

# **THEORY OF PLANETARY ATMOSPHERES**

**An Introduction to Their Physics  
and Chemistry**

*Second Edition*

*Joseph W. Chamberlain*

Department of Space Physics and Astronomy  
Wiess School of Natural Sciences  
Rice University  
Houston, Texas

*In collaboration with*

*Donald M. Hunten*

Department of Planetary Sciences  
Lunar and Planetary Laboratory  
University of Arizona  
Tucson, Arizona



ACADEMIC PRESS, INC.  
Harcourt Brace Jovanovich, Publishers  
San Diego New York Berkeley Boston  
London Sydney Tokyo Toronto

COPYRIGHT © 1987 BY ACADEMIC PRESS, INC.  
ALL RIGHTS RESERVED.  
NO PART OF THIS PUBLICATION MAY BE REPRODUCED OR  
TRANSMITTED IN ANY FORM OR BY ANY MEANS. ELECTRONIC  
OR MECHANICAL, INCLUDING PHOTOCOPY, RECORDING, OR  
ANY INFORMATION STORAGE AND RETRIEVAL SYSTEM, WITHOUT  
PERMISSION IN WRITING FROM THE PUBLISHER.

ACADEMIC PRESS, INC.  
1250 Sixth Avenue, San Diego, California 92101

*United Kingdom Edition published by*  
ACADEMIC PRESS INC. (LONDON) LTD.  
24-28 Oval Road, London NW1 7DX

**Library of Congress Cataloging in Publication Data**

Chamberlain, Joseph W. (Joseph Wyman), Date  
Theory of planetary atmospheres.

(International geophysics series ; v. )  
Includes bibliographies and index.  
1. Planets—Atmospheres. I. Hunten, Donald M.  
II. Title. III. Series.  
QB603.A85C48 1986 551.5'0999'2 86-10850  
ISBN 0-12-167251-4 (alk. paper)  
ISBN 0-12-167252-2 (paper ed.)

PRINTED IN THE UNITED STATES OF AMERICA

88 89 90 91 92

10 9 8 7 6 5 4 3 2

To  
O<sub>3</sub>, N<sub>2</sub>O, CO<sub>2</sub>, and <sup>14</sup>C;  
NO<sub>x</sub>, HO<sub>x</sub>, and ClO<sub>x</sub>;  
CCl<sub>4</sub>, CF<sub>2</sub>Cl<sub>2</sub>, and CFCl<sub>3</sub>;  
<sup>235</sup>U, Pu, D, and T;  
and many others  
of our effluent society  
without whom this book  
would not have been written.

## **PREFACE TO THE SECOND EDITION**

In the 8 years since the appearance of the first edition, there has been a virtual explosion in the literature of our subject. The Division for Planetary Sciences of the American Astronomical Society, only 15 years after splintering from the mother organization, is experiencing growing pains, with attendance so large that shortened papers and simultaneous sessions are necessary. This growth is due, of course, to the highly successful planetary explorations programs, principally the U. S. Pioneer and the Soviet Venera spacecraft sent to Venus and the Voyager missions to the Jovian planets, as well as the Viking missions to Mars (see Appendix IV).

This revision was therefore inevitably a major undertaking, comparable in scope to the preparation of the first edition, and even broader in its expanse of physics. At the outset the senior author recognized that he needed help and appealed to one of his oldest friends. Hence emerged the joint authorship of this edition.

The preparation of new material has been about equally divided, but we have each read the other's additions carefully and jointly take responsibility for any errors. We wish to thank Marilyn Chamberlain for assistance in organizing the indexes.

## PREFACE TO THE FIRST EDITION

As atmospheric physics has grown and become complicated, it has (like all subjects) encouraged its practitioners to specialize. No one understands the entire atmosphere very well; the last generalist was probably Aristotle. Yet the applied problems we face today often require that the research worker cross over imaginary disciplinary lines.

Our subject is, of course, nothing more than applied physics and chemistry. But in addition to those basic sciences the student of planetary atmospheres needs an overview of atmospheric structure and physical processes as presently understood. This book is intended to help fill that need for both graduate students and research scientists. Although the approach is mainly theoretical, very little basic physics is developed here. Material that is standard fare in third- and fourth-year physics courses is simply absorbed where needed.

The subject is developed as simply as I know how, without reducing it to a purely descriptive level. I frequently make radical assumptions that simplify the mathematics in order to illustrate a point, but I have attempted to alert the reader to the complexities that would have to be coped with at the research level.

The bibliographical notes for each chapter list some of the historically important papers, a selection of books and review articles, and a few other papers containing analyses or data discussed in the text. These selections are matters of personal judgment, but the interested student should be able to start his own literature survey for a selected topic with the material provided. For those readers who desire a more descriptive introduction to the subject to supplement their physical and chemical study, a number of excellent works are listed in Appendix V.

Several of my colleagues have read chapters of the text in draft and made constructive suggestions. I am especially indebted to Donald E. Anderson, Ralph J. Cicerone, Von R. Eshleman, Donald M. Hunten, Andrew A. Lacis, and Darrell R. Strobel for very critical and helpful readings. The text and the drawings have been prepared by Christine Dunning; I am most grateful to her for the high quality of her work and for a constant good humor, both of which lightened my burdens enormously.

# ***Chapter 1***

## **VERTICAL STRUCTURE OF AN ATMOSPHERE**

The simplest conceivable atmosphere is gravitationally bound (and therefore in hydrostatic equilibrium) and spherically symmetric. For the terrestrial planets, at least, solar radiation and the radiative properties of the atmospheric constituents fix the first-order description of the vertical thermal structure. An atmosphere controlled by sunlight can scarcely be spherically symmetric. Nevertheless, it is useful to think of a mean planetary atmosphere, with day-night and latitudinal variations occurring about the mean.

The *vertical structure* of an atmosphere is the run of pressure, temperature, density, and chemical composition with distance from the center of the planet (or with height above the surface). When these parameters are inferred in part from theory or when they are tabulated as mean or representative values, they constitute a *model atmosphere*.

Figure 1.1 shows the temperature profile for Earth's atmosphere; it serves to divide the atmosphere into different regions, where the controlling physics and chemistry differ.

The tropospheric temperature is governed by radiative and convective exchange. In the stratosphere trace amounts of  $O_3$  are formed by sunlight; the remarkable ability of  $O_3$  to absorb both ultraviolet and infrared radiation causes an inversion above the tropopause. The decrease in  $O_3$  production and the increased rate of cooling to space by  $CO_2$  reestablish a declining

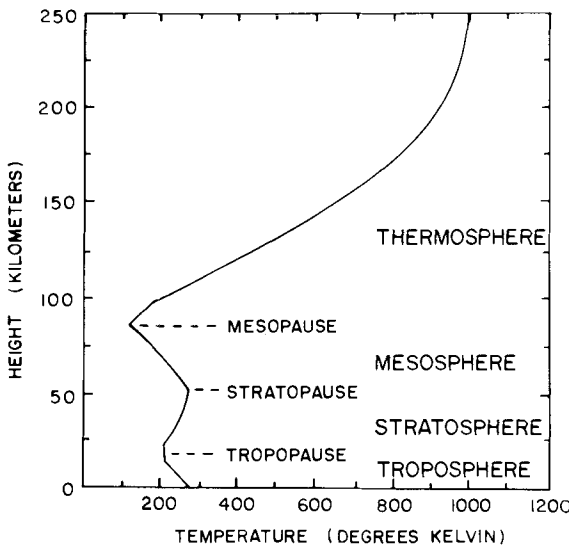


**Fig. 1.1** Schematic temperature profile for Earth's atmosphere showing the various regimes defined by the temperature gradient.

temperature in the mesosphere. Finally, heating by  $O_2$  photolysis and ionization increases the thermosphere temperatures to about  $1000^{\circ}\text{K}$ . We shall examine the main processes in these regions in turn.

## 1.1 Hydrostatic Equilibrium

The vertical distribution of pressure, temperature, and density in a static, spherical atmosphere with a specified composition are governed by three relationships. First we have hydrostatic equilibrium, in which the pressure gradient is

$$\frac{dp}{dr} = -\left(\frac{GM}{r^2}\right)(MN) = -g(r)\rho \quad (1.1.1)$$

Here  $\mathcal{M}$  is the mass of the planet and  $M$  is the mean mass of the molecules of a mixed atmosphere,  $N$  is their number density,  $\rho$  is the mass density, and  $r$  is the distance from the center of the (spherical) planet. Over height intervals  $\Delta r$  such that  $\Delta r \ll r$ , the local acceleration of gravity  $g(r) \approx \text{const.}$

For an equation of state, the perfect gas law is adequate:

$$p = NkT = \rho RT \quad (1.1.2)$$

where  $R = k/M$  (erg/gm deg) is the gas constant appropriate to the atmospheric composition. Then hydrostatic equilibrium gives

$$\frac{dp}{p} = -\frac{G\mathcal{M}M}{kT} \frac{dr}{r^2} \approx -\frac{gM}{kT} dz \equiv -\frac{dz}{H} \quad (1.1.3)$$

where  $z$  is height above the surface and  $H$  the (pressure) *scale height*.

A third relation must fix the temperature (cf. Section 1.2). If the mean mass and temperature are constant with height, we obtain the *barometric law*:

$$\begin{aligned} p(r) &= p(r_0) \exp\left(-\frac{G\mathcal{M}M}{kTr_0}(r - r_0)\right) \\ &\approx p(r_0) \exp\left(-\frac{r - r_0}{H}\right) \\ p(z) &= p(z_0) \exp\left(-\frac{z - z_0}{H}\right) \end{aligned} \quad (1.1.4)$$

Thus the *pressure scale height* ( $H = kT/Mg$ ) is an *e*-folding distance. In the general case the density distribution is

$$\begin{aligned} \frac{dN}{N} &= -\frac{dT}{T} - \frac{G\mathcal{M}M}{kT} \frac{dr}{r^2} \approx -\frac{dT}{T} - \frac{dz}{H} \\ &= -\left(\frac{1}{T} \frac{dT}{dz} + \frac{Mg}{kT}\right) dz = -\frac{dz}{H^*} \end{aligned} \quad (1.1.5)$$

which defines the *density scale height*  $H^*$ . The *integrated density* is the number of particles in a column above a specified height. It is, from (1.1.1),

$$\begin{aligned} \mathcal{N}(r) &\equiv \int_r^\infty N(r) dr = \int_0^{p(r)} \frac{r^2}{G\mathcal{M}M} dp \\ &\approx \frac{p(r)}{g(r)M} = N(r)H \end{aligned} \quad (1.1.6)$$

The integrated density is often written in terms of the height of a column under standard temperature and pressure conditions that would contain the same number of molecules or atoms. This is the equivalent thickness in “atmo-centimeters” (alternatively, “centimeter-atmospheres” or “centimeter-amagat”),

$$\xi = \frac{\mathcal{N}(z)}{N_0} \text{ atm-cm} \quad (1.1.7)$$

where  $N_0$  is Loschmidt’s number ( $2.687 \times 10^{19} \text{ cm}^{-3}$ ).

Without perfect mixing the mean mass  $M$  is a function of height,  $M(z)$ . At high altitudes the mixing processes are likely to be less important since the diffusion coefficient (Section 2.3.1) is large. Hence the atmosphere tends to separate out diffusively, and the composition changes as well through photochemical reactions. The gravity  $g$  is also a function of height [see (1.1.3)]. This effect is discussed in Section 7.1; the generalized barometric equation is (7.1.19).

## 1.2 Radiative Equilibrium

As a starting point we will regard the atmospheric temperature as governed by radiative equilibrium. Of course, it is not, but we will add convection later. In the ionosphere conduction becomes the dominant mechanism for heat transfer, and radiative equilibrium is not even a good starting approximation.

### 1.2.1 Equation of Radiative Transfer and Kirchhoff's Law

In a homogeneous medium (see Fig. 1.2) the monochromatic radiant intensity  $I_\nu$  (measured in  $\text{erg}/\text{cm}^2 \text{ sec sr Hz}$ ) changes along distance  $ds$  (mea-

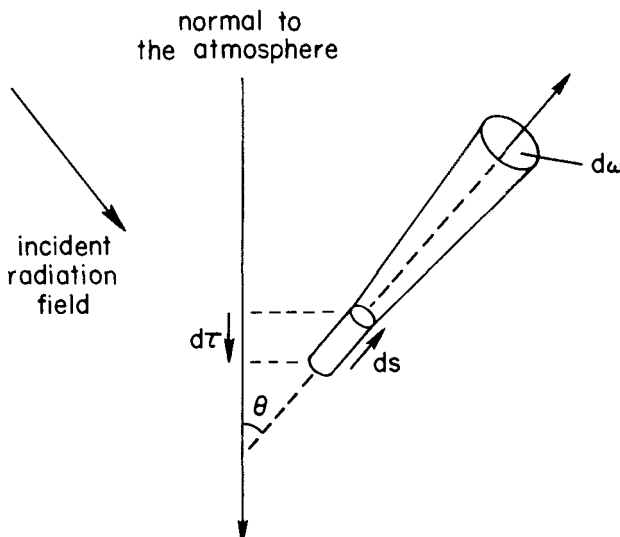


**Fig. 1.2** Geometry for the equation of radiative transfer. The element  $ds$  is always positive and taken in the direction of propagation of a light ray.

sured in the direction of propagation of the light ray and always positive) by amount  $dI_v$  given by

$$\frac{1}{\rho} \frac{dI_v}{ds} = -(\kappa_v + \sigma_v)I_v + j_v \quad (1.2.1)$$

where  $\kappa_v$  is the mass absorption coefficient and  $\sigma_v$  the mass scattering coefficient (both measured in  $\text{cm}^2/\text{gm}$ ), and  $j_v$  is the emission coefficient ( $\text{erg}/\text{gm sec sr Hz}$ ). The emission  $j_v$  may be due in part to scattering and in part to thermal excitation. The combination  $\kappa_v + \sigma_v$  is the *extinction coefficient*.

Let us look at a few special cases. If emission and scattering back into the original beam are negligible, as in viewing a single star against a black sky, we have  $j_v = 0$  and

$$I_v(s) = I_v(0)e^{-(\kappa_v + \sigma_v)\rho s} \quad (1.2.2)$$

which is *Lambert's exponential absorption law*.

If the source of emission includes scattering (as in the blue, sunlit sky), we have to specify a *scattering phase function*,  $p(\cos \Theta)$ , giving the angular distribution of scattered radiation. Thus, if  $j_v$  is entirely due to scattering, the emission term is

$$j_v = \frac{\kappa_v + \sigma_v}{4\pi} \int I_v(\cos \Theta)p(\cos \Theta)d\Omega' \quad (1.2.3)$$

where the phase function itself is normalized so that integrated over a sphere it is

$$\frac{1}{4\pi} \int p(\cos \Theta)d\Omega' = \frac{\sigma_v}{\kappa_v + \sigma_v} \equiv \tilde{\omega}_v \quad (1.2.4)$$

which is called the *albedo for single scattering*.

For the scattering atmosphere, then, the equation of transfer is, for radiation in direction  $\theta, \phi$ ,

$$\frac{dI_v(\theta, \phi)}{(\kappa_v + \sigma_v)\rho ds} = -I_v(\theta, \phi) + \frac{1}{4\pi} \int_0^{2\pi} \int_0^\pi I_v(\theta', \phi')p(\theta, \phi; \theta', \phi') \sin \theta' d\theta' d\phi' \quad (1.2.5)$$

At the other extreme from a scattering atmosphere is one in *local thermodynamic equilibrium* (LTE). It is assumed that at each point a local temperature  $T$  can be defined so that the emission is given by Kirchhoff's law,

$$j_v = \kappa_v B_v(T) \quad (1.2.6)$$

where the Planck function is

$$B_v(T) = \frac{2hv^3}{c^2} \frac{1}{e^{hv/kT} - 1} \quad (1.2.7)$$

We then have, since  $\sigma_v$  is assumed zero, the monochromatic radiation in LTE given by

$$\frac{dI_v(\theta, \phi)}{\kappa_v \rho ds} = -I_v(\theta, \phi) + B_v(T) \quad (1.2.8)$$

The LTE approximation can never be exact, and one problem is ascertaining how inexact it is. In complete thermodynamic equilibrium, the temperature is everywhere the same; in the atmosphere the temperature has a definite gradient. Also, atmospheric emission is not Planckian at any point; the radiation field in the ultraviolet and infrared are not characteristic of the same  $T$ . Finally, the local kinetic temperature (given by the Maxwellian distribution law) is not the same as the effective Planckian temperature (defined by the radiation field). In a real situation we must usually treat scattering and thermal emission together. For combined isotropic scattering and thermal emission the transfer equation is

$$\frac{dI_v}{(\kappa_v + \sigma_v)\rho ds} = -I_v + \frac{\tilde{\omega}_v}{4\pi} \int_0^{2\pi} \int_{-\pi/2}^{\pi/2} I_v(\theta', \phi') \sin \theta' d\theta' d\phi' + (1 - \tilde{\omega}_v)B_v \quad (1.2.9)$$

In the general case we define the source function (in the same units as  $I_v$ ) as the ratio of emission coefficient to opacity

$$\mathcal{J}_v = \frac{j_v}{\kappa_v + \sigma_v} \quad (1.2.10)$$

Then the general equation of transfer is

$$\frac{dI_v}{(\kappa_v + \sigma_v)\rho ds} = -I_v + \mathcal{J}_v \quad (1.2.11)$$

For isotropic scattering,

$$\mathcal{J}_v = \frac{\tilde{\omega}_v}{4\pi} \int I_v d\Omega \equiv \tilde{\omega}_v J_v \quad (1.2.12)$$

where  $J_v$  is the local mean intensity. For LTE,

$$\mathcal{J}_v = B_v(T) \quad (1.2.13)$$

and the combined case has

$$\mathcal{J}_v = \tilde{\omega}_v J_v + (1 - \tilde{\omega}_v) B_v \quad (1.2.14)$$

Defining a *slant optical thickness* from  $s$  to  $s'$  as

$$\tau_v(s, s') = \int_s^{s'} (\kappa_v + \sigma_v) \rho \, ds \quad (1.2.15)$$

we can write down the formal solution to Eq. (1.2.11) as

$$I_v(s) = I_v(0) e^{-\tau_v(s, 0)} + \int_0^s \mathcal{J}_v(s') e^{-\tau_v(s, s')} (\kappa_v + \sigma_v) \rho \, ds' \quad (1.2.16)$$

If the source function is known, we have the solution for the radiation field. In practice, the solution is not so simple because  $\mathcal{J}_v(s')$  depends on  $I_v(s')$  directly or on  $B_v(T)$  (which in turn depends on the heating from the radiation field) or both.

### 1.2.2 Monochromatic Radiative Equilibrium

In a plane-stratified atmosphere in which height  $z$  is measured upward, we measure optical depth  $\tau$  downward and zenith angle of the direction of radiation flow  $\theta$  from the upward vertical. Then  $ds = \sec \theta \, dz$  is always positive and the vertical optical thickness is

$$d\tau_v = -(\kappa_v + \sigma_v) \rho \, dz \quad (1.2.17)$$

Equation (1.2.8) for LTE conditions is then

$$\mu \frac{dI_v(\theta, \phi)}{d\tau_v} = I_v(\theta, \phi) - B_v(T) \quad (1.2.18)$$

where  $\mu = \cos \theta$ . Integrating over a sphere we have

$$\frac{d}{d\tau_v} (\pi F_v) = 4\pi (J_v - B_v) \quad (1.2.19)$$

where the mean intensity  $J_v$  is given by (1.2.12) and the net flux across an area parallel to the surface is

$$\pi F_v = 2\pi \int_{-1}^1 I_v(\mu) \mu \, d\mu \quad (1.2.20)$$

We may obtain an approximate solution by the *two-stream approximation* (see Fig. 1.3). Suppose that the upward radiant intensity is  $I_v(\mu, \tau) = I^+(\tau)$

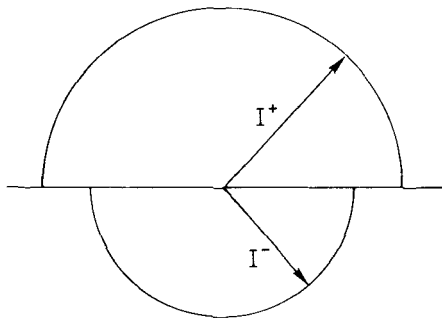


**Fig. 1.3** The two-stream approximation considers the radiation field to be composed of two simple streams, one upward and one downward.

for  $0 < \mu < +1$  and the downward radiation field is  $I_v(\mu, \tau) = I^-(\tau)$  ( $-1 < \mu < 0$ ). Then the mean intensity at depth  $\tau$  is

$$J_v \equiv \frac{1}{2} \int_{-1}^1 I_v(\mu) d\mu = \frac{1}{2}(I^+ + I^-) \quad (1.2.21)$$

and the net flux is

$$\pi F_v = \pi(I^+ - I^-) \quad (1.2.22)$$

To obtain a second relation between mean intensity and flux, we multiply (1.2.18) by  $\mu$  and integrate over a sphere. With (1.2.20) and (1.2.21) we have

$$2\pi \frac{d}{d\tau_v} \int_0^1 d\mu \mu^2 (I^+ + I^-) = 2\pi \int_0^1 d\mu \mu (I^+ - I^-) \quad (1.2.23)$$

or

$$\frac{4\pi}{3} \frac{dJ_v}{d\tau_v} = \pi F_v \quad (1.2.24)$$

Substituting (1.2.19) for  $J_v$  in this equation yields the flux equation

$$\frac{d^2 F_v}{d\tau_v^2} - 3F_v = -4 \frac{dB_v}{d\tau_v} \quad (1.2.25)$$

The concept of radiative equilibrium means that the net flux divergence is everywhere zero, with no energy lost or supplied by convection or conduction. It does not mean that the flux  $\pi F_v$  in each separate frequency everywhere is constant. Nevertheless, it is instructive to examine this case of *monochromatic radiative equilibrium* (MRE). With  $dF_v/d\tau_v = 0$  everywhere, our equation for the thermal radiation versus  $\tau_v$  is

$$\frac{dB_v}{d\tau_v} = \frac{3}{4} F_v = \text{const} \quad (1.2.26)$$

In applying boundary conditions we have to be careful that they do not conflict with assumptions already introduced in the two-stream approximation. Let us suppose that the ground is a black body at temperature  $T_g$  and a cold black sky ( $T = 0$ ) lies above the atmosphere. With Eqs. (1.2.21) and (1.2.22) we can write

$$J_v = I^- + \frac{1}{2}F_v = I^+ - \frac{1}{2}F_v \quad (1.2.27)$$

Then the transfer equation (1.2.19) gives

$$\begin{aligned} \frac{dF_v}{d\tau_v} &= 4(I^+ - B_v) - 2F_v \\ &= 4(I^- - B_v) + 2F_v = 0 \end{aligned} \quad (1.2.28)$$

Hence the upward intensity at the ground is

$$I_g^+ \equiv B_v(T_g) = B_v(T_1) + \frac{1}{2}F_v \quad (1.2.29)$$

where  $T_1$  is the air temperature at the ground, and the downward intensity at the top of the atmosphere is

$$I_0^- \equiv 0 = B_v(T_0) - \frac{1}{2}F_v \quad (1.2.30)$$

where  $T_0$  is the air temperature at  $\tau = 0$ .

The solution tells us that, to fit an LTE solution with the special case of MRE, there is a discontinuity in temperature at the ground, with  $T_g > T_1$ , and the air at the top approaches a value,  $T_0 \neq 0$ . The radiant flux leaving the atmosphere is

$$\pi I_0^+ = \pi B_v(T_0) + \frac{\pi}{2} F_v = 2\pi B_v(T_0) \quad (1.2.31)$$

or twice what an opaque black body at temperature  $T_0$  would emit.

The solution, then, from (1.2.26) and (1.2.30) is (see Fig. 1.4)

$$B_v(\tau_v) = B_v(T_0)(1 + \frac{3}{2}\tau_v) \quad (1.2.32)$$

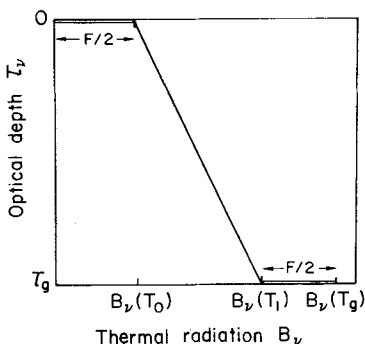


**Fig. 1.4** The MRE solution for  $T(\tau)$ , presented as  $B_v(T)$  vs.  $\tau_v$ . Note the discontinuity at the ground and the finite skin temperature at  $\tau = 0$ .

The atmospheric radiation  $\pi I_0^+$  is thus characteristic of the thermal emission at  $\tau_v = \frac{2}{3}$ .

A common name for  $T_0$  is the *Gold-Humphreys skin temperature*, or simply *skin temperature*. It can be derived on the assumption that a volume element in the stratosphere is heated by absorption of planetary radiation over a hemisphere and cooled by its own radiation over a sphere. By Kirchhoff's law, the absorption and emission are proportional as long as the same wavelength bands are involved, which is approximately true. Since the solid angles are in a ratio 1:2, the mean planetary temperature and the skin temperature are in the ratio  $1:2^{-1/4}$  [cf. (1.2.45)]. The principal reason for deviations from this result is additional heating by solar radiation; a prominent example is ozone heating on the Earth.

### 1.2.3 Local Thermodynamic Equilibrium for a Gray Atmosphere Heated from the Ground

We are now ready to examine how the interchange of radiation governs the temperature of an atmosphere when there is no direct solar absorption by the atmosphere, when there is no conduction or convection, and when scattering can be neglected. The transfer equation (1.2.8) for LTE is

$$\frac{\mu dI_v}{\kappa_v \rho dz} = -I_v + B_v \quad (1.2.33)$$

Integrating over frequency we have

$$\frac{\mu}{\rho} \frac{d}{dz} \left( \int_0^\infty \frac{I_v}{\kappa_v} dv \right) = -I + B \quad (1.2.34)$$

where

$$I = \int_0^\infty I_v dv, \quad B = \int_0^\infty B_v dv \quad (1.2.35)$$

By integrating over a sphere and setting the net flux constant, we have, analogously to Eq. (1.2.26),

$$-\frac{1}{\rho} \frac{d}{dz} \left( \int_0^\infty \frac{B_v}{\kappa_v} dv \right) = \frac{3}{4} F \quad (1.2.36)$$

where  $F = \int F_v dv$ . In the event  $\kappa_v = \text{const} (= \kappa)$  the transfer equation (1.2.33) is

$$\mu \frac{dI}{d\tau} = I - B \quad (1.2.37)$$

and the thermal radiation is given by

$$\frac{dB}{d\tau} = \frac{3}{4}F \quad (1.2.38)$$

where

$$d\tau = -\kappa\rho dz \quad (1.2.39)$$

Hence the gray solution is analogous to that for MRE given above.

It would seem that, with a mean absorption coefficient properly defined, any nongray atmosphere could be treated with the gray solution. Thus writing

$$d\tau = -\langle\kappa\rangle\rho dz \quad (1.2.40)$$

a comparison of (1.2.36) and (1.2.38) suggests

$$\frac{1}{\langle\kappa\rangle} = \frac{1}{B} \int_0^\infty \frac{B_v}{\kappa_v} dv \quad (1.2.41)$$

where  $B$  is given by (1.2.35). This  $\langle\kappa\rangle$  is the *Rosseland mean* used widely in astrophysics. The problem with it lies in the Eddington approximation. To conserve flux, the MRE equation (1.2.19) requires  $J_v = B_v$  precisely. But in LTE there is a gradual shift with depth in the frequency distribution of the radiation, since temperature varies with depth, and  $J_v$  cannot precisely equal  $B_v$  to conserve the flux in each frequency interval. But if there is approximate equality over the spectrum, the Rosseland mean is a good approximation. It works well for stellar atmospheres, but is not good for most terrestrial situations. Since  $T$  and  $B_v(T)$  vary with depth,  $\langle\kappa\rangle$  cannot be treated as constant with depth. Thus iterations are required to compute  $B_v(T)$  and  $\langle\kappa\rangle$  as functions of depth. An alternative and generally better procedure is to put  $\kappa_v$  on the right-hand side of (1.2.26) and integrate over  $v$ . Comparison with (1.2.38) gives

$$\langle\kappa\rangle = \frac{1}{F} \int_0^\infty \kappa_v F_v dv \quad (1.2.42)$$

which is the *Chandrasekhar mean* coefficient. Its difficulty is that  $F_v$  is not known in advance of solving the problem, requiring iterations, or other approximations.

We can now write the LTE gray-atmosphere solution and compare numerical results with temperatures in the Earth's atmosphere. Equation (1.2.38) gives a solution, similar to (1.2.32),

$$T^4(\tau) = T_0^4(1 + \frac{3}{2}\tau) \quad (1.2.43)$$

where  $T_0$  is the temperature of the upper boundary. Here the integrated black-body intensity is

$$B(\tau) = \frac{\sigma}{\pi} T^4(\tau) \quad (1.2.44)$$

The total radiant flux from the Earth can be expressed in terms of a *mean planetary emission temperature*, obtained by integrating Eq. (1.2.31) over frequency:

$$T_e^4 = 2T_0^4 \quad (1.2.45)$$

For a rotating planet of radius  $R$  at a uniform temperature over the sphere this temperature is related to the incident solar flux by

$$4\pi R^2 \sigma T_e^4 = (1 - \Lambda)\pi R^2(\pi \mathcal{F}_\odot) \quad (1.2.46)$$

where  $\Lambda$  is the effective planetary albedo and  $\pi \mathcal{F}_\odot$  is the incident solar flux. With  $\Lambda = 0.29$  for Earth, we find  $T_e = 255^\circ\text{K}$  and a boundary temperature  $T_0 = T_e/1.19 = 215^\circ\text{K}$ , which is close to the mid-latitude tropopause temperature. If we know the optical thickness of the atmosphere versus height, we can figure the temperature versus height—the lapse rate for radiative equilibrium. An example is given in Problem 1.3.

The discontinuity between the air and surface temperature can be expressed from (1.2.29) as

$$\begin{aligned} T_s^4 &= T^4(\tau_g) + \frac{1}{2}T_e^4 \\ &= T_0^4(2 + \frac{3}{2}\tau_g) \\ &= T_e^4(1 + \frac{3}{4}\tau_g) \end{aligned} \quad (1.2.47)$$

where  $\tau_g$  is the optical thickness at the ground. The deposition of sunlight striking the Earth is shown in Table 1.1.

Equations (1.2.43) and (1.2.47) illustrate how high temperatures can be attained near the ground if the infrared  $\tau$  is large and heating is from below.

TABLE 1.1 Approximate Percentage Deposition of Incident Solar Flux<sup>a</sup>

| Reflected to space | Absorbed by ground | Absorbed in troposphere | Absorbed above troposphere | Reradiated from ground to atmosphere |
|--------------------|--------------------|-------------------------|----------------------------|--------------------------------------|
| 40                 | 40                 | 18                      | 2                          | 25                                   |

<sup>a</sup> The solar constant outside the atmosphere is  $2 \text{ cal/min cm}^2 = 1.39 \times 10^6 \text{ erg/cm}^2 \text{ sec}$ ; the global average heat received is one fourth this amount.

Heating from this combination of a transparent atmosphere in the visible, where the sun's energy is a maximum, and of high opacity in the infrared, where the Earth's Planckian curve peaks, is known as the *greenhouse effect*. It has long been thought that the trapping of infrared by glass is not the important thing in warming greenhouses. Rather, it is said, the glass roof merely keeps the warm air from convecting away. Purists have fought a steadily losing battle to replace "greenhouse effect" with a less picturesque term. We prefer to think of atmospheres as warming by the greenhouse effect, even if greenhouses do not.

If there is no internal heat source, the emission temperature  $T_e$ , computed from (1.2.46), will be equivalent to the measured *bolometric temperature*  $T_b$ , which is obtained by measuring the mean planetary flux from thermal emission over all frequencies and setting it equal to  $\sigma T_b^4$ . In the case of Jupiter and possibly other major planets,  $T_b > T_e$ , indicating internal generation of heat (cf. Section 1.8.3).

If an atmosphere's thermal emission is measured only in a narrow frequency interval, its intensity gives a *brightness temperature*  $T_B$ , defined by  $I_\nu = B_\nu(T_B)$ . If the atmosphere were gray,  $I_\nu$  would be Planckian and  $T_B$  would be the same at all frequencies and the same as  $T_b$ . The brightness temperature of Venus in the microwave spectrum gave the first indication of its 750°K surface (cf. Section 1.8.1).

### 1.3 Convection in the Troposphere

As we have seen, a gray atmosphere in radiative equilibrium approaches a finite "skin temperature" at high altitude. This isothermal region is stable against convective circulation. At large  $\tau$ , however, the radiative gradient  $dT/dz$  becomes steep (i.e., negatively large). Hence, an optically thick, gray atmosphere can be convectively unstable at low altitudes; the temperature distribution that radiative exchange tends to establish is then too steep to be hydrostatically supported.

If an element of gas moves adiabatically, the first law of thermodynamics requires that

$$C_v dT = -p dV \quad (1.3.1)$$

where  $C_v$  is the specific heat at constant volume (erg/gm°K). If  $V$  is the *specific volume* containing a gram of molecules, then the perfect gas law gives

$$dV = \frac{N_0 k}{p} dT - \frac{N_0 k T}{p^2} dp \quad (1.3.2)$$

where  $N_0 = 1/M$  and  $M$  is the molecular mass. Since  $C_p = C_v + N_0k$  (erg/gm°K), we have the alternate thermodynamic relation

$$C_p dT = \frac{N_0 k T}{p} dp = V dp = \frac{1}{\rho} dp \quad (1.3.3)$$

With hydrostatic equilibrium, (1.1.1), the first law thus gives the *dry adiabatic temperature gradient*,

$$\frac{dT}{dz} = -\frac{g}{C_p} = -\frac{\gamma - 1}{\gamma} \frac{gM}{k} \quad (1.3.4)$$

where  $\gamma = C_p/C_v$ . For the Earth's troposphere this lapse rate (the negative of the temperature gradient) is 9.8°K/km.

For saturated air the first law includes the latent heat released by water condensing:

$$C_v dT = -p dV - L dw_s, \quad C_p dT = \frac{1}{\rho} dp - L dw_s \quad (1.3.5)$$

where  $w_s$  is the mass of saturated water per mass of air and  $L$  is the latent heat of vaporization. The *saturation adiabatic lapse rate* is then

$$-\frac{dT}{dz} = \frac{g/C_p}{1 + (L/C_p)(dw_s/dT)} \quad (1.3.6)$$

The wet lapse rate may be about half the dry rate or around 5°K/km. Since convection is partly moist and partly dry, the troposphere has an average value of 6.5°K/km. This value characterizes the static stability of the Earth's large-scale weather systems (see Section 2.2.4).

The temperature distribution in radiative-convective equilibrium is thus simply the adiabatic curve at low altitudes, merging into the purely radiative one at higher levels (see Fig. 1.5). Of an infinite number of parallel adiabatic atmospheres we must select the one that emits the same upward radiant flux as the radiative atmosphere itself. For example, curve 1 in Fig. 1.5 is tangent to the radiative curve and would not require a temperature discontinuity. But the adiabatic curve is everywhere below the radiative one and it clearly cannot supply the radiant flux required above point A to support the temperature there in radiative equilibrium.

A self-consistent solution is an adiabatic curve displaced to the right by an amount such that the flux boundary condition is satisfied. The temperature discontinuity at the ground must also be removed, since it is unstable convectively. The flux given by the various adiabatic distributions is readily computed from the formal solution to the transfer equation (1.2.16).

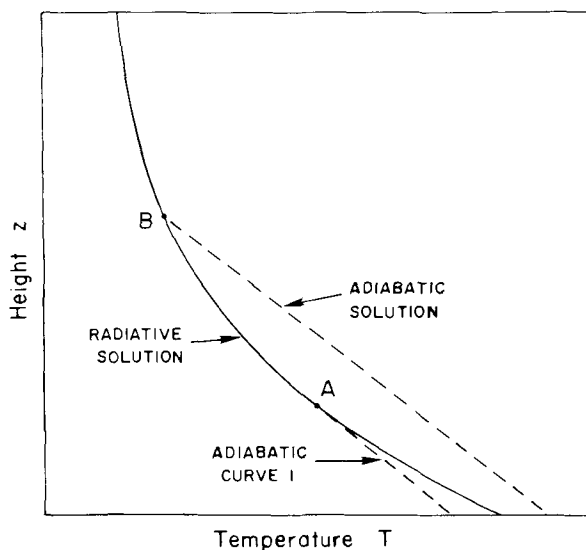


**Fig. 1.5** When convection is present the adiabatic portion of the curve not only extends to a point where the radiative solution is convectively stable; it must also supply the thermal radiation to sustain the profile above "B." Point *B* is called the *radiative-convective boundary*. The tropopause, defined as the base of the first isothermal region, is just above the top of the figure.

#### 1.4 Latitudinal Variations of the Tropopause and Departures from Grayness

The radiative-convective model with a gray atmosphere reproduces the main features of the troposphere temperature distribution, with the radiative "skin temperature" being identified with the near-isothermal region of the tropopause. This happy state of affairs does not hold, however, when we examine some of the finer features. Figure 1.6 shows isotherms on meridional cross sections for the various seasons. The heavy line shows the location of the tropopause. It is apparent from (1.2.45) and (1.2.46) that in the gray atmosphere, heated from below and without dynamical interchange latitudinally, the tropopause would be warmer in the tropics than in the Arctic simply because the ground temperature is higher. In fact, the tropic tropopause is around 15 km with  $T \approx 195^{\circ}\text{K}$ , whereas over the polar cap it is as low as 8 to 10 km and  $T \approx 225^{\circ}\text{K}$ .

Why should the tropopause be lower and warmer in the Arctic? There are several contributing factors. Quite likely the most important is the fact that the atmosphere is not only nongray but the distribution of the infrared active gases ( $\text{CO}_2$ ,  $\text{H}_2\text{O}$ , and  $\text{O}_3$ ) varies with latitude.

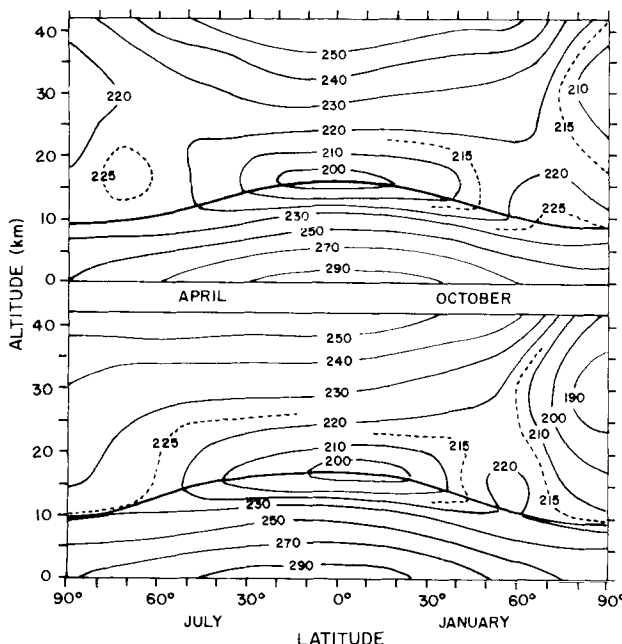


**Fig. 1.6** Distribution of the observed temperature ( $^{\circ}\text{K}$ ) in the northern hemisphere for different seasons. [Based on data assembled by J. LONDON; see MANABE and STRICKLER (1964).]

The departure from grayness itself diminishes the coupling between the ground and skin temperatures. With windows in the absorption spectrum, the ground can cool by radiating directly to space or to the stratosphere. The higher water vapor in the tropics inhibits this direct cooling of the ground but, more important, it increases the cooling of the upper troposphere. This dependence of absolute humidity on air temperature is probably the most important item governing tropopause height.

Another factor is the latitudinal dependence of stratospheric ozone. In a static atmosphere, ozone would be most abundant where it is most readily created—at lower latitudes. In fact (as we shall discuss in Section 3.3.2), it is more abundant at higher latitudes. The  $9.6 \mu\text{m}$  band of  $\text{O}_3$  is largely responsible for heating the lower stratosphere by absorbing surface infrared radiation in an otherwise clear window. In addition, we have so far neglected direct heating by the sun, but the existence of the stratosphere is primarily due to direct solar photolysis and heating. With ozone more abundant in the Arctic and distributed more toward low altitudes than in the tropics, it has a different effect on the temperature profile. The tropic tropopause is sharply defined, with an abrupt temperature inversion and rapid rise in the lower stratosphere. In the polar regions the lower stratosphere is nearly

isothermal, and these differences are probably due to the different ozone distributions.

Nevertheless, detailed model calculations have not given as satisfactory agreement as one would desire, suggesting other effects are contributing. The meridional circulation of the stratosphere is known to be important (see Section 3.3.2) and it probably has an influence on the tropopause height and temperature of the lower stratosphere. Also, convection is driven more strongly in the tropics, both because solar radiation is more abundant, and because of the cooling of the upper troposphere by the increased water vapor.

The interplay of all these effects requires elaborate computational models in which one feature is varied at a time to see what its effect is. Often the effects involve such complex feedbacks that the physics at work becomes obscure.

## 1.5 The Stratosphere: Absorption of Direct Solar Radiation

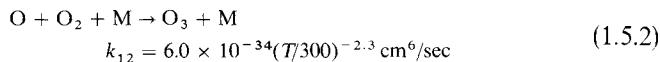
For an elementary examination of the stratospheric heating, we will oversimplify the problem while retaining enough of the relevant physics to see what is happening. In Chapter 3 the ozone-related chemistry is examined more thoroughly. (Also, the basic principles of photochemistry are reviewed in Section 3.1.) For now let us suppose that the only reactions of importance involve only oxygen: the so-called “Chapman reactions.”

### 1.5.1 Elementary Oxygen Chemistry

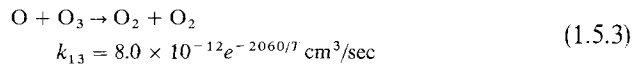
Molecular oxygen in the stratosphere is photodissociated by absorption in the Herzberg continuum:



Atomic oxygen then attaches to  $\text{O}_2$  in the presence of an unspecified third body M to form ozone,



where  $k_{12}$  is the three-body rate coefficient (see Section 3.1). Both kinds of “odd oxygen” (i.e., O and  $\text{O}_3$ ) are destroyed by



and  $\text{O}_3$  is converted back to O by



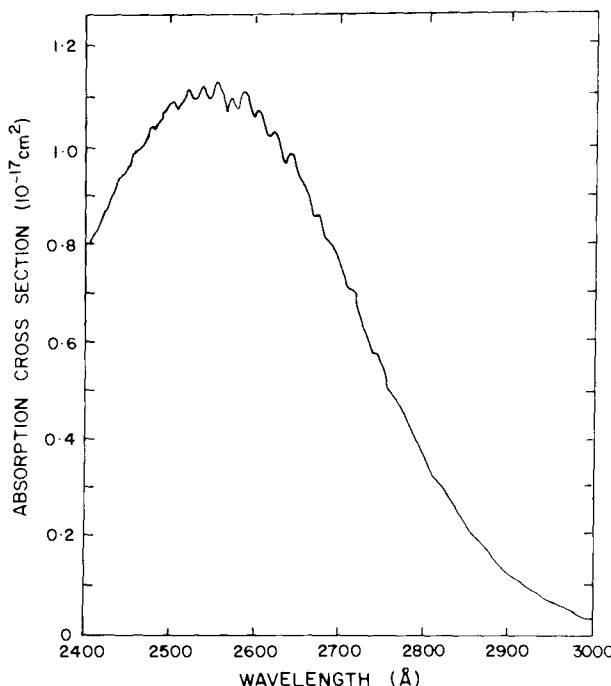


**Fig. 1.7** Absorption cross sections of the Hartley bands and continuum. [Measurements by E. C. Y. INN and TANAKA (1953), *J. Opt. Soc. Amer.* **43**, 870.]

The principal source of heating is this  $O_3$  dissociation, which occurs in the strong Hartley continuum, shown in Fig. 1.7. Over this region  $O_3$  is the only atmospheric substance strongly absorbing (Fig. 1.8).

Thus not only is this absorption responsible for heating the stratosphere, but the  $O_3$  there prevents sunlight in the 0.2–0.3  $\mu\text{m}$  region from reaching the ground. Since many forms of life (including the DNA molecule) cannot tolerate the ultraviolet, the 0.3 atm-cm or so in the stratosphere seems a very thin shield indeed. Only because  $O_3$  is a strong absorber in the Hartley region (cross section of  $10^{-18}$ – $10^{-17}$   $\text{cm}^2$ ) can so few molecules accomplish so much.

The  $O_2$  absorption (1.5.1), on the other hand, is intrinsically very weak. It is important to keep in mind that there are two photodissociation continua for  $O_2$  important in atmospheric physics (cf. Fig. 1.9). The stronger one, the *Schumann-Runge continuum*, lies at wavelengths shortward of 1750 Å (7.1 eV). It involves the electronic transition  $B^3\Sigma_u^- \leftarrow X^3\Sigma_g^-$  and hence is permitted as an electric-dipole transition. The measured cross section is in the range  $10^{-18}$ – $10^{-17}$   $\text{cm}^2$  and  $O_2$  dissociates into  $O(^3P) + O(^1D)$ , that is, one atom in the ground term and one in the metastable  $^1D$  term at 2 eV. This dis-

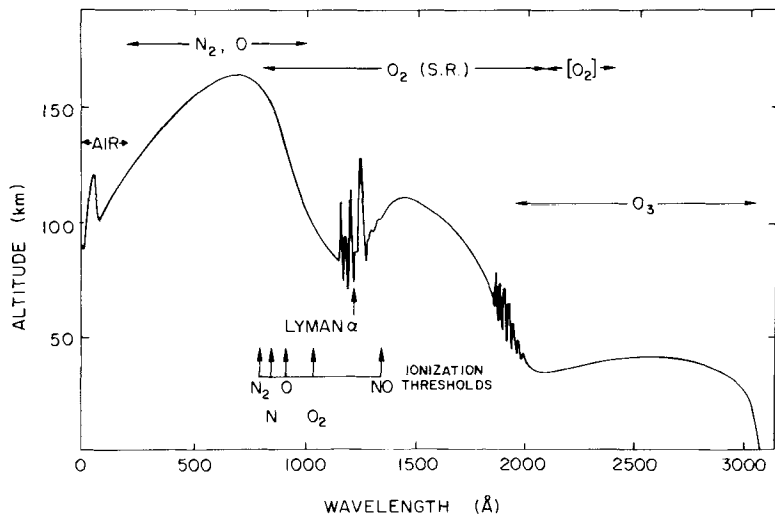


**Fig. 1.8** Altitude at which the intensity of solar radiation drops to  $1/e$  of its value outside Earth's atmosphere for vertical incidence. The Schumann-Runge and forbidden Herzberg  $O_2$  absorbing regions are denoted by S.R. and  $[O_2]$ , respectively. [Based on data assembled in 1961 by P. J. NAWROCKI, K. WATANABE, and L. G. SMITH; adapted from L. HERZBERG (1965), in "Physics of the Earth's Upper Atmosphere" (C. W. Hines *et al.*, eds.), p. 40. Prentice-Hall, Englewood Cliffs, New Jersey.]

sociation occurs in the 100 km region and sunlight at  $\lambda < 1750 \text{ \AA}$  is totally extinguished above the stratosphere.

The weaker absorption occurs at  $\lambda < 2420$  (5.1 eV). It involves the forbidden Herzberg continuum  $A^3\Sigma_u^+ \leftarrow X^3\Sigma_g^-$  whose cross section is  $10^{-24} - 10^{-23} \text{ cm}^2$ , and the dissociation products are both in the ground term  $O(^3P)$ .

When the source function (representing local scattering or emission) is negligible, the transfer equation (1.2.11) gives the absorption per unit volume as

$$\mu \frac{dI_v(z)}{dz} = -\kappa_v \rho I(z) \quad (1.5.5)$$

$$\mu \frac{dI_v(z)}{dz} = -\kappa_v \rho I_v(\infty) e^{-\tau_v/\mu} \quad (1.5.6)$$

We will pursue this equation further in discussing the formation of the ionosphere (Section 5.1.1), but for the moment we will simply note that, in a barometric atmosphere (1.4), the maximum absorption occurs at (see Problem 1.4).

$$\tau_v/\mu = \kappa_v \rho H/\mu = \alpha_v N(z) H/\mu = 1 \quad (1.5.7)$$

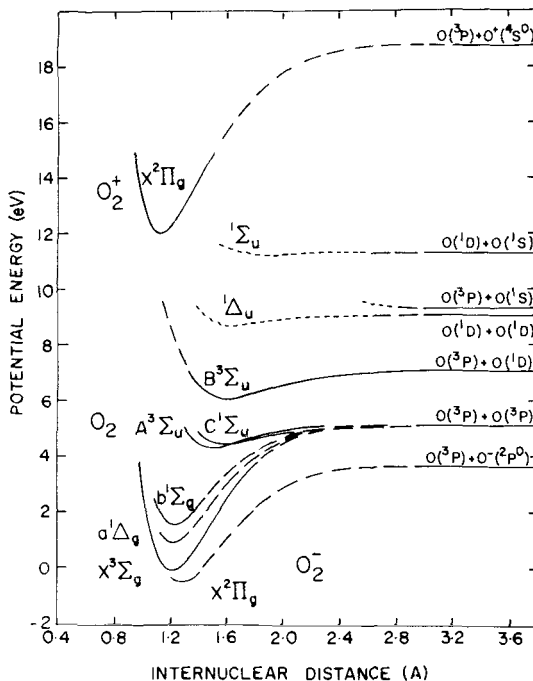


**Fig. 1.9** Simplified potential energy diagram for oxygen. Along the right side are listed the dissociation products; an energy level diagram of O appears as Fig. 6.3.

where  $\alpha_v$  ( $\text{cm}^2$ ) is the molecular cross section. Hence the Schumann–Runge dissociation peaks near 100 km; the Herzberg dissociation would peak in the 20–25 km region, except that O<sub>3</sub> absorption between 1800 and 2400 Å raises the  $\tau_v = 1$  level to about 40 km. The actual absorption coefficients are not gray and the destruction of O<sub>3</sub>, involving reactions (1.5.2), (1.5.3), and (1.5.4), places the maximum ozone abundance somewhat lower, around 25–30 km altitude.

We can make an approximate assessment of the ozone distribution with the above four equations in daytime photochemical equilibrium. First, O is created by dissociation (1.5.1) at a rate  $2J_2(z)$  ( $\text{sec}^{-1}$  per O<sub>2</sub> molecule), which depends on the photon flux ( $\text{cm}^{-2} \text{ sec}^{-1}$ ) of dissociating radiation at height  $z$  and the O<sub>2</sub> absorption cross section ( $\text{cm}^2$ ) in the Herzberg continuum. Similarly (1.5.4) proceeds at rate  $J_3$  ( $\text{sec}^{-1}$  per O<sub>3</sub> molecule). The destruction of O by the two-body reaction (1.5.3) is given by the rate coefficient  $k_{13}$  ( $\text{cm}^3/\text{sec}$ ), which is the mean of the O–O<sub>3</sub> association cross section times the velocity of collision. Cross sections for chemical reactions may have a strong velocity dependence, making the rate coefficients strongly tempera-

ture dependent. Finally, the three-body reaction (1.5.2) has a rate coefficient  $k_{12}$  (cm<sup>6</sup>/sec). Rate coefficients are discussed more thoroughly in Section 3.1.

Thus the net change in O abundance is

$$\frac{d[\text{O}]}{dt} = 2J_2(z)[\text{O}_2] + J_3(z)[\text{O}_3] - k_{13}[\text{O}][\text{O}_3] - k_{12}[\text{O}][\text{O}_2][\text{M}] \quad (1.5.8)$$

where brackets denote concentrations (molecule/cm<sup>3</sup>). Similarly, the  $\text{O}_3$  rate of change is

$$\frac{d[\text{O}_3]}{dt} = k_{12}[\text{O}][\text{O}_2][\text{M}] - k_{13}[\text{O}][\text{O}_3] - J_3[\text{O}_3] \quad (1.5.9)$$

In chemical equilibrium these two equations lead to

$$[\text{O}] = \frac{J_2[\text{O}_2]}{k_{13}[\text{O}_3]} \quad (1.5.10)$$

and

$$[\text{O}_3] = \frac{k_{12}[\text{O}][\text{O}_2][\text{M}]}{k_{13}[\text{O}] + J_3} \quad (1.5.11)$$

Below 60 km the term  $k_{13}[\text{O}] \ll J_3$  because of the low O abundance. Then we have

$$\frac{[\text{O}_3]_{\text{day}}}{[\text{O}_2]} \approx \left( \frac{k_{12}J_2[\text{M}]}{k_{13}J_3} \right)^{1/2} \quad (1.5.12)$$

and

$$[\text{O}]_{\text{day}} \approx \left( \frac{J_2J_3}{k_{12}k_{13}[\text{M}]} \right)^{1/2} \quad (1.5.13)$$

The daytime distribution of oxygen allotropes is shown in Fig. 1.10. At nighttime  $\text{O}_3$  grows at the expense of O through (1.5.2), which proceeds rapidly because  $\text{O}_2$  is large. Nevertheless, since  $[\text{O}] \ll [\text{O}_3]$  in the stratosphere, the resulting increase in  $\text{O}_3$  is relatively small. Were there a plentiful supply of O, the nighttime equilibrium of  $\text{O}_3$  would grow to

$$\frac{[\text{O}_3]_{\text{night}}}{[\text{O}_2]} \rightarrow \frac{k_{12}[\text{M}]}{k_{13}} \quad (1.5.14)$$

but in the stratosphere the O rapidly disappears at night and the  $\text{O}_3$  becomes essentially inert.

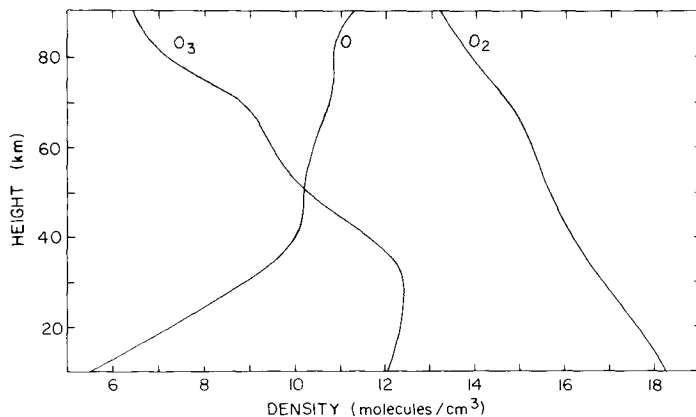


**Fig. 1.10** Daytime equilibrium of oxygen allotropes according to the Chapman theory. The abscissa is  $\log_{10} N$ . [Calculations by D. R. BATES (1954) in "The Earth as a Planet" (G. P. Kuiper, ed.), p. 581, Univ. Chicago Press, Chicago.]

### 1.5.2 Stratospheric Heating

A calculation of the stratospheric temperature profile is not a simple task even with simplified photochemistry, the absence of vertical mixing, and ignored meridional dynamics. While the solar heating is not too complicated (although the solar-energy input at each level must be averaged over the day for any latitude and time of year) the infrared net cooling (or heating) is less straightforward. For example, weak rotational lines in the  $15\ \mu\text{m}$  fundamental band of CO<sub>2</sub> and lines in isotopic bands and weak *hot bands* (which arise from an excited lower vibrational level) are important in radiating directly to space, whereas stronger transitions in CO<sub>2</sub>, H<sub>2</sub>O, and O<sub>3</sub> provide a complex interchange of radiation within the atmosphere. The problem can be handled only by intricate computer codes.

With it understood that these complexities are being greatly oversimplified, we can at least examine the fundamental physics of solar heating. The Herzberg O<sub>2</sub> continuum is screened by not only the overhead O<sub>2</sub> but by O<sub>3</sub>. Hence we have

$$J_2(z) = J_2^{(0)} \exp\left(-\frac{\tau_2(\text{O}_2, z)}{\mu} - \frac{\tau_2(\text{O}_3, z)}{\mu}\right) \quad (1.5.15)$$

where  $J_2^{(0)}$  is the value outside the atmosphere. The extinction due to O<sub>2</sub> is

$$\tau_2(\text{O}_2, z) = \alpha_2(\text{O}_2) \int_z^{\infty} [\text{O}_2(z')] dz \quad (1.5.16)$$

and that due to  $O_3$  is

$$\tau_2(O_3, z) = \alpha_2(O_3) \int_z^\infty [O_3(z)] dz \quad (1.5.17)$$

The extinction of  $J_3(z)$  is similarly defined by

$$\tau_3(O_3, z) = \alpha_3(O_3) \int_z^\infty [O_3(z)] dz \quad (1.5.18)$$

where  $\alpha_3$  is the average absorption cross section in the Hartley continuum.

The evaluation of (1.5.12) for  $[O_3]$  thus involves  $[O_3]$  on the right-hand side, but we may proceed by successive approximations. Let us begin by making the obviously crude assumption that all constituents follow the same atmospheric scale height  $H$ . Then (1.5.12) gives for a first approximation

$$\frac{[O_3(z)]_{\text{day}}}{[O_2(z)]} \approx \left( \frac{k_{12}[M(z_0)]J_2^{(0)}}{k_{13}J_3^{(0)}} \right)^{1/2} e^{-(z-z_0)/2H} \exp\left(-\frac{\tau_0}{2\mu} e^{-(z-z_0)/H}\right) \quad (1.5.19)$$

where

$$\tau_0 = \tau_2(O_2, z_0) + \tau_2(O_3, z_0) - \tau_3(O_3, z_0) \quad (1.5.20)$$

Equation (1.5.19) has the form of a so-called “Chapman layer,” which we will encounter again in ionosphere theory (see Section 5.1.1). The simple exponential represents diminished absorption with increasing altitude simply because of the decreasing abundance of the absorber. The compound exponential is due to attenuation of sunlight, which causes the “layer” to diminish deep in the atmosphere. The relative abundance of  $[O_3]$  would, in this approximation, peak at  $\tau_0/\mu = 1$ ; that is, at the  $\tau_0$  “absorption” peak [see Eq. (1.5.6)]. The absolute  $[O_3]$  peak, however, is at  $\tau_0/\mu = 3$ , or well below the  $\tau_0$  “absorption” peak. The reader should be aware that (1.5.19) is a poor approximation for a real ozone layer since  $\tau_0$  itself depends on  $[O_3]$ .

The instantaneous heating rate from dissociation is then

$$\left( \frac{dT}{dt} \right)_{\text{heat}} = \frac{[O_2(z)]}{\rho(z)C_p} \left( J_2(z)hv_2 + J_3(z)hv_3 \frac{[O_3(z)]_{\text{day}}}{[O_2(z)]} \right) \quad (1.5.21)$$

where  $\rho(z)$  is the local mass density,  $C_p$  is the specific heat of air ( $\text{erg/gm}^\circ\text{K}$ ), and  $v_2$  and  $v_3$  are average frequencies of the  $O_2$  Herzberg and  $O_3$  Hartley continua, respectively. It is a good approximation to assume that all the solar energy absorbed in the stratosphere goes into heating. Part of it appears as kinetic energy at the moment of dissociation; part goes into metastable states, such as  $O(^1D)$ , and is collisionally deactivated (i.e., transformed into heat); and part (the dissociation energy itself) appears as heat when the dissociation products react chemically to re-associate by (1.5.2) and (1.5.3).

To find the equilibrium temperature we equate the heat absorbed to that emitted. At high altitudes the infrared region of the atmosphere becomes

optically thin and radiates directly to space. This assumption is occasionally used to examine small fluctuations in heating and temperature and is called the *transparent approximation*. Assuming grayness for the emitting gases, we have [cf. (1.2.44)]

$$4\pi\kappa B(z) \equiv 4\kappa\sigma T^4 = C_p \left( \frac{dT}{dt} \right)_{\text{cool}} \quad (1.5.22)$$

where  $\kappa$  ( $\text{cm}^2/\text{gm}$ ) is the absorption coefficient. The actual atmosphere is far from gray and a *linear* or *Newtonian* law of cooling is often adopted:

$$C_p \left( \frac{dT}{dt} \right)_{\text{cool}} = aT \quad (1.5.23)$$

where  $a$  is a constant ( $\sim 4\kappa\sigma T_0^{-3}$ ). An example of the use of these simplified equations is given in Problem 1.6. The average overhead absorption for atmospheric gases in the infrared is shown in Fig. 1.11.

### 1.5.3 Water in the Stratosphere

The predominant carrier of radiative energy in the troposphere is  $\text{H}_2\text{O}$ , although  $\text{CO}_2$  is also important, especially at higher altitudes. In the stratosphere and above,  $\text{H}_2\text{O}$  is much less important owing to its small mixing

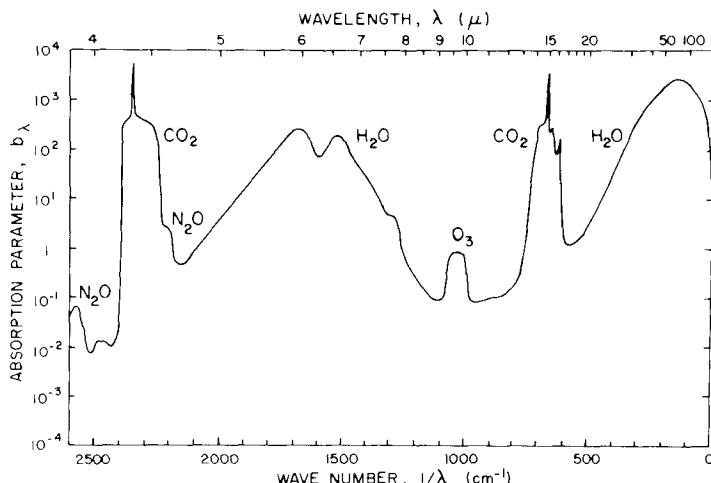


**Fig. 1.11** An indication of the absorbing properties of the lower atmosphere is  $b_\lambda$ , where  $1/b_\lambda$  is the thickness in atmospheres that would give 50 percent absorption and 50 percent transmission. In this limited sense,  $b_\lambda$  is a kind of optical thickness, even though over finite wavelength intervals the atmosphere does not absorb according to the Lambert exponential-attenuation law (1.2.2). [Adapted from C. W. ALLEN (1973), "Astrophysical Quantities," 3rd ed., p. 130, Athlone Press, London.]

ratio. The mixing ratio of stratospheric H<sub>2</sub>O is about  $5 \times 10^{-6}$  by volume and this amount would produce a saturated vapor pressure at the low temperature of the tropical tropopause ( $\sim 195^{\circ}\text{K}$  at 15 km). Hence it is commonly thought that the tropopause acts as a kind of cold trap. Any higher fraction of water would eventually find condensation nuclei, condense as ice, and fall out.

## 1.6 The Mesopause: Vibrational Relaxation of CO<sub>2</sub>

Above the stratosphere the heating is mainly due to the absorption of solar ultraviolet by ozone and CO<sub>2</sub> absorption at 15  $\mu\text{m}$ ; the latter band also dominates the cooling. The ratio [O<sub>3</sub>]/[CO<sub>2</sub>] diminishes slowly with increasing altitude, and the ratio of heating to cooling does the same. The temperature thus monotonically decreases at an average gradient of about  $-5^{\circ}\text{K}/\text{km}$ , quite stable in comparison with the dry adiabatic gradient (1.3.4) of  $-9.8^{\circ}\text{K}/\text{km}$ .

The direct absorption of sunlight is thus small, and radiation transport, primarily in the 15  $\mu\text{m}$  band of CO<sub>2</sub>, becomes dominant in governing the temperature distribution.

### 1.6.1 The CO<sub>2</sub> $\nu_2$ Fundamental Transition

The CO<sub>2</sub> molecule is linear (see Fig. 1.12). Consequently, the  $\nu_1$  mode, symmetric vibration, has no dipole moment for <sup>16</sup>O<sup>12</sup>C<sup>16</sup>O, and the vibration-rotation spectrum is absent, just as it is for homonuclear diatomic molecules. The  $\nu_2$  or bending mode has the lowest fundamental, occurring at 667.3 cm<sup>-1</sup> or 15  $\mu\text{m}$ . The  $\nu_2$  degeneracy (meaning the energy is equivalent for a vibration in the plane of the page and one perpendicular to it) is removed with rotation. Hence the transition is formally written (0 1<sup>1</sup> 0)  $\rightleftharpoons$  (0 0<sup>0</sup> 0),

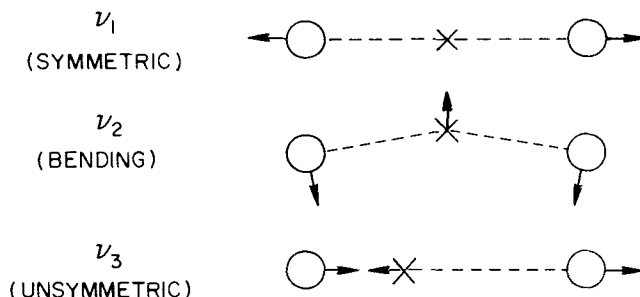


**Fig. 1.12** Vibrational modes for the linear OCO molecule.

where the principal numbers are the three vibrational quantum numbers  $v_i$ , and where the superscript is  $l$ , the quantum number specifying the *angular momentum of vibration* ( $0 \leq l \leq v_2$ ). The  $v_3$  mode, unsymmetric vibration, is  $(0\ 0^0\ 1) \rightleftharpoons (0\ 0^0\ 0)$ , which occurs at  $2350\text{ cm}^{-1}$  or  $4.3\text{ }\mu\text{m}$  and is an order of magnitude stronger in absorption. But because the  $15\text{ }\mu\text{m}$  band is more readily excited at the low mesospheric temperatures, is strong enough to be optically thick, and remains in local thermodynamic equilibrium (LTE) with the atmosphere to higher altitudes, it is the more important. The latter point requires some discussion, for the breakdown of LTE occurs through the phenomenon of *vibrational relaxation*.

### 1.6.2. Kirchhoff's Law and Vibrational Relaxation

In treating radiation in the troposphere (see Section 1.2.3), where many substances (e.g.,  $\text{H}_2\text{O}$ ,  $\text{CO}_2$ ) are radiatively active, we adopted a gray-atmosphere approximation for the infrared. Now we are concerned with a single vibrational transition for transporting heat, and it might seem that the use of Kirchhoff's law is no longer appropriate. We will demonstrate here that the approaches of thermodynamics and molecular physics are equivalent.

First, assume there is no scattering. The emitted radiation ( $\text{erg}/\text{cm}^3\text{ sec sr Hz}$ ) from unit volume is given by the emission coefficient of (1.2.1),

$$dI_v/ds = \rho j_v \quad (1.6.1)$$

where by (1.2.6),  $j_v = \kappa_v B_v$ . Integrating over the band profile (which we cannot now regard as gray but must represent with a realistic  $\kappa_v$  variation), we have an omnidirectional emission of energy density  $E$  in the entire  $v' = 1 \rightarrow v = 0$  band of

$$\frac{dE(1,0)}{dt} \equiv \int_{\text{sphere}} \int_{\text{band}} \frac{dI_v}{ds} dv d\Omega = 4\pi \rho B_v \int_v \kappa_v dv \quad (1.6.2)$$

where  $B_v$  comes out of the integrals since we are concerned with isotropic emission over a small frequency interval wherein  $B_v \approx \text{const}$ . Making use of the identity

$$\rho \kappa_v = N(v) \alpha_v(v, v') \quad (1.6.3)$$

to write the absorption coefficient in terms of the molecular cross section  $\alpha_v(v, v')$ , and the  $\text{CO}_2$  population in the lower vibrational level  $N(v)$ , we have

$$\frac{dE(1,0)}{dt} = \frac{4\pi N(0) 2hv^3}{c^2(e^{hv/kT} - 1)} \int \alpha_v(0, 1) dv \quad (1.6.4)$$

The integrated absorption cross section is expressed commonly in a variety of equivalent ways, including the *band strength*  $S$ , the *oscillator strength*  $f$ , the Einstein *absorption coefficient*  $B$ , or (since the three Einstein coefficients are uniquely related) the emission *transition probability*  $A$ . Thus we may choose from

$$\begin{aligned} \int \alpha_v(0, 1) dv &= S(0, 1) \\ &= \frac{\pi e^2}{mc} f(0, 1) \\ &= \frac{h\nu}{4\pi} B(0, 1) = \frac{c^2}{8\pi\nu^2} \frac{\tilde{\omega}(1)}{\tilde{\omega}(0)} A(1, 0) \end{aligned} \quad (1.6.5)$$

where  $\tilde{\omega}$  represents the *statistical weight* of a level. Opting for the transition probability, we write

$$\frac{dE(1, 0)}{dt} = \frac{N(1)A(1, 0)h\nu}{1 - e^{-h\nu/kT}} \text{ erg/cm}^3 \text{ sec} \quad (1.6.6)$$

since in thermodynamic equilibrium the relative populations of levels  $v$  and  $v'$  are given by Boltzmann's excitation equation,

$$\frac{N(v')}{N(v)} = \frac{\tilde{\omega}(v')}{\tilde{\omega}(v)} \exp\left(-\frac{h\nu(v')}{kT}\right) \quad (1.6.7)$$

For a diatomic molecule we can regard the vibrational levels (summed over all rotational levels) as having the same statistical weights,  $\tilde{\omega}(v') = \tilde{\omega}(v)$ .

From the approach of molecular physics, the rate of energy emission from  $v' = 1 \rightarrow v = 0$  is

$$\frac{dE(1, 0)}{dt} = N(1)[A(1, 0) + B_v(T)B(1, 0)]h\nu \quad (1.6.8)$$

where  $B(1, 0)$  is the *Einstein coefficient for stimulated emission*, and we take the incident intensity as Planckian and characteristic of the local temperature. The Einstein relationships are

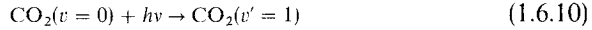
$$\tilde{\omega}(1)B(1, 0) = \tilde{\omega}(0)B(0, 1) = \frac{\tilde{\omega}(1)c^2}{2h\nu^3} A(1, 0) \quad (1.6.9)$$

With  $B_v$  given by (1.2.7), Eq. (1.6.8) reduces to (1.6.6).

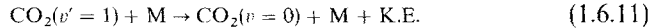
Of course, it is scarcely surprising that the two approaches are equivalent when one considers that we have assumed Planckian radiation and a Boltzmann distribution of level populations. These conditions are, after all, used to establish the relationships among the Einstein  $A$  and  $B$ 's. Conversely, if the radiation field is far from isotropic or not characteristic of the local

temperature or if collisions are not frequent enough to maintain the Boltzmann distribution (1.6.7), the Kirchhoff relationship does not apply and we must look at the molecular physics to ascertain the emission.

Let us examine the collision and radiation physics to see when thermodynamic equilibrium becomes a poor approximation. Radiation is transferred to heat by absorption,



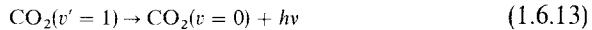
followed by collisional deactivation,



where K.E. ( $= h\nu$ ) is the kinetic energy supplied to the gas. The rate coefficient for deactivation is  $\eta(1, 0)$  ( $\text{cm}^3/\text{sec}$ ) so that

$$\frac{d[\text{CO}_2(1)]}{dt} = -[\text{CO}_2(1)][\text{M}]\eta(1, 0) \text{ cm}^{-3} \text{ sec}^{-1} \quad (1.6.12)$$

On the other hand, absorption by (1.6.10) may be followed by spontaneous emission,



in which case there is no radiation transferred into kinetic energy and the combination (1.6.10) plus (1.6.13) amounts to scattering. Neglecting the small stimulated-emission term in the denominator of (1.6.6), the loss of  $\text{CO}_2(v' = 1)$  by spontaneous emission is

$$\frac{d[\text{CO}_2(1)]}{dt} = -[\text{CO}_2(1)]A(1, 0) \quad (1.6.14)$$

which gives an albedo for single scattering of

$$\tilde{\omega}^* = \frac{A(1, 0)}{A(1, 0) + \eta(1, 0)[\text{M}]} \quad (1.6.15)$$

which is independent of frequency within the 1-0 band.

The equation of transfer (1.2.11), with (1.6.14) and (1.2.17), is then

$$\mu \frac{dI_v}{d\tau_v} = I_v - \tilde{\omega}^* J_v - (1 - \tilde{\omega}^*) B_v \quad (1.6.16)$$

When  $\tilde{\omega}^* \approx 0$  the coupling of the gas to the radiation field is strong; this is the state of LTE. But when  $\tilde{\omega}^* \approx 1$ , the upper state scatters the incident photons and the kinetic temperature of the gas is not strongly affected by the incident radiation.

The shift from  $\tilde{\omega}^* \approx 0$  to  $\tilde{\omega}^* \approx 1$  is called *vibrational relaxation* [meaning that vibrational populations are no longer governed by the Boltzmann

equation (1.6.7)], and it occurs at

$$[M] \lesssim \frac{A(1,0)}{\eta(1,0)} \quad (1.6.17)$$

For the  $v_2$  band of  $\text{CO}_2$ , the band strength is  $S(0,1) = 2.37 \times 10^{-7} \text{ cm}^2/\text{sec}$ , giving  $A(1,0) = 1.35 \text{ sec}^{-1}$ . Adopting  $\eta(1,0) = 2.5 \times 10^{-15} \text{ cm}^3/\text{sec}$ , we find relaxation occurs for densities  $[M] \lesssim 10^{15} \text{ cm}^{-3}$ , which occurs around 70–75 km.

Above this altitude radiative absorption is negligible compared with collisional excitation, although the gas still radiatively cools by emission of energy at the rate

$$\frac{dE(1,0)}{dt} = \eta(0,1)\tilde{\omega}^*[M][\text{CO}_2]hv \quad (1.6.18)$$

where the excitation rate coefficient is related to the deactivation coefficient (through thermodynamic considerations of detailed balancing) by

$$\tilde{\omega}(0)\eta(0,1) = \tilde{\omega}(1)\eta(1,0)e^{-hv/kT} \quad (1.6.19)$$

When the relative populations are not in thermodynamic equilibrium, they must in general be determined by the relative importance of collisions and the radiation field. If the local kinetic temperature is  $T$  and radiation characteristic of some other temperature  $T_0$  is incident from below, the excitation is

$$\frac{N(1)}{N(0)} = \frac{\tilde{\omega}(1)}{\tilde{\omega}(0)} \left( (1 - \tilde{\omega}^*)e^{-hv/kT} + \frac{\tilde{\omega}^*}{2} e^{-hv/kT_0} \right) \quad (1.6.20)$$

in lieu of the Boltzmann equation (1.6.7). The  $\frac{1}{2}$  factor enters because the gas is irradiated only from below; the equation is based on negligible induced emission (see Problem 1.9).

The temperature of the upper mesosphere will thus decrease upwards until heating from the thermosphere offsets the radiant losses. To estimate where this occurs we must first look at the thermospheric processes.

## 1.7 Ionization, Dissociation, and Heat Transfer in the Thermosphere

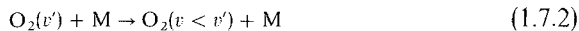
Above 80 km in the Earth's atmosphere the direct absorption of solar energy again becomes important for two reasons: Photoionization, at the lower altitudes mainly by X-rays, and photodissociation in the Schumann–Runge continuum of  $\text{O}_2$ . (The principles of photochemistry are reviewed in Section 3.1.)

### 1.7.1 Absorption of Sunlight

The heating that occurs from photoionization involves a number of processes. First is ejection of the electron itself. For an example, let us take the O<sub>2</sub> molecule, although N<sub>2</sub>, O, and minor constituents are also ionized by X-rays and NO is ionized by the strong solar Ly  $\alpha$  emission of hydrogen at 1215 Å. Thus photoionization,



where the ionization potential is about 12 eV and the electron carries away additional kinetic energy. This energy is fed into the neutral gas by collisions that excite electronic states or high vibrational levels. A small amount of the energy is lost to space by molecular radiation, but N<sub>2</sub> and O<sub>2</sub> have no vibrational-rotational spectra, since they are *homonuclear* and have no dipole moment. Hence the excitation energy is converted to kinetic energy by energy exchange,



or, through atom-atom interchange,



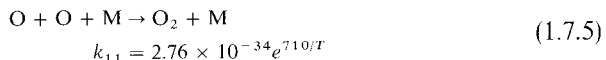
How the energy of ionization is converted to heat depends somewhat on the altitude. Below the 90 km region recombination occurs through (a) *electron attachment* to a neutral molecule followed by (b) *mutual neutralization*, a collision between a negative and a positive ion that leaves neutral products. Most of the ionization potential is thus released in the same region where ionization occurs.

At higher altitudes negative ions do not form readily and the positive charge is predominantly on O<sup>+</sup>, O<sub>2</sub><sup>+</sup>, or NO<sup>+</sup>. However, O<sup>+</sup> is very slow to recombine and sooner or later loses its charge to a molecule. Recombination is rapid for charged molecules, proceeding by, for example,



*dissociative recombination*.

Thus the difference between the ionization energy ( $\sim 12$  eV) and the dissociation energy ( $\sim 5$  eV) is released in the ionization region, but the reassociation energy is released lower, in the 100 km region, where oxygen associates by



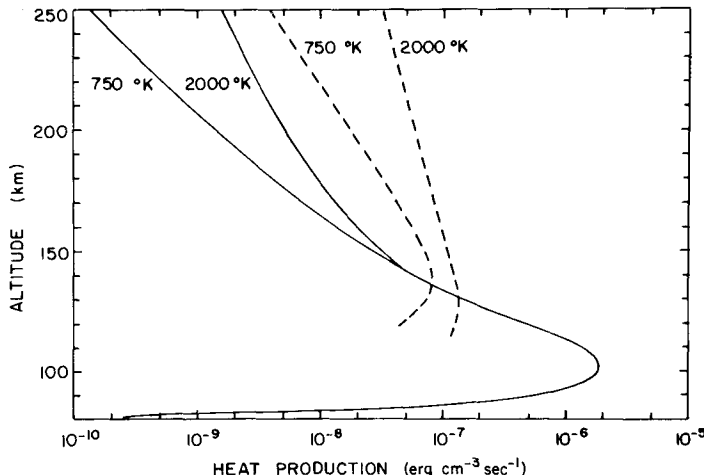


**Fig. 1.13** Deposition of heat in the upper atmosphere for an overhead sun ( $\mu = 1$ ) and heating efficiency  $\varepsilon = 0.3$ , computed for two models having temperatures in the high thermosphere and exosphere of 750 and 2000°K. The curves give the second term on the right of (1.7.19). Solid curves—Schumann–Runge continuum; dashed curves—ionization by  $\lambda < 1026 \text{ \AA}$ . [Calculations by P. M. BANKS and G. KOCKARTS (1973), “Aeronomy,” **B**, p. 19, Academic Press, New York.]

In the same way  $\text{O}_2$  is dissociated in the Schumann–Runge continuum and somewhat higher in altitude than the main level of re-association. The vertical interchange of matter, either by molecular diffusion, large-scale wind systems, or eddy mixing, thus plays a significant role in the heat deposition. Figure 1.13 shows heating rates computed for two assumed temperature and density distributions. The Schumann–Runge region is important in the lower thermosphere, and the 80–1026 Å interval that produces ionization dominates in the middle and upper thermosphere. The heating efficiency was taken as 30 percent. The remainder of the incident energy is either radiated away or transported downward in the form of chemical energy to the region where O atoms readily associate.

## 1.7.2 Oxygen Chemistry and Distribution in the Thermosphere

The strong Schumann–Runge continuum (see Section 1.5.1) at  $\lambda < 1750 \text{ \AA}$  produces



with  $J_2(\infty) \sim 4 \times 10^{-6} \text{ sec}^{-1}$ . The  $\text{O}({}^1\text{D})$  term lies 1.96 eV above ground. It is the upper term of the red 6300 and 6364 Å forbidden lines that appear in

both the airglow and aurora. Association occurs in the presence of a third body by (1.7.5) and by *radiative association*,



although the latter is unimportant compared with the three-body process except well above the main dissociation region. Neglecting (1.7.7) we have an equilibrium distribution of

$$\frac{[\text{O}]}{[\text{O}_2]} = \left( \frac{J_2}{k_{11}[\text{O}_2][\text{M}]} \right)^{1/2} \quad (1.7.8)$$

However, the diffusive separation of gases becomes important in the same region (around 100–110 km) where dissociation peaks. The theoretical time for uniformly mixed  $\text{O}_2$  and O to approach diffusive equilibrium at 115 km is about 10 days, which is also the lifetime of an  $\text{O}_2$  molecule against photo-dissociation. But in the 100–115 km region, the ratio  $[\text{O}_2]/[\text{O}] \approx \frac{1}{3}$  and is nearly constant. Hence the characteristic time for the lower thermosphere to become thoroughly mixed, from large scale circulation and turbulence, may also be the order of 10 days, with diffusion, mixing, and  $\text{O}_2$  photolysis having comparable time scales. In the next chapter we discuss diffusion and mixing more thoroughly. For now we note that somewhere between 115 and 150 km the diffusion time (which varies as the density) becomes sufficiently short that mixing is overcome and  $\text{O}_2$ , O, and  $\text{N}_2$  are all in diffusive equilibrium, meaning that each gas follows hydrostatic equilibrium, (1.1.5), independently for its own mass  $M_j$ . The atmospheric scale height is then (cf. Problem 1.1)

$$H = \left( \sum_j \frac{N_j/N}{H_j} \right)^{-1} \quad (1.7.9)$$

where  $H_j = kT/M_jg$ .

There is no  $\text{N}_2$  continuum where solar ultraviolet radiation is strong enough to dissociate it, but N atoms are formed through photoionization,



which occurs for  $\lambda < 796 \text{ \AA}$ , followed by dissociative recombination,



Once formed, N can re-associate by the three-body process, but it also reacts with oxygen, forming nitric oxide by



and



which is very slow at 300°K. However, ion-neutral reactions are the dominant source of N atoms,



and



although the latter reaction is probably very slow. Dissociative recombination of  $\text{NO}^+$  yields the N atom preferentially in the  ${}^2\text{D}$  state.

A different type of production mechanism involves  $\text{N}({}^2\text{D})$  formed by recombination, (1.7.11). The  ${}^2\text{D}$  term is metastable, at 2.37 eV above ground,  $\text{N}({}^4\text{S})$ . Once formed it can react with  $\text{O}_2$ ,



Nitric oxide formed in the thermosphere is important to the formation of the lower ionosphere, and we shall return to it in Chapter 5.

### 1.7.3 Radiative Exchange and Loss

Some of the processes mentioned above emit radiation as they occur. Electron attachment to form a negative ion may proceed either by emitting a stabilizing photon or in the presence of a third body. *Three-body association*, (1.7.5), may leave  $\text{O}_2$  in the ground state,  $X\ {}^3\Sigma_g^-$ , but it can just as well associate into one of the other (excited) states that correspond to two ground-term  $\text{O}({}^3\text{P})$  atoms (see Fig. 1.9). In that case the excited molecule might emit radiation in one of the  $\text{O}_2$  band systems observed in the airglow (see Section 6.1.2), and this loss represents energy not available for thermospheric heat.

The net heating efficiency must also include the loss of infrared radiation due to thermal collisions, such as the  $\text{CO}_2$  loss above its level of vibrational relaxation. But the abundant molecules  $\text{N}_2$  and  $\text{O}_2$  are forbidden to radiate in the infrared by electric-dipole transitions and the minor constituents that can radiate ( $\text{NO}$ ,  $\text{CO}$ , etc.) are rare in the Earth's atmosphere. Carbon monoxide rotational spectra are probably important in cooling the high atmospheres of Mars and Venus.

Nitric oxide has a vibration-rotation band at  $5.3\ \mu\text{m}$  whose importance could not be assessed until the NO concentration was established. It is, in fact, highly variable; one sample calculation leads to a loss of  $0.45\ \text{erg cm}^{-2}\ \text{s}^{-1}$ . Prior to 1980, the principal radiative loss for the upper thermosphere of Earth was thought to be a forbidden (by electric-dipole radiation) transition between two of the fine-structure levels,  $J = 1 \rightarrow J = 2$ , of the ground term of

$O(^3P_{2,1,0})$  (cf. Fig. 6.3). The transition occurs at  $63 \mu\text{m}$ . The level separation (0.02 eV) is comparable to atmospheric thermal energies (0.02 eV =  $232^\circ\text{K}$ ). Because the radiative lifetime is so long ( $1/A = 3.1 \text{ hr}$ ) compared with the time between thermal collisions, the levels of the  $O$  ground term are in a Boltzmann distribution. Hence the emission rate at  $63 \mu\text{m}$  is

$$\frac{dE(1,2)}{dt} = [\text{O}] \frac{\tilde{\omega}_1 \exp(-E_1/kT)}{\sum_{J=0}^2 \tilde{\omega}_J \exp(-E_J/kT)} A(1,2) E_1 \quad (1.7.18)$$

where  $E_J$  is the energy of the  $J$ th level above ground ( $J = 2$ ). The cooling effect of this radiation is important, however, only above the level where the transition ceases to be optically thick and this consideration limits the cooling to the  $F$  region (see Problem 1.7). The  $J = 0 \rightarrow J = 1$  transition at  $147 \mu\text{m}$  also occurs, but is less important.

#### 1.7.4 Conductive Flow of Heat and Location of the Mesopause

With a positive temperature slope, preventing convection, and a not very effective exchange of heat by radiation, the primary energy transfer in the lower thermosphere is by conduction. The instantaneous rate of heating is

$$\rho \frac{\partial}{\partial t} (C_p T) = \frac{\partial}{\partial z} \left( K \frac{\partial T}{\partial z} \right) + \sum_i \pi \mathcal{F}_i \varepsilon_i \alpha_i N(z) e^{-\tau_i(z)/\mu} - \mathcal{R}(z) \quad (1.7.19)$$

We here divide the solar flux into a number of spectral intervals  $\pi \mathcal{F}_i$ , chosen so that the absorption coefficient has little variation within each one. Thus  $\pi \mathcal{F}_i$  is the solar energy flux ( $\text{erg/cm}^2 \text{ sec}$ ) within each interval,  $\varepsilon_i$  is the fraction of absorbed solar energy that appears locally as heat, and  $\tau_i(z)$  is the vertical optical thickness in the ultraviolet intervals. With  $\alpha_i$  the mean absorption cross section ( $\text{cm}^2/\text{molecule}$ ), we have  $d\tau_i = -N(z)\alpha_i dz$ . Also  $K(T)$  is the thermal conductivity ( $\text{erg/cm sec}^\circ\text{K}$ ) and  $\mathcal{R}(z)$  is the radiant heat loss ( $\text{erg/cm}^3 \text{ sec}$ ).

In a steady state, averaged over a day, this equation integrates to

$$K \frac{dT}{dz} = \frac{1}{2} \sum_i \pi \mathcal{F}_i \varepsilon_i \langle \mu \rangle \left[ 1 - \exp\left(\frac{-\tau_i}{\langle \mu \rangle}\right) \right] - \int_z^\infty \mathcal{R}(z) dz \quad (1.7.20)$$

which is equivalent to the downward conductive heat flux. The use of an average solar zenith angle,  $\cos^{-1}\langle \mu \rangle$ , is an approximation (as is the factor  $\frac{1}{2}$  for nighttime). The flux should actually be integrated through the day with  $\mu = \mu(t)$ .

It is clear that at high altitude the right side vanishes and  $T \rightarrow T_{\text{ex}}$ , the exospheric temperature. At other heights  $z$ , the gradient must be large enough

to sustain a downward flow of heat equivalent to the total ultraviolet energy absorbed above  $z$  less the infrared loss.

Figure 1.13 shows where the energy is absorbed in the two intervals 80–1026 Å and the Schumann–Runge region,  $\lambda < 1750$  Å. The ionization energy varies with solar activity, but is the order of 2 erg/cm<sup>2</sup> sec. The Schumann–Runge flux is the order of 15 erg/cm<sup>2</sup> sec. The radiant loss from 63 μm radiation of O is probably only a few tenths of an erg/cm<sup>2</sup> sec, although that could be important above 150 km. The high altitudes are well insulated from the mesosphere by the thick thermosphere through which heat must flow to escape. Consequently, small changes in the heat absorbed or emitted can have a big impact on the local temperature.

$K(T)$  can be represented by the expression

$$K(T) = AT^s \quad (1.7.21)$$

where values of the empirical constants  $A$  and  $s$  are given in Table 1.2. The net heat flux deposited above 120 km, where  $T \approx 325^\circ\text{K}$ , is therefore

$$K(T) \frac{dT}{dz} = \frac{1}{2}\pi\mathcal{F}\varepsilon\langle\mu\rangle \gtrsim 0.4 \text{ erg/cm}^2 \text{ sec} \quad (1.7.22)$$

in order to support a gradient of at least 15°K/km, higher gradients occurring with high solar activity. Thus the ionization energy alone deposited above 120 km can probably account for the gradient with, say,  $\langle\mu\rangle = \frac{1}{2}$  and  $\varepsilon = 0.8$ .

The gradient at 90 km is only some 10°K/km, but a glance at Fig. 1.13 shows that the overhead heat input has increased manyfold. Even with some differences in efficiency, the conclusion is clear that radiative loss is important in the 100 km region. The location of the mesopause is given by the altitude at which the entire thermospheric flux has been radiated away by CO<sub>2</sub>, at 15 μm.

With CO<sub>2</sub> in vibrational relaxation, Eqs. (1.6.18) and (1.6.19) give the mesopause condition as

$$f(\text{CO}_2)\eta(1,0)hv \int_{z_0}^{\infty} N^2(z)e^{-hv/kT} dz = \frac{1}{2}\pi\mathcal{F}\varepsilon\langle\mu\rangle \quad (1.7.23)$$

TABLE 1.2 Constants in the Expression for Thermal Conductivity<sup>a</sup>

|            | Gas                             |      |                 |      |                |                |
|------------|---------------------------------|------|-----------------|------|----------------|----------------|
|            | N <sub>2</sub> , O <sub>2</sub> | O    | CO <sub>2</sub> | H    | H <sub>2</sub> | H <sub>2</sub> |
| Range (°K) |                                 |      |                 |      | > 150          | < 150          |
| $A$        | 36                              | 54   | 0.82            | 235  | 252            | 68.6           |
| $s$        | 0.75                            | 0.75 | 1.28            | 0.75 | 0.751          | 1.0            |

<sup>a</sup> Equation (1.7.21). The units of  $A$  are erg cm (cm<sup>2</sup> sec °K)<sup>-1</sup>.

where  $f(\text{CO}_2)$  is the mixing ratio of  $\text{CO}_2$  ( $3 \times 10^{-4}$ ) and  $\eta(1,0) = 2.5 \times 10^{-15} \text{ cm}^3/\text{sec}$ . The conductive flux on the right is about  $3.4 \text{ erg/cm}^2 \text{ sec}$ . Evaluating the integral in the isothermal approximation (1.1.4) at  $T_0 = 175^\circ\text{K}$  (the solution is not sensitive to  $T_0$ ) we find

$$N(z_0) = 1.3 \times 10^{14} \text{ cm}^{-3} \quad (1.7.24)$$

which occurs around 85 km.

The heat equation (1.7.22) can be solved analytically for a simplified but moderately realistic situation (see Problem 1.11). The thermosphere is represented as a conducting slab obeying (1.7.21) with the heat source concentrated at the top (the thermopause) and the sink at the bottom (the mesopause, at  $T_0$ ). The vertical coordinate is transformed to pressure by the hydrostatic equation (1.1.3):

$$\ln p = \ln p_0 - \int_{z_0}^z \frac{dz}{H} \quad (1.7.25)$$

Substitution of (1.7.22), with its right-hand side set equal to  $Q$ , followed by integration, yields

$$T^s = T_0^s + (skQ/AMg) \ln(p_0/p) \quad (1.7.26)$$

Because pressure is proportional to integrated density [Eq. (1.1.6)], the ratio of pressures is the same as the ratio of optical depths. To find the thermopause temperature  $T_1$ , we assume that this level is at a slant optical depth of unity; thus,  $p_0/p_1 = \tau_0/\langle\mu\rangle$ , where  $\tau_0$  is the optical depth at the mesopause for the softest ultraviolet radiation ( $\sim 200\text{--}1000 \text{ \AA}$ ).

A full numerical solution, including heat sources and sinks within the thermosphere, is easy using a similar technique. However, it still includes many uncertainties in the solar flux, the heating efficiency, and the mesopause conditions; in reality, the approximate analytic solution may be all that is justified.

## 1.8 Atmospheric Structure of Venus, Mars, and Mercury

### 1.8.1 Venus

The high temperature of the surface,  $733^\circ\text{K}$  at 92 bars, was first deduced from its emission in the microwave radio spectrum, to which the atmosphere is nearly transparent. Although only a few percent of the solar flux reaches the ground, the high temperature is due to a greenhouse effect. The gas is nearly all  $\text{CO}_2$ , with about 3%  $\text{N}_2$  (see Table 4.1).

The first measurements of the temperature profile were made by radio occultation (cf. Section 5.2.2) of Mariner 5 and by *in-situ* sensing on the

Venera 8 probe. Both kinds of measurement have since been repeated; the data in Fig. 1.14 are from the Pioneer Venus probes and orbiter. The lapse rate below 60 km is close to the adiabatic value but is actually less on average by about  $1^{\circ}\text{K}/\text{km}$ . There are thin layers typically around 20 and 50 km that are significantly unstable. Horizontally, this whole region is globally uniform to within about  $5^{\circ}\text{K}$ . Both this uniformity and the vertical structure represent the effects of dynamical activity.

The 50–65 km region is occupied by a dense, nearly uniform, cloud with an optical depth of about 20. Thin haze extends to much higher altitudes, 80–90 km. The principal cloud material is concentrated  $\text{H}_2\text{SO}_4$ , with approximately one  $\text{H}_2\text{O}$  molecule per  $\text{H}_2\text{SO}_4$  molecule. The yellow color is most commonly attributed to sulfur, and there is evidence of a third component,

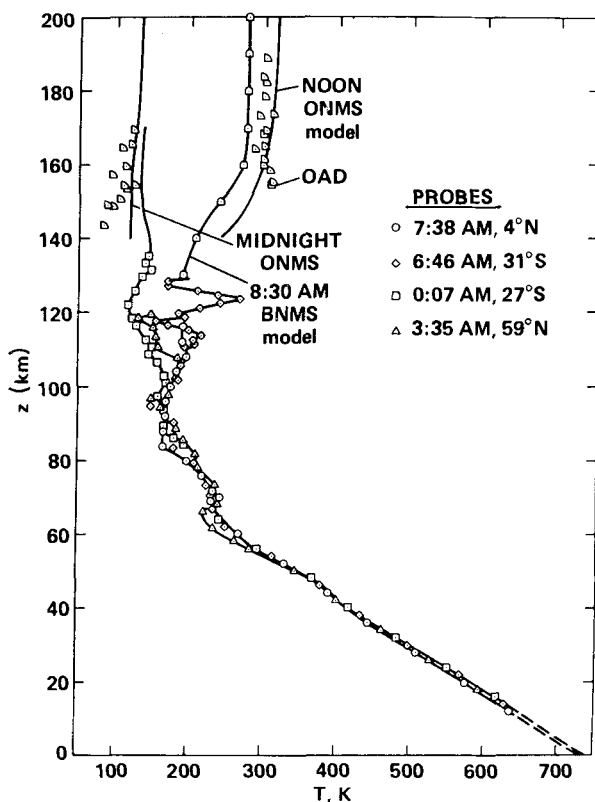


**Fig. 1.14** Temperature profiles of the Venus atmosphere from the surface to 200 km, compiled by Seiff from Pioneer Venus observations. The acronyms refer to various experiments: B, probe bus; O, orbiter; NMS, neutral mass spectrometer; and AD, atmospheric drag. [After HUNTER *et al.* (1983).]

also solid, near the cloud base. The first identification of sulfuric acid was from the refractive index (1.45) and near-infrared reflectivity (cf. Section 5.2.2), and several probe experiments have provided ample confirmation.

Winds have been measured at the cloud top by the tracking of features, and down to the surface by the tracking of probes. The flow is almost exactly zonal and retrograde (east to west). Although the direction is the same as for Venus' rotation, the speeds at the cloud top are much greater; the period is about 4 days rather than 243 days (sidereal). This speed of 100 m/sec decreases roughly linearly with height, reaching unmeasurably small values (less than 10–20 cm/sec) at around 5–10 km. These speeds refer to low latitudes; further north and south, the speeds diminish somewhat more slowly than they would for a solid shell. Above 65 km there is no direct information, but there are indications of a maximum speed of 120 m/sec followed by a decline.

Figure 1.14 shows a nearly monotonic decline of temperature from 65 to 100 km; there is no signature of a stratosphere, and we shall refer to the entire region as the mesosphere. As in the troposphere, any diurnal variation is very small.

On the day side the temperature begins to rise above 100 km, reaching an asymptotic value of 300°K at about 170 km. This thermosphere is therefore not nearly as well developed as the Earth's (compare Figs. 1.14 and 1.1). The night sides show an even more striking difference. The diurnal variation of exospheric temperature on Earth is around 200°K, or 20%. On Venus it is again 200°K, but this is now a factor of 3. Another view of this variation is shown in Fig. 1.15, which covers  $2\frac{1}{2}$  Venus days with daily measurements based on the scale height of atomic oxygen:  $T = MgH/k$  with  $M = 16$  amu (cf. Eq. 1.1.3). The term "thermosphere" (heat-sphere) becomes rather

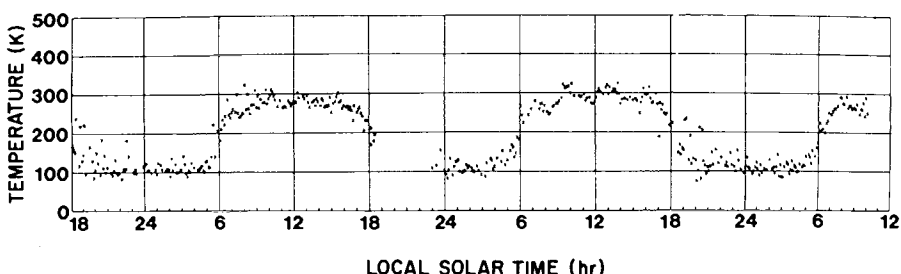


**Fig. 1.15** Diurnal variation of the exospheric temperature derived from constituent scale heights measured by the Pioneer Venus orbiter mass spectrometer. One point is shown for each Earth day; the time covered is about  $2\frac{1}{2}$  Venus days. [After HUNTEMAN *et al.* (1983).]

strained on the night side, and “cryosphere” is in common use. The same word is conventionally applied to regions of ice and snow on the Earth, but confusion is unlikely.

The composition of the upper thermosphere and lower exosphere are shown in Fig. 1.16. The cutoff at 150 km represents the lower altitude limit of the Pioneer Venus Orbiter and is already well above the homopause. Dashed and solid curves represent mean conditions near noon and midnight, where O becomes the dominant constituent at 157 and 140 km. The vastly different scale heights correspond to the different temperatures. Figure 1.17 shows the H density at 165 km as a function of hour angle (midnight at 0 and 24, noon at 12). For this gas, the effect of differing scale heights is small, and the maximum densities are on the night side. However, the peak is around 4 a.m., not midnight. A similar offset bulge is seen in airglow at 1980 Å (the 0-1 band of the NO  $\delta$  system) which is excited in recombination of N and O atoms.

Data for the lower thermosphere are very limited. As Fig. 1.14 indicates, some temperature profiles were obtained by analysis of the drag on the Pioneer Venus probes. In addition, a mass spectrometer on the probe carrier (or bus) measured helium and CO<sub>2</sub> down to 130 km, which is below the homopause. Along with some airglow data, these results can be used to constrain an aeronomical model and give the results shown in Fig. 1.18 (also, cf. Section 2.3.5).

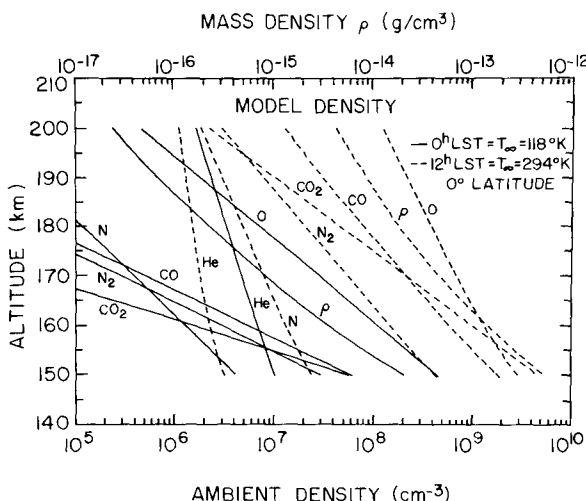


**Fig. 1.16** Model densities for the thermosphere derived by a global fit to data of the Pioneer Venus orbiter mass spectrometer. Recalibration suggests that all densities should be multiplied by 1.63. [After NIEMANN *et al.* (1980).]

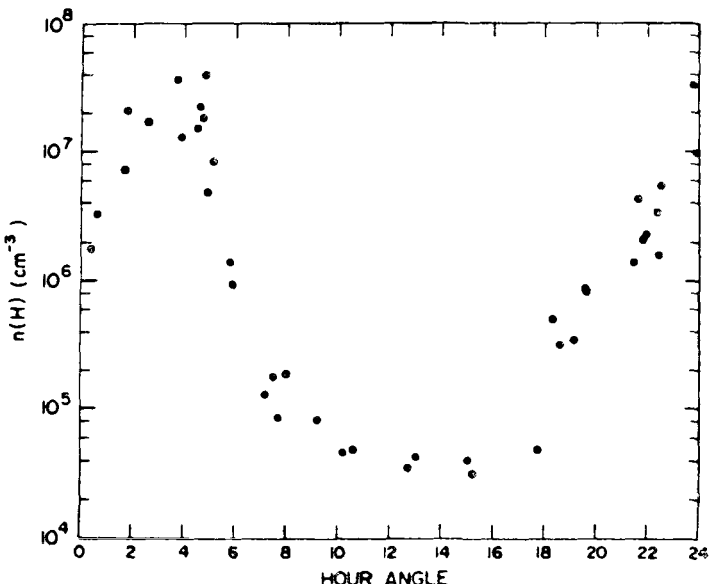


**Fig. 1.17** Diurnal variation of H on Venus near 165 km derived from other ions and the O density according to (5.1.42b). [After BRINTON *et al.* (1980).]

### 1.8.2 Venus' Thermosphere and Cryosphere

The large diurnal density ratio evident in Fig. 1.17 is accompanied by an even larger pressure ratio that is proportional to both density and temperature ratios [Eq. (1.1.2)]. Strong day-to-night winds would therefore be expected and were, in fact, predicted before there were any data for the night side. The pressure differences are, however, much greater than predicted. There are no wind measurements at thermospheric heights, but the nightside maximum of H (Fig. 1.17) and the NO airglow maximum give strong indications that the expected winds do exist. The displacement of both maxima away from midnight indicates that the flow is unsymmetrical and suggests that there is a superposed rotation. A sketch of the proposed flow field is shown in Fig. 1.19. The direction of the rotation is the same as that of the planet and the cloud tops. The speed can be estimated by the following argument. The rotation speed must be around one-half the day-night wind speed to cause the observed displacement of the maxima. If the wind speed is 100–200 m/sec (approaching the speed of sound), the rotation would be 50–100 m/sec. The corresponding period is around 6 days.

The circulation must be closed by a night-to-day flow, which is expected to be in the upper mesosphere around 90 km. As the major gases descend to

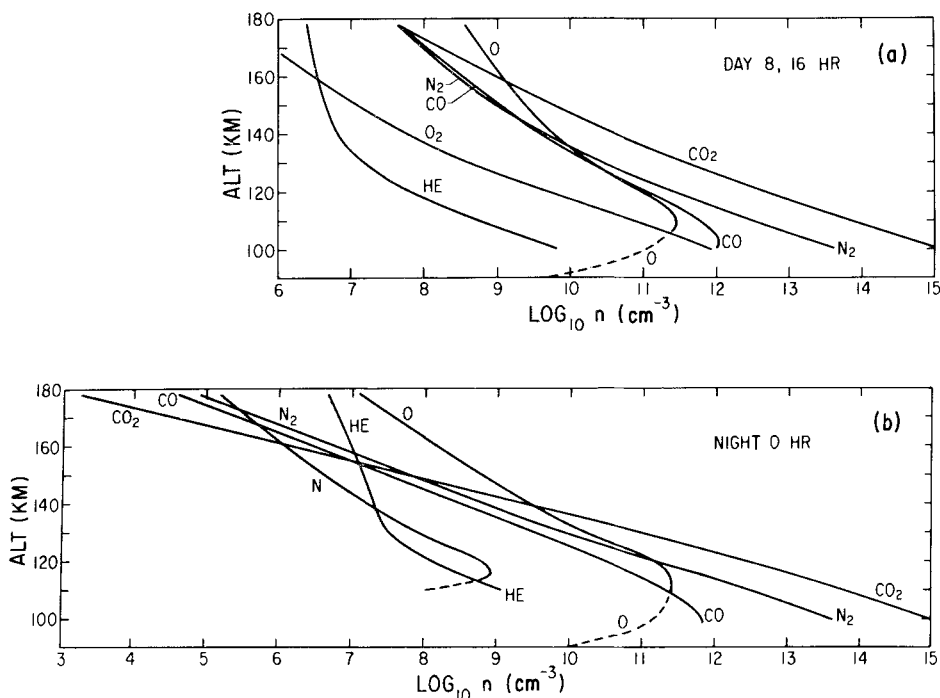


**Fig. 1.18** Densities for the Venus thermosphere on the day and night sides obtained from one-dimensional models based on Pioneer Venus and airglow data. [After MASSIE *et al.* (1983).]

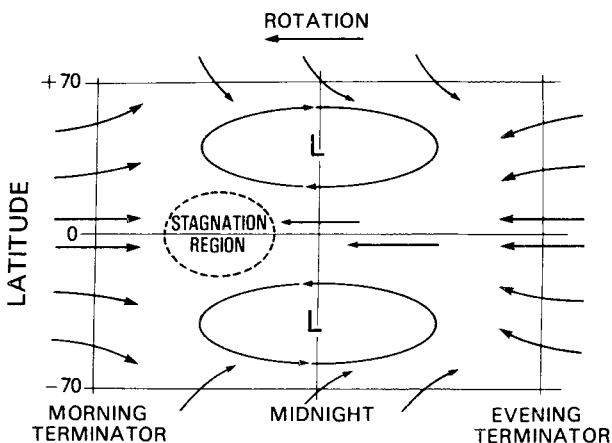


**Fig. 1.19** Schematic horizontal flow field for the nightside Venus thermosphere. [After NIEMANN *et al.* (1980).]

complete this circulation, they leave behind the lighter ones (H, He, N, O) to form the observed bulges. Horizontal flow in a diffusively separated region has the unusual property that the amount of each gas carried along is proportional to its scale height as well as its number density. This effect is called *wind-induced diffusion* or a *Johnson pump mechanism*.

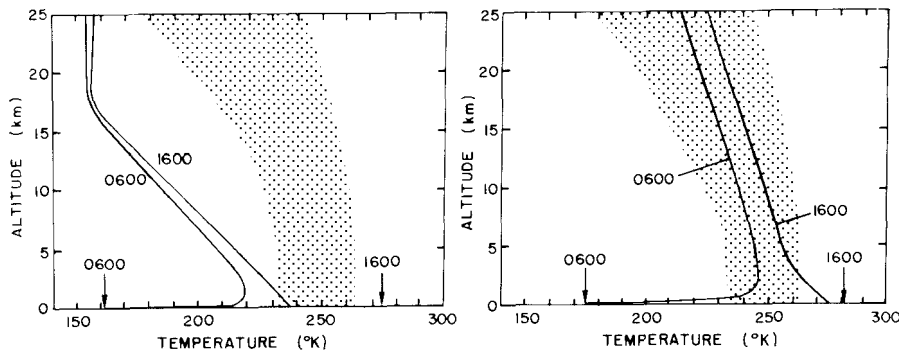
The heat balance of Venus' thermosphere offers two unsolved problems: the existence of the nightside cryosphere and the low temperature even on the day side. Substitution of the appropriate parameters into (1.7.26) gives a thermospause temperature of 414°K (Problem 1.12). Even though the heating efficiency is taken to have the remarkably low value of 0.1, this temperature does not agree with the observed global mean of 213°K or even the dayside value of 300°K. Heat transport may be dominated by the global circulation discussed above.

The cryosphere is totally out of the framework of Section 1.7.4, which assumes downward conduction as the principal heat sink. With the observed negative temperature gradient, conduction becomes a source, not a sink. Additional heat is brought in by the winds from the day side. It has been suggested that these winds may be slower than the 100–200 m/sec given by straightforward theory. The flow could become turbulent, which in itself slows down the net motion and also may generate a turbulent viscosity. Another, not entirely distinct, possibility is forced vertical mixing, which in the limit could give a temperature gradient approaching the adiabat. The only heat sink seems to be thermal radiation, principally in the 15  $\mu\text{m}$  bands of CO<sub>2</sub> (Section 1.6), even though it is necessarily very weak at temperatures as low as 125°K.

### 1.8.3 Mars

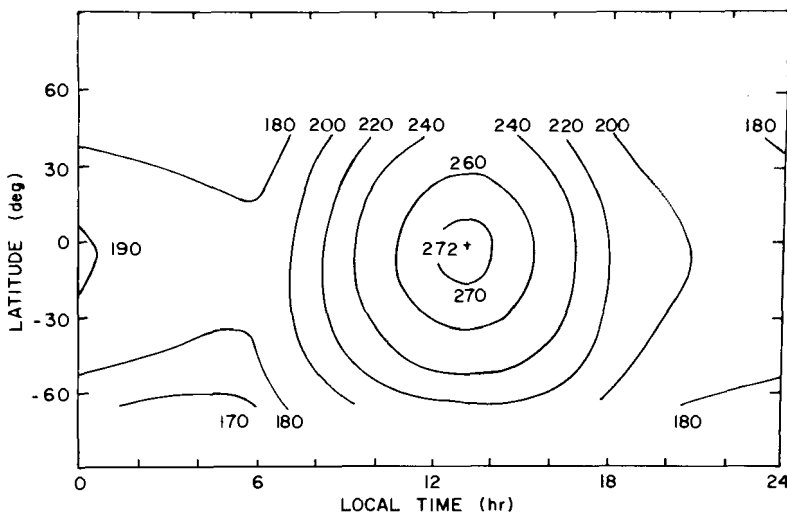
Like Venus, Mars has a CO<sub>2</sub> atmosphere with a few percent N<sub>2</sub> (Table 4.1). The surface pressure is, however, far lower, around 6 mbar at a mean level. Temperatures can be measured up to 25 km by radio occultation, and two profiles up to 200 km were obtained during the Viking entries.

Figure 1.20 shows a shaded area that includes the temperature measurements with height at various positions and times of day for dusty conditions. The temperature gradient is not even close to the predicted adiabatic lapse rate of 5°K/km for a clear CO<sub>2</sub> atmosphere in radiative-convective equilibrium. The actual temperature profile is due mainly to absorption of direct solar radiation by dust in the atmosphere. The effect is important even when the atmosphere appears to be clear; although the lapse rate is more nearly adiabatic for clear conditions, it is seldom steeper than 3°K/km. Models of the large-scale circulation (Section 2.5) also give a smaller lapse rate than does convection.



**Fig. 1.20** Temperature profiles for Mars showing the effect of direct solar heating due to dust absorption. The shaded areas show the region of Mariner 6 and 7 observations. The curves at the left are calculated for a clear  $\text{CO}_2$  atmosphere and at the right for one containing dust. [Calculations are due to GIERASCH and GOODY (1972).]

Because the surface pressure is so low, the greenhouse effect is weak, and the surface temperatures undergo large diurnal variations during the Martian day of 24.660 hr (Fig. 1.21). The Viking entry results are shown in Fig. 1.22. From 0 to 120 km, a combination of directly sensed data and densities from drag deceleration was used. At greater heights, individual densities were obtained by a mass spectrometer. The atmosphere was much less dusty for these 1976 measurements than for the 1969 results, shown in Fig. 1.20, and



**Fig. 1.21** Surface temperatures on Mars, calculated for a clear atmosphere based on Mariner 9 infrared radiometer observations. [Adapted from KIEFFER *et al.* (1973).]

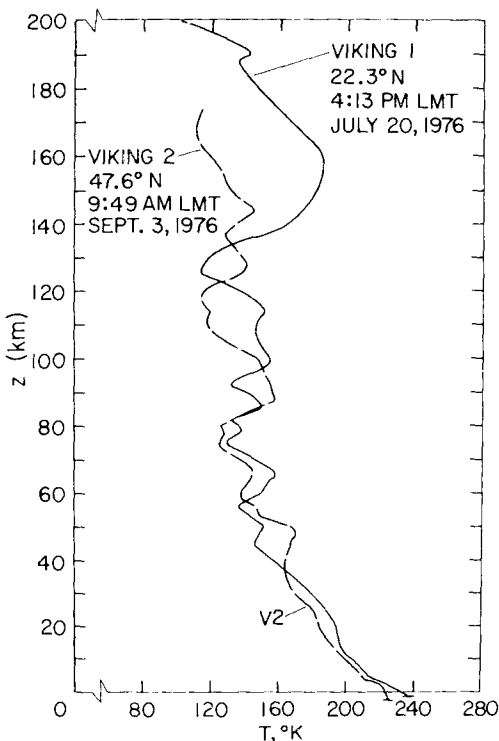


**Fig. 1.22** Martian temperature profiles from synthesis of Viking entry data. [After SEIFF and KIRK (1977).]

has a correspondingly larger lapse rate. As for Venus, there is no stratosphere and a very poorly defined mesopause. There is no evidence of a thermosphere in the Viking 2 data; even for Viking 1 the typical temperature is only 160°K.

Water vapor is present in small, highly variable quantities. It can be observed from Earth when the Doppler shift is large enough to move the Martian absorption lines away from the telluric ones (Fig. 4.11). It was also studied in detail by the Viking Orbiters. In the illuminated part of the winter hemisphere the abundance can drop below 1  $\mu\text{m}$  of precipitable water ( $10^{-4} \text{ g cm}^{-2}$ ); the largest value seen by Viking was 100  $\mu\text{m}$  near the north polar cap just after it had shrunk to its smallest size. This residual cap was therefore deduced to be water ice. A value around 10  $\mu\text{m}$  is fairly typical.

The atmosphere is always dusty, and dust storms on several scales are frequent. The largest scale covers the whole planet; one of these global storms was in progress in 1969 when Mariners 6 and 7 arrived, and only the tops of four huge volcanoes could be seen. Clouds and hazes of water frost are frequent, and  $\text{CO}_2$  itself condenses over the winter pole. These polar caps disappear, except for small remnants, in the summer season. The marked

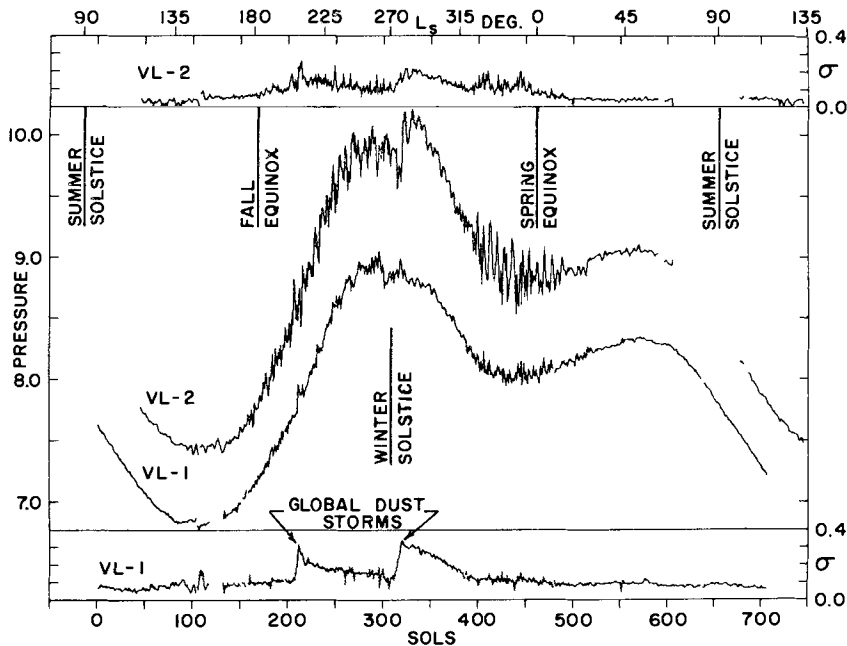


**Fig. 1.23** The annual cycles of atmospheric pressure at the two Viking landers. The strips at top and bottom show the standard deviation for each Martian day. [After HESS *et al.* (1980).]

effect on the atmospheric pressure is seen in the data from the Viking landers in Fig. 1.23. Both vehicles were in valleys and, therefore, obtained pressures appreciably greater than the more typical 6 mbar.

Figure 1.23 also shows the effects of Martian weather in the irregular oscillations of pressure about a smooth curve and in the upper and lower data sets which show the variability of pressure within each sol (Martian day). These fluctuations are particularly marked during two global dust storms.

The global circulation is similar to that of the Earth in many ways. Although the latent-heat effects of water are essentially lacking, there is the new feature of migration of 25% of the atmosphere into and out of the polar caps. The enhanced weather activity during late fall and late winter are evident in the pressure data of Lander 2, which was closer to the cap than Lander 1.

#### 1.8.4 Mars' Thermosphere

The composition of the region above 120 km is shown in Fig. 1.24 for Viking 1 conditions with a thermopause temperature of just over 200°K.

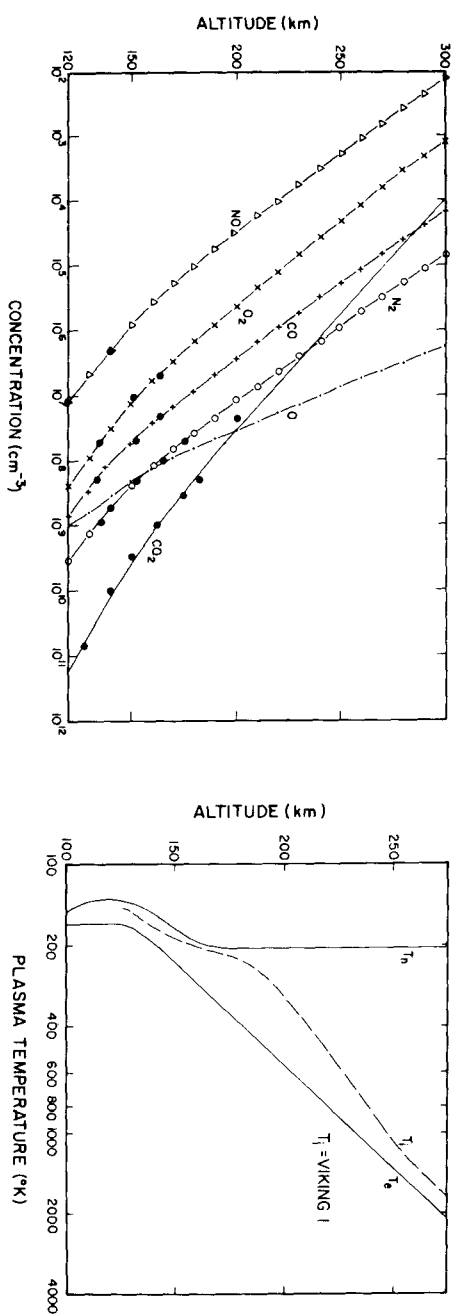


Fig. 1.24 Model Martian thermosphere consistent with neutral and ion data from the two Viking landers. Neutral, ion, and electron temperatures are shown at the right. [After HANSON *et al.* (1971).]

Mass spectrometric data are shown as black dots, and the model as a whole is consistent with ionospheric data. Except for the larger scale heights and the presence of NO, the resemblance to Venus (Figs. 1.16 and 1.17) is close.

However, closer examination shows that Mars is relatively deficient in O and CO. A conventional place to make the comparison is at a  $\text{CO}_2$  column density of  $4 \times 10^{16} \text{ cm}^{-2}$ , which is at unit zenith optical depth for ionizing radiation, and can therefore be loosely called the *ionospheric peak*. The height happens to be near 140 km for the day sides of both planets. According to Fig. 1.16, the O and CO mixing ratios on Venus are 13% and 9%, respectively; Fig. 1.24 shows 1.5% and 0.6%, respectively. The ratios are both near 10, most of which is explained by the ratio of solar fluxes, 4.5, responsible for the photolysis of  $\text{CO}_2$ . The remaining factor of 2 must reflect different sink strengths, which are almost entirely due to downward transport of the gases out of the region where they are produced. This transport must be about twice as effective on Mars as on Venus.

We now return to the thermospheric temperature profiles shown in Fig. 1.22. They were observed less than two months apart, and both refer to the day side. The mesopause height, computed as in Section 1.7.4, is about 100 km. Thus, even the Viking 1 profile bears very little resemblance to a terrestrial thermosphere such as shown in Fig. 1.1—anything resembling a mesopause is seen only at 130 km.

The temperature rise across the thermosphere should be nearly the same for Mars and Venus (Problem 1.12). Mars, therefore, seems to violate the model of Section 1.7.4 even more thoroughly than Venus. Further information is available from radio occultation studies with the Viking orbiters and Mariner 4, 6, 7, and 9. These results are collected in Fig. 1.25, along with a representation of solar activity. The measured quantity is the topside scale height of the electron density, shown on the left of the figure proper. A temperature can be obtained only through a model, and the one adopted for the scale on the far left assumes an atmosphere of pure  $\text{CO}_2$ , with ions of  $\text{CO}_2^+$  only. The 1978 point from Viking is 200°K. On both Mars and Venus,  $\text{O}^+$  and  $\text{O}_2^+$  are important, and a model including them gives a lower temperature for the same observed electron scale height. A representative value from Fig. 1.22 is 150°K or perhaps slightly less. To a first approximation, therefore, the temperature scale in Fig. 1.25 should be multiplied by 0.75. The highest point (1969) becomes 300°K. This is comparable to the Venus temperatures in 1980, also a year of high solar activity. However, Venus conditions since then seem to be much less variable than indicated for Mars.

There are no data at all for the nightside thermosphere; the electron density has never been high enough to detect. The rapid rotation of Mars leaves only 12 hours for cooling, which should be slow at the low

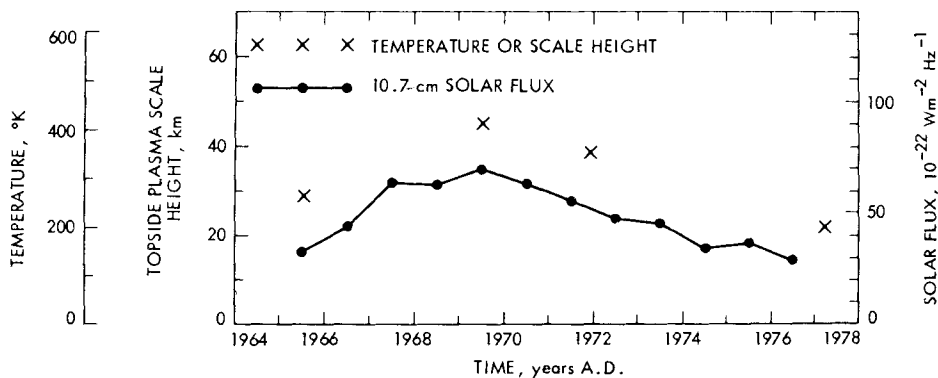


**Fig. 1.25** Ionospheric scale heights from Mariner and Viking radio occultations with a solar-flux index for comparison. The temperature scale is valid only for pure  $\text{CO}_2$  ions, as discussed in the text:  $\times$ , temperature or scale height; ●, 10.7 cm solar flux. [After FJELDBØ *et al.* (1977).]

temperatures observed on the day side. This argument suggests that the diurnal variation should be small, but our understanding is too poor for a confident prediction.

### 1.8.5 Mercury and Moon

These two objects have much in common, but the Moon lacks a planetary magnetic field and has much less atmosphere. The rest of this section will therefore be devoted to Mercury. An upper bound ( $2 \times 10^{-12}$  bar) to the total pressure follows from the absence of detectable absorption at the limb below 950 Å. The corresponding bound on the number density is  $4 \times 10^7 \text{ cm}^{-3}$ . However, resonance scattering by H and He at 1216 and 584 Å gives densities of 8 and  $4500 \text{ cm}^{-3}$  on the day side. There is much more helium on the night side, as inferred from its twilight effects. The larger density, at the much lower temperature, is required to balance the fluxes across the terminator. This problem is treated in Section 7.2.5.

Ground-based observations have found the Na Fraunhofer D lines in emission. The mechanism is almost certainly resonant scattering of sunlight by sodium vapor in Mercury's atmosphere. The total column abundance is estimated at  $8.1 \times 10^{11} \text{ atom/cm}^2$ , which corresponds to a surface density at the subsolar point of about  $1.5 \times 10^5 \text{ atom/cm}^3$ . Thus, sodium is at least a major constituent of Mercury.

Later Earth-based spectra also showed the potassium resonance lines at 7699 Å. The column abundance ratio is approximately  $[\text{Na}]/[\text{K}] = 100$ .

## 1.9 Atmospheric Structure in the Outer Solar System

The four Jovian planets, Jupiter, Saturn, Uranus, and Neptune, have extremely deep atmospheres of H<sub>2</sub> with roughly 10% (by number) He. They contain (or are expected to contain at deeper levels) the hydrides of the abundant elements C, N, and O—that is, methane (CH<sub>4</sub>), ammonia (NH<sub>3</sub>), and water vapor (H<sub>2</sub>O). Their mixing ratios tend to be around 0.1% on Jupiter and Saturn and may rise to 1% or even more on Uranus and Neptune. All but methane are nearly absent above levels of a few tenths of a bar, and this gas is nearly transparent above 1400 Å. Ultraviolet solar radiation is therefore much more prevalent in the stratospheres and mesospheres than on the terrestrial planets (although the incident fluxes are much smaller, 0.1–4% of the values on Earth).

Titan, the large satellite of Saturn, has a very substantial atmosphere of N<sub>2</sub> with a few percent of methane. In the Jovian system, Io has a thin SO<sub>2</sub> atmosphere, and the other three Galilean satellites (Europa, Ganymede, and Callisto) have exposed ice and, therefore, undoubtedly at least some water vapor. Methane is seen on Triton and Pluto.

The data shown above for Venus and Mars are heavily based on direct measurements within the atmospheres. No such data are available in the outer solar system. Remote-sensing data from spacecraft are available for the Jupiter, Saturn, and Uranus systems. Neptune will be visited in 1989. For Pluto, all the data come from Earth and Earth orbit. (See Appendix IV.)

### 1.9.1 Jupiter

The temperature profile in Fig. 1.26 was obtained by inversion of infrared radiances, combined with radio-occultation data to fix the helium abundance (Section 4.4). The evidence for the three cloud layers is more or less indirect; their composition is based almost entirely on expected abundances combined with vapor pressures. The presence of at least two separate layers is supported by imaging, inferences from spectroscopy, and infrared radiometry, and there is some evidence for three layers.

If Jupiter has a surface, it may be at a depth of tens of thousands of kilometers and a pressure of a magabar. Heights must therefore be measured from a totally arbitrary level, and there is no unanimity on which level to choose. The primary scale in Fig. 1.26 is the logarithm of pressure, plotted downward, and this practice is common. The height reference is the estimated H<sub>2</sub>O cloud base; other choices are 1 bar, the ammonia cloud top, 1 mbar (as in Fig. 1.27), and 1 μbar.

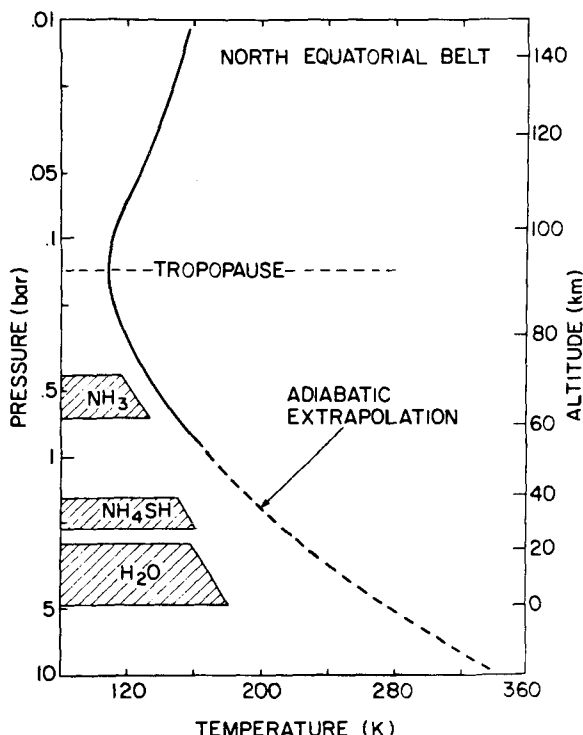


**Fig. 1.26** Jovian temperatures and schematic cloud structure, based primarily on Voyager infrared data. The height scale starts at the cloud base, approximately 5 bars. [After KUNDE *et al.* (1982).]

Figure 1.26 shows the tropopause at about 140 mbar and 105°K. The radiative-convective boundary is probably near 400 mbar, the ammonia cloud top. Jupiter's internal heat flux (Table 1.3) is sufficient to ensure convective transport at depths below a few bars, to which solar radiation is expected to penetrate. A very slightly superadiabatic lapse rate is therefore expected at all depths below 400–600 mbar. In practice, the difference is so small that the adiabatic profile can be used. This lapse rate is 1.9°K/km to temperatures of a few hundred degrees; at deeper levels the specific heats begin to rise and real-gas effects become appreciable.

The internal heat flux is obtained from the difference between the observed effective temperature  $T_{\text{eff}}$ , 125°K, and the solar-equilibrium temperature, 106°K, obtained from (1.2.46). It is believed that Jupiter is still in a late phase of its *Helmholtz contraction* from an initial state of much lower density and is converting the released gravitational energy into heat.

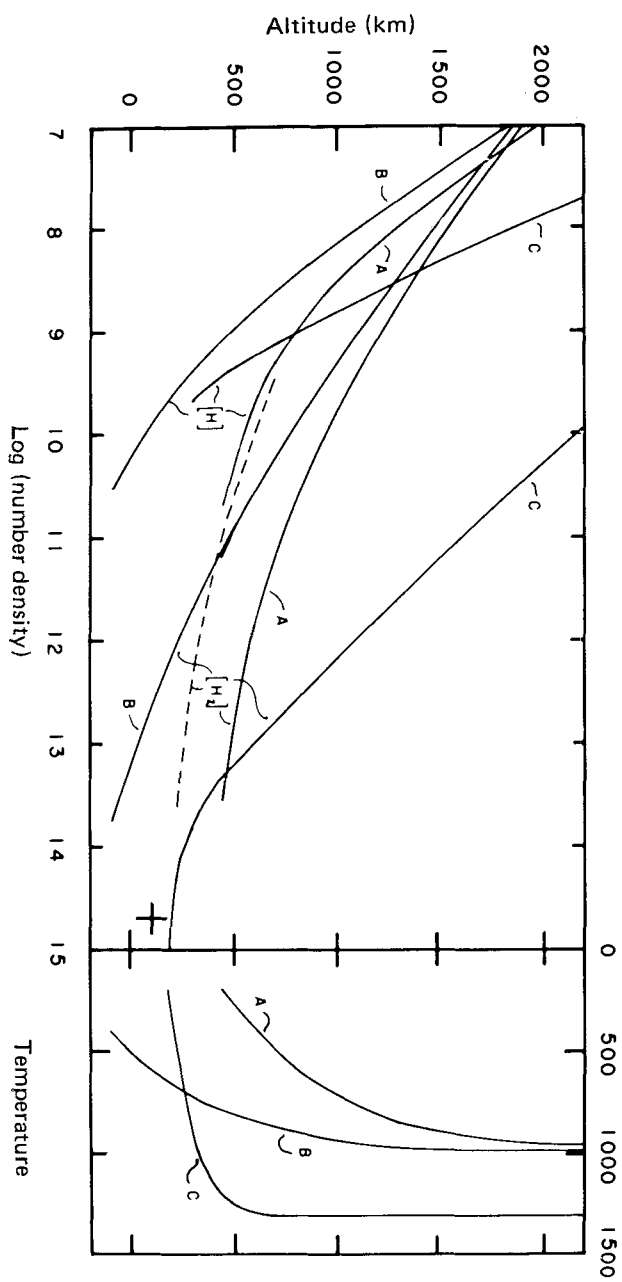


**Fig. 1.27** Jovian thermosphere, based on Voyager ultraviolet occultation data; the + point is from earth-based stellar occultations. Curves A and B fit the above data; curve C would be required to fit ionospheric data with no vertical transport other than diffusion. Helium is omitted because the observations were not sensitive to it. [After McCONNELL *et al.* (1982).]

**TABLE 1.3** Characteristics of the Jovian Planets

|  | Jupiter  | Saturn | Uranus | Neptune |
|--|----------|--------|--------|---------|
| Mean density ( $\text{g/cm}^3$ )                       | 1.34     | 0.70   | 1.58   | 2.30    |
| Effective temperature ( $^\circ\text{K}$ )             | 124.4    | 95.0   | 58     | 55.5    |
| Equilibrium temperature ( $^\circ\text{K}$ )           | 109.5    | 82.3   | 57     | 46      |
| Total flux/solar heat                                  | 1.668    | 1.78   | <1.3   | 1.1     |
| Internal flux ( $\text{erg cm}^{-2} \text{sec}^{-1}$ ) | 5444     | 2000   | <180   | 285     |
| Adiabatic lapse rate ( $^\circ\text{K}/\text{km}$ )    | 1.9      | 0.84   | 0.85   | 0.86    |
| Tropopause temperature ( $^\circ\text{K}$ )            | 105      | 85     | 54     | 52      |
| Tropopause pressure (mbar)                             | 140      | 80     | 100    | 200     |
| Exospheric temperature ( $^\circ\text{K}$ )            | 700–1000 | 420    | 700    | —       |

Figure 1.26 shows a well-developed stratosphere, whose full extent is not included. Radio-occultation data extend somewhat higher and, along with other data, suggest a stratopause at about 1 mbar and  $160\text{--}170^\circ\text{K}$  overlain by an isothermal mesosphere. There are two principal heat sources, both from solar radiation: the  $3.3\text{ }\mu\text{m}$  band ( $v_3$  fundamental) of methane and absorption in the ultraviolet and blue, which is attributed to a dust or smog of photochemical origin and greatly reduces the planetary albedo below that of the known atmospheric gases alone. Similar smogs are observed on Titan and Saturn; they are undoubtedly generated in the photochemistry of methane.

Cooling of the stratosphere and mesosphere is dominated by the  $7.7\text{ }\mu\text{m}$  ( $v_4$  fundamental) of methane and the  $12.2\text{ }\mu\text{m}$  ( $v_9$  band) of ethane ( $\text{C}_2\text{H}_6$ ). Although this latter molecule, which is of photochemical origin, is scarce, its band has a much better overlap with the Planck function than the methane band, and it therefore plays an important role. In the upper mesosphere, acetylene ( $\text{C}_2\text{H}_2$ ) is expected to become more and more abundant and exceed the ethane in the mesopause region. Acetylene has its  $v_5$  band at a still longer wavelength,  $13.7\text{ }\mu\text{m}$ , and probably controls the level at which all the heat from the thermosphere can be radiated (Section 1.6.2). These abundance estimates are entirely theoretical and very uncertain, and the mesopause level is therefore equally uncertain.

Pioneers 10 and 11, as well as Voyagers 1 and 2, measured the topside ionosphere by radio occultation (Section 5.3.3). If the scale height can be interpreted in terms of a proton-electron plasma, the temperatures found are  $750\text{--}1000^\circ\text{K}$ . It is expected that this plasma temperature is not significantly greater than the gas temperature. A serious observational difficulty is exhibited below the 1000-km level of Fig. 5.12. This part of the ionosphere is highly stratified, rendering analysis of the occultation data very difficult and the results uncertain. The reason is multipath propagation: more than one ray can reach the observer at a given instant. This difficulty is so severe that

the corresponding Voyager results have not been published, more than five years after the first encounter with Jupiter.

An important advance made by the Voyagers was to obtain solar and stellar occultations (properly called eclipses) in the ultraviolet region from 580 to 1600 Å, which includes the ionization continuum of all gases except helium, as well as bands and other continua at the longer wavelengths. Densities of H and H<sub>2</sub> obtained in this way are shown in Fig. 1.27 (curves A and B). The differences between these two sets of curves reflect the uncertainties of the analysis. The “plus” symbol in the lower right corner was obtained from Earth-based stellar occultation. Helium is present, but is not observable in the wavelength region used. Curves C are the densities required to explain the ionospheric densities by standard theory. It is clear that this theory does not include some important effect or effects, probably upward transport of plasma by winds or external electric fields. Nevertheless, as the right-hand panel of Fig. 1.27 shows, the exospheric temperature is still found to be of order 1000°K.

Application of (1.7.26) gives a predicted temperature rise across the thermosphere of about 15°K (Problem 1.13). Clearly a much stronger source of heat than solar ionizing radiation must be present. Suggested sources are dissipation of gravity waves generated in the troposphere, or soft electrons, either precipitating from outside the atmosphere or accelerated *in situ* by electric fields. They must be soft (that is, very easily absorbed) so that their energy will be dissipated at high altitudes; this energy could be a few electron volts up to a few tens of electron volts. Other phenomena (intense day airglow; high-latitude auroras) also suggest the presence of nonthermal electrons, some of which must have energies greater than the 12 eV photons that are observed. If the heat is deposited at the same height as solar ionizing energy, the flux required is 0.25–0.5 erg cm<sup>-2</sup> sec<sup>-1</sup> (cf. Problem 1.13).

## 1.9.2 Saturn, Uranus, and Neptune

Representative temperature profiles for Saturn are shown in Fig. 1.28. The tropopause temperature is around 85°K at the 80 mbar level. Cloud layers are expected at the same temperatures shown for Jupiter in Fig. 1.26. The ammonia layer, at 150°K, would therefore be somewhat deeper than 1 bar. The base of the H<sub>2</sub>O cloud (280°K) is at 11 bars, if the lapse rate is adiabatic as expected. The internal heat flux is about one-third of Jupiter’s and therefore a similar fraction of the absorbed solar energy (Table 1.3). However, models of Saturn’s Helmholtz contraction do not provide nearly this amount of energy. Instead, it is believed that Saturn is in the process of differentiating: at great depths, helium becomes insoluble in hydrogen, forming droplets that

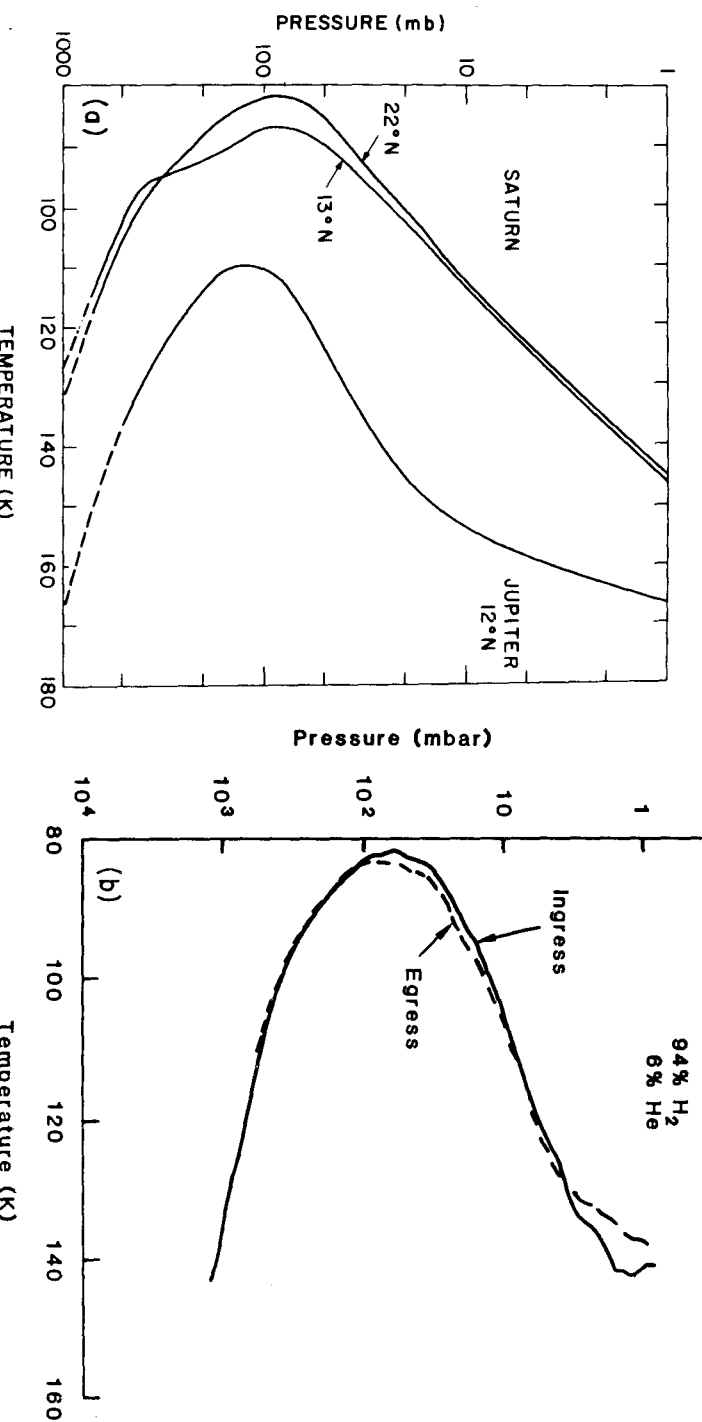
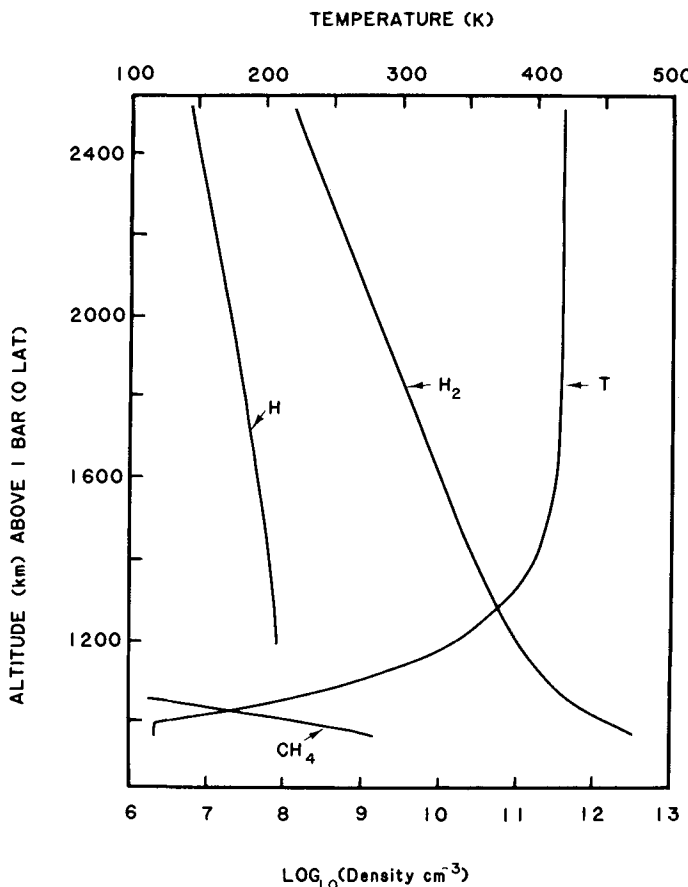


Fig. 1.28 Saturn temperature profiles obtained from (a) infrared and (b) radio-occultation data. [After HANEL *et al.* (1981) and TYLER *et al.* (1982).]

sink and release gravitational energy. Jupiter's interior is too hot for this to happen. Considerable support for the presence of differentiation is given by Saturn's helium abundance, which is considerably less than that of Jupiter (Table 4.1).

A stratospheric temperature rise is evident in Fig. 1.28, with a suggestion in the radio data of a stratopause near 1 mbar. There are no stellar occultation data to give a guide to mesopause conditions, but it appears that the mesospheric temperature could be around 150°K.

Data for the thermosphere and exosphere are shown in Fig. 1.29; as for Fig. 1.27, helium is omitted because the ultraviolet occultation experiment



**Fig. 1.29** Saturn's thermosphere from ultraviolet occultation. As in Fig. 1.27, the experiment was insensitive to helium. [After SMITH *et al.* (1983).]

could not observe it. Just as for Jupiter, the exospheric temperature is far higher than expected for solar heating alone, and all the remarks about this area made for Jupiter apply equally well to Saturn and Uranus.

Uranus and Neptune have considerably larger mean densities than Jupiter and Saturn (Table 1.3). Moreover, they have less gravitational compression, and must therefore contain much less hydrogen and helium in proportion to the heavier ice- and rock-forming elements. Methane abundances are much greater (1% or more); ammonia and water vapor are not observable at the low temperatures of these atmospheres.

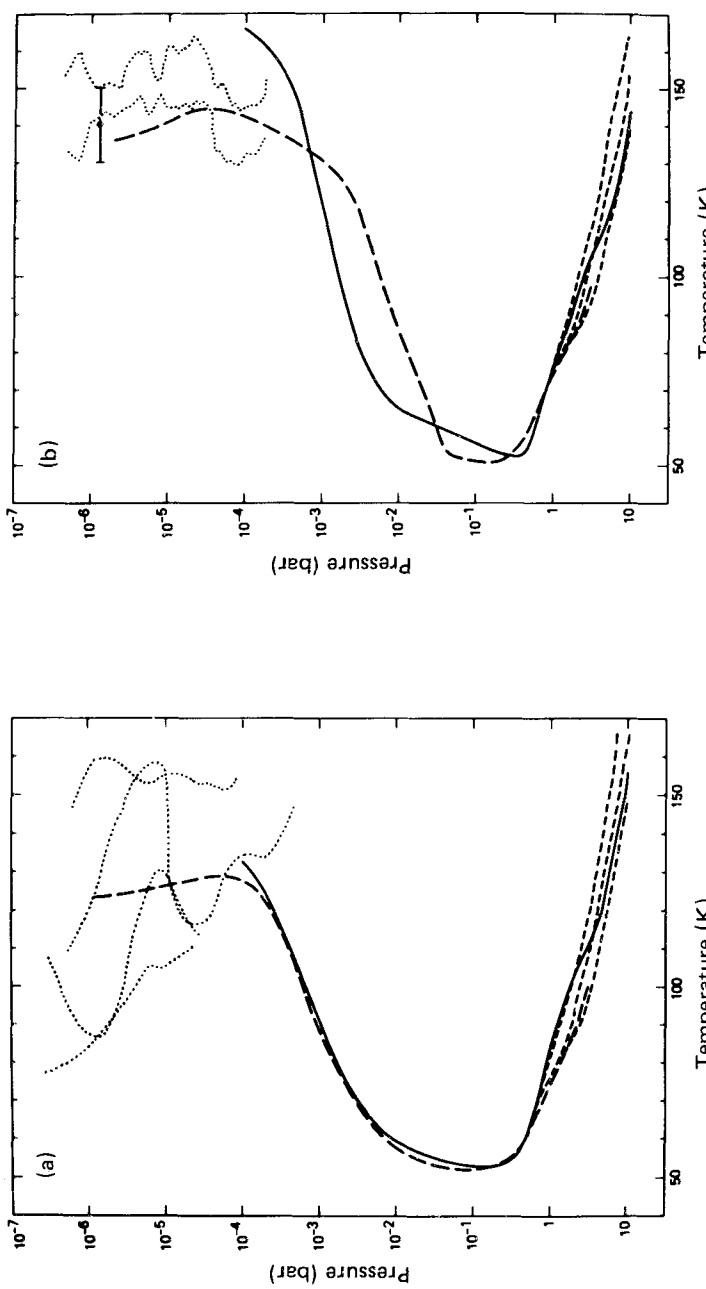
Temperature profiles are shown in Fig. 1.30. The solid and dashed curves are obtained by inversion of Earth-based infrared data, which have almost no information content for pressures below 1–10 mbar. In the mesospheres, the dotted curves represent results from stellar occultations. Usable events are much more common for Uranus and Neptune than for brighter planets, because much fainter stars can be observed. At the very cold temperatures reached in these atmospheres, condensation of methane becomes likely. This effect is responsible for the differences among the various curves of Fig. 1.30 in the 70–100°K (1–3-bar) region, which pertain to mixing ratios of 0.2, 2, and 4%, reading downward. These values refer to the deeper atmospheres and are reduced at the higher levels by cloud formation; the clouds appear between the bends in the curve.  $\text{H}_2\text{O}$  clouds could form below the 100-bar level and might extend as deep as 500 bars if the abundance is several percent. Clouds have been photographed on Neptune but not on Uranus; Neptune also shows photometric variations that are absent on Uranus.

As Table 1.3 indicates, Neptune has a detectable internal heat flux, while Uranus does not. It is therefore conceivable that the lapse rate on Uranus becomes subadiabatic for pressures greater than a few bars. It is equally possible that the true heat flow is just below the detection limit.

Both planets have stratospheres, although the lower, near-isothermal part is almost certainly much deeper on Uranus. Both mesospheres seem to be at 140–150°K. The Voyager encounter with Uranus obtained results analogous to Fig. 1.29, but with an exospheric temperature of 700°K. Both the high temperature and the presence of discrete aurora suggest nonsolar heat sources as on Jupiter and Saturn.

All four Jovian planets have nearly the same mesospheric temperature, despite solar and planetary heat sources varying by a factor of 30. The likely explanation lies in the spectral location of the  $\text{C}_2\text{H}_6$  and  $\text{C}_2\text{H}_2$  bands discussed in Section 1.9.1. At 150°K, the peak of the Planck function is at 19  $\mu\text{m}$ , and it only barely overlaps the 12.2  $\mu\text{m}$  band of ethane; if the temperature drops, the overlap quickly disappears. Thus, there is a very effective thermostat which can accommodate a wide range of heat inputs.

Fig. 1.30 Temperature profiles for (a) Uranus and (b) Neptune from Earth-based infrared and stellar-occultation data. [After ORTON and APPLEY (1984).]



One unique property of Uranus is its obliquity, which puts the axis almost in the orbital plane. Each hemisphere suffers an intense, 42-year winter which must have profound effects on the stratosphere and mesosphere. At higher pressures, the effects are minimized by a long thermal time constant. Further discussion appears in Section 2.7.

### 1.9.3 Titan

Titan can be regarded as a terrestrial planet located in the outer solar system. Its mean density suggests roughly equal proportions of rocky and icy material. The atmosphere is mostly N<sub>2</sub>, with a surface at 1496 mbar and 94.0°K. Methane absorptions are prominent in the spectrum; the abundance is around 1 % in the stratosphere and perhaps 3 % near the surface. As these figures imply, a methane cloud layer is suspected to be present, but it is hidden by a thick, pervasive hydrocarbon smog which gives the body a dark orange (really, brown) color. The smog occupies the upper troposphere and middle stratosphere; the cloud, if present, would be in the middle troposphere. A very close pass by Voyager 1 gave excellent infrared data and radio and ultraviolet occultations. Figure 1.31 shows the radio temperature profile, which includes information from the infrared. The tropopause is at 42 km, 128 mbar, 71.4°K. Temperatures around 170°K are reached near 1 mbar, which is probably the stratopause level.

The ultraviolet occultation probed the upper thermosphere and exosphere. The temperatures shown on Fig. 1.32 are very similar to that found at the stratopause. Application of the hydrostatic equation (Problem 1.14) shows

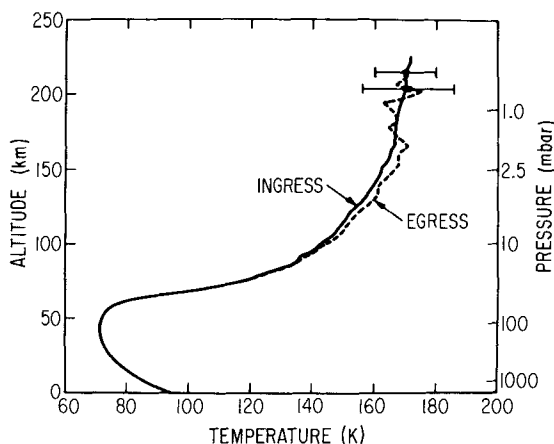


**Fig. 1.31** Titan temperatures by radio occultation for a mean mass of 28 amu consistent with infrared results. [After HUNTEMAN *et al.* (1984).]

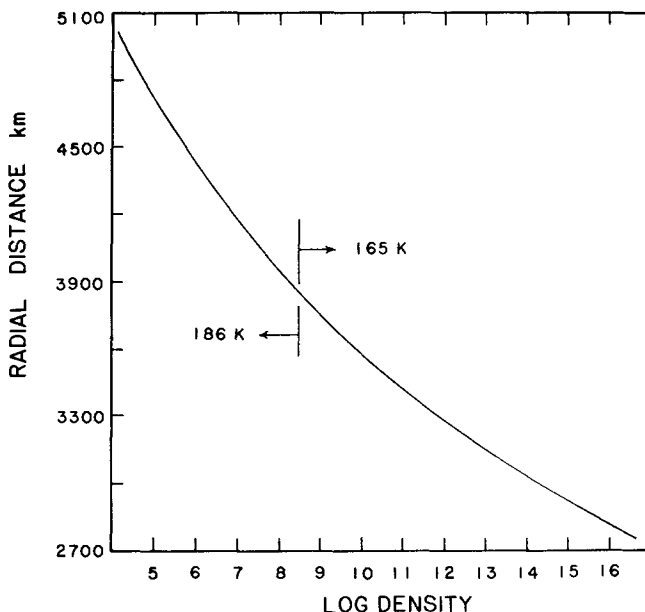


**Fig. 1.32** Density (primarily  $N_2$ ) of Titan's upper atmosphere from Voyager ultraviolet occultation. To compare the heights with Fig. 1.31, subtract 2575 km. [After SMITH *et al.* (1982).]

that the mean temperature between these levels is also similar. This whole region is unlikely to be strictly isothermal, but there is no further information. The density profile in Fig. 1.32 is noticeable curved, even though it is made up of two isothermal sections. The reason is the large variation of gravity with height in this extended atmosphere.

No ionosphere could be detected at a sensitivity level of  $2000 \text{ cm}^{-3}$ . There are two reasons: the regions probed were near sunset and dawn, and this molecular atmosphere (including methane and other hydrocarbons) provides very fast recombination. Figure 1.32 indicates a temperature step of  $21^\circ\text{K}$  at a density of  $3 \times 10^8 \text{ cm}^{-3}$ , which could perhaps represent a thermosphere, but this density is much less than normal for such a region. In any case, there is no sign of the many hundred degrees of temperature rise seen on Jupiter and Saturn.

Titan's stratosphere is the site of very active hydrocarbon photochemistry (Section 6.4.3). The principal products are the brown smog and ethane,  $C_2H_6$ , at the expense of methane, which must be replenished from below. The amount of ethane accumulated over the age of the solar system amounts to several hundred meters of liquid, which presumably exists at the surface along with dissolved methane, nitrogen, and heavier molecules.

### 1.9.4 Pluto, Triton, and the Galilean Satellites

Pluto's near-infrared spectrum shows several weak but well-defined methane absorptions. The shapes of the bands are more consistent with gas than ice as the absorber; moreover, at the expected temperature ( $57^{\circ}\text{K}$ ), any ice would have a substantial vapor pressure. If all the absorption is attributed to gas, the abundance is  $2700 \pm 700$  atm-cm, and the surface pressure is  $150 \mu\text{bar}$ . Because of Pluto's large orbital eccentricity, its equilibrium temperature varies appreciably. The measurements quoted here were made in 1980, near the warmest part of the cycle. Considerably lower atmospheric pressures probably occur at other times in Pluto's year.

Triton, the largest satellite of Neptune, also shows methane absorptions, but they are weaker and change appreciably as different sides of Triton face the Earth. The most likely explanation is that at least a major part of the absorption occurs in methane ice, which would be more abundant on one side. It is also possible that there are large topographic differences between the two hemispheres, with more gas over the lower one. In addition, an absorption at  $2.16 \mu\text{m}$  seems to be due to liquid or solid  $\text{N}_2$ . The vapor pressure at  $64^{\circ}\text{K}$  is  $130 \text{ mbar}$ , but the actual temperatures may be somewhat lower, especially at high latitudes and at night. The methane partial pressure should be about  $10^{-3}$  times smaller.

Jupiter's Galilean satellites fall into two very different groups: Europa, Ganymede, and Callisto, which exhibit water-ice absorptions, and Io, whose surface is mostly sulfur and  $\text{SO}_2$ . At Io's subsolar temperature, the vapor pressure of  $\text{SO}_2$  is about  $10^{-7} \text{ bar}$ . This figure is very sensitive to the assumed albedo, and if the  $\text{SO}_2$  frost is concentrated in white patches, which would be colder than average, the estimated subsolar pressure drops to  $7 \times 10^{-9} \text{ bar}$ . Near the terminator the vapor pressure drops to  $10^{-11} \text{ bar}$ , and on the night side it is less than  $10^{-16} \text{ bar}$ . In addition, at any one time there are several volcanoes (or geysers) erupting to heights as great as  $300 \text{ km}$  and probably ejecting large quantities of  $\text{SO}_2$  vapor. Whether the actual pressures resemble the vapor pressures is uncertain and is a subject of lively discussion. It has been suggested that the  $\text{SO}_2$  frost is located deep in a porous surface, where its temperature excursions would be greatly reduced. Also, if the pressure gradients are large, strong winds will blow away from the subsolar region and will tend to equalize the pressures. Photochemical action on  $\text{SO}_2$  must produce at least some  $\text{O}_2$  (see Section 6.4.4), which could contribute appreciably to the total pressure, especially on the night side.

Empirical information is indirect and ambiguous enough to permit more than one interpretation. Pioneer 10 observed ionospheres at both limbs by radio occultation, and they can be accounted for by electron bombardment of a  $10^{-11} \text{ bar}$  atmosphere. The infrared instrument on Voyager 1 detected  $\text{SO}_2$

directly, with a surface pressure around  $10^{-7}$  bar, but the line of sight passed through a volcanic plume, which may have been the cause of the absorption. There is no specific reason to apply the same explanation to the Pioneer results, although it cannot be ruled out.

The computed exospheric temperature is  $1000^{\circ}\text{K}$ , consistent with the large extent of the ionosphere. The temperature is high because  $\text{SO}_2$  absorbs strongly at much longer wavelengths than the gases found in any of the planets.

Io's orbit is surrounded by a torus containing atoms and ions of O, S, and Na. The ionized part, or plasma, is at a temperature of  $50,000^{\circ}\text{K}$  or 4 eV, and it radiates copiously in the  $600\text{--}1000\text{ \AA}$  region. There can be no doubt that Io is the source of the material, but the mechanisms at work have not been fully identified. There is little doubt that a major one is sputtering, or ejection by impact of energetic positive ions.

No atmospheres have been detected on Europa, Ganymede, or Callisto. An ultraviolet occultation measurement from Voyager 1 set an upper limit for Ganymede of  $10^{-11}$  bar (except for gases that absorb strongly only below  $910\text{ \AA}$ ). All three bodies have water-ice absorptions in their spectra, and should have partial pressures of water vapor in the neighborhood of  $10^{-15}$  bar, which could be increased by sputtering. Photolysis and escape of hydrogen should generate an  $\text{O}_2$  atmosphere. The surface pressure is computed to be about  $10^{-12}$  bar (see Section 6.4.4). Alternatively, if the  $\text{H}_2\text{O}$  abundance is  $10^{-14}$  bar or greater, the  $\text{O}_2$  is predicted to jump to  $10^{-6}$  bar, which is far above the Voyager limit for Ganymede.

## BIBLIOGRAPHICAL NOTES

### Section 1.2 Radiative Equilibrium

Atmospheric radiation is the subject of three major books:

GOODY, R. M. (1964), "Atmospheric Radiation," Clarendon Press, Oxford,  
is mainly a theoretical account of absorption and heat transfer by atmospheric gases.

KONDRATYEV, K. YA. (1969), "Radiation in the Atmosphere," Academic Press, New York,  
deals more with measurements, radiation scattering, global heat balance, and so forth.

ZUEV, V. E. (1974), "Propagation of Visible and Infrared Radiation in the Atmosphere,"  
Wiley, New York,

treats absorption and scattering as well, but the author devotes the final third of his book to the propagation of laser beams.

Radiative transfer is treated extensively in all the above books, but the standard reference is

CHANDRASEKHAR, S. (1950), "Radiative Transfer," Clarendon Press Oxford, (reprinted  
by Dover, New York, 1960).

The common belief that the heating of a greenhouse is due to the inhibition of convection by

the roof can be traced to experiments described in 1909 by R. W. Wood. This view has been challenged by

SILVERSTEIN, S. D. (1976), Effect of infrared transparency on the heat transfer through windows: A clarification of the greenhouse effect, *Science* **193**, 229–231,

who finds that the infrared radiative blanketing is not trivial and the physical analogy with the atmosphere is fairly appropriate after all.

Radiative-convective equilibrium has been the subject of many computer modeling studies. Notable as one of the first thorough attempts along these lines is

MANABE, S. and STRICKLER, R. F. (1964), Thermal equilibrium of the atmosphere with a convective adjustment, *J. Atmos. Sci.* **21**, 361–385.

A thorough review of modeling techniques and results is

RAMANATHAN, V. and COAKLEY, J. A., JR. (1978), Climate modeling through radiative-convective models, *Rev. Geophys. Space Phys.*, **16**, No. 4 (Nov).

Some of the modelling has been concerned with climatic variations due to compositional changes (see Section 7.5).

### Section 1.3 Convection in the Troposphere

The breakdown of radiative equilibrium by convective activity was first noted by R. EMDEN in 1913. The surge of theoretical activity following discovery of the stratosphere in 1900 is documented by GOODY (op. cit. Chapter 8).

### Section 1.4 Latitude Variations of the Tropopause

The problem of the latitude variation of the tropopause and its dependence on departures from grayness was treated by

GOODY, R. M. (1949), The thermal equilibrium at the tropopause and the temperature of the lower stratosphere, *Proc. Roy. Soc. A* **197**, 487–505.

### Section 1.5 The Stratosphere

The photochemical theory for oxygen in the stratosphere is due to

CHAPMAN, S. (1930a), A theory of upper-atmospheric ozone, *Mem. R. Meteorol. Soc.* **3**, 103–125.

CHAPMAN, S. (1930b), On ozone and atomic oxygen in the upper atmosphere, *Phil. Mag.* **10**, 369–383.

CHAPMAN, S. (1931a), Some phenomena of the upper atmosphere (Bakerian Lecture), *Proc. Roy. Soc. A* **132**, 353–374.

and to

WULF, O. R. and DEMING, L. S. (1936a), The theoretical calculation of the distribution of photochemically-formed ozone in the atmosphere, *Terr. Magn.* **41**, 299–310.

WULF, O. R. and DEMING, L. S. (1936b), The effect of visible solar radiation on the calculated distribution of atmospheric ozone, *ibid.* pp. 375–378.

WULF, O. R. and DEMING, L. S. (1937), The distribution of atmospheric ozone in equilibrium with solar radiation and the rate of maintenance of the distribution, *ibid.* **42**, 195–202.

The concept that ionizing or dissociating radiation will create “layers” in the atmosphere was first stated quantitatively in

LENARD, P. (1911), Über die Absorption der Nordlichtstrahlen in der Erdatmosphäre, *SitzungsBer. d. Heidelberger Akad. d. Wissenschaften* **12**, 1–9,

and developed more fully for electromagnetic radiation in the first full-length book on radio propagation,

PEDERSON, P. O. (1927), “The Propagation of Radio Waves,” Copenhagen, Danmarks Naturvidenskabelige Samfund A, Nr. 15a, 15b.

However, it was CHAPMAN who developed the theory to an incredible degree of completeness, including the numerical integration of the equations for a rotating Earth. The "Chapman-layer" papers are

CHAPMAN, S. (1931b), The absorption and dissociative or ionizing effect of monochromatic radiation in an atmosphere on a rotating Earth, *Proc. Phys. Soc.* **43**, 26–45.

CHAPMAN, S. (1931c), The absorption and dissociative or ionizing effect of monochromatic radiation in an atmosphere on a rotating Earth, *Proc. Phys. Soc.* **43**, 483–501.

It was first proposed that the water vapor at the tropopause is saturated and that this cold trap limits the abundance of H<sub>2</sub>O at higher altitudes by E. GOLD in 1909 in a report to the British Association in Winnipeg. The concept is developed in

GOLD, E. (1913), The international kite and balloon ascents, *Geophys. Mem.* 1, No. 5, M.O. 210e (cf. p. 129ff.)

From a series of 16 ascents into the stratosphere between 1943 and 1945 during which humidity measurements were made, BREWER concluded that the low temperature of the tropical tropopause provides the cold trap and that meridional circulation accounts for the low humidity and high ozone content at higher latitudes:

BREWER, A. W. (1949), Evidence for a world circulation provided by the measurements of helium and water vapour distribution in the stratosphere, *Quart. J. Roy. Meteorol. Soc.* **75**, 351–363.

### Section 1.6 The Mesopause

The concept of the cold mesopause being strongly influenced by the onset of vibrational relaxation was developed by

CURTIS, A. R. and GOODY, R. M. (1956), Thermal radiation in the upper atmosphere, *Proc. Roy. Soc. A* **236**, 193–206.

### Section 1.7 The Thermosphere

The importance of conduction in maintaining the high temperatures in the thermosphere (which at that time could be only indirectly inferred) was first demonstrated in a classic paper by

SPITZER, L. (1949), The terrestrial atmosphere above 300 km, in "The Atmospheres of the Earth and Planets," (G. P. Kuiper, ed.), pp. 211–247, Univ. Chicago Press, Chicago, [2nd ed., 1952].

Thermospheric theory has since been developed extensively, most notably by

BATES, D. R. (1951), The temperature of the upper atmosphere, *Proc. Phys. Soc. B* **64**, 805–821.

BATES, D. R. (1959), Some problems concerning the terrestrial atmosphere above about the 100 km level, *Proc. Roy. Soc. A* **253**, 451–462,

NICOLET, M. (1960), The properties and constitution of the upper atmosphere, in "Physics of the Upper Atmosphere," (J. A. Ratcliffe, ed.), pp. 17–71, Academic Press, New York.

The heating of an upper atmosphere by the dissipation of mechanical energy is discussed and compared with radiation sources and sinks by

LEOVY, C. B. (1975), Some energy sources and sinks in the upper atmosphere, in "Atmospheres of Earth and the Planets," (B. M. McCormac, ed.), pp. 73–86, D. Reidel Publ. Co., Dordrecht, The Netherlands.

The treatment here of the mesopause condition, defining the mesopause as the height where vibrationally relaxed CO<sub>2</sub> has emitted the entire conductive flux drained from the thermosphere, follows

CHAMBERLAIN, J. W. (1962), Upper atmospheres of the planets, *Astrophys. J.* **136**, 582–593.

Radiation by NO is computed and compared with that by O in

KOCKARTS, G. (1980), Nitric oxide cooling in the terrestrial thermosphere, *Geophys. Res. Lett.* **7**, 137–140.

The derivation of Eq. (1.7.26) follows

HUNTER, D. M. and DESSLER, A. J. (1977), Soft electrons as a possible heat source for Jupiter's thermosphere, *Planet. Space Sci.* **25**, 817–821.

It is based on a less restricted development by

GROSS, S. H. (1972), On the exospheric temperature of hydrogen-dominated planetary atmospheres, *J. Atmos. Sci.* **29**, 214–218.

### Section 1.8.1 Venus

Radio emission from Venus and its interpretation in terms of the temperature and pressure at the planet's surface are discussed by

BARRETT, A. H. and STAELIN, D. H. (1964), Radio observations of Venus and the interpretations, *Space Sci. Rev.* **3**, 109–135,

WOOD, A. T., JR.; WATTSON, R. B.; and POLLACK, J. B. (1968), Venus: Estimates of the surface temperature and pressure from radio and radar measurements, *Science* **162**, 114–116.

Result of the Soviet Venera experiments have been summarized in

AVDUEVSKY, V.; MAROV, M. YA.; and ROZHDESTVENSKY, M. (1970), A tentative model of the atmosphere of planet Venus based on the results of measurements of spaceprobes Venera 5 and Venera 6, *J. Atmos. Sci.* **27**, 561–568.

MAROV, M. YA.; AVDUEVSKY, V.; KERZHANOVICH, V.; ROZHDESTVENSKY, M.; BORODIN, N.; and RYABOV, O. (1973), Venera 8: Measurements of temperature, pressure, and wind velocity on the illuminated side of Venus, *J. Atmos. Sci.* **30**, 1210–1214,

AVDUEVSKY, V.; MAROV, M. YA.; MOSKIN, B. E.; and RONOMOV, A. E. (1973), Venera 8: Measurements of solar illumination through the atmosphere of Venus, *J. Atmos. Sci.* **30**, 1215–1218.

The Mariner observations of Venus' temperature profile are reported in

FJELDBO, G.; KLIORE, A.; and ESHLEMAN, V. (1971), The neutral atmosphere of Venus as studied with the Mariner 5 radio occultation experiments, *Astron. J.* **76**, 123–140,

HOWARD, H. T., et al. (1974), Venus: Mass, gravity field, atmospheric, and ionosphere as measured by the Mariner 10 dual-frequency radio system, *Science* **183**, 1297–1301.

The temperature of the upper atmosphere of Venus is examined theoretically by

DICKINSON, R. E. (1976), Venus mesosphere and thermosphere temperature structure, *Icarus* **27**, 479–493.

Pioneer Venus probe and orbiter results are collected in a special issue of *J. Geophys. Res.* (1980) **85**(A13), 7573–8337.

Figures 1.16 and 1.19 are from

NIEMANN, H. B.; KASPRZAK, W. T.; HEDIN, A. E.; HUNTER, D. M.; and SPENCER, N. W. (1980), Mass spectrometric measurements of the neutral gas composition of the thermosphere and exosphere of Venus, *J. Geophys. Res.* **85**, 7817–7827.

Figure 1.17 is from

BRINTON, H. C.; TAYLOR, H. A., JR.; NIEMANN, H. B.; MAYR, H. G.; NAGY, A. F.; CRAVENS, T. E.; and STROBEL, D. F. (1980), Venus nighttime hydrogen bulge, *Geophys. Res. Lett.* **7**, 865–868.

A monograph incorporating Pioneer Venus and Soviet results is

HUNTER, D. M.; COLIN, L.; DONAHUE, T. M.; and MOROZ, V. I., eds (1983), "Venus," Univ. Arizona Press, Tucson, Arizona.

Figures 1.14 and 1.15 are from pp. 259 and 354. Figure 1.18 is from

MASSIE, S. T.; HUNTER, D. M.; and SOWELL, D. R. (1983), Day and night models of the Venus thermosphere, *J. Geophys. Res.* **88**, 3955–3969.

### Section 1.8.3 Mars

Infrared radiometer and radio occultation experiments on the Martian surface and atmosphere by Mariner 4 (1965), Mariners 6 and 7 (1969), Mariner 9 (1971–1972), and the Soviet Mars 2 and 3 (1971–1972) have been reviewed in

BARTH, C. A. (1974), The atmosphere of Mars, *Ann. Rev. Earth Planet. Sci.* **2**, 333–367.

The analysis of the low-atmosphere temperatures in terms of heating by dust absorption is due to

GIERASCH, P. J., and GOODY, R. M. (1972), The effect of dust on the temperature of Martian atmosphere, *J. Atmos. Sci.* **29**, 400–402.

Surface temperatures measured by Mariner 9 have been analyzed in

KIEFFER, H. H.; CHASE, S. C.; MINER, E.; MÜNCH, G.; and NEUGEBAUER, G. (1973), Preliminary report on infrared radiometric measurements from the Mariner 9 spacecraft, *J. Geophys. Res.* **78**, 4291–4312.

Viking results are reported in three special issues of *J. Geophys. Res.* (1977), **82**(28), 3951–4684; (1979), **84**(B6), 2793–3007; (1979), **84**(B14), 7909–8519. See, in particular,

HANSON, W. B.; SANATANI, S.; and ZUCCARO, D. R. (1977), The martian ionosphere as observed by the Viking retarding potential analyzers, *J. Geophys. Res.* **82**, 4351–4363.

SEIFF, A., and KIRK, D. B. (1977), Structure of the atmosphere of Mars in summer at mid-latitudes, *J. Geophys. Res.* **82**, 4364–4378.

FJELDBO, G.; SWEETNAM, D.; BRENKLE, J.; CHRISTENSEN, E.; FARLESS, D.; MEHTA, J.; SEIDEL, B.; MICHAEL, W., Jr.; WALLIO, A.; and GROSSI, M. (1977), Viking radio occultation measurements of the Martian atmosphere and topography: Primary mission coverage, *J. Geophys. Res.* **82**, 4317–4324.

Water-vapor results are discussed by

JAKOSKY, B. M., and BARKER, E. S. (1984), Comparison of ground-based and Viking Orbiter measurements of Martian water vapor: variability of the seasonal cycle, *Icarus* **57**, 322–334.

Figure 1.23 is from

HESS, S. L.; RYAN, J. A.; TILLMAN, J. E.; HENRY, R. M.; and LEOVY, C. B. (1980), The annual cycle of pressure on Mars measured by Viking Landers 1 and 2, *Geophys. Res. Lett.* **7**, 197–200.

### Section 1.8.5 Mercury and Moon

The Mariner 10 results on Mercury's atmosphere are discussed in

KUMAR, S. (1976), Mercury's atmosphere: A perspective after Mariner 10, *Icarus* **28**, 579–591.

BROADFOOT, A. L. (1976), Ultraviolet spectroscopy of the inner solar system from Mariner 10, *Rev. Geophys. Space Phys.* **14**, 625–627.

BROADFOOT, A. L.; SHEMANSKY, D. E.; and KUMAR, S. (1976), Mariner 10: Mercury's atmosphere, *Geophys. Res. Lett.* **3**, 577–580.

The detection of sodium in the atmosphere of Mercury was reported by

POTTER, A., and MORGAN, T. (1985), Discovery of sodium in the atmosphere of Mercury, *Science* **229**, 651–653.

Potassium was found slightly later:

POTTER, A. and MORGAN, T. (1986), Potassium in the atmosphere of Mercury, *Icarus*, **67**, 336–340.

### Section 1.9.1 Jupiter

A radiative-transfer analysis for deriving the structure of the troposphere and mesosphere of Jupiter is given in

WALLACE, L.; PRATHER, M.; and BELTON, M. J. S. (1974), The thermal structure of the atmosphere of Jupiter, *Astrophys. J.* **193**, 481–493.

The mesosphere and thermosphere results quoted here are from

STROBEL, D. F., and SMITH, G. R. (1973), On the temperature of the Jovian atmosphere, *J. Atmos. Sci.* **30**, 718–725.

The problems associated with the use of radio occultation experiments to obtain temperature profiles on Jupiter are discussed in

HUBBARD, W. B.; HUNTEM, D. M.; and KLORE, A. (1975), Effect of the Jovian oblateness on Pioneer 10/11 radio occultations, *Geophys. Res. Letts.*, **2**, 265–268,

HUNTEM, D. M. and VEVERKA, J. (1976), Stellar and spacecraft occultations by Jupiter: A critical review of derived temperature profiles, in "Jupiter," ed. T. Gehrels, pp. 247–283, Univ Arizona Press, Tucson,

ESHLEMAN, V. R. (1975), Jupiter's atmosphere: Problems and potential of radio occultation, *Science* **189**, 876–878.

A more recent review is

TRAFTON, L. M. (1981), The atmospheres of the outer planets and satellites, *Rev. Geophys. Space Phys.* **19**, 43–89.

Voyager results are reported in a special issue of *J. Geophys. Res.* (1981) **86**(A10), 8121–8844.

Figure 1.26 is from

KUNDE, V.; HANEL, R.; MAGUIRE, W.; GAUTIER, D.; BALUTEAU, J. P.; MARTEN, A.; CHEDIN, A.; HUSSON, N.; and SCOTT, N. (1982), the tropospheric gas composition of Jupiter's north equatorial belt ( $\text{NH}_3$ ,  $\text{PH}_3$ ,  $\text{CH}_3\text{D}$ ,  $\text{GeH}_4$ ,  $\text{H}_2\text{O}$ ) and the Jovian D/H isotopic ratio, *Astrophys. J.* **263**, 443–467.

The discussion of Jupiter's ionosphere follows

MCCONNELL, J. C.; HOLBERG, J. B.; SMITH, G. R.; SANDEL, B. R.; SHEMANSKY, D. E.; and BROADFOOT, A. L. (1982), A new look at the ionosphere of Jupiter in light of the UVS occultation results, *Planet. Space Sci.* **30**, 151–167.

### Section 1.9.2 Saturn, Uranus, and Neptune

A comprehensive monograph, incorporating Voyager results, is

GEHRELS, T., and MATTHEWS, M. S. eds. (1984), "Saturn," Univ. Arizona Press, Tucson, Arizona.

Special issues of journals are

*Icarus* (1983) **53** (2), 163–387, *J. Geophys. Res.* (1982) **88**(A11), 8625–9018.

Figures 1.28 and 1.29 are from

HANEL, R. A.; CONRATH, B.; FLASAR, F. M.; KUNDE, V.; MAGUIRE, W.; PEARL, J.; PIRRAGLIA, J.; SAMUELSON, R.; HERATH, L.; ALLISON, M.; CRUIKSHANK, D.; GAUTIER, D.;

- GIERASCH, P.; HORN, L.; KOPPANY, R.; and PONNAMPERUMA, C. (1981), Infrared observations of the Saturnian system from Voyager 1, *Science* **212**, 192–200.  
 TYLER, G. L.; ESHELMAN, V. R.; ANDERSON, J. D.; LEVY, G. S.; LINDAL, G. F.; WOOD, G. E.; and CROFT, T. A. (1982), Radio science with Voyager 2 at Saturn: Atmosphere and ionosphere and the masses of Mimas, Tethys, and Iapetus, *Science* **315**, 553–558.  
 SMITH, G. R.; SHEMANSKY, D. E.; HOLBERG, J. B.; BROADFOOT, A. L.; SANDEL, B. R.; and MCCONNELL, J. C. (1983), Saturn's upper atmosphere from the Voyager 2 EUV solar and stellar occultations, *J. Geophys. Res.* **88**, 8667–8678.

An excellent pre-Voyager review for Uranus and Neptune is

BERGSTRAHL, J. T., ed. (1984), "Uranus and Neptune," NASA CP-2330.

Figure 1.30 is from the chapter in this volume by

ORTON, G. S. and APPLEBY, J. F. (1984), Temperature structures and infrared-derived properties of the atmospheres of Uranus and Neptune, pp. 89–155.

Voyager Uranus results are in

*Science* (1986) **233**, 39–109.

### Section 1.9.3 Titan

In addition to the references above for Saturn, there is a collection of papers on Titan in *J. Geophys. Res.* (1982) **87**(A3), 1351–1418.

A comprehensive review is

HUNTER, D. M.; TOMASKO, M. G.; FLASAR, F. M.; SAMUELSON, R. E.; STROBEL, D. F.; and STEVENSON, D. J. (1984), Titan, in Gehrels and Matthews, *ibid.*, pp. 671–759.

Figure 1.32 is from

SMITH, G. R.; STROBEL, D. F.; BROADFOOT, A. L.; SANDEL, B. R.; SHEMANSKY, D. E.; and HOLBERG, J. B. (1982), Titan's upper atmosphere: Composition and temperature from the EUV solar occultation results, *J. Geophys. Res.* **87**, 1351–1359.

### Section 1.9.4 Pluto, Triton, and the Galilean Satellites

Several papers on Pluto appear in *Icarus* (1980) **44**(1), 1–71.

Triton is reviewed by

CRUIKSHANK, D. P. (1984), Physical properties of Neptune's satellites, in "Uranus and Neptune," (J. T. Bergstrahl, ed.), NASA CP 2330, pp. 425–436.

Many reviews exist for Io, its plasma torus, and their interaction with the Jovian atmosphere. Chapters may be found in

MORRISON, D., ed. (1982), "Satellites of Jupiter," Univ. Arizona Press, Tucson, Arizona.

DESSLER, A. J., ed. (1983), "Physics of the Jovian magnetosphere," Cambridge Univ. Press, Cambridge.

BURNS, J. A., and MORRISON, D., eds. (1985), "Satellites of the Solar System," Univ. Arizona Press, Tucson, Arizona.

## PROBLEMS

**1.1 Diffusive equilibrium.** Show that for an atmosphere in diffusive equilibrium the atmospheric scale height is

$$H = \left( \sum_j \frac{N_j/N}{H_j} \right)^{-1}$$

where  $H_j = kT/M_j g$ .

**1.2 Linear variation of scale height.** Over a region where the temperature changes linearly with height and where  $g(r) \approx \text{const}$ , show that

$$\frac{p}{p_0} = \left( \frac{H}{H_0} \right)^{-1/\beta} \quad \text{and} \quad \frac{N}{N_0} = \left( \frac{H}{H_0} \right)^{-(1+\beta)/\beta}$$

where  $\beta = dH/dr$  and  $p_0$ ,  $N_0$ , and  $H_0$  denote values at a starting distance  $r_0$ .

**1.3 Radiative equilibrium.** Assume that solar radiation is absorbed only at the Earth's surface where the albedo is 40%. The re-radiated energy is absorbed mainly by water vapor, which we approximate as a gray absorber with a density scale height of 2 km and a total  $\tau_g = 2$ . Plot the temperature distribution with height for radiative equilibrium. What is the temperature discontinuity at the ground? What is the gradient in the air temperature near the ground?

**1.4 Chapman Layer.** Show that the maximum absorption in a barometric atmosphere occurs at  $\tau_v/\mu = 1$  [Eq. (1.5.7)].

**1.5 Chapman stratospheric chemistry.** With the Chapman reactions, what is the daytime rate of change of  $\text{O}_2$ ? Show that this equation adds no new information, beyond what is given by the analogous equations for O and  $\text{O}_3$ , but merely confirms the conservation of matter.

**1.6 Stratospheric heating.** (a) With the data given below and model atmosphere in Appendix III, find  $J_2(z)$  and  $J_3(z)$ . (b) Use the  $J$ 's to recompute  $[\text{O}_3]$  with the "gray u.v." approximation and Chapman chemistry and compare the results for self-consistency with  $[\text{O}_3]$  in the assumed model. (c) What are the heating rates in degrees per day? What portion arises from  $\text{O}_2$  dissociation? (d) Assuming a transparent "gray i.r." atmosphere, compute the temperatures and compare with the model. Show that the  $\kappa_v$  assumed is consistent with the assumption of optical thinness. Data provided:

$$\begin{aligned} \alpha_2(\text{O}_3) &= 1 \times 10^{-18} \text{ cm}^2 \quad (1800-2400 \text{ \AA}) \\ \alpha_2(\text{O}_2) &= 5 \times 10^{-24} \text{ cm}^2 \\ \alpha_3(\text{O}_3) &= 5 \times 10^{-18} \text{ cm}^2 \quad (2200-2900 \text{ \AA}) \\ J_2^{(0)} &= 6 \times 10^{-10} \text{ sec}^{-1} \\ J_3^{(0)} &= 4 \times 10^{-3} \text{ sec}^{-1} \\ k_{12} &= 6.0 \times 10^{-34} (T/300)^{-2.3} \text{ cm}^6/\text{sec} \\ k_{13} &= 8.0 \times 10^{-12} e^{-2060/T} \text{ cm}^3/\text{sec} \\ \langle \mu \rangle &= \frac{1}{2} \\ \kappa_v(\text{i.r.}) &= 1 \times 10^{-3} \text{ cm}^2/\text{gm} \end{aligned}$$

**1.7 Thermospheric forbidden oxygen emission.** The triplet ground term,  ${}^3\text{P}_{2,1,0}$ , of O has the  $J = 1$  level at 0.0197 eV and  $J = 0$  at 0.0281 eV. The transition probabilities are  $A(1,2) = 8.95 \times 10^{-5} \text{ sec}^{-1}$  and  $A(0,1) = 1.70 \times 10^{-5} \text{ sec}^{-1}$ . (a) What is the rate of emission in the two transitions at 200 km? Take  $T = 915^\circ\text{K}$  and  $[\text{O}] = 4 \times 10^9 \text{ cm}^{-3}$ . (b) What is the overhead optical thickness in the centers of each of the two lines? Assume pure Doppler broadening.

**1.8 Mesopause condition.** Compute and make a log plot of the  $15\mu\text{m}$   $\text{CO}_2$  thermal emission rate in the 70–100 km region with the model in Appendix III. Estimate a slope for the curve around 85–90 km and use it to integrate the emission. Find a value of  $z_0$  that satisfies the mesopause condition and compare with the solution (1.7.24).

**1.9 Vibrational relaxation.** Write the equation for statistical equilibrium for the excited vibrational level of the  $v_2$  fundamental of  $\text{CO}_2$  at temperature  $T$ . Assume that it is illuminated

from below by black-body radiation at temperature  $T_0$  and allow for induced emission as well as absorption. Show that in the limit of low  $T_0$  the population is given by (1.6.20).

**1.10 Analytic model thermosphere** [after Bates (1959)]. (a) The *geopotential distance* above height  $z_0$  is defined as

$$\zeta = \int_{z_0}^z \frac{g(z)}{g(z_0)} dz$$

Show that the height may be written as

$$z - z_0 = \frac{\zeta}{1 - \frac{\zeta}{r_0 + z_0}}$$

where  $r_0$  is the radius of the planet. (b) Let the temperature be represented by the formula

$$T(z) = T(\infty)[1 - a \exp(-\tau\zeta)]$$

where  $a$  and  $\tau$  are specified constants:

$$a \equiv 1 - \frac{T(z_0)}{T(\infty)}$$

$$\tau \equiv \frac{(dT/dz)_0}{T(\infty) - T(z_0)}$$

Show by integrating (1.1.5) that the number density of a constituent in diffusive equilibrium is

$$N(z) = N(z_0) \left( \frac{1-a}{\exp(\tau\zeta) - a} \right)^{1+\gamma} \exp(\tau\zeta)$$

where

$$\gamma = \frac{1-a}{\tau H_0}$$

and  $H_0$  is the pressure scale height of the constituent at  $z_0$ . (c) Take  $T(\infty) = 1000^\circ\text{K}$  and at  $z_0 = 120 \text{ km}$  take the O density as  $N_0 = 9.3 \times 10^{10} \text{ cm}^{-3}$ ,  $T(z_0) = 360^\circ\text{K}$  and  $(dT/dz)_{z_0} = 12^\circ\text{K}/\text{km}$ . Compute the temperature and O density at  $\zeta = 79$  and  $359 \text{ km}$  and compare with the model in Appendix III.

**1.11 Thermospheric temperature profile.** (a) Complete the derivation of Eq. (1.7.26). Indicate how the differential equation, including sources and sinks, could be set up for a numerical finite-difference solution. (b) Using the heat flux from Eq. (1.7.22) and the conductivity for O from Table 1.2, estimate the thermospause temperature for the Earth. (To ascertain the optical depth use a cross section of  $10^{-17} \text{ cm}^2$  and work out the column density from the data in the Appendices.) Repeat with twice the heat flux and compare with the actual Earth at solar minimum and maximum. (c) Mars and Venus both have CO<sub>2</sub> atmospheres and, therefore, differ in Eq. (1.7.26) only in  $Q$  and  $g$ . Would you expect similar thermopause temperatures? Why does gravity play this kind of role?

**1.12 Venus thermopause temperature.** Proceed as in Problem 1.11, but include a heating efficiency of 0.1 and other parameters adjusted to Venus (solar flux; CO<sub>2</sub> atmosphere;  $T_0 = 180^\circ\text{K}$ ;  $\tau_0/\langle\mu\rangle = 250$ ).

**1.13 Jupiter thermopause temperature.** Evaluate Eq. (1.7.26) for Jupiter with the following data: heating efficiency, 0.82; mesopause temperature,  $150^{\circ}\text{K}$ , and mesopause density,  $5 \times 10^{13} \text{ cm}^{-3}$ .

**1.14 Titan mesosphere mean temperature.** Voyager observations give  $(p, T)$  equal to  $(1.0 \text{ mbar}, 167^{\circ}\text{K})$  at  $190 \text{ km}$ , and  $(6.2 \times 10^{-9} \text{ mbar}, 165^{\circ}\text{K})$  at  $1265 \text{ km}$ . With the hydrostatic equation and a mean mass of  $28 \text{ amu}$ , find the mean temperature of the region between. Do not forget the variation of gravity with height (cf. Problem 1.10).

# **Chapter 2**

## **HYDRODYNAMICS OF ATMOSPHERES**

### **2.1 Basic Equations**

#### **2.1.1 Equations in an Inertial Frame**

The basic equations relating mass density  $\rho$ , pressure  $p$ , temperature  $T$ , and the three velocity components of  $\mathbf{v}$  ( $u, v, w$ ) are the equations of continuity, motion, state, and energy conservation. The continuity equation expresses the conservation of mass,

$$\frac{\partial \rho}{\partial t} = -\nabla \cdot (\rho \mathbf{v}) \quad (2.1.1)$$

which states that the local rate of increase in mass density is equivalent to the fluid's "convergence." Alternatively, it is common to write continuity in terms of the *substantial derivative*, taken along the path followed by an element of fluid. Thus

$$\frac{d\rho}{dt} \equiv \frac{\partial \rho}{\partial t} + \mathbf{v} \cdot \nabla \rho = -\nabla \cdot (\rho \mathbf{v}) + \mathbf{v} \cdot \nabla \rho \quad (2.1.2)$$

Expanding the divergence we have

$$\frac{d\rho}{dt} = -\rho \nabla \cdot \mathbf{v} \quad (2.1.3)$$

In the special case of an incompressible fluid,

$$\nabla \cdot \mathbf{v} = 0 \quad (2.1.4)$$

*Euler's equation* of motion for an ideal gas (i.e., one with no viscosity) is established by equating the force (per unit volume) on a fluid to the external force ( $\rho\mathbf{g}$ ) plus the pressure gradient:

$$\begin{aligned} \rho \frac{d\mathbf{v}}{dt} &\equiv \rho \left( \frac{\partial \mathbf{v}}{\partial t} + (\mathbf{v} \cdot \nabla) \mathbf{v} \right) \\ &= -\nabla p + \rho\mathbf{g} \end{aligned} \quad (2.1.5)$$

If the fluid is not frictionless, we must add a term accounting for the viscous transfer of momentum from one element of fluid to another. The viscosity stress tensor (which enters the equation in a manner analogous to the role of pressure) must have terms proportional to

$$\frac{\partial v_i}{\partial x_j} + \frac{\partial v_j}{\partial x_i} \quad (2.1.6)$$

since internal friction arises only when there is a relative motion between different parts of the fluid. For an incompressible fluid, terms with  $i = j$  vanish because of Eq. (2.1.4) and the equation of motion becomes the *Navier-Stokes equation*,

$$\frac{\partial \mathbf{v}}{\partial t} + (\mathbf{v} \cdot \nabla) \mathbf{v} = -\frac{1}{\rho} \nabla p + \mathbf{g} + \frac{\eta}{\rho} \nabla^2 \mathbf{v} \quad (2.1.7)$$

The proportionality constant  $\eta$  is the *dynamic viscosity* (gm/cm sec) while the ratio

$$\nu = \eta/\rho \quad (2.1.8)$$

is the *kinematic viscosity* (cm<sup>2</sup>/sec).

When the heat remains constant within all elements of the system and there is no interchange of heat by conduction and radiation, we have the special situation that the flow of gas is isentropic and adiabatic. An atmosphere scarcely conforms to these conditions, but in many problems the departures are not serious and the approximation is useful. Thus temperature is given by (1.3.4) (or its equivalent for moist air), and our set of equations is completed with the perfect gas law, (1.1.2). Integrating (1.3.3) we obtain the adiabatic condition for dry gas,

$$Tp^{-(\gamma-1)/\gamma} = \text{const.} \quad \text{or} \quad p\rho^{-\gamma} = \text{const.} \quad (2.1.9)$$

There are other problems, such as those dealing with instabilities and their driving forces, where one cannot take an adiabatic law but can regard the gas as "almost incompressible." That is, one takes  $\rho$  as a constant except in the buoyancy term of (2.1.7). This approach gives the *Boussinesq approximation*. Continuity is given by Eq. (2.1.4) and the Navier-Stokes equation

becomes

$$\frac{\partial \mathbf{v}}{\partial t} + (\mathbf{v} \cdot \nabla) \mathbf{v} = -\frac{1}{\rho_0} \nabla p + \left(1 + \frac{\delta\rho}{\rho_0}\right) \mathbf{g} + v \nabla^2 \mathbf{v} \quad (2.1.10)$$

where  $\rho = \rho_0 + \delta\rho$ . Energy conservation in a moving element with energy inflow gives

$$\rho_0 C_p \left( \frac{\partial T}{\partial t} + \mathbf{v} \cdot \nabla T \right) = \nabla \cdot (K \nabla T) + \rho_0 \mathbf{v} \cdot \mathbf{g} + Q \quad (2.1.11)$$

where  $K$  is the coefficient of thermal conductivity and where  $Q$  represents the source terms arising from the heat of viscous dissipation and radiation. For the troposphere and stratosphere, conduction is unimportant and radiation is the dominant term on the right.

## 2.1.2 Motion in a Rotating Atmosphere

As seen in a coordinate system  $\Sigma'$  rotating with angular velocity  $\Omega$  in an inertial frame  $\Sigma$ , a particle has a velocity  $v'$  such that

$$\mathbf{v} = \mathbf{v}' + \boldsymbol{\Omega} \times \mathbf{r} \quad (2.1.12)$$

Thus the absolute velocity is the velocity of a particle relative to Earth plus the Earth's rotational velocity. Differentiating a vector  $\mathbf{A}$  in the rotating system  $d'\mathbf{A}/dt$  also requires an adjustment for the rotation:

$$\frac{d\mathbf{A}}{dt} = \frac{d'\mathbf{A}}{dt} + \boldsymbol{\Omega} \times \mathbf{A} \quad (2.1.13)$$

in general, or

$$\frac{d\mathbf{v}}{dt} = \frac{d'\mathbf{v}}{dt} + \boldsymbol{\Omega} \times \mathbf{v} \quad (2.1.14)$$

in particular. Then with (2.1.12) we have

$$\begin{aligned} \frac{d\mathbf{v}}{dt} &= \frac{d'}{dt}(\mathbf{v}' + \boldsymbol{\Omega} \times \mathbf{r}) + \boldsymbol{\Omega} \times (\mathbf{v}' + \boldsymbol{\Omega} \times \mathbf{r}) \\ &= \frac{d'\mathbf{v}'}{dt} + 2\boldsymbol{\Omega} \times \mathbf{v}' - \Omega^2 \mathbf{R} \end{aligned} \quad (2.1.15)$$

since  $\boldsymbol{\Omega} \times (\boldsymbol{\Omega} \times \mathbf{r}) = -\Omega^2 \mathbf{R}$ , where  $\mathbf{R}$  is the distance from the axis of rotation. Equation (2.1.15) gives the acceleration of a particle in an inertial system as composed of the acceleration measured in the rotating system plus the Coriolis and centrifugal terms.

The Navier–Stokes equation for a rotating planet is thus given by writing (2.1.7) for  $d\mathbf{v}/dt$  in (2.1.15). We find

$$\frac{d'\mathbf{v}'}{dt} = -2\boldsymbol{\Omega} \times \mathbf{v}' - \frac{1}{\rho} \nabla p + \mathbf{g}_e + v\nabla^2\mathbf{v}' \quad (2.1.16)$$

where the centrifugal force has been absorbed into the gravitational term by writing an effective gravity,

$$\mathbf{g}_e = \mathbf{g} + \Omega^2\mathbf{R} \quad (2.1.17)$$

In planetary problems it is conventional to take rotating coordinates  $x$ ,  $y$ , and  $z$  (components of  $\mathbf{r}'$ ) as aligned eastward, northward, and upward. Then the velocities are correspondingly  $u = d'x/dt$ ,  $v = d'y/dt$ , and  $w = d'z/dt$ . These velocities are not Cartesian, however, and the acceleration components in spherical coordinates are (for  $\mathbf{v}' = \hat{\mathbf{i}}u + \hat{\mathbf{j}}v + \hat{\mathbf{k}}w$ )

$$\begin{aligned} \frac{d'\mathbf{v}'}{dt} &= \left( \frac{d'u}{dt} - \frac{uv \tan \phi}{a} + \frac{uw}{a} \right) \hat{\mathbf{i}} \\ &\quad + \left( \frac{d'v}{dt} + \frac{u^2 \tan \phi}{a} + \frac{vw}{a} \right) \hat{\mathbf{j}} \\ &\quad + \left( \frac{d'w}{dt} - \frac{u^2 + v^2}{a} \right) \hat{\mathbf{k}} \end{aligned} \quad (2.1.18)$$

where  $a$  is the planetary radius and  $\phi$  is latitude.

We now expand the various force terms. Thus we have

$$\boldsymbol{\Omega} \times \mathbf{v}' = \Omega(w \cos \phi - v \sin \phi) \hat{\mathbf{i}} + u \sin \phi \hat{\mathbf{j}} - u \cos \phi \hat{\mathbf{k}} \quad (2.1.19)$$

and we can usually write

$$\mathbf{g}_e = -g \hat{\mathbf{k}} \quad (2.1.20)$$

(where  $g \approx 980 \text{ cm/sec}$  at Earth's surface). Finally we have the equation for the eastward, northward, and upward components of the momentum equation. Omitting the primes for derivatives in the rotating system, we have

$$\frac{du}{dt} - \frac{uv \tan \phi}{a} + \frac{uw}{a} = -\frac{1}{\rho} \frac{\partial p}{\partial x} + 2\Omega v \sin \phi - 2\Omega w \cos \phi + v \nabla^2 u \quad (2.1.21)$$

$$\frac{dv}{dt} + \frac{u^2 \tan \phi}{a} + \frac{vw}{a} = -\frac{1}{\rho} \frac{\partial p}{\partial y} - 2\Omega u \sin \phi + v \nabla^2 v \quad (2.1.22)$$

and

$$\frac{dw}{dt} - \frac{u^2 + v^2}{a} = -\frac{1}{\rho} \frac{\partial p}{\partial z} - g + 2\Omega u \cos \phi + v \nabla^2 w \quad (2.1.23)$$

The curvature terms (those in  $a^{-1}$ ) are quadratic and awkward to handle, but can often be ignored. The acceleration term is also nonlinear, since (for example),

$$\frac{du}{dt} = \frac{\partial u}{\partial t} + u \frac{\partial u}{\partial x} + v \frac{\partial u}{\partial y} + w \frac{\partial u}{\partial z} \quad (2.1.24)$$

These velocity interaction terms are called “inertial” in turbulence theory and “advective” in atmospheric dynamics.

## 2.2 Horizontal Circulation of the Troposphere

### 2.2.1 Geostrophic Winds and the Gradient Flow

To simplify the horizontal equations of motion (2.1.21) and (2.1.22) we first examine the magnitude of the various terms. On a laboratory scale when the flow is not turbulent, energy dissipation occurs by the conversion of ordered, laminar flow directly into random molecular motions (i.e., heat) through the ordinary molecular viscosity. For air,  $\eta \sim 2 \times 10^{-4}$  gm/cm sec and at STP,  $v \sim 0.15$  cm<sup>2</sup>/sec, which makes the friction term negligible. In a turbulent atmosphere, however, there is an analogous, large-scale dissipation of ordered flow (when there are wind shears) into turbulent eddies of various sizes. The kinetic energy in this spectrum of eddies migrates from larger eddies toward smaller ones (from the more ordered flow into the more disordered), ultimately ending up as heat through the molecular viscosity. But from the point of view of atmospheric winds, the kinetic energy is lost at the rate it is convected into turbulence of any size. Without going into the mechanism of inertial transfer of energy, we can describe it phenomenologically by an *eddy viscosity*  $v_E$ . This viscosity operates on a scale,  $l \sim 3 \times 10^3$  cm in the troposphere, called the *mixing length*, which is analogous to the mean free path in molecular viscosity. Eddy viscosity is important in the lowest kilometer of the atmosphere; since wind velocities must vanish at the surface, wind shears are large in this *boundary layer* of the atmosphere. In this region  $v_E$  is found empirically to be the order of  $5 \times 10^4$  cm<sup>2</sup>/sec and with wind gradients  $\Delta u/\Delta z$  and  $\Delta v/\Delta z \sim 5$  m/sec km,  $\nabla^2 u \sim \nabla^2 v \sim 5 \times 10^{-8}$  cm<sup>-1</sup> sec<sup>-1</sup>. The friction term is of order  $3 \times 10^{-3}$  cm/sec<sup>2</sup> and has to be considered. Higher in the troposphere it is usually negligible and we shall not consider the dissipation term further in this section. Incidentally, turbulent eddies are responsible for transporting mass and energy, as well as momentum, and in those connections we shall later have need for the *eddy diffusion coefficient* (see Section 2.3.2) and the *coefficient of thermal diffusivity* (see Section 2.6).

On a planetary scale ( $L \sim 10^8$  cm) typical horizontal velocities  $u$  and  $v$  are  $10^3$  cm/sec ( $\approx 20$  knots), but mean vertical motions  $w$  are much smaller. Thus omitting the curvature terms and the small Coriolis term in  $\Omega w$ , we obtain the simplified equations

$$\frac{du}{dt} = 2\Omega v \sin \phi - \frac{1}{\rho} \frac{\partial p}{\partial x} \quad (2.2.1)$$

and

$$\frac{dv}{dt} = -2\Omega u \sin \phi - \frac{1}{\rho} \frac{\partial p}{\partial y} \quad (2.2.2)$$

With an advective time scale the order of  $L/V \sim 10^5$  sec ( $\sim 1$  day),  $\Omega \sim 10^{-4}$  sec $^{-1}$ , and pressure differences  $\Delta p \sim 10^4$  dynes/cm $^2$  ( $\sim 10^{-2}$  atm), the acceleration terms are an order of magnitude smaller than the force terms. Thus these typical synoptic characteristics of terrestrial weather indicate that the pressure gradients are nearly balanced by so-called *geostrophic winds* arising from the Coriolis force. Knowing the pressure distribution allows one to derive, in a purely diagnostic fashion, the zonal ( $u$ ) and meridional ( $v$ ) winds.

The relative magnitude of the acceleration term ( $V/t \sim V^2/L$ ) and the Coriolis term at mid-latitudes ( $\Omega V$ ) is the Rossby number

$$R_0 = V/L\Omega \quad (2.2.3)$$

A value of  $R_0 \ll 1$  indicates that the geostrophic approximation is good.

The analogous approximation for the vertical pressure gradient is simply hydrostatic equilibrium because of the dominance of  $g$  in (2.1.23). To a good approximation, therefore,

$$\frac{1}{\rho} \frac{\partial p}{\partial z} = -g \quad (2.2.4)$$

The above simplified equations of horizontal motion may be rewritten vectorially as

$$\frac{d\mathbf{V}}{dt} = f \mathbf{V} \times \hat{\mathbf{k}} - \frac{1}{\rho} \nabla p \quad (2.2.5)$$

where  $\mathbf{V} = \hat{\mathbf{i}}u + \hat{\mathbf{j}}v$ ,  $\nabla = \hat{\mathbf{i}}\partial/\partial x + \hat{\mathbf{j}}\partial/\partial y$ , and the Coriolis parameter is

$$f \equiv 2\Omega \sin \phi \quad (2.2.6)$$

A set of *natural coordinates* simplifies the discussion (see Fig. 2.1). The unit vector  $\hat{\mathbf{i}}$  is tangent to the flow,  $\hat{\mathbf{n}}$  is positive to the left of the flow, and  $\hat{\mathbf{k}}$  is

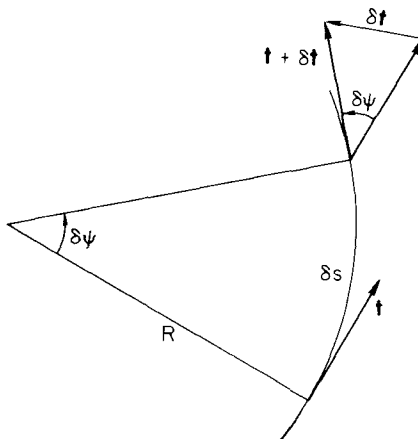


**Fig. 2.1** Curvilinear coordinates, showing the differential change in the unit tangent vector  $\hat{t}$ . [Adapted from HOLTON (1972).]

vertically upward (normal to the page). Then  $\mathbf{V} = V\hat{t}$  and, as in polar coordinates,  $\delta\hat{t} = \hat{n}\delta\psi = \hat{n}\delta s/R$ . Hence

$$\begin{aligned}\frac{d\mathbf{V}}{dt} &= \hat{t} \frac{dV}{dt} + V \frac{\hat{n}}{R} \frac{ds}{dt} \\ &= \hat{t} \frac{dV}{dt} + \hat{n} \frac{V^2}{R}\end{aligned}\quad (2.2.7)$$

The Coriolis force is  $f\mathbf{V} \times \hat{k} = -fV\hat{n}$ , so that (2.2.5) can be written as the scalar equations,

$$\frac{dV}{dt} = -\frac{1}{\rho} \frac{\partial p}{\partial s} \quad (2.2.8)$$

and

$$\frac{V^2}{R} = -fV - \frac{1}{\rho} \frac{\partial p}{\partial n} \quad (2.2.9)$$

The equations of motion are now given in terms of forces parallel and normal to the flow, respectively.

The geostrophic approximation, in which  $d\mathbf{V}/dt = 0$ , thus gives  $p = \text{const.}$  along the direction of flow. The magnitude of the velocity is

$$V_g = -\frac{1}{\rho f} \frac{\partial p}{\partial n} \quad (2.2.10)$$

the flow governed by the Coriolis force being perpendicular to the pressure gradient.

The special case of a vanishing horizontal pressure gradient is considered in Problem 2.1. If, on the other hand, the horizontal scale of a disturbance is very small, the Coriolis force is negligible. Then Eq. (2.2.9) gives

$$V = \left( -\frac{R}{\rho} \frac{\partial p}{\partial n} \right)^{1/2} \quad (2.2.11)$$

and the motion is also perpendicular to the pressure gradient with the pressure decreasing toward the center of rotation. Thus the force of the pressure gradient inward balances the outward centrifugal force. This *cyclostrophic flow* can be in either direction (cyclonic or anticyclonic) and is descriptive of tornados and dust devils.

The *gradient wind* is given by the full solution of (2.2.9), which describes the balance of centrifugal force with Coriolis force and the normal component of the pressure gradient:

$$V = -\frac{fR}{2} \pm \left( \frac{f^2 R^2}{4} - \frac{R}{\rho} \frac{\partial p}{\partial n} \right)^{1/2} \quad (2.2.12)$$

A physical solution must have  $V \geq 0$ . In Fig. 2.1 we have chosen the convention of taking  $R$  as positive when it is antiparallel to  $\mathbf{n}$ —that is, for counterclockwise motion. In this case ( $R > 0$ ) in the northern hemisphere ( $f > 0$ ), we have  $V > 0$  only if  $\partial p / \partial n < 0$ , which gives a low pressure (the *regular low*) at the center of curvature (see Fig. 2.2). Only the positive root is allowed.

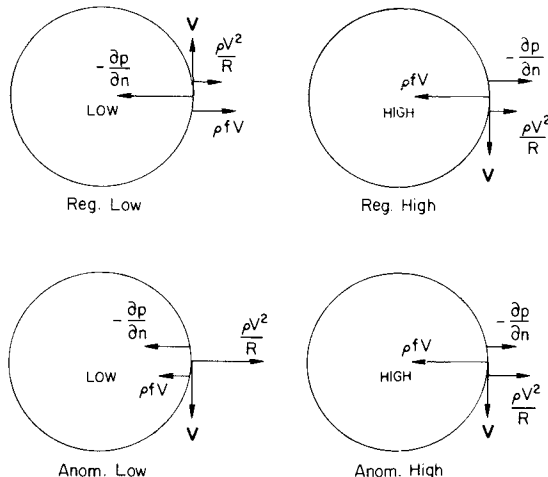


**Fig. 2.2** The four classes of gradient flow, showing how the pressure gradient is balanced by the Coriolis and centrifugal forces normal to the direction of flow. See Eq. (2.2.9). [Adapted from HOLTON (1972).]

On the other hand, if the curvature is clockwise ( $R < 0$ ), there are three possible solutions: (a)  $\partial p/\partial n > 0$ , which also (with the positive root) gives a low pressure, the *anomalous low*, at the center; (b)  $\partial p/\partial n < 0$ , which gives high-pressure solutions for either (b.1) the positive root or *anomalous high* or (b.2) the negative root or *regular high*.

For cases (b), either high-pressure solution, the pressure gradient is restrained by the condition that the radical must be real, or

$$\frac{\partial p}{\partial n} < \frac{\rho R f^2}{4} \quad (2.2.13)$$

Thus the pressure in a high tends to be nearly constant at the center with little concomitant wind.

## 2.2.2 Hadley Circulation

In 1735 Hadley proposed that the trade winds were driven by upward and poleward motion of air heated near the surface in the tropics. This air is diverted eastward by the Coriolis force and is replaced by air moving southwestward (in the northern hemisphere) near the surface (see Fig. 2.3). These *Hadley cells*, in tending to conserve their angular momentum about the rotational axis, thus have a zonal as well as meridional component. These cells were known not to extend to the polar regions because there is predominantly descending air around  $\pm 30^\circ$  latitude. However, cold surface air in the polar regions moves toward lower latitudes causing air motions towards the poles in the high troposphere.

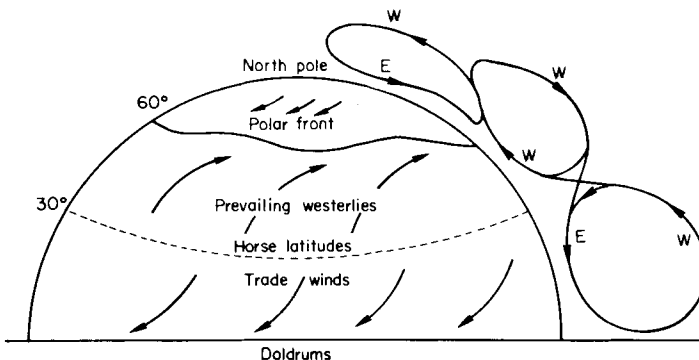


**Fig. 2.3** The three-cell circulation scheme, illustrating tropical convection with subsidence in the “horse latitudes,” ascent in the zone of polar fronts, and subsidence over the polar cap. The notations W and E refer to the directions from which the prevailing winds arise. [Adapted from C.-G. ROSSBY (1941), in “Yearbook of Agriculture, Climate, and Man,” G. Hambridge, ed., pp. 599–655, U.S. Gov. Printing Off., Washington, D.C.]

These two sets of convection cells are driven by solar energy, with heat being converted to kinetic energy. An intermediate cell develops between the Hadley and polar cells with low-level air drifting northward and eastward. This mid-latitude or *Ferrel cell* must be supplied kinetic energy for its maintenance. Mid-latitude circulation is dominated, however, by other dynamical forces than cellular overturning. Thus a simple conservation of angular momentum within the mid-latitude cell would require the surface westerlies to diminish in strength and even change to easterlies at high altitude, whereas in fact the westerlies increase in velocity with height. The reason for this increase is described below.

### 2.2.3 Thermal Wind: Jet Streams

As a practical matter it is convenient to examine horizontal circulations relative to surfaces of constant pressure (*isobars*) rather than constant altitude. Hence to use *isobaric* coordinates we need to make the transformations (see Fig. 2.4)

$$\left(\frac{\partial p}{\partial x}\right)_z = - \left(\frac{\partial p}{\partial z}\right)_x \left(\frac{\partial z}{\partial x}\right)_p \quad (2.2.14)$$

With the hydrostatic approximation (2.2.4), we have

$$\frac{1}{\rho} \left(\frac{\partial p}{\partial x}\right)_z = g \left(\frac{\partial z}{\partial x}\right)_p \quad (2.2.15)$$

Thus the geostrophic wind (2.2.10) becomes

$$u = - \frac{g}{f} \left(\frac{\partial z}{\partial y}\right)_p \quad \text{and} \quad v = \frac{g}{f} \left(\frac{\partial z}{\partial x}\right)_p \quad (2.2.16)$$

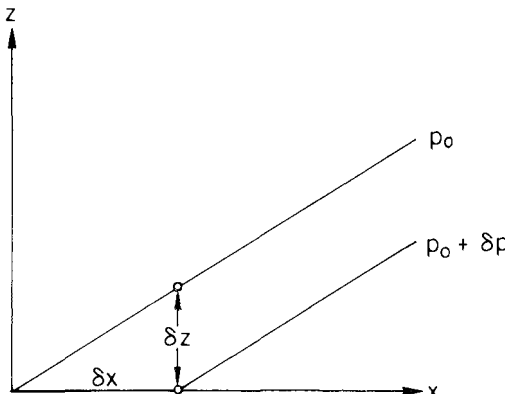


**Fig. 2.4** Isobaric coordinates, showing the relation of constant-pressure surfaces to  $x, z$ , coordinates. See Eq. (2.2.14). [After HOLTON (1972).]

The *geopotential* is the work required to raise unit mass from the surface to height  $z$ , namely,

$$\Phi \equiv \int_0^z g dz = - \int_{p_0}^p \frac{dp}{\rho} \quad (2.2.17)$$

Thus in isobaric coordinates the geostrophic wind is

$$u = - \frac{1}{f} \left( \frac{\partial \Phi}{\partial y} \right)_p \quad \text{and} \quad v = \frac{1}{f} \left( \frac{\partial \Phi}{\partial x} \right)_p \quad (2.2.18)$$

Since

$$\frac{\partial \Phi}{\partial p} = - \frac{RT}{p} \quad (2.2.19)$$

differentiation of (2.2.18) yields

$$\begin{aligned} p \frac{\partial u}{\partial p} &\equiv \frac{\partial u}{\partial \ln p} = - \frac{p}{f} \frac{\partial}{\partial p} \left( \frac{\partial \Phi}{\partial y} \right)_p = \frac{p}{f} \left[ \frac{\partial}{\partial y} \left( \frac{RT}{p} \right) \right]_p \\ &= \frac{R}{f} \left( \frac{\partial T}{\partial y} \right)_p \end{aligned} \quad (2.2.20)$$

and

$$\frac{\partial v}{\partial \ln p} = - \frac{R}{f} \left( \frac{\partial T}{\partial x} \right)_p \quad (2.2.21)$$

These *thermal wind equations* give the vertical wind shear due to nonuniform horizontal heating. Integrating these equations vertically over a slab having a mean temperature  $T$  and extending from pressure  $p_1$  up to  $p_2$  ( $< p_1$ ), we obtain a zonal velocity increment of

$$u(z_2) - u(z_1) = - \frac{R}{f} \left( \frac{\partial T}{\partial y} \right)_p \ln \frac{p_1}{p_2} \quad (2.2.22)$$

with a similar expression for meridional flow.

In a so-called *barotropic atmosphere* the density and pressure are assumed to be uniquely related, or  $\rho \equiv \rho(p)$ . In this situation an isobaric surface has a uniform density and therefore temperature. Consequently, the right side of (2.2.22) vanishes, geostrophic flow is uniform with height, and there is no thermal wind (i.e., vertical shear). In the more realistic *baroclinic atmosphere*, density depends on temperature as well as pressure, or  $\rho = \rho(p, T)$ , and thermal winds can exist.

Figure 2.5 shows mean meridional cross sections of temperature and wind velocity. The pole-to-equator temperature gradient  $(\partial T / \partial y)_p$  is much

larger in middle latitudes in January than in July and gives rise to a strong jet stream around 12 km and latitude  $30^{\circ}$ . In summer the jet stream weakens and moves northward and downward (see Problem 2.4). In Fig. 2.5 the discontinuity or "gap" in the tropopause, near the core of the jet stream, is a characteristic feature.

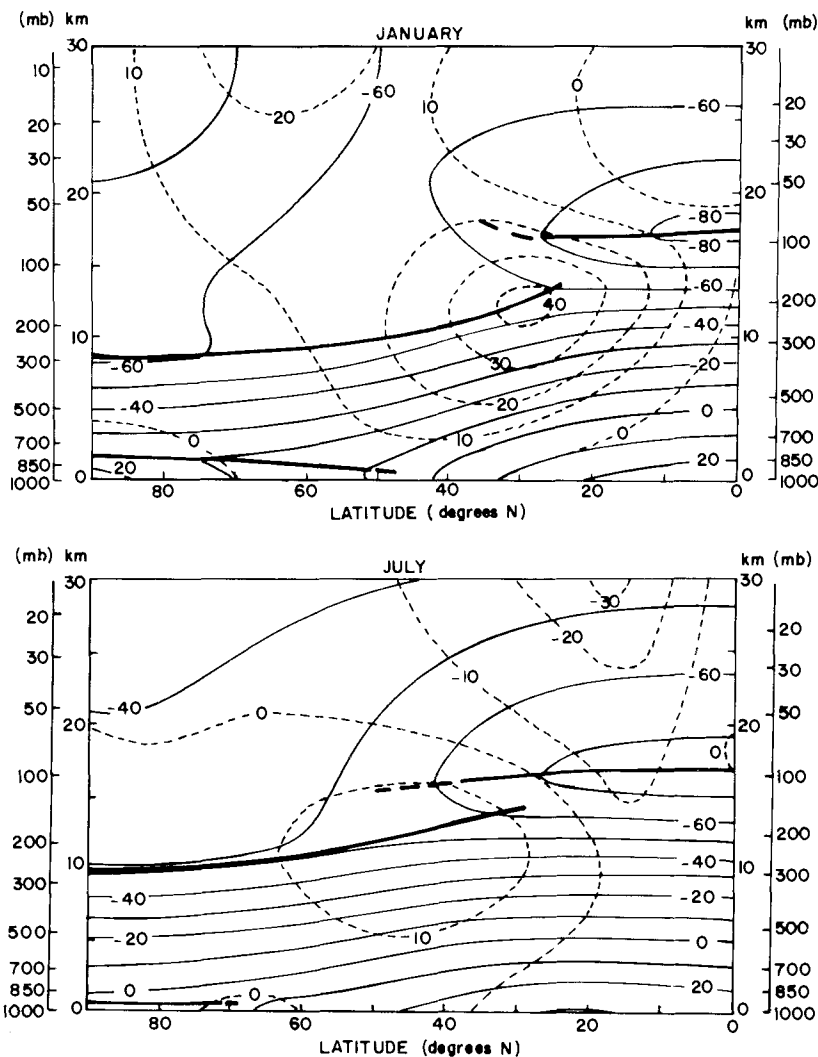


**Fig. 2.5** Meridional cross section of zonal winds (dashed lines in meters per second) and isotherms (solid lines in degrees Centigrade). Heavy solid lines representing the tropopause show mid-latitude discontinuities or "gaps." Note the seasonal change in the peak of the thermal wind (jet stream). [Adapted from "Arctic Forecast Guide," Navy Weather Research Facility, April 1962.]

### 2.2.4 Propagation of Disturbances on the Planetary Scale

We return now to the full set of hydrodynamic equations and write them in *isobaric coordinates*—that is, relative to surfaces of constant pressure rather than constant height. Restoring the acceleration term to the velocity equations (2.2.18) recovers the simplified equations of motion, (2.2.1) and (2.2.2):

$$\frac{du}{dt} - fv = -\left(\frac{\partial \Phi}{\partial x}\right)_p \quad (2.2.23)$$

and

$$\frac{dv}{dt} + fu = -\left(\frac{\partial \Phi}{\partial y}\right)_p \quad (2.2.24)$$

By (2.2.17), the hydrostatic approximation is

$$\frac{\partial \Phi}{\partial p} = -\frac{1}{\rho} = -\frac{RT}{p} \quad (2.2.25)$$

Also, with the vertical velocity being negligible in this approximation, we can simplify the equation of continuity, (2.1.3), by writing  $-(1/g) \partial p / \partial z$  for  $\rho$  and reversing the order of differentiation. Thus continuity becomes

$$\left(\frac{\partial u}{\partial x} + \frac{\partial v}{\partial y}\right)_p + \frac{\partial \omega}{\partial p} = 0 \quad (2.2.26)$$

where  $\omega \equiv dp/dt$  is the pressure change along the trajectory of a parcel of air. If the atmosphere is nearly adiabatic, the thermodynamic relation (1.3.3) is

$$C_p \frac{d \ln T}{dt} \approx R \frac{d \ln p}{dt} \quad (2.2.27)$$

and the set of equations is completed with the perfect gas law, (1.1.2),

$$T = p/\rho R \quad (2.2.28)$$

In these equations the substantial derivative, taken along the trajectory, is

$$\frac{d}{dt} \equiv \left(\frac{\partial}{\partial t}\right)_p + u\left(\frac{\partial}{\partial x}\right)_p + v\left(\frac{\partial}{\partial y}\right)_p + \omega \frac{\partial}{\partial p} \quad (2.2.29)$$

in lieu of (2.1.24), since  $p$  and  $\omega$  now play the role formerly held by  $z$  and  $w$ . In the equations of motion and continuity, the density does not enter, and there is no time derivative in the continuity equation, which leads to considerable simplification. It should be emphasized that all velocities and spatial gradients are measured with respect to isobaric surfaces, not horizontal surfaces.

The independent variables are now  $x$ ,  $y$ ,  $p$ , and  $t$  whereas the dependent variables are  $u$ ,  $v$ ,  $\omega$ ,  $\rho$ ,  $T$ , and  $\Phi$  (where  $\Phi$ , being essentially  $z$ , has interchanged roles with  $p$ ).

It is sometimes convenient to replace temperature  $T$  with the concept of *potential temperature*  $\theta$ , which is the temperature a volume of dry air at  $p$ ,  $T$  would have if compressed to pressure  $p_0 = 1$  atm. The substitution of  $\theta$  for  $T$  leads us to alternate forms of the fifth and sixth equations of this section. Thus from (2.2.27) or its integrated form (2.1.9), we write

$$\theta \equiv T \left( \frac{p_0}{p} \right)^{(\gamma-1)/\gamma} \approx \text{const.} \quad (2.2.30)$$

where  $(\gamma - 1)/\gamma \equiv R/C_p$ . Then (2.2.28) substituted into (2.2.30) relates  $\theta$  and  $\rho$  by

$$\theta = \frac{p}{\rho R} \left( \frac{p_0}{p} \right)^{R/C_p} \quad (2.2.31)$$

In developing the concept of geostrophic wind, we noted that some terms in the equations are found empirically to be small. The remaining terms then tell how the atmosphere generally behaves—that is, to the first order, winds are produced by pressure gradients and the Earth's rotation. If we had a synoptic picture of the pressure the world over, we could construct a corresponding snapshot of the flow. The analysis would be diagnostic but not predictive. It would tell us nothing about the pressure and wind fields the next day.

We will now extract from the six basic equations two simplified expressions that allow prediction. Of course, the actual solution of such equations requires an enormous set of starting data, and a large computer is required to obtain even fragmentary solutions. In the following we will concentrate on predicting the two dependent variables,  $\Phi$ , the geopotential, and  $\omega = dp/dt$ , the vertical motion. We start with the thermodynamic equation (2.2.30) which we will write in terms of  $\Phi$  by using the hydrostatic relation (2.2.25).

Differentiating the logarithm of (2.2.31) yields, for example,

$$\left( \frac{\partial \ln \theta}{\partial x} \right)_p = - \left( \frac{\partial \ln \rho}{\partial x} \right)_p \quad (2.2.32)$$

The thermodynamic equation states simply that the external heat input is small, or  $d \ln \theta / dt \approx 0$ . Expanding this derivative with (2.2.29) and substituting with (2.2.32) and analogous derivatives, we obtain

$$\left( \frac{\partial}{\partial t} \ln \rho \right)_p + u \left( \frac{\partial \ln \rho}{\partial x} \right)_p + v \left( \frac{\partial \ln \rho}{\partial y} \right)_p \approx \omega \frac{\partial \ln \theta}{\partial p} \quad (2.2.33)$$

The hydrostatic equation (2.2.25) eliminates  $\rho$  for  $\Phi$ , giving after some simplification

$$\frac{\partial}{\partial t} \left( -\frac{\partial \Phi}{\partial p} \right) + u \frac{\partial}{\partial x} \left( -\frac{\partial \Phi}{\partial p} \right) + v \frac{\partial}{\partial y} \left( -\frac{\partial \Phi}{\partial p} \right) \approx \sigma \omega \quad (2.2.34)$$

where

$$\sigma = -\frac{\partial \theta / \partial p}{\rho \theta} \quad (2.2.35)$$

is the *static stability parameter*. When  $\partial \theta / \partial p < 0$  (so that  $\sigma > 0$ ) a volume of air in adiabatic motion is stable to a small vertical displacement. Adopting the geostrophic velocity (2.2.18) for  $u, v$ , we have

$$\frac{\partial}{\partial t} \left( -\frac{\partial \Phi}{\partial p} \right) \approx -\frac{1}{f} (\hat{\mathbf{k}} \times \nabla_p \Phi) \cdot \nabla_p \left( -\frac{\partial \Phi}{\partial p} \right) + \sigma \omega \quad (2.2.36)$$

where  $\nabla_p$  signifies a gradient along an isobar.

Since  $\sigma$  is a function of  $\Phi$  (see Problem 2.5), this equation involves only the two dependent field variables  $\Phi$  and  $\omega$ . By Eq. (2.2.25)  $\partial \Phi / \partial p$  is proportional to temperature. Hence (2.2.36) essentially gives the local change of temperature due to the *advection* of temperature by the geostrophic wind on the same isobaric surface plus the adiabatic heating (or cooling) from descending (or rising) air. Had we explicitly carried an external heating (or cooling) term in the thermodynamic equation (2.2.27) or (2.2.30), in lieu of writing an approximate equality, a corresponding additional term would appear in (2.2.36).

Just as the thermodynamic equation is the basis for one  $\Phi$  vs.  $\omega$  relationship, (2.2.36), the equations of motion will provide another. Using (2.2.23) and (2.2.24), we find an expression for the local rate of change in the vertical component of the *vorticity vector*,  $\zeta = \hat{\mathbf{k}} \cdot \nabla \times \mathbf{V}$ :

$$\begin{aligned} \frac{\partial \zeta}{\partial t} &= \frac{\partial}{\partial t} \left( \frac{\partial v}{\partial x} - \frac{\partial u}{\partial y} \right) \\ &= -\mathbf{V} \cdot \nabla_p (\zeta + f) - \omega \frac{\partial \zeta}{\partial p} - (\zeta + f) \nabla_p \cdot \mathbf{V} \\ &\quad + \left[ \frac{\partial u}{\partial p} \left( \frac{\partial \omega}{\partial y} \right)_p - \frac{\partial v}{\partial p} \left( \frac{\partial \omega}{\partial x} \right)_p \right] \end{aligned} \quad (2.2.37)$$

Since  $\zeta$  is measured in the rotating coordinate system, it is a *relative vorticity* and  $\zeta + f$ , including the Coriolis motion, is the *absolute vorticity*. Thus the first term on the right is the horizontal advection term for vorticity and the next term represents vertical advection of vorticity. The final two terms are called the divergence and twisting terms.

The vertical advection and twisting terms are small, and normally  $\zeta \ll f$ . Hence a simplified version of the vorticity equation is

$$\frac{\partial \zeta}{\partial t} \approx -\mathbf{V} \cdot \nabla_p(\zeta + f) + f \frac{\partial \omega}{\partial p} \quad (2.2.38)$$

where the velocity divergence has been eliminated by the equation of continuity, (2.2.26).

Just as we obtained a geostrophic velocity,  $\mathbf{V}_g = (1/f)\mathbf{k} \times \nabla_p \Phi$ , by setting the acceleration term equal to zero, so can we obtain a geostrophic vorticity,  $\zeta_g = (1/f)\nabla_p^2 \Phi$ , from (2.2.23) and (2.2.24). Putting these approximate values in the simplified vorticity equation gives the *quasi-geostrophic vorticity equation*,

$$\frac{\partial}{\partial t}(\nabla_p^2 \Phi) \approx -(\hat{\mathbf{k}} \times \nabla_p \Phi) \cdot \nabla_p \left( \frac{1}{f} \nabla_p^2 \Phi + f \right) + f^2 \frac{\partial \omega}{\partial p} \quad (2.2.39)$$

Equations (2.2.36) and (2.2.39) govern the time changes in  $\Phi$  and  $\omega$ . It is possible to proceed further and eliminate one or the other dependent variable to obtain separate equations for  $\partial \Phi / \partial t$ , the *geopotential tendency*, and  $\omega \equiv dp/dt$ , the vertical motion. Thus by differentiating (2.2.36) with respect to  $p$  and for constant  $\sigma$ , we can eliminate  $\omega$ , obtaining an equation for  $\partial \Phi / \partial t$ ,

$$\left( \nabla_p^2 + \frac{f^2}{\sigma} \frac{\partial^2}{\partial p^2} \right) \frac{\partial \Phi}{\partial t} = -f \mathbf{V}_g \cdot \nabla_p \left( \frac{1}{f} \nabla_p^2 \Phi + f \right) - \frac{f^2}{\sigma} \frac{\partial}{\partial p} \left( \mathbf{V}_g \cdot \nabla_p \frac{\partial \Phi}{\partial p} \right) \quad (2.2.40)$$

Taking the spatial and pressure dependencies of the geopotential tendency to vary sinusoidally, we write

$$\frac{\partial \Phi}{\partial t} = (\text{const.}) \sin kx \sin ly \sin \frac{p\pi}{p_0} \quad (2.2.41)$$

where the  $p$  variation is an approximation based on the supposition that the vertical scale of disturbances is one or two scale heights (i.e., about the tropospheric height). (The wavenumbers  $k$  and  $l$  are defined by  $k = 2\pi/L_x$  and  $l = 2\pi/L_y$ , where the  $L$ 's are wavelengths.) Hence the left side of (2.2.40) is proportional to  $-\partial \Phi / \partial t$ .

On the right side of (2.2.40), the first term represents advection of vorticity by the geostrophic wind (see Fig. 2.6). Thus barometric highs and lows are carried either upstream or downstream, depending on the relative importance of the relative geostrophic vorticity  $\zeta = \nabla_p^2 \Phi / f$  and planetary vorticity  $f$  and on the wavelength of the disturbance.

The second term on the right side gives the growth (or decay) of a high- or low-pressure system. By (2.2.25),  $\partial \Phi / \partial p$  is essentially the temperature, so

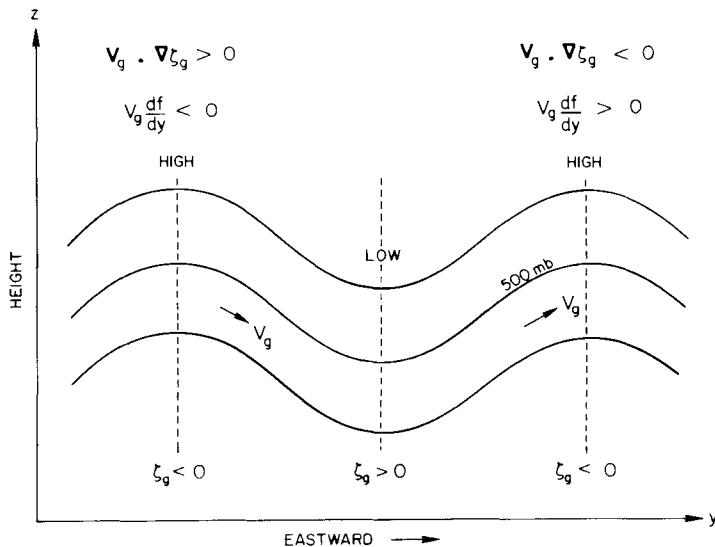


**Fig. 2.6** Schematic isobars near the 500 mb level in the  $x,z$  plane, showing regions of positive and negative advectons of relative and planetary vorticity. [After HOLTON (1972).]

that this second term gives the height (i.e., pressure) gradient of temperature advection. For example, if cold air is advected into the lower regions of a low-pressure system, the thickness of the air column is reduced and the height of a fixed pressure is lowered—the low-pressure system thus grows.

In a similar manner we could solve (2.2.36) and (2.2.39) for  $\omega$  as a function of  $\Phi$ . That is, the vertical motion depends exclusively on the geopotential field. It may also be shown that the resulting  $\omega$  ensures that the vorticity remains geostrophic and the temperature distribution with height remains hydrostatic. For further discussion and application of these diagnostic equations to the development of *baroclinic disturbances* the reader may consult the bibliographical notes.

Disturbances in the pressure field (other than compressional or sound waves) propagate in various forms of waves. *Gravity waves* are the familiar waves that propagate on the surface of water, but they also affect the interior of a fluid. In a stratified fluid such as the atmosphere, these waves may propagate nearly vertically as well as horizontally. A disturbance set up, say, by air flowing over a mountain range will propagate upward and be refracted toward the horizontal with increasing height. At high altitudes dissipation of the wave may be an important source of local energy.

A second type of wave responsible for free oscillations of the atmosphere is the *Rossby* or *planetary wave*. The driving mechanism is the latitudinal

variation of the Coriolis force, which causes the Rossby wave to propagate slowly (a few meters per second) westward (relative to the mean zonal flow).

We can see how the Rossby wave develops by examining a very simple situation: an atmosphere with constant density and no vertical motion. Operating on (2.2.1) with  $\partial/\partial y$  and on (2.2.2) with  $\partial/\partial x$  and subtracting gives

$$\frac{d}{dt} \left( \frac{\partial v}{\partial x} - \frac{\partial u}{\partial y} \right) + f \left( \frac{\partial v}{\partial y} + \frac{\partial u}{\partial x} \right) + v \frac{\partial f}{\partial y} = 0 \quad (2.2.42)$$

The first parenthetical term is the relative vorticity, and the second term vanishes by continuity. We then have

$$\frac{d(\zeta + f)}{dt} = 0 \quad (2.2.43)$$

Which also follows directly from Eq. (2.2.37). We now let  $f$  be linear with  $y$ ,  $f = f_0 + \beta y$  (known as the  $\beta$ -plane approximation), and assume a uniform zonal flow  $u_1$ , upon which is superimposed a perturbed flow  $u'$ ,  $v'$  such that  $u = u_1 + u'$ ,  $v = v'$ . The above conservation of absolute vorticity then yields

$$\left( \frac{\partial}{\partial t} + u_1 \frac{\partial}{\partial x} \right) \left( \frac{\partial v'}{\partial x} - \frac{\partial u'}{\partial y} \right) + \beta v' = 0 \quad (2.2.44)$$

We now introduce a stream function  $\psi$ , which relates  $u'$  and  $v'$  and which automatically satisfies continuity:

$$u' = -\frac{\partial \psi}{\partial y}, \quad v' = \frac{\partial \psi}{\partial x} \quad (2.2.45)$$

The wave equation for  $\psi$  is then

$$\left( \frac{\partial}{\partial t} + u_1 \frac{\partial}{\partial x} \right) \left( \frac{\partial^2 \psi}{\partial x^2} + \frac{\partial^2 \psi}{\partial y^2} \right) + \beta \frac{\partial \psi}{\partial x} = 0 \quad (2.2.46)$$

For a solution of the form  $\psi = \text{Re}[\psi_0 \exp i(\omega t + kx + ly)]$  to be possible, the dispersion relation,

$$c \equiv -\frac{\omega}{k} = u_1 - \frac{\beta}{k^2 + l^2} \quad (2.2.47)$$

must be satisfied. The velocity relative to the mean zonal flow is  $c - u_1$ , where  $c$  is phase velocity toward  $+x$ . Hence Rossby waves drift to the west.

If we write the horizontal momentum equations (2.2.1) and (2.2.2) for perturbations  $u'$ ,  $v'$ ,  $p'$  and then use the equatorial  $\beta$ -plane approximation ( $f = \beta y$ ), we may show that, for a solution with  $v' = 0$  and  $u' = \text{Re}[u'_0 \exp i(\omega t - kx)]$ , the amplitude has a latitude dependence of  $\exp(-\beta y^2 k/2\omega)$ . A

satisfactory solution exists only for  $k > 0$ ; hence, the wave must be eastward moving. These are the *Kelvin waves*.

A similar kind of atmospheric disturbance, because it also has wavelengths of the order of the planetary diameter, is the *atmospheric tide*. Indeed, tidal motions are special cases of gravity waves. Tidal waves are almost imperceptible in the troposphere, except in the tropics, but they are important on Mars and in the Earth's upper atmosphere. Tides are driven by solar heating as well as by the gravitational forces of the sun and moon.

## 2.3 Vertical Transport

### 2.3.1 Molecular Diffusion

Assume that a minor constituent has a density distribution  $N_1(z)$  in an atmosphere where its density distribution in diffusive equilibrium would be  $N_{1E}(z)$ . It will have an upward flux  $\Phi$ , which can be written in terms of an upward diffusion velocity  $w$ , given by the diffusion equation

$$\Phi_1 \equiv N_1 w_1 = -DN_{1E} \frac{\partial(N_1/N_{1E})}{\partial z} \quad (2.3.1)$$

Here  $D$  (cm<sup>2</sup>/sec) is the coefficient of diffusion, which varies inversely with the total ("background") density  $N(z)$ . For an atmosphere in hydrostatic equilibrium the distribution  $N_{1E}(z)$  is given by (1.1.5) and

$$\Phi_1 = -N_1 D \left( \frac{1}{N_1} \frac{\partial N_1}{\partial z} + \frac{M_1 g}{kT} + \frac{1}{T} \frac{\partial T}{\partial z} \right) \quad (2.3.2)$$

where  $M_1$  is the mass of the diffusing gas. The second and third terms on the right compose the reciprocal of the *density scale height*  $H_{1E}^*$  of an equilibrium distribution [different from the usual pressure scale height  $H$  unless the atmosphere is isothermal—cf. (1.1.5)]. Hence a convenient form of (2.3.2) is

$$\Phi_1 \equiv N_1 w_1 = N_1 D \left( \frac{1}{H_1^*} - \frac{1}{H_{1E}^*} \right) \quad (2.3.3)$$

It is often desirable to compare diffusion with other physical processes, such as dissociation or recombination. For these purposes we may use the concept of *time of diffusion*,  $\tau_{\text{dif}} \sim H_1^*/w_1$ , or, since the value is approximate in any case,  $H^2/D$ . The diffusion coefficient is inversely proportional to the total density  $N$  and can conveniently be written  $D = b/N$ , where  $b$  is a binary parameter that is best obtained empirically from data on diffusion, viscosity, and thermal conductivity. Appendix VII gives a selection of values for  $b$  and

an equation for estimating it for gas pairs lacking adequate data. Molecular diffusion becomes important above 90 km in the Earth's atmosphere.

The discussion so far has dealt with diffusion due to concentration gradients relative to the equilibrium gradient. Diffusion may also occur due to temperature gradients. To allow for thermal diffusion we merely add a term  $(\alpha_T/T) dT/dz$  within the parentheses of (2.3.2) and onto the definition of  $1/H_{1E}^*$ . The coefficient  $\alpha_T$  is the *thermal diffusion factor* [cf. Eq. (7.3.3)].

### 2.3.2 Eddy Diffusion

The equations of motion are not very useful for describing turbulence or mixing of the atmosphere because of the complexity that arises from the inertial interaction of different mass elements. Hence it is useful to simplify mixing by assigning it the kind of averaged macroscopic properties that molecular diffusion possesses. Substituting an *eddy diffusion coefficient*,  $K$  ( $\text{cm}^2/\text{sec}$ ) everywhere for  $D$  and the total density  $N(z)$  for  $N_{1E}(z)$  in (2.3.1) will, in form at least, accomplish this objective. Then in (2.3.2) we replace  $K$  for  $D$  and  $M \equiv \langle M \rangle$  for  $M_1$ . The resulting equation reads

$$\Phi_1 \equiv N_1 w_1 = -K(z)N(z) \frac{d}{dz} \left( \frac{N_1}{N} \right) \quad (2.3.4)$$

The total flux can be obtained by adding (2.3.1) and (2.3.4), as shown explicitly in (2.3.1). In principle,  $K$  can be regarded as having been derived from the mixing-length hypothesis outlined in Appendix VII. It is preferable simply to regard it as being defined by (2.3.4), giving the relation between the gradient of the mixing ratio and the flux. On this view, estimates of these two quantities can be used to derive values of  $K$ , and examples of this procedure are given in the next section.

### 2.3.3 Solutions of the Diffusion Equation

Considerable insight into atmospheric behavior can be obtained by means of analytic solutions for idealized situations, with a single minor constituent in a static background gas whose scale height  $H$  is independent of height. At altitudes below 90 km, eddy diffusion dominates; at higher altitudes it is necessary to include molecular diffusion as well. A constant flux  $\Phi$  can be regarded as a solution of a continuity equation with no sources or sinks, which does not need to be explicitly considered. More realistic cases can be solved numerically; multiple minor constituents may be coupled through their continuity equations (see Section 3.3). If the background gas, or more

than one major constituent, is also flowing, the situation becomes even more complicated but can still be handled.

If  $N_1/N$ , the mixing ratio, is replaced by  $f$ , (2.3.4) can be written as

$$df/dz = -\Phi/KN \quad (2.3.5)$$

This equation can be immediately integrated if  $K$  and  $\Phi$  are constant and  $N = N_0 e^{-h} = N_0 \exp[-(z - z_0)/H]$ :

$$f = A - \int \frac{\Phi}{KN} dz = A - \frac{\Phi H}{KN_0} e^h \quad (2.3.6)$$

The dimensionless height  $h$  is in units of the scale height  $H$  above the reference level  $z_0$ . The constant of integration  $A$  depends on boundary conditions. Multiplication by  $n$  gives

$$N_1 = AN_0 e^{-h} - (\Phi H/K) \quad (2.3.7)$$

Solutions of this class of problem always exhibit these two terms, one that has a height-independent mixing ratio and an exponential density profile and one that depends on the flux. The magnitude of the first term depends on the boundary conditions. For a flux of zero, this mixed term is the only one, as it should be. A downward flux is negative and gives a positive second term, which can be the dominant one, with a constant density; this situation is commonly found when a source lies some distance above a sink. Within the source and sink regions, the flux is not constant and the simple solution is not valid, but between them it is often useful.

A simple extension is to represent the height variation of  $K$  by an exponential, say  $K = K_0 e^{ah}$ ; the analog of (2.3.7) is

$$N_1 = AN_0 e^{-h} - \frac{\Phi H}{K(1-a)} \quad (2.3.8)$$

More complex forms for  $K$ , including discontinuities, can be handled by splitting the atmosphere into layers, with the solutions matched at the interfaces and  $\Phi$  constant throughout. Some examples are shown in Fig. 2.7. The solid line in Fig. 2.7c resembles the solution for a source in the stratosphere with a sink at the ground; the level “0” represents the tropopause, where  $K$  changes from  $10^5 \text{ cm}^2 \text{ sec}^{-1}$  below to a few thousand above. The sources of ozone catalysts discussed in Section 3.2 are of this general sort.

There is a class of multiple constituents that can be handled by lumping them together and treating their transport as a group. A prime example is hydrogen compounds; others are odd nitrogen and chlorine compounds. The number density of total hydrogen, or  $N_t$ , is defined as the weighted sum of the

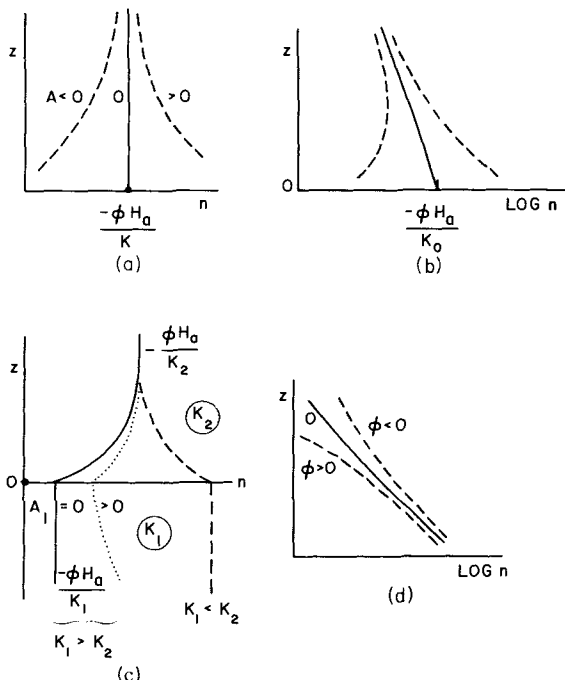


**Fig. 2.7** Solutions of the eddy-diffusion equation for simplified atmospheric models: (a) Downward flux and  $K$  constant; (b) constant downward flux,  $K$  increasing exponentially with height (read  $H_p$  for  $H_a$ ); (c) same as (a), but with two layers of differing  $K$ ; and (d) constant downward and upward flux, constant  $K$ . [After HUNTER (1975a).]

number densities of all hydrogen compounds; each weight is the number of H atoms in the compound. This definition can be multiplied by a constant or differentiated to obtain a total mixing ratio, a total flux, or its derivative. Thus, if an eddy equation like (2.3.5) is written for each constituent, the weighted sum of all these equations is

$$df/dz = -\Phi_J/KN \quad (2.3.9)$$

For most atoms, the total flux is zero, and it immediately follows that the mixing ratio must be height independent as long as eddy mixing dominates its behavior. For hydrogen there is an upward flux to supply its escape; the gradient of mixing ratio can be estimated from (2.3.9) and turns out to be negligible. There is however a very large negative gradient of the water-vapor mixing ratio, from a percent or so near the ground to 4 ppm in the lower stratosphere. In this region there is an additional major downward flux, due to precipitation, that is not described by (2.3.5) and not included in (2.3.9), which therefore does not apply. It does, however, apply very well throughout.

the stratosphere and mesosphere, failing again where molecular diffusion begins to become important.

To handle molecular diffusion and the transition from eddy diffusion, it is necessary to include Eq. (2.3.2) with the additional term for thermal diffusion discussed below it. This combination of molecular and eddy diffusion is somewhat heuristic but does provide a specific framework:

$$D\left(\frac{1}{N_1} \frac{dN_1}{dz} + \frac{1}{H_1} + \frac{1+\alpha}{T} \frac{dT}{dz}\right) + K\left(\frac{1}{N_1} \frac{dN_1}{dz} + \frac{1}{H} + \frac{1}{T} \frac{dT}{dz}\right) = -\frac{\Phi}{N_1} \quad (2.3.10)$$

The hydrostatic solution  $N_1^0$  is defined as the solution of this equation for zero flux:

$$D\left(\frac{1}{N_1^0} \frac{dN_1^0}{dz} + \frac{1}{H_1} + \frac{1+\alpha}{T} \frac{dT}{dz}\right) + K\left(\frac{1}{N_1^0} \frac{dN_1^0}{dz} + \frac{1}{H} + \frac{1}{T} \frac{dT}{dz}\right) = 0 \quad (2.3.11)$$

Subtraction of these two equations gives

$$(D+K)\left[\frac{1}{N_1} \frac{dN_1}{dz} - \frac{1}{N_1^0} \frac{dN_1^0}{dz}\right] = -\frac{\Phi}{N_1} \quad (2.3.12)$$

The ratio of the two solutions is  $r = N_1/N_1^0$ ; the logarithmic derivative of the right-hand side of this expression is identical to the bracketed term in (2.3.12), which can therefore be written as

$$\frac{dr}{dz} = -\frac{\Phi}{N_1^0(D+K)} \quad (2.3.13)$$

The solution of (2.3.10) can therefore always be done in two steps: solve the static equation (2.3.11), obtaining  $N_1^0$ , and then solve (2.3.13) with any appropriate profile of  $\Phi$  and  $K$ . This procedure, which involves no approximations, is used below in Section 2.3.4.

Over the middle atmosphere (the stratosphere and mesosphere),  $K$  tends to increase with height, but  $D$  increases considerably faster, becoming the greater of the two very near 100 km. This level, the *homopause*, divides the *homosphere* from the *heterosphere*, where diffusive separation takes effect. (The homopause is often called “turbopause,” but we disagree with this usage because it implies a specific mechanism, turbulence, rather than simply describing the observed behavior of atmospheric gases.) The nature of the transition can be illuminated by a solution of (2.3.10), once more in the approximation of constant temperature and constant  $K$ . The reference level is taken at the homopause, so that  $D = Ke^h$ , and the mass ratio  $M_1/M$  is set equal to  $s$ . Equation (2.3.10) therefore becomes

$$\frac{dN_1}{dh} + \frac{1+s \exp(h)}{1+\exp(h)} N_1 = -\frac{\Phi H}{K} \frac{1}{1+\exp(h)} \quad (2.3.14)$$

which can be solved with the integrating factor  $e^h(1 + e^h)^{s-1}$  to give

$$\begin{aligned} N_1 &= Ae^{-h}(1 + e^h)^{1-s} + \frac{\Phi H}{K(1-s)} e^{-h} \\ &= Be^{-h}(1 + e^h)^{1-s} - \frac{\Phi H}{K(1-s)} e^{-h}[(1 + e^h)^{1-s} - 1] \end{aligned} \quad (2.3.15)$$

These two forms are equivalent; the first is useful for upward flux and the second for downward flux, although a binomial expansion is necessary to see that the final term does go over to  $(-\Phi H/K)$  for large negative  $h$ , as in (2.3.7). For zero flux, the asymptotes for large negative and positive  $h$  are:

$$\begin{aligned} n &\sim e^{-h}, & (h \ll 0) \\ n &\sim e^{-sh}, & (h \gg 0) \end{aligned} \quad (2.3.16)$$

Since  $s$  represents the mass ratio, the upper asymptote has the scale height of the minor gas, as it should.

The next section illustrates these solutions by applying them to various topics.

### 2.3.4 Application to the Lower Thermosphere

The first term in (2.3.15) applies to the distribution near the homopause of inert gases such as He and Ar. In turn, comparison with observed distributions gives an estimate of  $K$ . The solutions are illustrated in Fig. 2.8; the asymptotes intersect at  $h = 0$ , and the ratio of the actual density to this intersection is  $2^{1-s}$ , which is 1.81 for helium in nitrogen ( $s = \frac{1}{7}$ ) and 0.74 for Ar in nitrogen ( $s = \frac{10}{7}$ ). A striking example is found in the Jovian planets, where the major gas is  $H_2$  and  $s = 8$  for methane; the ratio is 0.0078. Thus, although two straight asymptotes with a corner at the homopause usually do represent the profile fairly well, there are important exceptions.

Although the globally averaged helium flux on the Earth must be very nearly zero, large local fluxes are found, upward at some times and places, and downward at others. Thus, a large number of data sets would have to be averaged to get a valid comparison with theory. Argon is much better behaved, and shows a homopause very close to 100 km. At this height, the diffusion coefficient is  $5 \times 10^5 \text{ cm}^{-2} \text{ sec}^{-1}$ , and therefore this must also be the value of  $K$  (on the assumption that it does not depend on height in this region).

Molecular oxygen flows upward in the lower thermosphere and is dissociated into atoms that flow down again, recombining in the 80–100 km region. These processes are illustrated in Fig. 2.9. The downward flux of O is

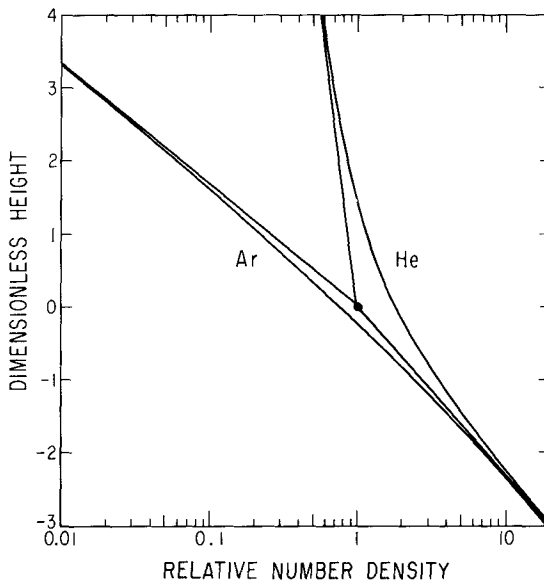


**Fig. 2.8** The solutions (2.3.15) for zero flux of helium and argon. The normalized height  $h$  is zero at the homopause and is in units of the scale height of the background atmosphere.

shown at the right, and is equal to twice the upward flux of  $O_2$ . The left panel illustrates the photolysis of  $O_2$  and the rates of the two principal reactions that recombine the atoms into molecules. The upward flux of  $O_2$  is accompanied by a reduction of its density below what it would otherwise be, and Eq. (2.3.13) can be used to calculate the magnitude of the effect if a profile of  $K$  is available. The subscript 2 is used for  $O_2$ . It is convenient to multiply both sides by the scale height  $H$  and then change  $dz/H$  to  $dh$ . Rather than use

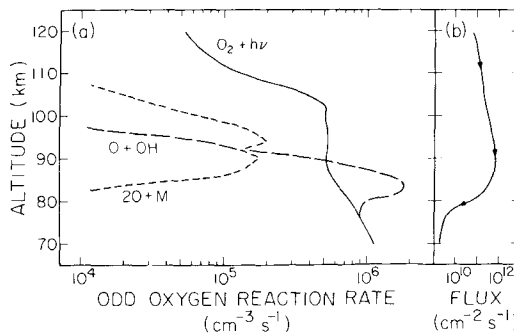


**Fig. 2.9** Odd oxygen in the Earth's lower thermosphere: (a) production (solid) and loss (dashed) rates and (b) flux of  $O$  atoms. [After ALLEN *et al.* (1981).]

the actual fluxes from Fig. 2.9, we shall crudely approximate them by a constant value,  $-2 \times 10^{11} \text{ cm}^{-2} \text{ sec}^{-1}$  for O and  $+1 \times 10^{11} \text{ for O}_2$ . For a reference level of 90 km,  $r$  is 1,  $D$  can be taken as  $10^5 e^h$  and  $N_2$ , the density of  $\text{O}_2$ , as  $2 \times 10^{13} e^h$ . With  $H = 8 \text{ km}$  and  $K = 5 \times 10^5 \text{ cm}^2 \text{ sec}^{-1}$ , (2.3.13) integrates to

$$\begin{aligned} r_2 - 1 &= -0.04 \int_0^h \frac{\Phi_2 H}{e^{-h}(e^h + 5)} dh \\ r_2 &= 1.072 - 0.04 \ln(e^h + 5) \end{aligned} \quad (2.3.17)$$

At  $h = 5$ ,  $z = 130 \text{ km}$ ,  $r_2$  is about 0.87; that is, the density of  $\text{O}_2$  is about 13 % less than it would be for no upward flux. The actual reduction may be somewhat greater if the calculation is done more carefully and extended to higher altitudes. The value for photochemical steady state is zero; thus, the combination of eddy and molecular diffusive fluxes has a first-order effect.

The atomic oxygen produced in the thermosphere flows down and begins to recombine at about 110 km; Fig. 2.9 illustrates the main processes and their rates as a function of height. A peak forms at about 100 km (Table III.4, Appendix III), and the density there can be estimated by a simple trick. At a peak, the gradient of density is zero, and the derivative terms in (2.3.10) drop out. If the temperature gradient is again ignored, the equation reduces to

$$N_1 = -kT\Phi/g(M_1 D + MK) \quad (2.3.18)$$

which is positive when the flux is negative. Inserting a flux of  $-4 \times 10^{11} \text{ cm}^{-2} \text{ sec}^{-1}$  from Fig. 2.9, with  $D$  evaluated at 100 km, we find  $N_1 = 4 \times 10^{11} \text{ cm}^{-3}$ , in satisfactory agreement with the value shown in Table III.4.

As these simplified examples show, assessment of tracer data can give information on the values of  $K$  at various heights. Figure 2.10 shows the results of such a study for the mesosphere and lower thermosphere, in which the tracers were O,  $\text{O}_2$ ,  $\text{CO}_2$ , Ar, and CO. For the stratosphere, suitable tracers are  $\text{CH}_4$ ,  $\text{N}_2\text{O}$ , and the chlorofluoromethanes.

### 2.3.5 Planetary Thermospheres

On Earth, as described in the previous section,  $\text{O}_2$  flows up into the thermosphere and is partially dissociated into O atoms, which flow down to levels where the density is great enough for them to recombine. At greater heights, diffusive separation ensures that O becomes the dominant constituent. On Mars and Venus,  $\text{CO}_2$  flows up, and CO and O flow down. On the Jovian planets,  $\text{H}_2$  flows up and H flows down. On all these planets, the eddy coefficient near the homopause can be estimated if adequate density measurements are available for the dissociation products. Although there are direct

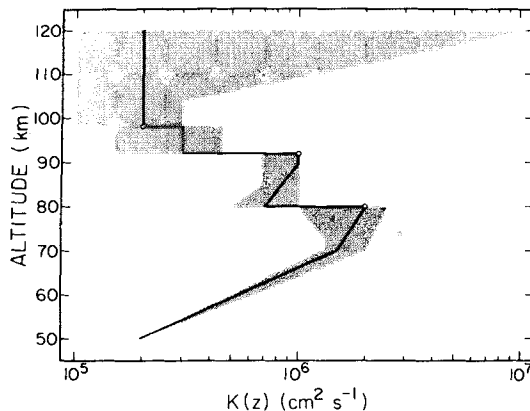


**Fig. 2.10** Profile of eddy coefficient  $K$  corresponding to Fig. 2.9. [After ALLEN *et al.* (1981).]

measurements of He, CO, and O on Venus, they must be supplemented by airglow data. On Mars, airglow is the principal source of information, and on the rest of the planets it is the only source. The situation on Jupiter, and possibly the other Jovian planets, is complicated by the presence of other sources of dissociation besides solar radiation (a common situation for objects far from the Sun).

On both Mars and Venus, the eddy coefficient is close to  $10^8 \text{ cm}^2 \text{ sec}^{-1}$ , more than two orders of magnitude greater than on the Earth. The helium data for Venus extend right through the homopause, and strongly suggest a height variation for  $K$  proportional to the inverse square root of density. However, there are also strong indications of a global thermospheric circulation, which may be an important factor in vertical as well as horizontal transport. Early results for Jupiter, based on Lyman-alpha data obtained from near Earth, suggested that  $K$  was near  $10^6 \text{ cm}^2 \text{ sec}^{-1}$ , but the values from Voyager are 1–2 orders of magnitude greater, depending partly on how much dissociation is attributed to auroral electrons. If the variation of  $K$  is real, it may be related to solar activity; it is also conceivable that the source of H is more variable than has been supposed.

## 2.4 Circulation of the Venus Atmosphere

There are several indications that Venus' atmosphere is dynamically active: (1) The temperature profile (see Section 1.8.1) is nearly adiabatic up to 50 km. Only 1 percent or so of the incident solar flux reaches the ground, most of the remainder being reflected to space by Mie scattering of the cloud droplets and Rayleigh scattering by the nearly 100 atmospheres of  $\text{CO}_2$ .

(2) Infrared thermal emission from the upper atmosphere and temperature measurements in deep atmosphere indicate small horizontal gradients, even though Venus' solar day is 117 days. (3) The very existence of clouds indicates large scale rising motions or at least small scale turbulence or both. (4) Fluctuations in radio signals suggest turbulent layers around 45 and 60 km altitude, but not in the deep atmosphere.

To understand the main physical processes at work we first examine the pertinent time scales. The thermal capacity above a level at pressure  $p$  for a hydrostatic atmosphere may be regarded [cf. (1.3.3) and (1.1.6)] as  $(C_p/R)pH$ . If the atmosphere radiates energy to space at a rate  $-\sigma T_e^4$  characteristic of some effective temperature  $T_e$ , given by (1.2.46), the cooling time scale (after solar heating stops) is

$$\tau_{\text{rad}} = \frac{\gamma p H}{(\gamma - 1)\sigma T_e^4} \approx 6 \times 10^4 T p \text{ (atm)} \quad (2.4.1)$$

since  $C_p/R = \gamma/(\gamma - 1)$ . At the surface  $\tau_{\text{rad}} > 10^2$  yr.

The dynamical time scale, as noted after (2.2.2), is

$$\tau_{\text{dyn}} = L/V \sim 10^5 \text{ sec} \quad (2.4.2)$$

for speeds of several meters per second.

The length of the Venus day is

$$\tau_{\text{day}} = 1.01 \times 10^7 \text{ sec} \quad (2.4.3)$$

Hence at height  $z \lesssim 45$  km,  $\tau_{\text{rad}} > \tau_{\text{day}}$  and it is not surprising that diurnal temperature changes are small. At the cloud level,  $z \approx 60$  km,  $\tau_{\text{rad}} \sim 0.5 \times 10^7$  sec and the small variation in thermal emission from that region indicates the presence of planetary scale winds. Indeed, Venera 9 and 10 measured zonal winds of 60 m/sec between 40 and 60 km.

The sidereal rotation period (244 days) is

$$2\pi/\Omega = \tau_{\text{rot}} = 2.11 \times 10^7 \text{ sec} \quad (2.4.4)$$

giving a Rossby number (2.2.3)

$$R_0 = \tau_{\text{rot}}/2\pi\tau_{\text{dyn}} \sim 3 \times 10^1 \quad (2.4.5)$$

which means that Coriolis forces are very small on Venus. Hence we conclude that the important parameter governing the circulation of the lower atmosphere is the *Golitsyn number*, the controlling parameter for a non-rotating planet,

$$G_0 = \tau_{\text{dyn}}/\tau_{\text{rad}} \quad (2.4.6)$$

If  $G_0 \gg 1$ , implying that the global circulation requires a long period compared with the time to transport heat radiatively, then radiative equilibrium

would govern the horizontal temperature variation (for a nonrotating planet). For  $G_0 \lesssim 1$  the motions will be important in transporting heat. On Venus  $G_0 \ll 1$  everywhere below the clouds. Thus in the lower atmosphere the time scales are ordered by

$$\tau_{\text{dyn}} \ll \tau_{\text{day}} \sim \tau_{\text{rot}} < \tau_{\text{rad}} \quad (2.4.7)$$

As with the Earth, the latitudinal imbalance between absorbed solar radiation and emitted infrared radiation requires the transport of heat poleward. On the Earth this meridional transport takes the form of a Hadley circulation at low latitudes, which gives way to baroclinic eddy transport at middle latitudes. The sloping convection associated with mid-latitude eddies is more efficient for transporting heat than the advection of a Hadley cell, when the atmosphere is rapidly rotating. However, on Venus the relative time scales suggest that a Hadley circulation would extend to polar latitudes. The primary circulation was thus thought to be a pair of Hadley cells, symmetric about the equator, with warm air rising in the equatorial region and sinking at the poles (Fig. 2.11). Although the rotation is slow enough to make Coriolis forces relatively unimportant, it appears to be fast enough to keep the equator uniformly heated, so that the meridional circulation was thought to be almost axially symmetric.

In spite of these reasonable expectations, the observations showed that the dominant circulation on Venus is a zonal westward "superrotation." Nevertheless, a weak meridional circulation must be present, since purely zonal winds cannot transport heat poleward. The observations do give strong evidence for a Hadley circulation at the cloud level, which is consistent with

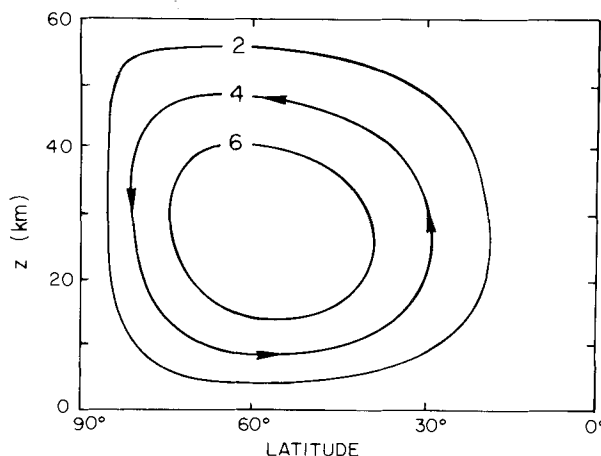


**Fig. 2.11** Streamlines in the Venus Hadley cell. [Based on calculations of E. KALNAY DE RIVAS (1973), *J. Atmos. Sci.* **30**, 763.]

most of the solar flux being absorbed there. (Below the clouds there is likely a series of alternating direct and reversed-flow meridional cells, including a ground-level Hadley cell.) The cloud-level Hadley cell and the atmospheric superrotation combine to produce the polar vortex (Fig. 2.12). The meridional winds near the cloud tops are only about 10 m/sec, an order of magnitude slower than the typical zonal wind.

In the 60 km region  $\tau_{\text{rad}} \sim 0.5 \times 10^7$  sec and

$$\tau_{\text{dyn}} \ll \tau_{\text{rad}} \lesssim \tau_{\text{day}} \sim \tau_{\text{rot}} \quad (2.4.8)$$

replaces (2.4.7). Thus diurnal heating is more likely to be faster than in the deep atmosphere. Before it was clearly realized that the clouds are in a different dynamical regime from the lower atmosphere, it was thought that

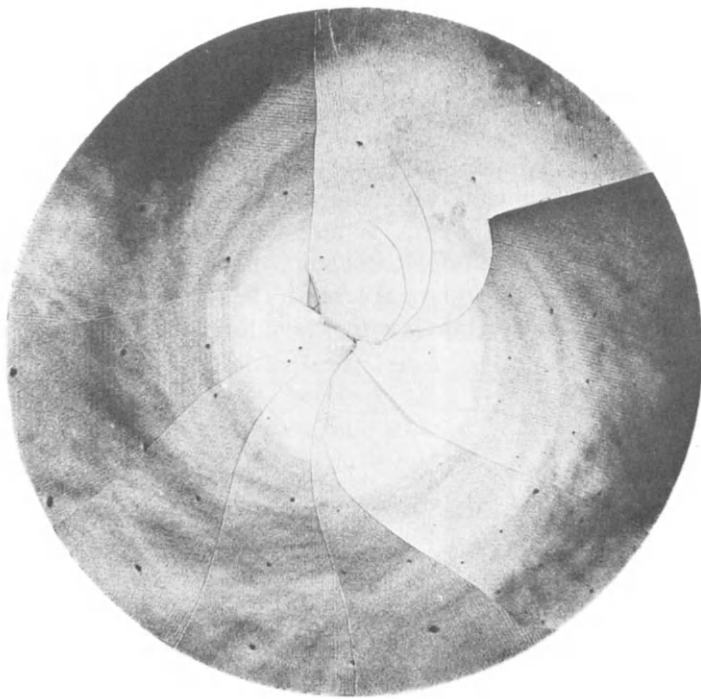


**Fig. 2.12** Space-time composite of ultraviolet images of the southern hemisphere of Venus as observed from Mariner 10. Note the counterclockwise (westward) flowing vortex centered on the south pole. Spiral streaks, resembling dense terrestrial stratus, converge into the vortex from low latitudes, akin to the spiral bands of a hurricane. The outer edge of the photograph is the equator. [Courtesy VERNER E. SUOMI and SANJAY S. LIMAYEH; also see *J. Atmos. Sci.* **34**, 205 (1977) and *Science* **201**, 1009–1011 (1978).]

the general circulation should lead to an absence (or at least a partial clearing) of clouds near the descending branch of the Hadley cell. The clouds may in fact be less dense, or lie lower, over the polar caps; but the matter now seems less important.

Mariner 10 observations disclosed a distinct pattern in the ultraviolet images of clouds centered on the sub-solar region that is probably due to convection. Also the near uniformity of thermal emission indicates a controlling influence of dynamics. The question arises as to what causes the ultraviolet contrast patterns, which do not appear in the visual or infrared. Probably there is an unidentified ultraviolet absorber; but perhaps the ultraviolet penetrates only into the uppermost thin haze. A highly irregular upper surface, with peaks and troughs due to convection, could produce highlights and shadows (planetary photometry is treated in Section 4.3.3).

The predominant feature of the upper-atmosphere dynamics is an approximate *four-day retrograde rotation*. Not only is such a motion well documented from telescopic photographs from Earth of cloud contrasts in the ultraviolet, but spectroscopic Doppler shifts and the zonal drifts of descending spacecraft indicate real but highly variable velocities of the order of 100 m/sec.

The high zonal wind speeds, many times faster than the retrograde rotation speed of the planet, give rise to their description as “superrotational.” Although the winds are mainly observed, naturally, near the cloud tops, interferometric tracking of Pioneer Venus probes and Veneras 8, 9, 10, and 12 yielded altitude profiles of the wind velocities, which steadily decrease from around 100 m/sec at the cloud tops to near zero in the lowest scale height.

Away from the equator, the zonal winds have an equatorward centrifugal force that is just balanced by the poleward force from the equatorward pressure gradient, since the Coriolis force is negligible. Thus, the equations of motion reduce to the simple case of cyclostrophic flow, Eq. (2.2.11), which may be written

$$\frac{u^2 \tan \phi}{a} = -\frac{1}{\rho} \left( \frac{\partial p}{\partial y} \right)_z \quad (2.4.9)$$

Invoking the hydrostatic equation (2.2.25) and the perfect gas law, we can obtain the thermal wind equation for cyclostrophic balance:

$$2u \frac{du}{d \ln p} = \frac{R}{\tan \phi} \frac{\partial T}{\partial \phi} \quad (2.4.10)$$

This equation is the analogue to (2.2.21) for the case of vanishing Coriolis force. Equation (2.4.10) describes the increasing speed of the zonal retrograde superrotation with height as the temperature decreases poleward (along constant pressure surfaces), as it does below 70 km.

Most of the speculation on the driving mechanism for the four-day rotation involves the sun's apparent motion, which is direct (west to east), as seem from Venus. The "moving flame" mechanism has solar energy deposited within the clouds and convected upward, but with an appreciable time lag. As a convecting volume expands and rises, it reacts on those convection cells preceding it. Thus the stream lines of upward convection following the sun's trace across the planet will be tilted away from the sun, or in the retrograde sense. It is still not established whether this or some other mechanism is responsible for the four-day effect. Other candidate processes, besides the transfer of momentum through a vertical succession of eddies, are (1) a coupling between the zonal flow and the mean meridional circulation (Hadley convection) and (2) upward propagating planetary-scale waves. The process maintaining the zonal circulation must be effective everywhere between the surface region and cloud levels and above, because all this atmosphere superrotates, except the lowest scale height.

Moving planetary waves, as well as atmospheric rotation, can be discerned from the ultraviolet albedo markings, with the displacements of the large-scale markings indicating the propagation of planetary-scale waves relative to the winds. A wide variety of planetary waves is observed and several causative mechanisms have been proposed, including resonant oscillations of the atmosphere, an instability in the mean circulation, a baroclinic instability, and a preferential response of the atmosphere (at 4–6-day periods) to forcing, over a broad spectrum of periods, by convective activity at cloud heights or by turbulent activity. Several specific interpretations have been offered to explain particular recurring patterns; for example, the Y morphology of the dark equatorial markings could be a combination of a midlatitude Rossby wave and a westward propagating equatorial Kelvin wave, with the Rossby wave shifted westward in phase by an appropriate amount.

Above 100 km the circulation is quite different because of the enormous temperature and pressure differences between the day and night sides. While the day-side thermosphere rises to 300°K, the night side temperature decreases above 100 km and drops to an asymptotic value of about 100°K, creating what has been called a night-side "cryosphere." These large day-night temperature differences create horizontal pressure gradients across the terminator. At 190 km the pressure at noon is three powers of 10 larger than it is at night. At both morning and evening terminators, the pressure gradients direct the flow from the day hemisphere to the night, providing as a first approximation a circulation from the subsolar to the antisolar points. There is a major vertical contraction of the atmosphere above 100 km as it crosses the terminators, arising from night-side cooling (by radiation in the 15  $\mu\text{m}$  band of CO<sub>2</sub>) and descending motion.

## 2.5 Diurnal Winds on Mars

The atmosphere of Mars, while composed primarily of CO<sub>2</sub>, is otherwise vastly different in character from Venus' atmosphere. With a surface pressure around 7.5 mb, it radiates heat rapidly. The temperature at the Viking I landing site (22.5° N) in early summer varies from 187°K at 05 00 local solar time to 242°K at 15 00 hours. The phase lag for the maximum temperature after local noon is not unlike the response over terrestrial deserts, but the 55°K amplitude suggests a cooling time of

$$\tau_{\text{rad}} \sim \tau_{\text{rot}} = 8.88 \times 10^4 \text{ sec} \quad (2.5.1)$$

On the other hand, Coriolis forces are important, as on Earth.

Well above the high mountains, the circulation may be relatively simple. Figure 2.13 shows, from results of computer modeling, that geostrophic winds, mainly due to latitudinal pressure gradients arising from uneven solar heating, yield weak easterlies in the summer hemisphere and stronger but irregular westerlies in the winter hemisphere.

Computer modeling of the Martian surface winds has also shown them to be critically dependent on the topography. In addition, both the numerical models and the pressure measurements show that the atmosphere is driven by thermal tides. Not only is there a diurnal (wavenumber 1 or  $l = 1/a \sin \phi$ ) component present, but there is an equally important semidiurnal (wavenumber 2) component. The Earth also shows the semidiurnal component, which is driven westward by solar heating but has a strong amplitude because of an accidental resonance with the horizontal channel formed by the ground and tropopause. The Martian semidiurnal mode is similar in character to Earth's but had not been predicted by the modeling.

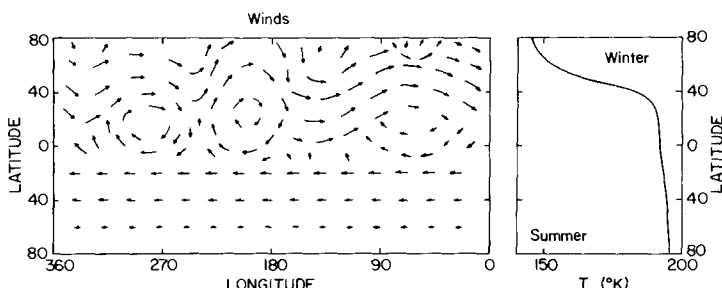


**Fig. 2.13** Schematic air flow on Mars well above the ground, computed for the southern summer solstice. The strong west winds in the middle and high latitudes of the winter hemisphere are produced by the net eastward Coriolis torque that accompanies the poleward transfer of air mass, caused in turn by condensation of CO<sub>2</sub> over the winter polar cap. [Based on numerical modeling by LEOVY and MINTZ (1969).]

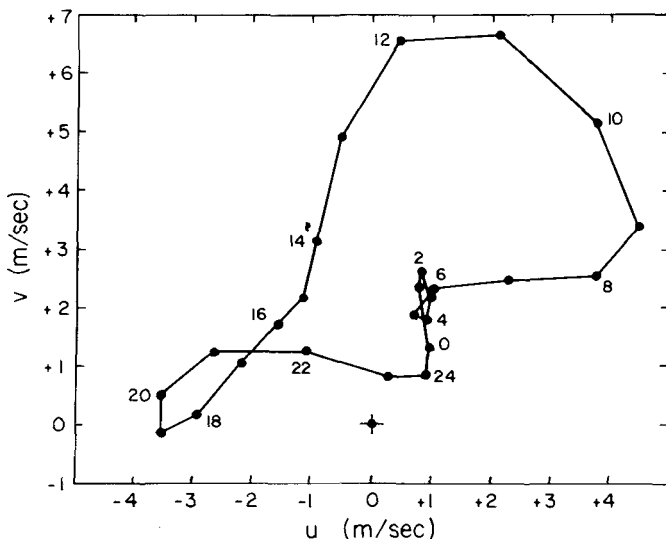


Fig. 2.14 Hodograph of the horizontal winds measured by Viking I. The values next to the points are times in hours from local midnight. The  $u$  (eastward) and  $v$  (northward) velocity components are found by drawing a vector from the cross to a point on the curve. [After HESS et al. (1976).]

The Earth's diurnal mode is also westward driven by the sun, but the Martian diurnal mode shows peculiarities in phase and in the direction of associated winds. Presumably it is either modified severely by Martian topography or it is in an eastward traveling mode—the so-called *Kelvin resonance mode*.

Figure 2.14 shows the predominant southwesterlies composing the winds through the Martian day. Observations over a short period at one station do not by themselves tell much of the general surface circulation on the planet. Nevertheless, they give the required data base for a comparison with numerical models that can then lead to a more confident evaluation of the planetary circulation.

The Viking landers also showed a slow but steady decrease of total pressure at their northern-hemisphere locations. The effect was expected, as the southern ice cap was growing by the condensation of  $\text{CO}_2$  from the atmosphere.

## 2.6 Convection in the Jovian Atmosphere

Jupiter, as the prototype for the major planets, offers many characteristics that are vastly different from those of terrestrial planets. It has a diameter 11.2 times the Earth's and a rotation period of less than 10 hr or

$$\tau_{\text{rot}} = 3.54 \times 10^4 \text{ sec} \quad (2.6.1)$$

Zonal speeds at the boundaries of the bright *zones* and dark *belts* may reach 100 m/sec, so that (for zonal motions, at least)

$$\tau_{\text{dyn}} \sim 10^6 \text{ sec} \quad (2.6.2)$$

and the Rossby number (2.2.3) is

$$R_0 \sim 10^{-2} \quad (2.6.3)$$

meaning the geostrophic velocity (2.2.10) should be a good approximation.

The Bond (omnidirectional) albedo has been accurately determined with the aid of the phase integral (see Section 4.3.3) measured by Pioneer 10 and is  $\Lambda_B = 0.45$ . Hence the equilibrium temperature (1.2.46) is  $T_e = 106^\circ\text{K}$ . However, photometry in the infrared from aircraft above the Earth's water vapor gives a radiation temperature of  $T = 124.4^\circ\text{K}$ , indicating that most of Jupiter's atmospheric heat energy comes from the interior, not from the sun (see Section 1.9.1).

It would appear also that convection is strong for two reasons: First, the bright zones are cooler and higher than the dark belts, their high albedo arising from solid  $\text{NH}_3$  crystals. Thus the zones are regions of upward motion and high pressure (see Fig. 2.15). Second, the strong zonal flow is evidently

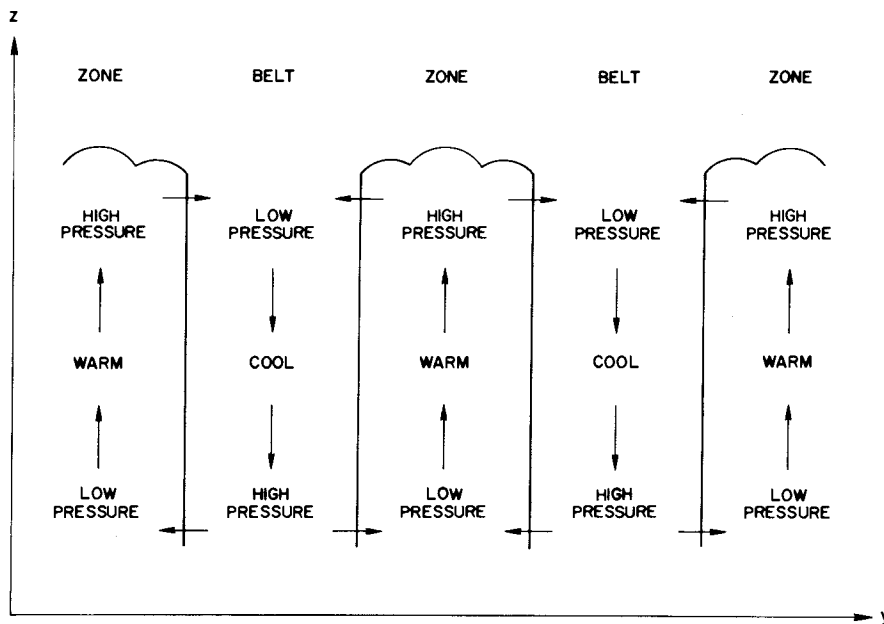


**Fig. 2.15** Schematic diagram of Jupiter's meridional circulation. [After STONE (1976).]

due to Coriolis interaction with meridional flow between zones and belts. The highest wind velocities are found along the transitions between zones and belts, with eastward velocities between a zone and a poleward belt, westward velocities between a zone and an adjacent equatorial belt.

On the other hand, if Jupiter were not strongly heated from the interior, one would not expect to find such strong convection. To understand how rotation inhibits convection, we refer to the vorticity equation (2.2.37), which came from the equations of motion (2.1.21–2.1.23) with the rotation terms (in  $a^{-1}$ ) and viscosity terms (in  $v$ ) discarded. As in the derivation of (2.2.38), let us discard terms in the square of the velocity (remembering that  $\omega = dp/dt$  is essentially a velocity in isobaric coordinates). Then for steady ( $\partial\zeta/\partial t = 0$ ), slow motions we have from (2.2.37)

$$\frac{\partial(\zeta + f)}{\partial t} \approx -\nabla_p \cdot [(\zeta + f)\mathbf{V}] \approx -f\nabla_p \cdot \mathbf{V} = 0 \quad (2.6.4)$$

(since  $\zeta\mathbf{V}$  is of second order in velocities), where  $\mathbf{V} = \hat{\mathbf{u}}u + \hat{\mathbf{j}}v$ . Then from the isobaric equation of continuity (2.2.26) we have

$$\partial\omega/\partial p = 0 \quad (2.6.5)$$

which states that an element of fluid must move along a line of constantly changing pressure,  $\omega \equiv dp/dt = \text{const}$ . Clearly the constant can only be zero, so that to a first approximation *all steady motions in a rotating atmosphere with zero viscosity must be barotropic* (i.e., two dimensional). This statement amounts to the *Taylor–Proudman theorem* in hydrodynamic stability theory.

In the atmospheres of Venus, Mars, and Earth (at least in middle latitudes) the barotropic atmosphere gives way to a *baroclinic* one in which temperature varies systematically with latitude at a given pressure level. This latitudinal variation  $(\partial T/\partial\phi)_p$  carries profound results for Earth and probably Mars. It gives rise to thermal winds or large velocity shears (see Section 2.2.3). In turn, small perturbations in velocity (or pressure or temperature) tend to become greatly amplified in regions where large shears already exist. These *baroclinic instabilities* set up strong disturbances consisting of cyclonic winds and turbulent mixing. Thus a baroclinic atmosphere, which violates the Taylor–Proudman theorem, can be established because convection is driven by horizontal gradients, the motion is not steady, and the eddy viscosity  $v_E$  (see Section 2.2.1) cannot be ignored. The important point is that, in a baroclinic atmosphere, convection is driven as a by-product of the horizontal temperature gradients.

It has been widely doubted in the past that Jupiter's atmosphere is driven by its baroclinicity, because it was not clear why the zones and belts should exist as they do and especially why the equatorial zone should have a strong

eastward flowing jet. Alternatively, if Jupiter is largely heated from below, the atmosphere could be convectively unstable (with a superadiabatic gradient) so that the static stability (2.2.35) is negative and convection is the primary driving force. The question is whether the rotation of Jupiter would prevent a primary convection from being established.

The circulation problem thus posed has some similarity to the *Bénard problem*, a classical problem in hydrodynamic instability. In its simplest form the Bénard problem deals with a horizontal layer of fluid heated from below. Because of thermal expansion the fluid at lower levels is lighter than at the top. But the convection tendency, which the fluid develops in order to correct this abnormal state of affairs, is inhibited by viscosity. Thus there will be some critical temperature gradient at which convection will begin. Smaller abnormal gradients of temperature will be stable, and the lighter, lower levels will support the heavier mass above.

The hydrodynamic equations for this problem may be solved in the Boussinesq approximation. The solutions are eigenvalue in nature and indicate that a fixed pattern of convection cells is set up when the unstable temperature gradient is achieved. Theory gives a critical value of the *Rayleigh number* at which convection will begin. The Rayleigh number is a combination of parameters in the problem,

$$R \equiv \frac{g\alpha\beta d^4}{v\chi} \quad (2.6.6)$$

where  $\alpha$  and  $\chi$  are coefficients of volume expansion and thermometric conductivity,  $\beta$  is the abnormal temperature gradient, and  $d$  the depth of the fluid. Without rotation, the critical value is  $R_c = 1100$ . The effect of rotation about a vertical axis is specified by another dimensionless parameter, the Taylor number,

$$Ta \equiv \frac{4\Omega^2 d^4}{v^2} = \left( \frac{fd^2}{v} \right)^2 \quad (2.6.7)$$

where  $\Omega$  becomes  $\Omega \sin \phi$  in the spherical problem. For example, when  $Ta = 2 \times 10^3$ , convection does not set in until  $R_c = 2376$ . As an example of the Taylor number, the Earth's boundary layer (see Section 2.2.1) has  $d \sim 10^5$  cm and  $v_E \sim 5 \times 10^4$  cm<sup>2</sup>/sec; with  $f \sim 10^{-4}$  /sec, we have  $Ta \sim 4 \times 10^2$ .

Computer modeling of the Bénard problem for a rotating spherical planet with nonisotropic *eddy viscosity*  $v_E$  and *thermal diffusivity*  $\chi_E$  indicates that turbulent convection will create the zones and belts, with the proper velocities. At high latitudes, the banded structure disappears, presumably because the Taylor number's dependence on latitude leads to a suppression of convection. Figure 2.16 shows the results of a computer simulation of circulation in the Jovian atmosphere.

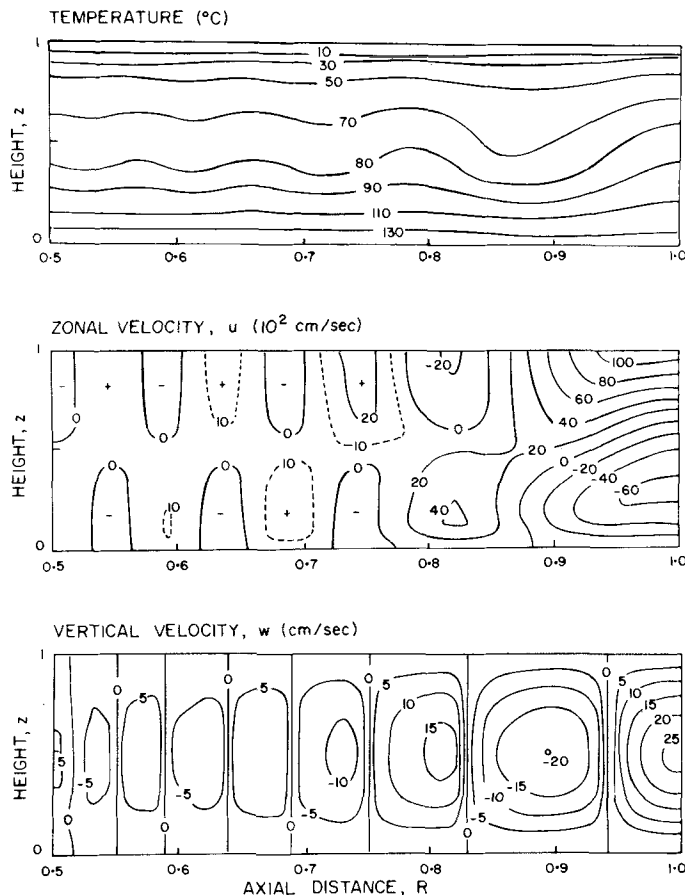


**Fig. 2.16** Contours of temperature, zonal winds, and vertical motions in a numerical simulation of Jupiter's atmosphere for a large-scale convection driven by internal heating. [Adapted from calculations by WILLIAMS and ROBINSON (1973).]

Near the equator there is an eastward jet of 100 m/sec at high levels with a retrograde motion of 60 m/sec below it. Between these jets and the inactive polar regions (beginning at  $\phi = \pm 45^\circ$ ) are alternating positive and negative zonal flow correlated with the banded structure. These upper level jets are countered by opposite flows below.

Attractive as it is, this model of free convection, driven by heating from below, has problems. The model calculations use the observable quantities to constrain the adopted parameters, but there is one observable quantity left over—the energy flux through the atmosphere. The main source of flux

in the model is the convective flow and the parameters that produce the right scales of the motions also produce much too much outward energy flow.

Other models of the general circulation of Jupiter involve a more stable dynamical situation than free, dry convection. Below the visible clouds (near the 300°K level; see Fig. 1.26) condensation of water is important. With moist convection much of the heat flux from below is latent rather than sensible heat. Very likely the banded structure of Jupiter is due to a large-scale convection pattern driven by the internal heat source but with the phase change of water playing a controlling thermodynamic role.

Baroclinic circulation arises from differential heating between the poles and equator. The zonal flow can thus be driven by horizontal heat transport, which is coupled with (and modifies) the vertical temperature gradients. However, baroclinic circulation models for Jupiter do not transfer zonal mean potential energy (e.g., temperature differences) directly into zonal winds, as in Hadley circulation. Instead, the zonal mean potential energy is first broken into smaller eddy-sized packets of varying temperature and pressure. This potential energy is, according to computer modeling, transformed into eddies of kinetic energy and thence into zonal winds, with strong vertical shear induced by the thermal wind equation (2.2.20). The eddies correspond to discrete cyclonic and anti-cyclonic storms seen in high-resolution imaging of the jets lying near the borders between the zones and belts. Larger storms that emerge from the computer modeling are long lived and may correspond to actual storms such as the Great Red Spot.

Baroclinic instabilities may become important at middle latitudes, where they would have the effect of over-riding (i.e., stabilizing) the convective overturning. However, as noted above, the horizontal temperature gradients are smaller than on Earth and Mars because of the larger scale of Jupiter and its internal heat source, and consequently baroclinic instabilities must have little effect in equatorial latitudes. On the other hand the equatorial jet could arise from a vertical transport of momentum by Rossby or gravity waves rather than convection.

Winds at the cloud deck of Jupiter, as disclosed by the zonal drift of eddies, have been analyzed with data from the 1979 Voyagers' imaging and infrared spectrometer experiments. The latter yields atmospheric temperature versus pressure, because the intensity at a given wavelength is emitted primarily from a given atmospheric thickness (i.e., where the optical thickness  $\tau \sim 1$ ). The upper tropospheric temperatures (see Fig. 1.26) are strongly coupled to the wind field at the cloud deck in the sense required to weaken the jets with increasing altitudes over several scale heights. With the baroclinic interpretation, both the thermal wind shear at middle latitudes and the activity of planetary waves near the equator are responses in the upper troposphere to driving forces in the deeper atmosphere.

## 2.7 Uranus and its Seasons

The axis of Uranus lies only 8 degrees out of its orbital plane. Each polar region therefore is exposed to 42 years of continuous sunlight, followed by 42 years of complete darkness. Averaged over a year, the solar input to the poles is greater than that to the equator; the factor is  $\pi/2$  for  $90^\circ$  obliquity. The meridional temperature gradient that drives the atmosphere therefore has the opposite sign to that found on most planets. The internal heat flux is unmeasurably small (Table 1.3) and probably has little or no effect on the circulation pattern. Even though Uranus' year is long, its radiative time constant is even longer, about 630 Earth years or 7.5 Uranus years (Problem 2.11). The fractional temperature change during half a year is therefore at most  $\exp -\frac{1}{15}$  or 7 %. For a mean temperature of  $58^\circ\text{K}$ , this amounts to  $4^\circ\text{K}$ , which could be further reduced by vertical or horizontal motions.

During 1966–1980, the microwave brightness temperature in the 10–20 cm wavelength range increased from  $180$  to  $270^\circ\text{K}$ , with a smaller decrease in 1983. During this whole period, the pole has been approaching the apparent center of the disk; the effect might therefore be seasonal, although it is clearly much greater than any likely change of physical temperature. One possibility is that the atmosphere was becoming more transparent, permitting the observed radiation to originate at a deeper, warmer level. The problem of time-dependent local convection has been studied in some detail. At high latitudes, solar heating of the higher levels during summer generates a subadiabatic lapse rate and shuts off the convection. Most of the convection takes place toward the end of winter, when the boundary temperature is lowest. However, the temperature excursion is still several degrees, and there remains a substantial drive for horizontal circulation.

Parameterized models for such circulation suggest that it should be able to reduce the pole-equator temperature difference to well under  $1^\circ\text{K}$  (the same conclusion holds for Neptune). Velocities could be small (less than 2 m/sec), and eddy scales or wavelengths should be less than 1000 km.

## BIBLIOGRAPHICAL NOTES

### Section 2.1 Basic Equations

An advanced but concise and clear text on hydrodynamics is

LANDAU, L. D., and LIFSHITZ, E. M. (1959), "Fluid Mechanics," Pergamon Press, New York.

### Section 2.2 Horizontal Circulation of the Troposphere

The pioneering paper on the general circulation is

HADLEY, G. (1735), Concerning the cause of the general trade-winds, *Phil. Trans. Roy. Soc. London* **39**, 58–60 [reprinted in *Smithsonian Inst. Misc. Collections* **51**, 5–7, 1910].

Modern meteorology was founded around the close of World War I by the Norwegian school at Bergen led by VILHELM BJERKNES. One of the principal papers of that period, by his son JACOB, identifies warm and cold fronts for the first time:

BJERKNES, J. (1919), On the structure of moving cyclones, *Geofys. Publ.* **1**, No. 2, 8 pp.

The importance of the Bergen school in modern meteorology is treated in a delightful article by

NAMIAS, J. (1981), The early influence of the Bergen school on synoptic meteorology in the United States, *Pageoph* **119**, 491–500.

Much of the present thinking on planetary flow patterns is due to ROSSBY (another product of Bergen) and his collaborators. Much of their work is reviewed in

ROSSBY, C.-G. (1949), On the nature of the general circulation of the lower atmosphere, in "The Atmospheres of the Earth and Planets," (G. P. Kuiper, ed.), pp. 16–48, Univ. Chicago Press, Chicago, [2nd ed., 1952].

The theory of planetary circulation is developed in

LORENZ, E. N. (1967), "The Nature and Theory of the General Circulation of the Atmosphere," World Meteorological Organization, Geneva.

Most of the discussion in Section 2.2 has been based on Chapters 2 through 7 of the excellent text

HOLTON, J. R. (1972), "An Introduction to Dynamic Meteorology," Academic Press, New York.

A more descriptive text, which in many ways is complementary to Holton, is

PALMÉN, E. and NEWTON, C. W. (1969), "Atmospheric Circulations Systems," Academic Press, New York.

That dynamical instabilities associated with mid-latitude westerlies were crucial to the origin and development of cyclonic disturbances was demonstrated in

CHARNEY, J. G. (1947), The dynamics of long waves in a baroclinic westerly current, *J. Meteorology* **4**, 135–162.

A number of classic papers in dynamic meteorology (including CHARNEY, 1947) are reprinted in

SALTZMAN, B. (ed.) (1962), "Theory of Thermal Convection," Dover, New York.

A theoretical comparative study of circulation in atmospheres of the solar system has been developed by

GOLITSYN, G. S. (1970), A similarity approach to the general circulation of planetary atmospheres, *Icarus* **13**, 1–24.

The role of planetary waves and tides at high altitudes is discussed in

VOLLAND, H. and MAYR, H. G. (1977), Theoretical aspects of tidal and planetary wave propagation at thermospheric heights, *Rev. Geophys. Space Phys.* **15**, 203–226.

HOUGHTON, J. T. (1977), "The Physics of Atmospheres," Cambridge Univ. Press, New York.

SALBY, M. L. (1984), Survey of planetary-scale traveling waves: The state of theory and observations, *Rev. Geophys. Space Phys.* **22**, 209–236.

### Section 2.3 Vertical Transport

The importance of molecular diffusion above 100 km in Earth's atmosphere was first emphasized by

NICOLET, M. and MANGE, P. (1954), The dissociation of oxygen in the high atmosphere, *J. Geophys. Res.* **59**, 15–45.

NICOLET, M. (1954), Dynamic effects in the high atmosphere, in "The Earth as a Planet," (G. P. Kuiper, ed.), Univ. Chicago Press, Chicago.

The standard theoretical work on molecular diffusion, viscosity, and conductivity is CHAPMAN, S. and COWLING, T. G. (1970), "The Mathematical Theory of Non-Uniform Gases," 3d. ed., Cambridge University Press, Cambridge.

The importance of eddy diffusion to atmospheric structure and composition was established by COLEGROVE, F. D.; HANSON, W. B.; and JOHNSON, F. S. (1965), Eddy diffusion and oxygen transport in the lower thermosphere, *J. Geophys. Res.* **70**, 4931–4941.  
COLEGROVE, F. D.; HANSON, W. B.; and JOHNSON, F. S. (1966), Atmospheric composition in the lower thermosphere, *ibid.* **71**, 2227–2236.

A general discussion of eddy diffusion is given in

HUNTER, D. M. (1975a), Vertical transport in atmospheres, in "Atmospheres of Earth and the Planets," (B. M. McCormac, ed.), pp. 59–72, D. Reidel Publ. Co., Dordrecht, The Netherlands.

Examples of analytic treatments may be found in

- HUNTER, D. M. (1975b), Estimates of stratospheric pollution by an analytic model, *Proc. Nat. Acad. Sci.* **72**, 4711–4715.  
WALLACE, L. and HUNTER, D. M. (1973), The Lyman-alpha albedo of Jupiter, *Astrophys. J.* **182**, 1013–1031.  
PRINN, R. G. (1974), Venus: Vertical transport rates in the visible atmosphere, *J. Atmos. Sci.* **31**, 1691–1697.  
PRINN, R. G. and BARSHAY, S. S. (1977), Carbon monoxide on Jupiter and implications for atmospheric convection, *Science* **198**, 1031–1034.

Argon (as well as oxygen) data for Earth are analyzed by

VON ZAHN, U. (1967), Mass spectrometric measurements of atomic oxygen in the upper atmosphere: A critical review, *J. Geophys. Res.* **72**, 5933–5937.

Figures 2.9 and 2.10 are from the comprehensive analysis of

ALLEN, M.; YUNG, Y. L.; and WATERS, J. W. (1981), Vertical transport and photochemistry in the terrestrial mesosphere and lower thermosphere (50–120 km), *J. Geophys. Res.* **86**, 3617–3627.

The Venus helium measurements through the homopause are described and discussed by

VON ZAHN, U.; FRICKE, K. H.; HUNTER, D. M.; KRANKOWSKY, D.; MAUERSBERGER, K.; and NIER, A. O. (1980), The upper atmosphere of Venus during morning conditions, *J. Geophys. Res.* **85**, 7829–7840.

More comprehensive analyses are given by

- MASSIE, S. T.; HUNTER, D. M.; and SOWELL, R. (1983), Day and night models of the Venus thermosphere, *J. Geophys. Res.* **88**, 3955–3969.  
YUNG, Y. L. and DEMORE, W. B. (1982), Photochemistry of the atmosphere of Venus: Implications for atmospheric evolution, *Icarus* **51**, 199–247.

The thermosphere of Mars was analyzed by

MCELROY, M. B. and McCONNELL, J. C. (1971), Dissociation of CO<sub>2</sub> in the Martian atmosphere, *J. Atmos. Sci.* **28**, 879–884.

An analysis of Jupiter's eddy coefficient is in

WALLACE, L. and HUNTER, D. M. (1973), *op. cit.*

Voyager data for Jupiter and Titan are discussed in

- McCONNELL, J. C.; HOLBERG, J. B.; SMITH, G. R.; SANDEL, B. R.; SHEMANSKY, D. E.; and BROADFOOT, A. L. (1982), A new look at the ionosphere of Jupiter in light of the UVS occultation results, *Planet. Space Sci.* **30**, 151–167,  
 SMITH, G. R.; STROBEL, D. F.; BROADFOOT, A. L.; SANDEL, B. R.; SHEMANSKY, D. E.; and HOLBERG, J. R. (1982), Titan's upper atmosphere: Composition and temperature from the EUV solar occultation results, *J. Geophys. Res.* **87**, 1351–1359.  
 YUNG, Y. L.; ALLEN, M.; and PINTO, J. P. (1984), Photochemistry of the atmosphere of Titan: Comparison between model and observations, *Astrophys. J. Suppl.* **55**, 465–506.

#### Section 2.4 Circulation of the Venus Atmosphere

The discussion of the circulation of Venus' atmosphere is drawn largely from

- SCHUBERT, G. (1983), General circulation and the dynamical state of the Venus atmosphere, in "Venus" (D. M. Hunten, L. Colin, T. M. Donahue, and V. I. Moroz, eds.), pp. 681–765, Univ. of Arizona Press, Tucson, Arizona.

Winds for the high atmosphere inferred from the temperature contrasts are treated in

- SEIFF, A. (1982), Dynamical implications of the observed thermal contrasts in Venus' upper atmosphere, *Icarus* **51**, 574–592.

Modeling considerations for the lower atmosphere are due to

- STONE, P. H. (1975), The dynamics of the atmosphere of Venus, *J. Atmos. Sci.* **32**, 1005–1016.

The four-day rotation of the upper atmosphere of Venus was established by

- BOYER, C. and CAMICHEL, H. (1961), Observations photographiques de la planète Vénus, *Ann. Astrophys.* **24**, 531–535.

The "moving flame" mechanism was developed by

- SCHUBERT, G. and WHITEHEAD, J. (1969), Moving flame experiment with liquid mercury: Possible implications for the Venus atmosphere, *Science* **163**, 71–72,  
 YOUNG, R. E. and SCHUBERT, G. (1973), Dynamical aspects of the Venus 4-day circulation, *Planet. Space Sci.* **21**, 1563–1580.

The term "cryosphere" for an upper atmosphere whose temperature decreases with altitude was proposed by

- SCHUBERT, G., et al. (1980), Structure and circulation of the Venus atmosphere, *J. Geophys. Res.* **85**, 8007–8025.

#### Section 2.5 Diurnal Winds on Mars

An excellent review, which incorporates material from the Viking missions, is

- LEOVY, C. B. (1979), Martian meteorology, *Ann. Rev. Astron. Astrophys.* **17**, 387–413.

A numerical model for the circulation of the Martian atmosphere was first developed by

- LEOVY, C. B. and MINTZ, Y. (1969), Numerical simulation of the atmospheric circulation and climate of Mars, *J. Atmos. Sci.* **26**, 1167–1190.

An improved model, with more realistic topography and an additional model layer to simulate the strong diurnal variations of wind and temperature in the boundary layer, is due to

- POLLACK, J. B.; LEOVY, C. B.; GREIMAN, P. W.; and MINTZ, Y. (1981), A Martian general circulation experiment with large topography, *J. Atmos. Sci.* **38**, 3–29.

Viking lander measurements of temperatures, winds, and pressures have been reported in

- HESS, S., et al. (1976), Mars climatology from Viking I after 20 sols, *Science* **194**, 78–81.

The theory of tides in atmospheres is developed in

CHAPMAN, S. and LINDZEN, R. S. (1970), "Atmospheric Tides," Gordon and Breach, New York.

A discussion of tides expected in the Martian atmosphere is given by

ZUREK, R. W. (1976), Diurnal tides in the Martian atmosphere, *J. Atmos. Sci.* **33**, 321–337.

HAMILTON, K. (1982), The effect of solar tides on the general circulation of the Martian atmosphere, *J. Atmos. Sci.* **39**, 481–485.

Planetary waves are discussed by

CONRATH, B. J. (1981), Planetary-scale wave structure in the Martian atmosphere, *Icarus* **48**, 246–255.

Growth of the ice caps is treated theoretically in

BRIGGS, G. A. (1974), The nature of the residual Martian polar caps, *Icarus* **23**, 167–191

### Section 2.6 Convection in the Jovian Atmosphere

The nature of Jupiter's circulation was investigated before Pioneer and Voyager with the collective empirical evidence assembled by

CHAPMAN, C. R. (1969), Jupiter's zonal winds: Variation with latitude, *J. Atmos. Sci.* **26**, 986–990.

The first dynamical discussion of the banded structure along the lines illustrated in Fig. 2.11 is due to

HESS, S. L. and PANOFSKY, H. A. (1951), The atmospheres of the other planets, in "Compendium of Meteorology," pp. 391–400, Amer. Meteor. Soc., Boston.

Interpretation of the zonal flow as a baroclinic mechanism was discussed by

GIERASCH, P. J. and STONE, P. H. (1968), A mechanism for Jupiter's equatorial acceleration, *J. Atmos. Sci.* **25**, 1169–1170.

STONE, P. H. (1972a), A simplified radiative-dynamical model for the static stability of rotating atmospheres, *J. Atmos. Sci.* **29**, 405–418.

STONE, P. H. (1972b) A non-geostrophic baroclinic stability: part III. The momentum and heat transports, *ibid.* **29**, 419–426.

The Bénard problem with rotation is treated in

CHANDRASEKHAR, S. (1961), "Hydrodynamic and Hydromagnetic Stability," Clarendon Press, Oxford.

The convective model discussed here is due to

WILLIAMS, G. P. and ROBINSON, J. B. (1973), Dynamics of a convectively unstable atmosphere: Jupiter? *J. Atmos. Sci.* **30**, 684–717.

A qualitatively similar model is suggested in

BUSSE, F. H. (1976), A simple model of convection in the Jovian atmosphere, *Icarus* **29**, 255–260.

The controlling influence of the latent heat of water on the Jovian meteorology was proposed by

BARCILON, A. and GIERASCH, P. J. (1970), A moist Hadley cell model for Jupiter's cloud bands, *J. Atmos. Sci.* **27**, 550–560.

The role of water in a large-scale convective circulation has been examined by

GIERASCH, P. J. (1976), Jovian meteorology: Large-scale moist convection, *Icarus* **29**, 445–454.

After the publication of WILLIAMS and ROBINSON (1973), Williams ran computer models based on conventional (i.e., terrestrial) meteorological equations scaled to Jupiter. He found that the banded structure and oval-shaped disturbances (including the Great Red Spot) may be characteristic of turbulent barotropic vorticity exchanges in a rapidly rotating atmosphere. As on Earth, baroclinic instability would be the primary energy conversion process, and strong convection would not be required. A summary is given in

WILLIAMS, G. P. (1975), Jupiter's atmospheric circulation, *Nature* **257**, 778 (only).

and detailed discussions are found in

WILLIAMS, G. P. (1978), Planetary circulations: 1. Barotropic representations of Jovian and terrestrial turbulence, *J. Atmos. Sci.* **35**, 1399–1426,

WILLIAMS, G. P. (1979), Planetary circulations: 2. The Jovian quasi-geostrophic regime, *J. Atmos. Sci.* **36**, 932–968.

This work inspired a revival of interest in baroclinic models:

GIERASCH, P. J.; INGERSOLL, A. P.; and POLLARD, D. (1979), Baroclinic instabilities in Jupiter's zonal flow, *Icarus* **40**, 205–212.

CONRATH, B. J.; GIERASCH, P. J.; and NATH, N. (1981), Stability of zonal flows on Jupiter, *Icarus* **48**, 256–282.

The role of waves in a baroclinic atmosphere has been discussed by

CHARNEY, J. G. (1947), The dynamics of long waves in a baroclinic westerly current, *J. Meteorol.* **4**, 135–163.

MAXWORTHY, T. (1975), A wave driven model of the Jovian equatorial jet, *Planet. Space Sci.* **23**, 1223–1233.

MAXWORTHY, T.; REDEKOPP, L. G.; and WEIDMAN, P. D. (1978), On the production and interaction of planetary solitary waves: Applications to the Jovian atmosphere, *Icarus* **33**, 388–409.

INGERSOLL, A. P. and CUONG, P. G. (1981), Numerical model of long-lived Jovian vortices, *J. Atmos. Sci.* **38**, 2067–2076.

Voyager observations of zonal winds and related temperature gradients are analyzed in

MITCHELL, J. L.; BEEBE, R. F.; INGERSOLL, A. P.; and GARNEAU, G. W. (1981), Flow fields within Jupiter's Great Red Spot and White Oval BC, *J. Geophys. Res.* **86**, 8751–8757.

INGERSOLL, A. P.; BEEBE, R. F.; MITCHELL, J. L.; GARNEAU, G. W.; YAGI, G. M.; and MULLER, J. P. (1981), Interaction of eddies and mean zonal flow on Jupiter as inferred from Voyager 1 and 2 images, *J. Geophys. Res.* **86**, 8733–8743.

PIRRAGLIA, J. A.; CONRATH, B. J.; ALLISON, M. D.; and GIERASCH, P. J. (1981), Thermal structure and dynamics of Saturn and Jupiter, *Nature* **292**, 677–679.

LIMAYE, S. S.; REVERCOMB, H. E.; SROMOVSKY, L. A.; KRAUSS, R. J.; SANTEK, D. A.; and SUOMI, V. E. (1982), Jovian winds from Voyager 2. Part I: Zonal mean circulation, *J. Atmos. Sci.* **39**, 1413–1432.

ALLISON, M. and STONE, P. H. (1983), Saturn meteorology: A diagnostic assessment of thin-layer configurations for the zonal flow, *Icarus* **54**, 296–308.

An excellent review of the dynamics of Jupiter's atmosphere is

STONE, P. H. (1976), The meteorology of the Jovian atmosphere, in "Jupiter," (T. Gehrels, ed.), pp. 586–617, Univ. Arizona Press, Tucson.

## Section 2.7 Uranus and its Seasons

That the temporal change of microwave emission might be of seasonal origin was suggested by

BRIGGS, F. H. and ANDREW, B. H. (1980), Microwave radiometry and interferometry of Uranus, *Icarus* **41**, 269–277.

The discussion of convection in the text follows

WALLACE, L. (1983), The seasonal variation of the thermal structure of the atmosphere of Uranus, *Icarus* **54**, 110–132.

and an earlier paper,

WALLACE, L. (1980), The structure of the Uranus atmosphere, *Icarus* **43**, 231–259.

The horizontal circulation of Uranus has been discussed by Stone (*op. cit.*, Section 2.6) and

STONE, P. H. (1973), The dynamics of the atmospheres of the major planets, *Space Sci. Rev.* **14**, 444–459.

STONE, P. H. (1975), The atmosphere of Uranus, *Icarus* **24**, 292–298.

A more recent update is

INGERSOLL, A. P. (1985), Atmospheric dynamics of Uranus and Neptune: Theoretical considerations, in “Uranus and Neptune” (J. T. Bergstrahl, ed.), pp. 263–269, NASA CP 2330.

## PROBLEMS

**2.1 Inertial oscillation.** Solve the simplified equation of horizontal motion for the case of uniform horizontal pressure and show that air parcels will move in anticyclonic (clockwise) circles with periods of one-half the rotation period of a Foucault pendulum.

**2.2 Tornado pressure.** A tornado rotates with constant angular velocity and has a uniform temperature. Find an expression for the outward pressure distribution in terms of the central pressure  $p_0$ . Take  $T = 300^\circ\text{K}$  and, at 0.1 km from the center, take  $p = 1 \text{ atm}$  and  $V = 10^4 \text{ cm/sec}$ . What is  $p_0$ ?

**2.3 Gradient flow.** (a) What is the geostrophic wind speed at the surface at  $\phi = 30^\circ$  when the pressure gradient is 1 mb/100 km? (b) What are the cyclonic and anticyclonic gradient wind speeds for the same conditions and a radius of curvature of 600 km?

**2.4 Jet stream.** What is the jet stream velocity (a) in summer at 250 mb (10 km) and  $\phi = 45^\circ$  if the mean  $dT/d\phi = -0.5^\circ\text{K}/\text{deg}$ , and (b) in winter at 200 mb (12 km) and  $\phi = 30^\circ$ , with  $dT/d\phi = -1^\circ\text{K}/\text{deg}$ . In both cases take the zonal wind to be a westerly of 10 m/sec at the 600 mb level. (c) Estimate the difference in fuel costs for a jet transport crossing the U.S. traveling eastward compared with westward in the winter jet stream. (Figure fuel consumption at 10,000 lb/hr; jet fuel costs about three-fourths the price of gasoline.)

**2.5 Static stability parameter (I).** Show that  $\sigma(\Phi)$  is

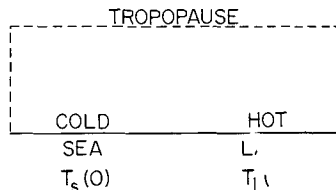
$$\sigma = \frac{1}{p^2} \left( \frac{\partial}{\partial \ln p} - \frac{R}{C_p} \right) \frac{\partial \Phi}{\partial \ln p}$$

**2.6 Static stability parameter (II).** Use the expression in Problem 2.5 to find  $\sigma(p)$  when the atmosphere is (a) adiabatic and (b) isothermal.

**2.7 Vorticity equation.** Show that the isobaric equations of motion give the vorticity equation (2.2.37).

**2.8 Sea breeze.** Idealize a cross section of a coastal region as being bounded on either side and the top by impenetrable walls. Over the sea the surface temperature is  $T_s(0) = 12^\circ\text{C}$ . Over land,  $T_l(0) = 27^\circ\text{C}$ . The surface pressure over both regions is nearly equal,  $p(0) \approx 1000 \text{ mb}$ , and

$T$  decreases with height over both regions at a rate  $dT/dz = -6.5^\circ\text{C}/\text{km}$ . (a) Find the pressures at 10 km over each region. (b) From considerations of continuity, what is the direction of circulation within the closed cell? (c) What will happen at night if the land air cools rapidly enough to become colder than the sea air?



**2.9 Eddy diffusion.** What is the density distribution for a minor constituent in an isothermal atmosphere when the flux is constant and the eddy diffusion coefficient varies as  $\exp[(z - z_0)/L]$  when (a)  $L = \frac{1}{2}H$  and (b)  $L = H$ ?

**2.10 Bénard cells.** Suppose that in the horizontal plane at the onset of convection the Bénard cells consist of a network of uniform, regular, and contiguous polygons. (Within each cell the convection flow is upward near the center and downward near the perimeter.) Show that these polygons can only be equilateral triangles, squares, or regular hexagons.

**2.11 Uranus' thermal time constant.** Calculate the fraction of thermal energy radiated in 1 sec using the Stefan-Boltzmann law; the reciprocal of this is the thermal time constant. For the heat capacity use a column one scale height deep with a molar specific heat  $C_p = 5R/2$ .

## **Chapter 3**

# **CHEMISTRY AND DYNAMICS OF EARTH'S STRATOSPHERE**

### **3.1 Principles of Photochemistry**

Photochemistry is concerned with chemical reactions that are initiated by the absorption of radiation. Thus schematically we write



meaning that molecule A absorbs a quantum of radiation and makes an energy transition to the excited molecular state designated A\*. The excited state could be an excited rotational or vibrational level, an excited electronic state, or it could be a dissociated or an ionized molecule. The *quantum yield* of the process (3.1.1) is the number of A\* molecules produced for each absorbed photon that has adequate energy to produce state A\*.

Once excited molecules are produced, they enter into secondary chemical reactions, forming species that would not exist (in the same proportions, at least) in a state of thermodynamic equilibrium at the local kinetic temperature. Hence photochemical processes are non-LTE mechanisms (see Section 1.2.1), and they have to be handled quantitatively by examining the rate at which each reaction occurs. This fact constitutes the basic complexity of photochemical theory.

Suppose reaction (3.1.1) has an absorption cross section  $\alpha(v)$  ( $\text{cm}^2$ ). If the total cross section of A at frequency  $v$  is  $\alpha_T(v)$ , the monochromatic quantum efficiency is  $\alpha(v)/\alpha_T(v)$ . The instantaneous rate of production of A\* (square

brackets denote concentration in molecules/cm<sup>3</sup>) is

$$\begin{aligned} \frac{d[A^*]}{dt} &= [A] \int_{v_0}^{\infty} \pi \mathcal{F}_v e^{-\tau_v/\mu} \alpha(v) dv \\ &\equiv [A] J \end{aligned} \quad (3.1.2)$$

Here  $hv_0$  is the threshold energy for reaction (3.1.1),  $\pi \mathcal{F}_v$  (photon/cm<sup>2</sup> sec Hz) is the photon flux per unit frequency interval outside the Earth's atmosphere. The vertical optical thickness is

$$\tau_v(z) = \sum_i \alpha_i(v) \int_z^{\infty} N_i(z') dz' \quad (3.1.3)$$

where the summation is taken over every constituent with abundance  $N_i$  that absorbs at frequency  $v$ . The factor  $1/\mu$  is the slant air-mass factor for the zenith angle  $\chi$  of the sun. Unless one is especially concerned with sunrise or sunset effects,  $\mu = \cos \chi$  is an adequate approximation. The second equality in (3.1.2) defines  $J$  (sec<sup>-1</sup>), the production rate of A\* per molecule of A. If A\* represents a partial or total dissociation of molecule A, then  $J$  is commonly called the *photolysis rate*.

A two-body reaction,



proceeds at the rate

$$\begin{aligned} \frac{d[C]}{dt} &= [A][B] \iint Q_{AB}(g) f_A(v_A) f_B(v_B) g d^3 v_A d^3 v_B \\ &\equiv [A][B] k_{AB} \end{aligned} \quad (3.1.5)$$

The  $f$ 's represent normalized distribution functions for the molecular velocities;  $g$  is the relative scalar velocity of collision, so that  $g = |\mathbf{v}_A - \mathbf{v}_B|$ ; and  $Q_{AB}(g)$  is the collision cross section. This cross section is zero at velocities

$$g < g_0 \equiv \left( \frac{2\varepsilon_0}{M_{AB}} \right)^{1/2} \quad (3.1.6)$$

where  $M_{AB}$  is the reduced mass of A and B, and  $\varepsilon_0$  is the *activation energy* that must be supplied to overcome any potential barrier that (3.1.4) might have (see Problem 3.1).

The *rate coefficient*  $k_{AB}$  (cm<sup>3</sup>/sec) defined by (3.1.5) is conventionally written to show a temperature dependence as

$$k_{AB} = a(T/300)^b e^{-c/T} \quad (3.1.7)$$

where  $T$  is expressed in degrees Kelvin. The quantity  $c$  is the activation energy in °K (i.e.,  $c = \varepsilon_0/k$ ) and the exponential is essentially a Boltzmann factor giving the fraction of a population that possesses the necessary kinetic energy to make a reaction occur.

In atmospheric physics it is occasionally desirable to refer a rate coefficient to the gas-kinetic rate for elastic collisions. Most atmospheric molecules have diameters several times that of the first Bohr orbit or cross sections of  $Q \approx 5 \times 10^{-15} \text{ cm}^2$ . At 300°K the mean speed of mass 28( $\text{N}_2$ ) is  $\langle v \rangle \sim 4 \times 10^4 \text{ cm/sec}$ . Hence the gas kinetic rate is about

$$k_{\text{g.k.}} = Q\langle v \rangle \approx 2 \times 10^{-10} (T/300)^{1/2} \text{ cm}^3/\text{sec} \quad (3.1.8)$$

Unless there are long-range (e.g., Coulomb) forces at work, this value is an upper limit for chemical rates.

By analogy with (3.1.5) we can define a rate coefficient for the three-body collision



in which M serves to stabilize intermediate products of the reaction and to help balance the kinetic energy and momentum. This reaction proceeds at the rate

$$d[\text{C}]/dt = [\text{A}][\text{B}][\text{M}]k_{\text{ABM}} \quad (3.1.10)$$

TABLE 3.1 *Dissociation Energies of Neutral Molecules<sup>a</sup>*

| Species  | Dissociation energy |           |         |
|--|---------------------|-----------|---------|
|  | eV/molecule         | kcal/mole | Å (vac) |
| H <sub>2</sub>                                       | 4.479               | 103.266   | 2768    |
| CO   | 11.111              | 256.163   | 1116    |
| N <sub>2</sub>                                       | 9.762               | 225.061   | 1270    |
| NO   | 6.509               | 150.055   | 1905    |
| O <sub>2</sub>                                       | 5.117               | 117.967   | 2423    |
| OH   | 4.395               | 101.33    | 2821    |
| ClO  | 2.73                | 63        | ~4540   |
| HCl  | 4.44                | 102       | ~2800   |
| HF   | 5.86                | 135       | ~2115   |
| H <sub>2</sub> O → H + OH                            | 5.117               | 117.98    | 2423    |
| HO <sub>2</sub> → O + OH                             | 2.73                | 63        | 4540    |
| CO <sub>2</sub> → CO + O                             | 5.455               | 125.750   | 2273    |
| NO <sub>2</sub> → NO + O                             | 3.117               | 71.86     | 3977    |
| N <sub>2</sub> O → N <sub>2</sub> + O                | 1.677               | 38.66     | 7393    |
| O <sub>3</sub> → O <sub>2</sub> + O                  | 1.052               | 24.25     | 11,785  |
| CH <sub>4</sub> → CH <sub>3</sub> + H                | 4.45                | 103       | ~2785   |
| H <sub>2</sub> O <sub>2</sub> → H <sub>2</sub> O + O | 1.43                | 33        | ~8700   |
| NO <sub>3</sub> → NO <sub>2</sub> + O                | 2.17                | 50        | ~5700   |
| HNO <sub>3</sub> → OH + NO <sub>2</sub>              | 2.30                | 53        | ~5400   |
| ClNO <sub>3</sub> → ClO + NO <sub>2</sub>            | 1.13                | 26.1      | ~10,970 |

<sup>a</sup> Wavelength equivalents of the dissociation energy are not necessarily the threshold wavelengths at which photodissociation actually occurs, because the cross section for photodissociation may be negligibly small at the wavelength corresponding to the dissociation energy.

Proceeding with our discussion of gas-kinetic collisions, we make an estimate for an upper limit to  $k_{ABM}$ . The two-body collision frequency for molecule A is

$$v_c(2) = \frac{1}{[A]} \frac{d[A]}{dt} = [B]k_{AB} \quad (3.1.11)$$

The mean time between collisions is  $v_c^{-1}$ , but the duration of a collision is of order  $\tau_{coll} = d/\langle v \rangle$ , where  $d (= 4 \times 10^{-8} \text{ cm})$  is the molecular diameter. Hence the probability that, during a two-body collision, a third body M will also be in the immediate neighborhood is  $\tau_{coll}/v_c^{-1}$ . The three-body collision frequency is thus  $v_c(2)$  times the number of collisions occurring during the time of the two-body collision, or

$$\begin{aligned} \frac{1}{[A]} \frac{d[A]}{dt} &= v_c(3) = v_c(2)[v_c(2)\tau_{coll}] \\ &= [B]k_{AB} \times [M]k_{AB} \times 1 \times 10^{-12} \end{aligned} \quad (3.1.12)$$

Comparison of this expression with (3.1.10) gives

$$k_{ABM} = 1 \times 10^{-12} k_{AB}^2 = 4 \times 10^{-32} (T/300) \text{ cm}^6/\text{sec} \quad (3.1.13)$$

where we use the gas-kinetic value for  $k_{AB}$ .

For gas-kinetic collisions, Eq. (3.1.5) and (3.1.10) give equal rates for

$$[M] = k_{AB}/k_{ABM} = 5 \times 10^{21} \text{ cm}^{-3} \quad (3.1.14)$$

Consequently, if all two-body reactions occurred at least once every  $10^2$  (gas-kinetic) collisions, three-body reactions would be negligible everywhere, even at the ground. But in some cases  $k_{AB}$  is extremely slow (for example,  $O + O \rightarrow O_2 + h\nu$  has  $k < 10^{-20} \text{ cm}^3/\text{sec}$ ), and the three-body process is the dominant mechanism.

Table 3.1 lists dissociation energies for the major, and a number of minor, constituents of Earth's atmosphere. Table 3.2 gives sample photolysis rates

**TABLE 3.2** Daily Mean Photolysis Rates<sup>a</sup> ( $\text{sec}^{-1}$ ) (Averaged Day-Night Rates at 30°N Latitude, Solar Declination +12°)

| Height<br><i>z</i> (km) | <i>J</i> (O <sub>2</sub> )<br>(1.5.1) | <i>J</i> (O <sub>3</sub> )<br>(1.5.4) | <i>J</i> (NO <sub>2</sub> )<br>(3.2.29) | <i>J</i> (N <sub>2</sub> O)<br>(3.2.49) | <i>J</i> (HNO <sub>3</sub> )<br>(3.2.32) |
|-------------------------|---------------------------------------|---------------------------------------|---|---|--|
| 60                      | 5.7(-10)                              | 4.0(-3)                               | 4.42(-3)                                | 2.9(-7)                                 | 5.3(-5)                                  |
| 50                      | 3.7(-10)                              | 2.9(-3)                               | 4.41(-3)                                | 2.4(-7)                                 | 4.4(-5)                                  |
| 40                      | 1.5(-10)                              | 5.9(-4)                               | 4.35(-3)                                | 1.4(-7)                                 | 2.4(-5)                                  |
| 30                      | 1.1(-11)                              | 8.6(-5)                               | 4.23(-3)                                | 1.6(-8)                                 | 3.2(-6)                                  |
| 20                      | 4.7(-14)                              | 3.2(-5)                               | 4.12(-3)                                | 7.7(-11)                                | 2.2(-7)                                  |

<sup>a</sup> Numbers in parentheses are powers of 10. Calculations from a 1973 program by McELROY *et al.* (1974). Revised cross sections (JOHNSON and SELWYN, 1975) reduce *J*(N<sub>2</sub>O) at 20 km and below. Scattering of sunlight will increase the *J*'s in some cases.

that bear on the chemistry discussed in this chapter. Appendix III presents a model atmosphere for average conditions at 45° latitude.

### 3.2 Catalytic Destruction of Ozone

#### 3.2.1 Pure Oxygen Chemistry

To recapitulate from Section 1.5.1 the four Chapman reactions involving only the allotropes of oxygen are (1.5.1–1.5.4) and have dissociation rates or rate coefficients of  $J_2$ ,  $k_{12}$ ,  $k_{13}$ , and  $J_3$ , respectively. The rates of change of  $[O]$  and  $[O_3]$  are given by (1.5.8–1.5.9) and the change in odd oxygen is

$$\frac{d([O] + [O_3])}{dt} = 2J_2[O_2] - 2k_{13}[O][O_3] \quad (3.2.1)$$

Throughout the stratosphere, O is in equilibrium with  $O_3$  and  $O_2$  because of the relatively small amounts of O that are present. However,  $O_3$  is not necessarily in photochemical equilibrium in the lower stratosphere.

Setting  $d[O]/dt = 0$  in (3.2.1) and (1.5.8), we can write from (3.2.1)

$$\frac{d[O_3]}{dt} = -\frac{2k_{13}J_3[O_3]^2}{k_{12}[O_2][M]} + 2J_2[O_2] \quad (3.2.2)$$

where we have used the empirical fact that  $k_{13}[O_3] \ll k_{12}[O_2][M]$ . An integration for  $[O_3]$  increasing with  $t$  yields

$$t - t_0 = \left( \frac{k_{12}[M]}{16k_{13}J_2J_3} \right)^{1/2} \ln \left\{ \left( \frac{[O_3]_{eq} + [O_3]}{[O_3]_{eq} - [O_3]} \right) \left( \frac{[O_3]_{eq} - [O_3]_0}{[O_3]_{eq} + [O_3]_0} \right) \right\} \quad (3.2.3)$$

where  $[O_3]_0$  is the abundance at  $t_0$  and  $[O_3]_{eq}$  is the equilibrium abundance of Eq. (1.5.12). Let  $\tau_{eq}$  be the time for  $O_3$  to increase from zero to 0.5  $[O_3]_{eq}$  (or, what is equivalent, the time to increase from 50 percent to 80 percent of  $[O_3]_{eq}$ —in either case the logarithm factor is  $\ln 3 = 1.10$ ). Then

$$\tau_{eq}(O_3) = \frac{0.275[O_3]_{eq}}{[O_2]J_2} \quad (3.2.4)$$

Figure 3.1 shows this  $\tau_{eq}$  as a function of height computed with  $J_2$ 's for different zenith angles. The figure has two important messages:

- (1) Below 30 km the lifetime  $\tau_{eq}$  is measured in weeks; below 25 km, in years. With such long photochemical lifetimes we shall find that dynamics (horizontal and vertical mixing) controls the distribution of ozone. A simple, local photochemical equilibrium—indeed, even a steady state—does not exist for  $O_3$  in the lower stratosphere. We will return to this matter in Section 3.3.2.

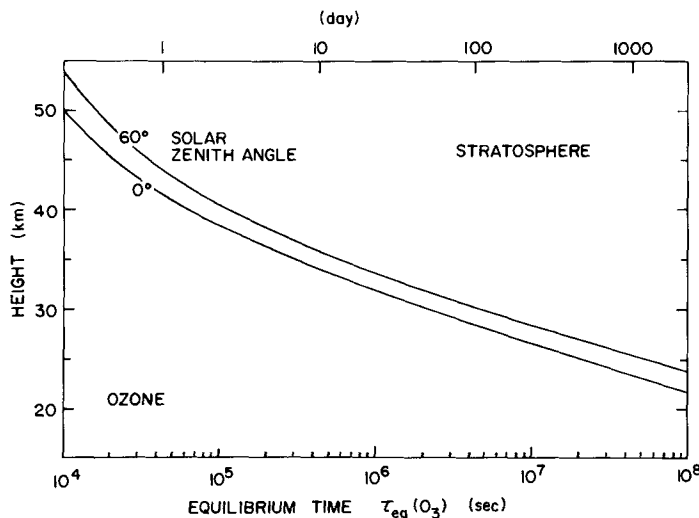


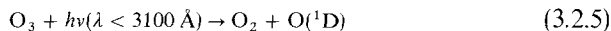
Fig. 3.1 Equilibrium time  $\tau_{eq}(O_3)$  for ozone in a pure oxygen atmosphere, as calculated from (3.2.4), where  $J_2$  is a function of zenith angle and height. [Adapted from NICOLET (1975).]

(2) Above 40 km a chemical equilibrium should exist, because the lifetimes for adjustment become less than a day. Nevertheless, the observed values of  $[O_3]$  are less than the values calculated from (1.5.12) and there seems to be no possibility that  $k_{12}$ ,  $k_{13}$ ,  $J_2$ , or  $J_3$  can be in error enough to make up the discrepancy. Thus pure oxygen chemistry presents an internal inconsistency. We will find the resolution of this dilemma in catalytic chemistry with minor constituents  $HO_x$ ,  $NO_x$ , and  $ClO_x$ . In this notation, for  $x$  read 0, 1, or 2; just as O and  $O_3$  constitute “odd oxygen” molecules,  $HO_x$ ,  $NO_x$ , and  $ClO_x$  represent odd hydrogen, odd nitrogen, and odd chlorine molecules.

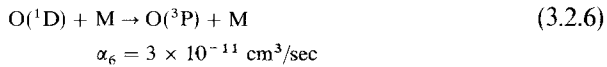
### 3.2.2 Photochemistry of Hydrogenous Radicals

The free radicals  $HO_x$  are H, OH (hydroxyl), and  $HO_2$  (hydroperoxyl). The single H atom makes these radicals highly reactive with odd oxygen O and  $O_3$ . The production of  $HO_x$  originates with the dissociation of  $H_2O$  and  $CH_4$  (methane).

The straightforward photodissociation of water into H + OH is shielded in the stratosphere by the Herzberg dissociation continuum of  $O_2$  and is less important than the following indirect process: Metastable O(<sup>1</sup>D) is produced in the photodissociation of ozone,



with rate  $J_3$ . The O(<sup>1</sup>D) atom has a radiative lifetime of nearly two minutes, but it is deactivated in much less than a second by collisions with O<sub>2</sub> and N<sub>2</sub> by

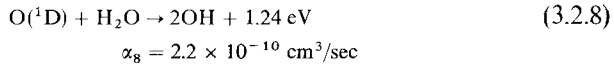


where  $\alpha$  represents the rate coefficient. Nevertheless, there is always a daytime trace abundance of

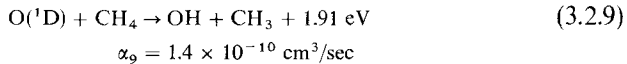
$$[\text{O}(\text{D})] = \frac{J_3[\text{O}_3]}{\alpha_6[\text{M}]} \quad (3.2.7)$$

which is about 10 cm<sup>-3</sup> at 30 km (cf. Fig. 3.3).

The O(<sup>1</sup>D) atoms, carrying 1.96 eV of excitation energy, then form OH by

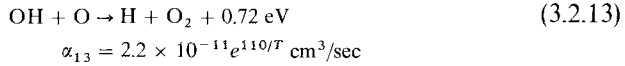
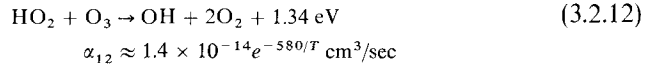
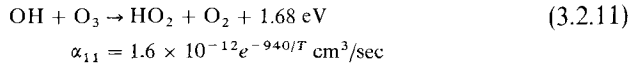
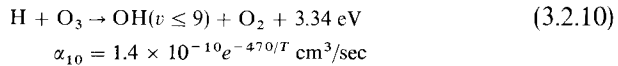


and

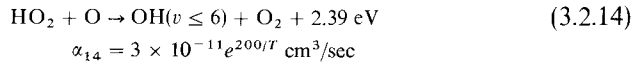


The latter reaction is the dominant destruction mechanism of CH<sub>4</sub> in the stratosphere; it becomes photodissociated only in the mesosphere, although at lower altitudes OH also destroys CH<sub>4</sub> [cf. reaction (3.3.2)]. Additional HO<sub>x</sub> is formed by the further oxidation of CH<sub>3</sub> (methyl radical).

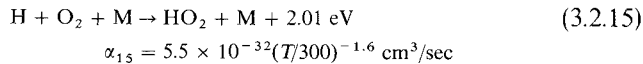
Once formed, HO<sub>x</sub> destroys odd oxygen with no destruction of HO<sub>x</sub> itself. At the stratopause level (~50 km), where HO<sub>x</sub> is most important, the reactions on O and O<sub>3</sub> are



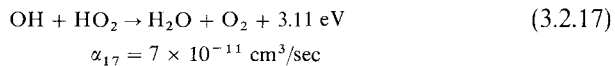
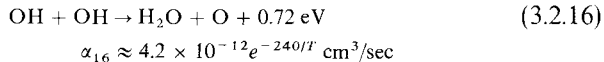
and



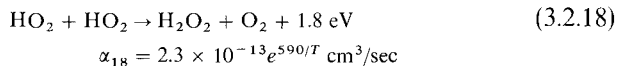
In addition,  $\text{HO}_x$  is internally redistributed without destroying odd oxygen by



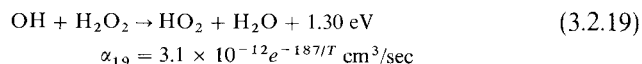
To complete the  $\text{HO}_x$  cycle in the stratosphere, the family is destroyed by



and



The  $\text{H}_2\text{O}_2$  (hydrogen peroxide) formed in the last reaction may be photo-dissociated into  $2\text{OH}$  or it may be attacked by  $\text{OH}$ ,



Destruction of  $\text{HO}_x$  may also occur through  $\text{CH}_4$ ; see (3.3.2) below.

Analysis of these reactions is best handled in two parts: first, the catalytic reactions on  $\text{O}$  and  $\text{O}_3$ , and second, the production and loss of  $\text{HO}_x$ . The catalytic reactions are shown schematically in Fig. 3.2. Where photochemical

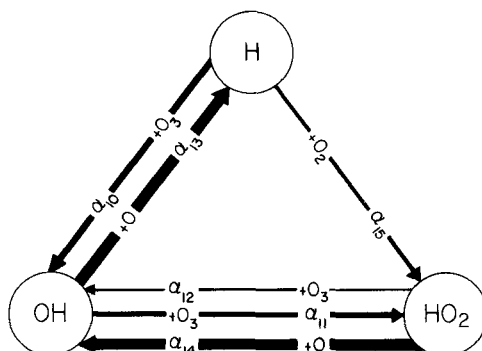


**Fig. 3.2** Internal reactions of the  $\text{HO}_x$  family. The widths of the arrows are rough indicators of the relative importance of the reactions near the stratopause ( $z \sim 50 \text{ km}$ ), where the influence of  $\text{HO}_x$  on odd oxygen is most important.

equilibrium prevails, we can readily write down the equilibrium abundance ratios. The  $[H]$  equilibrium gives

$$\frac{[OH]}{[H]} = \frac{\alpha_{10}[O_3] + \alpha_{15}[O_2][M]}{\alpha_{13}[O]} \quad (3.2.20)$$

With the low rate coefficients  $\alpha_{11}$  and  $\alpha_{12}$ , we have

$$\frac{[HO_2]}{[H]} = \frac{\alpha_{15}[O_2][M]}{\alpha_{14}[O]} \quad (3.2.21)$$

from the  $[HO_2]$  equilibrium.

Adding the hydrogenous reactions to the Chapman reactions, we find that  $[O_3]$  equilibrium yields

$$[O_3] = \frac{k_{12}[O][O_2][M]}{J_3 + k_{13}[O] + \alpha_{12}[HO_2] + \alpha_{11}[OH] + \alpha_{10}[H]} \quad (3.2.22)$$

where  $k_{13}[O] \ll J_3$  below 60 km, and  $[O + O_3]$  equilibrium gives

$$[O] = \frac{2J_2[O_2] - \alpha_{10}[H][O_3] - \alpha_{11}[OH][O_3] - \alpha_{12}[HO_2][O_3]}{2k_{13}[O_3] + \alpha_{13}[OH] + \alpha_{14}[HO_2]} \quad (3.2.23)$$

Anticipating our results somewhat, we can see that  $[H]$  will be very small because of the small  $[O]$  in (3.2.20–3.2.21). Also, we will be expecting other  $HO_x$  abundances of the order of  $10^7 \text{ cm}^{-3}$  or less. These values allow us to discard the terms in  $\alpha_{10}$ ,  $\alpha_{11}$ , and  $\alpha_{12}$  obtaining

$$\frac{[O_3]^2}{[O_2]^2} = \frac{k_{12}J_2[M]}{k_{13}J_3(1 + A)} \quad (3.2.24)$$

which is identical to the Chapman solution (1.5.12) except for the correction term,

$$A = \frac{\alpha_{13}[OH] + \alpha_{14}[HO_2]}{2k_{13}[O_3]} \quad (3.2.25)$$

Typical values at the 50 km stratopause are  $k_{13} \sim 5 \times 10^{-15} \text{ cm}^3/\text{sec}$ ,  $[O_3] \sim 5 \times 10^{10} \text{ cm}^{-3}$ , and  $\alpha_{13} \sim \alpha_{14} \sim 4 \times 10^{-11} \text{ cm}^3/\text{sec}$ . To have  $A \gtrsim 1$  requires  $[HO_x] \gtrsim 10^7 \text{ cm}^{-3}$ .

Returning now to the balance of production and loss of  $HO_x$ , we will omit the  $CH_4$  chemistry for simplicity. Then production is primarily by (3.2.8) and loss occurs mainly through (3.2.17), or

$$[O(^1D)][H_2O]\alpha_8 = [OH][HO_2]\alpha_{17} \quad (3.2.26)$$

With  $[O(^1D)]$  given in terms of the  $[O_3]$  mixing ratio by (3.2.7) and with  $[OH]$  and  $[HO_2]$  related by (3.2.20 and 3.2.21), we may solve for  $[HO_x]$ .

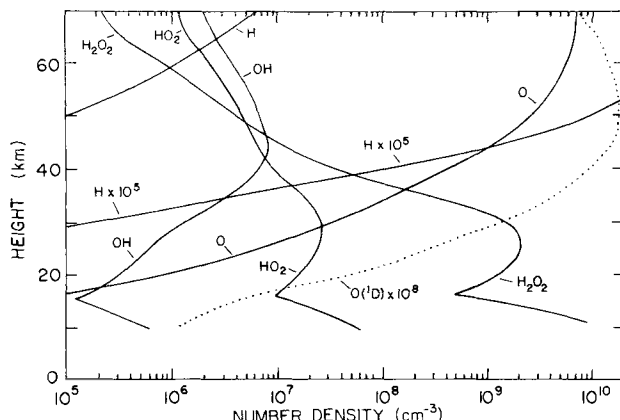


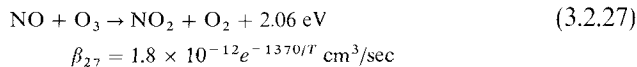
**Fig. 3.3** Model calculations of the distribution of hydrogenous radicals  $\text{HO}_x$ ,  $\text{H}_2\text{O}_2$ ,  $\text{O}({}^3\text{P})$ , and  $\text{O}({}^1\text{D})$  for the atmosphere at  $30^\circ$  latitude (24-hr averages). [After McELROY *et al.* 1974.]

Detailed calculations (including vertical mixing; see Section 3.3.1) as shown in Fig. 3.3 indicate that in the stratopause region ( $z \sim 50$  km) the  $\text{OH}$  and  $\text{HO}_2$  densities are of the order of  $10^7 \text{ cm}^{-3}$  and that  $\text{HO}_x$  is indeed an important sink for  $\text{O}$  and  $\text{O}_3$  in this region.

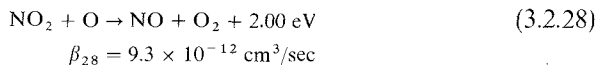
Referring again to Fig. 3.2 we see that the main reactions in the catalytic  $\text{HO}_x$  cycle proceed clockwise around the triangle. Both  $\alpha_{14}$  and  $\alpha_{13}$  destroy  $\text{O}$  and then the  $\text{HO}_x$  is rejuvenated by  $\alpha_{15}$ , which does not itself destroy odd oxygen. This three-way mechanism is in contrast to the  $\text{NO}_x$  and  $\text{ClO}_x$  cycles (to be discussed presently), which operate by two-way cycles. Thus  $\text{NO}_x$  operates on the analogs to  $\alpha_{11}$  and  $\alpha_{14}$ ;  $\text{ClO}_x$  operates on mechanisms like  $\alpha_{10}$  and  $\alpha_{13}$ . Although the main  $\text{HO}_x$  reactions in the stratosphere destroy  $\text{O}$ , these reactions must be regarded as destructive of  $\text{O}_3$  since  $\text{O}$  is a potential  $\text{O}_3$  molecule.

### 3.2.3 Oxides of Nitrogen

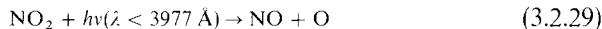
Odd oxygen is destroyed in a catalytic cycle by  $\text{NO}$  (nitric oxide) and  $\text{NO}_2$  (nitrogen dioxide):



and



where  $\beta$ 's represent the rate coefficients. The first reaction does not always result in a net loss of ozone, because most often  $\text{NO}_2$  is photodissociated,

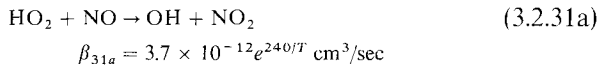


which is followed by

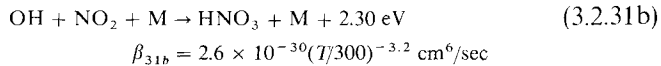


The sequence of reactions (3.2.27, 3.2.29, and 3.2.30) produces no net change in the products ( $\text{NO}$  and  $\text{O}_3$ ). Thus the process that limits the rate of  $\text{O}_3$  destruction is (3.2.28). Whenever it occurs not only is an  $\text{O}$  atom (which represents a potential  $\text{O}_3$  molecule) destroyed but a second  $\text{O}_3$  is destroyed by (3.2.27).

The interaction of minor, catalytic substances can be important if the rate coefficients are high or if there is no other route to reach a specific end result. Thus  $\text{HO}_x$  and  $\text{NO}_x$  are rearranged by



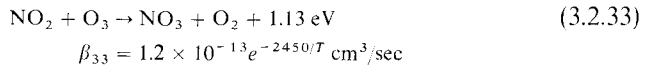
But the reaction is important mainly because (especially at night) a major fraction of  $\text{NO}_2$  in the lower stratosphere is bound as  $\text{HNO}_3$  (nitric acid) by



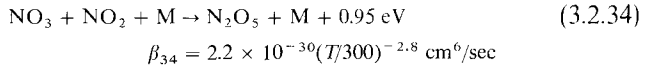
This  $\text{NO}_x$  is thereby removed temporarily from the catalytic cycle. In the daytime, photolysis of  $\text{HNO}_3$  restores  $\text{NO}_2$  by



Also,  $\text{NO}_x$  in the form of  $\text{NO}_2$  can be photodissociated, with the  $\text{O}$  atom producing an  $\text{O}_3$ . Thus the sequence (3.2.11, 3.2.31a, 3.2.29, and 3.2.30) is a *do-nothing cycle*, with all the original constituents recovered. Another reservoir for  $\text{NO}_2$ , especially at night, is  $\text{N}_2\text{O}_5$  (nitrogen pentoxide) by



followed by



In the day  $\text{NO}_2$  is recovered by



and



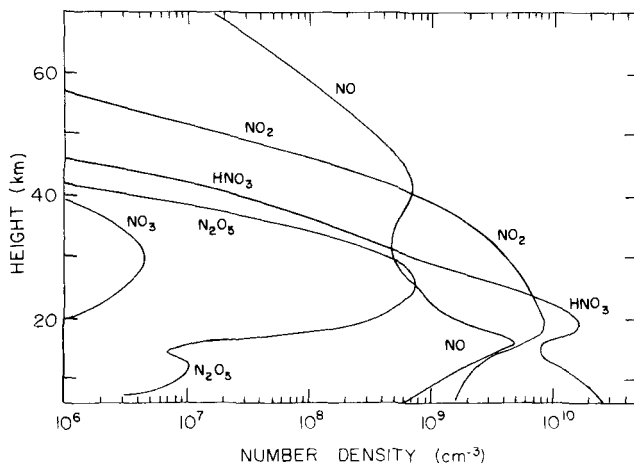


**Fig. 3.4** Model calculations of the distribution of nitrogen oxides  $\text{NO}_x$ ,  $\text{HNO}_3$ , and  $\text{N}_2\text{O}_5$  at 30° latitude (24-hr averages). [After McELROY *et al.* (1974).]

Because most of the radiation photolyzing  $\text{NO}_2$  by (3.2.29) is unattenuated by  $\text{O}_2$  or  $\text{O}_3$ , the daytime dissociation rate is high,  $J_{29} \approx 4 \times 10^{-3} \text{ sec}^{-1}$  or a lifetime of  $\tau(\text{NO}_2) = 1/J_{29} \sim 2 \times 10^2 \text{ sec}$ . Hence  $\text{NO}_2$  is in a daytime photoequilibrium of

$$\frac{[\text{NO}_2]}{[\text{NO}]} = \frac{\beta_{27}[\text{O}_3]}{\beta_{28}[\text{O}] + J_{29}} \approx \frac{\beta_{27}[\text{O}_3]}{J_{29}} \quad (3.2.37)$$

Figure 3.4 shows equilibrium abundances calculated with 24-hour averages of the dissociation rates  $J$  and with vertical eddy diffusion.

The net rates of production of  $\text{O}$  and  $\text{O}_3$ , including the Chapman reactions and the hydrogenous and nitrogenous chemistry, are

$$\begin{aligned} \frac{d[\text{O}]}{dt} &= 2J_2[\text{O}_2] + J_3[\text{O}_3] \sim k_{13}[\text{O}][\text{O}_3] - k_{12}[\text{O}][\text{O}_2][\text{M}] \\ &\quad - \alpha_{14}[\text{HO}_2][\text{O}] - \alpha_{13}[\text{OH}][\text{O}] + J_{29}[\text{NO}_2] - \beta_{28}[\text{NO}_2][\text{O}] \end{aligned} \quad (3.2.38)$$

and

$$\begin{aligned} \frac{d[\text{O}_3]}{dt} &= k_{12}[\text{O}][\text{O}_2][\text{M}] \sim k_{13}[\text{O}][\text{O}_3] - J_3[\text{O}_3] - \alpha_{12}[\text{HO}_2][\text{O}_3] \\ &\quad - \alpha_{11}[\text{OH}][\text{O}_3] \sim \alpha_{10}[\text{H}][\text{O}_3] - \beta_{27}[\text{NO}][\text{O}_3] \end{aligned} \quad (3.2.39)$$

which yield

$$\begin{aligned} \frac{d[\text{O} + \text{O}_3]}{dt} = & 2J_2[\text{O}_2] - [\text{O}_3](\alpha_{12}[\text{HO}_2] + \alpha_{11}[\text{OH}] + \alpha_{10}[\text{H}]) \\ & - [\text{O}](2k_{13}[\text{O}_3] + \alpha_{14}[\text{HO}_2] + \alpha_{13}[\text{OH}] + 2\beta_{28}[\text{NO}_2]) \end{aligned} \quad (3.2.40)$$

Discarding terms that will be numerically small (see Fig. 3.5), we have in equilibrium from (3.2.39)

$$[\text{O}_3] \approx \frac{k_{12}[\text{O}_2][\text{M}][\text{O}]}{J_3} \quad (3.2.41)$$

where, from (3.2.40),

$$[\text{O}] \approx \frac{J_2[\text{O}_2]}{[\text{O}_3]k_{13} + \beta_{28}[\text{NO}_2] + \frac{1}{2}(\alpha_{14}[\text{HO}_2] + \alpha_{13}[\text{OH}])} \quad (3.2.42)$$

Combining the last two expressions in the form of (3.2.24) gives the correction term to the Chapman solution as

$$A = \frac{\alpha_{13}[\text{OH}] + \alpha_{14}[\text{HO}_2] + 2\beta_{28}[\text{NO}_2]}{2k_{13}[\text{O}_3]} \quad (3.2.43)$$

which indicates the relative importance of  $\text{O}-\text{O}_3$  self-destruction and catalytic loss through  $\text{HO}_x$  and  $\text{NO}_x$ .

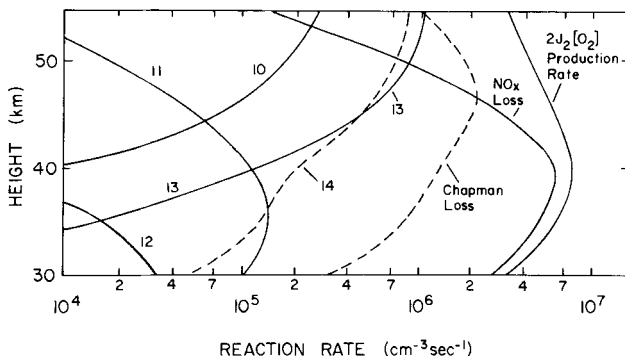
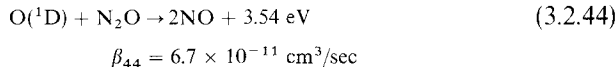


**Fig. 3.5** Rates of production and loss of odd oxygen. The (24-hr average) “production rate” by photodissociation is  $2J_2[\text{O}_2]$  and the “Chapman loss” is  $2k_{13}[\text{O}][\text{O}_3]$ ; see (3.2.1). The curve “ $\text{NO}_x$  loss” gives  $2\beta_{28}[\text{NO}_2][\text{O}]$ ; see the discussion following (3.2.30). The numbered curves give the contributions to the loss from  $\text{HO}_x$  reactions (3.2.10–3.2.14). For example, curve “10” is  $\alpha_{10}[\text{H}][\text{O}_3]$ . [Adapted from McELROY *et al.* (1974).]

### 3.2.4 Natural and Artificial Sources of Nitrogen Oxides

**Biological Production of N<sub>2</sub>O** The production and loss of the total NO<sub>x</sub> in the stratosphere depends critically on vertical transport. The principal production mechanism is from N<sub>2</sub>O (nitrous oxide), which is formed from biological activity on the surface, reacting with metastable oxygen:

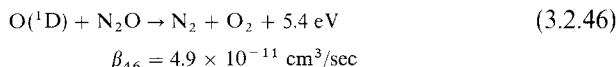


The reaction

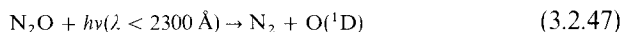


is exothermic but has a rate coefficient  $\beta_{45} \sim 10^{-31} \text{ cm}^3/\text{sec}$ , which corresponds to an activation energy of about 1.1 eV. The O(¹D) produced by ozone photolysis (3.2.5) evidently supplies this activation energy and the rate  $\beta_{44}$  is very rapid.

In addition, N<sub>2</sub>O is destroyed in the stratosphere by



for which the same remarks apply. However, the principal destruction mechanism is photodissociation,



Thus the rate of production of NO<sub>x</sub> depends on the rate of production of N<sub>2</sub>O at the surface and its subsequent transport into the stratosphere.

The principal loss mechanism for NO<sub>x</sub> from the stratosphere is downward transport into the troposphere, where HNO<sub>3</sub>, being soluble in water, will rain out. Thus continuity (2.1.1) requires that

$$\frac{\partial [\text{NO}_x]}{\partial t} = -\frac{\partial}{\partial z}([\text{NO}_x]w) + 2\beta_{44}[\text{N}_2\text{O}][\text{O}(\text{¹D})] \quad (3.2.48)$$

Continuity equations involving chemical sources and sinks as well as mass flow are discussed further in Section 3.3.

**Aircraft Exhaust** The importance of NO<sub>x</sub> to the ozone balance has created concern over the role of high-altitude aircraft, and especially the prospective effects of large fleets of supersonic aircraft, because NO<sub>x</sub> is a principal constituent of engine exhausts. Deleterious effects might occur within a few decades of the onset of heavy contamination directly within the

stratosphere. The residence time depends on the height of injection. For  $\text{NO}_x$  injected into the stratosphere, it is several years, and for injection above 20 km it is tens of years, with  $\text{NO}_x$  increasing over long periods. Engine exhausts in the troposphere are not particularly harmful to stratospheric ozone because most of the  $\text{NO}_x$  rains out eventually and is not readily transported into the stratosphere. Indeed, engine exhausts in the troposphere lead to the production of ozone (cf. Section 7.4.4).

**Industrial Fertilizers** The major source of  $\text{NO}_x$  being plant activity in the manufacture of  $\text{N}_2\text{O}$  has raised the unsettling question of whether artificial fertilizers, being applied to soils in enormous quantities the world over, will eventually contribute to deterioration of ozone. The first process of converting nitrogen into a form suitable for plant use is *fixation*, basically the conversion of even nitrogen  $\text{N}_2$  into odd nitrogen  $\text{NH}_4$  (ammonium). Fixation occurs naturally through certain bacteria operating on the roots of legumes and through combustion. Fixed nitrogen is used by plants to synthesize proteins and nucleic acids. Micro-organisms may then convert the organic  $\text{NH}_4$  into inorganic  $\text{NO}_3^-$  (nitrate), a process called *nitrification*. The final step in this biologic cycle is *denitrification*, the reduction, again with microbial assistance, of  $\text{NO}_3^-$  to  $\text{N}_2$  and  $\text{N}_2\text{O}$ . The net result is that atmospheric  $\text{N}_2$  going through the cycle does not all return as  $\text{N}_2$ , but some of it becomes  $\text{N}_2\text{O}$ .

It appears that industrial fertilizers now account for an amount of fixed nitrogen fed to the soil that is comparable to the natural production. However, there are major uncertainties in attempting to extrapolate this result into an eventual increase in  $\text{N}_2\text{O}$  flowing into the stratosphere. The role of fixed nitrogen in the sea is poorly understood, even as to whether it represents a source or sink of atmospheric  $\text{N}_2\text{O}$ . The branching ratio in denitrification to yield  $\text{N}_2$  and  $\text{N}_2\text{O}$  is clearly a critical number, but it must depend on the chemical processes involved, which are poorly understood. The subject of the biogeochemistry of  $\text{N}_2\text{O}$  is likely to attract much attention in the future.

**Nuclear Explosions** A possible artificial source of  $\text{NO}_x$  in the stratosphere is the explosion of nuclear weapons in or below the stratosphere. Defensive engagements with nuclear devices launched to intercept offensive missiles in the high atmosphere form commonplace scenarios for military planning by nuclear equipped nations. The explosive power of the interceptor must be in the megaton (MT) range to assure an adequate production of radiation to "kill" the intruder warhead. It seems clear that any such massive release of energy in the stratosphere will seriously wound the ozone layer and expose the entire world to intense solar ultraviolet radiation. (One MT of TNT explosive is equivalent to  $4.2 \times 10^{22}$  erg.)

In 1962 the United States conducted megaton atmospheric tests in the tropics and in 1961–62 the Soviet Union exploded several large bombs in the Arctic, including one thought to exceed 50 MT of yield. In calculating what effects would be expected, there are two critical questions: How much  $\text{NO}_x$  is produced? and How high would the explosion debris rise?

The first question seems to be well answered. At high temperatures within the fireball, the  $\text{NO}_x$  abundance can be rather accurately estimated by thermodynamic equilibrium distributions of molecular energies. For  $T \lesssim 2000^\circ\text{K}$ , the reactions that destroy NO become very slow, and the  $[\text{NO}]$  stabilizes at about 1 percent.

The second question is more ambiguous. Most of the United States' experience with large tests has been in the tropics, where the tropopause is higher and colder than in the fall in the Arctic (where the largest Soviet tests occurred). Possibly the fireball did not rise as high as scaling from low-latitude experience would suggest. If the injected  $\text{NO}_x$  did not reach photochemical altitudes, the catalytic cycle (3.2.27–3.2.28) could not operate. At lower Arctic altitudes the  $[\text{O}]$  is already depleted and  $[\text{O}_3]$  is essentially inert. Hence the destructive catalytic effects would await the transport of the weapon-produced  $\text{NO}_x$  to lower latitudes and higher altitudes.

Analysis of ozone observations around the period of the tests by several groups has led to inconclusive results of whether the bombs' effects were evident or not. Possibly as much as 5 percent effect could have been expected. The data, always noisy and hard to average satisfactorily, may have been confused also by massive eruptions of the Mt. Agung volcano in early 1963 and an apparent breakdown of the so-called *quasi-biennial oscillation* of the atmosphere and the associated fluctuation of total ozone.

**Galactic Cosmic Rays** Still another type of variation is that produced by variable cosmic-ray ionization. It is potentially important in that (a) it may reveal observationally how the stratospheric ozone responds to a known change in  $\text{NO}_x$  production, (b) it may be the physical explanation for the long suspected 11-year variation in total ozone, and (c) it has led to some speculative mechanisms for long-term changes in terrestrial climate controlled by the stratosphere.

The basic source of variations in the low-energy component of Galactic cosmic rays (GCR) striking the Earth is the heliomagnetic field imbedded in the solar wind. During times of high solar activity, the solar wind and its magnetic field are strong. Then low-energy GCR's are shielded from the Earth, especially over the polar cap, where the terrestrial magnetic field is most receptive to cosmic rays. The small amount of ionization produced in the stratosphere is thus considerably less than at sunspot minimum (see Fig. 3.6).

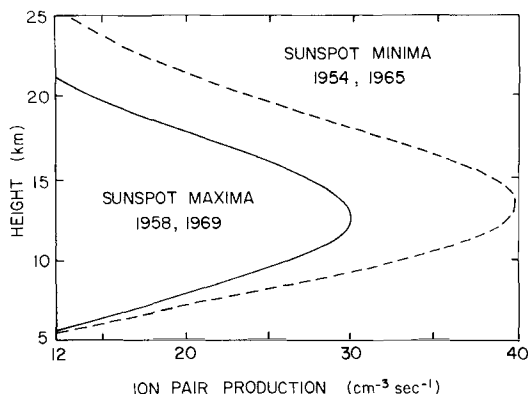
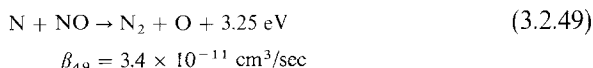
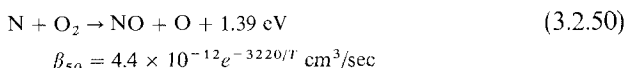


**Fig. 3.6** Height distribution of the ionization produced in the atmosphere by cosmic rays over Thule, Greenland (near the north geomagnetic pole) during times of high and low solar activity. The reduction in Galactic cosmic rays during high solar activity is attributed to screening of the Earth by magnetic fields associated with the solar wind. [Adapted from G. BRASSEUR and M. NICOLET (1973), *Planet Space Sci.* **21**, 939; based on data from H. V. NEHER (1971), *J. Geophys. Res.* **76**, 1637.]

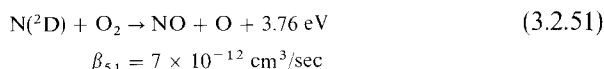
Cosmic rays produce one ion-pair for each 35 eV lost in transit through the atmosphere. By various collision processes, this ionization results in the production of free N atoms, about 1.4 atom/ion-pair. These atoms may either destroy  $\text{NO}_x$  by



or create it by



The same reaction with excited N atoms,



goes much faster, with the 2.37 eV of the  ${}^2\text{D}$  term countering the high activation energy. The matter is of some importance, because perhaps half the N atoms produced will be in a metastable state and will not be readily deactivated before a chemical encounter.

The  $\text{NO}_x$  is thus modulated with an 11-year period, mainly over the polar caps. With this fluctuating component being transported out of the polar

cap by horizontal motions on a time scale  $\tau$  of a few months or a year, the  $[\text{NO}_x]$  varies as

$$\frac{\partial [\text{NO}_x]}{\partial t} = \mathcal{J}_0 + \mathcal{J}_1 e^{i\omega t} - \frac{[\text{NO}_x]}{\tau} \quad (3.2.52)$$

The  $\mathcal{J}$ 's represent production rates by cosmic rays and the frequency is  $\omega = 2\pi/11 \text{ yr}^{-1}$ . We assume a solution varying as  $e^{i(\omega t - \delta)}$ , where  $\delta$  is the lag of maximum  $\text{NO}_x$  concentration behind maximum production (or sunspot minimum). The solution for the oscillating component is

$$[\text{NO}_x] = \frac{\mathcal{J}_1 \tau}{(1 + \omega^2 \tau^2)^{1/2}} \cos(\omega \tau - \delta) \quad (3.2.53)$$

where

$$\delta = \tan^{-1} \omega \tau \quad (3.2.54)$$

At lower latitudes, outside the polar cap, there is an additional phase lag due to meridional transport and eventual loss to the troposphere. Finally, there is a lag between sunspot maximum and solar wind maximum. Hence the  $[\text{NO}_x]$  minimum (i.e.,  $[\text{O}_3]$  maximum) occurs at a time following sunspot maximum given by

$$\Delta t = \delta/\omega + \delta_\theta/\omega + (\Delta t)_{\text{sw}} \quad (3.2.55)$$

where  $\delta/\omega \sim 1 \text{ yr}$  is the lag between production and maximum NO concentration,  $\delta_\theta/\omega$  is the additional latitude-dependent lag for meridional transport, and  $(\Delta t)_{\text{sw}} \sim 1 \text{ yr}$  is the solar-wind lag.

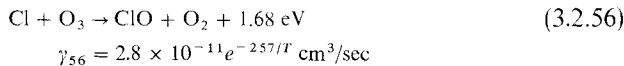
Observations of total ozone variations indicate that the phase shifts are about as predicted and that the effect is stronger at higher latitudes. So many factors evidently enter into ozone variability that it is difficult to extract convincing periodicities from examining even smoothed data, and it is sometimes helpful to seek periodicities and phase effects suggested by physical theory.

**Solar Cosmic Rays** A different kind of cosmic-ray effect likely arises from bursts of particles from solar flares. These solar cosmic rays occur mainly at peaks of solar activity and therefore will be out of phase with the maximum GCR's, which peak during sunspot minimum. Further, they have lower energies than even low-energy GCR's and are deposited higher in the stratosphere. In the mesosphere they are associated with polar-cap radio absorption (PCA events). The ionization occurs in rather short bursts of a few hours, but solar cosmic rays in that short period produce ionization equivalent to the excess ionization from several months of GCR modulation. Thus there are two distinct cosmic-ray effects, with quite different characteristics, that may produce natural and observable variations in ozone.

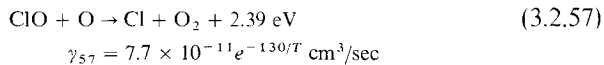
**Impact of NO<sub>x</sub> on Climate?** The awareness that particle bombardment of the stratosphere could reduce its ozone abundance has led to speculative proposals for causes of climate modification. One proposal concentrates on the climatic effects that would accompany changes in the solar and terrestrial magnetic fields. For example, drastic reductions in the geomagnetic field strength could admit substantial increases in the GCR radiation and reduce the protective ozone cover. The diminished ozone would lead to a cooler stratosphere, which would normally be accompanied by cooler surface temperatures because of reduced greenhouse heating in the 9.6  $\mu\text{m}$  band of O<sub>3</sub>. A further speculative suggestion is that a stratosphere cooler than the present one might lead to greater condensation of ice haze, which would increase the Earth's albedo, or reduced stratospheric H<sub>2</sub>O vapor, which would permit more tropospheric cooling. Such climate mechanisms always involve complex feedbacks, both positive and negative, a fact that makes the subject exceedingly difficult to handle quantitatively.

### 3.2.5 Chlorine and the Halomethanes

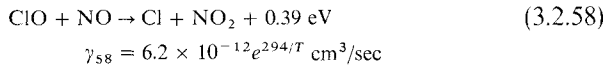
Once released in the stratosphere a free chlorine atom Cl reacts immediately with ozone, starting the ClO<sub>x</sub> cycle, by



where  $\gamma$  is the rate coefficient. Then ClO (chlorine monoxide) may either complete the catalytic cycle directly,

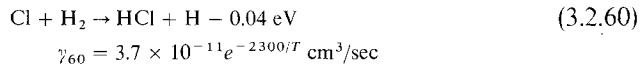
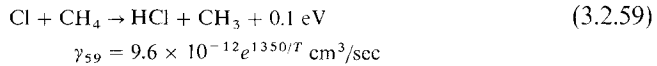


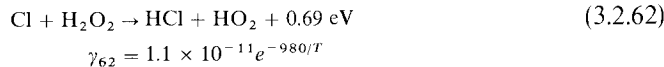
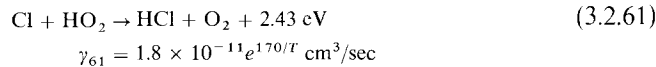
or it may branch to



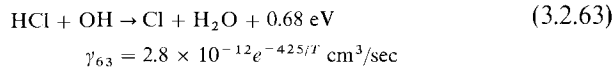
The latter branch may complete the cycle either by (3.2.28), with the net result of destroying two odd oxygens, or by (3.2.29)–(3.2.30), which restores the lost O<sub>3</sub>.

Chlorine is lost from the stratosphere mainly in the form of inactive HCl (hydrogen chloride), which is transported downward into the troposphere and is removed by rainout. The main reactions transforming Cl into HCl are

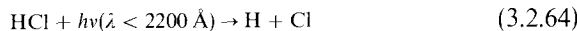




Active Cl is regenerated from HCl by



and



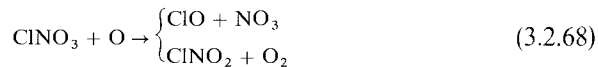
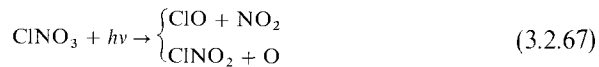
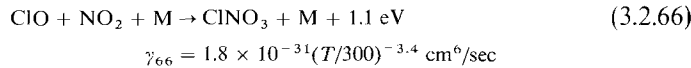
Incidentally, each of the catalytic cycles depends crucially on  $[\text{OH}]$ . Thus OH plays a direct role in the  $\text{HO}_x$  cycle through reactions  $\alpha_{11}$  and, more importantly,  $\alpha_{13}$ ; it is the principal sink for  $\text{HO}_x$  through reaction  $\alpha_{17}$ ; it converts active  $\text{NO}_2$  into inactive  $\text{HNO}_3$  by reaction  $\beta_{31b}$ ; and it releases Cl from HCl by reaction  $\gamma_{63}$ .

Purely chemical equilibrium of HCl does not exist in the stratosphere because the chemical sink terms are so small that the dynamical flow has to be included everywhere. The equation of continuity (2.1.1), with the chemical sources and sinks added, is

$$\frac{\partial [\text{HCl}]}{\partial t} = -\nabla([\text{HCl}]w_{\text{HCl}}) - [\text{HCl}](J_{64} + \gamma_{63}[\text{OH}]) \\ + [\text{Cl}](\gamma_{59}[\text{CH}_4] + \gamma_{60}[\text{H}_2] + \gamma_{61}[\text{HO}_2] + \gamma_{62}[\text{H}_2\text{O}_2]) \quad (3.2.65)$$

Because  $[\text{O}_3] \gg [\text{O}]$  and the  $\text{Cl} + \text{O}_3$  reaction is fast, chlorine is about evenly divided between the forms  $\text{ClO}$  and  $\text{HCl}$ ;  $[\text{Cl}]$  is very small. At 35 km the lifetime of Cl is  $\tau(\text{Cl}) = 1/\gamma_{56}[\text{O}_3] \sim 1/20 \text{ sec}$ , while  $\tau(\text{ClO}) = (\gamma_{57}[\text{O}] + \gamma_{58}[\text{NO}])^{-1} \sim 40 \text{ sec}$  and  $\tau(\text{HCl}) = 1/\gamma_{63}[\text{OH}] \sim 3 \times 10^5 \text{ sec}$ .

Another reservoir for Cl is  $\text{ClNO}_3$  (chlorine nitrate). It is formed and removed by



$$\gamma_{68} = 3.0 \times 10^{-12} e^{-810/T} \text{ cm}^3/\text{sec}$$

The importance of these reactions is not only that they reduce slightly the amount of active  $\text{ClO}_x$ , but that they also reduce  $\text{NO}_x$ , especially in the lower stratosphere. Hence we have the interesting phenomenon of two ozone-destroying catalysts tending to cancel one another out. Other examples of *nonlinear or coupled catalytic chemistry* may involve such substances as  $\text{HOCl}$  and  $\text{HO}_2\text{NO}_2$ , as well as  $\text{HNO}_3$  (see 3.2.31a,b).

At the present time it is not clear whether Cl is a major sink for  $\text{O}_3$ , compared with  $\text{NO}_x$ . The natural abundance of atmospheric Cl (mainly in the forms  $\text{HCl}$  and  $\text{CH}_3\text{Cl}$ ), arising principally from volcanic emission, is probably small and the artificial (anthropogenic) sources have not yet become serious. With an estimated abundance at 35 km of  $[\text{ClO}] \approx 2 \times 10^7 \text{ cm}^{-3}$ , the loss rate of  $\text{O}_3$  from the  $\text{ClO}_x$  cycle is only

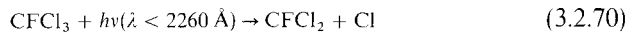
$$d[\text{O}_3]/dt = -2\gamma_{57}[\text{ClO}][\text{O}] \approx 4 \times 10^5 \text{ sec}^{-1} \quad (3.2.69)$$

which is smaller by a factor 2 than the Chapman loss rate,  $2k_{13}[\text{O}_3][\text{O}]$ , and an order of magnitude smaller than the  $\text{NO}_x$  loss rate,  $2\beta_{28}[\text{NO}_2][\text{O}]$  (see Fig. 3.5). There are, however, major uncertainties in these estimates, and the destruction of  $\text{O}_3$  due to natural  $\text{NO}_x$  now seems less important, according to detailed model calculations, than it did a few years earlier, partly because of the nonlinear catalyst interactions.

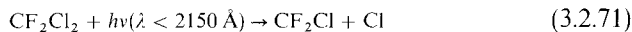
The principal sources of Cl in the stratosphere are the *halomethanes* (or *halogenated methanes*), molecules in which halogens take the place of one or more hydrogen in  $\text{CH}_4$  (methane). The most important of these molecules in the troposphere are  $\text{CFCl}_3$  (trichlorofluoromethane, often called "F-11"),  $\text{CF}_2\text{Cl}_2$  (dichlorofluoromethane—"F-12"),  $\text{CCl}_4$  (carbon tetrachloride), and  $\text{CH}_3\text{Cl}$  (methyl chloride). [In this shorthand identifying system, *F* apparently originated from E. I. duPont de Nemours and Company's trademark name *Freon*, which is in common use, although over 20 companies the world over manufacture these substances; the first digit is the number of H atoms plus one; the second is the number of fluorine atoms. For more complex fluorocarbons a "hundreds" digit is prefixed to specify the number of carbon atoms minus one.]

In recent years F-11 and F-12 have attracted wide popular and scientific attention as being potentially harmful to stratospheric ozone if their manufacture and release into the atmosphere continues at the rates existing in the mid-1970s. The molecule  $\text{CF}_2\text{Cl}_2$  is the most widely used halomethane, both as a refrigerant and as a propellant in aerosol sprays, whereas  $\text{CFCl}_3$  is used primarily in sprays. These *chlorofluoromethanes* or *fluorocarbons*, as they are often called, were developed in 1930 in a chemical search for a refrigerant that was both nontoxic and nonflammable, and being chemically inert is precisely the reason they cause a stratospheric problem. The molecules are practically insoluble so that the oceans are not an effective sink. Free

molecules of these synthetic gases cannot be photodissociated in the troposphere, but upon diffusing into the stratosphere, they are photolyzed by



and



(These wavelengths are the observed ones; the bond dissociation energies are considerably smaller.) Also,  $\text{CCl}_4$ , being fully halogenated, is highly inert in the troposphere and in the stratosphere undergoes



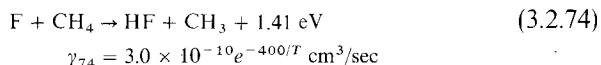
The radicals thus formed immediately react with  $\text{O}_2$  to release another Cl atom. While  $\text{CCl}_4$  may arise in part naturally, its main origin seems to be its industrial manufacture, which has a very long history. There have been some laboratory experiments that indicate visual sunlight can dissociate the halomethanes if the molecules become first adsorbed onto sand or quartz. This area of surface photochemistry is likely to become an important one.

The partially halogenated  $\text{CH}_3\text{Cl}$  may be produced naturally in the troposphere and it may be a minor source of Cl for the stratosphere. However, the molecule can be attacked by OH in the troposphere and probably has a lifetime against chemical destruction there of under a year. The halomethanes are part of a broader class of substance widely used industrially, the *halocarbons* (*halogenated hydrocarbons*, e.g.,  $\text{CH}_2\text{ClCH}_2\text{Cl}$ ). However, only the fully halogenated methanes,  $\text{CFCl}_3$ ,  $\text{CF}_2\text{Cl}_2$ , and  $\text{CCl}_4$ , are now thought to pose a problem because of their tropospheric indestructibility. The partially halogenated methanes  $\text{CHFCl}_2$  (*F-21*) and  $\text{CHF}_2\text{Cl}$  (*F-22*) are attacked by OH in the troposphere and may serve as substitutes to *F-11* and *F-12* in some uses. On the other hand, OH is showing signs of becoming overworked as a tropospheric cleansing agent, largely for the demands placed on it by  $\text{CH}_4$  and CO. A shortage of OH would lead to a new set of problems; see Section 7.4.2.

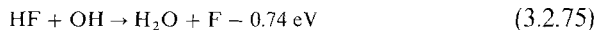
The fluorine atoms in the halomethanes are in principle just as destructive of  $\text{O}_3$  as is Cl. Thus, as in reactions  $\gamma_{56}$  and  $\gamma_{57}$  we have



In practice this  $\text{FO}_x$  cycle is unimportant because the analog to  $\gamma_{59}$ ,



proceeds very rapidly. And once formed, HF (hydrogen fluoride) is not attacked by the analog to  $\gamma_{63}$  to regenerate F because



is comfortably endothermic.

On the other hand, bromine atoms released into the atmosphere could be an efficient catalytic destroyer of ozone. The sources of bromine in the air are marine aerosols, combustion of leaded gasoline, and the use of the halomethane  $\text{CH}_3\text{Br}$  (methyl bromide) as an agricultural fumigant. In the stratosphere bromine chemistry is similar to chlorine chemistry.

### 3.3 Stratospheric Motions

#### 3.3.1 Vertical Mixing

With the concept of eddy diffusion (see Section 2.3.2) the degree of mixing can be ascertained from the measured vertical distribution of some minor substance whose chemistry is understood. Then the derived coefficient for eddy diffusion,  $K(z)$ , may be used to model the distributions of other minor constituents. This approach is based on the supposition that vertical and horizontal transport are independent, which would require that the atmosphere be uniform horizontally (i.e., zonally and meridionally). This is not generally true, of course, but the *one-dimensional dynamic model* can be very useful if its limitations are appreciated. Thus if  $K(z)$  is derived from a substance that has a latitudinal or day-night variation, it may not be appropriate for another substance whose horizontal variations would provide different dynamical sources or sinks (which are absorbed in the coefficient  $K$ ).

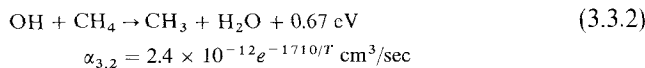
In the troposphere convective mixing is very rapid and  $K \sim 3 \times 10^5 \text{ cm}^2/\text{sec}$ . In the stratosphere the stable temperature gradient inhibits mixing, which then occurs only because of planetary-scale pressure waves. Just above the tropopause  $K \sim 2 \times 10^3 \text{ cm}^2/\text{sec}$ . However, at 40 km these waves have associated vertical wavelengths of about 5 km; if we take the mixing length  $l$  (Section 2.2.1) to be half a wavelength and vertical motions of  $w \sim 0.5 \text{ cm/sec}$ , we have  $K \sim wl \sim 10^5 \text{ cm}^2/\text{sec}$ . As waves are propagated upward their energy varies as the square of their amplitude, or as  $\rho l^2$ , and hence for energy to be approximately conserved, we expect  $K$  to vary roughly as  $\rho^{-1/2}$ . (In practice the wave energy is not strictly conserved if some of it is dissipated into eddy motions.)

For a chemical constituent that is not conserved, the equation of continuity (2.1.1) must include chemical production ( $P$ ) and loss ( $L$ ) terms. For a minor constituent of density  $N_1$ ,

$$\begin{aligned}\frac{\partial N_1}{\partial t} &= -\frac{\partial}{\partial z}(N_1 w_1) + P(N_1) - L(N_1) \\ &= 0 \quad (\text{in steady state})\end{aligned}\tag{3.3.1}$$

This must be coupled with the eddy equation (2.3.4). For a multicomponent system, each component has such a pair of coupled first-order differential equations; the whole system is coupled through the production and loss terms in (3.3.1). Equation (2.3.4) can be differentiated with respect to height and substituted in (3.3.1), but the resulting second-order equation is often more difficult to solve than the original pair. [However, see Eqs. (5.1.26) and (5.1.29).]

The eddy diffusion coefficient  $K(z)$  so far cannot be obtained from a knowledge of atmospheric motions and must be estimated from tracers. A good tracer must be uniformly distributed around the globe, must have a chemical loss time well matched to the mixing time  $H^2/K$  (Section 2.3.1), and must have a simple, well-understood chemistry. These requirements are best met for the stratosphere by  $\text{N}_2\text{O}$  (nitrous oxide) and  $\text{CH}_4$  (methane). Both are produced at many places in or just below the surface and are destroyed but not produced in the stratosphere. Nearly all the  $\text{N}_2\text{O}$  is lost by photolysis. For methane, the principal loss in the stratosphere occurs through oxidation by (3.2.9) forming  $\text{OH}$ , as well as through destruction of  $\text{OH}$  by



and, in the mesosphere, by photodissociation. Thus the chemical term is

$$-L(\text{CH}_4) = -[\text{CH}_4]\{\alpha_9[\text{O}^1\text{D}] + \alpha_{3.2}[\text{OH}] + J(\text{CH}_4)\}\tag{3.3.3}$$

where diurnal averages are used for the densities of  $\text{O}^1\text{D}$  and  $\text{OH}$  and for the photolysis rate  $J(\text{CH}_4)$ . Measurements of  $\text{CH}_4$  versus height are used first in (3.3.1) to calculate the flux profile, and then in (2.3.4) to obtain values of  $K(z)$ . More often, however, such an inversion is not practical, and it is necessary to assume  $K$ , compute the distribution of tracer, compare with the data, and iterate. Results obtained in this way are shown in Fig. 2.10.

In Eq. (3.3.3) the term in curly brackets is the reciprocal chemical lifetime  $\tau_{\text{chem}}^{-1}$ . The dynamical time associated with mixing (see Section 2.3.1) is  $\tau_{\text{mix}} \sim H^2/K$ . Figure 3.7 compares these lifetimes for an eddy mixing coefficient derived from  $\text{CH}_4$  measurements. It appears that  $K$  is nearly constant

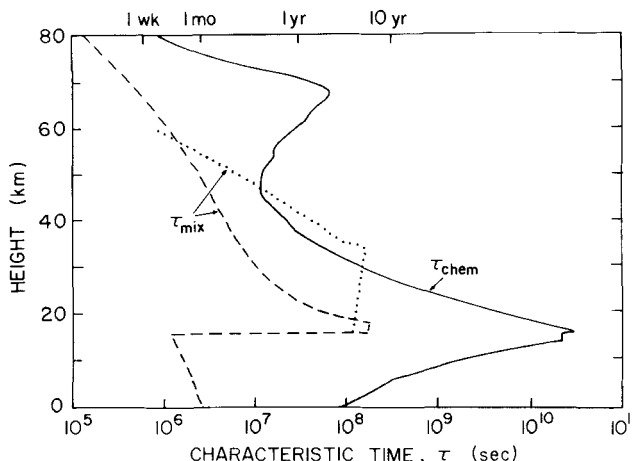


**Fig. 3.7** Comparison of the characteristic time for vertical mixing,  $\tau_{\text{mix}} = H^2/K$ , with the chemical time for destruction of  $\text{CH}_4$  given by (3.3.3). The two curves for mixing are for two assumed height dependences of  $K$ . [Adapted from WOFSY and McELROY (1973).]

( $2 \times 10^3 \text{ cm}^2/\text{sec}$ ) just above the tropopause; it then starts to increase upward. There may be a real change in dynamical regime around 20 km because the lower stratosphere is driven by tropospheric dynamics, but the middle stratosphere is driven by its own internal heat sources. In any case  $\text{CH}_4$  is mixed throughout the stratosphere in times that are short compared with the chemical lifetime and it thus serves (as does  $\text{N}_2\text{O}$ ) as an effective tracer, being essentially inert between 10 and 30 km.

The one-dimensional ("1-D") model can be extended to take account of diurnal changes in dissociating radiation. For substances that change rapidly at sunrise and sunset, this kind of approach may be necessary, as daily averages could give misleading results. It is sometimes possible to reduce the necessary number of diffusion equations by the use of lumped constituents, such as the *odd oxygen* of Eq. (3.2.1).

### 3.3.2 Meridional Circulation and Stratospheric Exchange with the Troposphere

That meridional circulation in the stratosphere is extremely important to the distribution of ozone can be readily appreciated by examination of Fig. 3.8. The region of production of ozone by photolysis of  $\text{O}_2$  [reaction (1.5.1) followed by (1.5.2)] lies above 20 km at the equator and above 25 km over the polar caps. The ozone concentrations are a maximum in the spring polar regions, which lie well outside the region of production. Large concentrations also occur in the temperate zones, but well below the photo-

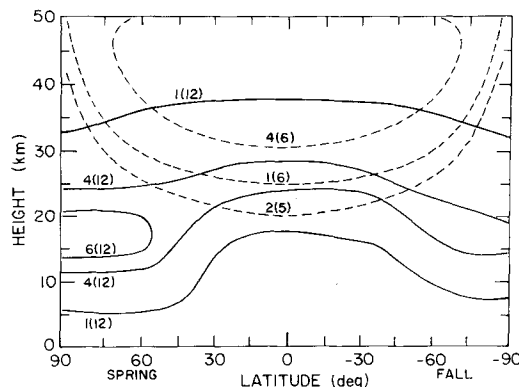


**Fig. 3.8** Regions of ozone production and residence. Zonal average ozone concentrations (solid lines) are shown in molecules/cm<sup>3</sup>. Zonal average production rates (dashed lines) are given in molecules/cm<sup>3</sup> sec. An average production rate of  $3 \times 10^4$  molecules/cm<sup>3</sup> sec is equivalent to  $1 \times 10^{12}$  molecule/cm<sup>3</sup> yr. A number such as  $4 \times 10^{12}$  is written 4(12). [Adapted from JOHNSTON (1975).]

chemically active altitudes. During the southern hemisphere spring, Fig. 3.8 is more or less reversed, so there are clearly major meridional shifts of stratospheric air mass over periods of a few months.

Figure 3.1 shows the photochemical time scales of Eq. (3.2.4), which gives the characteristic time to approach photochemical equilibrium. Figure 3.9 gives a slightly different calculation, the instantaneous photochemical lifetime, defined by

$$\tau_{\text{phot}}^{-1}(O_3) = \frac{1}{[O_3]} \frac{d[O_3]}{dt} = \frac{2J_2[O_2]}{[O_3]} \quad (3.3.4)$$

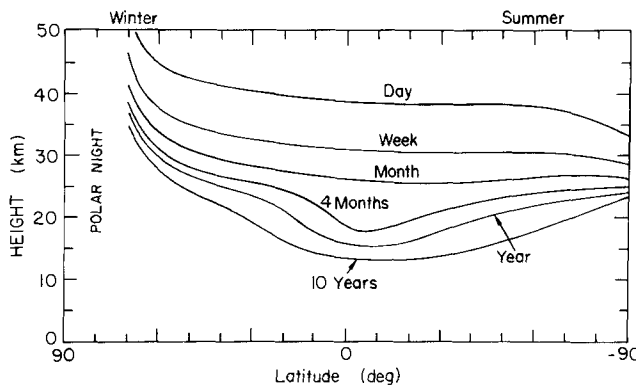


**Fig. 3.9** Photochemical times  $\tau_{\text{phot}}(O_3)$  for local replacement of ozone, zonally averaged for January 15. [After JOHNSTON (1975).]

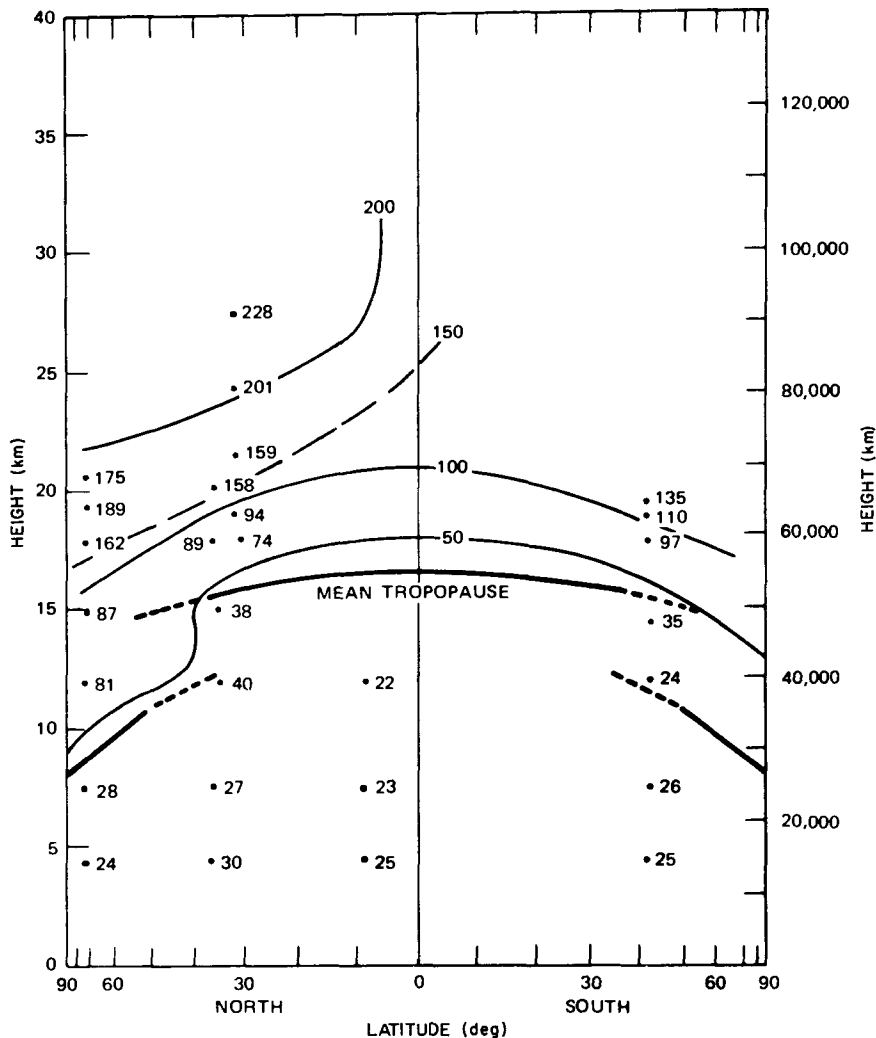


Fig. 3.10 Atmospheric  $^{14}\text{C}$  sampling and extrapolation of measurements for March–May, 1961. [After K. TELEGADAS (1973), U.S.A.W.C., Health and Safety Laboratory Report No. 243.]

where the concentrations and rates are daily averages for a particular day. Where the photochemical lifetime exceeds a month (below about 30 km at mid-latitudes), the ozone is under dynamical control. At higher altitudes than 30 km (except in the polar night), ozone is primarily under photochemical control. We could obtain average vertical and meridional ("2-D") flow from observing how ozone or some other substance flows through the stratosphere, making the photochemical adjustments as in 1-D analyses.

Most of the direct quantitative evidence for stratospheric motions comes

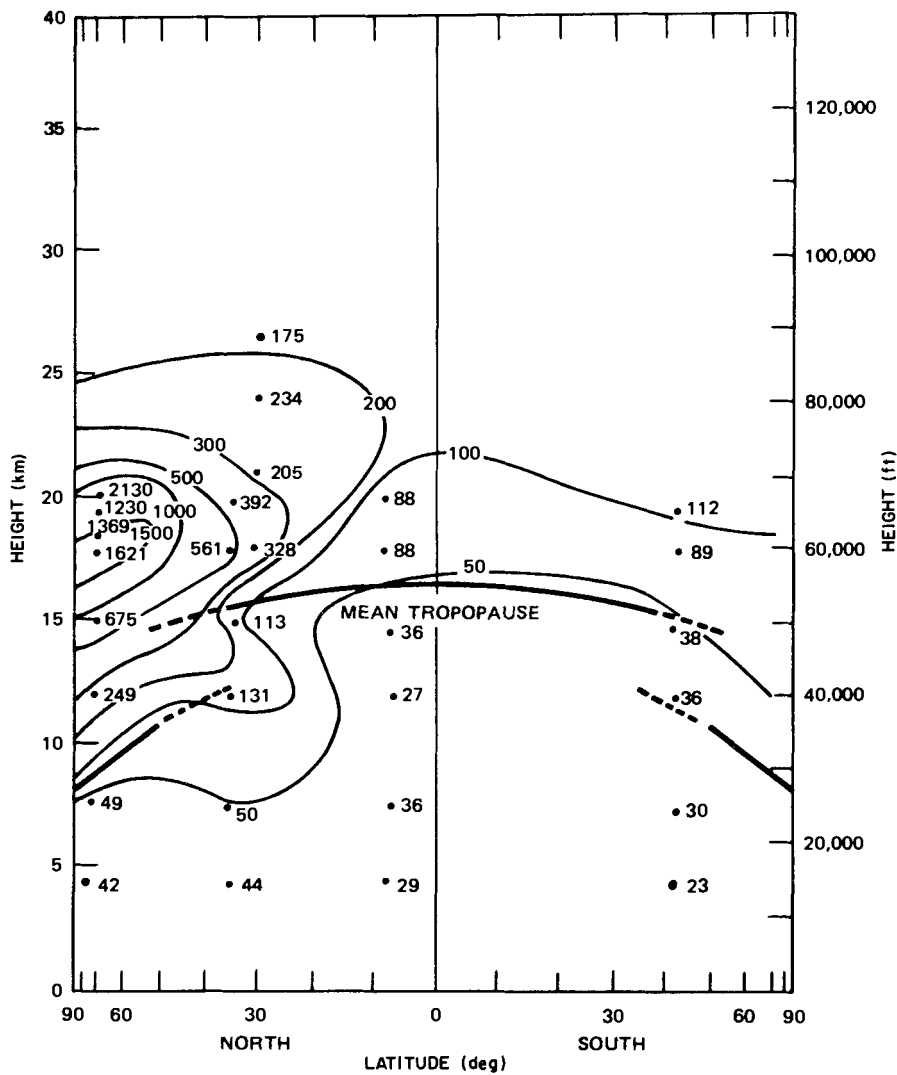


Fig. 3.11 Atmospheric  $^{14}\text{C}$  sampling and extrapolation of measurements for March–May, 1962. [After K. TELEGADAS (1973), U.S.A.W.C., Health and Safety Laboratory Report No. 243.]

from monitoring radioactive debris injected into the stratosphere from nuclear explosions. This motion is a combination of a mean circulation and eddy diffusion and of settling of particulate matter. Meridional winds are highly variable but the mean circulation is very small, and a large number of accurate measurements of tracers would be necessary to reconstruct it. Adequate measurements are not available for most of the stratosphere (see Figs. 3.10–3.13) but temperature measurements are (e.g., Fig. 2.5). Hence

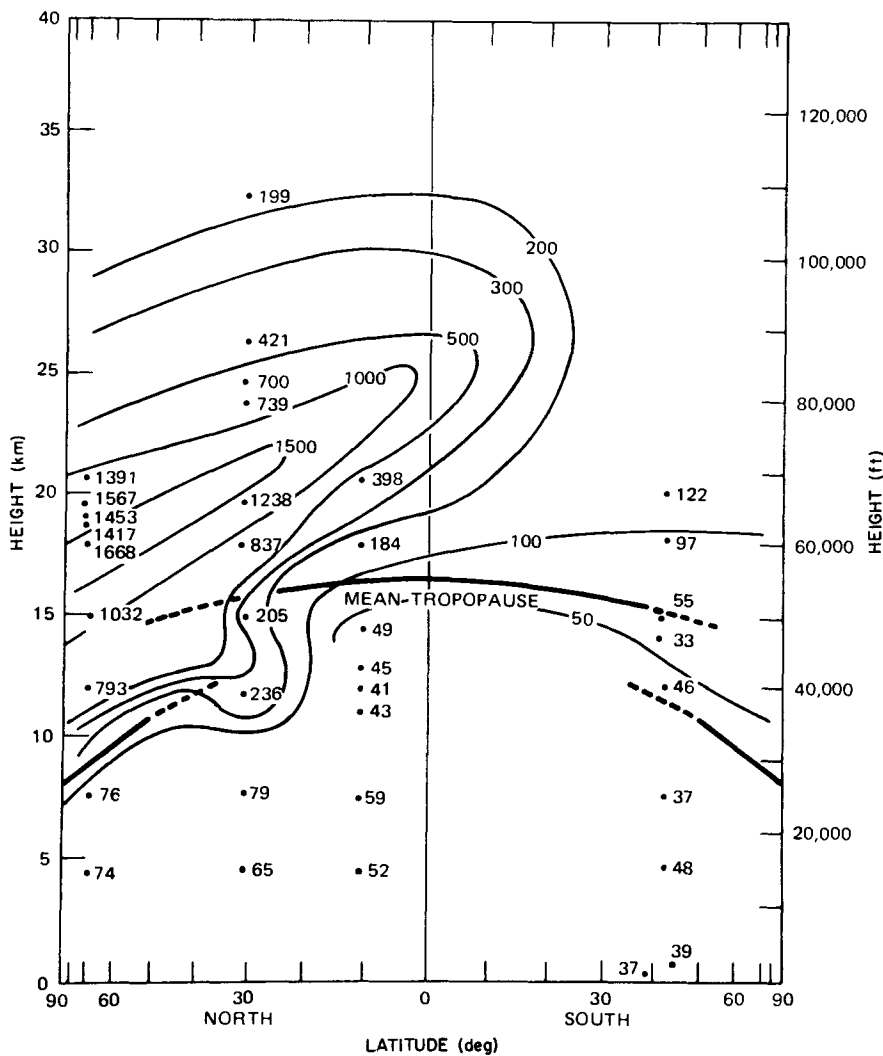
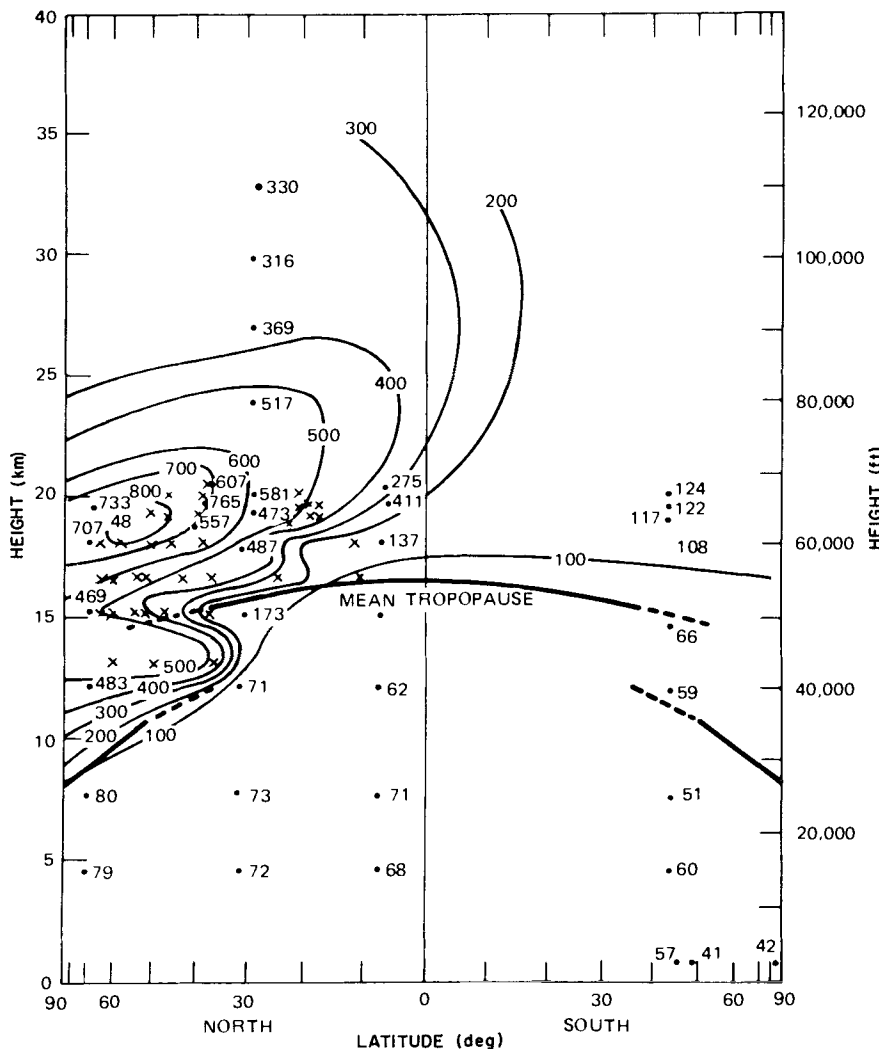


Fig. 3.12 Atmospheric  $^{14}\text{C}$  sampling and extrapolation of measurements for March–May, 1963. [After K. TELEGADAS (1973), U.S.A.W.C., Health and Safety Laboratory Report No. 243.]

one can utilize the thermodynamic equation (2.1.11) with radiative heating and cooling and eddy heat transport on the right. When averaged zonally and over one season, say, this equation is

$$\frac{\partial T}{\partial t} + v \frac{\partial T}{r \cos \phi d\phi} + w \left( \frac{\partial T}{\partial z} + \frac{g}{C_p} \right) = \frac{Q}{\rho C_p} \quad (3.3.5)$$



**Fig. 3.13** Atmospheric  $^{14}\text{C}$  sampling and extrapolation of measurements for March–May, 1964. [After K. TELEGADAS (1973), U.S.A.W.C., Health and Safety Laboratory Report No. 243.]

where  $\phi$  is latitude and  $Q$  is the net rate of heat supply. Combining this equation with continuity (2.1.1),

$$\frac{\partial(\rho v \cos \phi)}{r \cos \phi \partial \phi} + \frac{\partial(\rho w)}{\partial z} = 0 \quad (3.3.6)$$

allows one to solve for the velocities of heat advection and so construct the stream lines of mass flow.

Results of such a calculation are shown in Figs. 3.14–3.17 for the four seasons. It seems clear from these figures that the meridional circulation in the lower stratosphere, to above the 25 km level, is governed by tropospheric circulation. The spring and fall maps clearly show the Hadley, Ferrel, and polar convection cells, with the first two (in each hemisphere) protruding well into the stratosphere. The summer Hadley cell almost disappears and its mass flux is negligible, but the winter Hadley cell transfers tropospheric air upward and poleward, at the rate of  $8 \times 10^{12}$  gm/sec between the tropopause and the 25 km level. This three month season thus interchanges  $6 \times 10^{19}$  gm of air between troposphere and stratosphere, which is 15% of the stratospheric air mass in one hemisphere. Altogether the Hadley cells transfer 35 to 40 percent of the mass equivalent of the stratosphere through the tropopause per year.

The upward flow from the tropical branch of the Hadley cell is not a slow continuous flow, like the mean flow of Figs. 3.14–3.17. The tropical updrafts occur mainly as cumulus towers that penetrate the tropopause. The downward branch in the subtropics is more uniform, but there is also some downward flow around the tropical cumulus towers.

Were the mean circulation the only exchange mechanism between tropospheric and stratospheric air masses, the residence time, defined by

$$\tau_{\text{exch}}^{-1} = -\frac{1}{\mathcal{M}} \frac{d\mathcal{M}}{dt} \quad (3.3.7)$$

where  $\mathcal{M}$  is the total stratospheric air mass ( $10^{21}$  gm) would be three years. The actual mean residence time of pollutants between the tropopause and 25 km is 1 to 2 years, the difference being due largely to eddy diffusion on the size scale of cyclones and anticyclones. (Small-scale eddy diffusion at the tropopause is unimportant for purposes of mass transfer.)

Another mechanism for transporting mass across the tropopause is the seasonal shifting of the tropopause height (Figs. 3.14–3.17). Between  $30^\circ$  and  $55^\circ$  latitude the winter stratosphere gains mass and the summer stratosphere loses it.

The upper stratosphere is driven by radiative heating and cooling. The warm summer stratosphere rises and moves over the equator, descending into the winter hemisphere in a single-cell pattern.

The mass transferred from the summer to winter stratospheric hemisphere is  $6 \times 10^{12}$  gm/sec, with one third this amount crossing the equator above 35 km. Thus the total mass transferred in six months is about  $5-8 \times 10^{19}$  gm, or 10 to 15 percent of the hemispheric mass.

Water vapor distribution in the stratosphere poses special problems. The volume mixing ratios (i.e., the number density of  $\text{H}_2\text{O}$  molecules to air molecules) is generally in the range  $1-8 \times 10^{-6}$  up to about 40 km and it

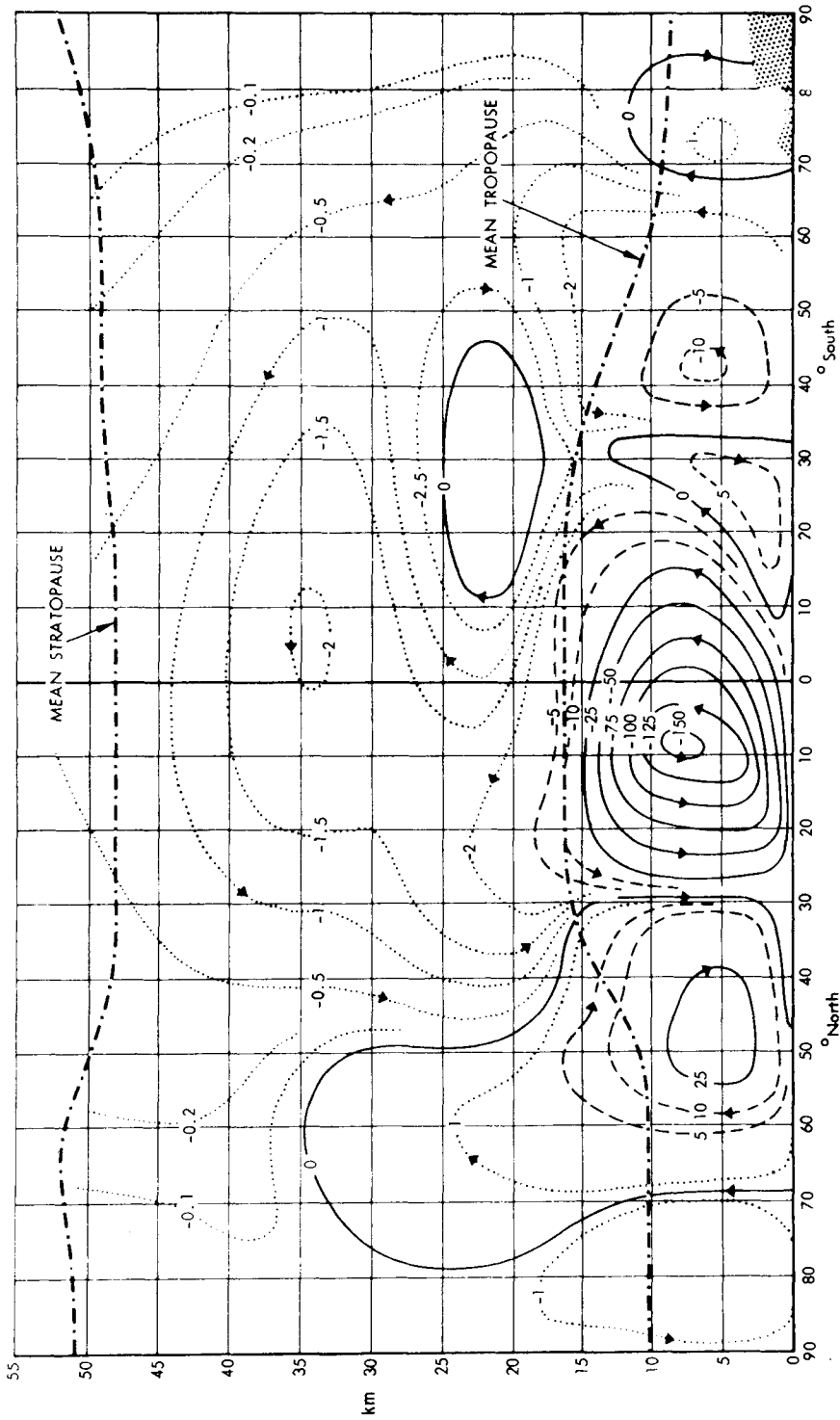


Fig. 3.14 Mean meridional circulation for December-February. Mass flow is given in units of  $10^{12}$  gm/sec. [After J. F. LOUIS in E. R. REITER et al. (1975), Chap. 6, CIAP Monograph No. 1, U.S. Dept. Transport., Washington, D.C.]

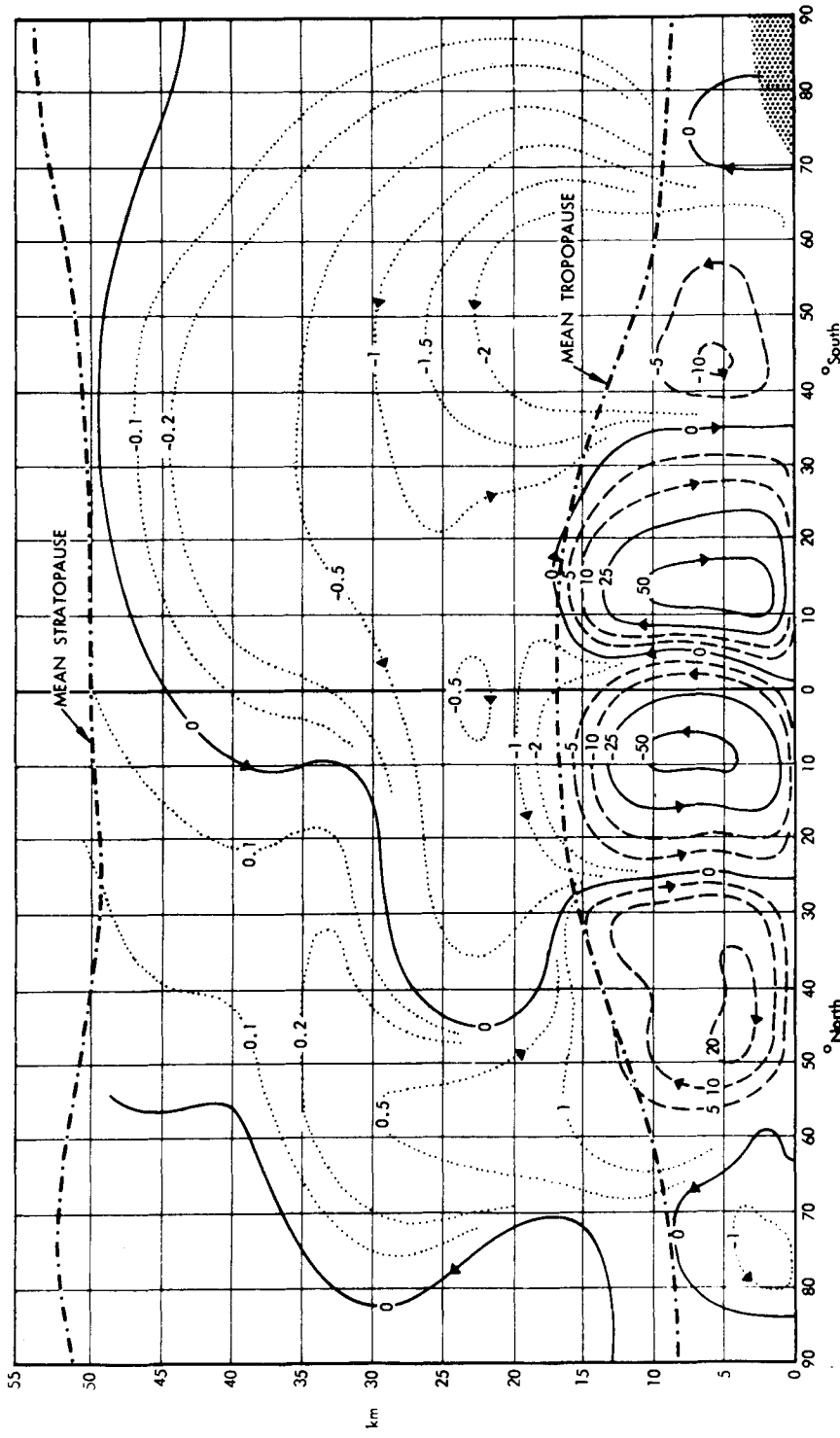


Fig. 3.15 Mean meridional circulation for March-May. Mass flow is given in units of  $10^{-12}$  gm/sec. [After J. F. LOUIS in E. R. REITER *et al.* (1975), Chap. 6, CLAP Monograph No. 1, U.S. Dept. Transport, Washington, D.C.]

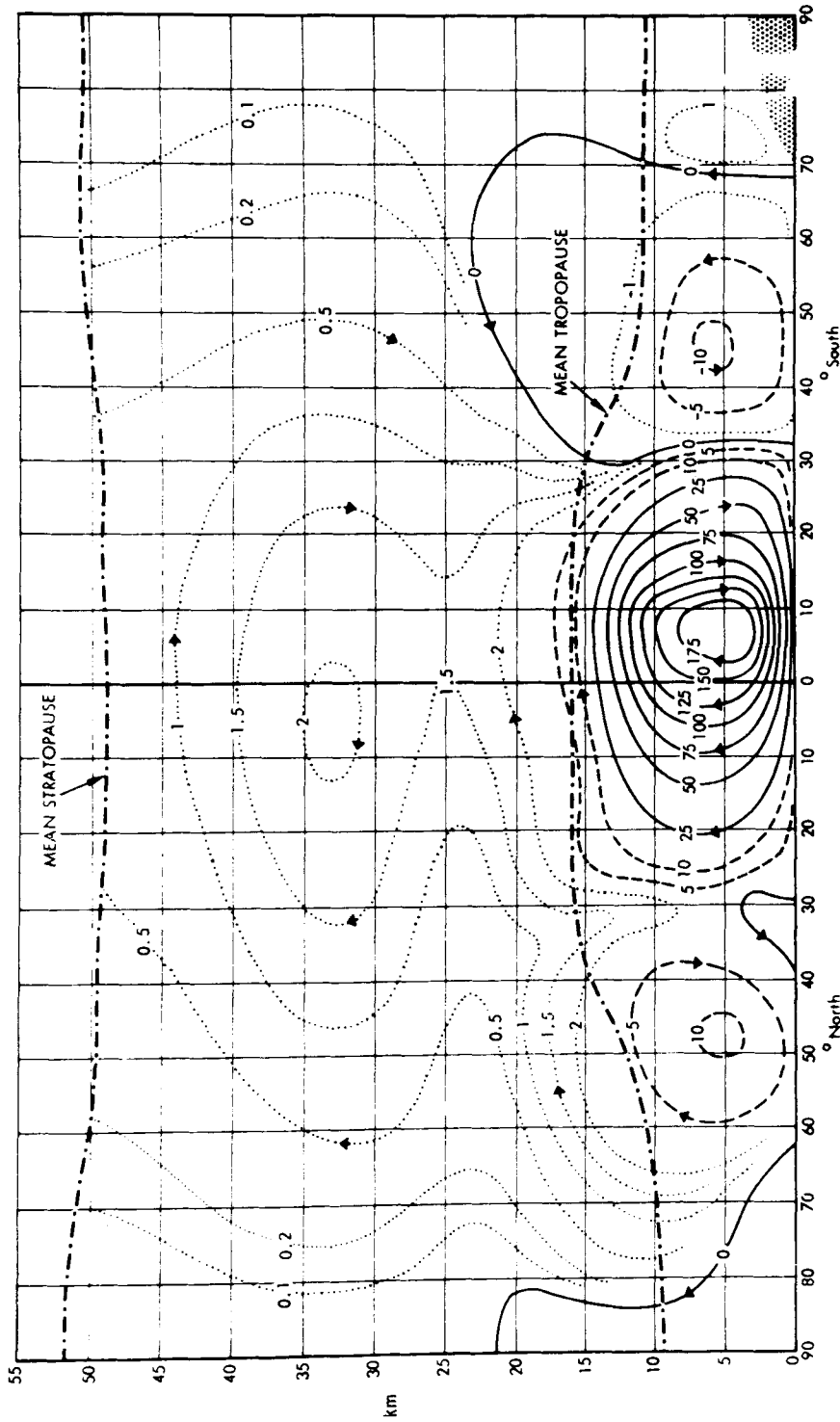


Fig. 3.16 Mean meridional circulation for June-August. Mass flow is given in units of  $10^{12}$  gm/sec. [After J. F. LOUIS in E. R. REITER *et al.* (1975), Chap. 6, CIAP Monograph No. 1, U.S. Dept. Transport, Washington, D.C.]

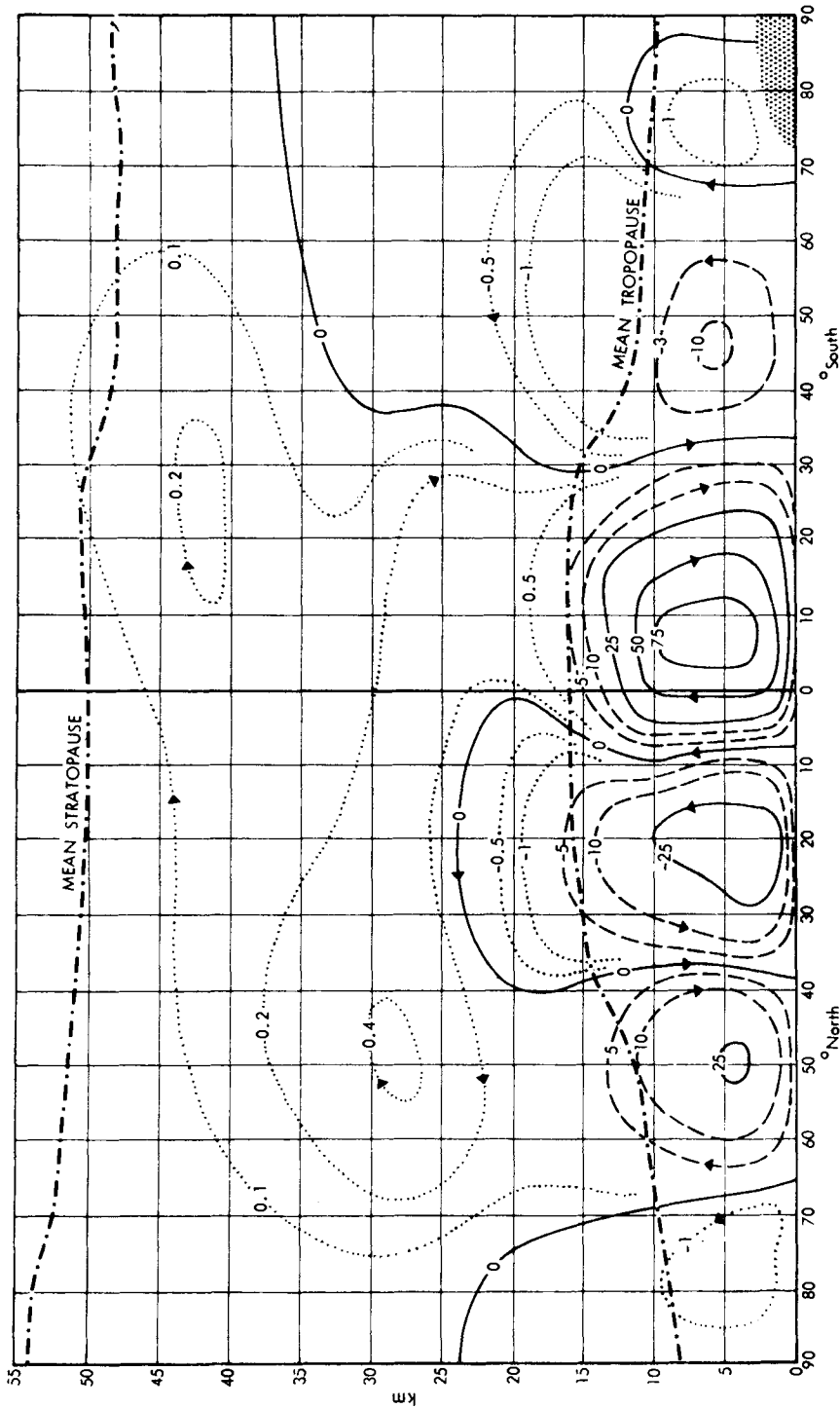


Fig. 3.14 Mean meridional circulation for September-November. Mass flow is given in units of  $10^{-12}$  gm/sec. [After J. F. LOUIS in E. R. REITER et al. (1975), Chap. 6, CIAP Monograph No. 1, U.S. Dept. Transport., Washington, D.C.]

possibly increases gradually from the tropopause to the 40 km level. Beyond that, measurements by different workers are often seriously divergent from one another and consequently the questions of whether real, major fluctuations in humidity occur and whether latitudinal or secular trends exist are largely unresolved.

## BIBLIOGRAPHICAL NOTES

### Section 3.1 Principles of Photochemistry

This subject is treated in depth in

CALVERT, J. G. and PITTS, J. N., Jr. (1966), "Photochemistry," Wiley, New York.

The subject is developed with emphasis on planetary chemistry in a series of articles in

LEVINE, J. S., ed. (1985), "The Photochemistry of Atmospheres," Academic Press, Orlando, 518 pp.

### Section 3.2 Catalytic Destruction of Ozone

A major review of this topic is

NICOLET, M. (1975), Stratospheric ozone: An introduction to its study, *Rev. Geophys. Space Phys.* **13**, 593-636.

This paper provides references to over 350 research papers. Compilations of chemical rate coefficients will be found in

HAMPSON, R. F. and GARVIN, D. (1975), "Chemical Kinetic and Photochemical Data for Modelling Atmospheric Chemistry," NBS Tech. Note 866, Natl. Tech. Infor. Serv., Springfield, Virginia 22151.

ANDERSON, L. G. (1976), Atmospheric chemical kinetics data survey, *Rev. Geophys. Space Phys.* **14**, 151-171.

A "workshop" organized by NASA has collected together the best laboratory values (as of June 1977) of stratospheric rate constants, absorption cross sections and quantum yields, tropospheric abundances of constituents that can cause stratospheric contamination, and a few photodissociation rates. The latter include the effects of sunlight scattering by the atmosphere or clouds (which increases the effective *J*-values). The committee's report is available (for \$9) as

HUDSON, R. D., ed. (1977), "Chlorofluoromethanes and the Stratosphere." NASA Reference Publ. 1010, 266 pp., Nat. Tech. Inform. Service, Springfield, Virginia 22151.

The rate coefficients quoted in this chapter and Section 1.5.1 (for the Chapman reactions) are from a 1983 compilation,

DEMURE, W. B.; MOLINA, M. J.; WATSON, R. T.; GOLDEN, D. M.; HAMPSON, R. F.; KURYLO, M. J.; HOWARD, C. J.; and RAVISHANKARA, A. R. (1983), Chemical kinetics and photochemical data for use in stratospheric modeling, Jet Propulsion Laboratory Publ. 83-62, Pasadena, California.

A later version of the same publication was issued in 1985 as JPL Publication 85-37.

The National Research Council occasionally issues updates of its evaluation of the danger of ozone depletion and associated medical effects:

Environmental Studies Board, N.R.C. (1984), "Causes and Effects of Changes in Stratospheric Ozone: Update 1983," National Academy Press, Washington, D.C.

NASA has organized an international Ozone Assessment, which involved the participation of 150 scientists from a dozen countries. The report is

WATSON, R. T., *et al.*, (eds). (1986), "Present State of Knowledge of the Upper Atmosphere: Processes That Control Ozone and Other Climatically Important Trace Gases," NASA Reference Publication 1162.

A survey of ion-molecule reactions of importance in geophysical and astrophysical applications is

ANICICH, V. G. and HUNTRESS, W. T., Jr. (1986), A survey of biomolecular ion-molecular reactions for use in modeling the chemistry of planetary atmospheres, cometary comae, and interstellar clouds, *Astrophys. J. Suppl.*, in press.

#### **Section 3.2.1 Pure Oxygen Chemistry**

The early (1930s) work on ozone photochemistry by S. CHAPMAN and by O. R. WULF and L. S. DEMING is documented in Chapter 1.

#### **Section 3.2.2 Hydrogenous Radicals**

The relationship between hydroxyl chemistry and ozone in the upper stratosphere and mesosphere was first developed by

BATES, D. R. and NICOLET, M. (1950), The photochemistry of water vapor, *J. Geophys. Res.* **55**, 301–327.

#### **Section 3.2.3 Oxides of Nitrogen**

The enormous impact of the nitrogen oxides on stratospheric ozone was first recognized by

CRUTZEN, P. J. (1970), The influence of nitrogen oxides on the atmospheric ozone content, *Quart. J. Roy. Meteorol. Soc.* **96**, 320–325.

Shortly afterwards, the potential for contamination of the stratosphere by NO<sub>x</sub> emission from aircraft was signaled by

JOHNSTON, H. S. (1971), Reduction of stratospheric ozone by nitrogen oxide catalysts from supersonic transport exhausts, *Science* **173**, 517–522.

The latter paper was largely responsible for setting in motion a chain of environmental studies by the U.S. Department of Transportation, the National Academy of Sciences, and other bodies that has in turn greatly accelerated activity in stratospheric research. The role of HO<sub>x</sub> and NO<sub>x</sub> chemistry in ozone depletion has been developed most thoroughly for a given season and latitude in

MCELROY, M. B.; WOFSY, S. C.; PENNER, J. E.; and MCCONNELL, J. C. (1974), Atmospheric ozone: Possible impact of stratospheric aviation, *J. Atmos. Sci.* **31**, 287–303,

and for the global average in

JOHNSTON, H. S. (1975), Global ozone balance in the natural stratosphere, *Rev. Geophys. Space Phys.* **13**, 637–649.

The importance of the reaction of the minor constituents HO<sub>2</sub> and NO was established by the measurement of the large rate coefficient  $\beta_{31a}$  by

HOWARD, C. J. and EVENSON, K. M. (1977), Kinetics of the reaction of HO<sub>2</sub> with NO, *Geophys. Res. Lettrs.* **4**, 437–440.

A number of papers dealing with stratospheric nitrogen oxides and their relationship to ozone appear in a special issue dedicated to the scientific accomplishments and to the memory of John F. Noxon:

*J. Geophys. Res.* **91**, No. D5, 30 April (1986), pp. 5321–5485.

### Section 3.2.4 Natural and Artificial Sources of Nitrogen Oxides

The role of aircraft exhausts in supplying the stratosphere directly with NO<sub>x</sub> has been widely studied since the original paper by

JOHNSTON, H. S. (1971), op. cit.

Particular reference should be made to the model calculations of

MCELROY, M. B., et al. (1974), op. cit.

More recent two-dimensional (vertical and meridional) computer modeling with updated rate coefficients and chemical interactions between NO<sub>x</sub> and other minor constituents indicates much less O<sub>3</sub> reduction than did earlier estimates for NO<sub>x</sub> injection below 20 km according to

HIDALGO, H. and CRUTZEN, P. J. (1977), The tropospheric and stratospheric composition perturbed by NO<sub>x</sub> emissions of high-altitude aircraft, *J. Geophys. Res.* **82**, 5833–5866.

This revised chemistry would also reduce the ozone destruction in the lower stratosphere following a tropospheric explosion of a nuclear weapon. After the Johnston (1971) paper it was immediately noted in three independent papers that NO is formed chemically in the stratosphere from inert N<sub>2</sub>O produced in the soil:

CRUTZEN, P. J. (1971), Ozone production rates in an oxygen, hydrogen, nitrogen oxide atmosphere, *J. Geophys. Res.* **76**, 7311–7327,

MCELROY, M. B. and MCCONNELL, J. C. (1971), Nitrous oxide: A natural source of stratospheric NO, *J. Atmos. Sci.* **28**, 1095–1098,

NICOLET, M. and VERGISON, E. (1971), L'oxyde azoteux dans la stratosphère, *Aeronom. Acta* **90**, 1–16.

That the agricultural source of N<sub>2</sub>O might be stimulated by the wide use of chemical fertilizers was first noted by

CRUTZEN, P. J. (1974), Estimates of possible variations in total ozone due to natural causes and human activities, *Ambio* **3**, 201–210,

and has been investigated in detail by

MCELROY, M. B.; ELKINS, J. W.; WOFSY, S. C.; and YUNG, Y. L. (1976), Sources and sinks for atmospheric N<sub>2</sub>O, *Rev. Geophys. Space Phys.* **14**, 143–150,

LIU, S. C.; CICERONE, R. J.; DONAHUE, T. M.; and CHAMEIDES, W. L. (1977), Sources and sinks of atmospheric N<sub>2</sub>O and the possible ozone reduction due to industrial fixed nitrogen fertilizers, *Tellus* **29**, 251–263,

CRUTZEN, P. J. and EHHLALT, D. H. (1977), Effects of nitrogen fertilizers and combustion on the stratospheric ozone layer, *Ambio* **6**, 112–117,

MCELROY, M. B.; WOFSY, S. C.; and YUNG, Y. L. (1977), The nitrogen cycle: Perturbations due to man and their impact on atmospheric N<sub>2</sub>O and O<sub>3</sub>, *Phil. Trans. Roy. Soc.* **B277**, 159–181.

The difficulties in assessing the effects of fertilizer on stratospheric ozone have been constructively addressed by

JOHNSTON, H. S. (1977), Analysis of the independent variables in the perturbation of stratospheric ozone by nitrogen fertilizers, *J. Geophys. Res.* **82**, 1767–1772.

Photodissociation of N<sub>2</sub>O was formerly thought to occur shortward of 3400 Å and therefore be important in the troposphere, but the wavelength limit of (3.2.47) was established by

JOHNSTON, H. S. and SELWYN, G. S. (1975), New cross sections for the absorption of near ultraviolet radiation by nitrous oxide (N<sub>2</sub>O), *Geophys. Res. Lettrs.* **2**, 549–551.

The role of nuclear explosions was first noted by

FOLEY, H. M. and RUDERMAN, M. A. (1973), Stratospheric NO production from past nuclear explosions, *J. Geophys. Res.* **78**, 4441–4450,

and subsequent work has been evaluated by

BAUER, E. and GILMORE, F. R. (1975), Effect of atmospheric nuclear explosions on total ozone, *Rev. Geophys. Space Phys.* **13**, 451–458.

A sobering analysis of the devastating effects on the world-wide stratosphere that would be caused by a major nuclear exchange between two countries is given in

NATIONAL ACADEMY OF SCIENCES (1975), "Long-term worldwide effects of multiple nuclear-weapons detonations," N.A.S. Washington, D.C. 20418.

Galactic cosmic rays as a source of  $\text{NO}_x$  was first noted by

WARNECK, P. (1972), Cosmic radiation as a source of odd nitrogen in the stratosphere, *J. Geophys. Res.* **77**, 6589–6591.

Extensive calculations of the distribution of this source in the atmosphere have been made by

NICOLET, M. (1975), On the production of nitric oxide by cosmic rays in the mesosphere and stratosphere, *Planet. Space Sci.* **23**, 637–649.

The established 11-year variation of cosmic rays was considered as a mechanism for causing the cyclic fluctuations in total ozone by

RUDERMAN, M. A. and CHAMBERLAIN, J. W. (1975), Origin of the sunspot modulation of ozone: Its implications for stratospheric NO injection, *Planet. Space Sci.* **23**, 247–268.

Solar cosmic rays have been proposed as an observable source of ozone reduction by

CRUTZEN, P. J.; ISAKSEN, I.S.A.; and REID, G. C. (1975), Solar proton events: Stratospheric sources of nitric oxide, *Science* **189**, 457–459.

and observations from Nimbus 4 have shown an ozone reduction associated with a major solar proton event according to

HEATH, D. F.; KRUEGER, A. J.; and CRUTZEN, P. J. (1977), Solar proton event: Influence on stratospheric ozone, *Science* **197**, 886–889.

A possible role of Galactic and solar cosmic rays in inducing climatic variations has been suggested by

CHAMBERLAIN, J. W. (1977), A mechanism for inducing climatic variations through the stratosphere: Screening of cosmic rays by solar and terrestrial magnetic fields, *J. Atmos. Sci.* **34**, 737–743.

### Section 3.2.5 Chlorine and the Halomethanes

The potential importance of chlorine chemistry to stratospheric ozone was first declared publicly at an international symposium in Kyoto, September, 1973, by R. S. STOLARSKI and R. J. CICERONE. However, the chemistry in the published version of that paper is considerably revised from that in the original oral presentation. Another paper in the symposium proceedings discusses  $\text{ClO}_x$  chemistry and was submitted for publication a few weeks after the Kyoto conference. Apparently the two groups were working independently on the problem and must share credit for recognition of the important reactions. The published papers are

WOFSY, S. C. and McELROY, M. B. (1974),  $\text{HO}_x$ ,  $\text{NO}_x$ , and  $\text{ClO}_x$ : Their role in atmospheric photochemistry, *Canad. J. Chem.* **52**, 1582–1591,

STOLARSKI, R. S. and CICERONE, R. J. (1974), Stratospheric chlorine: A possible sink for ozone, *Canad. J. Chem.* **52**, 1610–1615.

A third paper in the same proceedings discusses  $\text{ClO}_x$  chemistry briefly as a result of the Stolarski and Cicerone presentation.

That the synthetic halomethanes evidently have no natural sink other than stratospheric photolysis and that they therefore pose a serious threat to the environment was first announced in

MOLINA, M. J. and ROWLAND, F. S. (1974), Stratospheric sink for chlorofluoromethanes: Chlorine atom catalyzed destruction of ozone, *Nature* **249**, 810–812.

An exceptionally thorough analysis of the Cl chemistry and projection of the environmental hazard is given in

ROWLAND, F. S. and MOLINA, M. J. (1975), Chlorofluoromethanes in the environment, *Rev. Geophys. Space Phys.* **13**, 1–35.

The formation of  $\text{ClNO}_3$  (chlorine nitrate) was the first recognized example of self-cancellation of two ozone-destroying catalysts ( $\text{ClO}_x$  and  $\text{NO}_x$ ); see

ROWLAND, F. S.; SPENCER, J. E.; and MOLINA, M. J. (1976), Stratospheric formation and photolysis of chlorine nitrate, *J. Phys. Chem.* **80**, 2711–2713.

The magnitude of the day/night ratio of  $\text{ClO}$  has been measured, and it provides a key check on the quantitative chemistry of chlorine in the stratosphere:

SOLOMON, P. M.; DE ZAFRA, R.; PARRISH, A.; and BARRETT, J. W. (1984), Diurnal variation of stratospheric chlorine monoxide: A critical test of chlorine chemistry in the ozone layer, *Science*, **224**, 1210–1214.

Volcanic gases as a possible source of stratospheric chlorine have been considered in

STOLARSKI, R. S. and CICERONE, R. J. (1974), op. cit.,

RYAN, J. A. and MUKHERJEE, N. R. (1975), Sources of stratospheric gaseous chlorine, *Rev. Geophys. Space Phys.* **13**, 650–658.

Measurements of photoabsorption cross sections for several halomethanes are reported in

ROWLAND, F. S. and MOLINA, M. J. (1975), op. cit.,

ROBBINS, D. E. and STOLARSKI, R. S. (1976), Comparison of stratospheric ozone distributions by fluorocarbons 11, 12, 21, and 22, *Geophys. Res. Lettrs.* **3**, 603–606.

Bromine in the atmosphere and its possible influence on the stratosphere is treated in

WORSY, S. C.; MC ELROY, M. B.; and YUNG, Y. L. (1975), The chemistry of atmospheric bromine, *Geophys. Res. Lettrs.* **2**, 215–218.

### Section 3.3 Stratospheric Motions

The use of vertical profiles of trace constituents for the stratosphere to derive vertical mixing rates is developed in

WORSY, S. C. and MC ELROY, M. B. (1973), On vertical mixing in the upper stratosphere and lower mesosphere, *J. Geophys. Res.* **78**, 2619–2624.

HUNTER, D. M. (1975), Estimates of stratospheric pollution by an analytic model, *Proc. Nat. Acad. Sci. USA* **72**, 4711–4715.

For the mesosphere, see

ALLEN, M.; YUNG, Y. L; and WATERS, J. W. (1981), Vertical transport and photochemistry in the terrestrial mesosphere and lower thermosphere (50–120 km), *J. Geophys. Res.* **86**, 3617–3627.

Stratospheric circulation and exchange with the troposphere is reviewed in

REITER, E. R. (1975), Stratospheric-tropospheric exchange processes, *Rev. Geophys. Space Phys.* **13**, 459–474.

A theoretical discussion of stratospheric meteorology and general circulation is given in

HOLTON, J. R. (1975). "The Dynamic Meteorology of the Stratosphere and Mesosphere," American Meteorological Society, Boston.

The propagation of gravity waves in the stratosphere is reviewed by

WALLACE, J. M. (1973), General circulation of the tropical lower stratosphere, *Rev. Geophys. Space Phys.* **11**, 191–222.

The status of knowledge on the distribution of water vapor is summarized in

HARRIES, J. E. (1976), The distribution of water vapor in the stratosphere, *Rev. Geophys. Space Phys.* **14**, 565–575.

## PROBLEMS

**3.1 Threshold kinetic energy.** If two molecules of mass  $M_A$  and  $M_B$  have relative velocities  $g$  along a line connecting their centers, show that the threshold velocity for a chemical reaction is given by (3.1.6).

**3.2 Reaction energies.** (a) Compare the heat energy released in the conversion of  $O_3 + O$  into  $2O_2$  by direct annihilation (1.5.3) with the catalytic processes using hydrogenous radicals (3.2.11 and 3.2.14) and the nitrogen oxides (3.2.27 and 3.2.28). (b) Which of the following reactions is exothermic? By how much?

- (1)  $NO_3 + NO_3 \rightarrow 2NO_2 + O_2$
- (2)  $N_2O_5 + O \rightarrow 2NO_2 + O_2$

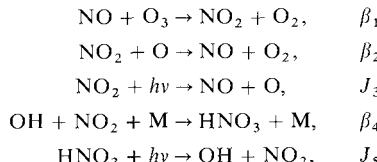
**3.3 Equilibrium ozone with  $ClO_x$**  [after NICOLET (1975)]. Write the equilibrium  $O_3$  abundance in the form (3.2.24) and find the correction term for a linear combination of Chapman,  $HO_x$ ,  $NO_x$ , and  $ClO_x$  chemistry, considering only the principal reactions.

**3.4 Eddy diffusion with a source function: (I) Analytic.** Solve Eq. (3.2.48) for  $[NO_x] \equiv N_1(z)$  in a steady state where  $\mathcal{J} \equiv [N_2O][O(^1D)]\beta_{44}$  is a constant value in the range  $z_0 < z < z_t$  and zero outside. Take  $H(z)$  and  $K(z) = \text{const}$  in this range. At high altitudes  $N_1(z)/N(z) = \text{a constant mixing ratio}$  (i.e., we neglect photodissociation) and the  $z_0$  plane is a perfect sink, with  $N_1(z \leq z_0) = 0$ .

**3.5 Eddy diffusion: (II) Numerical.** Approximate values for the lower stratosphere are  $\mathcal{J} = 33 \text{ cm}^{-3} \text{ sec}^{-1}$ ,  $H = 6.7 \text{ km}$ ,  $K = 3 \times 10^3 \text{ cm}^2/\text{sec}$ , and  $z_0 = 16 \text{ km}$ . Also take  $z_t = 40 \text{ km}$ .

- (a) What is the altitude of the maximum  $[NO_x]$ ?
- (b) Sketch  $[NO_x]$  between 16 and 40 km and compare with values estimated from Fig. 3.4.
- (c) Explain qualitatively how  $[O(^1D)]$  and  $[N_2O]$  must vary with altitude and why, therefore,  $\mathcal{J} = \text{const}$  is a fair approximation in this region.

**3.6 Nonlinear interaction of  $NO_x$  and  $ClO_x$ .** (a) Consider  $[NO_x] = [NO] + [NO_2] + [HNO_3]$  to be in photochemical equilibrium with the following reactions and rates or rate coefficients:



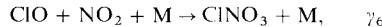
The catalytic loss rate of  $O_3$  depends on  $[NO_2]$ . Show that the ratio of  $NO_2$  to total odd nitrogen is

$$\frac{[NO_2]}{[NO_x]} \equiv R = \left[ 1 + \frac{[OH][M]\beta_4}{J_5} + \frac{[O]\beta_2 + J_3}{[O_3]\beta_1} \right]^{-1}$$

(b) If Cl is added to the system the total odd nitrogen is

$$[\text{NO}_x] = [\text{NO}] + [\text{NO}_2] + [\text{HNO}_3] + [\text{ClNO}_3]$$

and we now consider, in addition to the above reactions,



Show that if the total odd nitrogen remains fixed when Cl is added, the  $[\text{NO}_2]$  is reduced such that

$$Q \equiv \frac{[\text{NO}_2](\text{with Cl})}{[\text{NO}_2](\text{without Cl})} = (1 + R \cdot S)^{-1}$$

where  $S$  is proportional to  $[\text{ClO}]$ .

**3.7 Upward diffusion with photochemical loss.** Over a height interval  $z_0$  to  $z$  an atmosphere has a constant scale height  $H$  and vertical eddy diffusion coefficient  $K$ . In this region a minor constituent with number density  $N_1(z)$  is photodissociated with a rate  $J$ , also independent of  $z$ . (a) Show that in equilibrium the density distribution has the solution

$$N_1(z) = N_1(z_0)e^{-\alpha(z-z_0)/H}$$

where  $\alpha$  is a constant and  $\alpha \geq 1$ . (b) Relate  $\alpha$  to the characteristic times of mixing  $\tau_{\text{mix}}$  and photo-dissociation  $\tau_{\text{dis}}$ , and find  $\alpha$  when  $\tau_{\text{dis}} = \tau_{\text{mix}}$ .

**3.8 Diurnal variation.** Consider the formation of  $\text{NO}_2$  in the day by



and its removal, day and night, by



The rate coefficient  $\beta_2$  for reaction (2) is constant. The production rate  $J_1(t)$  in the 24-hour day of the Arctic summer is approximated by a sinusoidal variation,

$$J(t) = \frac{1}{2}J_{\text{max}}(1 - \cos \omega t)$$

where  $t$  is measured from midnight and  $\omega = (2\pi/24) \text{ hr}^{-1}$ . Regard all substances except  $\text{NO}_2$  as constant. (a) How long after noon does  $[\text{NO}_2]$  reach a maximum? Take  $\beta_2 = 5 \times 10^{-30} \text{ cm}^6/\text{sec}$ ,  $[\text{M}] = 10^{18} \text{ cm}^{-3}$ ,  $[\text{OH}] = 10^7 \text{ cm}^{-3}$ ,  $[\text{HNO}_3] = 10^{10} \text{ cm}^{-3}$ ,  $J_{\text{max}} = 2 \times 10^{-5} \text{ sec}^{-1}$ . (b) What is the ratio of the maximum to minimum  $[\text{NO}_2]$ ?



## ***Chapter 4***

# **PLANETARY ASTRONOMY**

This chapter deals with the remote sensing of planetary atmospheres by radiation. This radiation frequently contains the signatures of atmospheric characteristics (e.g., composition, temperature, pressure) integrated over a range of depth; proper interpretation of the data may be a formidable problem.

### **4.1 Radiative Transfer in an Optically Thick Atmosphere**

#### **4.1.1 Equation of Transfer**

In the formation of a spectral absorption line by planetary gases, there may be scattering centers in the atmosphere as well as absorbers. We will suppose that the scattering, whether it be by gas (*Rayleigh scattering*) or aerosols (*Mie scattering*), does not change the frequency of the photon. In this sense the scattering is called *coherent*.

With a scattering and absorbing atmosphere illuminated by the sun (cf. Fig. 4.1), the general equation of transfer (1.2.11),

$$\mu \frac{dI}{d\tau} = I - \mathcal{J} \quad (4.1.1)$$

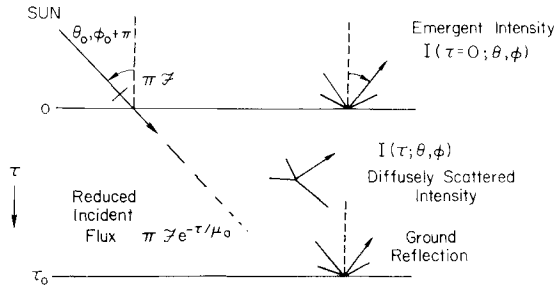


**Fig. 4.1** Scattering of sunlight in an optically thick atmosphere. The direction of propagation of diffuse intensity  $I$  is toward  $\theta, \phi$ ; however, the (downward) direction of the incident solar flux (measured across an area normal to the solar direction) is toward  $\theta_0 + \pi, \phi_0$ , since  $\theta_0$  is conventionally taken as the solar zenith angle, i.e., the angle between local zenith and the sun. Equation (4.1.2) relates the intensity toward  $\theta, \phi$  to that toward  $\theta', \phi'$  and to the incident flux from direction  $\theta_0, \phi_0 + \pi$ .

becomes (1.2.5) with a term added to the source function  $\mathcal{J}$  to account for unscattered solar radiation:

$$\begin{aligned} \mu \frac{dI(\theta, \phi)}{d\tau} &= I(\theta, \phi) - \frac{1}{4\pi} \int_0^{2\pi} \int_0^\pi I(\theta', \phi') p(\theta, \phi; \theta', \phi') \sin \theta' d\theta' d\phi' \\ &\quad - \frac{\pi \mathcal{F}}{4\pi} e^{-\tau/\mu_0} p(\theta, \phi; \theta_0 + \pi, \phi_0) \end{aligned} \quad (4.1.2)$$

Here  $I$  (erg/cm<sup>2</sup> sec sr Hz) is the monochromatic specific intensity at optical depth  $\tau$  (we will omit the subscript  $v$  used in Section 1.2), the element of vertical optical thickness is  $d\tau = -(\kappa + \sigma)\rho dz$ , the direction cosines are  $\mu = \cos \theta$ , where  $\theta$  is the zenith angle of the observer,  $\mu_0 = \cos \theta_0$ , where  $\theta_0$  is the zenith angle of the sun,  $p$  is the scattering phase function normalized by (1.2.4),  $\sigma$  is the mass scattering coefficient (cm<sup>2</sup>/gm) and  $\kappa$  the absorption coefficient, and  $\pi \mathcal{F}$  (erg/cm<sup>2</sup> sec Hz) is the solar flux crossing an area taken normal to the incident beam. The extra term in the solar flux enters as a matter of convenience. Where there is a parallel beam of incident radiation, its specific intensity is infinite. Hence we divide the radiation field into the unscattered part  $\pi \mathcal{F} e^{-\tau/\mu_0}$  and the diffuse field  $I$  that has experienced at least one scattering. That the flux term is equivalent to an additional intensity in the direction  $\theta_0 + \pi, \phi_0$  may be verified by writing the solar intensity as  $\pi \mathcal{F} \delta(\mu' - \mu_0) \delta(\phi' - \phi_0)$ , where  $\delta$  is the Dirac  $\delta$ -function.

With the single-scattering albedo defined as

$$\tilde{\omega} = \frac{\sigma}{\kappa + \sigma} \quad (4.1.3)$$

the equation for isotropic scattering ( $p \equiv \text{const} = \tilde{\omega}$ ) becomes

$$\mu \frac{dI(\mu)}{d\tau} = I(\mu) - \frac{\tilde{\omega}}{2} \int_{-1}^1 I(\mu) d\mu - \frac{\tilde{\omega}}{4} \mathcal{F} e^{-\tau/\mu_0} \quad (4.1.4)$$

We must bear in mind that  $I$  is a function of depth  $\tau$  as well as direction, even though the  $\tau$  dependence is not explicitly stated.

#### 4.1.2 Gaussian Quadrature Formula

Approximate solutions of the integro-differential equation (4.1.4) may be obtained by dividing the radiation field into  $2n$  discrete streams and replacing the integral with a sum. Let  $f(x)$  be a polynomial of degree  $2m - 1$ , completely specified by  $2m$  numbers,

$$f(x) = c_0 + c_1 x + \cdots + c_{2m-1} x^{2m-1} \quad (4.1.5)$$

We wish to replace the integral with a sum such that

$$\int_A^B f(x) dx = \sum_{j=1}^n a_j f(x_j) \quad (4.1.6)$$

If we were to use Newton's method to evaluate the integral, we would have to specify the function at  $n = 2m$  evenly spaced points  $x_j$ , and the weighting factors in the summation would all be  $a_j = (B - A)/2m$ .

Gauss' method reduces the number of points  $x_j$  required for an exact evaluation of (4.1.6) to only  $n = m$  by selecting the optimum values of the *division points* for a  $2m - 1$  degree polynomial. Thus the integral of an arbitrary function  $f(x)$  specified at  $n$  points,  $x_j (j = 1 \dots n)$ , will be accurate for a polynomial of degree  $2n - 1$  if the  $x_j$  and  $a_j$  are selected by Gauss' method.

To see how this method works, let us put (4.1.5) into (4.1.6) and evaluate the  $l$ th term. For the integral to be accurately represented by the summation, (4.1.6) must be exact for each term in the polynomial:

$$c_i \int_A^B x^l dx = c_i (a_1 x_1^l + a_2 x_2^l + \cdots + a_n x_n^l), \quad l = 0, 1, \dots, 2m - 1 \quad (4.1.7)$$

Thus we have  $2m$  such equations ( $l = 0$  to  $2m - 1$ ) and we wish to solve them for  $a_1 \dots a_m$  and  $x_1 \dots x_m$ . By scaling the function  $f(x)$  and translating the origin we can always write the integral over a finite interval in terms of limits  $A, B = -1, +1$ . Writing

$$\alpha_l \equiv \int_{-1}^1 x^l dx, \quad l = 0, 1, \dots, 2m - 1 \quad (4.1.8)$$

we define a set of  $m$  constants  $d_l$  by the  $m$  equations

$$\alpha_{i+m} + \sum_{l=0}^{m-1} d_l \alpha_{i+l} = 0, \quad i = 0, 1, \dots, m-1 \quad (4.1.9)$$

From (4.1.7.) this equation becomes

$$\begin{aligned} & \sum_{j=1}^n a_j x_j^{i+m} + \sum_{l=0}^{m-1} d_l \sum_{j=1}^n a_j x_j^{i+l} \\ &= \sum_{j=1}^n a_j x_j^i \left( x_j^m + \sum_{l=0}^{m-1} d_l x_j^l \right) = 0 \end{aligned} \quad (4.1.10)$$

The terms in parentheses are of the form of a polynomial of degree  $m$ . Thus with the  $m$  values of  $d_l$  obtained from solving (4.1.9), we can find the  $n (=m)$  division points  $x_j$  from the  $m$  solutions of the equation

$$x_j^m + \sum_{l=0}^{m-1} d_l x_j^l = 0 \quad (4.1.11)$$

Once the  $d_l$ 's and  $x_j$ 's are determined, we can find the  $n$  Gaussian weighting factors from  $n$  of the  $2n$  equations (4.1.7),

$$\alpha_l = \sum_{j=1}^n a_j x_j^l, \quad l = 0, 1, \dots, 2n-1 \quad (4.1.12)$$

where  $\alpha_l$  is found from (4.1.8). (Only  $n$  of these equations are linearly independent.)

The division points and weighting factors are determined once and for all for a given degree  $n$  and specified integration limits (conventionally  $-1$  and  $+1$ ) and are tabulated in various books on mathematical functions. An example of the calculation, use, and accuracy of Gaussian integration is given in Problem 4.1.

#### 4.1.3 Solution for Isotropic Scattering in the First Approximation

As in our discussion of thermal radiation (see Section 1.2) we can gain an insight into radiative transfer problems with a very simple two-stream solution, even though quantitative accuracy may require more elaborate computations. The transfer equation for isotropic scattering, (4.1.4), with Gaussian summation is

$$\mu_i \frac{dI(\mu_i)}{d\tau} = I(\mu_i) - \frac{\tilde{\omega}}{2} \sum_j a_j I(\mu_j) - \frac{\tilde{\omega}}{4} \mathcal{F} e^{-\tau/\mu_0}, \quad i = \pm 1, \pm 2, \dots, \pm n \quad (4.1.13)$$

For  $n = 1$  the summation is a two-point Gaussian sum, with  $a_{\pm 1} = 1$  and  $\mu_{\pm 1} = \pm 3^{-1/2}$ . If the two hemispheres are regarded as independent, one finds  $\mu_{\pm 1} = \pm \frac{1}{2}$ , a value which usually gives superior results. However, the value  $\pm 3^{-1/2}$  so permeates the literature that we shall usually adopt it.

Our procedure is first to obtain a solution of the associated homogeneous equation and then add a particular solution for the full equation. The homogeneous equation

$$\mu_i \frac{dI_i}{d\tau} = I_i - \frac{\tilde{\omega}}{2}(I_1 + I_{-1}), \quad i = \pm 1 \quad (4.1.14)$$

has a solution of the form  $g_i e^{-k\tau}$ , where

$$g_i = \frac{\text{const.}}{1 + \mu_i k} \quad (4.1.15)$$

However, this solution is compatible with (4.1.14) only for certain *characteristic values* of  $k$ . By putting the assumed solution, with  $g_i$  as given above, back into (4.1.14), we obtain the *characteristic equation*

$$1 - \mu_1^2 k^2 = \tilde{\omega} \quad (4.1.16)$$

which has two solutions for  $k$  that differ only in sign. Thus the homogeneous equation has the solution

$$I_i = \frac{\tilde{\omega} \mathcal{F}}{4} \left( \frac{Le^{-k\tau}}{1 + \mu_i k} + \frac{L'e^{k\tau}}{1 - \mu_i k} \right) \quad (4.1.17)$$

where  $k = [3(1 - \tilde{\omega})]^{1/2}$  and where the constants  $\tilde{\omega} \mathcal{F}/4$  have been extracted for later convenience.

A particular integral for the full equation (4.1.13) is

$$I_i = \frac{\tilde{\omega} \mathcal{F}}{4} h_i e^{-\tau/\mu_0} \quad (4.1.18)$$

Substitution gives

$$h_i = \frac{\gamma}{1 + \mu_i/\mu_0} \quad (4.1.19)$$

where  $\gamma$  is a constant. However, this constant is not an arbitrary integration constant. The first approximation ( $n = 1$ ) replaces an integro-differential equation with two coupled, first-order differential equations (4.1.14) and

both integration constants have been obtained from the homogeneous solution. Putting (4.1.18) with  $h_i$  given by (4.1.19) into (4.1.13) defines the constant,

$$\gamma = \left( 1 - \frac{\tilde{\omega}}{1 - \mu_1^2/\mu_0^2} \right)^{-1} = \frac{1 - 3\mu_0^2}{1 - k^2\mu_0^2} \quad (4.1.20)$$

The particular solution is therefore

$$I_i = \frac{\tilde{\omega}\mathcal{F}}{4} \frac{(1 - \mu_1^2/\mu_0^2)e^{-\tau/\mu_0}}{(1 - \tilde{\omega} - \mu_1^2/\mu_0^2)(1 + \mu_i/\mu_0)} \quad (4.1.21)$$

The full solution consists of (4.1.17) and (4.1.21); these equations do not give the intensity  $I(\mu)$  for arbitrary  $\mu$  but only the two-stream intensities  $I(\pm\mu_1)$ . However, we can use these two-stream solutions to obtain the source function and then use the formal solution of the transfer equation (1.2.16) to obtain  $I(\mu)$ .

We first apply the boundary conditions to evaluate the integration constants  $L$  and  $L'$ . Because there is no downward diffuse radiation at the top of the atmosphere,  $I_{-1}(\tau = 0; \mu_i = -\mu_1) = 0$ , which gives

$$L + L' + (1 - \tilde{\omega})^{1/2}(L - L') = \frac{\gamma\tilde{\omega}u_0/\mu_1}{1 - \mu_0/\mu_1} = \frac{\tilde{\omega}\sqrt{3}\mu_0(1 + \sqrt{3}\mu_0)}{1 - k^2\mu_0^2} \quad (4.1.22)$$

The second boundary condition is that the ground albedo is some value  $\Lambda$ . If the incident solar flux reaching the ground (where  $\tau = \tau_0$ ) is reflected by *Lambert's reflection law* (i.e., isotropically), then the albedo condition is

$$I_1(\tau = \tau_0; \mu_1 = +\mu_1) = \Lambda [I_{-1}(\tau_0; -\mu_1) + \mu_0\mathcal{F}e^{-\tau_0/\mu_0}] \quad (4.1.23)$$

We are now ready to define the optically thick atmosphere as one in which  $\exp(-\tau_0) \ll \exp(-k\tau_0)$ , which in turn requires a high scattering albedo, or  $1 - \tilde{\omega} \ll 1$ . In this case, condition (4.1.23) yields

$$L' = Le^{-2k\tau_0}\zeta(\Lambda, \tilde{\omega}) \quad (4.1.24)$$

where

$$\zeta(\Lambda, \tilde{\omega}) = \frac{(1 - \tilde{\omega})^{1/2}(1 + \Lambda) - (1 - \Lambda)}{(1 - \tilde{\omega})^{1/2}(1 + \Lambda) + (1 - \Lambda)} \quad (4.1.25)$$

The source function is

$$\begin{aligned} \mathcal{J} &= \frac{\tilde{\omega}}{2}(I_{+1} + I_{-1}) + \frac{\tilde{\omega}}{4}\mathcal{F}e^{-\tau/\mu_0} \\ &= \frac{\tilde{\omega}^2\mathcal{F}}{4} \left[ \frac{Le^{-k\tau} + L'e^{k\tau}}{1 - \mu_1^2k^2} + \frac{e^{-\tau/\mu_0}}{1 - \tilde{\omega} - \mu_1^2/\mu_0^2} \right] + \frac{\tilde{\omega}\mathcal{F}}{4}e^{-\tau/\mu_0} \end{aligned} \quad (4.1.26)$$

We can eliminate  $\mu_1$  with (4.1.16) and (4.1.20). The formal solution (1.2.16) then yields the upward intensity

$$\begin{aligned} I(\tau, +\mu) &= \int_{\tau}^{\tau_0} e^{-(\tau' - \tau)/\mu} \mathcal{J}(\tau') d\tau'/\mu \\ &= \frac{\tilde{\omega}\mathcal{F}}{4} \left[ \frac{Le^{-k\tau}}{1+k\mu} + \frac{L'e^{k\tau}}{1-k\mu} + \frac{\gamma e^{-\tau/\mu_0}}{1+\mu/\mu_0} \right] \quad (0 < \mu \leq 1) \end{aligned} \quad (4.1.27)$$

and the downward intensity

$$\begin{aligned} I(\tau, -\mu) &= \int_0^{\tau} e^{-(\tau - \tau')/\mu} \mathcal{J}(\tau') d\tau'/\mu \\ &= \frac{\tilde{\omega}\mathcal{F}}{4} \left[ \frac{L}{1-k\mu} (e^{-k\tau} - e^{-\tau/\mu}) + \frac{L'}{1+k\mu} (e^{k\tau} - e^{-\tau/\mu}) \right. \\ &\quad \left. + \frac{\gamma}{1-\mu/\mu_0} (e^{-\tau/\mu_0} - e^{-\tau/\mu}) \right] \quad (0 < \mu \leq 1) \end{aligned} \quad (4.1.28)$$

The emergent intensity at the top of the atmosphere can be written in the convenient form

$$I(0, +\mu) = \frac{\tilde{\omega}\mathcal{F}}{4} \frac{\mu_0}{\mu + \mu_0} \frac{(1 + 3^{1/2}\mu)(1 + 3^{1/2}\mu_0)}{(1 + k\mu)(1 + k\mu_0)} [1 + P(\tilde{\omega}, \mu, \mu_0)] \quad (4.1.29)$$

where

$$P = \frac{2k(\mu + \mu_0)[1 - (1 - \tilde{\omega})^{1/2}]\zeta(\Lambda, \tilde{\omega})e^{-2k\tau_0}}{(1 - k\mu)(1 - k\mu_0)[1 + (1 - \tilde{\omega})^{1/2}]} \quad (4.1.30)$$

Except for the flux projection factor  $\mu_0$  in the numerator of (4.1.29), the emergent intensity is completely symmetrical in  $\mu$  and  $\mu_0$ . This feature is common to radiative transfer problems and is known as the *principle of reciprocity*. Defining

$$H_1(\tilde{\omega}, \mu) \equiv \frac{1 + \sqrt{3}\mu}{1 + k\mu} \quad (4.1.31)$$

we may write the emergent intensity as

$$I(0, +\mu) = \frac{\tilde{\omega}\mathcal{F}}{4} \frac{\mu_0}{\mu + \mu_0} H_1(\tilde{\omega}, \mu) H_1(\tilde{\omega}, \mu_0) (1 + P) \quad (4.1.32)$$

In the limit  $\tau_0 \rightarrow \infty$ , then  $P = 0$  and the  $H_1$  functions give the solution for a semi-infinite atmosphere. With the Ambartzumian-Chandrasekhar *principles of invariance* the transfer equation (4.1.4) can also be formulated as an integral equation. Exact solutions of the integral equation for the emergent intensity in the case of semi-infinite atmospheres are given in terms of certain tabulated *Chandrasekhar H functions*, of which  $H_1$  is the leading term. Indeed, an idea of the accuracy of the first approximation is

afforded by the consideration that  $H_1(\tilde{\omega}, \mu)$  is accurate to within about 10 percent. For example,  $H(\tilde{\omega} = 1, \mu = 1) = 2.91$ , which is 7 percent higher than (4.1.31). Somewhat better accuracy can be achieved while still retaining the analytic simplicity of the first approximation by replacing (4.1.31) with

$$H_1(\tilde{\omega}, \mu) = \frac{H(1, \mu)}{1 + k\mu} \quad (4.1.33)$$

where  $H(1, \mu)$  is the tabulated exact  $H$  function for conservative scattering.

Figure 4.2 shows plots of  $H$  functions for isotropic scattering for several values of  $\tilde{\omega}$ . The dotted lines show the approximation  $H_1$  of (4.1.31), which is written for  $\mu_1 = 3^{-1/2}$ , and the dashed lines show the values for  $\mu_1 = \frac{1}{2}$ , much closer to the true curves. Normalizing them at the right axis according to (4.1.33) would bring them rather close together, but they still fall below the true curves at angles near the horizon. The  $H$  function gives the ratio of observed intensity from a source above the slab with the slab present and absent; since the source is observed in both cases,  $H$  is never less than 1. Near the zenith,  $H$  can be as high as 2.9, because the scattered light is directed this way at the expense of angles near the horizon.

With  $H_1$  so defined, Eq. (4.1.32) is accurate to a few percent for  $\tau_0 \gtrsim 3$  and  $\tilde{\omega} \gtrsim 0.9$ . Note that the additional term  $P$  for the finiteness of the atmosphere

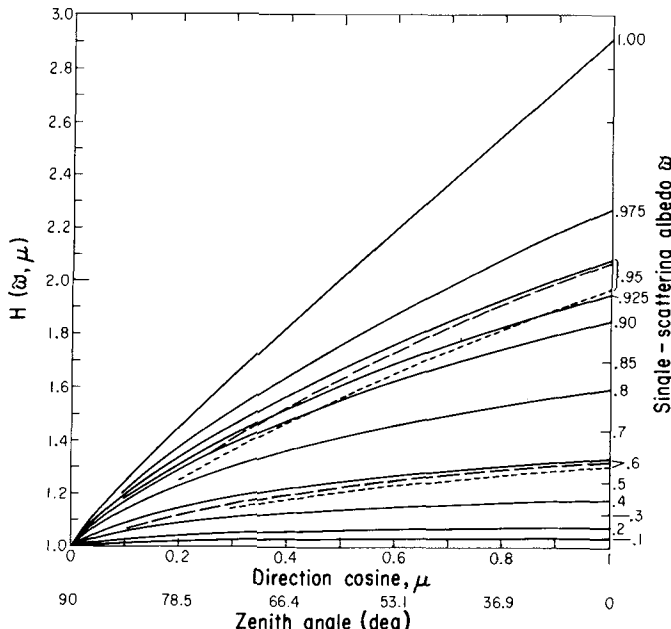


Fig. 4.2 Chandrasekhar  $H$  functions for isotropic scattering.

is by (4.1.30) proportional to  $\zeta$  of (4.1.25) and can be either positive or negative. We obtain  $P = \zeta = 0$  when the ground albedo is

$$\Lambda = \frac{1 - (1 - \tilde{\omega})^{1/2}}{1 + (1 - \tilde{\omega})^{1/2}} \quad (4.1.34)$$

Therefore a finite but thick atmosphere with this ground albedo will reflect radiation in the same manner as a semi-infinite one. It is apparent physically why condition (4.1.34) is independent of  $\tau_0$ : It simulates the albedo for a semi-infinite atmosphere that is diffusely illuminated from above (Problem 4.4).

#### 4.1.4 Anisotropic Scattering

In general we can express any phase function  $p(\cos \Theta)$  as a series of Legendre polynomials with arguments

$$\cos \Theta = \mu\mu' + (1 - \mu^2)^{1/2}(1 - \mu'^2)^{1/2} \cos(\phi - \phi') \quad (4.1.35)$$

In the simplest example of  $p = \tilde{\omega}(1 + a\cos \Theta)$ , for constants  $\tilde{\omega}$  and  $a$  ( $-1 \leq a \leq 1$ ), we may represent the scattered intensity as the sum of two components,

$$I(\tau, \mu, \phi) = I^{(0)}(\tau, \mu) + I^{(1)}(\tau, \mu)\cos(\phi - \phi_0) \quad (4.1.36)$$

The equation of transfer (4.1.2) now becomes two independent equations (Problem 4.6). The azimuth-independent intensity is given by

$$\begin{aligned} \mu \frac{dI^{(0)}(\mu)}{d\tau} &= I^{(0)}(\mu) - \frac{\tilde{\omega}}{2} \int_{-1}^{+1} I^{(0)}(\mu') d\mu' - \frac{\tilde{\omega}a\mu}{2} \int_{-1}^{+1} I^{(0)}(\mu')\mu' d\mu' \\ &\quad - \frac{\tilde{\omega}(1 - a\mu\mu_0)\mathcal{F}e^{-\tau/\mu_0}}{4} \end{aligned} \quad (4.1.37)$$

and the azimuth-dependent term has a coefficient satisfying

$$\begin{aligned} \mu \frac{dI^{(1)}(\mu)}{d\tau} &= I^{(1)}(\mu) - \frac{\tilde{\omega}a(1 - \mu^2)^{1/2}}{4} \int_{-1}^{+1} I^{(1)}(\mu')(1 - \mu'^2)^{1/2} d\mu' \\ &\quad - \frac{\tilde{\omega}a\mathcal{F}}{4} (1 - \mu^2)^{1/2}(1 - \mu_0^2)^{1/2} e^{-\tau/\mu_0} \end{aligned} \quad (4.1.38)$$

Both  $I^{(0)}$  and  $I^{(1)}$  may be solved separately just as for the isotropic case above. For a semi-infinite atmosphere the emergent intensity  $I^{(0)}$  is

$$I^{(0)}(0, \mu) = \frac{\tilde{\omega}\mathcal{F}}{4} \frac{\mu_0}{\mu + \mu_0} H^{(0)}(\mu)H^{(0)}(\mu_0)[1 - c_0(\mu + \mu_0) - a(1 - \tilde{\omega})\mu\mu_0] \quad (4.1.39)$$

where

$$c_0 = \frac{\tilde{\omega} \alpha_i^{(0)} a (1 - \tilde{\omega})}{2 - \tilde{\omega} \alpha_0^{(0)}} \quad (4.1.40)$$

and where  $\alpha_n^{(0)}$  is the  $n$ th moment of  $H^{(0)}$  (see expression in Problem 4.5).

The solution for  $I^{(1)}$  is

$$I^{(1)}(0, \mu) = \frac{\tilde{\omega} a \mathcal{F}}{4} \frac{\mu_0}{\mu + \mu_0} (1 - \mu^2)^{1/2} (1 - \mu_0^2)^{1/2} H^{(1)}(\mu) H^{(1)}(\mu_0) \quad (4.1.41)$$

In the first approximation these two sets of  $H$  functions are given by equations like (4.1.31) but where the characteristic equations yield  $k$ 's given by

$$k^{(0)} = [(1 - \tilde{\omega})(3 - \tilde{\omega}a)]^{1/2}, \quad k^{(1)} = (3 - \tilde{\omega}a)^{1/2} \quad (4.1.42)$$

Solutions of these equations, even in the first approximation, can readily yield information on differences in scattering for forward ( $a > 0$ ) and backward ( $a < 0$ ) phase functions.

More realistic phase functions, such as those appropriate to *Mie scattering* by droplets (see Section 4.3.2), are much more difficult to handle and it is frequently necessary to resort to complex computer programs. However, in many cases a satisfactory approximation is a solution expressed in terms of the *asymmetry factor*  $\langle \cos \Theta \rangle$  of the scattering phase function. Thus the degree of anisotropy in  $p(\cos \Theta)$  can be crudely described by the mean,

$$g \equiv \langle \cos \Theta \rangle = \frac{1}{2\tilde{\omega}} \int_{-1}^1 p(\cos \Theta) \cos \Theta d(\cos \Theta) \quad (4.1.43)$$

where  $p(\cos \Theta)$  is normalized to  $\tilde{\omega}$  by (1.2.4). Thus  $g = 0$  corresponds to isotropic scattering,  $g \rightarrow 1$  for strongly forward-elongated phase functions that are typical of small drops, and  $g \rightarrow -1$  for strongly backward scattering.

For the function  $p(\cos \Theta) = \tilde{\omega}(1 + a \cos \Theta)$ , we find  $g = a/3$  is restricted to the range  $\pm \frac{1}{3}$ . A fairly simple analytic function that gives the full range of possible  $g$ 's is the *Henyey-Greenstein phase function*

$$p(\cos \Theta) = \frac{\tilde{\omega}(1 - g^2)}{(1 + g^2 - 2g \cos \Theta)^{3/2}} \quad (4.1.44)$$

Two-term Henyey-Greenstein phase functions can simulate particles that have both forward and backward peaks.

The reflected radiation from an optically thick atmosphere is not strongly dependent on the precise phase function but does vary with  $g$ . Hence two different phase functions will produce similar radiation fields if their  $g$ 's (and the parameters  $\tilde{\omega}$  and  $\tau_0$ ; see below) are the same. Indeed, the similarity

of two atmospheres may be carried further. If the  $g$  is changed, it is possible to adjust the albedo  $\tilde{\omega}$  to compensate for that change. In this way problems may frequently be reduced to an *equivalent problem* for isotropic scattering. The similarity relations are

$$\tilde{\omega}' = \frac{(1-g)\tilde{\omega}}{1-g\tilde{\omega}} \quad (4.1.45)$$

$$\tau_0' = (1-g\tilde{\omega})\tau_0 \quad (4.1.46)$$

where primes refer to the isotropically scattering case and  $\tau_0$  is the total optical thickness of the atmosphere.

#### 4.1.5 Numerical Methods in Radiative Transfer

There are many approaches possible for solving the transfer equation (4.1.2). One procedure in common use is to solve the equation rigorously for a very thin layer, then apply a mathematical algorithm to extend the solution for the thin layer to layers of any desired optical thickness. If we choose the optical thickness of an atmospheric layer to be so small ( $\tau \sim 10^{-5}$ ) that only single scattering occurs, the integral in (4.1.2) is zero, and the transfer equation has the form

$$dy/dx + f(x)y = Q(x) \quad (4.1.47)$$

By multiplying through by the integrating factor  $\exp[\int f(x) dx]$ , we can put (4.1.47) in the form of an exact differential,

$$d(ye^{\int f(x) dx}) = e^{\int f(x) dx}Q(x)dx \quad (4.1.48)$$

Introducing the physical variables in (4.1.48), we find

$$d(Ie^{-\tau/\mu}) = -e^{-\tau/\mu} \frac{\pi \mathcal{F}}{4\pi\mu} p(\cos \Theta) e^{-\tau/\mu_0} d\tau \quad (4.1.49)$$

Then, applying the boundary conditions of

$$\begin{aligned} I(\tau = 0) &= 0, & \mu < 0 \\ I(\tau) &= 0, & \mu > 0 \end{aligned} \quad (4.1.50)$$

we obtain

$$I = \frac{\mu_0 \mathcal{F}}{4(\mu + \mu_0)} \{1 - e^{-\tau/\mu - \tau/\mu_0}\} p(\cos \Theta) \quad (4.1.51)$$

for the reflected intensity, and

$$I = \frac{\mu_0 \mathcal{F}}{4(\mu - \mu_0)} \{e^{-\tau/\mu} - e^{-\tau/\mu_0}\} p(\cos \Theta) \quad (4.1.52)$$

for the transmitted intensity.

The expressions (4.1.51) and (4.1.52) for single scattering by a very thin layer are exact in the sense that no approximation regarding the phase function  $p$  has been introduced. The next step in the procedure calls for evaluating the single-scattering expressions at specified Gaussian quadrature points and inserting these values in a *doubling equation algorithm*. The doubling procedure accounts for multiple scattering between the two thin layers that are being added, and returns values for the reflected and transmitted intensities valid for an optical thickness of  $2\tau$ . By successive doublings of the initial layer, the scattering properties for layers of large optical thickness can be rapidly obtained. Similarly, a vertically inhomogeneous atmosphere can be treated by combining layers of different properties. (The  $H$  functions, of course, are defined only for vertically homogeneous atmospheres.)

The remainder of this section describes a convenient numerical method for generating numerical solutions in the two-stream (or “first”) approximation. This *Feautrier method* can also be used in an  $n$ -stream version, but the two-stream version has substantial accuracy and is simple enough to run on any personal computer. It is limited to isotropic scattering, but the properties of each layer can be different. The pair of equations obtained from (4.1.13) is

$$\mu_{\pm 1} \frac{dI_{\pm 1}}{d\tau} = I_{\pm 1} - \frac{\tilde{\omega}(\tau)}{2} (I_1 + I_{-1}) - \frac{\tilde{\omega}(\tau) \mathcal{F}}{4} e^{-\tau/\mu_0} \quad (4.1.53)$$

which is identical with (4.1.14) except that the last term has not been dropped. We replace  $I_1 + I_{-1}$  by  $P$  [not the same  $P$  as in (4.1.30)] and recognize that  $\mu_{-1} = -\mu_1$ . The difference of the two equations is

$$\mu_1 \frac{d}{d\tau} (I_1 + I_{-1}) = \mu_1 \frac{dP}{d\tau} = I_1 - I_{-1} \quad (4.1.54)$$

and the sum can be combined with (4.1.54) to eliminate  $I_1 - I_{-1}$ :

$$\mu_1^2 \frac{d^2 P}{d\tau^2} = P[1 - \tilde{\omega}(\tau)] - \frac{\tilde{\omega}(\tau) F}{2} \exp(-\tau/\mu_0) \quad (4.1.55)$$

The second derivative can be replaced by its finite difference equivalent on a grid of constant spacing  $\Delta\tau$ :

$$\left(\frac{\mu_1}{\Delta\tau}\right)^2 (P_{i+1} - 2P_i + P_{i-1}) = P_i(1 - \tilde{\omega}_i) - \frac{\tilde{\omega}_i F}{2} \exp(-\tau_i/\mu_0) \quad (4.1.56)$$

where the subscripts  $i$  represent quantities at grid points  $\tau_i$ . Equation (4.1.56) plus the upper and lower boundary conditions form a tridiagonal matrix which suggests the relation

$$P_i = P_{i-1} A_{i-1} + B_{i-1} \quad (4.1.57)$$

Recursion relations for  $A$  and  $B$  are obtained by eliminating  $P_{i+1}$  from (4.1.56) and (4.1.57)

$$A_{i-1} = \left[ (1 - \tilde{\omega}_i) \left( \frac{\Delta\tau}{\mu_1} \right)^2 + 2 - A_i \right]^{-1} \quad (4.1.58)$$

and

$$B_{i-1} = A_{i-1} \left[ B_i + \frac{\tilde{\omega}_i F}{2} \left( \frac{\Delta\tau}{\mu_1} \right)^2 \exp(-\tau_i/\mu_0) \right] \quad (4.1.59)$$

The boundary conditions require some care. We formulate the lower boundary condition first for a finite slab with a surface of albedo  $\Lambda$  below it. If the lowest grid point is indexed  $i = l$ , the boundary is placed at  $b = l - \frac{1}{2}$ , and the upward intensity is  $I_1(\tau_b) = \Lambda I_{-1}(\tau_b)$ . Then (4.1.54) and (4.1.57) give

$$A_{l-1} = \frac{2\mu_1(1 + \Lambda) - (1 - \Lambda)\Delta\tau}{2\mu_1(1 + \Lambda) + (1 - \Lambda)\Delta\tau}, \quad B_{l-1} = 0 \quad (4.1.60)$$

Equations (4.1.58–4.1.60) allow the evaluation of all the  $A$  and  $B$ . For a semi-infinite atmosphere the application of the lower boundary condition requires some experimentation. For  $\tilde{\omega} \lesssim 0.995$  it is sufficient to put the deepest grid point at  $\tau = 30$  and to represent the atmosphere below as homogeneous with  $\tilde{\omega} = \tilde{\omega}_l$ .

The upper boundary condition  $I_{-1}(\tau = 0) = 0$  is imposed between the two top grid points chosen so that  $\tau_1 + \tau_2 = 0$ . Then (4.1.54) in finite difference form combined with (4.1.57) for  $i = 2$  gives

$$P_1 \left( \frac{2 + \Delta\tau/\mu_1}{2 - \Delta\tau/\mu_1} - A_1 \right) = B_1 \quad (4.1.61)$$

which allows the calculation of  $P_1$ ; the remaining  $P$  can be obtained from (4.1.57) and  $I_1(\tau = 0) = (P_1 + P_2)/2$ .

An analytic solution to (4.1.55) for a single layer with constant  $\tilde{\omega}$  is

$$\begin{aligned} P &= A^+ \exp[+(1 - \tilde{\omega})^{1/2}\tau/\mu_1] \\ &\quad + A^- \exp[-(1 - \tilde{\omega})^{1/2}\tau/\mu_1] + \frac{\tilde{\omega}F/2 \exp(-\tau/\mu_0)}{(1 - \tilde{\omega}) - (\mu_1/\mu_0)^2} \end{aligned} \quad (4.1.62)$$

where  $A^+$  and  $A^-$  are to be determined by the boundary conditions. The layers may then be combined by requiring continuity in  $P$  and  $dP/d\tau$  at the

boundaries and applying upper and lower boundary conditions on  $I_1$  and  $I_{-1}$ . This yields a matrix which allows the determination of  $A^+$  and  $A^-$  in each of the layers and completely specifies  $P(\tau)$ .

Once the values of  $P$  have been obtained, as in any other method they are substituted into (4.1.4) to obtain  $I(\mu)$  at directions other than  $\mu_1$ . The traditional choice for  $\mu_1$ , used throughout the present section, is  $3^{-1/2}$ , but  $\frac{1}{2}$  is actually superior. They correspond, respectively, to a two-point quadrature over the entire sphere and two single-point quadratures, one for each hemisphere.

## 4.2 Spectroscopy

### 4.2.1 Optically Thin Continuum

Consider the radiation entering a thin atmosphere defined by  $\tau_c \ll 1$  at continuum frequencies  $\nu$ —well removed from spectral absorption lines. The light is diffusely reflected from the surface, or possibly from cloud tops, and observed at some angle  $\theta$  from the local zenith (see Fig. 4.1). The *absorption profile* in a spectral line relative to the neighboring continuum is

$$\begin{aligned} s_\nu &\equiv \frac{I_c - I_\nu}{I_c} \\ &= 1 - \exp\left[-\tau_\nu\left(\frac{1}{\mu_0} + \frac{1}{\mu}\right)\right] \end{aligned} \quad (4.2.1)$$

The factor  $(\mu_0^{-1} + \mu^{-1})$  for observation at a particular point on the disk is the air-mass factor  $\eta$ . For observations that cover the entire disk at full phase the mean air-mass factor is  $\langle \eta \rangle = 4$  in the optically thin limit (see below).

The entire area absorbed in one spectral line in Fig. 4.3 is the *equivalent width*  $W$ , so called because it is the width (in  $\nu$  or  $\lambda$  units) of a totally black

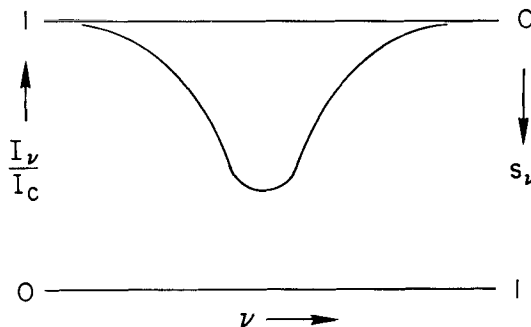


**Fig. 4.3** Schematic profile of a spectral absorption line.

line ( $I_v = 0$ ) having the same area as the real profile. Without high spectral resolution it is not possible to measure profiles directly, but the equivalent width represents total energy loss and is independent of the spectral resolution.

In the limit of very weak lines such that the optical thickness in the line center  $\tau_0 \ll 1$ , we have

$$W \equiv \int_0^\infty s_v dv \approx \eta \int_0^\infty \tau_v dv = \eta \mathcal{N} S \quad (4.2.2)$$

where  $\mathcal{N}$  is the *integrated overhead density* (1.1.6) and  $S$  ( $\text{cm}^2/\text{sec}$ ) is the line *strength* or integrated cross section (1.6.5).

For stronger absorption, as the center of the line profile approaches blackness or *saturation*,  $W$  can clearly not continue to increase linearly with  $\eta \mathcal{N} S$ . The plot of  $W$  vs.  $\eta \mathcal{N} S$  is called the *curve of growth*. Its form depends in turn on the shape of the line absorption coefficient. For collisional broadening, usually the most important type of line broadening in planetary absorption spectra, the absorption cross section follows the Lorentz profile,

$$\alpha_v = \frac{S\Gamma/4\pi^2}{(v - v_0)^2 + (\Gamma/4\pi)^2} \quad (4.2.3)$$

where  $\Gamma$  is the *collisional damping constant*. Many writers use  $\alpha_L$ , the Lorentz width, instead of  $\Gamma/4\pi$ . As  $\eta \mathcal{N} S$  is increased (say, for different lines in a spectrum), the curve of growth begins to level out as the line core becomes saturated. However, the broad wings can still absorb additional radiation. Somewhat arbitrarily let us define the absorbing wings as beginning at the point  $v_1$  ( $\equiv v_1$ ), where the effective optical thickness drops to unity,  $\eta \tau_v = \eta \mathcal{N} \alpha_v = 1$ , or

$$v_1 - v_0 \approx \pm (\eta \mathcal{N} S \Gamma / 4\pi^2)^{1/2} \quad (4.2.4)$$

Thus after the line's core becomes saturated the equivalent width is given by total absorption from the center  $v_0$  to  $v_1$  and linearly from  $v_1$  onward:

$$\begin{aligned} W &\approx 2 \int_0^{|v_1 - v_0|} dv + \frac{2\eta \mathcal{N} S \Gamma}{4\pi^2} \int_{|v_1 - v_0|}^\infty \frac{d(v - v_0)}{(v - v_0)^2} \\ &= \frac{2}{\pi} (\eta \mathcal{N} S \Gamma)^{1/2} \end{aligned} \quad (4.2.5)$$

and strong, pressure-broadened lines are said to be on the square-root portion of the curve of growth.

A more accurate derivation of (4.2.5) replaces  $2/\pi$  with  $1/\sqrt{\pi}$ , a correction of 13 percent. Writing  $\mathcal{N} \alpha_v$  from (4.2.3) for  $\tau_v$  in (4.2.1) yields the *Ladenberg-Reiche formula*,

$$W = \eta \mathcal{N} S e^{-2\eta \mathcal{N} S / \Gamma} [J_0(i2\eta \mathcal{N} S / \Gamma) - iJ_1(i2\eta \mathcal{N} S / \Gamma)] \quad (4.2.6)$$

where  $J_0$  and  $J_1$  are Bessel functions of the first kind. Limiting cases follow from asymptotic expressions for  $J_0$  and  $J_1$ . For  $\eta\mathcal{N}S/\Gamma \ll 1$ , we recover (4.2.2); for  $\eta\mathcal{N}S/\Gamma \gg 1$  we obtain

$$W \approx \left( \frac{\eta\mathcal{N}S\Gamma}{\pi} \right)^{1/2} \quad (4.2.7)$$

in place of (4.2.5).

The air mass factor  $\eta$  is still  $\mu_0^{-1} + \mu^{-1}$  for observations of a single region on the disk, and for observations of the entire disk at full phase,  $\langle \eta^{1/2} \rangle$  is proportional to  $\langle \mu^{-1/2} \rangle$ . That is,  $\eta^{1/2}$  in (4.2.7) must be replaced with

$$\begin{aligned} \langle \eta^{1/2} \rangle &= 2 \int_0^1 \eta^{1/2} \mu \, d\mu \\ &= 2 \int_0^1 \left( \frac{2}{\mu} \right)^{1/2} \mu \, d\mu = \frac{4\sqrt{2}}{3} \end{aligned} \quad (4.2.8)$$

So far, we have ignored the fact that the optical path length traverses a range of pressure, but  $\Gamma$  varies as the pressure and an effective pressure for the entire atmosphere is needed. As noted earlier, the problem does not arise if there is no saturation. If the lines are strong, the *Strong-Plass formula* gives the absorption  $W$  in terms of the damping constant  $\Gamma_0$  at the ground (or other reflecting surface):

$$W = \frac{\Gamma_0}{2\sqrt{\pi}} \frac{\gamma(2\eta\mathcal{N}S/\Gamma_0 + \frac{1}{2})}{\gamma(2\eta\mathcal{N}S/\Gamma_0)} \quad (4.2.9)$$

where  $\gamma$  is the gamma function. In the limit of  $\eta\mathcal{N}S/\Gamma \ll 1$ , we have  $\gamma(\frac{1}{2}) = \sqrt{\pi}$  and  $\gamma(2\eta\mathcal{N}S/\Gamma_0) = (2\eta\mathcal{N}S/\Gamma_0)^{-1}$ , which yields  $W = \eta\mathcal{N}S$ , a result in agreement with (4.2.2) and independent of the pressure. For strong lines,  $\eta\mathcal{N}S/\Gamma_0 \gg 1$ , the asymptotic dependence of the gamma function gives

$$W \approx \left( \frac{\eta\mathcal{N}S\Gamma_0}{2\pi} \right)^{1/2} \quad (4.2.10)$$

Equation (4.2.10) is sometimes called the *Curtis-Godson approximation*. Comparing this formula with (4.2.7) indicates that  $\Gamma = \Gamma_0/2$ . The effective pressure for pressure-broadened lines in a barometric atmosphere is one-half the ground pressure (see Problem 4.7).

Absorption in a strong band does not distinguish between effects of the abundance  $\mathcal{N}$  and the pressure. Weak bands, on the other hand, are sensitive only to  $\mathcal{N}$  but are simply harder to observe. Thus telescopic observations of the strong 1.6  $\mu\text{m}$  bands on Mars indicated a number of years ago that

$$f(\text{CO}_2)p_0^2 = 90 \text{ (mb)}^2 \quad (4.2.11)$$

if the pressure broadening were mainly due to N<sub>2</sub>. (Here  $f$  is the CO<sub>2</sub> mixing ratio.) However, self-broadening by CO<sub>2</sub> is about 2.2 times as effective as broadening by N<sub>2</sub>. With this correction, (4.2.11) becomes

$$f(\text{CO}_2)[1 + 1.2f(\text{CO}_2)]p_0^2 = 90 \text{ (mb)}^2 \quad (4.2.12)$$

which gives  $p_0 \gtrsim 6.4$  mb as the lower pressure limit for a pure CO<sub>2</sub> atmosphere. On the other hand, with the CO<sub>2</sub> abundance estimated telescopically from the weak 8689 Å band, it appeared that  $p_0$  was in the range 10–20 mb. More refined spectroscopic analyses and direct spacecraft measurements have now confirmed the lower pressure limit and the preponderance of CO<sub>2</sub> in the Martian atmosphere.

Relative absorption of the different lines in a band may also be used to derive *rotational temperatures* for an atmosphere at the level of band absorption. The relative absorption of the  $J$ th rotational level in the ground state follows the Boltzmann distribution,

$$N(J) = \text{const.}(2J + 1)\exp[-BJ(J + 1)hc/kT] \quad (4.2.13)$$

where  $B$  is the rotational constant and  $2J + 1$  is the statistical weight of the level. The relative line strengths for a particular branch of the band may be written  $S(JJ')/(2J + 1)$ . Hence we have, for an optically thin atmosphere,

$$W(JJ') = \text{const.}S(JJ')\exp[-BJ(J + 1)hc/kT] \quad (4.2.14)$$

(Such a distribution can be seen in Fig. 4.12, where the lines become stronger at low  $J$  because of the strength factor and then fall off again as the Boltzmann factor takes over.) Thus a plot of  $\log[W(JJ')/S(JJ')]$  against  $J(J + 1)$  gives a straight line whose slope is inversely proportional to the temperature. In the square-root limit of (4.2.7) we have  $W(JJ') = \text{const.}(\mathcal{N}S)^{1/2}$  and the temperature is found from plotting  $\log[W/S^{1/2}]$  against  $\frac{1}{2}J(J + 1)$ .

If the pressure is extremely low, even strong lines will not show appreciable pressure broadening. Saturated lines will have an asymptotic run of  $W(\mathcal{N})$  that depends on the Doppler profile. For example, consider the Martian CO<sub>2</sub> lines shown in Fig. 4.12 on p. 191. Here the pressure is only 6 mbar, and the effective pressure in the sense of (4.2.10), the Curtis-Godson approximation, is 3 mbar. The corresponding curve of growth (in Fig. 4.13) shows the linear region and the beginning of saturation. The approach to the square-root region is visible in the solid curve near the right, while the dashed line indicates the zero-pressure limit, where the only significant contribution to the line shape is the Doppler broadening due to the thermal motions of the molecules. The absorption coefficient has the form of a Gaussian with a full width at half maximum of  $2\alpha_D(\ln 2)^{1/2}$ , where the Doppler width in wave

numbers is  $\alpha_D = (v_0/c)(2kT/M)^{1/2}$ ;  $v_0$  is the wave number at line center. Carrying through a derivation similar to that giving (4.2.7), we find that the equivalent width for strong absorption is asymptotically  $W = 2\alpha_D[\ln(\eta\mathcal{N}S/\alpha_D\pi^{1/2})]^{1/2}$ .

In Fig. 4.13, on page 192, the various plotted points come from lines of different strengths and, for the inset, different air masses. They are also influenced by the thermal distribution of rotational levels (4.2.13).

#### 4.2.2 Optically Thick Continuum

For an optically thick (semi-infinite) atmosphere the absorption profile of a spectral line, Eq. (4.2.1), has the form

$$\begin{aligned} s_v \equiv \frac{I_c - I_v}{I_c} &= 1 - \frac{\tilde{\omega}_v H(\tilde{\omega}_v, \mu) H(\tilde{\omega}_v, \mu_0)}{\tilde{\omega}_c H(\tilde{\omega}_c, \mu) H(\tilde{\omega}_c, \mu_0)} \\ &\approx \sqrt{3}(\mu + \mu_0)[(1 - \tilde{\omega}_v)^{1/2} - (1 - \tilde{\omega}_c)^{1/2}] \\ &\quad + (1 + 3\mu\mu_0)[(1 - \tilde{\omega}_v) - (1 - \tilde{\omega}_c)] \\ &\quad - 3(\mu + \mu_0)^2[(1 - \tilde{\omega}_v) - (1 - \tilde{\omega}_v)^{1/2}(1 - \tilde{\omega}_c)^{1/2}] \end{aligned} \quad (4.2.15)$$

where we have used (4.1.32) with  $P = 0$  and expanded (4.1.33) for the  $H$  functions for the case  $1 - \tilde{\omega} \ll 1$  (i.e., for weak lines and a weakly absorbing continuum). This equation is more complicated than that for a simple reflecting surface with a thin atmosphere. Note that the angular dependence is in the opposite sense, with the strength of absorption increasing with increasing  $\mu$  and  $\mu_0$  (instead of increasing with increasing  $1/\mu$  and  $1/\mu_0$ ). The reason for this behavior is due to the fact that larger values of  $\mu$  and  $\mu_0$  are associated with radiation deeper in the atmosphere since the first (or last) scattering occurs at about  $\tau/\mu_0$  (or  $\tau/\mu$ ) = 1. Radiation that penetrates deeper will have more chances for scatterings, therefore a higher probability of becoming absorbed.

A second difference is that the degree of absorption no longer depends only on the gaseous absorption coefficient  $\alpha_v$ , or even the total albedo in the line  $\tilde{\omega}_v$ , but it depends as well on the absorption in the continuum  $\tilde{\omega}_c$ .

Let us now write the albedo in terms of absorption coefficients. Since we have two albedos in the problem, we need to divide the absorption coefficient  $\kappa$  into two parts, so that  $\kappa$  now becomes  $\kappa + \alpha_v$ . If  $\alpha_v$  is the molecular absorption cross section of (4.2.3), then  $\alpha_v = N\alpha_{v0}/\rho$  is the gaseous mass absorption coefficient ( $\text{cm}^2/\text{gm}$ ), where  $N$  is the number density of absorbing molecules and  $\rho$  is the mass density (including particles and gas). Similarly let  $\sigma$  and  $\kappa$  be the mass scattering and absorption coefficients of aerosols or other

scattering particles in the atmosphere. Then the albedo within the absorption line is

$$\tilde{\omega}_v = \frac{\sigma}{a_v + \kappa + \sigma} \quad (4.2.16)$$

and in the continuum,

$$\tilde{\omega}_c = \frac{\sigma}{\kappa + \sigma} \quad (4.2.17)$$

It is convenient to refer the line albedo to the value at the line center,

$$\tilde{\omega}_0 = \frac{\sigma}{a_0 + \kappa + \sigma} \quad (4.2.18)$$

and write  $\alpha_v = \alpha_0/x^2$ , where

$$x^{-2} = \frac{(\Gamma/4\pi)^2}{(v - v_0)^2 + (\Gamma/4\pi)^2} \quad (4.2.19)$$

The radiative transfer theory is developed, of course, for the parameters  $\tilde{\omega}_0$  and  $\tilde{\omega}_c$ . Our concern with the gaseous absorption in the atmosphere makes it desirable to work in parameters proportional to  $a_0$ . Thus line absorption can be expressed in terms of a dimensionless *line absorption parameter* [see (4.2.3)]:

$$u \equiv \frac{a_0}{\kappa + \sigma} = \frac{\tilde{\omega}_c - \tilde{\omega}_0}{\tilde{\omega}_0} = \frac{4S}{\Gamma} \frac{N}{\rho(\kappa + \sigma)} = \frac{4S\mathcal{N}_s}{\Gamma} \quad (4.2.20)$$

The ratio

$$\mathcal{N}_s \equiv N/\rho(\kappa + \sigma) \text{ (molecules/cm}^2\text{)} \quad (4.2.21)$$

is the *specific abundance*, the amount of absorbing gas in a column of unit cross section and with a length of unit optical thickness in the continuum [=  $1/\rho(\kappa + \sigma)$ ]. This quantity is the scattering atmosphere's analog to gaseous abundance above a reflecting surface in a transparent atmosphere.

A second auxiliary parameter to accompany  $u$  (in place of using  $\tilde{\omega}_c$  or  $\tilde{\omega}_0$ ) is the *absorption-ratio parameter*,

$$q \equiv \frac{a_0}{\kappa} = \frac{u}{1 - \tilde{\omega}_c} \quad (4.2.22)$$

which measures the relative importance of line and continuum absorption. Any two of the four parameters  $\tilde{\omega}_0$ ,  $\tilde{\omega}_c$ ,  $u$ , and  $q$  define the profile. In the case of weak lines wherein  $u \ll 1$ , we may replace  $(1 - \tilde{\omega}_v)$  with

$$(1 - \tilde{\omega}_v) \approx (1 - \tilde{\omega}_c) + u/x^2 \quad (4.2.23)$$

Then with (4.2.22), the equivalent width obtained from (4.2.15) may be written in terms of the two parameters  $\tilde{\omega}_c$  and  $q$ :

$$\begin{aligned} W &= \int_0^\infty s_v dv \\ &= \frac{\Gamma}{2\pi} \int_1^\infty \frac{dx x}{(x^2 - 1)^{1/2}} \left\{ \sqrt{3}(\mu + \mu_0)(1 - \tilde{\omega}_c)^{1/2} [(1 + q/x^2)^{1/2} - 1] \right. \\ &\quad + (1 + 3\mu\mu_0)(1 - \tilde{\omega}_c)q/x^2 - 3(\mu + \mu_0)^2(1 - \tilde{\omega}_c)[(1 + q/x^2) \right. \\ &\quad \left. \left. - (1 + q/x^2)^{1/2}] \right\} \end{aligned} \quad (4.2.24)$$

We now examine two limiting sub-cases of the weak-line limit; we will suppose that either the continuum absorption is much weaker or much stronger than the line absorption. If the continuum absorption is the stronger, then  $q \ll 1$ ; the profile is Lorentzian,

$$s_v = \left\{ \frac{1}{2}\sqrt{3}(\mu + \mu_0)(1 - \tilde{\omega}_c)^{1/2}q + [1 - \frac{3}{2}(\mu^2 + \mu_0^2)](1 - \tilde{\omega}_c)q \right\}/x^2 \quad (4.2.25)$$

and the equivalent width is linear in  $\mathcal{N}_s$  and independent of  $\Gamma$ :

$$W = [(1 - \tilde{\omega}_c)^{-1/2} \frac{1}{2}\sqrt{3}(\mu + \mu_0) + 1 - \frac{3}{2}(\mu^2 + \mu_0^2)]\mathcal{N}_s S \quad (4.2.26)$$

The dominant term is clearly the first one, except at  $\mu \approx 0 \approx \mu_0$ . For a given position ( $\mu$  and  $\mu_0$ ) on the planet this linear curve of growth is indistinguishable from the weak-line case in the reflecting-surface model, although the variation with the geometry is different. The cause of the linearity of (4.2.26) is a bit more subtle than the linearity in optically thin atmospheres. But before we discuss the physical mechanics of line formation (see Section 4.2.3), we shall examine the other weak-line case.

If the continuum absorption is very weak compared with that at the line's center,  $q \gg 1$ . Then except in the far wings (i.e., except where  $x \gtrsim \sqrt{q}$ ) the profile is

$$\begin{aligned} s_v &\approx \sqrt{3}(\mu + \mu_0)(1 - \tilde{\omega}_c)^{1/2} [1 + \sqrt{3}(\mu + \mu_0)(1 - \tilde{\omega}_c)^{1/2}] \left( 1 + \frac{x^2}{2q} - \frac{x}{\sqrt{q}} \right) \frac{\sqrt{q}}{x} \\ &\quad + [1 - 3(\mu^2 + \mu\mu_0 + \mu_0^2)](1 - \tilde{\omega}_c) \frac{q}{x^2} \end{aligned} \quad (4.2.27)$$

The dominant term varies as  $|v - v_0|^{-1}$  over most of the profile (Fig. 4.4). This situation is unique to the scattering, optically thick atmosphere. It is most clearly seen in the limit of  $\tilde{\omega}_c = 1$ , where (except for  $\mu \approx 0 \approx \mu_0$ )

$$s_v \rightarrow \sqrt{3}(\mu + \mu_0)(u^{1/2}/x) \quad (4.2.28)$$

The latter profile gives an equivalent width that diverges logarithmically. With a finite continuum absorption, however, the profile at large  $x$  varies as  $1/x^2$  and the equivalent width is finite. Nevertheless, the broad, slowly diminishing profile can cause measurements of the equivalent width to be uncertain because of uncertainty in where the line merges into the continuum.

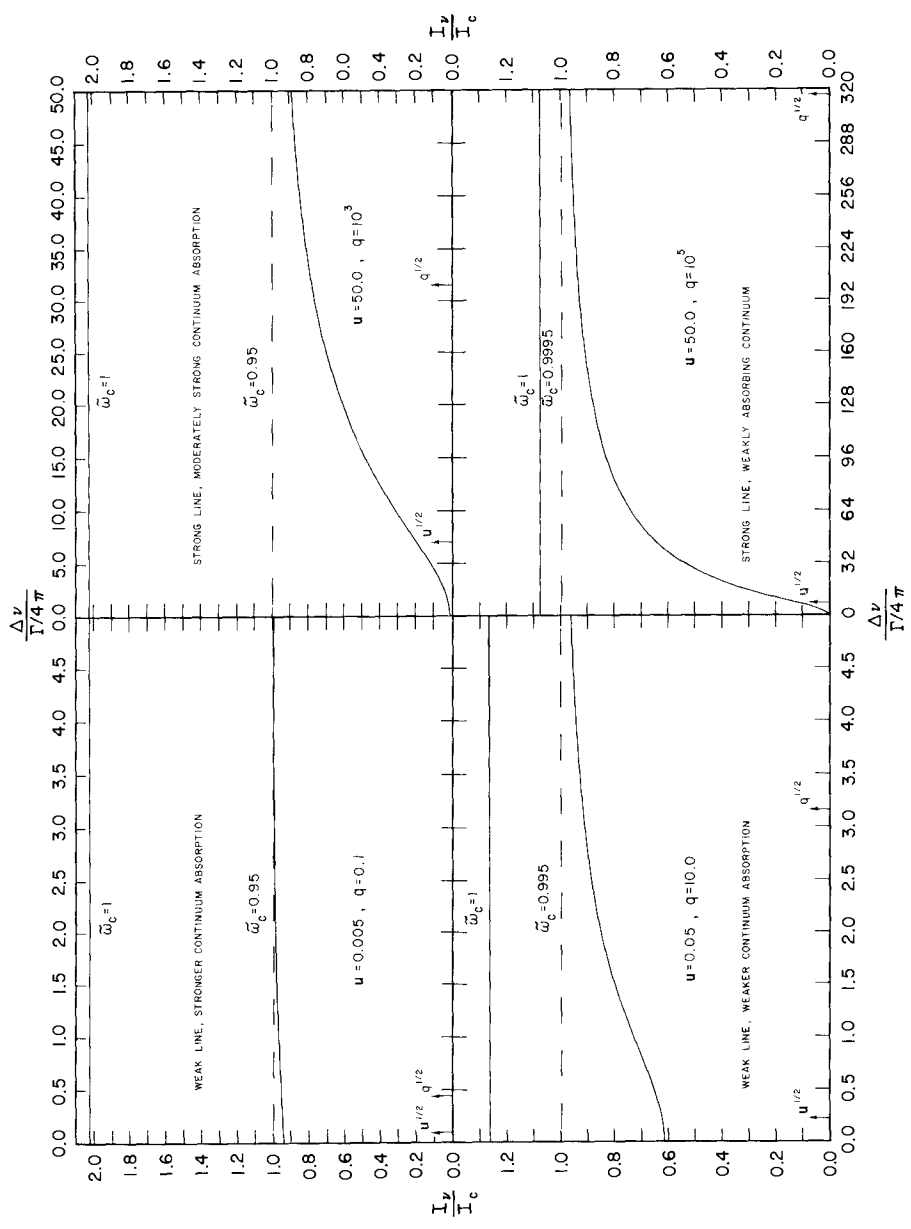
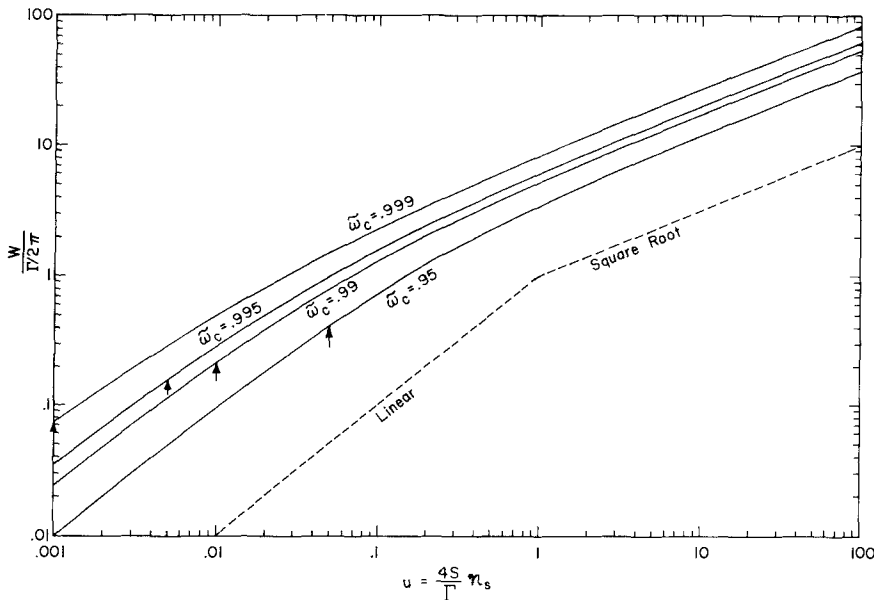


Fig. 4.4 Line profiles for different combinations of the continuum albedo  $\tilde{\omega}_c$  and line absorption parameter  $u$ . Note the distance from the line center  $\Delta\nu$  is given in dimensionless units. The profiles are for semi-infinite atmospheres with  $\mu = \mu_0 = 1$ . In each case the intensity that would be observed for a continuum albedo of unity is shown relative to the actual continuum for albedo  $\tilde{\omega}_c$ . Values of  $u^{1/2}$  and  $q^{1/2}$  are indicated by arrows on the abscissa scale. [After CHAMBERTAIN (1970).]



**Fig. 4.5** Curves of growth for semi-infinite atmospheres with  $\mu = \mu_0 = 1$ . Dashed lines are parallel to the asymptotic dependences. Arrows denote the points where  $q = 1$ , which is roughly the point where the changeover from square-root to linear dependence occurs. [After CHAMBERLAIN (1970).]

Integrating (4.2.27) yields

$$W \approx (\mu + \mu_0) \{1 + [3(1 - \tilde{\omega}_c)]^{1/2}(\mu + \mu_0)\} \ln \left( \frac{4S\mathcal{N}_s}{\Gamma(1 - \tilde{\omega}_c)} \right) \left( \frac{3}{4\pi^2} \mathcal{N}_s S \Gamma \right)^{1/2} + \mathcal{N}_s S [1 - 3(\mu^2 + \mu\mu_0 + \mu_0^2)] \quad (4.2.29)$$

Thus the curve of growth (Fig. 4.5) is in the square-root regime (except for  $\mu \approx 0 \approx \mu_0$ ), but for quite a different reason than we found for (4.2.7). There the line saturation in the core was responsible for the diminished rate of increase in the curve of growth. Here the lines are assumed to be unsaturated and the square-root law is due to the  $|v - v_0|^{-1}$  shape of the profile, which is due in turn to the diffuse scattering within the atmosphere (see discussion in the following section).

In (4.2.26) and (4.2.29) the air-mass factor is

$$\eta = \mu + \mu_0 \quad (4.2.30)$$

which gives a distinctive variation of the spectrum across the disk and with phase. For integrated observations of the whole disk at full phase,  $\langle \eta \rangle = \frac{4}{3}$  if the continuum reflection is uniform over the disk, and  $\langle \eta \rangle = \frac{3}{2}$  if the

continuum is weighted by  $\mu_0$  (which would give the continuum limb darkening of a Lambertian surface) with the center of the image showing the strongest absorption. We can get a rough idea of the phase variation from its trend near the center of the planetary image, viz., at  $\mu = \mu_0 = \cos(\Phi/2)$ , where  $\Phi$  is the *phase angle* (the angle between the sun and observer as seen from the planet). Thus with  $\langle \eta \rangle \approx \text{const} \cos(\Phi/2)$ , the absorbing spectrum is strongest at full phase ( $\Phi = 0$ ) and weakest at the crescent ( $\Phi \sim \pi$ ) (cf. Fig. 4.6).

A more accurate integration, obtained by weighting the continuum with a limb-darkening factor  $\mu_0$ , is

$$\begin{aligned}\langle \eta \rangle &= \frac{\iint (\mu + \mu_0) \mu \mu_0 \sin \theta d\theta d\phi}{\iint \mu \mu_0 \sin \theta d\theta d\phi} \\ &= \frac{3\pi}{8} \frac{(1 + \cos \Phi)^2}{(\pi - \Phi) \cos \Phi + \sin \Phi}\end{aligned}\quad (4.2.31)$$

Here  $\theta$  is co-latitude and  $\phi$  is longitude. Then  $\mu = \sin \theta \cos \phi$  and  $\mu_0 = \sin \theta \cos(\Phi - \phi)$ ;  $\phi$  is integrated between  $\Phi - \frac{1}{2}\pi$  and  $\frac{1}{2}\pi$  and  $\theta$  from 0 to  $\pi$ . It is possible to calibrate one spectrum relative to another taken at a different phase by the superimposed solar (Fraunhofer) lines. A long series of such spectra first disclosed that Venus' clouds do not reflect as a sharp deck of cumulus, but act instead like a thin haze in which unit optical thickness extends over a linear thickness the order of a scale height or more. Were the clouds more compact and dense, sunlight would traverse more of Venus' air above the cloud tops than below and the analog to  $\langle \eta \rangle \approx \text{const} \cos(\Phi/2)$  would be  $\langle \eta \rangle \approx \text{const} \sec(\Phi/2)$ , which is opposite to the observed trend.

An approximate analytic theory has been developed for strong, saturated lines, as well, but curves of growth are best calculated numerically. Once the curve of growth reaches the square-root regime, strong lines continue to vary as  $(\mathcal{N}S\Gamma)^{1/2}$ . The physical cause for this variation is, for the saturated core, the same as for the optically thin case; that is, the transition frequency  $v$  between core and wing varies as  $(\mathcal{N}S\Gamma)^{1/2}$ . In addition, the wide, intermediate region between saturated core and linear wing follows the square-root absorption because of multiple scattering. For strong lines

$$W \approx \frac{1}{2}(\mathcal{N}_s S \Gamma)^{1/2} f(\tilde{\omega}_c, \mu, \mu_0) \quad (4.2.32)$$

where  $f$  is a monotonically increasing function of  $\mu + \mu_0$  and is unity at  $\mu = 0 = \mu_0$ .

#### 4.2.3 Radiative Transfer as a Random Walk of Photons

The square-root dependence of the absorption on the amount of absorber, (4.2.29), even for weak, unsaturated lines, is a pervasive feature of radiative

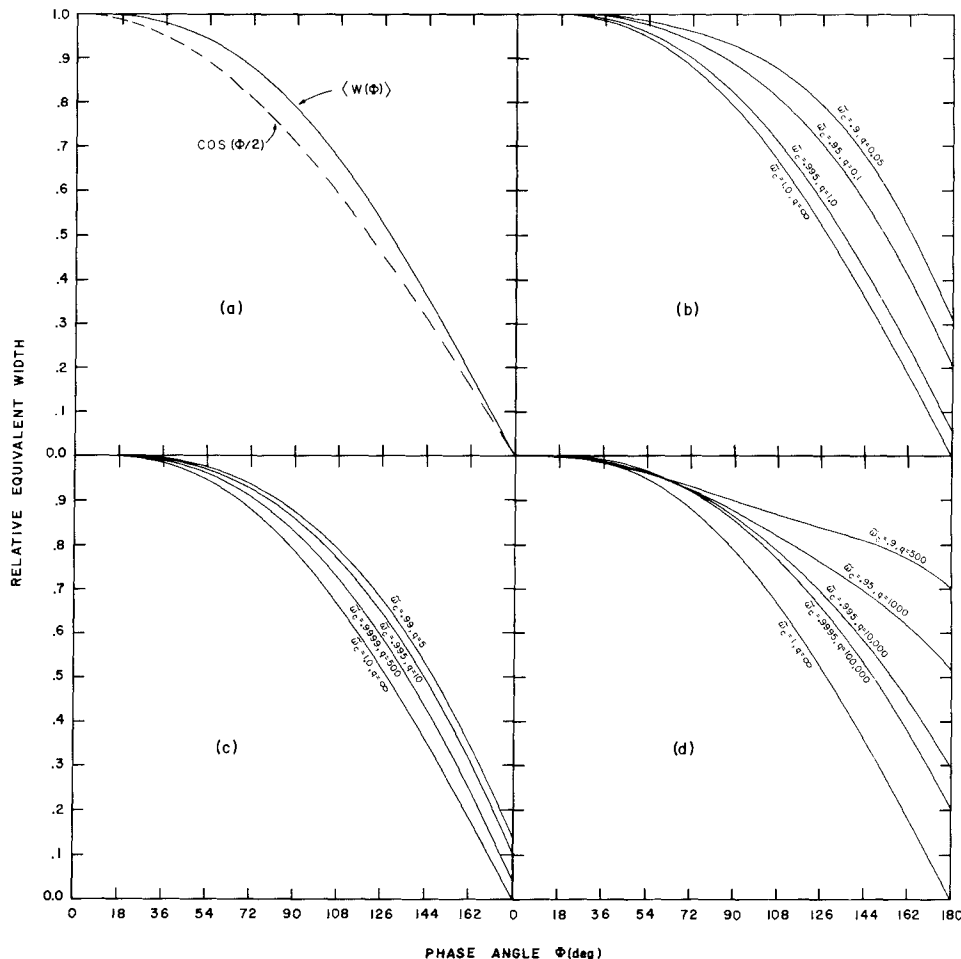


**Fig. 4.6** Phase variations of equivalent width for absorption lines in the integrated light of a planet. Angle  $0^\circ$  corresponds to full phase;  $180^\circ$  is new phase. Curves in (a) are for  $W$  varying as  $\mu + \mu_0$  and the continuum reflected according to Lambert's law. Dashed line is the rough approximation of  $\mu = \mu_0 = \cos(\Phi/2)$ ; solid line is computed with (4.2.31). Curves in (b), (c), and (d) are for isotropic scattering and apply, respectively, to very weak lines ( $u = 0.005$ ), moderately weak lines ( $u = 0.05$ ), and very strong lines ( $u = 50$ ). [After CHAMBERLAIN (1970).]

transfer problems. To see physically how this dependence arises, and why a linear absorption law emerges for the case where the continuum absorption dominates that in the line, (4.2.26), it is useful to look at the simple one-dimensional flight of a photon initially deposited at point  $s = 0$  in a medium wherein it can be scattered a distance of unit length either upward or downward every time it meets a scattering particle. By a succession of  $n$  such scatterings it eventually arrives at point  $s$  (see Fig. 4.7).

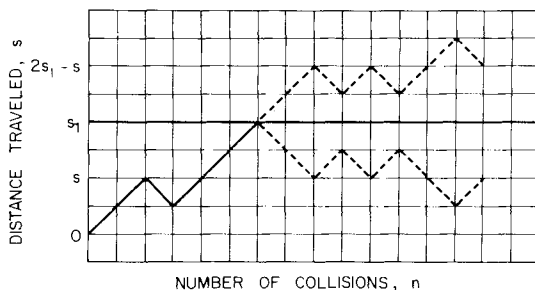


**Fig. 4.7** A particle starts a random walk at  $s = 0$ . If  $s_1$  is an absorbing screen, the particles that would otherwise reach  $s$  after  $n$  (by the lower dashed path) must be subtracted from  $p(s, n)$  to give the effect of the screen. Trajectories above and below  $s_1$  are symmetric.

Stochastic theory gives the probability for this photon arriving at point  $s$  after  $n$  scatterings as

$$\begin{aligned} P(s, n) &= \frac{n!}{\left[\frac{1}{2}(n+s)\right]! \left[\frac{1}{2}(n-s)\right]! 2^n} \\ &\approx \left(\frac{2}{\pi n}\right)^{1/2} e^{-s^2/2n} \end{aligned} \quad (4.2.33)$$

where the approximation is the asymptotic value for large  $n$  obtained by Stirling's formula.

Let us now introduce an absorbing screen at position  $s_1$ . We must now subtract all those trajectories that would otherwise intersect  $s_1$  before reaching  $s$  on the  $n$ th collision. But the unbounded scattering medium is symmetric in the trajectories on either side of  $s_1$ . Therefore, the number to be subtracted from  $P(s, n)$  is just the number that would have reached the point at  $s_1 + (s_1 - s)$  after  $n$  scatterings, since all such particles have necessarily crossed  $s_1$  on the way. Thus we have the probability for the photon at  $s$  after  $n$  scatterings with a sink at  $s_1$  to be

$$\begin{aligned} P(s, n; s_1) &= P(s, n) - P(2s_1 - s, n) \\ &= \left(\frac{2}{\pi n}\right)^{1/2} [e^{-s^2/2n} - e^{-(2s_1 - s)^2/2n}] \end{aligned} \quad (4.2.34)$$

In the atmosphere a distance  $s$  measured from the source corresponds to  $s_1 - \tau/\mu_1$ , since the mean scattering distance in the vertical direction (that is, the unit of length) is  $\mu_1 = 1/\sqrt{3}$ , and since the top of the atmosphere is at  $s_1$  from the source. The incident photons are deposited at  $\tau/\mu_0 = 1$  or  $\tau = \mu_0$ ; this depth corresponds to  $s = 0$ , so that  $s_1$  becomes  $\mu_0/\mu_1$ . Similarly, photons leaving the atmosphere have their last scattering at  $\tau = \mu$  or  $s = (\mu_0 - \mu)/\mu_1$ . The probability that a photon will arrive at the top of the atmosphere after

$n$  scatterings must be multiplied by the probability that it was not destroyed in one of those scatterings. Hence the probability of a photon emerging from the atmosphere after  $n$  scatterings is

$$P[\sqrt{3}(\mu - \mu_0), n; \sqrt{3}\mu_0] = \left( \frac{2}{\pi n} \right)^{1/2} \tilde{\omega}^n \left[ \exp\left(-\frac{3(\mu_0 - \mu)^2}{2n}\right) - \exp\left(-\frac{3(\mu_0 + \mu)^2}{2n}\right) \right] \quad (4.2.35)$$

To find the number of scatterings per incident photon we compare (4.2.35) with the value for  $\tilde{\omega} = 1$ , since in that limit all incident photons eventually re-emerge. Thus the mean number of scatterings is, for large  $n$  and  $\tilde{\omega} \sim 1$ ,

$$\begin{aligned} \langle n \rangle &\approx \frac{\int_1^\infty dn n^{-1/2} e^{n \ln \tilde{\omega}} [1 - 3(\mu_0 - \mu)^2/2n]}{\int_1^\infty dn n^{-3/2} [1 - 3(\mu_0 - \mu)^2]} \\ &\approx \frac{\sqrt{\pi} [1 + 3(\mu_0 - \mu)^2(1 - \tilde{\omega})]}{(1 - \tilde{\omega})^{1/2} [2 - (\mu_0 - \mu)^2]} \end{aligned} \quad (4.2.36)$$

When the absorption is weak, the total absorption is the mean number of scatterings times the fractional energy lost per scattering, or

$$\langle n \rangle (1 - \tilde{\omega}) = \frac{[\pi(1 - \tilde{\omega})]^{1/2}}{2 - (\mu_0 - \mu)^2} \quad (4.2.37)$$

This is an approximate mean-free-path theory for the  $\langle n \rangle$  of photons that can escape, but it does not give the correct angular distribution; it demonstrates, however, the origin of the square-root absorption law as being due to the decreasing number of scatterings with increasing  $(1 - \tilde{\omega})$ . In the case of negligible continuum absorption ( $\tilde{\omega}_c = 1$ ), the leading term of (4.2.15) varies as  $(1 - \tilde{\omega}_v)^{1/2}$ . We can define a *sink function* analogously to the source function (4.1.26) but with  $(1 - \tilde{\omega})$  replacing  $\tilde{\omega}$ . This sink function is simply the amount of absorption occurring at each depth. Figure 4.8 shows two sink functions that are nearly proportional to  $1 - \tilde{\omega}_v$  high in the atmosphere, but at great depths the amount of absorption is diminished as the absorption coefficient is increased, causing the total absorption to vary as  $(1 - \tilde{\omega})^{1/2}$ .

We can now understand why the line absorption varies as  $\mathcal{N}_s S / (1 - \tilde{\omega}_c)^{1/2}$  instead of as  $(\mathcal{N}_s S)^{1/2}$  for the case where the line absorption is much weaker than the continuum absorption, (4.2.25–4.2.26). In that case the number of scatterings as given by (4.2.36) is governed by  $(1 - \tilde{\omega}_c)^{-1/2}$ , but the line absorption is now only  $\langle n \rangle u$ , where  $u$  is given by (4.2.20). Thus the statistical wanderings of photons through the atmosphere are affected very little by the line absorption. The dominant process of radiation transfer is now the scattering as modified by the photon sink due to *continuum* absorption. The line absorption makes only a small perturbation and hence has a linear

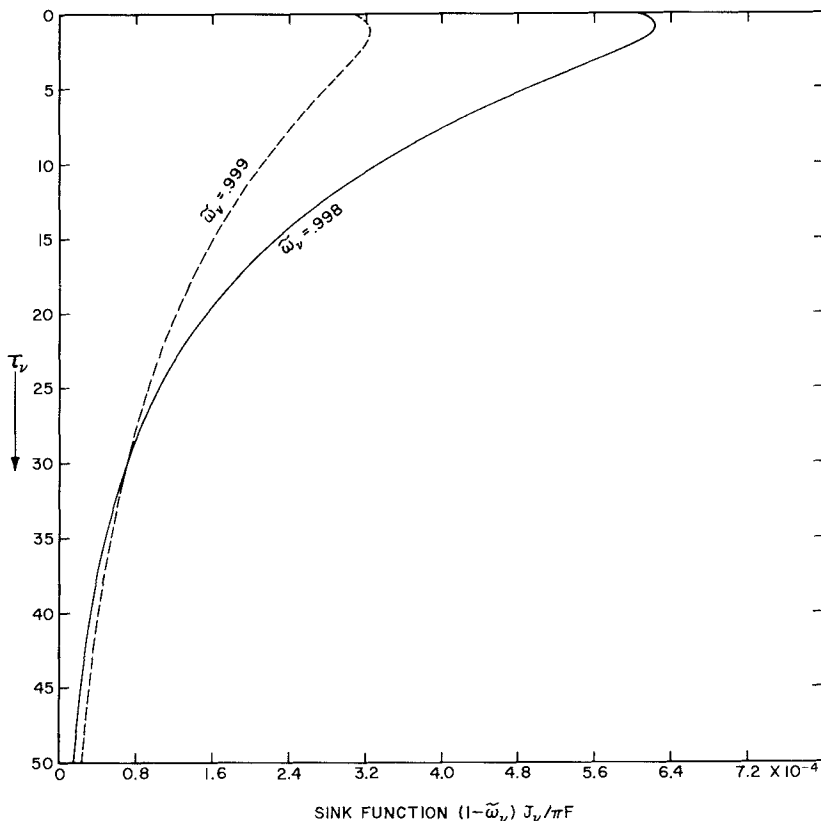


**Fig. 4.8** Comparison of two sink functions (the rate of absorption per unit optical thickness). [After CHAMBERLAIN (1970).]

effect on the number of photons escaping. This linearity is thus physically distinct from that produced by a thin atmosphere, a conclusion also emphasized by the qualitatively different air-mass dependence  $\eta$ .

#### 4.2.4 Atmospheric Spectra and Abundances of the Elements

The absorption spectra of Mars and Venus are dominated by  $\text{CO}_2$  bands. Strong bands in the far infrared totally dominate Venus' spectrum, and even the weak bands in the near infrared (see Fig. 4.9) appear clearly. The absorption occurs in a scattering atmosphere and the penetration of sunlight into the atmosphere depends on the albedo  $\tilde{\omega}_v$ . In the visual continuum  $\tilde{\omega}_c \approx 1$  and appreciable light (the order of a few percent of the solar flux above the atmosphere) reaches the surface of Venus.

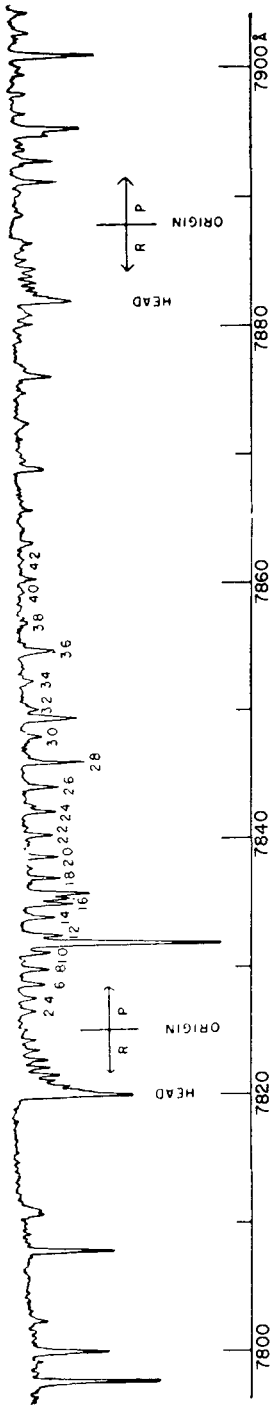


**Fig. 4.9** Vibration-rotation bands of  $\text{CO}_2$  in spectrum of Venus. The two bands have heads at 7882.8 and 7820.0 Å arising from transitions from the ground vibrational level to  $[5v_3 + (v_1, 2v_2)]$ , where the  $v_1$  and  $2v_2$  levels are in Fermi resonance (see Fig. 1.12). Only the even numbered rotational lines are present. Plate obtained by T. Dunham, Jr. with the 2.5-m (100-in.) telescope at Mt. Wilson in 1938; plate dispersion, 4.4 Å/mm.

In the centers of the absorption lines, the penetration is only to a scale height or two below the apparent cloud tops. The CO<sub>2</sub> bands appear very roughly as though they were absorbed by 10–20 km of CO<sub>2</sub> at about 0.1 atmospheric pressure. Hence it is common to see quoted in the older literature CO<sub>2</sub> abundances “above the cloud tops” of a few atm-km. In a purely scattering atmosphere such a concept is meaningless.

In recent years high-resolution *Fourier spectroscopy* with a Michelson interferometer (see Fig. 4.10) has disclosed a number of minor constituents, and entry probes have produced *in situ* measurements of abundances (see Table 4.1).

The spectrum of Mars is more straightforward to interpret, but, having a total abundance equivalent to less than 10<sup>-2</sup> atmospheres, its absorptions are very weak. For example, from the Earth H<sub>2</sub>O appears as weak satellite lines that are Doppler shifted from the telluric absorptions (Fig. 4.11). The lines of the principal constituent, CO<sub>2</sub>, are considerably stronger, even the high overtones shown in Figs. 4.12 and 4.13. For these bands, the telluric absorption is negligible. Stronger bands at 1.6 and 2.0 μm are strongly pressure-broadened in both atmospheres, and the greater pressure on Earth broadens them to a point where the telluric corrections are no longer small. These are the bands referred to in (4.2.11). The Vikings 1 and 2 carried mass spectrometers to the surface, providing additional abundance ratios (Table 4.1.).

The red and infrared spectrum of Jupiter (see Fig. 4.15) is dominated by CH<sub>4</sub> (methane) and NH<sub>3</sub> (ammonia). The bands are complex and often difficult to interpret because the molecular structure involved in the transitions is not completely understood. However, it was long apparent, from thermodynamic considerations of the relative amounts of different molecules that would exist in equilibrium at Jovian temperatures, that the main constituent must be H<sub>2</sub>. This molecule was indeed detected in high abundance by its near-infrared quadrupole lines, discussed in the next section. It also dominates the far-infrared spectrum (Section 4.4), observed from the ground, from aircraft, and from planetary probes such as the Voyagers. The best

**Fig. 4.10** The  $J = 4$  line in the *R* branch of the 1.7 μm band of HCl on Venus, showing the isotope splitting, obtained with a Michelson interferometer. The frequency scale is cm<sup>-1</sup>. From the bottom upward, the spectra are of Venus (two tracings), the sun, and the ratio Venus/sun. [After CONNES *et al.* (1969).]

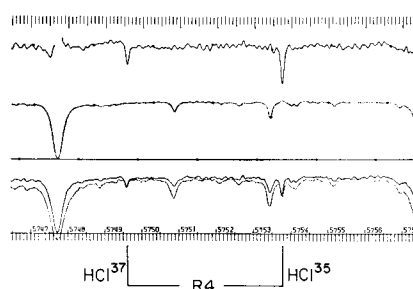


**TABLE 4.1** *Fractional Composition of Planetary Atmospheres<sup>a</sup>*

|                                      | Earth             | Venus    | Mars     | Titan   |
|--------------------------------------|-------------------|----------|----------|---------|
| Pressure (mbar)                      |                   |          |          |         |
| Surface                              | 1013              | 92,000   | 6        | 1496    |
| Cloud top                            | —                 | ~200     | —        | ~10     |
| Major Gases, %                       |                   |          |          |         |
| CO <sub>2</sub> , (CH <sub>4</sub> ) | 0.03 <sup>b</sup> | 96.5     | 95.3     | (2–10)  |
| N <sub>2</sub>                       | 78                | 3.5      | 2.7      | 65–98   |
| O <sub>2</sub>                       | 21                | <0.1 ppm | 0.13     | —       |
| H <sub>2</sub> O                     | 0.2 <sup>c</sup>  | ≤100 ppm | ≤100 ppm | —       |
| Ar                                   | 0.9               | 70 ppm   | 1.6      | 0–25?   |
| Trace Gases <sup>d</sup> (ppm)       |                   |          |          |         |
| H <sub>2</sub>                       | 0.5               | ?        | ~10      | 2000    |
| He                                   | 5                 | ~12      | —        | —       |
| CO                                   | 0.2               | 50       | 700      | ~100    |
| NO                                   | 0.0005            | —        | ~3       | —       |
| O <sub>3</sub>                       | 0.4               | —        | ~0.01    | —       |
| HCl                                  | —                 | 0.6      | —        | —       |
| HF                                   | —                 | 0.005    | —        | —       |
| Ne                                   | 18.2              | 7        | 2.5      | —       |
| Kr                                   | 1.14              | ≤1       | 0.3      | —       |
| Xe                                   | 0.087             | <0.1     | 0.08     | —       |
|                                      | Jupiter           | Saturn   | Uranus   | Neptune |
| Major gases (%)                      |                   |          |          |         |
| H <sub>2</sub>                       | 88.8              | 93.2     | ~85      | ~90     |
| He                                   | 11.1              | 6.7      | ~15      | ~10     |
| CH <sub>4</sub>                      | 0.195             | 0.1–0.2  | 0.1–1    | 0.1–1   |
| NH <sub>3</sub>                      | 0.18              | <0.1     | —        | —       |
| H <sub>2</sub> O                     | ~0.01             | —        | —        | —       |
| Trace Gases <sup>e</sup>             |                   |          |          |         |
| PH <sub>3</sub>                      | 0.6 ppm           | 1–2 ppm  | —        | —       |
| GeH <sub>4</sub>                     | 0.7 ppm           | —        | —        | —       |

<sup>a</sup> Volume mixing ratios. For Mercury see Section 1.8.5. For Io, the other Galilean satellites, and Pluto, see Section 1.9.4. See Appendix III for more details on Earth's atmosphere.

<sup>b</sup> Equivalent of about 50 bars in the crust.

<sup>c</sup> Equivalent of 270 bars in the oceans.

<sup>d</sup> Titan also has a trace (1.5 ppb) of CO<sub>2</sub> and nine organic species produced photochemically, ranging from C<sub>2</sub>H<sub>6</sub> (20 ppm) to C<sub>4</sub>H<sub>2</sub> and HC<sub>3</sub>N (a few ppb).

<sup>e</sup> Trace gases in the major planets also include C<sub>2</sub>H<sub>6</sub>, C<sub>2</sub>H<sub>2</sub>, and probably many compounds mentioned in note <sup>d</sup>.

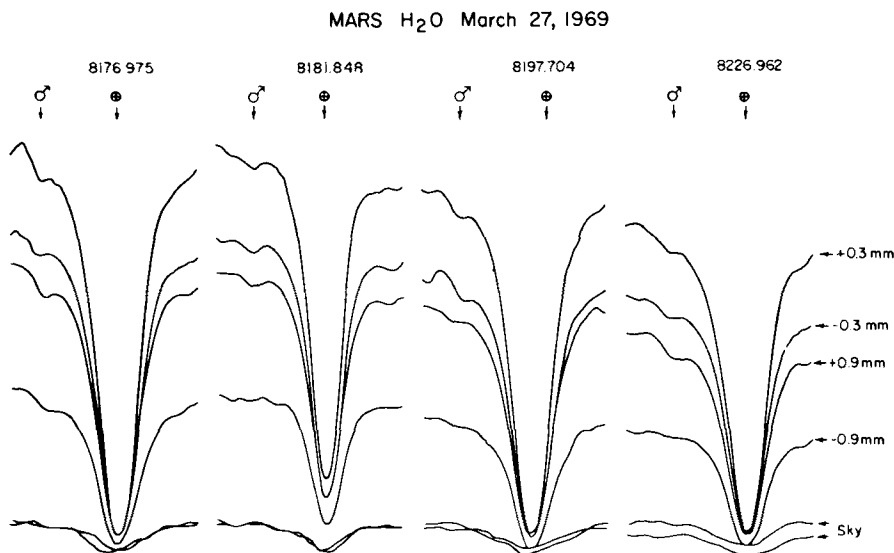


**Fig. 4.11** Water vapor in the spectrum of Mars. These tracings of four of the strongest lines in the 8200 Å band were made at different positions on the photographic plate, corresponding to different latitudes on Mars. The Martian absorption shows as a weak, Doppler-shifted indentation on the shoulder of the strong telluric absorption. Spectra obtained with the 2.7-m telescope at McDonald Observatory; dispersion, 1.9 Å/mm. [After R. G. TULL (1970) *Icarus*, 13, 43.]

remotely sensed estimates of the He/H<sub>2</sub> ratio are obtained by simultaneous analysis of these data and those from radio occultation.

With the spectrographic slit focused along Jupiter's equator, it is easy to distinguish Jovian absorptions from Fraunhofer (solar) lines. Because of its large radius and 10-hr rotation period, the Doppler shift between the east and west limbs gives a definite slant to the lines. The solar radiation, being reflected from a moving object, has twice the Doppler shift that is characteristic of the rotational speed. Hence the Fraunhofer lines have twice the tilt of the Jovian absorptions.

Interpretation of the Jovian spectrum is confounded by several factors other than the complexity of the main absorptions. The principal high clouds are formed by NH<sub>3</sub> and the atmosphere is a scattering one. The banded structure of these clouds makes the depth of penetration of sunlight highly variable from place to place. Also different wavelengths penetrate to different depths giving large differences in determinations of the [NH<sub>3</sub>]/[CH<sub>4</sub>] ratio.

The presence of He has also long been inferred, but its direct observation was made possible only by the observation from Pioneer 10 of the airglow

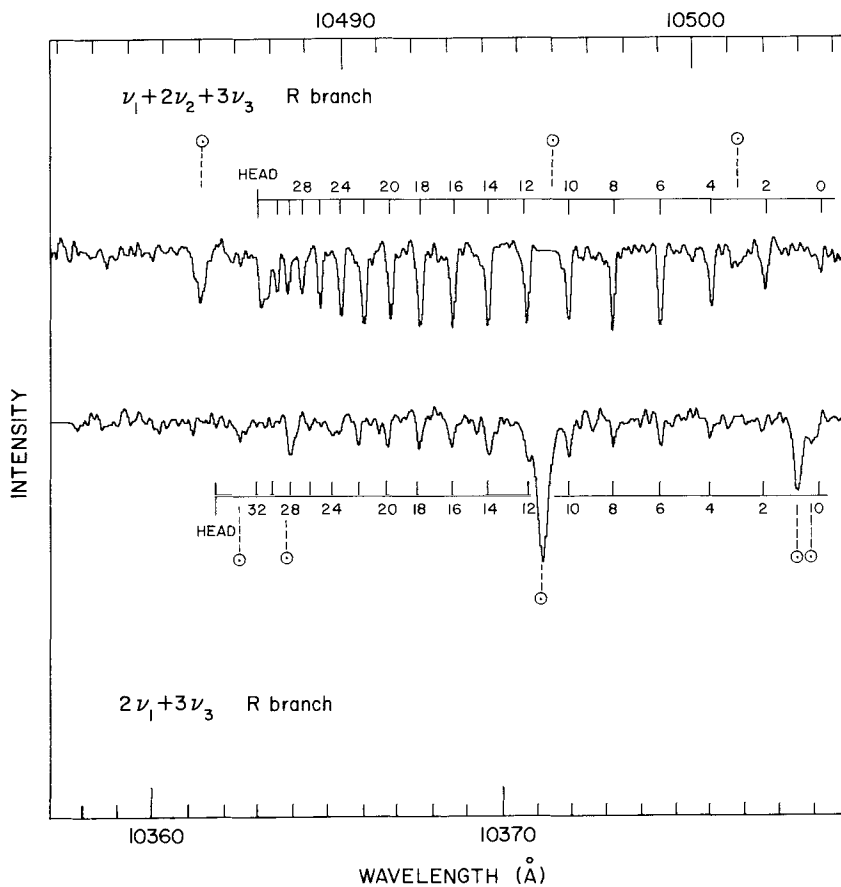


**Fig. 4.12** Two  $\text{CO}_2$  bands in the spectrum of Mars. Solar lines (one of which has been eliminated) are flagged. [After BELTON *et al.* (1968).]

scattering in the resonance transition at  $584 \text{ \AA}$  (see discussion in Section 6.3.1). This broadband measurement was greatly refined by the ultraviolet spectrometers on the Voyagers.

Emphasis so far has been on the analysis of light scattered from a surface or atmosphere. Transmission measurements are also possible in special circumstances when a rocket or spacecraft observes the Sun or a star through an atmosphere at the limb. Although properly called eclipses, such experiments are usually referred to as optical occultations. The wavelength region is usually the ultraviolet, in some cases to wavelengths as short as  $55 \text{ nm}$  which are available only from the Sun because light from stars below  $91 \text{ nm}$  is absorbed by interstellar hydrogen. This range is particularly interesting

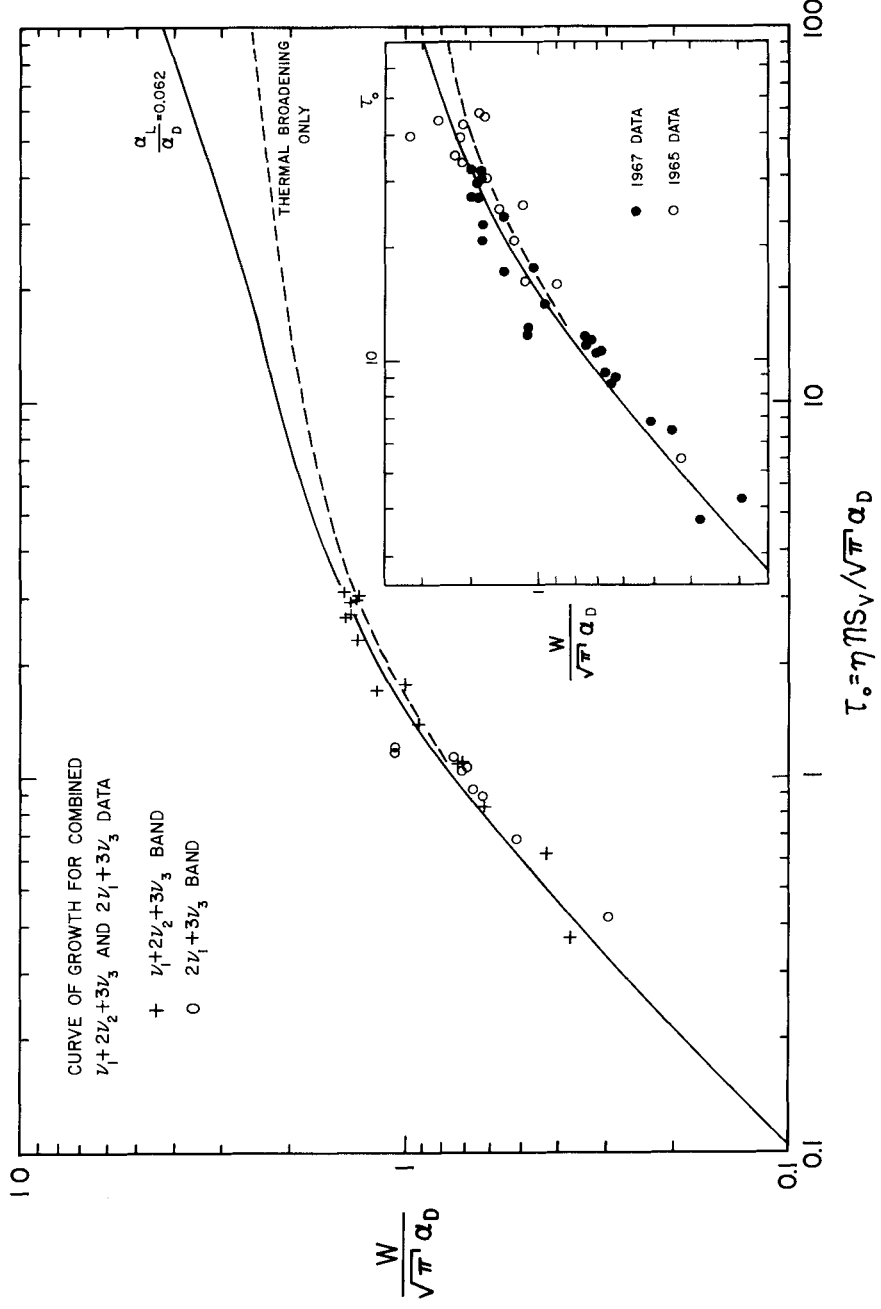


Fig. 4.13 Curves of growth for the lines of Fig. 4.12. The inset includes lines observed with a larger air mass. [After BELTON *et al.* (1968).]

because all gases are strong absorbers in their ionizing continua; it has been used to set very tight upper limits for Mercury and Ganymede. Voyager experiments have been successful at Jupiter, Saturn, and Titan. For the two planets the principal absorbers are H, H<sub>2</sub>, and CH<sub>4</sub>. The H<sub>2</sub> absorption is by the Lyman bands between 91 and 111 nm, which are composed of a small number of widely spaced lines. A very long path length is required to give observable absorption at the low spectral resolution that was available. The other two gases have continua that are much easier to deal with.

At Titan the principal absorbers were N<sub>2</sub> in its ionization continuum below 90 nm, CH<sub>4</sub> up to 140 nm, and acetylene, C<sub>2</sub>H<sub>2</sub>, with banded absorption between 100 and 150 nm.

The only other application of the method (before the Voyager encounter with Uranus in 1986) has been to the Earth, where the principal targets have been O<sub>2</sub> and O<sub>3</sub>. Many more molecules have been observed in the infrared, both from the surface and from high-altitude platforms, with the Sun well above the horizon and occasionally at zenith angles slightly greater than 90°.

#### 4.2.5 Laboratory Data on Molecular Absorption

Interpretation of a planetary spectrum requires several kinds of laboratory data. The wavelengths of the absorption identify the molecule. Information on the quantum levels (particularly their energies and statistical weights) is needed for analysis of rotational temperatures according to (4.2.13) and (4.2.14), where the energies are represented by  $hcBJ(J + 1)$ . The band strength  $S$  of Eq. (4.2.2) and the Lorentz broadening parameters  $\Gamma/4\pi = \alpha_L$  of Eq. (4.2.3) must be measured for each band and sometimes for each individual line in a band. It has often been the case (and still is) that planetary data, once obtained, cannot be analyzed until much later, when the relevant laboratory measurements have been made.

It would take far too much space to present a critical review of the data for all molecules of planetary interest. This brief summary must be supplemented by additional material, some of which is discussed in the Notes to this chapter.

Molecular energy states fall into three classes which generally occupy very different regions of the spectrum. Most rotational levels are spaced by a few cm<sup>-1</sup>, and the absorptions are therefore in the millimeter region, which makes this region very important in radio astronomy. Hydrides, and especially H<sub>2</sub>, absorb at much higher frequencies (inversely proportional to the moment of inertia) than most other molecules. For example, H<sub>2</sub> lines at 354 and 587 cm<sup>-1</sup> (28.2 and 17.0 μm) are important in the physics of the Jovian planets.

Vibrational levels have a typical spacing of 600–1500 cm<sup>-1</sup> and thus wavelengths of 17–7 μm for molecules typically found in atmospheres. Rotational sublevels are superposed on them; it is the multitude of closely spaced wavelengths from all these levels that gives the banded appearance of a vibrational-rotational transition. Polyatomic molecules have several normal modes of vibration, and the same number of *fundamentals*; however, some of the transitions may not appear in the infrared spectrum because of selection rules. The three normal modes of CO<sub>2</sub> are illustrated in Fig. 4.12. Near multiples of the fundamentals exist, giving *overtones* in the spectrum, and *combinations* correspond to the simultaneous change of more than one vibrational quantum number. For some important molecules, notably H<sub>2</sub>O and CH<sub>4</sub>, such bands extend all the way into the visible; near-infrared bands of CO<sub>2</sub> and H<sub>2</sub>O are shown in Figs. 4.9, 4.11, and 4.12. Electronic levels are of similar nature to the familiar levels of atoms, but each one has vibrational and rotational fine structure so that a single electronic transition corresponds to a band system spread over a considerable range of wavelengths. Some band systems have a corresponding continuum, usually in the ultraviolet, which can be regarded as a state of vibration so intense that an atom flies away from the molecule. The dissociation continua discussed in Chapters 1 and 6 are of this nature.

Absorptions by molecules of atmospheric interest are summarized in Table 4.2.

TABLE 4.2 Selected Molecular Bands

| Gas              | Wavelengths <sup>a</sup> , (μm)   | Where found <sup>b</sup> |
|------------------|---|--------------------------|
| CO <sub>2</sub>  | VR, ν <sub>2</sub> , 15; ν <sub>3</sub> , 4.3; to 0.78  | V, E, M                  |
| H <sub>2</sub> O | VR, ν <sub>1</sub> , 2.73; ν <sub>2</sub> , 6.3; ν <sub>3</sub> , 2.66; to 0.6<br>R, 10–1000; C, 8–12 | V, E, M, J               |
| N <sub>2</sub> O | VR, ν <sub>1</sub> , 7.8; ν <sub>2</sub> , 17; ν <sub>3</sub> , 4.5; to 2.11                          | E                        |
| O <sub>3</sub>   | VR, ν <sub>3</sub> , 9.6; E, 0.3–0.34<br>C, 0.2–0.3; 0.5–0.7  | E, M                     |
| SO <sub>2</sub>  | VR, ν <sub>1</sub> , 8.7; ν <sub>2</sub> , 19.3; ν <sub>3</sub> , 7.35<br>E, 0.2–0.32                 | V, I                     |
| CH <sub>4</sub>  | VR, ν <sub>3</sub> , 3.3; ν <sub>4</sub> , 7.66; to 0.49  | E, J, S, U, N, P, T      |
| NH <sub>3</sub>  | Inversion, 13 mm; R, 40–503<br>VR, ν <sub>2</sub> , 8–12; 0.65, 0.76                                  | E, J                     |
| H <sub>2</sub>   | Rotation 28, 17;<br>VR (1, 0)–(4–0) 2.4, 1.2, 0.82, 0.62  | J, S, U, N, T            |
| O <sub>2</sub>   | Atmospheric, 0.76; IR atmospheric, 1.27;<br>Sohumann–Runge, 0.175–0.2                                 | E, M                     |

<sup>a</sup> R, rotation; VR, vibration-rotation; E, electronic; C, continuum.

<sup>b</sup> V, Venus; E, Earth; M, Mars; J, Jupiter; S, Saturn; U, Uranus; N, Neptune; P, Pluto; I, Io; T, Titan;

In molecules that lack a dipole moment, notably *homonuclear molecules* such as N<sub>2</sub>, O<sub>2</sub>, and H<sub>2</sub>, rotational and vibrational transitions are forbidden. Even isotopic variants such as <sup>14</sup>N<sup>15</sup>N absorb only weakly. The symmetric molecules do have a quadrupole moment, and the quadrupole transitions of H<sub>2</sub> are measurable in the Jovian planets. This molecule also has a strong *pressure-induced absorption (enforced dipole transitions)* caused by destruction of the symmetry during collisions. Because these collisions are extremely brief, the absorptions are correspondingly broad, in accordance with the uncertainty principle. (They can be seen in Fig. 4.22 extending from 300 to 800 cm<sup>-1</sup>.) The quadrupole lines, on the other hand, exhibit the curious phenomenon of *collisional narrowing*, which greatly complicates the computation of their curves of growth; it is even worse for a scattering atmosphere.

Ordinary *pressure broadening* occurs (classically) because the phase of a passing wave train is suddenly altered; a Fourier analysis transforms the altered wave trains into a broadened frequency distribution. However, in certain cases this effect occurs only infrequently. In addition for molecules that are not isolated, the ability to absorb at a certain Doppler displacement depends not only on the molecule having the proper translational velocity, but on its capability to change its translational energy so as to conserve energy and momentum with the photon. For a molecule with a mean free path the order of the wavelength or smaller, this factor (it turns out, from a quantum treatment) increases the likelihood of absorbing a photon near the line center.

The prominent bands of methane that occur in the visible and up to about 1.0 μm (see Figs. 4.14 and 4.15) are inherently diffuse; that is, the absorption in small spectral regions within them obeys a simple exponential law. Attempts to assign them to individual overtones and combinations show that the number of possible assignments can be in the thousands, each with a large number of individual lines. It is therefore plausible that they contain so many individual lines that they overlap completely, even at very low pressure, and absorb as a slowly varying continuum. These bands therefore give an unambiguous measure of the methane abundance, with no need to know the pressure. The bands further into the infrared appear to behave more conventionally.

Ammonia has an important band at even lower frequencies than its rotation spectrum. It is called the *inversion band*, because classically it corresponds to an oscillation of the N atom through the plane defined by the three H atoms. Centered at a wavelength of 13 mm, it is collisionally broadened at pressures of several bars to cover the whole microwave region, and gives the dominant opacity for this region in most of the Jovian planets (see Fig. 4.24). Conversely, flux measurements give important information on both the ammonia abundance and the deep temperature structure.

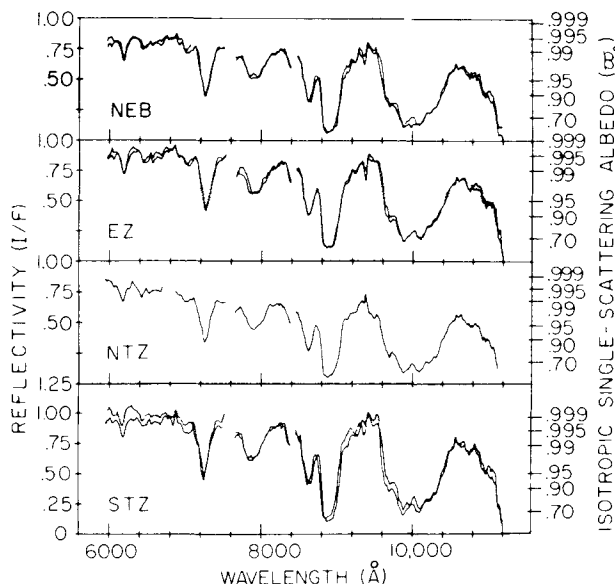


**Fig. 4.14** The reflectivities of four areas of Jupiter, showing the broad methane bands. [After PILCHER *et al.* (1973).]

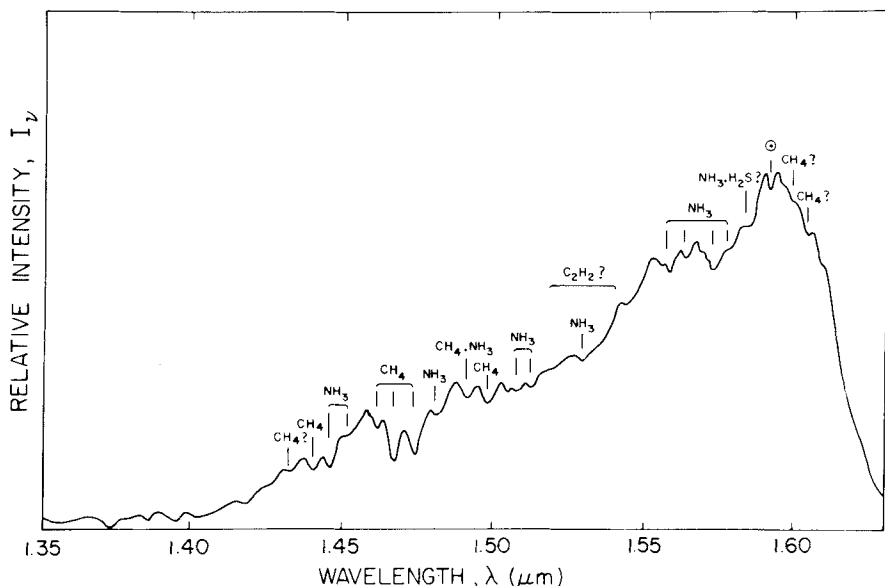


**Fig. 4.15** Infrared spectrum of Jupiter, 1.35–1.63  $\mu\text{m}$ . [Adapted from D. P. CRUIKSHANK and A. B. BINDER (1969), Comm. Lunar Planetary Lab. No. 103, Univ. Arizona, Tucson.]

Electronic transitions are seen in atmospheres principally in emission, as airglow or aurora, except for their dissociation continua. One notable absorption does occur in O<sub>2</sub>, the Atmospheric band system in the red, which is a quadrupole transition. Very strong in the Earth's atmosphere, it has been detected in the spectrum of Mars at times of large Doppler shift, and has set a very tight upper limit for oxygen on Venus. Energy level diagrams for O<sub>2</sub> are given in Figs. 1.9 and 6.4.

### 4.3 Photometry and Polarimetry

#### 4.3.1 Determination of the Scattering Function from Spectral Variations

The variation of a planetary spectrum with the planet's phase (see Fig. 4.6) will depend (for an optically thick atmosphere) on the nature of the scattering phase function  $p(\cos \Theta)$ . One could in principle solve the transfer equation for various functions  $p(\cos \Theta)$ , fit the results with observations across the disk or at different phases, and so deduce the correct  $p$ . In practice this has not been a fruitful endeavor. Among the various parameters entering the spectroscopic theory, there are compensating trade-offs so that isotropic scattering can be forced to fit most of a given set of observations by adjusting unknowns. The *similarity relations* (Section 4.1.4) give, for example, the line albedo  $\tilde{\omega}'$  and total thickness  $\tau_0'$  of an isotropically scattering atmosphere that will mimic the reflected intensity from an atmosphere scattering anisotropically and with a different albedo  $\tilde{\omega}_v$  and thickness  $\tau_0$ . There is also the possibility that the vertical mixing of aerosols and gas is inhomogeneous, which complicates interpretation.

In any case there are more sensitive methods for deriving the scattering phase function. Of some use is the photometry of the planet at different scattering angles and in different colors. More powerful is the method of polarimetry.

Once having a scattering function the number of adjustable parameters in the theory is helpfully narrowed but still not necessarily uniquely fixed because observations inherently are not as homogeneous as one could wish. The theoretical spectra may be obtained through large computing programs with accurate Mie-scattering phase functions, but for most purposes it is sufficient to use simplified functions  $p(\cos \Theta)$  that can be solved more readily but which contain the essential features of the Mie scattering.

#### 4.3.2 Scattering by Particles (Mie Scattering)

In discussions of scattering, either of two angles may be used. Phase functions are usually expressed in terms of a scattering angle  $\Theta$ , which is the

deviation of a scattered ray relative to the direction of an unscattered ray (cf. Fig. 6.6). On the other hand, the phase angle  $\Phi$  is the angle at the scattering center between the direction of the source of the incident ray and the direction of its emergence. At full phase the phase angle is  $\Phi = 0$ ; in general  $\Phi = \pi - \Theta$ .

The scattering diagram for a particular particle depends on its size, shape, and orientation, the wavelength of light, and on the real and imaginary parts of the index of refraction. However, for particles that are large compared with the wavelength, we can make a simplification by calculating the scattering diagram with ray optics. This is not to imply that the answer will be entirely correct, since interference between various emerging rays still must be considered.

Figure 4.16 shows the different components of light scattered by a sphere. The  $l = 0$  ray is diffraction, which is concentrated in the forward direction and is unpolarized (for natural incident light). The intensity and polarization of light reflected and refracted may be computed separately for components of the intensity perpendicular and parallel to the plane of scattering from the well-known *Fresnel reflection coefficients*. The external reflection ( $l = 1$ ) amounts to only a few percent for an index of refraction  $n \lesssim 1.5$ , but it is highly polarized. The most important internal rays are those refracted twice with no internal reflections ( $l = 2$ ). These rays account for the strong forward scattering that is prevalent in *Mie scattering* (scattering by spherical drops) when the size parameter,

$$x \equiv 2\pi r/\lambda \quad (4.3.1)$$

is large. The light that is internally reflected once ( $l = 3$ ) or twice ( $l = 4$ ) accounts for only a small fraction of the scattered intensity but for spheres

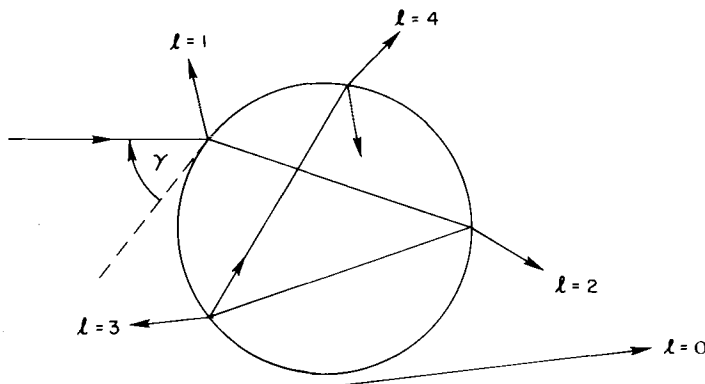


**Fig. 4.16** Paths of light rays scattered by a sphere according to geometrical optics. [Adapted from HANSEN and TRAVIS (1974).]

the resulting concentration of the light into a small angle gives rise to the primary and secondary rainbows.

Rainbows in general arise from a concentration of internally reflected rays at a maximum or minimum angle of deviation. Thus for  $n = \frac{4}{3}$  (appropriate for water) as the angle  $\gamma$  in Fig. 4.16 varies from normal ( $\gamma = 90^\circ$ ) to grazing incidence, the  $l = 3$  ray decreases from a scattering angle  $\Theta = 180^\circ$  (back-scattering) to  $137^\circ$ , the angle of minimum deviation, and then increases. The concentration of scattering around  $\Theta = 137^\circ$  is the primary rainbow. Spherical scatterers tend to focus reflected rays at  $\Theta \sim 180^\circ$ . This phenomenon is the *glory*, which is often seen from aircraft flying over sunlit clouds and appears as a brightening of the clouds near the edge of the aircraft shadow. Occasionally colored rings are visible.

Precise values for the phase function and polarization generally require the use of Mie computations. However, a number of features, such as the rainbow, that do not involve interference phenomena are adequately represented by geometrical optics. This is especially true when the particles are substantially larger than the wavelength of light and also when the dispersion in particle sizes is sufficiently large to wash out the interference effects. Figure 4.17 shows an example of calculations with Mie theory compared with geometrical optics.

### 4.3.3 Photometry of Planets

The scattering phase functions in common use because of their elementary nature are (a) isotropic,  $p(\cos \Theta) = \tilde{\omega}$ ; (b) the Rayleigh phase function,

$$p(\cos \Theta) = \frac{3}{4}(1 + \cos^2 \Theta) \quad (4.3.2)$$

which takes no account of the polarization produced by the scattering; (c) Rayleigh scattering,

$$p_l(\cos \Theta) = \frac{3}{4} \cos^2 \Theta, \quad p_r(\cos \Theta) = \frac{3}{4} \quad (4.3.3)$$

which treats the electric vectors in the plane of scattering ( $E_l$ ) and perpendicular to it ( $E_r$ ) separately, since the scattered light is polarized; and (d) the first-order anisotropic phase function,

$$p(\cos \Theta) = \tilde{\omega}(1 + a \cos \Theta), \quad -1 < a < 1 \quad (4.3.4)$$

From solutions of the transfer equation, one can compute for any of these functions the total flux reflected by the planet toward the Earth as a function of planetary phase  $\Phi$ . Integrating the reflected intensity over co-latitude  $\theta$  and longitude  $\phi$  (both coordinates referred to the Earth–planet–sun plane

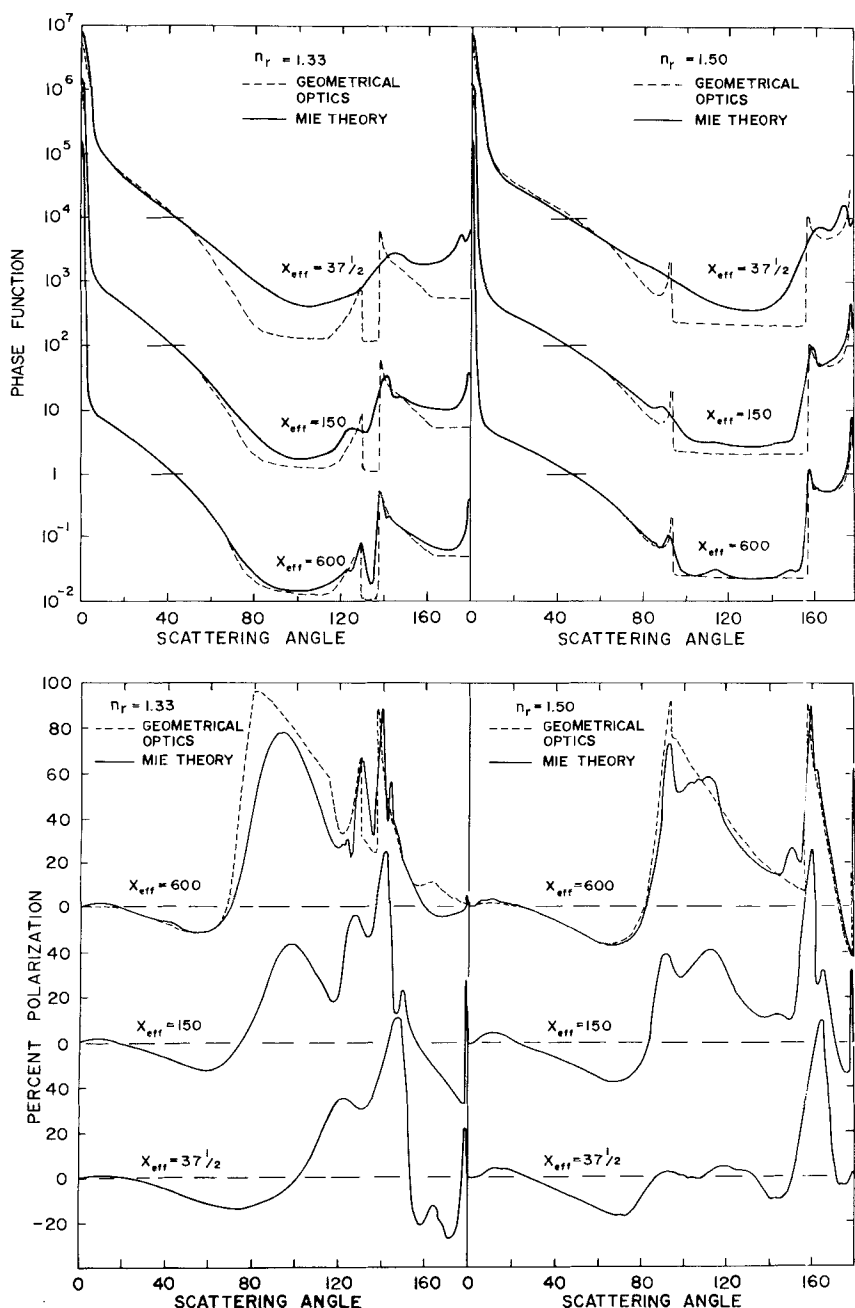


**Fig. 4.17** Comparison of geometrical optics with Mie theory. The phase functions (upper figure) and polarization (lower) are computed for single scattering by spheres with a distribution of sizes given by  $N(x) = x^6 \exp(-9x/x_{\text{eff}})$ , and real indices of refraction  $n_r$ . For the phase function the scale applies to the curves with  $x_{\text{eff}} = 600$ ; the other curves are successively displaced upward by factors of  $10^2$ . [After HANSEN and TRAVIS (1974).]

rather than to a rotational axis), we have the flux referred to unit planetary radius,

$$j(\Phi) = \int_{\Phi-\pi/2}^{\pi/2} d\phi \int_0^\pi d\theta \sin \theta \mu I(\mu, \psi; \mu_0) \quad (4.3.5)$$

where  $\mu = \sin \theta \cos \phi$  is the factor projecting the spherical area onto the disk and  $\psi$  is the local azimuthal angle that enters for anisotropic scattering.

Knowing  $j(\Phi)$  we can integrate it over a sphere to find the total radiant flux to all space. The ratio of the total reflected flux in all directions to the incident solar flux received by a sphere of unit radius is the *Bond albedo*:

$$\begin{aligned} \Lambda_B &\equiv \frac{2\pi \int_0^\pi j(\Phi) \sin \Phi d\Phi}{\pi \mathcal{F} \int_0^{2\pi} \int_0^1 \mu_0 d\mu_0 d\psi_0} \\ &= \left[ \frac{j(0)}{\pi \mathcal{F}} \right] \left[ 2 \int_0^\pi \frac{j(\Phi)}{j(0)} \sin \Phi d\Phi \right] \\ &= \lambda(0)q \end{aligned} \quad (4.3.6)$$

where  $\lambda(0)$  and  $q$  represent the two expressions in square brackets, respectively.

The factor  $\lambda(0)$  is the *geometric albedo*; for a highly reflecting atmosphere  $\lambda(0)$  is in the range 0.65–0.80, depending on the phase function  $p(\cos \Theta)$  (see Problem 4.10).

The *phase integral*  $q$  can be obtained theoretically from (4.3.5). However, ground-based measurement of the phase variation  $j(\Phi)$  is difficult, and for the outer planets is limited to rather small angles. Thus spacecraft measurements are necessary to obtain reliable values of  $j(\Phi)$ , and, in turn, the Bond albedo, which is necessary for estimating the thermal balance of a planet (see Section 1.2).

Center-to-limb photometry is also capable in principle of yielding the scattering phase function, which is of value as an indicator of the size of scattering particles as well as necessary to derive  $\Lambda_B$ . The difficulty in practice is that the information from near the limb of the planet is hard to obtain with precision, and the data do not therefore give enough information to discriminate among a variety of possible forms of  $p(\cos \Theta)$ .

The thermal infrared emission of Jupiter has been investigated from the ground (mainly in the 2.8–13  $\mu\text{m}$  wavelength region), from high-altitude aircraft (20–500  $\mu\text{m}$ ), and from Pioneers 10 and 11 (20 and 45  $\mu\text{m}$ ). The effective radiating temperature of the planet is  $T_e = 134^\circ\text{K}$  according to Earth-based data and  $125^\circ\text{K}$  according to the Pioneer measurements. Both values are significantly higher than can be accounted for by absorption and reradiation of sunlight. The planet emits about twice the energy it absorbs and the conclusion must be that Jupiter generates this energy from its interior by gravitational contraction, much as does a newly forming star.

#### 4.3.4 Polarimetry of Venus

Because the electric (and magnetic) vibrations of light can have preferred directions, radiation toward a given direction is not a simple scalar with magnitude  $I$ . In general, a radiation field is the sum of an unpolarized and an elliptically polarized component. Elliptical polarization has a phase relationship between the electrical oscillations along the major and minor axes of the ellipse. Four quantities are required to define the field. They are the intensities ( $I_l, I_r$ ) polarized in specified directions (cf. Fig. 4.18), the position  $\chi$  of the plane of polarization (the major axis of the ellipse), and the phase lag  $\delta$  between the electrical oscillations  $E_l(t)$  and  $E_r(t)$ . (When the major and minor axes of the polarization ellipse are not along the reference axes  $l$  and  $r$ , this phase difference will not generally be  $\pi/2$ .)

In place of two intensities ( $I_l, I_r$ ) we could use total intensity ( $I = I_l + I_r$ ) and the difference  $Q \equiv I_l - I_r$  or the polarization  $P = Q/I$ . There are major conveniences in handling multiple scattering of polarized light if the angles ( $\chi, \delta$ ) are also replaced by quantities having intensity units. Thus we shall develop the four *Stokes parameters*:

$$\begin{aligned} I &= I_l + I_r \\ Q &= I_l - I_r \\ U &= Q \tan 2\chi \\ V &= E_l^{(0)} E_r^{(0)} \sin \delta \end{aligned} \quad (4.3.7)$$

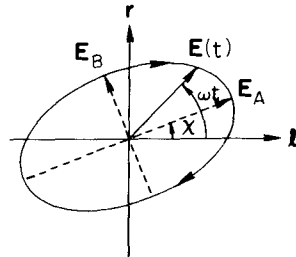
for amplitudes  $E^{(0)}$ . Defining ellipticity as

$$\tan \beta = E_B^{(0)} / E_A^{(0)} \quad (4.3.8)$$

we shall find that the plane of polarization  $\chi$ , phase lag  $\delta$ , and ellipticity angle  $\beta$  are all related. This interrelationship makes it possible to work with  $\beta$  in (4.3.7) in lieu of  $\delta$ . If we express the plane of polarization by

$$\begin{aligned} E_A(t) &= E^{(0)} \cos \beta \sin \omega t \\ E_B(t) &= E^{(0)} \sin \beta \cos \omega t \end{aligned} \quad (4.3.9)$$

**Fig. 4.18** The polarization ellipse in the plane perpendicular to wave propagation. The axes  $l$  and  $r$  are fixed. The angle  $\chi$  gives the direction of maximum linear polarization. The vector  $\mathbf{E}(t)$  is the resultant of the electric oscillations along the major and minor axes. The arrows on the ellipse give the convention for right-hand polarization when the wave propagation is into the paper.



we can obtain amplitudes in the longitudinal and perpendicular coordinate system in the form

$$\begin{aligned} E_l &= E_A \cos \chi + E_B \sin \chi \\ E_r &= E_A \sin \chi - E_B \cos \chi \end{aligned} \quad (4.3.10)$$

Substituting (4.3.9) and averaging over an oscillation yields

$$\begin{aligned} I_l &\equiv \langle E_l^2 \rangle = \frac{1}{2} E^{(0)2} (\cos^2 \beta \cos^2 \chi + \sin^2 \beta \sin^2 \chi) \\ I_r &\equiv \langle E_r^2 \rangle = \frac{1}{2} E^{(0)2} (\cos^2 \beta \sin^2 \chi + \sin^2 \beta \cos^2 \chi) \end{aligned} \quad (4.3.11)$$

With  $I = \frac{1}{2} E^{(0)2}$ , we readily verify the first Stokes parameter (4.3.7). The second takes the form

$$Q \equiv I_l - I_r = I \cos 2\chi \cos 2\beta \quad (4.3.12)$$

If on the  $l$  and  $r$  axes the phases of oscillation are correlated, we may write those oscillations as

$$\begin{aligned} E_l(t) &= E_l^{(0)} \sin(\omega t - \varepsilon_l) \\ E_r(t) &= E_r^{(0)} \sin(\omega t - \varepsilon_r) \end{aligned} \quad (4.3.13)$$

where  $\delta = \varepsilon_r - \varepsilon_l$ . One may show (Problem 4.11) that this representation is consistent with (4.3.10) if

$$\begin{aligned} \tan \varepsilon_l &= -\tan \beta \tan \chi \\ \tan \varepsilon_r &= \tan \beta \operatorname{ctn} \chi \end{aligned} \quad (4.3.14)$$

and

$$E_l^{(0)} E_r^{(0)} \cos \delta = \frac{1}{2} E^{(0)2} \sin 2\chi \cos 2\beta \quad (4.3.15)$$

Thus from (4.3.12) the third Stokes parameter is

$$\begin{aligned} U &\equiv Q \tan 2\chi = I \sin 2\chi \cos 2\beta \\ &= E_l^{(0)} E_r^{(0)} \cos \delta \end{aligned} \quad (4.3.16)$$

and the fourth is

$$\begin{aligned} V &\equiv E_l^{(0)} E_r^{(0)} \sin \delta = I \sin 2\beta \\ &= Q \tan 2\beta \sec 2\chi \end{aligned} \quad (4.3.17)$$

Conversely, in terms of the four parameters  $I$ ,  $Q$ ,  $U$ , and  $V$ , we may obtain the plane of polarization from

$$\tan 2\chi = U/Q \quad (4.3.18)$$

the polarization from

$$P = Q/I \quad (4.3.19)$$

the ellipticity from

$$\sin 2\beta = \frac{V}{(Q^2 + U^2 + V^2)^{1/2}} \quad (4.3.20)$$

and the phase lag from

$$\tan \delta = \tan 2\beta \sec 2\chi \quad (4.3.21)$$

The polarization of a planet for scattered sunlight can thus be treated as we would treat scattering of the intensity without polarization, except that all four intensity components of the “vector intensity,”

$$\begin{aligned} \mathbf{I} &= (I, Q, U, V) \\ &= (I_l, I_r, U, V) \end{aligned} \quad (4.3.22)$$

must be treated separately. For example, the scattering through angle  $\Theta$  for Rayleigh scattering is given by

$$\left( \frac{d\omega'}{4\pi} \sigma \right) \mathbf{R} \mathbf{I} d\omega \quad (4.3.23)$$

where the scattering matrix is

$$\mathbf{R} = \frac{3}{2} \begin{pmatrix} \cos^2 \Theta & 0 & 0 & 0 \\ 0 & 1 & 0 & 0 \\ 0 & 0 & \cos \Theta & 0 \\ 0 & 0 & 0 & \cos \Theta \end{pmatrix} \quad (4.3.24)$$

This matrix replaces the partial phase functions of (4.3.3). For incident natural light,  $I_{||} = I_{\perp} = \frac{1}{2}I$  and  $U = V = 0$ , and the matrix reduces to the simpler case. But for multiple scattering the complete matrix is necessary to follow the polarization vector.

Venus provides a particularly illuminating example of the information contained in polarized light and the numerical difficulty in retrieving this information. Until the 1920s it was debatable whether sunlight reflected by Venus was in fact polarized. However, when B. Lyot developed a precision polarimeter capable of accuracies of about 0.1 percent, it was revealed that Venus has well-defined polarization features as a function of phase angle. Moreover, the fortuitous location of Venus as an interior planet provides a nearly complete phase angle coverage as viewed from Earth. But it was not until recently that sufficiently large computers became available to perform the Mie-scattering computations to adequately model the polarization by the Venus cloud particles. The results (see Fig. 4.19) showed conclusively

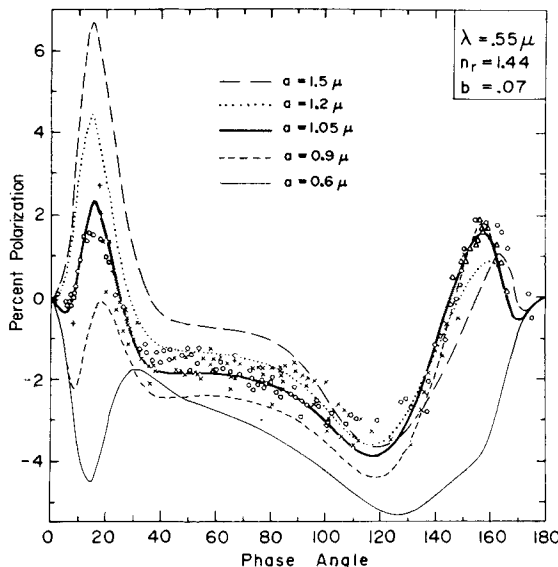


**Fig. 4.19** Polarization of Venus. Observational points and calculations centered at  $\lambda = 0.55 \mu\text{m}$ . All curves for spheres with refractive index of 1.44. The different curves show effect of radius of sphere. Distribution of sizes is  $n(r) = \text{const } r^{11.3} e^{-r/0.07a}$ . Rayleigh fractional contribution to scattering is about 0.009. [After HANSEN and HOVENIER (1974).]

that: (1) the cloud particles in the visible cloud-top were spherical; (2) the effective radius of the particles was  $\sim 1 \mu\text{m}$ ; (3) the particle size distribution was very narrow with an effective variance of only  $\sim 0.07$ ; (4) the refractive index decreased from 1.46 at  $\lambda = 0.365 \mu\text{m}$  to 1.43 at  $\lambda = 0.99 \mu\text{m}$ ; and (5) that the cloud optical thickness of unity occurs at a pressure of  $\sim 50 \text{ mb}$ . The precise limits on the refractive index had the effect of eliminating all previously suggested cloud particle compositions except for concentrated sulfuric acid,  $\text{H}_2\text{SO}_4 \cdot (\text{H}_2\text{O})$ , which provides a good fit to the observed polarization.

The successful analysis of Venus polarization, however, is not likely to be repeated for other planets in the solar system. The precision and uniqueness of the results obtained for Venus depends largely on the fact that the cloud particles proved to be spherical—as indicated by the characteristic features such as the rainbow and the anomalous diffraction and their wavelength dependence. On planets such as Mars and Jupiter we would expect to find irregular dust and ice particles rather than spherical (liquid) particles. This irregularity would have the effect of introducing additional parameters with compensating trade-offs, making the analysis much more complicated and less unique.

## 4.4 Thermal Radiation

### 4.4.1 Equation of Transfer

The thermal emission from an atmosphere carries the signature of the temperature profile, and is widely used for remote sensing of planets including the Earth, where it is applied both from the surface and from orbit. It is important to find spectral regions with suitable opacities (a general term for absorption coefficients) and to have accurate knowledge of their values. Opacities are discussed in Section 4.4.2.

The starting point is (1.2.18), the monochromatic equation of transfer for LTE, in which the source function is equal to the Planck function  $B_v(T)$ . The intensity at zenith angle represented by  $\mu$  is given by

$$\mu \frac{dI_v}{d\tau_v} - I_v = -B_v(T) \quad (4.4.1)$$

With the integrating factor  $\exp(-\tau_v/\mu)$ , this equation becomes

$$\mu \frac{d}{d\tau_v} (I_v e^{-\tau_v/\mu}) = -B_v(T) e^{-\tau_v/\mu} \quad (4.4.2)$$

We are usually interested in the outgoing intensity  $I_v(0)$  at the top of the atmosphere, where  $\tau_v = 0$ . Integrating from 0 to  $\infty$ , we obtain

$$I_v(0) = \int_0^\infty B_v(T) e^{-\tau_v/\mu} \frac{d\tau_v}{\mu} \quad (4.4.3)$$

(The term on the left at  $\tau_v = \infty$  has vanished.) For observation from the surface, we use  $\tau'_v = \tau_g - \tau_v$  as the variable, where  $\tau_g$  is the optical depth at the ground, and recognize that the downcoming intensity is zero at  $\tau_v = 0$ ,  $\tau'_v = \tau_g$ . Also, since  $\mu$  is negative for downgoing radiation, we use  $\mu' = -\mu$ . The integral of (4.4.2) is then

$$I_v(\tau'_v = 0) = \int_0^{\tau_g} B_v(T) e^{-\tau'_v/\mu'} \frac{d\tau'_v}{\mu'} \quad (4.4.4)$$

Equations (4.4.3) and (4.4.4) have the same form, in which the volume emission  $B_v(T) d\tau_v/\mu$  is exponentially attenuated over the slant path  $\tau_v/\mu$ , and all the contributions are summed to give the intensity. This deceptively simple explanation is possible because of the special properties of LTE.

The literature of this subject often uses the symbol  $\tau$  for transmission, which in our notation would be  $e^{-\tau}$ . Transmission, which will be represented here by  $T'$ , is a more general concept because it is not restricted to

monochromatic radiation; it can be computed in curve-of-growth situations and for groups of lines in a wavelength band. For monochromatic radiation,

$$dT' = d(e^{-\tau/\mu}) = -e^{-\tau/\mu} d\tau/\mu \quad (4.4.5)$$

Thus, (4.4.3) can be written as

$$I_v(0) = \int_{\infty}^0 B_v(T) dT' \quad (4.4.6)$$

where the limits have been interchanged to take account of the minus sign in (4.4.5). In turn,  $dT'$  can be written as  $(dT'/dp)dp$ ;  $(dT'/d \ln p) d \ln p$ ; or  $(dT'/dz)dz$ . The last two choices give convenient vertical scales, since  $(-\log p)$  and height are roughly equivalent; the pressure scale has major advantages when the atmosphere is not isothermal.

For simplicity, the following example uses a height scale and a constant temperature and scale height  $H$ . The barometric equation (1.1.4) therefore applies to number density  $N$  as well as pressure. As in Section 5.1.1, we write

$$d\tau_v = \kappa_v = N(z)\sigma_v \quad (4.4.7)$$

where  $\sigma_v$  is the absorption cross section; scattering is negligible in all cases of interest here. With this substitution, (4.4.3) becomes

$$I_v(0) = \frac{\sigma_v N(z_0)}{\mu} \int_0^{\infty} B_v(T) \exp\left(-\frac{z-z_0}{H} - \frac{\tau_v}{\mu}\right) dz \quad (4.4.8)$$

The integrand has the form of a Chapman function, whose properties are discussed in Section 5.1.1. The reference height  $z_0$  is chosen to coincide with the peak of the function, which is illustrated in Fig. 4.20.

The exponential factor (Chapman function in this example) multiplying  $B_v(T)$  in (4.4.8) is called the *weighting function* or the *kernel*, and the entire integrand is the *contribution function*. The form of the weighting function is different if the atmosphere is not isothermal or if the absorption cross section is not independent of pressure. In many important cases (pressure-broadened line wings, for example), the absorption cross section is proportional to pressure, and the optical depth to its square. This case again can give a Chapman-like weighting function, but exactly half as thick.

If the atmosphere is not isothermal,  $B_v(T)$  is a function of height, and the contribution function differs from the weighting function, sometimes quite drastically. Conversely, if wavelengths can be observed that have strongly different opacities, their contribution functions will be at different heights. Mathematical inversion of such a data set can therefore give a temperature profile for part of the atmosphere (Section 4.4.3). As a first, rather crude, approximation the brightness temperature at a given wavelength can be assigned to an effective level, which is at the peak of the corresponding

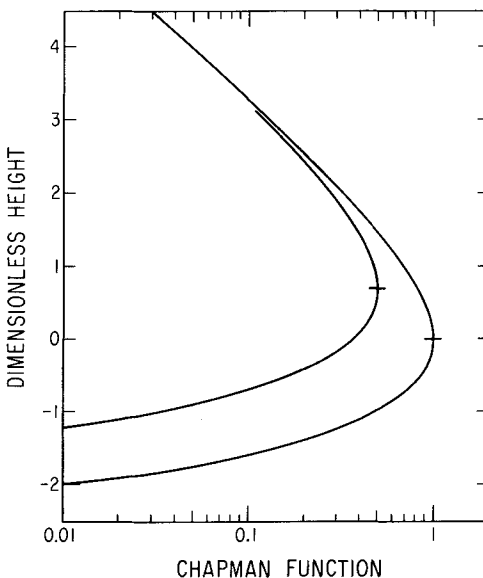


**Fig. 4.20** Chapman weighting functions  $\text{Ch}(z)$  for  $\mu = 1$  and  $0.5$ .

weighting function. This level is at *unit slant optical depth* (5.1.4 and 5.1.5). The dark Fraunhofer lines in the solar spectrum illustrate this principle. Wavelengths with stronger absorption appear darker and must “originate” from a greater height. This part of the solar atmosphere therefore has a negative temperature gradient. Bright lines, seen in the ultraviolet and in other stars, come from the *chromosphere*, a still higher region with a positive temperature gradient. Exactly analogous phenomena are found in planetary atmospheres, but at the much longer wavelengths that correspond to their lower temperatures.

#### 4.4.2 Thermal Opacities

The thermal, or *planetary*, region of the spectrum is important in two contexts. First, the opacities must be known for studies of heat transport by radiation, such as those discussed in Section 1.2. Second, for remote sensing based on (4.4.3) or (4.4.4) the opacity at each wavelength used must be known so that optical depth can be converted to pressure, or composition if the temperature profile is already known. The following comments should be read in conjunction with Table 4.2 above; for further information the Notes at the end of the chapter can be consulted. To be of interest in the present context, a band must have a significant overlap with the Planck function at

the planetary temperature. The corresponding wavelengths are greater than 4–5  $\mu\text{m}$  for terrestrial planets, and 10–15  $\mu\text{m}$  in the outer solar system. Although emitted fluxes are very small at radio wavelengths, they can still be measured with sensitive receivers.

On Earth the two significant absorbers are  $\text{H}_2\text{O}$  and  $\text{CO}_2$ . In the troposphere the 15  $\mu\text{m}$  band complex of  $\text{CO}_2$  is too opaque to have any significant effect; the mean free path of the radiation is so short that energy transport is negligible. Conversely, in the stratosphere there is not enough  $\text{H}_2\text{O}$  to be effective, and the  $\text{CO}_2$  becomes dominant. Even though this gas absorbs strongly only over a spectral region about 1  $\mu\text{m}$  wide, there is enough energy transported to dominate the thermal structure of the entire stratosphere and mesosphere (cf. Sections 1.5 and 1.6). For  $\text{H}_2\text{O}$  the important features are the 6.25  $\mu\text{m}$  fundamental, the rotation band extending from 10  $\mu\text{m}$  into the radio region, and a continuum centered near 10  $\mu\text{m}$ . The Earth's greenhouse effect is attributable almost entirely to them.

For Mars and for Venus above the clouds,  $\text{CO}_2$  is the most important source of gaseous opacity; the only major difference is the abundance of nearly 100% instead of the Earth's 330 ppm. Even this difference is reduced by the effect of pressure broadening on the Earth. In the deep atmosphere of Venus, many more  $\text{CO}_2$  bands, as well as pressure-induced features, become important, as do absorption by water vapor and cloud particles.

Temperature sounding from space on all three planets is carried out by picking regions within the  $\text{CO}_2$  fundamental that have absorption coefficients covering the widest possible range. The Earth and Mars spectra in Fig. 4.21 show this band as an absorption, indicating a negative temperature gradient in both middle atmospheres. Microwave lines are also used for sounding from the ground:  $\text{H}_2\text{O}$  on Earth and CO on all three planets. In this region the actual shape of a line is readily resolved by a radio receiver, and the phenomenon that gives height discrimination is pressure broadening. Radiation near the line center is weighted to high altitudes; farther out, it comes from lower altitudes. Practical effects limit the pressure range to roughly  $10^{-6}$ – $10^{-3}$  bar (on Earth, 90–30 km). The reason for the low-altitude limit is that the line becomes too broad to be measurable as a line; for the same reason, tropospheric absorption does not seriously interfere with the experiment.

In the Jovian planets the most important thermal opacity is due to the pressure-induced dipole transitions of  $\text{H}_2$ , which occupy the entire region from 300 to 800  $\text{cm}^{-1}$ . Several Voyager spectra of Jupiter, shown in Figs. 4.21 and 4.22, illustrate this feature, along with many others. The absorption is strongest at the transition frequencies, 354 and 587  $\text{cm}^{-1}$ , with the rotational quantum number  $J$  changing from 0 to 2 and 1 to 3, respectively. Changes by one unit are strongly forbidden; to that extent, it is convenient to think in

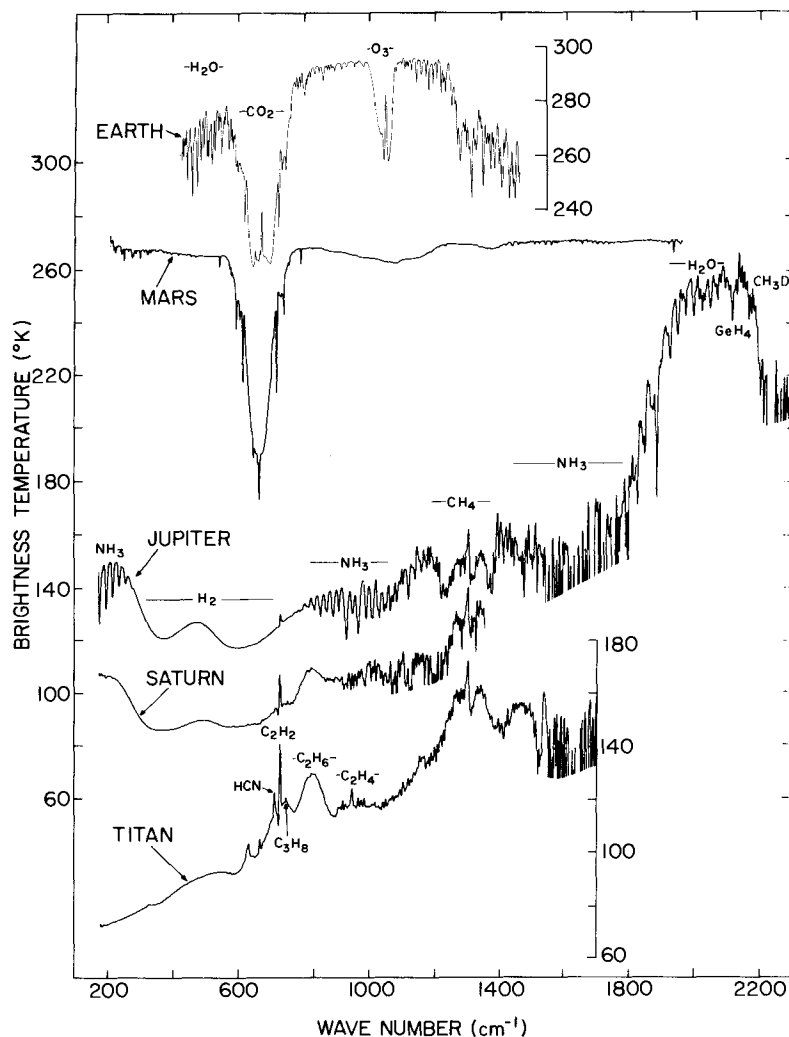


**Fig. 4.21** Spectra in the thermal infrared, plotted as brightness temperatures, for four planets and Titan. Features that show as “absorptions” are formed in a region of negative temperature gradient (troposphere); those that show as “emissions” are from a warm stratosphere. [After HANEL (1983).]

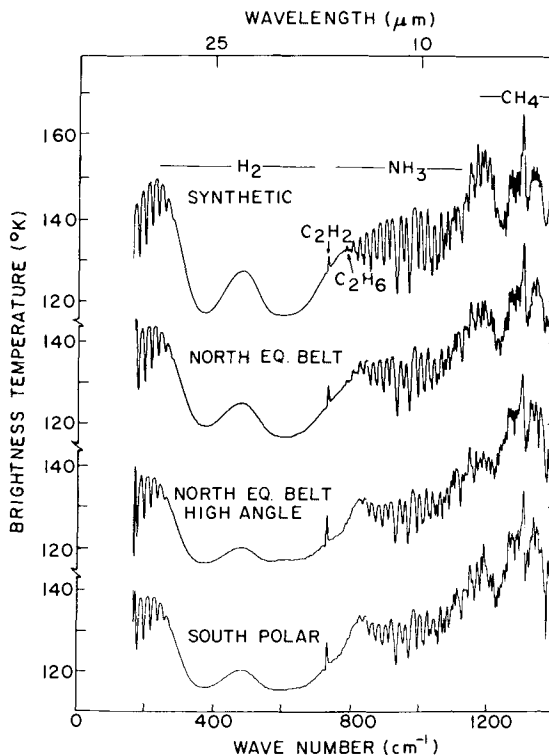


**Fig. 4.22** Thermal emission spectra of Jupiter observed by Voyager 1. [After HANEL *et al.* (1979).]

terms of two distinct forms of  $H_2$ : ortho-hydrogen with odd  $J$  and para-hydrogen with even  $J$  (Appendix VIII). Thus, the low-frequency line belongs to the para form, and the high-frequency to the ortho. Since the strongest absorption corresponds to the lowest brightness temperatures, the lines must be formed in a region of negative temperature gradient, namely the upper troposphere. In the two lowest tracings of Fig. 4.22, the viewing angle is far from vertical; the contrast is considerably reduced because the level of formation is moving up into a region of reduced temperature gradient (the tropopause). This effect is dramatically shown in Fig. 4.23, where a curve is shown for an emission angle of 78 degrees.

Figure 4.22 shows bands of ammonia flanking the hydrogen lines; the rotation band is at the left and a series of vibration-rotation bands at the right. These bands are not very useful for atmospheric sounding because ammonia is very inhomogeneously distributed. The highest brightness temperature of all is in the methane fundamental at  $7.8 \mu m$ , and indicates the

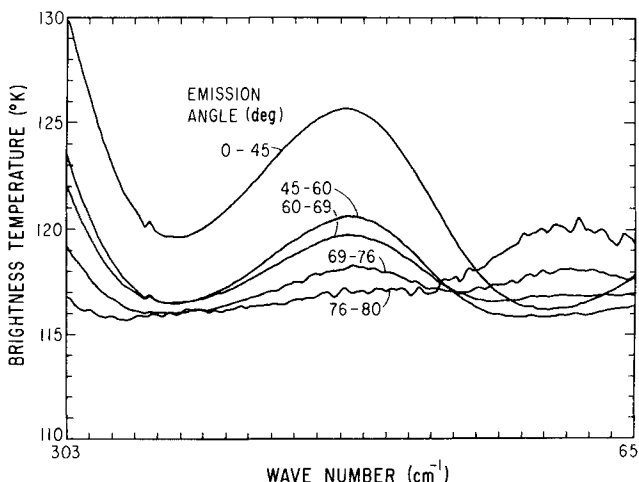


**Fig. 4.23** Region of the H<sub>2</sub> bands in the Voyager data for Jupiter averaged in different ranges of emission angle by S. T. Massie.

presence of a warm stratosphere. Although this band is not ideal for temperature sounding, it is the best available. Stratospheric emissions due to ethane (C<sub>2</sub>H<sub>6</sub>) and acetylene (C<sub>2</sub>H<sub>2</sub>) can be seen just below 800 cm<sup>-1</sup>. A much richer spectrum is found at Titan, and a dozen simple organic molecules have been identified in its stratosphere.

Sensing in the 1–5 bar region depends on the opacity due to the pressure-broadened far wings of the ammonia inversion band. The long-wave wing of this absorption extends from the band center (13 mm) to at least 21 cm, the limit of current observing techniques applied from Earth. There are serious uncertainties in the line shape so far from center, and corresponding limitations in what can be deduced about the planets (see the Section 4.4.3). The spectrum of Jupiter shown in Fig. 4.24 illustrates the increase of brightness temperature to longer wavelengths as the emission arises from greater depths.

The thermal opacity for the Jovian planets is controlled almost entirely by the H<sub>2</sub> pressure-induced absorption. Because the variation with wavelength is relatively small, an equivalent gray opacity (1.2.41) can be readily defined and used with confidence. The principal limitation occurs at the higher temperatures found at deeper levels; the line shape changes appreciably, and the nearly perfect overlap with the Planck function begins to be lost. However, at these depths the opacity is so large in any case that most of the heat flux must be carried by convection. For Jupiter, the optical depth at pressure  $p$  (bars) is  $4.22p^2$ ; unit optical depth therefore occurs at 0.49 bar for vertical emission.

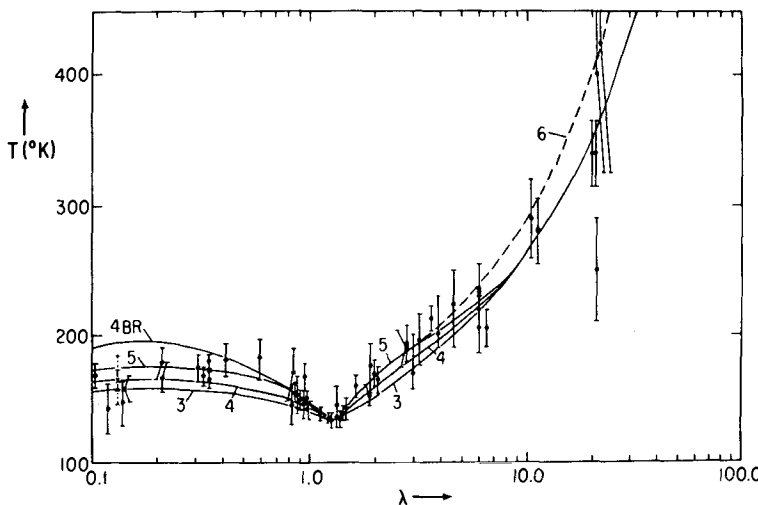


**Fig. 4.24** Radio brightness temperatures of Jupiter compared with models assuming various ammonia absorption coefficients. The absorption is due to the wings of the inversion band centered on 1.3 cm. [After MASSIE and DE PATER (1985).]

#### 4.4.3 Inversion of Thermal Data

As mentioned in Section 4.4.1, a mathematical inversion process is used to convert measured fluxes at suitably chosen wavelengths into an atmospheric temperature profile. As a crude first approximation, brightness-temperature plots such as those in Fig. 4.22 can be interpreted as giving the temperatures at the levels where the optical depth is unity. Similarly, if there are data at different emission angles (as illustrated in Fig. 4.23), even a single wavelength can be used. The inversion procedure is used to sharpen the vertical resolution to less than the width of the weighting functions, which is 2.45 or 1.22 scale heights when optical depth is proportional to pressure or its square. Weighting and contribution functions for Jupiter are shown in Fig. 4.25; there are two in the  $H_2$  region and two in the  $CH_4$  band. The latter band is very temperature sensitive, because it lies near the high-frequency edge of the Planck function at Jovian temperatures; there is a corresponding large difference at high altitudes between the weighting and contribution functions, as comparison of the two panels of Fig. 4.25 reveals.

Given (in this example) four measured intensities (or “radiances”) at the chosen frequencies, one then writes down four copies of the integral (4.4.3), along with the appropriate four relationships between optical depth and pressure. These simultaneous equations must then be solved for the height profile of  $B_v(T)$  and therefore of  $T$ . Since the equations are nonlinear, this

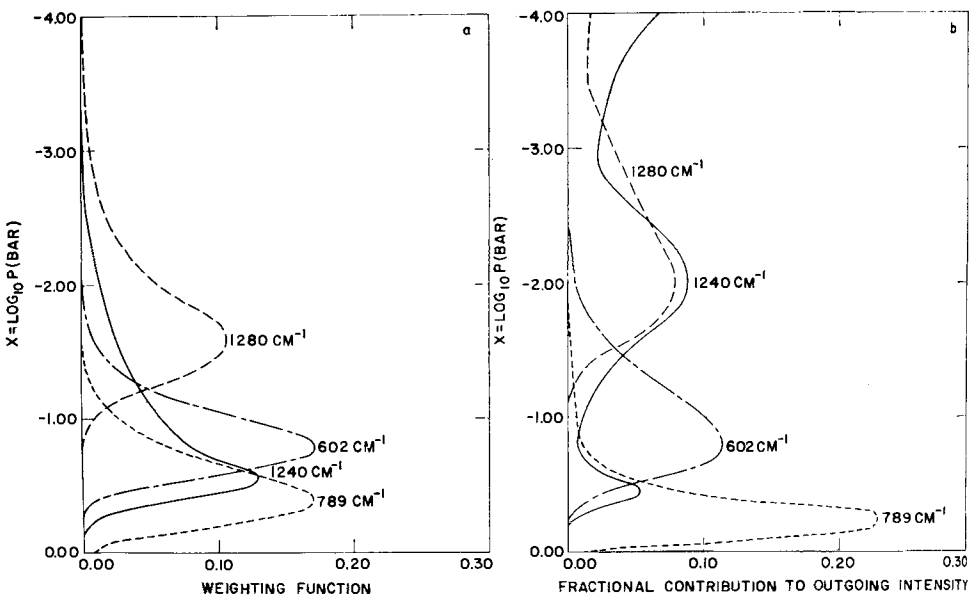


**Fig. 4.25** Weighting and contribution functions for Jupiter. [After ORTON (1977).]

inversion is far from simple; inversion theory is a substantial scientific discipline in its own right. The actual process is carried out in a computer by iteration, until successive iterations agree within some criterion. Although a relaxation algorithm due to Chahine is popular, many workers assert that a matrix-inversion procedure is superior, particularly in being less dependent on an initial guess for the temperature profile. There are also divergent opinions about the attainable height resolution, but as a rule of thumb it is unlikely to be better than one-half the width of the weighting function. The signal-to-noise ratio is decreased as the resolution is improved, but noise is not as important as the inability to resolve details in the profile.

Inversion of radio data such as shown in Fig. 4.24 can be carried out in the same way, but the more usual procedure is to synthesize a spectrum on the assumption of an adiabatic lapse rate and some ammonia abundance. A good fit can be obtained for some range of abundances with corresponding changes in the temperature at a reference level. The temperature at 1 bar is reasonably well known from the infrared data, and the ammonia abundance therefore can be obtained. For Jupiter and Saturn the values are around twice what would be expected for solar abundances, and the lapse rate is close to adiabatic over the 1–5 bar range. Much smaller abundances seem to exist on Uranus and Neptune, where the brightness temperatures are found to be relatively large.

There are some differences in the pressure-induced opacity of H<sub>2</sub>, depending on whether the inducing collision is with He or another H<sub>2</sub> molecule. Although the differences are small and the method is easily upset by unknown opacities, it has been applied to Jupiter and Saturn with reasonable results. Current practice is to combine the infrared data with results from radio occultation. To a first approximation, the radio experiment gives the scale height and therefore the ratio of temperature to molecular weight, while the infrared gives temperature as such. Thus, the molecular weight and therefore the helium-hydrogen ratio can be obtained.

#### 4.4.4 Radio and Stellar Occultations

An occultation occurs when a spacecraft or star passes behind the limb of a planet. Two effects take place: differential refraction reduces the apparent brightness of the source; and the waves are delayed, observable as a phase shift when the source is a spacecraft. The latter effect is discussed in Section 5.2 in the context of ionospheric measurements, but the principles are the same. With a stellar source, only the reduction of intensity can be measured. Its origin is illustrated in Fig. 4.26: a ray passing deeper in the atmosphere is refracted through a larger angle; by the time the two rays reach the Earth at distance  $D$ , their separation  $dy$  is greater than their original separation  $dz = dr_1$ . The intensity of the source is thus reduced by the factor  $dy/dz$ ; from Fig. 4.26, it can be seen that

$$\frac{dz}{dy} = \frac{I_*}{I} = 1 + D \frac{d\theta}{dz} \quad (4.4.9)$$

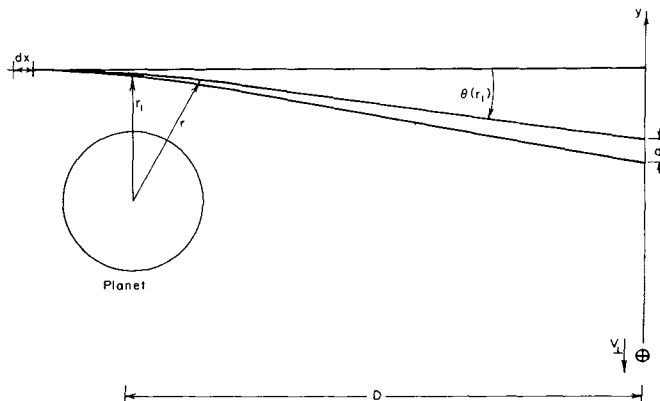


Fig. 4.26 Geometry of an atmospheric occultation.

In this illustration, the star is taken to be at infinity. For a spacecraft event,  $D$  is the distance from the limb to the spacecraft, and the Earth is effectively at infinity.

The refractive index  $n$  of a gas is always very close to unity, and it is convenient to work with the refractivity,  $N = n - 1$ , which is proportional to density. Thus,  $N$  obeys the same barometric equation (1.1.5) as the number density shown in that equation. Some workers use  $10^6 N$ , but this convention is not followed here. For simplicity we shall take the atmosphere as isothermal. The refraction angle  $\theta$  is given by (5.2.31):

$$\theta = \frac{d}{dz} \int_{-\infty}^{\infty} (n - 1) dz = \frac{d}{dz} [N_0(2\pi r H)^{1/2}] = -N_0 \left( \frac{2\pi r}{H} \right)^{1/2} \quad (4.4.10)$$

where  $dp$  has been replaced by  $dz$ , the horizontally integrated density is given in (6.2.6), and differentiation of  $N$  with respect to height has been replaced by division by  $-H$ . The subscript zero refers to conditions at the minimum height of the ray. The sign convention makes  $\alpha$  negative as drawn in Fig. 4.26. A second differentiation gives

$$\frac{d\theta}{dz} = -\frac{\theta}{H} \quad (4.4.11)$$

this relation can also be obtained from (5.2.29). Substitution in (4.4.9) gives

$$\frac{I_*}{I} = 1 + D \frac{|\theta|}{H} \quad (4.4.12)$$

Thus, half the original intensity is seen when the refraction angle  $|\theta|$  is equal to  $H/D$ , the angle subtended by an atmospheric scale height at the distance  $D$ . Typical values are  $4 \times 10^{-8}$  and  $1.5 \times 10^{-4}$  rad for the Earth–Jupiter and spacecraft–Jupiter distances. The corresponding density levels are near the mesopause and the stratopause.

For an isothermal atmospheric region, the shape of the light curve can be matched to (4.4.12) to give the scale height near the half-intensity level. In the general case, (4.4.9) is valid and can be solved in successive layers (“onion-peeling”) or by an integral inversion; in either case a density profile is obtained. Further processing can invoke hydrostatic equilibrium as an additional constraint, with a final result of a profile of  $T/M$ . As mentioned above, other information about the molecular weight  $M$  is needed to give actual temperatures; or if a temperature is known,  $M$  can be found.

All methods of remote sensing are strewn with pitfalls, and this one is no exception, as emphasized by its extensive literature, which should be consulted for details.

## BIBLIOGRAPHICAL NOTES

**Section 4.1 Radiative Transfer in an Optically Thick Atmosphere**

The basic text is

CHANDRASEKHAR, S. (1950), "Radiative Transfer," Clarendon Press, Oxford (reprinted by Dover, New York, 1960).

This classic treatise develops solutions with exact  $H$ -functions for simple phase functions, as well as solutions in the  $n$ th approximation. Finite atmospheres are also treated there with the exact formalism and solved in terms of so-called  $X$ - and  $Y$ -functions.

A review and extensive bibliography of theoretical calculations for scattering with a variety of phase functions is given in

IRVINE, W. M. (1975), Multiple scattering in planetary atmospheres, *Icarus* **25**, 175–204.

The similarity relations for scattering by atmospheres with different phase functions, albedos, and thicknesses are discussed in

VAN DE HULST, H. C. and GROSSMAN, K. (1968), Multiple light scattering in planetary atmospheres, in "The Atmospheres of Venus and Mars," (J. C. Brandt and M. B. McElroy, eds.), pp. 35–55, Gordon and Breach, New York.

For the accurate solution of realistic problems of planetary atmospheres, with scattering phase functions such as (4.1.44), the function introduced by L. G. HENYET and J. L. GREENSTEIN [(1941), *Astrophys. J.* **93**, 70] it is necessary to employ numerical techniques. Computational methods in wide use are the *doubling method* and the related *adding method* in which the single-scattering properties of an optically thin layer are used to derive the cumulative scattering of a large number of layers (see Section 4.1.5, due to A. A. LACIS). The concept originated with

STOKES, G. G. (1862), On the intensity of the light reflected from or transmitted through a pile of plates, *Proc. Roy. Soc. (London)* **11**, 545–556,

and was introduced to atmospheric physics by

BELLMAN, R. E.; KALABA, R.; and UENO, S. (1963), Invariant imbedding and diffuse reflection from a two-dimensional flat layer, *Icarus* **1**, 297–303;

TWOMEY, S.; JACOBOWITZ, H.; and HOWELL, H. B. (1966), Matrix methods for multiple-scattering problems, *J. Atmos. Sci.* **23**, 289–296;

VAN DE HULST, H. C. and GROSSMAN, K. (1968), Multiple light scattering in planetary atmospheres, in "The Atmospheres of Venus and Mars," (J. C. Brandt and M. B. McElroy, eds.), pp. 35–55, Gordon and Breach, New York.

The numerical technique has been developed for planetary atmospheres by

HANSEN, J. E. (1969), Radiative transfer by doubling very thin layers, *Astrophys. J.* **155**, 565–573;

HANSEN, J. E. (1971), Multiple scattering of polarized light in planetary atmospheres, Part I. The doubling method, *J. Atmos. Sci.* **28**, 120–125,

HANSEN, J. E. and TRAVIS, L. D. (1974), Light scattering in planetary atmospheres, *Space Sci. Rev.* **16**, 527–610.

An implementation of the invariant imbedding technique is described by

SATO, M.; KAWABATA, K.; and HANSEN, J. E. (1977), A fast invariant imbedding method for multiple scattering and an application to equivalent widths of CO<sub>2</sub> lines on Venus, *Astrophys. J.* **216**, 947–962.

A survey of practical but approximate methods is included in

WALLACE, L. and HUNTER, D. M. (1978), The Jovian spectrum in the region 0.4–1.1  $\mu\text{m}$ : The C/H ratio, *Rev. Geophys. Space Phys.* **16**, 289–319.

The discussion of the two-stream Feautrier method is taken from this paper. The two-term Henyey-Greenstein (TTHG) function and its expansion in spherical harmonics are given by

KATTAWAR, G. W. (1975), A three-parameter analytic phase function for multiple scattering calculations, *J. Quant. Spectrosc. Radiat. Transfer* **15**, 839–849.

Because clouds may be optically thin over distances of a scale height or because two or more distinct cloud levels may be present, some numerical models have been developed for vertically inhomogeneous atmospheres—meaning that the relative absorption and scattering varies with depth. Among these models are

DANIELSON, R. E. and TOMASKO, M. G. (1969), A two-layer model of the Jovian clouds. *J. Atmos. Sci.* **26**, 889–897;

COCHRAN, W. D. (1977), Jupiter: An inhomogeneous atmospheric model analysis of spatial variations of the  $\text{H}_2(4-\text{O})\text{S}(1)$  line, *Icarus* **31**, 325–347;

DANIELSON, R. E.; COCHRAN, W. D.; WANNIER, P. G.; and LIGHT, E. S. (1977), A saturation model of the atmosphere of Uranus, *Icarus* **31**, 97–109.

#### Section 4.2 Spectroscopy

Curves of growth, radiative transfer, and absorptions in the Earth's atmosphere are extensively discussed by

GOODY, R. M. (1964), "Atmospheric Radiation," Clarendon Press, Oxford;

KONDRATYEV, K. YA. (1969), "Radiation in the Atmosphere," Academic Press, New York;

LOIU, K.-N. (1980), "An Introduction to Atmospheric Radiation," Academic Press, New York;

The solution (4.2.6) for the equivalent width of an absorption line with Lorentz broadening in a nonscattering atmosphere was first obtained by

LADENBERG, R. and REICHE, F. (1913), Über Selektive Absorption, *Ann. Physik* **42**, 181–209.

For a barometric atmosphere the solution (4.2.9) was obtained by

STRONG, J. and PLASS, G. N. (1950), The effect of pressure broadening of spectral lines on atmospheric temperature, *Astrophys. J.* **112**, 365–379.

[The strong-line limit (4.2.10) was later given by CURTIS, A. R. (1952), *Q. J. Roy. Met. Soc.* **78**, and by GODSON, W. L. (1953), *ibid.* **79**, 367.]

The complications inherent in both the spectroscopic and the photometric techniques used to estimate the total pressure of the Martian atmosphere from ground-based observations are reviewed in

CHAMBERLAIN, J. W. and HUNTER, D. M. (1965), Pressure and  $\text{CO}_2$  content of the Martian atmosphere: A critical discussion, *Rev. Geophys.* **3**, 299–317.

With refined observations of  $\text{CO}_2$ , relative altitudes of surface features on Mars were first obtained by

BELTON, M. J. S. and HUNTER, D. M. (1971), The distribution of  $\text{CO}_2$  on Mars: Spectroscopic determination of surface topography, *Icarus* **15**, 204–232.

It was first noted that a weak line formed in an atmosphere scattering with  $\tilde{\omega}_c \approx 1$  should vary as the square root of the absorption coefficient (4.2.28) in

VAN DE HULST, H. C. (1949), Scattering in the atmospheres of the Earth and the planets, in "The Atmospheres of the Earth and Planets," (G. P. Kuiper, ed.), pp. 49–111, Univ. Chicago Press, Chicago [2nd ed., 1952].

The phase variation and spectroscopic temperatures of a long series of near-infrared CO<sub>2</sub> spectra of Venus (obtained by Kuiper) were interpreted in terms of multiple scattering in a hazy atmosphere by

CHAMBERLAIN, J. W. and KUIPER, G. P. (1956), Rotational temperature and phase variation of the carbon dioxide bands of Venus, *Astrophys. J.* **124**, 399–405.

Little notice was taken of the importance of multiple-scattering analysis in optically thick atmospheres over the next decade. Observers and analysts alike continued to compare Venus' spectra with those from the laboratory and inferred the "amount of CO<sub>2</sub> above the Venus clouds." The situation changed dramatically with the publication of an interpretational paper,

CHAMBERLAIN, J. W. (1965), The atmosphere of Venus near her cloud tops, *Astrophys. J.* **141**, 1184–1205.

The curve-of-growth theory presented here follows

CHAMBERLAIN, J. W. (1970), Behavior of absorption lines in a hazy planetary atmosphere, *Astrophys. J.* **159**, 137–158.

Carbon dioxide was found in the spectrum of Venus with infrared-sensitive photographic plates that recorded the same bands shown in Fig. 4.8 by

ADAMS, W. S. and DUNHAM, T., JR. (1932), Absorption bands in the infra-red spectrum of Venus, *Publ. Astr. Soc. Pacific* **44**, 243–245.

The Mars data shown in Figs. 4.12 and 4.13 are described by

BELTON, M. J. S.; BROADFOOT, A. L.; and HUNTER, D. M. (1968), Abundance and temperature of CO<sub>2</sub> on Mars during the 1967 opposition, *J. Geophys. Res.* **73**, 4795–4806.

Figure 4.14 is from

PILCHER, C. B.; PRINN, R. G.; and MCCORD, T. B. (1973), Spectroscopy of Jupiter: 320 to 11,200 Å, *J. Atmos. Sci.* **30**, 302–307.

A number of planetary spectra are reproduced and their interpretation discussed by

HUNTER, D. M. (1971), Composition and structure of planetary atmospheres, *Space Sci. Rev.* **12**, 539–599.

The highest resolution planetary spectra are those obtained with a Michelson interferometer by the technique commonly called *Fourier spectroscopy*. In particular, the spectra of the brighter planets are recorded in

CONNES, P.; CONNES, J.; and MAILLARD, J. P. (1969), "Atlas des spectres infrarouges de Vénus, Mars, Jupiter et Saturn," Centre National de la Recherche Scientifique, Paris.

The atmospheric abundances in Table 4.1 are based on tabulations and summaries in

ALLEN, C. W. (1973), "Astrophysical Quantities," 3d. ed., Athlone Press, London, p. 119; HUNTER, D. M. (1971), op. cit.;

MCELROY, M. B.; KONG, T. Y.; and YUNG, Y. L. (1976), Composition and structure of the Martian upper atmosphere: Analysis of results from Viking, *Science* **194**, 1295–1298; RIDGWAY, S. T.; LARSON, H. P.; and FINK, U. (1976). The infrared spectrum of Jupiter, in "Jupiter," (T. Gehrels, ed.), pp. 384–417. Univ. Arizona Press, Tucson,

- VON ZAHN, U.; KUMAR, S.; NIEMANN, H.; and PRINN, R. G. (1983), Composition of the Venus atmosphere, in "Venus" (D. M. Hunten, L. Colin, T. M. Donahue, and V. I. Moroz, eds.), pp. 299–430, Univ. of Arizona Press, Tucson, Arizona,
- OWEN, T.; BIEMANN, K.; RUSHNECK, D. R.; BILLER, J. E.; HOWARTH, D. W.; and LAFLEUR, A. L. (1977), The composition of the atmosphere at the surface of Mars, *J. Geophys. Res.* **82**, 4635–4639,
- HUNTER, D. M.; TOMASKO, M. G.; FLASAR, F. M.; SAMUELSON, E. E.; STROBEL, D. F.; and STEVENSON, D. J. (1984), Titan, in "Saturn" (T. Gehrels and M. S. Matthews, eds.), pp. 671–759, Univ. of Arizona Press, Tucson, Arizona,
- GAUTIER, D.; CONRATH, B. J.; FLASAR, M.; HANEL, R.; KUNDE, V.; CHEDIN, A.; and SCOTT, N. (1981), The helium abundance of Jupiter from Voyager, *J. Geophys. Res.* **86**, 8713–8720,
- GAUTIER, D.; BEZARD, B.; MARTEN, A.; BALUTEAU, J. P.; SCOTT, N.; CHEDIN, A.; KUNDE, V.; and HANEL, R. (1982), The C/H ratio on Jupiter from the Voyager infrared investigation, *Astrophys. J.* **257**, 901–912,
- KUNDE, V.; HANEL, R.; MAGUIRE, W.; GAUTIER, D.; BALUTEAU, J. P.; MARTEN, A.; CHEDIN, A.; HUSSON, N.; and SCOTT, N. (1982), The tropospheric composition of Jupiter's north equatorial belt, *Astrophys. J.* **263**, 443–467.
- PRINN, R. G.; LARSON, H. P.; CALDWELL, J. J.; and GAUTIER, D. (1984), Composition and chemistry of Saturn's atmosphere, in "Saturn" (T. Gehrels and M. S. Matthews, eds.), pp. 88–149, Univ. of Arizona Press, Tucson, Arizona.

The problems of interpreting Jupiter's spectrum are treated by

- TEIFEL, V. G. (1976), Morphology of molecular absorption on the disk of Jupiter, in "Jupiter," (T. Gehrels, ed.), pp. 441–485, Univ. Arizona Press, Tucson,
- WALLACE, L. (1976), The thermal structure of Jupiter in the stratosphere and upper troposphere, in "Jupiter," (T. Gehrels, ed.), pp. 284–303, Univ. Arizona Press, Tucson.
- WALLACE, L. and HUNTER, D. M. (1978), The Jovian spectrum in the region 0.4–1.1  $\mu$ : The C/H ratio, *Rev. Geophys. Space Phys.* **16** (No. 3, Aug.), 289–319.

The phenomenon of collisional narrowing of the Doppler profile was developed by

- DICKE, R. H. (1953), The effects of collisions on the Doppler width of spectral lines, *Phys. Rev.* **89**, 472–473

and applied to a curve of growth for H<sub>2</sub> in a scattering model of Jupiter's atmosphere by

- FINK, U. and BELTON, M. J. S. (1969), Collision-narrowed curves of growth for H<sub>2</sub> applied to new photoelectric observations of Jupiter, *J. Atmos. Sci.* **26**, 952–962.

The quadrupole and pressure-induced dipole spectra of H<sub>2</sub> are discussed in

- HERZBERG, G. (1952), Laboratory absorption spectra obtained with long paths, in "The Atmospheres of the Earth and Planets," (G. P. Kuiper, ed.), pp. 406–416, Univ. Chicago Press, Chicago, 2nd ed.,
- BIRNBAUM, A. and POLL, J. D. (1969), Quadrupole transitions in the H<sub>2</sub>, HD, and D<sub>2</sub> molecules, *J. Atmos. Sci.* **26**, 943–945.

Most of the gases in Table 4.2 are discussed in

- GOODY, R. M. (1964), *op. cit.*

Wavelengths and energy levels, but not strengths, can be found in

- HERZBERG, G. (1945), "Infrared and Raman spectra of polyatomic molecules," Van Nostrand-Reinhold, Princeton, New Jersey.

Wavenumbers, strengths, and other parameters for a huge number of Earth atmospheric lines are contained on the "AFGL tape," available from the U.S. Air Force Geophysics Laboratory, Bedford, Massachusetts. A description of the first version is in

MCCLATCHY, R. A.; BENEDICT, W. S.; CLOUGH, S. A.; BURCH, D. E.; CALFEE, R. F.; FOX, K.; ROTHRMAN, L. S.; and GARING, J. S. (1973), AFCRL atmospheric absorption line parameters compilation, AFCRL-TR-73-0096; Environmental Research Papers No. 434.

Other references are

- WALLACE, L. and HUNTER, D. M. (1978), *op. cit.*,  
 GEHRELS, T., ed. (1976), "Jupiter," pp. 319-371, 384-417, Univ. of Arizona Press, Tucson, Arizona,  
 GILLE, J. C. and LEE, T. H. (1969), The spectrum and transmission of ammonia under Jovian conditions, *J. Atmos. Sci.* **26**, 932-940,  
 DE PATER, I. and MASSIE, S. T. (1985), Models of the millimeter-centimeter spectra of the Jovian planets, *Icarus* **62**, 143-171.  
 BELTON, M. J. S. (1982), An interpretation of the near-ultraviolet absorption spectrum of SO<sub>2</sub>: Implications for Venus, Io, and laboratory measurements, *Icarus* **52**, 149-165,  
 KRASNOPOLSKY, V. A. (1985), Chemical composition of Venus clouds, *Planet. Space Sci.* **33**, 109-117.

#### Section 4.3 Photometry and Polarimetry

Scattering by particles is most thoroughly treated in VAN DE HULST, H. C. (1957), "Light Scattering by Small Particles," Wiley, New York.

On a more elementary level is

MCCARTNEY, E. J. (1976), "Optics of the Atmosphere: Scattering by Molecules and Particles," Wiley, New York.

Mie scattering by an atmosphere in which the particles are not of uniform size is treated in

DEIRMENDJIAN, D. (1969), "Electromagnetic Scattering on Spherical Polydispersions," American Elsevier, New York,

WICKRAMASINGHE, N. C. (1973), "Light Scattering Functions with Applications in Astronomy," Wiley, New York.

The fundamentals of planetary photometry are thoroughly reviewed in

HARRIS, D. L. (1961), Photometry and colorimetry of planets and satellites, in "Planets and Satellites," (G. P. Kuiper and B. M. Middlehurst, eds.), pp. 272-342, Univ. Chicago Press, Chicago.

That the "surface" temperatures of Jupiter and Saturn were extremely low—comparable to the values that would be maintained by solar radiation—was first shown (from a reduction of Lowell Observatory radiometric measurements) by

MENZEL, D. H. (1923), Water-cell transmissions and planetary temperatures, *Astrophys. J.* **58**, 65-74.

On the basis of these results Menzel later gave the first convincing arguments that the major planets are composed largely of hydrogen (rather than having terrestrial compositions with hot, gaseous interiors to account for their low densities) in

MENZEL, D. H. (1930), Hydrogen abundance and the constitution of the giant planets, *Publ. Astr. Soc. Pacific* **42**, 228-232.

Thermal infrared observations from Pioneer, their interpretation in terms of an effective temperature, and references to earlier Earth-based measurements are given in

INGERSOLL, A. P.; MÜNCH, G.; NEUGEBAUER, G.; and ORTON, G. S. (1976), Results of the infrared radiometer experiment on Pioneers 10 and 11, in "Jupiter," (T. Gehrels, ed.), pp. 197-205, Univ. Arizona Press, Tucson.

That Jupiter is heated from below was inferred from the cloud activity and potential energy considerations by

KUIPER, G. P. (1952), Planetary atmospheres and their origin, in "The Atmospheres of the Earth and Planets," (G. P. Kuiper, ed.), pp. 306–405, Univ. Chicago Press, Chicago, 2nd ed. (cf. pp. 326, 376).

Kuiper was reluctant to attach too much importance to radiometric temperatures measured in the 8–12  $\mu\text{m}$  window. That a genuine discrepancy with the solar-equilibrium temperature existed and must indicate internal heating was first emphasized by

ÖPIK, E. J. (1962), Jupiter: Chemical composition, structure, and origin of a giant planet, *Icarus* **1**, 200–257.

High-resolution photometry of Venus from Mariner 10, with emphasis on the mysterious dark markings that appear in the ultraviolet wavelengths, is discussed by

HAPKE, B. (1976), Photometry of Venus from Mariner 10, *J. Atmos. Sci.* **33**, 1803–1815.

The formulation of radiative transfer in terms of the parameters originally devised in 1852 by G. G. STOKES is due to

CHANDRASEKHAR (1950), op. cit. pp. 24–35.

Scattering by planetary atmospheres, with emphasis on the polarization produced by Mie scattering, is reviewed in

HANSEN, J. E. and TRAVIS, L. D. (1974), op. cit.

Multiple-scattering calculations, compared with observations, established that the index of refraction for the Venus aerosols is  $1.46 \pm 0.015$  in the blue and  $1.43 \pm 0.015$  in the near infrared and that the sizes of the droplets are concentrated around  $1.05 \mu\text{m}$  radius. This polarization analysis is due to

HANSEN, J. E. and HOVENIER, J. W. (1974), Interpretation of the polarization of Venus, *J. Atmosph. Sci.* **31**, 1137–1160.

On the basis of this analysis, sulfuric acid,  $\text{H}_2\text{SO}_4$ , was proposed as the source of Venus' visual clouds independently by

SILL, G. T. (1972), Sulfuric acid in the Venus clouds, *Com. Lunar Planet. Lab.* Univ. Arizona, Tucson, **9**, No. 171, 191–198,

YOUNG, A. T. (1973), Are the clouds of Venus sulfuric acid? *Icarus* **18**, 564–582.

The power of polarization studies of scattering atmospheres was first demonstrated by

LYOT, B. (1929), Recherches sur la polarisation de la lumière des planètes et de quelques substances terrestres. *Ann Observ. Paris (Meudon)* **8**, 161 pp. [English translation, NASA TT T-187 (1964)].

#### Section 4.4 Thermal Radiation

Figure 4.21 is from a useful review by

HANEL, R. A. (1983), Planetary exploration with spaceborne Michelson interferometers in the thermal infrared, in "Spectrometric Techniques," vol. III (G. A. Vanasse, ed.), pp. 43–135, Academic Press, New York.

Figure 4.22 is from

HANEL, R., CONRATH, B., FLASAR, M., KUNDE, V., LOWMAN, P., MAGUIRE, W., PEARL, J., PIRRAGLIA, J., SAMUELSON, R., GAUTIER, D., GIERASCH, P., KUMAR, S., and PONNAMPERUMA, C. (1979), Infrared observations of the Jovian system from Voyager 1, *Science* **204**, 972–976.

Figures 4.23 and 4.24 are from

MASSIE, and DE PATER, *op. cit.*, Section 4.2.

ORTON, G. S. (1977), Recovery of the mean Jovian temperature structure from inversion of spectrally resolved thermal radiance data, *Icarus* **32**, 41–57.

The proposal for thermal sounding based on Eq. (4.4.3) was made by

KAPLAN, L. D. (1959), Inference of atmospheric structure from remote radiation measurements, *J. Opt. Soc. Am.* **49**, 1004–1007.

The serious mathematical problems of getting a useful result were first overcome by

CHAHINE, M. (1968), Determination of the temperature profile of an atmosphere from its outgoing radiance, *J. Opt. Soc. Am.* **58**, 1634–1637,

CHAHINE, M. (1970), Inverse problems in radiative transfer: determination of atmospheric parameters, *J. Atmos. Sci.* **27**, 960–967.

A clear exposition of the problems, their causes and cures, is given by

TWOMEY, S. (1977), "Introduction to the Mathematics of Inversion in Remote Sensing and Indirect Measurements," Elsevier, Amsterdam.

Another useful book is

DEEPAK, A., ed. (1977), "Inversion Methods in Atmospheric Remote Sensing," Academic Press, New York.

An example of microwave sounding of H<sub>2</sub>O on Earth is

BEVILACQUA, R. M.; OLIVERO, J. J.; SCHWARTZ, P. R.; GIBBONS, C. J.; BOLOGNA, J. M.; and THACKER, D. J. (1983), An observational study of water vapor in the mid-latitude mesosphere using ground-based microwave techniques, *J. Geophys. Res.* **88**, 8523–8534.

A survey of the occultation method is given by

HUNTER, D. M. and VEVERKA, J. (1976), Stellar and spacecraft occultations by Jupiter: A critical review of derived temperature profiles, in "Jupiter" (T. Gehrels, ed.), pp. 247–283, Univ. of Arizona Press, Tucson, Arizona.

The method currently used to analyze stellar occultations is derived and discussed in

FRENCH, R. G.; ELLIOT, J. L.; and GIERASCH, P. J. (1978), Analysis of stellar occultation data: Effects of photon noise and initial conditions, *Icarus* **33**, 186–202.

Combined analysis of infrared and radio measurements is described by

GAUTIER, D. *et al.*, *op. cit.*, (1981).

## PROBLEMS

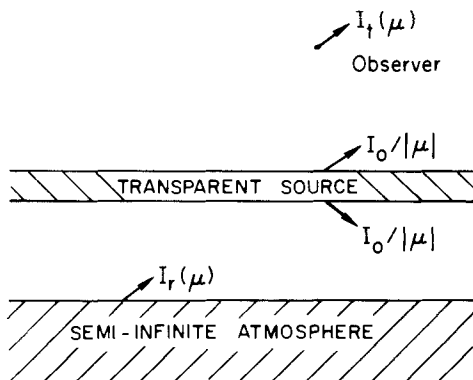
**4.1 Gaussian quadrature.** (a) Find the division points and weighting factors for a three-point quadrature. Show that the three unused equations (4.1.12) satisfy the  $a_j$ 's found from the other three. (b) Use the Gaussian quadrature to evaluate  $\int_{-1}^1 e^x dx$  and compare the result with the exact value and with the approximate value obtained from a series expansion of  $e^x$  to terms in  $x^5$ .

**4.2 Diffuse reflection.** A semi-infinite atmosphere is illuminated by a parallel beam of light with incident flux  $\pi\mathcal{F}$  (measured across an area normal to the beam). The beam is incident from a zenith angle  $\cos^{-1}\mu_0$ . (a) What is the albedo of the atmosphere for this incident radiation in the first approximation when the scattering albedo is  $\bar{\omega} = 1$ ? (b) Evaluate this albedo for  $\mu_0 = 1, 1/\sqrt{3}, \frac{1}{2}$ , and 0.1 and comment on what these results connote about the accuracy of the first approximation.

**4.3 Physical meaning of the  $H$ -functions** [after CHANDRASEKHAR (1950)]. A layer that emits airglow in all directions, with an angular distribution of intensity  $I_s(\mu) = I_0/|\mu|$ , lies above the semi-infinite, isotropically scattering atmosphere. An observer in space sees a total intensity  $I_t(0, +\mu) = I_s(\mu) + I_r(0, +\mu)$ , where  $I_r$  is the intensity diffusely reflected by the atmosphere. Solve the transfer equation in the first approximation for  $I_r$  and show that the relative enhancement to the observed intensity provided by the atmosphere is

$$I_t(+\mu)/I_s(\mu) = H_1(\mu)$$

where  $H_1$  is given by (4.1.31). (Note: This result actually holds to all orders of approximation. Hence the reflectivity of an atmosphere, for the source distribution assumed here, provides a physical meaning for the Chandrasekhar  $H$ -functions.)



**4.4 Atmospheric albedo ( $I$ ).** A semi-infinite atmosphere is illuminated from above by isotropic radiation of total flux  $\pi\mathcal{F}$  (measured across a surface parallel to the top of the atmosphere). (a) Solve the transfer equation in the first approximation and apply the boundary conditions to fix the two integration constants. (b) Find the source function and the upward radiation field  $I(\tau, +\mu)$ . (c) What is the albedo  $\Lambda$  of the atmosphere for this incident radiation field? Evaluate  $\Lambda$  to order  $(1 - \tilde{\omega})$  for the case when  $(1 - \tilde{\omega}) \ll 1$ , and show that  $\Lambda$  is almost, but not quite, the same as (4.1.34).

**4.5 Atmospheric albedo (II).** Show that the albedo  $\Lambda$  in Problem 4.4 can be written as

$$\Lambda = 1 - 2\alpha_1(1 - \tilde{\omega})^{1/2}$$

where  $\alpha_n$  is the  $n$ th moment of the  $H$ -functions. In the first approximation

$$\alpha_n = \int_0^1 \mu^n H_1(\mu) d\mu$$

where  $H_1$  is given by (4.1.31).

**4.6 Anisotropic scattering.** (a) Show that the transfer equation with  $I(\tau, \mu)$  divided into azimuth-dependent and -independent parts, (4.1.36), may be written as the two equations (4.1.37) and (4.1.38). (b) Solve the transfer equation (4.1.2) in the optically thin limit (where only single scattering need be considered) and obtain expressions (4.1.51) and (4.1.52) for the reflected and transmitted intensities.

**4.7 Effective damping constant.** Consider a barometric (constant temperature) atmosphere in which the absorption cross section of a well-mixed absorber everywhere has a Lorentz profile (4.2.3) with  $\Gamma$  proportional to the local pressure. The continuum is optically thin. (a) Show that the effective optical thickness as seen from outside the atmosphere is

$$\eta\tau_v = \frac{2\eta S \mathcal{N}}{\Gamma_0} \ln \left[ 1 + \left( \frac{\Gamma_0/4\pi}{v - v_0} \right)^2 \right]$$

where  $\Gamma_0$  is the value at the ground, and compare with  $\eta\tau_v$  for an atmosphere of constant density. (b) In the manner of Eq. (4.2.4) find the frequency displacement where the optical thickness is unity and show that for strongly absorbing lines the equivalent width is the same as for a constant-density atmosphere, except that  $\Gamma$  is replaced with  $\Gamma_0/2$ .

**4.8 Air-mass factor.** (a) Show that  $\langle \eta \rangle$ , as given by the first equality of (4.2.31), has the same phase variation, relative to the value at full phase, for any zonal strip (i.e., a band with boundaries of constant latitude). (b) Show that within any zonal strip  $\eta$  is a maximum where  $\mu = \mu_0$ .

**4.9 Spectra with anisotropic scattering.** Use the first approximation to compare the variation of a weak line from center to limb for a planet at full phase  $\Phi = 180^\circ$  when  $\tilde{\omega}_c = 1.00$  for forward scattering ( $a = 1$ ) and backward scattering ( $a = -1$ ). Explain why the line absorption is stronger for  $a = +1$  in the center of the image.

**4.10 Bond albedo.** In the case of a planet reflecting as a Lambertian surface (i.e., isotropically) with a ground albedo  $\Lambda$ , show that the geometric albedo is  $\lambda(0) = \frac{2}{3}\Lambda$ , the phase integral is  $q = \frac{3}{2}$ , and hence the Bond albedo is  $\Lambda_B = \Lambda$ .

**4.11 Stokes parameters.** (a) Show that phase lag  $\delta$ , polarization angle  $\chi$ , and ellipticity angle  $\beta$  are related by (4.3.15) and that  $U$  is given by (4.3.16). (b) Derive (4.3.17).

## ***Chapter 5***

# **IONOSPHERES**

### **5.1 Formation of Ionospheric Regions**

Discovery of the ionosphere has an interesting history that is summarized on pp. 270–1. The Earth's ionosphere is divided into several regions designated by the letters D, E, and F, the latter being subdivided into F1 and F2. Historically, the division arose from the successive plateaus of electron density  $N_e$  observed on records of the time delay (i.e., *virtual height*) of radio reflections as the transmitted signal was swept through frequency; see Fig. 5.1. (The *critical frequency* at which reflection occurs varies as  $N_e^{1/2}$ . Thus higher frequencies penetrate farther into the ionosphere and are reflected by higher  $N_e$ ; cf. Section 5.2.) The E “layer” was the first to be detected and was so labeled as being the atmospheric layer reflecting the E vector of the radio signal. Later the lower D and higher F layers were discovered.

Distinct ionospheric regions develop because (a) the solar spectrum deposits its energy at various heights depending on the absorption characteristics of the atmosphere, (b) the physics of recombination depends on the density, and (c) the composition of the atmosphere changes with height. Thus the four main ionospheric regions can be associated with different governing physical processes, and this physics (rather than simple height differentiation) is the basis for labeling an ionospheric region on another planet as a D, E, F1, or F2 region.

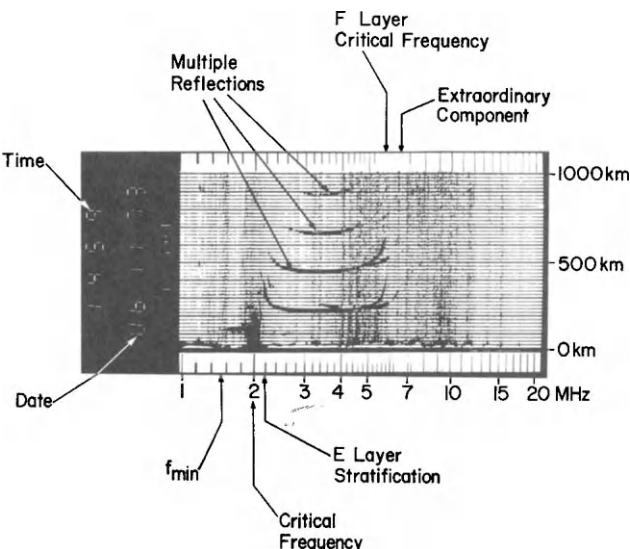


**Fig. 5.1** Ionogram, giving the virtual height of reflection *versus* the transmitted frequency ( $f$ ). As increasing frequency approaches the critical frequency for F-region reflection, the signal rises steeply on the record and then disappears as reflection becomes impossible. This record was obtained at Slough in England U.T. 1459 hours, Nov. 6, 1973, and thus indicates daytime conditions. Below about 1.6 MHz (in the AM radio band) D-region absorption prevents the signal from being reflected. The “ordinary” and “extraordinary” polarization components transmit differently because of differing refractive indices. The echo reflections at about two, three, and four times the height of the main reflections arise from multiple reflections between ionosphere and ground. (Courtesy, H. RISHBETH and Science Research Council, Appleton Laboratory, Slough, United Kingdom.)

Even though ionospheric recombination does not necessarily vary as the square of the electron density  $N_e$ , that dependence is common under uncomplicated circumstances. Hence it is phenomenologically useful to consider recombination as occurring at a rate described by an *effective recombination coefficient*  $\alpha_{\text{eff}}$  so that  $N_e$  can be described by

$$\frac{dN_e}{dt} = q - \alpha_{\text{eff}} N_e^2 \quad (5.1.1)$$

where  $q$  is the production rate of free electrons. Table 5.1 gives a thumbnail sketch of the Earth's ionospheric regions with characteristic values, determined observationally, of  $\alpha_{\text{eff}}$ . Tables 5.2 and 5.3 show the frequency ranges used for different communication purposes, which are largely dictated by the properties of the ionosphere. In the following sections we will develop the basic physical processes that give the unique characteristics to each ionospheric region.

TABLE 5.1 *The Ionosphere*

| Region | Nominal height of layer peak (km) | $N_e^{(\max)}$ ( $\text{cm}^{-3}$ )                    | $\alpha_{\text{eff}}$ ( $\text{cm}^3/\text{sec}$ ) | Ion production  | Recombination   |
|--------|-----------------------------------|--|--|---|---|
| D      | 90<br>Lower following solar flare | $1.5 \times 10^4$ (noon);<br>absent at night           | $3 \times 10^{-8}$                                 | Ionization by solar X-rays, or Ly $\alpha$ ionization of NO. Enhanced ionization following solar flares due to X-ray ionization of all species. Electron attachment to O and O <sub>2</sub> forms negative ions; ratio of negative ions to electrons increases with depth and at night.   | Electrons form negative ions, which are destroyed by photodetachment (daytime only), associative detachment (O + O <sup>-</sup> → O <sub>2</sub> + e), and mutual neutralization (O <sup>-</sup> + X <sup>+</sup> → O + X). |
| E      | 110                               | $1.5 \times 10^5$ (noon);<br>$< 1 \times 10^4$ (night) | $10^{-8}$  | Ionization of O <sub>2</sub> may occur directly by absorption in the first ionization continuum ( $h\nu > 12.0 \text{ eV}$ ). Coronal X-rays also contribute, ionizing O, O <sub>2</sub> , and N <sub>2</sub> . Nighttime E and sporadic E (thin patches of extra ionization) are due to electron and meteor bombardment. Some E <sub>s</sub> radio reflections may be due to turbulence in normal E layer. | Dissociative recombination<br>O <sub>2</sub> <sup>+</sup> + e → O + O and<br>NO <sup>+</sup> + e → N + O.   |
| F1     | 200                               | $2.5 \times 10^5$ (noon);<br>absent at night           | $7 \times 10^{-9}$                                 | Ionization of O by Lyman "continuum" or by emission lines of He. This ionization probably accompanied by N <sub>2</sub> ionization, which disappears rapidly after sunset.  | O <sup>+</sup> ions readily transfer charge to NO and perhaps to O <sub>2</sub> <sup>+</sup> . Most of the ionization is thus in molecular form and disappears by dissociative recombination.                               |
| F2     | 300                               | $10^6$ (noon)<br>$10^5$ (midnight)                     | $10^{-10} - 10^{-9}$                               | Variabile; probably decreases with increasing height.<br>Height and electron density highly variable. Large daily, seasonal, and sunspot-cycle variations are combined with general erratic behavior.   | Recombination of molecular ions as in F1; but limiting process is here charge transfer, giving an attachment-like recombination law.  |

**TABLE 5.2** Designations of Radio Bands

| Frequency designation | Frequency range | Wavelength designation | Common uses in communications                        |
|-----------------------|-----------------|------------------------|--|
| Very low (VLF)        | 3–30 kHz        | ten-kilometric         | Maritime mobile; radio navigation                    |
| Low (LF)              | 30–300 kHz      | kilometric             | Maritime mobile; radio navigation                    |
| Medium (MF)           | 300–3000 kHz    | hectometric            | Commercial AM broadcast                              |
| High (HF)             | 3–30 MHz        | decametric             | Short-wave broadcast                                 |
| Very high (VHF)       | 30–300 MHz      | metric                 | TV; FM radio; space to Earth                         |
| Ultra high (UHF)      | 300–3000 MHz    | decimetric             | TV channels 14–69; navigation; space to Earth; radar |
| Super high (SHF)      | 3–30 GHz        | centimetric            | Spacecraft communication; radar                      |
| Extremely high (EHF)  | 30–300 GHz      | millimetric            | Spacecraft communication; radar                      |

**TABLE 5.3** Microwave Bands<sup>a</sup>

| Designation | Frequency range<br>(GHz) |
|-------------|--------------------------|
| P           | 0.225 – 0.390            |
| L           | 0.390 – 1.550            |
| S           | 1.55 – 5.20              |
| X           | 5.20 – 10.90             |
| K           | 10.90 – 36.00            |
| Q           | 36.0 – 46.0              |
| V           | 46.0 – 56.0              |
| W           | 56.0 – 100.0             |

<sup>a</sup> See Westman, H. P. (ed.) (1970), "Reference Data for Radio Engineers", 5th ed.

### 5.1.1 Chapman Layer: The E and F1 Regions

Let us write the cross section for photoionization of a particular atom or molecule with number density  $N(z)$  at a given frequency as  $\sigma_v$  ( $\text{cm}^2$ ) and the total absorption coefficient as  $\kappa_v$  ( $\text{cm}^{-1}$ ). If the ionizable gas is the only constituent absorbing, then  $\kappa_v \equiv N(z)\sigma_v$ . However, in the more general

case the rate of photoionization for incident monochromatic radiation is

$$q(z, \mu_0) = N(z)\sigma_v\pi\mathcal{F}_v \exp\left[-\int_z^\infty \kappa_v(z') dz'/\mu_0\right] (\text{cm}^{-3} \text{ sec}^{-1}) \quad (5.1.2)$$

where  $\pi\mathcal{F}_v$  is the solar photon flux (photon/cm<sup>2</sup> sec) outside the atmosphere, and  $\mu_0 = \cos \chi_0$  for solar zenith angle  $\chi_0$ . If in addition we take the atmosphere to be isothermal and consider only a single, ionizable constituent, we have

$$q(z, \mu_0) = \pi\mathcal{F}_v\sigma_v N(z_0) \exp\left[-\frac{z - z_0}{H} - \frac{\sigma_v N(z_0)H}{\mu_0} e^{-(z - z_0)/H}\right] \quad (5.1.3)$$

where  $H$  is the scale height of the absorber and  $z_0$  is an arbitrary reference height. The first term in brackets is the decrease of the ionizable constituent with height and the second term represents the increase of unattenuated solar flux with height. Differentiating places the maximum production at  $z_{\max}$  given by

$$e^{(z_{\max} - z_0)/H} = \frac{N(z_0)H\sigma_v}{\mu_0} \quad (5.1.4)$$

Since the vertical optical thickness is

$$\tau_v(z) = N(z_0)H\sigma_v e^{-(z - z_0)/H} \quad (5.1.5)$$

the maximum ionization occurs where the slant optical thickness is  $\tau_v/\mu_0 = 1$ . Hence from (5.1.3) we can write the maximum production as

$$\begin{aligned} q(z_{\max}, \mu_0) &= \pi\mathcal{F}_v\sigma_v N(z_0) \exp\left[-\frac{z_{\max} - z_0}{H} - 1\right] \\ &= \frac{\pi\mathcal{F}_v\mu_0}{H} e^{-1} \end{aligned} \quad (5.1.6)$$

where we make use of (5.1.4).

We now write the maximum production for an overhead sun as

$$q_M \equiv q(z_{\max}, \mu_0 = 1) = \frac{\pi\mathcal{F}_v}{He} \quad (5.1.7)$$

and let  $z_M$  be the height  $z_{\max}$  for  $\mu_0 = 1$ . Then (5.1.3) takes the convenient form

$$q(z, \mu_0) = q_M \exp\left[1 - \frac{z - z_M}{H} - \frac{1}{\mu_0} e^{-(z - z_M)/H}\right] \quad (5.1.8)$$

This is the *Chapman production function* illustrated in Fig. 4.20.

If the recombination varies as  $N_e^2$  with a coefficient  $\alpha$  as in (5.1.1), the electron density at any height in equilibrium is

$$N_e(z, \mu_0) = \left( \frac{q_M}{\alpha} \right)^{1/2} \exp \left\{ \frac{1}{2} \left[ 1 - \frac{z - z_M}{H} - \frac{1}{\mu_0} e^{-(z-z_M)/H} \right] \right\} \quad (5.1.9)$$

We can now note three important characteristics for this idealized *Chapman layer*. Expanding the exponential about  $z_M$  for small distances compared with  $H$  gives for an overhead sun ( $\mu_0 = 1$ )

$$\begin{aligned} N_e(z, 1) &\approx \left( \frac{q_M}{\alpha} \right)^{1/2} \exp \left[ -\frac{1}{4} \left( \frac{z - z_M}{H} \right)^2 \right] \\ &\approx \left( \frac{q_M}{\alpha} \right)^{1/2} \left[ 1 - \left( \frac{z - z_M}{2H} \right)^2 \right] \end{aligned} \quad (5.1.10)$$

Thus the electron distribution is parabolic around the peak of the layer.

Secondly, from (5.1.6) the production varies as  $\cos \chi_0$ ; hence the daily, seasonal, and latitudinal variation of  $N_e$  will vary as  $(\cos \chi_0)^{1/2}$  for a layer in quasi-equilibrium with the ionizing flux.

Finally, by setting the arbitrary reference height  $z_0 = z_{\max}$  in (5.1.4) we find

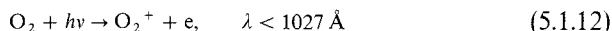
$$N(z_{\max}) = \mu_0 / H \sigma_v \quad (5.1.11)$$

Thus in principle the measurement of  $z_{\max}$  through the day could, if the theory were rigorously correct, lead to a determination of  $N$  (density of the ionizable constituent) versus  $z$  in the neighborhood of the layer peak. In practice, such an analysis becomes complicated by vertical oscillations due to atmospheric tides.

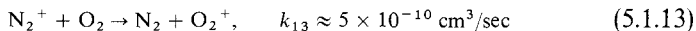
The elementary theory given above requires many refinements to be useful:

- (1) The plane-parallel geometry in which the absorbing path varies as  $\sec \chi_0$  is clearly invalid near sunrise and sunset.
- (2) The actual atmosphere has a time lag in responding to the solar zenith angle and is not in quasi-equilibrium.
- (3) The thermosphere is not isothermal, so that  $H$  varies with  $z$ .
- (4) The ionizing radiation usually covers a wide range of frequency and is not monochromatic as assumed.
- (5) The ionization does not remain at the altitude where it is produced, but moves up or down by ambipolar diffusion (with positive ions and electrons traveling together as a single gas).
- (6) Recombination is not strictly proportional to  $N_e^2$ ; this point will be examined further in the next section, for in some situations it is a very poor approximation.

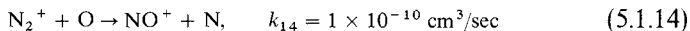
The E and F1 regions are basically Chapman layers. The E region (90--140 km) is physically the simplest. Ions are produced mainly from O<sub>2</sub> molecules by *photoionization*,



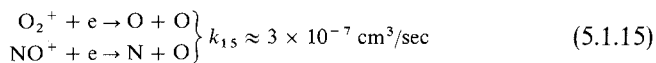
Additional ionization by coronal X-rays leads to O<sub>2</sub><sup>+</sup> and NO<sup>+</sup> ions by rapid *charge-exchange*, such as



or *atom-ion interchange*,



The molecular ions O<sub>2</sub><sup>+</sup> and NO<sup>+</sup> are of comparable density in the daytime E region (Fig. 5.2). Recombination occurs through *dissociative recombination*,



Thus  $k_{15}$  essentially accounts for  $\alpha_{\text{eff}} \sim 10^{-8} \text{ cm}^3/\text{sec}$  in the E region (Table 5.1). The E region also has a minor, long-lived component of metallic ions,

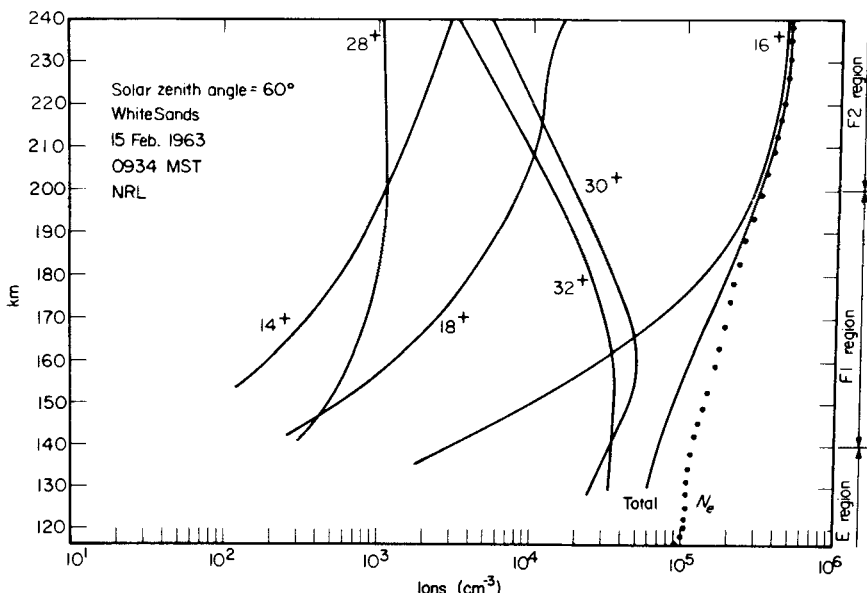


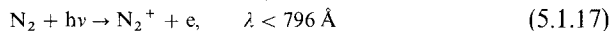
Fig. 5.2 Daytime positive ion concentrations obtained by a rocket-borne mass spectrometer. Probable identifications of the ionic mass numbers are N<sup>+</sup>(=14<sup>+</sup>), O<sup>+</sup>(=16<sup>+</sup>), H<sub>2</sub>O<sup>+</sup>(=18<sup>+</sup>—probably carried by the rocket), N<sub>2</sub><sup>+</sup>(=28<sup>+</sup>), NO<sup>+</sup>(=30<sup>+</sup>), O<sub>2</sub><sup>+</sup>(=32<sup>+</sup>). The  $N_e$  curve was obtained from an ionogram. [After HOLMES, J. C., JOHNSON, C. Y.; and YOUNG, J. M. (1965), in "Space Research," (D. G. King-Hele *et al.*, eds.), North Holland, Amsterdam, 5, 756.]

responsible for most mid-latitude sporadic E—thin patches of ionization superimposed on the regular E layer (cf. Section 5.3.2).

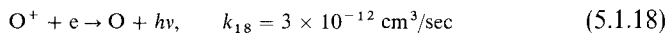
In the F1 region (140–200 km) the principal ion formed is  $O^+$  by



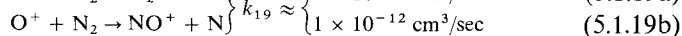
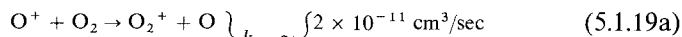
with some contribution from



The ionizing solar flux comes from the Lyman continuum,  $\lambda < 911 \text{ \AA}$ , and a large number of emission lines, among which He I (584 \AA) and He II (304 \AA) are especially prominent. The distinguishing feature between E and F1 is that the principal photoionized constituent is different. Hence the ionizing wavelengths and their depth of penetration into the atmosphere are different. In addition, there is a gradual change vertically through the F1 region in the mechanism of recombination. The atomic ions originally produced in F1 must transfer their charge to molecules prior to recombination, since *radiative recombination*,



is extremely slow. Thus F1 recombines by a two-step mechanism: *atom-ion interchange*,



followed by dissociative recombination, (5.1.15).

The lifetime for an  $O^+$  ion against destruction by (5.1.19) at 180 km is

$$\tau(O^+) = \frac{1}{k_{19a}[O_2] + k_{19b}[N_2]} \approx \frac{1}{0.0098 + 0.0067} \sim 60 \text{ sec} \quad (5.1.20a)$$

The lifetime in the day of the molecular ion is

$$\begin{aligned} \tau(NO^+) &= \frac{1}{k_{15}N_e} \\ &\approx \frac{1}{3 \times 10^{-7} \times 2.5 \times 10^5} \sim 10 \text{ sec} \end{aligned} \quad (5.1.20b)$$

Thus the ions are locked up in the atomic form, with (5.1.19) being the rate-limiting process in the upper F1 region. Consequently,  $\alpha_{\text{eff}} < k_{15}$  in F1 (Table 5.1).

In the lower F1 region (say, around 140 km), the lifetime of the atomic ion  $O^+$  is down by a factor of ten, whereas the molecular ions last somewhat

longer, because the electron density is reduced. Therefore, the molecular ions are dominant, even though it is primarily the atoms that are photoionized, and (5.1.15) is the rate limiting step. Thus, recombination changes from being limited by dissociative recombination in the lower F1 region to limitation by atom-ion interchange in the upper F1.

### 5.1.2 Low Attenuation Layer and Bradbury Recombination: The F2 Region

In the F2 region three things occur that cause the ionization profile to differ from that in F1. First, the atmosphere becomes optically thin to most ionizing radiations. Thus the second term in brackets in (5.1.3)—the second exponential—vanishes.

Second, of the two processes atom-ion interchange (5.1.19) and dissociative recombination (5.1.15), the former becomes totally dominant at high altitudes in limiting the rate of recombination. Consequently, the electron density changes at the rate

$$\frac{dN_e}{dt} = \pi \mathcal{F}_v \sigma_v [\text{O}]_0 e^{-(z-z_0)/H(\text{O})} - N_e k_{19} [\text{X}]_0 e^{-(z-z_0)/H(\text{X})} \quad (5.1.21)$$

where X represents  $\text{N}_2$  and  $\text{O}_2$  and where  $[\text{O}]_0$  and  $[\text{X}]_0$  are densities at  $z_0$ . Thus,  $k_{19}[\text{X}]_0$  is the weighted rate, in the sense defined by (5.1.20a), and  $H(\text{X})$  is the weighted scale height of  $\text{O}_2$  and  $\text{N}_2$ , as defined by (1.7.9).

The recombination term thus varies as the first power of  $N_e$ . The height variation of  $N_e$  for a neutral atmosphere in diffusive equilibrium and for ions in local chemical equilibrium is then

$$\begin{aligned} N_e(z) &= \text{const. exp} \left\{ (z - z_0) \left[ \frac{1}{H(\text{X})} - \frac{1}{H(\text{O})} \right] \right\} \\ &= \text{const. exp} \left\{ (z - z_0) \frac{g}{kT} [M(\text{X}) - M(\text{O})] \right\} \end{aligned} \quad (5.1.22)$$

Hence the electron density in chemical equilibrium would increase indefinitely with height.

This awkward state of affairs brings up the third point about F2. Clearly  $N_e$  cannot increase upward indefinitely and the mechanism that stops the increase is ambipolar diffusion. At some point the dynamical time for diffusive flow (Section 2.3.1) will become shorter than the chemical time, (5.1.20). Then the upward trend of  $N_e(z)$  will approach a diffusive equilibrium with a scale height appropriate to the ion-electron gas. Therefore, F2 cannot be treated with chemical equilibrium only. Because the recombination rate

varies as  $\beta N_e$ , where  $\beta$  is a decreasing function of height, dynamics is an essential feature of an F2 region.

In general, the linear recombination law (which also applies for different reasons in the D region; see Section 5.1.4) is known as *Bradbury* or  $\beta$  recombination, to distinguish it from the conventional  $\alpha$  recombination of Eq. (5.1.1). In the unrealistic case where  $\beta$  is independent of height, the height variation of (5.1.8) produces a Chapman-like shape of ionization density. More importantly, if we choose a fairly realistic height dependence for  $\beta$  and allow realistically for ambipolar diffusion, we also recover the Chapman height profile, as we shall now demonstrate.

### 5.1.3 Ambipolar Diffusion: Nighttime Recombination at High Altitudes

We can most simply examine the role of dynamics in structuring a high-altitude F2 layer by removing the electron production term of (5.1.21) that is, by considering recombination at night. The diffusion equation (see Section 2.3.2) will involve the scale height for the ion-electron gas in hydrostatic equilibrium. If we suppose that the neutral parent molecules, their positive ions, and the electrons all have the same temperature (as defined, say, by their mean kinetic energies), then the isothermal scale height of the ion-electron plasma ( $H_i$ ) will be twice that of the parent neutral gas ( $H_1$ ).

This result comes about from the fact that the electrons, with mass  $m \ll M$  (where  $M$  is the ion and neutral mass), tend to develop a very large scale height ( $kT/mg$ ) but are restrained from doing so by the electrostatic attraction of the ions. Thus for the ions hydrostatic equilibrium (1.1.1) becomes, for equal electron and ion densities,

$$dp_i/dz = -gN_eM + N_eeE \quad (5.1.23)$$

and, for the electrons,

$$dp_e/dz = -gN_em - N_eeE \approx -N_eeE \quad (5.1.24)$$

where  $E$  is the electrostatic field generated by the gravitational tendency for separation. Eliminating  $E$  and using the perfect gas law (1.1.2), we obtain an isothermal hydrostatic equilibrium for the plasma of

$$\frac{1}{N_e} \frac{dN_e}{dz} = -\frac{gM}{2kT} \equiv -\frac{1}{H_i} \quad (5.1.25)$$

Comparison with (1.1.5) shows that  $H_i = 2H_1$ .

Generally, temperatures of the neutral gas, positive ions, and electrons can be different. Typically, the electrons and ions are hotter than the neutral gas by several hundred degrees for the Earth and several thousand degrees for

Venus. There may also be two or more ionized species present. The treatment of these more generalized cases is a straightforward extension of the simple problem above (see Problem 5.1). For  $O^+$  ions in the Earth's thermosphere, the electric field is  $E = gM/2e = 8 \times 10^{-9}$  V/cm or 80 mV/100 km. The potential drop across the main portion of the ionosphere is therefore a few tenths of a volt. This special case of diffusive equilibrium is called *electrostatic equilibrium*.

The equation of continuity (2.1.1) with a loss term due to recombination and one-dimensional diffusion thus gives

$$\frac{\partial N_e}{\partial t} = -\beta(z)N_e + \frac{\partial}{\partial z} \left[ D(z) \left( \frac{\partial N_e}{\partial z} + \frac{N_e}{2H_1} \right) \right] \quad (5.1.26)$$

where the diffusion velocity is substituted from (2.3.1). The height dependence of the recombination coefficient is given by (5.1.21), which we write as

$$\beta(z) = k_{19}[X]_0 e^{-(z-z_0)/H(X)} \equiv \beta_0 e^{-(z-z_0)/H(X)} \quad (5.1.27)$$

The diffusion coefficient varies inversely as the total density. We will assume that the major constituent is the ionizable one—in the case of Earth's F2 it is O with scale height  $H_1$ . A magnetic field will inhibit diffusion of ions across the field lines. For  $O^+$  diffusing through O, the coefficient is

$$\begin{aligned} D(z) &= \frac{2.3 \times 10^{18} \sin^2 i}{[O(z)]} \\ &= D_0 e^{(z-z_0)/H_1} \end{aligned} \quad (5.1.28)$$

where  $i$  is the *inclination* (to the horizontal) of the field lines.

Thus we are concerned with two scale heights:  $H_1$  for the ionizable neutral gas, which is also the major constituent, and  $H(X)$  for the minor molecular constituent involved in the first step of recombination, atom-ion interchange (or charge exchange) (5.1.19). Continuity (5.1.26) thus gives

$$\frac{\partial N_e}{\partial t} = D_0 e^{(z-z_0)/H_1} \left( \frac{\partial^2 N_e}{\partial z^2} + \frac{3}{2H_1} \frac{\partial N_e}{\partial z} \right) + N_e \left( \frac{D_0 e^{(z-z_0)/H_1}}{2H_1^2} - \beta_0 e^{-(z-z_0)/H(X)} \right) \quad (5.1.29)$$

This equation is linear in  $N_e$ , making it possible to extract the time dependence, leaving a characteristic-value equation for  $N_e(z)$ .

Assuming the solution

$$N_e(z, t) = \sum_{j=0}^{\infty} N_j(z) e^{-\lambda_j t} \quad (5.1.30)$$

for constants  $\lambda_j$ , we have the equation for  $N_j(z)$ ,

$$\begin{aligned} H_1^2 e^{(z-z_0)/H_1} \left( \frac{\partial^2 N_j}{\partial z^2} + \frac{3}{2H_1} \frac{\partial N_j}{\partial z} \right) \\ - \left( \frac{H_1^2 \beta_0}{D_0} e^{-(z-z_0)/H(X)} - \frac{1}{2} e^{(z-z_0)/H_1} - \frac{H_1^2}{D_0} \lambda_j \right) N_j = 0, \quad j = 0, 1, \dots, \infty \end{aligned} \quad (5.1.31)$$

A change of variables removes the first derivative term:

$$y_j = N_j e^{(z-z_0)/4H_1}, \quad x = e^{-(z-z_0)/H_1} \quad (5.1.32)$$

Also if we consider the special case of  $H_1 = H(X)$  (which implies mixing and is not realistic for Earth's F2 region but nevertheless shows the kind of solution that emerges), we have

$$\frac{\partial^2 y_j}{\partial x^2} + \left( \frac{3}{16x^2} + \frac{H_1^2 \lambda_j}{D_0 x} - \frac{H_1^2 \beta_0}{D_0} \right) y_j = 0 \quad (5.1.33)$$

which is readily demonstrated by writing  $N_j = y_j x^{1/4}$  (Problem 5.2).

This equation has the same form as the familiar *radial wave equation* for the hydrogen atom. We seek a solution subject to two boundary conditions. First, as  $z \rightarrow \infty$  the diffusion velocity must not be infinite. Hence the term in brackets in (5.1.26) must vanish, which in turn requires that all components of  $N_e$  approach diffusive equilibrium or

$$N_j \rightarrow \text{const. } e^{-(z-z_0)/2H_1} = \text{const. } x^{1/2} \quad (5.1.34)$$

The second boundary condition requires that  $N_e$  remain bounded at low altitudes ( $z \rightarrow -\infty$ ). In terms of the  $y_j(x)$  variable of (5.1.32), these conditions are

$$\begin{aligned} y_j &\rightarrow \text{const. } x^{1/4}, & x \rightarrow 0 \\ y_j &\rightarrow 0, & x \rightarrow \infty \end{aligned} \quad (5.1.35)$$

The eigenfunctions of (5.1.33) are given in terms of generalized Laguerre polynomials,  $L_j^{-1/2}(v)$ :

$$N_j = A_j v^{1/2} e^{-v/2} L_j^{-1/2}(v) \quad (5.1.36)$$

Here  $A_j$  is a constant to be fixed by the initial electron distribution and the independent variable is

$$v = 2H_1 \left( \frac{\beta_0}{D_0} \right)^{1/2} x = 2H_1 \left( \frac{\beta_0}{D_0} \right)^{1/2} e^{-(z-z_0)/H_1} \quad (5.1.37)$$

The polynomial may be written in a power series,

$$L_j^{-1/2}(v) = 1 + a_1 v + a_2 v^2 + \cdots + a_j v^j \quad (5.1.38)$$

where the coefficients are related by the recursion relation,

$$a_{m+1} = \frac{m-j}{(m+1)(m+\frac{1}{2})} a_m, \quad m = 0, 1, \dots; \quad a_0 = 1 \quad (5.1.39)$$

The eigenvalues are

$$\lambda_j = \frac{2(\beta_0 D_0)^{1/2}}{H_1} (j + \frac{1}{4}), \quad j = 0, 1, \dots \quad (5.1.40)$$

From (5.1.30) and (5.1.40) it is apparent that solutions for large  $j$  represent short-lived fluctuations. A short time after sunset the higher-order solutions will vanish and  $N_e$  can be expressed as a linear combination of the first two or three eigenfunctions. Figure 5.3 shows  $N_0$ ,  $N_1$ , and  $N_2$  on an arbitrary scale of unity for the maximum of each curve. We assume for illustration that  $[O(z_0 = 300 \text{ km})] = 3 \times 10^9 \text{ cm}^{-3}$ ,  $H_1 = 50 \text{ km}$ ,  $D_0 = 7 \times 10^8 \text{ cm}^2/\text{sec}$ , and  $\beta_0 = 10^{-4} \text{ sec}^{-1}$ .

As  $N_2$  and  $N_1$  decay with lifetimes, respectively, of  $1/\lambda_2 = 1.1 \text{ hr}$  and  $1/\lambda_1 = 2.0 \text{ hr}$ , the peak altitude rises provided  $A_2$  and  $A_1$  are positive. The relative importance of these "overtone" solutions will be governed by the initial distribution of  $N_e$  and the  $A_j$ 's can be negative provided  $N_e$  is everywhere and at all times positive.

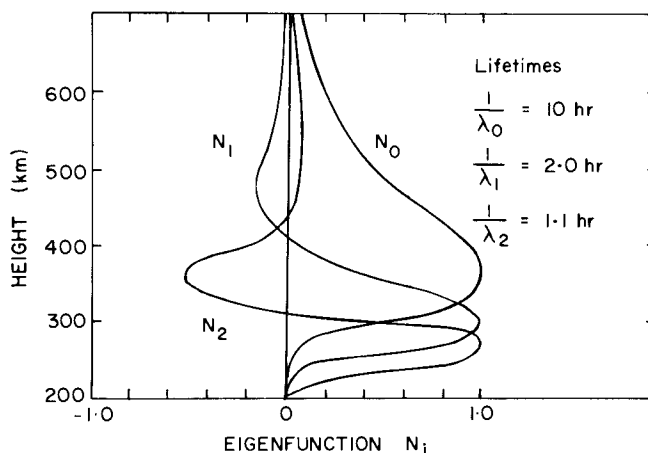


**Fig. 5.3** The first three eigenfunctions for the decay of an idealized nighttime F region.  
[Adapted from CHAMBERLAIN (1961).]

After several hours

$$N_e \rightarrow N_0 e^{-\lambda_0 t} \quad (5.1.41)$$

The maximum height and shape of F2 then no longer changes with time. The peak has risen to 365 km and  $N_e$  decays with a lifetime of  $\lambda_0^{-1} = 10$  hr. The distribution with height from (5.1.36) is

$$N_0(z) = \text{const } e^{-(z-z_0)/2H_1} \exp[-H_1(\beta_0/D_0)^{1/2}e^{-(z-z_0)/H_1}] \quad (5.1.42a)$$

which is in the form of a Chapman layer (5.1.9). Around the peak the electron distribution is parabolic and at high altitudes it is in diffusive equilibrium.

Mathematically the eigenvalue nature of the solution is a result of the linearity of (5.1.26). Physically this linearity means that for each eigenfunction the relative decay rate,  $N_j^{-1} \partial N_j / \partial t = -\lambda_j$ , is a constant with time and height. Thus when only the zeroth-order solution remains, the flux convergence of diffusive flow is exactly compensated, at every height, by recombination loss—except for a constant diffusive loss rate  $\lambda_0$  arising from a constant downward flow velocity (see Problem 5.2). Consequently, the layer retains a constant shape.

With this approximation of a mixed thermosphere [i.e.,  $H_1 = H(X)$ ], the ionization peak occurs where  $D(z)/H_1^2 = 4\beta(z)$ . Well below the peak, the loss of ions is governed by recombination; at very high altitudes the loss is due to vertical ambipolar diffusion. Hence, it was to be expected that the peak would occur near the height where the diffusion time  $H_1^2/D(z)$  is comparable to the recombination time  $1/\beta(z)$  [i.e.,  $\beta(z) \sim D(z)/H_1^2$ ].

For a more realistic model in which  $H_1 = 2H(X)$ , corresponding to diffusion through O and recombination of electrons with  $O_2^+$ , the eigenvalues cannot be obtained analytically but can be found numerically with a variational principle. The solution gives  $(4\beta_0 H_1^2/D_0)^{2/3} \lambda_0/\beta_0 = 1.06$  for the lowest eigenvalue, and this corresponds to a lifetime of  $1/\lambda_0 = 15$  hr. [Since  $D^2(z)/\beta(z)$  is independent of height, it makes no difference at what height  $\beta_0$  and  $D_0$  are evaluated.]

This simplified treatment ignores the important effects of horizontal winds which, by moving the ions across magnetic-field lines, produce a vertical component of the Lorentz force,  $ev \times \mathbf{B}/c$ .

Another item omitted from this discussion is the presence of  $H^+$  ions (or protons). Because O and H have ionization potentials that are equal (to within a small fraction of thermal energies), the reaction



is accidentally resonant. Writing the rate coefficients for forward and backward reactions as  $k_f$  and  $k_b$ , we have

$$[O^+][H]k_f = [O][H^+]k_b \quad (5.1.42c)$$

When the ionization potentials of two species are essentially identical, the ratio of neutral/ion depends, in thermodynamic equilibrium according to the Saha ionization formula, only on the ratio of statistical weights in the ground states. That ratio in turn establishes the ratio of reaction rates, which is valid for all conditions, not merely thermodynamic equilibrium. Thus, we have for the case at hand,

$$\begin{aligned} \frac{[\text{O}^+]/[\text{O}]}{[\text{H}^+]/[\text{H}]} &= \frac{k_b}{k_f} = \frac{\tilde{\omega}(^4\text{S})/\tilde{\omega}(^3\text{P})}{\tilde{\omega}(\text{H}^+)/\tilde{\omega}(^2\text{S})} = \frac{\frac{4}{9}}{\frac{1}{2}} \\ &= \frac{8}{9} \end{aligned} \quad (5.1.42d)$$

Although this equilibrium ratio is valid at high temperatures, say well above 1000°K, in the daytime there is a net production and upward flux of protons due to the photoionization of O in the region of the F2 peak. At night these protons descend again, produce O<sup>+</sup>, and help to sustain the nighttime ionosphere. This effect occurs because at low temperatures the Boltzmann factors operating between the ground-term oxygen triplet and the hydrogen doublet become important, and the ratio of (5.1.42d) falls to 0.55 at 300°K, producing the upward daytime flux. In addition, the content of the upper ionosphere is proportional to temperature.

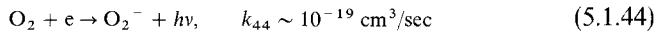
### 5.1.4 Ion Chemistry in the D Region

The distinguishing feature of the D region (75–90 km) is the predominance of negative ions. In addition, the chemistry of both positive and negative ions is complicated because many reactions are possible at the relatively high pressure in this region. These details are summarized in the latter part of this section; we begin the discussion here with a simplified overview.

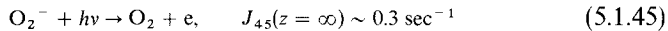
The N<sub>2</sub> molecule does not form a stable negative ion but O<sub>2</sub> does. These ions are formed by *three-body attachment*,



(The third body may also be N<sub>2</sub> but the rate coefficient is then substantially lower.) The three-body process is more important at D-region densities ([O<sub>2</sub>] ≈ 10<sup>13</sup>–10<sup>14</sup> cm<sup>-3</sup>) than *radiative attachment*,



The electrons may be removed from O<sub>2</sub><sup>-</sup> in the daytime by *photodetachment* (the inverse of the above process),

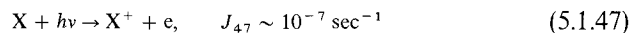


and in day and night by *collisional detachment* [the inverse of (5.1.43)],

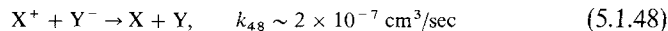


The electron affinity (i.e., ionization potential) of  $\text{O}_2^-$  is 0.43 eV. (The rate of  $k_{46}$  is extremely sensitive to temperature and the quoted value is an estimate for 200°K obtained from considerations of detailed balancing; see Problem 5.3.) Because this reaction is so slow, similar reactions with minor constituents (or molecules in metastable states) may be more significant detachment processes at night.

Positive ions and electrons are created through photoionization of  $\text{N}_2$  and  $\text{O}_2$  by X-rays and by Lyman alpha ionization of the minor constituent NO:



The ultimate loss of ionization occurs when the positive ions are neutralized, not simply when the free electrons disappear by attachment. The main recombination process when electrons are attached to molecules forming negative ions is *mutual neutralization*,



In addition to recombining by attachment (5.1.43) followed by mutual neutralization (5.1.48), free electrons can disappear directly through dissociative recombination (5.1.15), and this reaction must be considered for the daytime equilibrium.

On the basis of this limited chemistry we can set up equations for the time variation of the density of free electrons  $N_e$ , positive ions  $N^+$ , and negative ions  $N^-$ . We write the ratio

$$\lambda \equiv N^-/N_e \quad (5.1.49)$$

If the free-electron population is produced by (5.1.45), (5.1.46), and (5.1.47) and destroyed mainly by (5.1.43), we have

$$\frac{dN_e}{dt} = J_{45}\lambda N_e + k_{46}\lambda[\text{O}_2]N_e + J_{47}[\text{X}] - k_{43}[\text{O}_2]^2N_e \quad (5.1.50)$$

The loss process for free electrons (5.1.43) is linear with  $N_e$  and thus follows the  $\beta$ - or Bradbury-recombination law discussed in Section 5.1.2. Positive ions are destroyed only by (5.1.48) so that

$$\begin{aligned} \frac{dN^+}{dt} &\equiv (1 + \lambda)\frac{dN_e}{dt} + N_e \frac{d\lambda}{dt} \\ &= J_{47}[\text{X}] - k_{48}\lambda(1 + \lambda)N_e^2 \end{aligned} \quad (5.1.51)$$

or

$$\frac{dN_e}{dt} = \frac{J_{47}[X]}{1 + \lambda} - k_{48}\lambda N_e^2 - \frac{N_e}{1 + \lambda} \frac{d\lambda}{dt} \quad (5.1.52)$$

Written in this form the *effective production rate* of electrons, for constant  $\lambda$ , is [see (5.1.1)]

$$q_{\text{eff}} = \frac{J_{47}[X]}{1 + \lambda} \quad (5.1.53)$$

and the *effective recombination rate* is

$$\alpha_{\text{eff}} = k_{48}\lambda \quad (5.1.54)$$

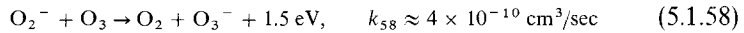
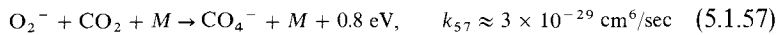
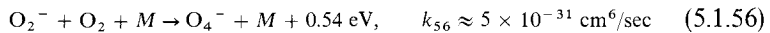
At night the  $J$ 's vanish and Eq. (5.1.50) indicates that free electrons rapidly disappear after sunset. One can solve (5.1.50) and (5.1.52) simultaneously for quasi-equilibrium to find daytime values of  $N_e$  and  $\lambda$  as functions of height and solar zenith angle. For many years it seemed that the  $O_2^-$  chemistry summarized above accounted for the D-region ionization in a satisfactory way. However, reaction (5.1.45) detaches the electron with visual light and detailed observations of two types failed to conform to expectations. First, twilight observations of the D region following ionization surges caused by particle bombardment from solar flares (*polar-cap absorption* or *PCA events*) showed the free electrons disappearing earlier than expected. Second, high-altitude nighttime tests of nuclear weapons in 1962 did not produce the extensive radio blackouts expected on the following mornings when sunlight could photodetach the high levels of ionization produced by gamma rays from the weapon. (Radio propagation effects are discussed in Section 5.2.) Both effects indicated that the electrons were bound to molecules that required ultraviolet rather than visual light to photodetach the electrons. The negative ions must therefore have electron affinities of several eV.

Laboratory work has greatly clarified the problem but has also shown it has surprising complexity. Figure 5.4 shows the chain of reactions that leads to the formation of  $NO_2^-$  and  $NO_3^-$  ions, which have electron affinities of 2.5 and 3.6 eV, respectively.

The  $O_2^-$  ion when formed may react with O to release the electron,



which merely starts the process over again by (5.1.43). But  $O_2^-$  may also react with  $O_2$  or  $CO_2$  or undergo charge transfer with  $O_3$ :



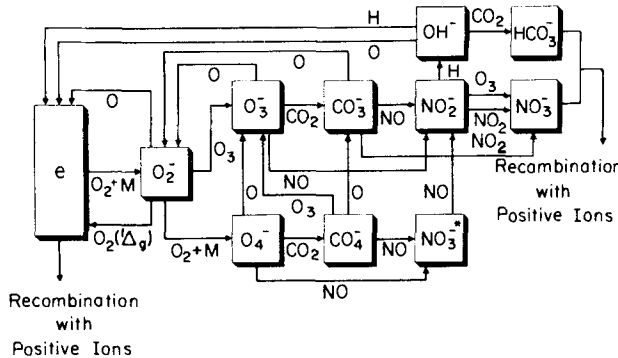
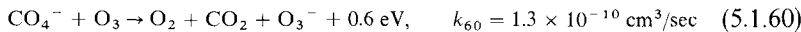


Fig. 5.4 Schematic diagram of negative-ion reactions in the D region with hydration neglected. [After FERGUSON (1974).]

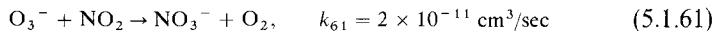
The O<sub>4</sub><sup>-</sup> of (5.1.56) is connected to CO<sub>4</sub><sup>-</sup> by



and CO<sub>4</sub><sup>-</sup> reacts with ozone by



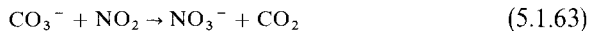
The terminal ion is probably formed by



and



followed by

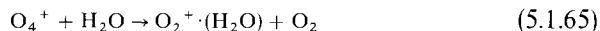


The ion chemistry is further complicated by hydration. The large dipole moment of H<sub>2</sub>O allows it to become attached readily to positive and negative ions alike, and clusters of even three or more water molecules can develop. The presence of the hydration affects the electron affinity and reaction rates of the molecule.

Positive-ion chemistry is also complicated. The N<sub>2</sub><sup>+</sup> and O<sub>2</sub><sup>+</sup> will readily transfer positive charge to NO, which has a lower ionization potential. Mass spectrometers flown on rockets have shown, however, that water-derived ions H<sub>3</sub>O<sup>+</sup>, H<sub>5</sub>O<sub>2</sub><sup>+</sup>, and H<sub>7</sub>O<sub>3</sub><sup>+</sup> are dominant. The principal reactions appear to be ion-molecule association,



followed by hydration,



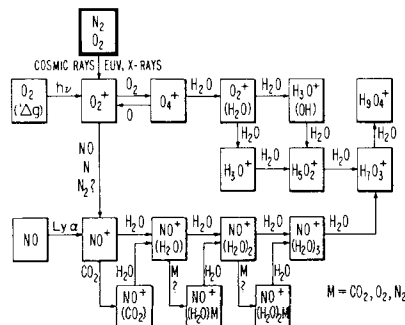


**Fig. 5.5** Schematic diagram of positive-ion reactions in the D region with hydration neglected. [After FERGUSON (1971).]

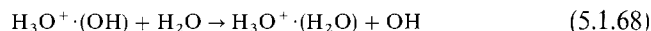
and either



or



followed by



Continued interaction with  $\text{H}_2\text{O}$  builds up the heavier ions. Figure 5.5 shows alternate sequences of positive-ion reactions.

## 5.2 Radio Waves in an Ionized Atmosphere

In an ionized medium, the real index of refraction is less than unity and can even drop to zero. This characteristic, which occurs in the medium- and high-frequency (MF and HF) ranges of the spectrum (0.3–30 MHz) in the Earth's ionosphere, makes radio sounding of the ionosphere the powerful technique it is. The index of refraction is also affected by a magnetic field, which greatly complicates the theory.

For later reference we write Maxwell's equations in Gaussian units (where current density  $\mathbf{J}$  is given in electromagnetic units and conductivity  $\sigma$  is in electrostatic units). The electric field is  $\mathbf{E}$ ; magnetic induction is  $\mathbf{B}$ ; permeability,  $\mu$ ; dielectric constant or permittivity,  $\kappa$ ; and  $e$  is the positive elementary charge. Ampere's law is

$$\nabla \times \left( \frac{\mathbf{B}}{\mu} \right) = 4\pi\mathbf{J} + \frac{1}{c} \frac{\partial(\kappa\mathbf{E})}{\partial t} \quad (5.2.1)$$

Faraday's law is

$$\nabla \times \mathbf{E} = -\frac{1}{c} \frac{\partial \mathbf{B}}{\partial t} \quad (5.2.2)$$

the magnetic lines of force are continuous, or

$$\nabla \cdot \mathbf{B} = 0 \quad (5.2.3)$$

and electrostatic lines of force start and stop on charges, or

$$\nabla \cdot (\kappa \mathbf{E}) = e4\pi(N_i - N_e) \quad (5.2.4)$$

where  $N_i$  and  $N_e$  are singly-charged ion and electron number densities. In a stationary atmosphere with no magnetic field, Ohm's law is

$$\mathbf{J} = \sigma \mathbf{E}/c \quad (5.2.5)$$

When there is no net charge ( $N_i = N_e$ ) and when  $\mu$  and  $\kappa$  are independent of time and position, we obtain the common wave equation by taking the curl of (5.2.2). Then eliminating the resulting term in  $\nabla \cdot \mathbf{E}$  with (5.2.4),  $\nabla \times \mathbf{B}$  with (5.2.1), and  $\mathbf{J}$  with (5.2.5) yields

$$\nabla^2 \mathbf{E} - \frac{\mu\kappa}{c^2} \frac{\partial^2 \mathbf{E}}{\partial t^2} - \frac{4\pi\sigma\mu}{c^2} \frac{\partial \mathbf{E}}{\partial t} = 0 \quad (5.2.6)$$

When  $\sigma$  is sufficiently large, the second term is negligible and  $\mathbf{E}$  is governed by a heat-conduction or diffusion equation. When  $\sigma = 0$  and  $\mu\kappa$  is real, (5.2.6) is the ordinary wave equation, and the phase velocity is  $c/n$ , where  $n = (\kappa\mu)^{1/2}$  is the ordinary index of refraction of the medium.

### 5.2.1 An Ionosphere with No Magnetic Field: Critical Reflection

Let us examine propagation of a radio wave in a uniform, ionized medium (where uniformity means that any departures from homogeneity are on a scale large compared with the wavelength). With  $\mu = 1$  the wave equation is

$$\nabla^2 \mathbf{E} = \frac{\kappa}{c^2} \frac{\partial^2 \mathbf{E}}{\partial t^2} \quad (5.2.7)$$

The oscillating  $\mathbf{E}$  field sets electrons in motion. When these electrons collide with the gas molecules with a collision frequency  $v_c$ , two related things occur. The amount of energy re-emitted as electromagnetic radiation is diminished and the electron's motion lags behind the phase of the incident wave. Thus

using complex exponentials to treat the phase will lead to a real (negative) exponential that we can identify with the absorption coefficient of the atmosphere.

Writing  $\mathbf{E}(t) = \mathbf{E}_0 e^{-i\omega t}$ , where  $\omega = 2\pi v$  and  $v$  is the radiation frequency (cycle/sec  $\equiv$  hertz), the equation of motion of an electron is

$$m \frac{d^2 \mathbf{x}}{dt^2} = -e \mathbf{E}_0 e^{-i\omega t} - mv_c \frac{d\mathbf{x}}{dt} \quad (5.2.8)$$

where  $\mathbf{x}$  is the electron displacement from its neutral position and  $m$  is the electron mass. We are supposing that in a collision the electron loses all its momentum. The steady-state solution must clearly vary as  $e^{-i\omega t}$  and is

$$\mathbf{x} = \frac{-i}{v_c - i\omega} \frac{e}{\omega m} \mathbf{E}_0 e^{-i\omega t} \quad (5.2.9)$$

To see how the  $\mathbf{E}$  field itself varies, we relate the dielectric constant to the polarization  $\mathbf{P}$ , here caused by the displacement of electrons from their electrically neutral position. Thus we have

$$\kappa \equiv 1 + 4\pi \frac{\mathbf{P}}{\mathbf{E}} = 1 - \frac{4\pi N_e e \mathbf{x}}{\mathbf{E}} = 1 + \frac{i4\pi \sigma_p}{\omega} \quad (5.2.10)$$

where we define

$$\sigma_p = \frac{N_e e^2 (v_c + i\omega)}{m(\omega^2 + v_c^2)} \quad (5.2.11)$$

That the quantity  $\sigma_p$  is a complex conductivity can be seen from Ohm's law, (5.2.5), where the polarization current,  $(1/c) d\mathbf{P}/dt = -(N_e e/c) d\mathbf{x}/dt$ , replaces the conduction current  $\mathbf{J}$  (also see Problem 5.5).

The wave equation (5.2.7) has a plane-wave solution

$$E(z, t) = E_0 \exp[-i\omega(t - \kappa^{1/2} z/c)] \quad (5.2.12)$$

where  $z$  is the distance along the path of propagation. From (5.2.10) and (5.2.11), the real part of  $\kappa$  is

$$\kappa_0 = 1 - \frac{4\pi N_e e^2}{m(v_c^2 + \omega^2)} = 1 - \frac{\omega_0^2}{\omega^2 + v_c^2} \quad (5.2.13)$$

where the *plasma frequency* is

$$\omega_0 = (4\pi N_e e^2 / m)^{1/2} \quad (5.2.14)$$

To obtain the real index of refraction and the absorption coefficient, we write  $\kappa^{1/2} = n + ig$  or  $\kappa = n^2 - g^2 + i2ng$ . Then we have from (5.2.10).

$$\kappa = \kappa_0 + i4\pi\sigma_0/\omega \quad (5.2.15)$$

where the real part of  $\sigma_P$  is

$$\sigma_0 = \frac{N_e e^2 v_c}{m(\omega^2 + v_c^2)} \quad (5.2.16)$$

Solving simultaneously for  $n^2$  and  $g$  in terms of  $\kappa_0$  and  $\sigma_0$  we obtain the real index of refraction  $n$  from

$$n^2 = \frac{\kappa_0}{2} + \left( \frac{\kappa_0^2}{4} + \frac{4\pi^2 \sigma_0^2}{\omega^2} \right)^{1/2} \quad (5.2.17)$$

The absorption coefficient is obtained by considering the attenuation with distance of the mean intensity (averaged over an oscillation). Thus from (5.2.12)  $I = \frac{1}{2}\mathbf{E} \cdot \mathbf{E}^* = I_0 \exp(-2\omega g z/c)$  and the volume absorption coefficient is

$$k = \frac{2\omega g}{c} = \frac{4\pi\sigma_0}{cn} (\text{cm}^{-1}) \quad (5.2.18)$$

At high collision frequencies  $v_c \gg \omega$ , (5.2.16) gives the kinetic theory value of  $\sigma_0$  proportional to  $1/v_c$ . When the collision frequency is low ( $v_c \ll \omega$ ), the conductivity  $\sigma_0$  varies directly as  $v_c$ ; that is, collisions are required for the electrons to carry any net conduction current. But since  $\sigma_0$  is small,

$$n \equiv \kappa_0^{1/2} = (1 - \omega_0^2/\omega^2)^{1/2} \quad (5.2.19)$$

and waves with a circular frequency  $\omega < \omega_0$  cannot propagate in the medium. In the ionosphere waves will be prohibited from entering the region where  $\omega_0 \geq \omega$  by refraction or reflection. If the incident angle, measured from the normal, is  $\theta_0$ , the wave will, according to Snell's law, be turned back at an electron density corresponding to  $n = \sin \theta_0$ . For the particular case of vertical incidence ( $\theta_0 = 0$ ), *critical reflection* occurs when  $\omega_0 = \omega$  and  $n = 0$ . The electron density required to reflect a wave with frequency  $v = \omega/2\pi$  is, from (5.2.14),

$$N_e = \frac{\pi m v^2}{e^2} = 1.24 \times 10^4 v^2 \quad (5.2.20)$$

where  $v$  is measured in megahertz and  $N_e$  in electron/cm<sup>3</sup>. The absorption coefficient for  $v_c \ll \omega$  is

$$k = \frac{4\pi N_e e^2 v_c}{mc\omega(\omega^2 - \omega_0^2)^{1/2}} \quad (5.2.21)$$

At  $\omega \approx \omega_0$  the coefficient is large, high attenuation being associated with a low  $n$ . At frequencies well above the local plasma frequency ( $\omega \gg \omega_0$ ), the absorption varies as  $\omega^{-2}$ . Thus high-frequency (short-wave) radio is less susceptible to daytime D-region absorption than is the medium-frequency commercial broadcast band.

The cyclic plasma frequency  $\omega_0/2\pi$  is the natural (plane-wave) frequency for coherent oscillation of electrons in the plasma. The *critical frequency*  $v_0$  of an ionized layer is the maximum frequency ( $\omega/2\pi$ ) reflected and hence the maximum value of  $\omega_0/2\pi$  in the layer.

The theory for the dispersion relation (5.2.17) in the presence of an external magnetic field will be examined in Section 5.2.5.

### 5.2.2 Refraction for Grazing Incidence: Spacecraft Occultations

One of the most powerful tools for sensing atmospheres of other planets with spacecraft has been the occultation of SHF and UHF radio waves. The technique is especially valuable when it has been possible to use two frequencies, the higher one (the X band at 8400 MHz) being nearly unaffected by the ionosphere and the lower UHF frequency (the S band at 2300 MHz) being somewhat altered. These frequencies are coherent at a ratio of 3/11.

In the following we will consider the radio signals to be transmitted from Earth to the spacecraft (the uplink mode) with the information received by the spacecraft being read out at a later time. This was in fact the procedure used on Mariner 5 (Venus). Later occultation experiments were designed for downlink operation, or sometimes an uplink-downlink round trip, with a transponder on the spacecraft returning a signal to Earth. The basic theory is, of course, independent of the sense of transmission.

Suppose the signal transmitted from Earth is received and recorded by the spacecraft. As the spacecraft passes behind the planet (Fig. 5.6), the

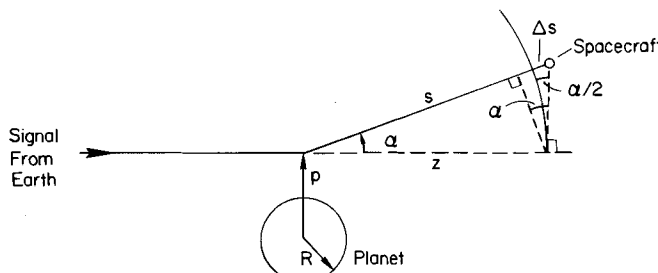


**Fig. 5.6** Geometry of refraction of a radio wave passing through an ionosphere to a spacecraft receiver. The angle of refraction is  $\alpha$  for a ray that has an impact parameter  $p$ .

atmosphere affects the signal in two related ways: the changing index of refraction causes the signal to be deflected and its phase to be shifted. The phase shift is the quantity measured.

Since the phase velocity is  $c/n$ , an unmodified wave will arrive at the spacecraft at time  $t$  and distance  $s$  from the transmitter with phase  $\phi_0 = -(\omega t - \omega s/c)$ , whereas the wave passing through an atmosphere with index  $n$  will have an altered phase of  $\phi_1 = -(\omega t - n\omega s/c)$ . Thus the phase shift is

$$\phi \equiv \phi_1 - \phi_0 = \frac{\omega}{c} \int_{-\infty}^{\infty} (n - 1) ds \quad (5.2.22)$$

For  $n < 1$  the phase velocity of the wave is advanced and therefore the phase shift is negative (a given phase arrives earlier than it would for an unmodified wave).

The phase shift and angle of refraction are related through the index of refraction, but the refraction angle  $\alpha$  also affects the total path length and thereby produces an additional phase shift. Therefore, we must first express  $\alpha$  in terms of the phase shift (5.2.22) caused by the changed phase velocity. Then we can find the additional effect due to the path length. The angle of refraction is obtained from Snell's law, but because  $n$  steadily changes through the atmosphere, the total deviation is a bit complicated. Consider the refraction occurring as a ray enters a thin layer between  $r$  and  $r'$  (Fig. 5.7). From the triangle OAB we have

$$\frac{r}{\sin \psi} = \frac{r'}{\sin \theta} \quad (5.2.23)$$

and Snell's law gives

$$n' \sin \theta' = n \sin \psi \quad (5.2.24)$$

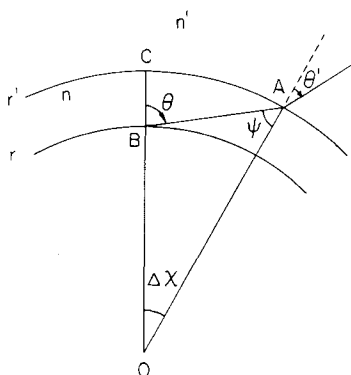


**Fig. 5.7** Refraction of a ray as it passes from a region of refractive index  $n'$  into a thin spherical shell with index  $n$ .

Eliminating  $\psi$  gives

$$nr \sin \theta = n'r' \sin \theta' \quad (5.2.25)$$

With  $n' = n + \Delta n$ , and so forth, the differential form of (5.2.25) becomes

$$\frac{dr}{r} + \frac{dn}{n} + \frac{d\theta}{\tan \theta} = 0 \quad (5.2.26)$$

The differential refraction is

$$\Delta\alpha \equiv \theta' - \psi \equiv \theta' - (\theta - \Delta\chi) \quad (5.2.27)$$

and from the small triangle ABC in Fig. 5.7 we have

$$r' \Delta\chi \approx \Delta r \tan \theta \quad (5.2.28)$$

Removing  $dr/r$  with (5.2.28) and writing  $d\theta + d\chi$  in terms of  $d\alpha$  by (5.2.27), we obtain from (5.2.26)

$$d\alpha = -\tan \theta dn/n \quad (5.2.29)$$

Now suppose that in traversing a shell of thickness  $dr$  the ray covers a total distance  $ds$  and experiences a change in index of  $dn$ . We wish to find the change in index of refraction over a given ray path  $ds$  when the *impact parameter*  $p$  is changed by amount  $dp$ , since  $p$  is the coordinate that observationally is known. From Fig. 5.8 the segment of ray path  $ds$  through the shell  $dr$  is displaced out of the shell if the impact parameter is increased by  $dp$ , or

$$\frac{dn}{ds} = -\frac{dn}{dr} \cos \theta = -\left(\frac{dn}{dp} \frac{1}{\sin \theta}\right) \cos \theta \quad (5.2.30)$$

Consequently, the total angle of refraction when  $n \approx 1$  (i.e., for  $\omega$  far from the critical frequency) is given by

$$\begin{aligned} \alpha &= -\int \frac{dn}{n} \tan \theta = -\int_{-\infty}^{\infty} \frac{\tan \theta}{n} \frac{dn}{ds} ds \\ &= \int_{-\infty}^{\infty} \frac{1}{n} \frac{dn}{dp} ds = \frac{d}{dp} \int_{-\infty}^{\infty} (n-1) ds \\ &= \frac{c}{\omega} \frac{d\phi}{dp} \end{aligned} \quad (5.2.31)$$

This expression relates the refraction angle to the phase advancement due to the change in phase velocity caused by the lower index  $n$ . As noted above, offsetting this effect is a phase retardation due to the bending of the ray, which increases the distance traversed compared with the straight-line

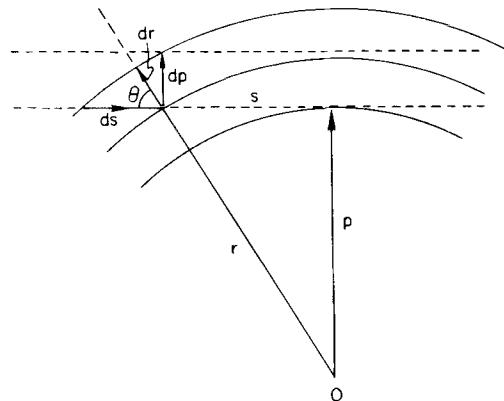


**Fig. 5.8** Geometry associated with the change in the refractive index accompanying a change  $dp$  in the impact parameter as the spacecraft moves behind (or out from) the planet. (Note that  $ds$  is always positive in the direction of propagation; for instance, we have  $0 \leq \theta \leq \pi/2$ , but for emergence the angle as shown must be regarded as  $\theta + \pi$ .)

distance. In Fig. 5.6 the increased distance of transmission due to the deflection  $\alpha$  is

$$\Delta s = \alpha z(\alpha/2) = \frac{1}{2}z\alpha^2 \quad (5.2.32)$$

The total or integrated phase lag due to the velocity change and the path length change is, from (5.2.31) and (5.2.32), respectively,

$$\phi = \frac{\omega}{c} \int (n - 1) ds + \frac{\omega}{c} \frac{z\alpha^2}{2} \quad (5.2.33)$$

With  $\alpha$  related to  $n$  by (5.2.31) and  $n$  given by (5.2.19) and (5.2.14), we obtain for  $\omega \gg \omega_0$

$$\phi = -\frac{\omega}{c} I + \frac{z\omega}{2c} \left( \frac{dI}{dp} \right)^2 \quad (5.2.34)$$

where

$$I \equiv - \int (n - 1) ds = \frac{e^2}{2\pi m v^2} \int_{-\infty}^{\infty} N_e(s) ds \quad (5.2.35)$$

The first term in (5.2.34) is normally the dominant one, and hence the phase shift is negative. The use of two frequencies simplifies the determination of the phase shift. If only one frequency is used the spacecraft's position must be known with high accuracy. Thus the simultaneous measurement of  $\phi(t)$  with position  $p(t)$  allows one to infer the tangentially integrated electron density, or  $I(p)$ , for varying impact parameters  $p$ , and hence reconstruct  $N_e$ .

*versus* height  $r$  above the center of the planet. A simple example is given in Problem 5.7.

In addition to the phase shift and deflection, differential refraction causes focusing and defocusing as the ray passes through the ionosphere and defocusing in the lower atmosphere (where  $n > 1$ ). Thus the signal strength, as well as the phase, changes during occultation entry and exit.

The above discussion in terms of phase emphasizes the physical effects at work. For actually reducing observations a much more practical approach is to measure the Doppler shift in frequency at the spacecraft. The relative motion of Earth and spacecraft is known from the spacecraft's ephemeris. Because of the bending of the ray through angle  $\alpha$  the spacecraft will detect a slight Doppler shift in the direction perpendicular to the Earth-spacecraft direction; it is equivalent to the rate of change of phase,  $d\phi/dt = (d\phi/dp)/(dp/dt)$ , in (5.2.31). This Doppler shift gives the deflection angle  $\alpha(p)$ , which in turn is related to the index  $n$  by (5.2.31), and it is not necessary to work with the two-term solution for  $\phi$  (5.2.34).

### 5.2.3 Partial Reflection from Sharp and Diffuse Surfaces

Critical reflection, developed in Section 5.2.1, is a highly efficient mechanism. However, just as in ordinary optics, some reflections occur whenever a wave crosses a boundary between two indices of refraction. The effect is important in reflection by relatively thin ionospheric layers, such as one type of sporadic  $E$ . At one time it aroused interest in accounting for radar reflections from so-called *radio-aurorae*: areas of ionization aligned along the magnetic field and created by the same particle bombardment that creates visual aurorae. Radio-aurorae are observed at quite high frequencies. If a 400 MHz signal were due to critical reflection, it would require  $N_e \approx 2 \times 10^9 \text{ cm}^{-3}$ . On the other hand, much lower densities can, under the right circumstances, reflect such waves. The right circumstances are that the sheet of ionization have a rather distinct "surface" and that this surface be aligned perpendicular to the radar beam. Hence radio-aurorae are most commonly seen poleward of the radar. As we shall see, however, partial reflection from a diffuse surface tends to be very inefficient because of interference. (Radio-aurorae probably arise from inhomogeneous patches of ionization and not plane sheets; cf. Section 5.2.4.)

The Fresnel formulae for reflected and refracted amplitudes in the general case of arbitrary angles of incidence and polarization are developed in texts on electromagnetism. For our purposes a brief review for normal incidence will suffice. The formulae arise from the requirements that the tangential components of  $\mathbf{E}$  and  $\mathbf{H}$  ( $= \mathbf{B}/\mu$ ) be continuous across a boundary. In general

we can write  $\mathbf{H} = n\hat{\mathbf{k}} \times \mathbf{E}$ , where  $\hat{\mathbf{k}}$  is a unit vector parallel to the direction of propagation, since  $\mathbf{E}$  and  $\mathbf{H}$  both have plane-wave solutions and are related by Faraday's law (5.2.2).

The incident electric amplitude (from a region with index  $n_1$ ) is  $E_0'$ ; the transmitted (to a region with  $n_2$ ) is  $E_0''$ ; the reflected,  $E_0'''$ . Thus the two conditions require

$$\begin{aligned} E_0 + E_0'' &= E_0' \\ n_1 E_0 - n_1 E_0'' &= n_2 E_0' \end{aligned} \quad (5.2.36)$$

Eliminating  $E_0'$  we have the reflection coefficient for the intensity,

$$R = \left( \frac{E_0''}{E_0} \right)^2 = \left( \frac{1 - n_2/n_1}{1 + n_2/n_1} \right)^2 \quad (5.2.37)$$

When  $n_2 \rightarrow 0$  the boundary is totally (i.e., critically) reflecting.

Suppose now the wave enters from a region where  $n_1 = 1$  into one where  $n_2$  is given by (5.2.19). For the case of  $n_2 \approx 1$  (i.e.,  $\omega$  far above the critical frequency  $\omega_0$ ), (5.2.14) gives

$$1 - n_2 = \frac{N_e e^2}{2\pi m v^2} \quad (5.2.38)$$

and the reflection coefficient for a sharp surface is

$$R = \frac{N_e^2 e^4}{16\pi^2 m^2 v^4} = 4 \times 10^{-10} \frac{N_e^2}{v^4} \quad (5.2.39)$$

where the numerical value applies when  $N_e$  is in electron/cm<sup>3</sup> and  $v$  in MHz. Thus at 100 MHz and  $N_e = 5 \times 10^6$  cm<sup>-3</sup>, we have  $R = 10^{-4}$ , but  $R$  decreases rapidly toward higher frequencies.

The difficulty with auroral reflections is that the boundaries between different indices of reflection are diffuse, not sharp. This complication does not generally enter the problem in optical reflection and we shall examine it in some detail. So long as there are no irregularities in electron density in a plane perpendicular to the direction of propagation, we may use the wave equation (5.2.7). Again, ignoring absorption and taking  $\kappa = \kappa_0$  from (5.2.13), we have

$$\frac{\partial^2 \mathbf{E}(z, t)}{\partial z^2} = \frac{\omega^2 - \omega_0^2}{\omega^2 c^2} \frac{\partial^2 \mathbf{E}(z, t)}{\partial t^2} \quad (5.2.40)$$

Removing the time dependence by  $E(z, t) = E_1(z) \exp(-i\omega t)$  gives the amplitude equation

$$\frac{\partial^2 E_1(z)}{\partial z^2} + \frac{\omega^2}{c^2} E_1(z) = \frac{\omega_0^2(z)}{c^2} E_1(z) \quad (5.2.41)$$

If  $\omega_0^2(z)$  were a step function with value  $\omega_0^2(z) = 0$  for  $z < 0$  and  $\omega_0^2 = \text{const}$  for  $z > 0$ , then (5.2.41) admits plane-wave solutions. Outside the scattering medium ( $z < 0$ ) we have simply

$$E_1(z) = E_0 e^{i\omega z/c} + E_0'' e^{-i\omega z/c} \quad (5.2.42)$$

With  $\omega_0^2(z)$  gradually changing with  $z$ , the perturbed wave is the summation of the perturbations produced by every individual element of volume. Thus we have

$$E_1(z) = E_0 e^{i\omega z/c} - \int_{-\infty}^{\infty} G(z|z_0) \frac{\omega_0^2(z_0)}{c^2} E_1(z_0) dz_0 \quad (5.2.43)$$

where  $G(z|z_0)$  is the perturbation in the wave amplitude at  $z$  produced by a single perturbation in the index of refraction at  $z_0$ . This *Green's function* is a solution of the equation

$$\frac{d^2 G}{dz^2} + \frac{\omega^2}{c^2} G = -\delta(z - z_0) \quad (5.2.44)$$

which describes a simple oscillator with a  $\delta$ -function driving force. Its solution is

$$G(z|z_0) = -\frac{c}{2i\omega} e^{i\omega|z-z_0|/c} \quad (5.2.45)$$

From (5.2.43) the solution, with  $\omega_0$  given in terms of  $N_e$  by (5.2.14), is

$$\begin{aligned} E_1(z) &= E_0 e^{i\omega z/c} + \frac{2\pi e^2}{i\omega mc} \int_{-\infty}^z e^{i\omega(z-z_0)/c} E_1(z_0) N_e(z_0) dz_0 \\ &\quad + \frac{2\pi e^2}{i\omega mc} \int_z^{\infty} e^{i\omega(z_0-z)/c} E_1(z_0) N_e(z_0) dz_0 \end{aligned} \quad (5.2.46)$$

The first term on the right side is the plane wave incident from  $z = -\infty$ . In the limit of  $z \rightarrow -\infty$ , (5.2.46) gives both the incident and reflected wave. Suppose the scattering region has only a minor perturbation on the incident wave (as when  $\omega \gg \omega_0$ ), then we can adopt the *Born approximation* and write

$$E_1(z_0) \approx E_0 e^{i\omega z_0/c} \quad (5.2.48)$$

and the reflected wave amplitude at  $z \rightarrow -\infty$  is

$$E_0'' = \frac{2\pi e^2 E_0}{i\omega mc} \int_{-\infty}^{\infty} e^{i2\omega z_0/c} N_e(z_0) dz_0 \quad (5.2.49)$$

The reflection coefficient becomes, with an integration by parts,

$$R = \left( \frac{E'_0}{E_0} \right)^2 = \frac{e^4}{16\pi^2 m^2 v^4} \left| \int_{-\infty}^{\infty} e^{i2\omega z_0/c} \frac{dN_e(z_0)}{dz_0} dz_0 \right|^2 \quad (5.2.50)$$

Unless the boundary is much sharper than a wavelength, interference between waves reflected from different distances into the boundary drastically reduces the reflected amplitude. When  $dN_e/dz_0 = N_e \delta(z_0)$ —when the boundary is sharp—equation (5.2.50) reduces to the Fresnel formula (5.2.39).

If  $v$  is near the critical frequency  $\omega_0/2\pi$  for the maximum  $N_e$  in the reflecting volume, as it is in observations of *sporadic E*, the Born approximation (5.2.48) is not valid. As in the analogous situation for scattering in quantum-mechanical problems, one may then resort to the so-called WKB approximation.

#### 5.2.4 Incoherent Scattering and Small-Scale Irregularities

The ionosphere so far has been treated as a fluid medium—a *plasma*. Under certain circumstances the ionosphere ceases to behave as a unified plasma and electrons or ions respond individually to an electromagnetic impulse. The coherent response of a plasma to a wave arises because all electrons in a small region of dimension  $a \ll \lambda$ , where  $\lambda$  is the wavelength, are subjected to the same external driving force. If, however, the wavelength is sufficiently small—say, smaller than interparticle spacings ( $\lambda \lesssim N_e^{-1/3}$ )—the concept of a fluid becomes meaningless and the wave interacts with individual electrons. In most situations, and certainly for the ionosphere, another limit, the Debye screening length  $\lambda_D$ , is a more severe restriction. That is, for the plasma to behave coherently the wave must have  $\lambda \gtrsim \lambda_D$  and usually we find  $\lambda_D > N_e^{-1/3}$ .

With the wavelength related to frequency by  $\lambda\omega/2\pi = c/n$  (the phase velocity), in a collisionless medium the dispersion relation (5.2.19) for the wave becomes

$$\frac{c}{\lambda} = \frac{(\omega^2 - \omega_0^2)^{1/2}}{2\pi} \quad (5.2.51)$$

Similarly, if we consider the mean motion of electrons in more detail, a pressure gradient term [see (2.1.5)] enters the derivation and competes with the electric force, leading to a dispersion relation for the electron oscillations:

$$\frac{\langle 3v^2 \rangle_{th}^{1/2}}{\lambda_e} \approx \frac{(\omega^2 - \omega_0^2)^{1/2}}{2\pi} \quad (5.2.52)$$

where  $\lambda_e$  is the wavelength of electron oscillations and  $\langle v^2 \rangle_{\text{th}}^{1/2}$  is their rms thermal velocity. For large electron oscillations  $\lambda_e$ , the frequency is  $\omega \approx \omega_0$ . But at high frequencies,  $\omega \gg \omega_0$ , the electrons have much shorter oscillations. The Debye screening length is the order of  $\langle v^2 \rangle_{\text{th}}^{1/2}/\omega_0$ ; specifically it is defined as

$$\lambda_D = \left( \frac{kT}{4\pi e^2 N_e} \right)^{1/2} = 6.90 \left( \frac{T}{N_e} \right)^{1/2} \quad (5.2.53)$$

For  $T = 10^3$ °K and  $N_e = 10^5 \text{ cm}^{-3}$ , we have  $\lambda_D = 0.7 \text{ cm}$ , whereas  $N_e^{-1/3} = 0.02 \text{ cm}$ . Within the distance  $\lambda_D$  the Coulomb field of an individual charge is distinguishable and the charge responds to an electromagnetic wave as an individual. Outside this distance the Coulomb field of an electron is damped by the cloud of other charges surrounding it and it is merely part of this element of fluid, responding to a wave as a body.

Electrons scatter unpolarized incident light through an angle  $\Theta$ , according to the Thomson differential cross section (Problem 5.9),

$$\frac{d\sigma}{d\Omega} = \left( \frac{e^2}{mc^2} \right)^2 \frac{1}{2}(1 + \cos^2 \Theta) (\text{cm}^2/\text{sr}) \quad (5.2.54)$$

where the factor  $\frac{1}{2}$  accounts for the equal division of incident flux into two perpendicular polarizations. If the total flux incident on a volume  $V$  is  $\pi F$  and if the electrons are far apart ( $\lambda \ll N_e^{-1/3}$ ), the total scattered intensity is simply additive:

$$I_{\text{sea}}(\Theta) = \frac{N_e V (1 + \cos^2 \Theta)}{2r^2} \left( \frac{e^2}{mc^2} \right)^2 (\pi F) \quad (5.2.55)$$

where  $r$  is the distance from the electron. The length  $e^2/mc^2 = 2.82 \times 10^{-13} \text{ cm}$  is the classical radius of the electron.

Incoherent scatter from high-power radars, whose frequency penetrates the F-region peak, is a means of sounding the topside of the ionosphere from the ground. (Another means involves the use of satellites viewing downward.) The velocity dispersion causes a narrow frequency band to be Doppler broadened on its return, providing information on the electron temperature. If the probing wavelength is  $\lambda \gtrsim \lambda_D$ , the electrons will not incoherently scatter, as noted above, and the scattering occurs mainly from ion-acoustic and ion-cyclotron waves. In this fashion it is possible to investigate the positive-ion species as well.

The scattering by a small volume  $V$  containing free electrons whose scattered waves interfere may be obtained by supposing that each electron Thomson-scatters independently and then adding  $\mathbf{E}$  vectors, with regard

for phase interference, much as we did in (5.2.49) for partial reflection. This technique is the *Rayleigh–Gans approximation*, valid for small phase shifts. Thus the scattered intensity is

$$I(\Theta) = \frac{V^2(1 + \cos^2 \Theta)}{2r^2} \frac{N_e^2 e^4}{m^2 c^4} (\pi F) |\mathcal{R}(\theta, \phi)|^2 \quad (5.2.56)$$

where the *interference factor* (which depends on the particular geometry) is

$$\mathcal{R}(\theta, \phi) = \frac{1}{V} \int e^{i\delta} dV \quad (5.2.57)$$

and  $\delta$  is the phase lag for each point in the cylinder referred to some origin. A simple example is given as Problem 5.10.

As another example, for a cylinder of length  $l$  and diameter  $d$  scattering backward ( $\Theta = \pi$ ), the interference factor is

$$\mathcal{R} = \frac{2}{x} J_1(x) \left( \frac{\pi}{2y} \right)^{1/2} J_{1/2}(y) \quad (5.2.58)$$

where  $J_1$  and  $J_{1/2}$  are Bessel functions,  $x = (2\pi d/\lambda) \cos \psi$ ,  $y = (2\pi l/\lambda) \sin \psi$ , and  $\pi/2 - \psi$  is the angle between the direction of incidence and the axis of the cylinder. To further simplify, suppose we observe at right angles to a cylinder. For example, a tube of ionization along a magnetic field line is probed with a radar beam approximately perpendicular to the field; then  $\psi \sim 0$ . For small dimensions ( $x \ll 1$  and  $y \ll 1$ ) and thin rods ( $d \ll l$  or  $x \ll y$ ), we have, by expanding the Bessel functions,

$$\mathcal{R} \approx \left( 1 - \frac{x^2}{8} \right) \left( 1 - \frac{y^2}{6} \right) \quad (5.2.59)$$

The intensity back-scattered by a single cylinder is then

$$I(\pi) = \frac{\pi^2 d^4 l^2 N_e^2 e^4}{16r^2 m^2 c^4} \left( 1 - \frac{\pi^2 d^2}{\lambda^2} \right) \left( 1 - \frac{4 \pi^2 l^2 \psi^2}{3 \lambda^2} \right) (\pi F) \quad (5.2.60)$$

If the cylinders of density  $N_e + \Delta N_e$  are embedded in a uniform background  $N_e$ , we simply replace  $N_e^2$  above with  $(\Delta N_e)^2$ . Irregularities in  $N_e$  play a major role in ionospheric observations. Certain types of sporadic  $E$ , the spread  $F$  phenomenon, and most radio-aurorae are almost certainly due to inhomogeneous patches of ionization, even though the origin of the irregularities may not be well understood.

Note that for the cylindrical geometry the dependence of the reflection on angle  $\psi$  enters with the length  $l$ . In the case of auroral reflections, the  $\psi$  dependence is called *aspect sensitivity*. The strongest reflections usually

occur when the beam is perpendicular to the field lines ( $\psi = 0$ ) and the intensity falls off rapidly away from this geometry.

### 5.2.5 Magneto-Ionic Theory for a Collisionless Ionosphere

The complete *Appleton formula* describes the propagation of a wave in an arbitrary direction in an ionized medium with an external magnetic field, including the effects of collisions. We have previously (see Section 5.2.1) examined the role of collisions when there is no external field, but in the interest of simplicity we will here omit collisional damping. In addition we will omit the second-order effects of the magnetic field perpendicular to the direction of propagation. The result, (5.2.70), is a simplified version of the Appleton dispersion relation.

The wave is assumed to be propagating in the  $z$  direction and the magnetic field  $\mathbf{B}$  is in an arbitrary direction, with components  $B_x$ ,  $B_y$ ,  $B_z$ . We take the permeability as  $\mu = 1$ . The equations of motion for an electron accelerated by the electric vector of the wave  $\mathbf{E}$  and subject to the constraint provided by the *Lorentz force*  $e\mathbf{v} \times \mathbf{B}/c$ , are

$$\begin{aligned}\frac{d^2x}{dt^2} &= -\frac{e}{m} E_x(t) - \frac{e}{mc} (\mathbf{v} \times \mathbf{B})_x \\ &= -\frac{e}{m} E_x(t) - \omega_z \frac{dy}{dt}\end{aligned}\quad (5.2.61)$$

and

$$\frac{d^2y}{dt^2} = -\frac{e}{m} E_y(t) + \omega_z \frac{dx}{dt} \quad (5.2.62)$$

where

$$\omega_z = eB_z/mc \quad (5.2.63)$$

is the *gyrofrequency*. We have neglected in the equations of motion a second-order effect caused by the external  $B_x$  and  $B_y$  components and the magnetic vector of the wave; they give rise to an oscillating  $z$ -component of electron motion. The important motion occurs in the  $xy$  plane; hence we can simplify the treatment by using complex quantities:

$$u \equiv x + iy, \quad E = E_x + iE_y, \quad B = B_x + iB_y \quad (5.2.64)$$

The equations of motion become

$$\frac{\partial^2 u}{\partial t^2} = \frac{\partial^2 x}{\partial t^2} + i \frac{\partial^2 y}{\partial t^2} = -\frac{e}{m} E(t) + i\omega_z \frac{\partial u}{\partial t} \quad (5.2.65)$$

Faraday's law (5.2.2) is

$$\frac{\partial E}{\partial z} = \frac{i}{c} \frac{\partial B}{\partial t} \quad (5.2.66)$$

and Ampère's law (5.2.1) is

$$\frac{\partial B}{\partial z} = i \frac{4\pi N_e e}{c} \dot{u} - \frac{i\kappa}{c} \frac{\partial E}{\partial t} \quad (5.2.67)$$

A solution to this set of three simultaneous equations is

$$\begin{aligned} E &= E_0 e^{\pm i\omega(t-nz/c)}, & B &= B_0 e^{\pm i\omega(t-nz/c)} \\ u &= u_0 e^{\pm i\omega(t-nz/c)} \end{aligned} \quad (5.2.68)$$

These waves in  $E$ ,  $B$ , and  $u$  travel in the  $+z$  direction. The ambiguity of sign in the exponent does not matter in the absence of a magnetic field, but the option gives rise to two solutions when  $B \neq 0$ . Thus substituting (5.2.68) into (5.2.65–5.2.67) yields

$$\begin{aligned} \frac{e}{m} E_0 - (\omega^2 \mp \omega\omega_z)u_0 &= 0 \\ nE_0 + iB_0 &= 0 \\ \kappa E_0 + inB_0 - 4\pi N_e e u_0 &= 0 \end{aligned} \quad (5.2.69)$$

For this set of equations to have a nontrivial solution, their determinant must vanish. Expansion of the determinant gives the two solutions for the index of refraction:

$$n^2 = \kappa - \frac{\omega_0^2}{\omega^2 \mp \omega\omega_z} \quad (5.2.70)$$

where the plasma frequency  $\omega_0$  is given by (5.2.14) and where  $\kappa = 1$  for the collisionless case. For a field of  $B_z = 1$  G,  $eB_z/mc = 17.6$  Mrad/sec. The Earth's field is 0.315 G at the magnetic equator and twice as strong at the poles. Thus the gyrofrequency  $\omega_z$  is of the same order as the plasma frequency  $\omega_0$  for the lower ionosphere and therefore of the same order as the frequencies  $\omega$  used to probe the ionosphere. [For  $B = 0.5$  G,  $\omega_0 = \omega_z$  corresponds to  $N_e = 2.43 \times 10^4$  cm<sup>-3</sup>; see (5.2.20).]

The radio wave probing an ionosphere with a magnetic field splits into two modes, as does an optical wave in an anisotropic double-refracting crystal. The ionosphere thus has *magnetic birefringence*. For  $\kappa = 1$ , the *ordinary wave* is defined by

$$n_+^2 = 1 - \frac{\omega_0^2}{\omega(\omega + \omega_z)} \quad (5.2.71)$$

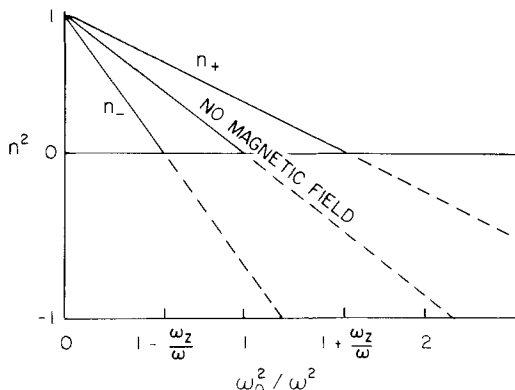


**Fig. 5.9** Variation of index of refraction with the plasma frequency  $\omega_0$  for propagation along the magnetic field and when  $\omega > \omega_z$  (wave frequency exceeds the gyrofrequency). In this situation the extraordinary wave would be critically reflected at a lower plasma frequency than the ordinary one. Compare Fig. 5.1.

which gives critical reflection ( $n_+ = 0$ ) for

$$\omega = \left( \omega_0^2 + \frac{\omega_z^2}{4} \right)^{1/2} - \frac{\omega_z}{2} \quad (5.2.72)$$

The *extraordinary wave* has

$$n_-^2 = 1 - \frac{\omega_0^2}{\omega(\omega - \omega_z)} \quad (5.2.73)$$

and this index becomes infinite for  $\omega = \omega_z$ . A linearly polarized wave transmitted into the ionosphere becomes split into right- and left-handed circularly polarized components, propagating with the two different velocities. (Right-handed polarization is a clockwise rotation when the wave is viewed toward the direction of propagation.) The wave returning to Earth may be drastically changed from the transmitted wave, frequently containing the separate circularly polarized components (see Fig. 5.1). Figure 5.9 illustrates dispersion relations for the ionosphere when propagation is along the magnetic field, which gives the main, first-order splitting of modes.

### 5.3 Ionospheres of Venus, Mars, and Jupiter

#### 5.3.1 Venus' and Mars' Chapman Layers

The compositions of Venus' and Mars' thermospheres are nearly identical: CO<sub>2</sub> and its dissociation products O and CO, and a few percent of N<sub>2</sub>. The production rates of O and CO are large, as discussed below, and their modest

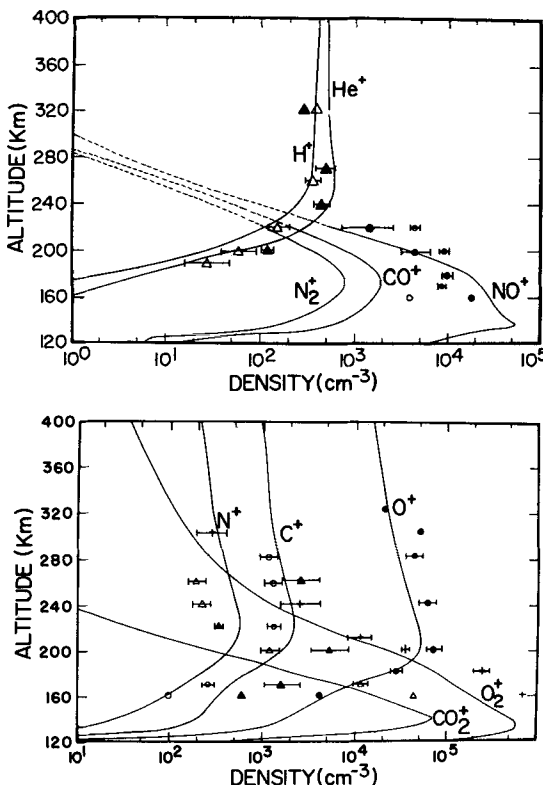


**Fig. 5.10** Calculated ion densities for Venus, with points indicating representative measurements [Pioneer Venus data; model by NAGY *et al.* (1980)].

densities can only be explained by rapid downward transport by eddy diffusion with  $K$  around  $10^8 \text{ cm}^2/\text{sec}$ , a hundredfold greater than for Earth. Recombination takes place at much lower levels (Section 6.4). Figures 5.10 and 5.11 show typical dayside ion densities measured by Pioneer Venus and Viking, along with results of theoretical computations.

Both ionospheres are basically of the Chapman type, with an  $\alpha$  recombination coefficient essentially independent of height. Because  $\text{CO}_2$  remains the dominant constituent far above the layers' peaks, it is the main ionizable source to high altitude. Photoionization of  $\text{CO}_2$  corresponds to the direct  $\text{O}_2$  and  $\text{N}_2$  ionization in the E region on Earth and, more importantly, an atomic ion does not assume the role that  $\text{O}^+$  does in Earth's F1. Thus, the physics of ion production and recombination indicates E-type regions. That the Martian ionosphere is indeed Chapman-like is substantiated by the daily variation of the height and electron density of the peak [see Eq. (5.1.6)].

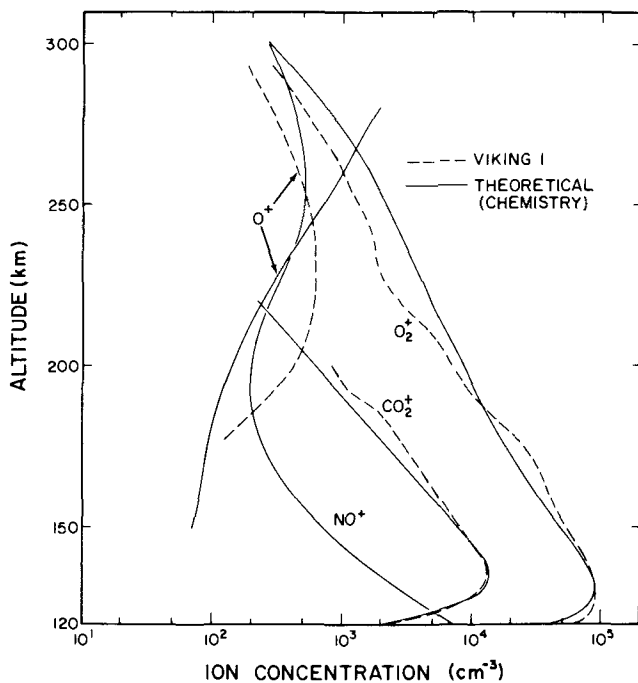
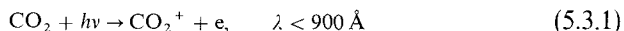


**Fig. 5.11** Ion densities for Mars, observed by Viking 1 (dashed lines) and calculated profiles (solid lines). [From HANSON *et al.* (1977)].

[Solar X-rays and ultraviolet longward of 900 Å (being absorbed by minor constituents) will be deposited much lower; this deposition produces an ionization enhancement corresponding to a second E region.] There are F2 regions, dominated by  $O^+$  in diffusive equilibrium, on both planets, but there are no F2 peaks. The  $O^+$  is more visible in Fig. 5.10 than in Fig. 5.11 because the data for Venus extend further into the F2 region. The Chapman nature of the Venus ionosphere has been thoroughly verified through the density and height variation of the peak with solar zenith angle [cf. Eq. (5.1.6)]. There are, in fact, small deviations for very low Sun that can be accounted for by an advanced model.

Ion production occurs by

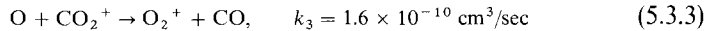


which has a rate outside the atmosphere at Venus of  $J_1 = 7.5 \times 10^{-7} \text{ sec}^{-1}$ , and

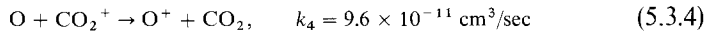


with  $J_2 = 4 \times 10^{-7} \text{ sec}^{-1}$ .

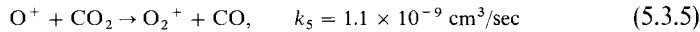
The main ambient ion is  $O_2^+$ , which is quickly formed by atom-ion interchange,



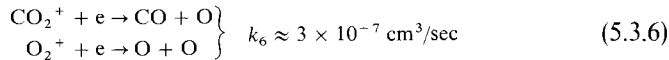
or by charge transfer



quickly followed by

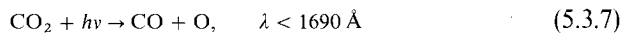


Both  $O_2^+$  and  $CO_2^+$  disappear by dissociative recombination,

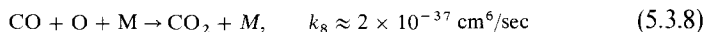


The small degree of  $CO_2$  dissociation in the ionospheres of both planets is surprising but well established from the intensities of the  $O(\lambda 1304)$  and  $CO$  (fourth positive and Cameron systems) airglow emissions (see Section 6.3). The  $O$  emission is excited primarily by fluorescence, and its brightness gives directly the  $O$  abundance and distribution.

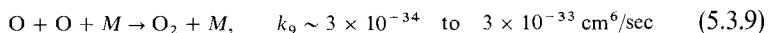
As shown in Figs. 1.18 and 1.24, the degree of  $CO_2$  dissociation in the thermospheres of both planets is modest, in great contrast to  $O_2$  on the Earth. Thus, although  $O$  is important in the ion chemistry, its direct ionization is negligible except at very high altitudes. Because diffusive separation of  $O$  and  $CO_2$  is very strong, the  $O$  mixing ratio must be specified at some particular height, such as the ionospheric peak. The peak heights and mixing ratios are 140 km, 13% for Venus, and 130 km, 2% for Mars (Sections 1.8.1 and 1.8.4). This difference is reflected in Figs. 5.10 and 5.11 by the smaller maximum density of  $O^+$  on Mars, but the composition near the main peak is almost unaffected. Dissociation of  $CO_2$  occurs in almost every ionization event and also in the direct process



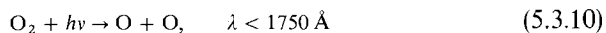
The inverse recombination reaction is negligibly slow:



Without a more efficient way of restoring  $CO_2$ , the  $O$  produced by (5.3.7) would become abundant enough to self-associate by



which is then balanced by



Thus one would have expected to find copious amounts of O, CO, and O<sub>2</sub> in the upper atmospheres of Venus and Mars. Instead, rapid downward eddy transport moves the products to lower altitudes. Although this conclusion was first reached for Mars, it is much more strongly based for Venus, where direct mass spectrometric measurements have been obtained for several constituents, including helium. It is not understood why the eddy mixing is so much stronger than on Earth. One possibility is that turbulent heating from the dissipation of planetary (Rossby) waves is more important at high altitudes than on Earth, where dissipation occurs in the stratosphere and mesosphere. Once transported to low altitudes O and CO can associate catalytically with the aid of OH chemistry (Section 6.4).

From (5.1.9) we see that, well above the electron peak,

$$N_e(z) \rightarrow \text{const} \exp\left(-\frac{z - z_M}{2H}\right) \quad (5.3.11)$$

or in a Chapman layer the electron density (fortuitously) approaches the diffusive-equilibrium value (for equal electron, ion, and neutral temperatures) in which the ion scale height is twice that of the neutral parent.

Thus, if the ion composition is known to be dominantly CO<sub>2</sub><sup>+</sup>, the temperature can be deduced. The seeming model independence is however illusory, and a glance at Figs. 5.10 and 5.11 reveals that temperatures obtained in this way, including those shown in Fig. 1.25, are invalid.

Inspection of Fig. 5.10 reveals that there are no observed data points above 320 km. For the two orbits represented, this level is the ionopause, the interface of the ionosphere with the solar wind. The ionopause height can depend strongly on solar wind conditions, specifically the dynamic pressure, with a standard deviation around 25 km. However, the average behavior has been well documented in several years of daily passes by the Pioneer Venus Orbiter; the height varies from 333 km near the subsolar point, through 610 km at 60° solar zenith angle, 846 km at the terminator, to 1200 km at 30° beyond the terminator. Somewhat similar effects would be expected for Mars, even though (unlike Venus) it may have a weak planetary magnetic field. However, no ionopause has ever been evident in radio-occultation data, and the two Viking landers entered on paths unsuitable for detecting it.

### 5.3.2 Nightside Ionization on Venus

A major surprise from the Venus Mariners was the detection of a nightside ionosphere with a peak  $N_e \sim 10^4 \text{ cm}^{-3}$  at 140 km altitude. Venus' sidereal period of rotation is  $P_{\text{sid}} \sim -244.3$  days (the minus sign meaning

westward or retrograde); its year is  $P_{\text{rev}} = 225$  days; hence its solar rotation period, given by

$$\frac{1}{P_{\text{sol}}} = \frac{1}{P_{\text{sid}}} - \frac{1}{P_{\text{rev}}} \quad (5.3.12)$$

is  $P_{\text{sol}} = -117$  day =  $-1.01 \times 10^7$  sec. The time required for rotation of a point on the terminator to the region of the Mariner 10 observations is about 10 percent of the rotation period, giving a co-rotation time scale of

$$\tau_{\text{CR}} \sim 10^6 \text{ sec} \quad (5.3.13)$$

Even a four-day co-rotation period, sometimes inferred for the middle atmosphere (see Section 2.4), gives a time scale of

$$\tau_{4d} \sim 3 \times 10^4 \text{ sec} \quad (5.3.14)$$

The dayside ionosphere contains predominantly the molecular positive ions  $\text{O}_2^+$  and  $\text{CO}_2^+$ , which recombine with free electrons by dissociative recombination (5.1.45) with rate coefficients  $\alpha_{\text{rec}} \sim 3 \times 10^{-7} \text{ cm}^3/\text{sec}$ . Hence an initial  $N_e(0) \sim 5 \times 10^5 \text{ cm}^{-3}$  at sunset will decay in four days to

$$\begin{aligned} N_e(\tau_{4d}) &= \left( \frac{1}{N_e(0)} + \alpha_{\text{rec}} \tau_{4d} \right)^{-1} \approx (\alpha_{\text{rec}} \tau_{4d})^{-1} \\ &= 10^2 \text{ cm}^{-3} \end{aligned} \quad (5.3.15)$$

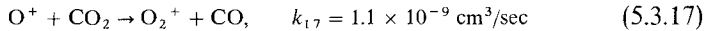
Thus to maintain the nightside ionization, it is necessary to transport the dayside ionization very rapidly, have a nonmolecular ion component that does not recombine so rapidly, or create ionization directly on the nightside. Before the Pioneer Venus Orbiter obtained *in-situ* measurements of the nightside ions, it seemed likely that they would be metallic ( $\text{Mg}^+$ ,  $\text{Na}^+$ ,  $\text{Si}^+$ ,  $\text{Fe}^+$ ). Metal ionization could be produced by charge transfer on the dayside and transported by rotation to the nightside, or it might be produced on the nightside itself by meteor ablation.

Such ions as these are known to be formed in the Earth's lower ionosphere as a result on meteor ablation, and they probably form one type of sporadic  $E$  seen most frequently in middle latitudes. Also, atomic ions recombine with free electrons by radiative recombination,

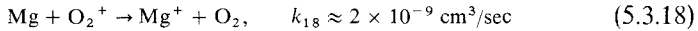
$$\text{Mg}^+ + e \rightarrow \text{Mg} + h\nu, \quad \alpha_{16} \sim 3 \times 10^{-12} \text{ cm}^3/\text{sec} \quad (5.3.16)$$

If this mechanism were the sole means of recombination, it would increase the ion lifetime to  $(N_e \alpha_{16})^{-1} \sim 10^6$  sec. For radiative recombination to be the rate-limiting mechanism, it would be necessary that the positive ions neither

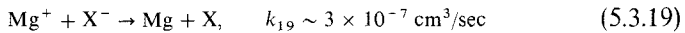
transfer their charge to a molecule nor be neutralized by association with a negative ion. Metallic ions have low ionization potentials and will not transfer their charge to other (molecular) constituents. On the other hand  $O^+$ , for example, is not long lived because of ion-atom interchange,



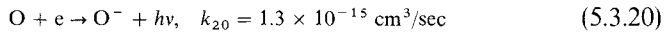
giving a lifetime for  $O^+$  of less than 0.1 sec. Indeed, the metals pick up charge on the dayside by exothermic charge transfer,



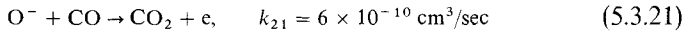
It is important that negative ions do not form rapidly. If they did, not only would free electrons (which are the charges observed by radio occultations) become depleted, but the positive ions would disappear rapidly by mutual neutralization,



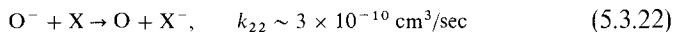
In the Earth's ionosphere the primary negative ion—the one most readily formed directly from electron attachment—is  $O_2^-$ . On Venus the  $O_2$  abundance is very small so that  $O^-$  becomes the primary ion, formed by radiative attachment,



But since O is also a minor constituent, the rate of formation is slow and, once formed,  $O^-$  is destroyed in seconds by



These two reactions alone would give  $[O^-]/N_e \sim 2 \times 10^{-6}$ . Alternatively,  $O^-$  might transfer its electron to a constituent with a higher electron affinity, as  $O_2^-$  does in the Earth's D region, so that the negative ions become relatively stable. The importance of mutual neutralization could then be increased. With charge transfer,



we would have a density  $[X^-] > [O^-]$  if the neutral parent had a mixing ratio  $[X]/[CO_2] \gtrsim 10^{-4}$ . In that case mutual neutralization would become more important than radiative recombination in removing metallic ions.

Whether the unknown substance X exists was never ascertained, because the main ions are not metallic in the first place. The nightside ions are predominantly  $O_2^+$  at the electron peak ( $N_e \sim 10^4 \text{ cm}^{-3}$ ,  $z \sim 145 \text{ km}$ ). At lower altitudes,  $NO^+$  and  $CO_2^+$  become significant; at heights above 160

km,  $O^+$  becomes the major ion. The favored mechanisms are a precipitating low-energy ( $\sim 30$  eV) electron flux of some  $3 \times 10^8 \text{ cm}^{-2} \text{ sec}^{-1}$  and a downward thermal  $O^+$  flux of about  $6 \times 10^7 \text{ cm}^{-2} \text{ sec}^{-1}$ . Possibly both are important at different places and times, with transport of  $O^+$  from the day side acting within a few tens of degrees of the terminator.

### 5.3.3 Jupiter's Giant Ionosphere

As discussed in Section 1.9.1, Jupiter provided another example of an upper atmosphere that did not fit theoretical expectations. The exospheric temperature deduced from the Pioneer 10 and 11 radio occultations, and confirmed by Voyager, is around  $1000^\circ\text{K}$  instead of the expected 200. The dashed line in Fig. 5.12 indicates a model fit to the data, in which the density scale for the neutral atmosphere was necessarily a free parameter. The Voyagers obtained independent information from ultraviolet occultations of the Sun and a star with another surprising result that the neutral densities are much smaller than had been assumed. These densities are shown in Fig. 1.27.

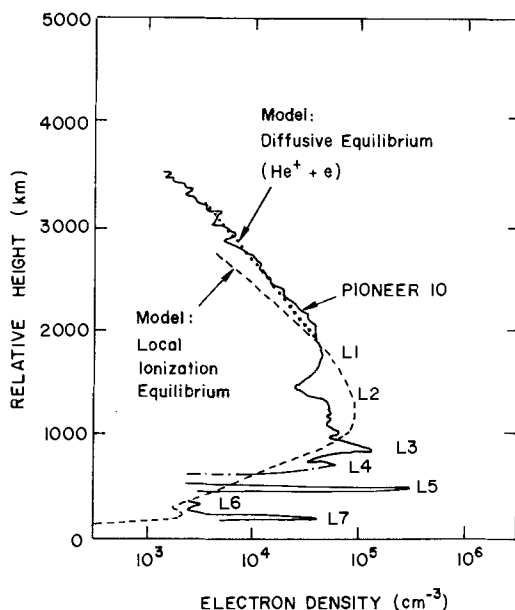


**Fig. 5.12** Model of the Jupiter ionosphere for an exosphere temperature of  $1050^\circ\text{K}$ . The model is calculated to fit observations of Pioneer 10 at latitude  $26^\circ\text{N}$  and a solar zenith angle of  $81^\circ$  (afternoon). The observed peaks (L1, L2, etc.) may or may not be real layers of ionization. [Adapted from ATREYA and DONAHUE (1976).]

The principal reactions producing ions in the Jovian atmosphere are photoionization,



and *dissociative photoionization*,



The latter process is important as the main source of *primary*  $\text{H}^+$  ions.

Of these primary ions,  $\text{H}_2^+$  disappears by



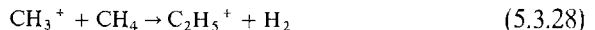
followed by



and to a smaller degree by dissociative recombination,



Also,  $\text{CH}_3^+$ , which is produced at comparatively low altitudes by solar Lyman  $\alpha$ , reacts with methane by



which is followed by dissociative recombination.

Of more interest are the atomic ions  $\text{H}^+$  and  $\text{He}^+$ , which may lend the lower Jupiter ionosphere an F1 character. The  $\text{He}^+$  ion mainly reacts with  $\text{H}_2$  to give a variety of products, the most important of which is



The protons react with  $\text{CH}_4$  to form molecular ions at low altitude; somewhat higher, they form a molecular ion by three-body association,



Above the electron peak, the molecular densities are probably too low for chemical reactions to be important compared with the slow radiative recombination,



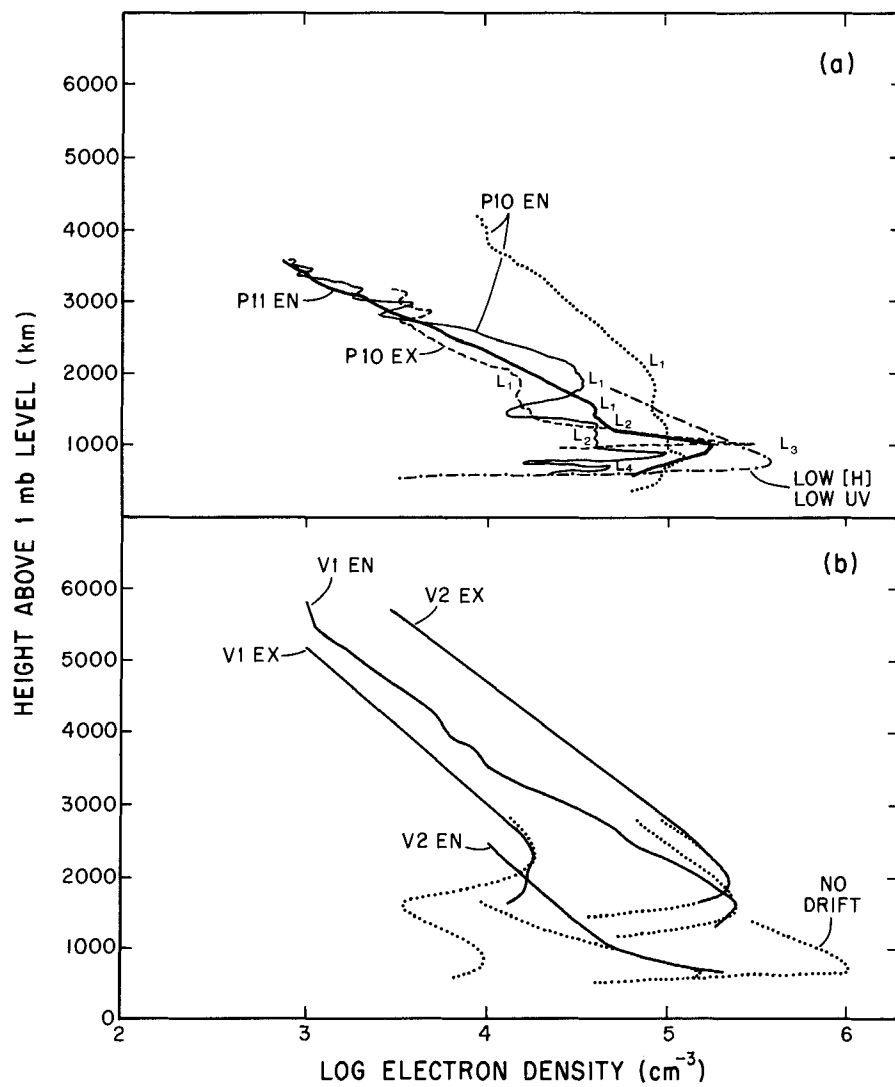


**Fig. 5.13** Jovian electron density profiles observed by Pioneers 10 and 11 (a) and Voyagers 1 and 2 (b). In (a), curves P10 EN are derived from the same data, and the dash-dot curve is a model based on Fig. 1.27 but with essentially no atomic hydrogen. The models in (b), also based on Fig. 1.27, are shown by dotted lines. [After MCCONNELL *et al.* (1982)].

which accounts for electron densities as high as  $10^5 \text{ cm}^{-3}$  on a planet so far (5 AU) from the sun.

One more reaction has been added to the list since the work represented above and in Fig. 5.12:



It is endothermic by 1.83 eV if the  $\text{H}_2$  is in its ground state, but exothermic for molecules excited to the fourth or higher vibrational level. Such levels are easily produced by electron impact, but by molecular symmetry cannot decay radiatively (cf. Section 4.2.5). At high altitudes, where collisions are rare, vibrationally excited molecules can survive for a long time, and (5.3.32) can be an important sink of protons. At lower altitudes, collisions with other  $\text{H}_2$  molecules can cause the vibrational excitation to be shared or degraded to kinetic energy.

Figure 5.13 gives another view of the Pioneer electron densities along with the four Voyager profiles. As in Fig. 1.27, heights are referred to the 1 mbar level. Models are indicated by the dash-dot line in Fig. 5.13a and by the dotted lines in Fig. 5.13b.

### 5.3.4 Titan's Ionosphere

The atmosphere of Titan contains very little  $\text{H}_2$ , and instead is mostly  $\text{N}_2$ ; the principal ion produced is therefore  $\text{N}_2^+$ . But the ionosphere is rich in hydrocarbons, because methane is lighter than nitrogen, and the  $\text{C}_2$  molecules are roughly the same mass. The methane mixing ratio near the exobase was measured at  $8 \pm 3\%$  by the Voyager 1 ultraviolet spectrometer in its solar occultation experiment. Secondary reactions with methane and hydrogen produce  $\text{CH}_3^+$ ,  $\text{CH}_2^+$ , and  $\text{N}_2\text{H}^+$ , all of which presumably have large recombination coefficients. The expected electron density for ion production by solar photons is around  $1000 \text{ cm}^{-3}$ , comfortably below the limit of 2000 set by radio occultation. However, electron impact could dominate the production and raise the predicted density much closer to the limit.

## BIBLIOGRAPHICAL NOTES

### Section 5.1 Formation of Ionospheric Regions

The existence of a conducting region in the atmosphere was first inferred by

STEWART, B. (1882). Hypothetical views regarding the connection between the state of the Sun and terrestrial magnetism. *Encyclopaedia Britannica* (9th ed.) **16**, 181–184. [The date 1878 appearing on the title page of the volume cannot apply to this article, which contains at least some material written later.]

Stewart's conclusion was based on daily changes in the geomagnetic field. Much earlier a mathematical method for separating the magnetic field into two parts—one internal and one external to the Earth's surface—had been developed by

GAUSS, C. F. (1839), Allgemeine Theorie des Erd-magnetismus, in "Resultate aus den Beobachtungen des magnetischen Vereins im Jahre 1838," publ. C. F. Gauss and W. Weber, Leipzig. [Reprinted in *Werke* 5, 119–180, Göttingen, *Kgl. Ges. Wiss.* 1877; English translation by Mrs. Sabine, revised by Sir John Herschel, "Scientific Memoirs," (R. Taylor, ed.), 2, 184–251, London, 1841.]

With adequate data at last accumulated, the method was further developed and applied by

SCHUSTER, A. (1889), The diurnal variation of terrestrial magnetism, *Phil. Trans. Roy. Soc. (London)* A180, 467–512.

who demonstrated conclusively that electric currents must be flowing overhead.

This geomagnetic history was not widely known outside the field, so when Marconi transmitted radio waves across the Atlantic on Dec. 12, 1901, an overhead conducting layer was invoked anew independently by

KENNELLY, A. E. (1902), On the elevation of the electrically conducting strata of the Earth's atmosphere, *Elec. World Eng.* 39, 473,

HEAVISIDE, O. (1902), Telegraphy I. Theory, *Encyclopaedia Britannica* (10th ed.) 33, 213–218.

Kennelly placed the layer at 80 km, much higher than had been thought likely by Stewart and Schuster.

Direct evidence for the existence of the Kennelly-Heaviside layer (called the E layer by Appleton) was obtained through comparing the fading of signals received on two types of directional antennas by

APPLETON, E. V. and BARNETT, M. A. F. (1925), On some direct evidence for downward atmospheric reflection of electric waves, *Proc. Roy. Soc. (London)* A109, 621–641,

SMITH-ROSE, R. L. and BARFIELD, R. H. (1927), Further measurements on wireless waves received from the upper atmosphere, *Proc. Roy. Soc. (London)* A116, 682–693.

The most direct means of sounding the ionosphere is the use of radio pulses of shorter duration than the transit time to the ionosphere and back. Measurement of the time delay then gives directly the apparent (*virtual*) height of reflection. The original experiments of this nature, which gave dramatic proof of the existence and location of ionized layers, were performed by

BREIT, G. and TUVE, M. A. (1926), A test of the existence of the conducting layer, *Phys. Rev.* 28, 554–575 (also *Nature* 116, 357 [1925]).

The theory of ionospheric layering was developed most thoroughly by

CHAPMAN, S. (1931), The absorption and dissociation or ionizing effect of monochromatic radiation in an atmosphere on a rotating Earth, *Proc. Phys. Soc.* 43, 26–45 and 483–501.

(The earlier history of the theory of layering is summarized in the notes to Section 1.5, The Stratosphere.)

Linear or  $\beta$  recombination was introduced in connection with D-region ionization and negative ion formation in

BRAIDBURY, N. E. (1938), Ionization, negative-ion formation, and recombination in the ionosphere, *Terr. Magn.* 43, 55–66.

That  $\beta$  recombination is also dominant in the high F2 region, where the positive ions are mainly atomic and where charge transfer is the rate-limiting process for ion destruction is a concept developed by

BATES, D. R. and MASSEY, H. S. W. (1946), The basic reactions in the upper atmosphere I, *Proc. Roy. Soc. (London)* A187, 261–296,

BATES, D. R. and MASSEY, H. S. W. (1947), The basic reactions of the upper atmosphere II, The theory of recombination in the ionized layers, *Proc. Roy. Soc. (London)* **A192**, 1–16.

The importance of  $N_2$  ionization and the rapid conversion of  $N_2^+$  to  $NO^+$  by atom-ion interchange (5.1.14) were first demonstrated from a model based on rocket observations of solar fluxes and neutral densities by

NORTON, R. B.; VANZANDT, T. E.; and DENISON, J. S. (1963), A model of the atmosphere and ionosphere in the E and F1 regions, *Proc. Intern. Conf. on the Ionosphere* pp. 26–34, *Inst. Phys. and Phys. Soc. (London)*.

Nighttime recombination in F2 and the formation of the F2 peak by ion diffusion was first developed in a reasonably accurate way by

DUNGEY, J. W. (1956), The effect of ambipolar diffusion in the night-time F layer, *J. Atm. Terr. Phys* **9**, 90–102.

His numerical solution is for the case  $H_1 = 2H(X)$ . The nighttime F2 solution given here is not highly accurate but it is probably the most realistic one that can be treated completely analytically. This discussion is based on

CHAMBERLAIN, J. W. (1961), "Physics of the Aurora and Airglow," Section 13.2, Academic Press, New York.

Electrostatic equilibrium was first developed for the ionized regions of a stellar atmosphere by

PANNEKOEK, A. (1922), Ionization in stellar atmospheres, *Bull. Astron. Insts. Netherlands* **1**, (19), 107–118,

ROSSELAND, S. (1924), Electrical state of a star, *Mon. Not., R. A. S.* **84**, 720–728.

The case of two ions was treated by

EDDINGTON, A. S. (1926), "The Internal Constitution of the Stars," 1959 reprint, pp. 272–276, Dover, New York.

The idea was rediscovered and applied to the ionosphere by

DUNGEY, J. W. (1955), Electrodynamics of the outer atmosphere, in "The Physics of the Ionosphere," pp. 229–236, The Physical Society, London.

Extension to the case of two ions was made by

MANGE, P. (1961), Diffusion in the thermosphere, *Ann. Geophys.* **17**, 63–77.

That the F2 peak ionization should be near the boundary of the regimes dominated by recombination and by diffusion (i.e., where  $\beta \sim D/H^2$ ) was noted by

RISHBETH, H. and BARRON, D. W. (1960), Equilibrium electron distributions in the ionospheric F2-layer, *J. Atmos. Terr. Phys.* **18**, 234–252.

The accidental resonance of reaction (5.1.42b), including the ratio of reaction rates given by (5.1.42d), was first developed by

CHAMBERLAIN, J. W. (1957), Excitation in nebulae: Charge transfer and the Cassiopeia radio source, *Astrophys. J.* **123**, 390–398.

The temperature dependence of the rates of the forward and back reactions are calculated and measured by

FEHSENFELD, F. C. and FERGUSON, E. E. (1972), Thermal energy reaction rate constants for  $H^+$  and  $CO^+$  with O and NO, *J. Chem. Phys.* **56**, 3066–3070.

The Saha ionization equation may be found in textbooks dealing with stellar atmospheres and in

ALLEN, C. W. (1978), "Astrophysical Quantities," 4th edition, Athlone Press, London.

Two types of observation in the early 1960s demonstrated that  $O_2^-$  could not be the dominant negative ion in the D region, but that a terminal ion of greater electron affinity must be formed. First, early observations of twilight variations of polar-cap absorption (PCA) events were interpreted as requiring solar ultraviolet, rather than visual, photodetachment by

REID, G. C. (1961), A study of the enhanced ionization produced by solar protons during a polar cap absorption event, *J. Geophys. Res.* **66**, 4071–4085.

Later, analysis of enhanced D-region radio absorption, produced by gamma rays from atmospheric nuclear tests in the Pacific in 1962, led to  $CO_3^-$ ,  $NO_2^-$ , and  $NO_3^-$  being invoked as possible terminal ions by

LELEVIER, R. E. and BRANSCOMB, L. M. (1968), Ion chemistry governing mesospheric electron concentrations, *J. Geophys. Res.* **73**, 27–41.

The complexity of the positive-ion make-up of the D region was demonstrated from rocket measurements by

NARCISI, R. S. and BAILEY, A. D. (1965), Mass spectrometric measurements of positive ions at altitudes from 64 to 112 kilometers, *J. Geophys. Res.* **70**, 3687–3700.

Development of D-region chemistry has depended crucially on the laboratory measurement of reaction rates. Reviews on the subject include

FERGUSON, E. E. (1971), D-region ion chemistry, *Rev. Geophys. Space Phys.* **9**, 997–1008,

FERGUSON, E. E. (1974), Laboratory measurements of ionospheric ion-molecule reaction rates, *Rev. Geophys. Space Phys.* **12**, 703–713,

REID, G. C. (1973), Ion chemistry of the D and E regions, in "Physics and Chemistry of Upper Atmospheres," (B. M. McCormac, ed.), pp. 99–109, D. Reidel Publ. Co., Dordrecht, The Netherlands.

The rate coefficients quoted here are taken from summary tables contained in

BORTNER, M. H. and BAURER, T. (eds.) (1972), "DNA Reaction Rate Handbook," Defense Nuclear Agency, Washington, D.C.

General and comprehensive surveys of ionospheric physics are provided by

BAUER, S. J. (1973), "Physics of Planetary Ionospheres," Springer-Verlag, Berlin,

RISHBETH, H. and GARRIOTT, O. K. (1969), "Introduction to Ionospheric Physics," Academic Press, New York.

## Section 5.2 Radio Waves in an Ionized Atmosphere

The theory underlying wave propagation in the ionosphere, including the differences in propagation parallel and perpendicular to a magnetic field, is contained in the classical treatment of the electron by

LORENTZ, H. A. (1909), "The Theory of Electrons and its Applications to the Phenomena of Light and Radiant Heat," B. G. Teubner, Leipzig.

The basic theory for radio propagation by way of the Kennelly–Heaviside layer was developed by

ECCLES, W. H. (1912), On the diurnal variations of the electric waves occurring in nature and on the propagation of electric waves around the bend of the Earth, *Proc. Roy. Soc. (London)* **A87**, 79–99,

It was first shown that a plasma has a real index of refraction less than unity and consequently refracts a wave incident on the ionosphere away from the vertical, leading to reflection, in

LARMOR, J. (1924), Why wireless electric rays can bend around the Earth, *Phil. Mag.* **48**, 1025–1036.

This paper introduced the famous critical-reflection equation (5.2.19) as well as the role of electron collisions in attenuating the wave. The importance of the magnetic field on radio propagation was immediately realized by

APPLETON, E. V. (1925), Geophysical influences on the transmission of wireless waves, *Proc. Phys. Soc.* **37**, 16D–22D,

NICHOLS, H. W. and SCHELLENG, J. C. (1925), Propagation of electric waves over the Earth, *Bell Syst. Tech. J.* **4**, 215–234.

The latter paper introduced a tensor for the dielectric properties of the nonisotropic magnetoplasma. The complete magneto-ionic theory for propagation of radio waves through an ionized medium in the presence of an external magnetic field is due to

APPLETON, E. V. (1932), Wireless studies of the ionosphere, *J. Inst. Elec. Engrs.* **71**, 642–650. [A summary of Appleton's derivation appears in

APPLETON, E. V. (1928), *U.R.S.I. Mém. Sci.* **1**, 2–3 (Papers Presented to the 1927 October General Assembly of the Intern. Sci. Radio Union); reprinted in

BOOKER, H. G. (1974), *J. Atmos. Terr. Phys.* **36**, 2113.]

Other papers of the period that considered the dispersion formula are

GOLDSTEIN, S. (1928), The influence of the Earth's magnetic field on electric transmission in the upper atmosphere, *Proc. Roy. Soc. (London)* **A121**, 260–285.

HARTREE, D. R. (1929), The propagation of electromagnetic waves in a stratified medium, *Proc. Phil. Soc.* **25**, 97–120,

HARTREE, D. R. (1931), The propagation of electro-magnetic waves in a refracting medium in a magnetic field, *Proc. Phil. Soc.* **27**, 143–162.

Some priority questions have been raised as to who first developed the complete dispersion formula [the extension of (5.2.70) to include the second-order effects]. An obscure paper by

LASSEN, H. (1927), Über den Einfluss des Erdmagnetfeldes auf die Fortpflanzung der elektrischen Wellen der drahtlosen Telegraphie in der Atmosphäre, *Elektr. Nachr. Technik.* **4**, 324–334,

contains a general dispersion relation, including some collisional and positive-ion effects, from which the Appleton formula can be deduced as a special case. The issue is clouded in that APPLETON (1932), following Hartree, incorrectly included the so-called "Lorentz polarization term," appropriate for a dielectric, while otherwise treating the medium as a conductor, although APPLETON's (1928) original note contains the correct expression. In addition, the birefringence character of a magnetoplasma was contained in the NICHOLS–SCHELLENG (1925) tensor. For further details see

BOOKER, H. G. (1974), Fifty years of the ionosphere, *J. Atmos. Terr. Phys.* **36**, 2113–2136.

RAWER, K. and SUCHY, K. (1976), Remarks concerning the dispersion of electromagnetic waves in a magnetized cold plasma, *J. Atmos. Terr. Phys.* **38**, 395–398.

Most textbooks on electromagnetism do not treat the *Appleton* (or, as it is frequently but incorrectly called, the *Appleton-Hartree*) formula, but a complete account of propagation in ionized media appears in

RATCLIFFE, J. A. (1959), "The Magneto-Ionic Theory and its Application to the Ionosphere," Cambridge University Press, Cambridge,

MITRA, S. K. (1952), "The Upper Atmosphere," 2d ed., Asiatic Society, Calcutta.

The theory of radio occultation of spacecraft by planets was developed by

FJELDBO, G.; ESHLEMAN, V. R.; GARRIOTT, O. K.; and SMITH, F. L., III (1965), The two-frequency bistatic radar-occultation method for the study of planetary ionospheres, *J. Geophys. Res.* **70**, 3701–3710,

ESHLEMAN, V. R. (1973), The radio occultation method for the study of planetary atmospheres, *Planet. Space Sci.* **21**, 1521–1531.

The method has been highly successful for Venus', Mars', and Jupiter's ionospheres. There have been problems in deriving the pressure-temperature curves for Jupiter below the ionosphere (where  $n > 1$ ) largely because of its oblateness. This difficulty was identified by

HUBBARD, W. B.; HUNTER, D. M.; and KLORE, A. (1975), Effect of the Jovian oblateness on Pioneer 10/11 radio occultations, *Geophys. Res. Lett.* **2**, 265–268.

A discussion of the oblateness problem and other sources of error, including a simplified explanation of the error magnification, is given by

ESHLEMAN, V. R. (1975), Jupiter's atmosphere: Problems and potential of radio occultation, *Science* **189**, 876–878.

The drastic reduction of partial reflection of radio waves from a diffuse surface compared with Fresnel reflection from a sharp surface was noted by

HERLOFSON, N. (1947), Interpretation of radio echoes from polar auroras, *Nature* **160**, 867–868.

Incoherent scatter as a method for sounding the top-side ionosphere, making use of expected small-scale irregularities to return very high frequency signals, was proposed by

GORDON, W. E. (1958), Incoherent scattering by free electrons with applications to space exploration by radar, *Proc. Inst. Radio Eng.* **46**, 1824–1829.

The first successful experiments were conducted by

BOWLES, K. L. (1958), Observation of vertical incidence scatter from the ionosphere at 41 Mc/s, *Phys. Rev. Letters* **1**, 454–455.

The Rayleigh–Gans approximation used here to estimate backscattering from small irregularities is developed in depth by

VAN DE HULST, H. C. (1957), "Light Scattering by Small Particles," Chapter 7, Wiley, New York.

### Section 5.3 Ionospheres of Venus, Mars, and Jupiter

A review of the ionospheres and upper atmospheres of Venus and Mars, with an extensive bibliography, is in

SCHUNK, R. W. and NAGY, A. F. (1980), Ionospheres of the terrestrial planets, *Rev. Geophys. Space Phys.* **18**, 813–852.

Additional material on the Mars ionosphere is reviewed by

BARTH, C. A. (1974), The atmosphere of Mars, *Ann. Rev. Earth Planet. Sci.* **2**, 333–367.

A review of the observations of Venus' ionosphere, with emphasis on the Pioneer Venus orbiter, is given in

BRACE, L. H.; TAYLOR, H. A., Jr.; GOMBOSI, T. I.; KLORE, A. J.; KNUDSEN, W. C.; and NAGY, A. F. (1983), The ionosphere of Venus: Observations and their interpretation, in "Venus" (D. M. Hunten, L. Colin, T. M. Donahue, and V. I. Moroz, eds.), pp. 779–840, Univ. Arizona Press, Tucson, Arizona.

The theory and model calculations of Venus' dayside ionosphere are treated in

NAGY, A. F.; CRAVENS, T. E.; SMITH, S. G.; TAYLOR, H. A., Jr.; and BRINTON, H. C. (1980), Model calculations of the dayside ionosphere of Venus: Ionic composition, *J. Geophys. Res.* **85**, 7795–7801,

NAGY, A. F.; CRAVENS, T. E.; and GOMBOSI, T. I. (1983), Basic theory and model calculations of the Venus ionosphere, in "Venus" (D. M. Hunten, L. Colin, T. M. Donahue, and V. I. Moroz, eds.), pp. 841–872, Univ. Arizona Press, Tucson, Arizona.

Figure 5.11 is from

HANSON, W. B.; SANATANI, S.; and ZUCCARO, D. R. (1977), The Martian ionosphere as observed by the Viking retarding potential analyzers, *J. Geophys. Res.* **82**, 4351–4362.

An early Venus model ionosphere is that of

KUMAR, S. and HUNTEM, D. M. (1974), Venus: An ionospheric model with an exospheric temperature of  $350^{\circ}\text{K}$ , *J. Geophys. Res.* **79**, 2529–2532.

The metallic-ion theory of Venus' nighttime ionosphere and the role of negative ions is treated in

BUTLER, D. M. and CHAMBERLAIN, J. W. (1976), Venus' night-side ionosphere: Its origin and maintenance, *J. Geophys. Res.* **81**, 4757–4760.

The role of metallic ions in the E region of Earth's ionosphere has been reviewed by

REID, G. C. (1973), *op. cit.*,

FERGUSON, E. E. (1972), Atmospheric metal ion chemistry, *Radio Sci.* **7**, 397–401.

Models of the nightside Venus ionosphere are discussed in

CRAVENS, T. E.; CRAWFORD, S. L.; NAGY, A. F.; and GOMBOSI, T. I. (1983), A two-dimensional model of the atmosphere of Venus, *J. Geophys. Res.* **88**, 5595–5606,

KUMAR, S. (1982), Venus nightside ionosphere: A model with KeV electron impact ionization, *Geophys. Res. Lett.* **9**, 595–598.

The radio-occultation data for the Jovian ionosphere have been analyzed by

FJELDBO, G.; KLIOR, A.; SEIDEL, B.; SWEETNAM, D.; and WOICESHYN, P. (1976), The Pioneer 11 radio occultation measurements of the Jovian ionosphere, in "Jupiter," (T. Gehrels, ed.), pp. 238–246, Univ. Arizona Press, Tucson.

The Jovian ionosphere has been modeled from the occultation data by

ATREYA, S. K. and DONAHUE, T. M. (1976), Model ionospheres of Jupiter, in "Jupiter," (T. Gehrels, ed.), pp. 304–318, Univ. Arizona Press, Tucson,

MCCONNELL, J. C. *et al.*, *op. cit.*, Section 1.9.1.

The proposal that there is anomalous heating of the Jovian thermosphere due to the dissipation of gravity waves was made on the basis of a stellar occultation that preceded the Pioneers and anticipated the radio-occultation results. The observations and theory, respectively, are in

VEVERKA, J.; ELLIOT, J.; WASSERMAN, L.; and SAGAN, C. (1974), The upper atmosphere of Jupiter, *Astron. J.* **179**, 73–84,

FRENCH, R. G. and GIERASCH, P. J. (1974), Waves in the Jovian upper atmosphere, *J. Atmos. Sci.* **31**, 1707–1712.

## PROBLEMS

**5.1 Charged-particle scale height.** (a) What is the scale height for a plasma in a gravitational field when there are two ions with density, mass, and temperature of  $N_1$ ,  $M_1$ , and  $T_i$  and  $N_2$ ,  $M_2$ ,  $T_i$ ? The electrons have density  $N_1 + N_2$ ,  $m_e \ll M_i$ , and  $T_e \neq T_i$ . All ions have a single charge  $+e$ . (b) In the special case where  $N_1 \gg N_2$  and  $T_e = T_i$ , show that the plasma has twice the scale height of the parent neutral of mass  $M_1$ . (c) Show that at high altitudes ( $z \gg z_M$ ) the distribution of  $N_e(z)$  given by (5.1.9) approaches diffusive equilibrium. Explain why (physically) this result comes about.

**5.1A Topside ionosphere.** (a) Calculate the rates of disappearance of  $\text{NO}^+$  by (5.1.15) and of  $\text{O}^+$  by (5.1.19) at heights of 120 and 180 km. Which step is rate-limiting at each height? (b)

Calculate the effective mass of  $H^+$  in a region with equal number densities of  $H^+$  and  $O^+$ , using the results derived in the first part.

**5.2 Decay of F2.** (a) Show that the change of variables (5.1.32) reduces (5.1.31) to the “radial wave equation” (5.1.33). (b) Show by substitution into (5.1.26) that the  $j = 0$  solution (5.1.42) gives a diffusive flux divergence that arises from a constant downward velocity  $w = -(\beta_0 D_0)^{1/2}$ . Show further that this divergence is balanced everywhere by  $\beta$ -recombination, except for a constant relative loss rate  $\lambda_0$ .

**5.3 Detailed balancing.** The Saha ionization equation for thermodynamic equilibrium is

$$\frac{N_{q+1} N_e}{N_q} = \frac{(2\pi m k T)^{3/2}}{h^3} \frac{2\tilde{\omega}_{q+1}}{\tilde{\omega}_q} \exp\left(-\frac{\chi_q}{kT}\right)$$

where  $N_q$  is the density of a species in the  $q$ th stage of ionization,  $N_{q+1}$  the density in the next higher stage,  $\chi_q$  the ionization potential from the ground state of stage  $q$ , and the  $\tilde{\omega}$ 's are the statistical weights of the ground states. (Actually the  $\tilde{\omega}$ 's should be replaced with temperature-dependent partition functions summed over all the rotational levels in the molecules.) In thermodynamic equilibrium (5.1.43) would be balanced by the inverse process (5.1.46) involving  $O_2(X^3\Sigma_g^-)$  and  $O_2^-(X^2\Pi_g)$ . With the rate coefficient  $k_{43}$  adopted, compute the rate coefficient  $k_{46}$  for  $T = 200^\circ K$  and  $150^\circ K$ . [Approximate the partition functions with  $\tilde{\omega}(O_2) = 1$  and  $\tilde{\omega}(O_2^-) = 2$ .]

**5.4 D-region chemistry.** Equations (5.1.50) and (5.1.51) give the rate of change of electrons and positive ions. (a) Using the reactions (5.1.43) through (5.1.48) [omitting (5.1.44)], write the analogous equation for negative ions. (b) Express this rate as a rate of change  $dN_e/dt$  in terms of  $N_e$  and  $\lambda$ , in the manner of (5.1.52). (c) Show that this equation introduces no new information beyond what is already known.

**5.5 Wave equation for a conducting fluid.** In the derivation of (5.2.11) for  $\sigma_p$  we assumed that the atmosphere is a dielectric and that the conduction current  $\mathbf{J}$  vanishes and  $\sigma = 0$ . Alternatively, consider the atmosphere to be a conductor with  $\kappa = 1$  (for the neutral component of the atmosphere) and  $\sigma \neq 0$  in (5.2.6), and regard the electron oscillations as contributing to the current  $\mathbf{J}$ . Show that then  $\sigma$  is given by (5.2.11) and  $\mathbf{E}$  is given by (5.2.12).

**5.6 Critical reflection and absorption loss.** The electron density in a medium is given by  $N_e(z) = az$ , where  $a$  is a constant gradient. A radio wave of circular frequency  $\omega$  is transmitted from the point  $z = 0$  along the  $+z$  axis and is eventually reflected at distance  $z = m\omega^2/4\pi e^2 a$ . Assuming that the beam remains perfectly collimated, find the signal loss of returned/transmitted power due to absorption if  $v_c \ll \omega$ . (Regard  $v_c$  as a constant.)

**5.7 Phase lag for radio occultation.** Suppose the electron density in a planetary atmosphere follows an isothermal scale height with constant gravity ( $H \ll r$ ). For a circular frequency  $\omega \equiv 2\pi v$  [that everywhere meets the condition  $\omega \gg \omega_0(r)$ ], show, using only the first term of (5.2.34), that the electron density is related approximately to the phase lag  $\phi$  produced by grazing incidence, tangential at  $r$ , by

$$N_e(r) = -\frac{mv_c \phi}{e^2(2\pi r H)^{1/2}}$$

**5.8 Partial reflection.** The electron density across a diffuse “surface” has a gradient

$$\frac{dN_e}{dz} = \frac{N_0}{a\sqrt{\pi}} \exp\left(-\frac{-z^2}{a^2}\right)$$

where  $a$  is a constant and  $N_0$  is  $N_e(z)$  as  $z \rightarrow \infty$ ;  $N_0$  is well below the value required for critical reflection. Show that the reflected intensity is reduced from the value for a sharp surface by a factor  $\exp(-8\pi^2 a^2/\lambda^2)$ , where  $\lambda$  is the wavelength in vacuum.

**5.9 Thomson scattering.** (a) Given the total cross section for scattering by a single electron

$$\sigma = \frac{8\pi}{3} \left( \frac{e^2}{mc^2} \right)^2$$

show that the differential cross section is given by (5.2.54) when the incident radiation is unpolarized. (b) With this differential cross section, show that a beam incident along the  $x$  axis and plane polarized with  $\mathbf{E}$  parallel to the  $z$  axis has the same total cross section as given above.

**5.10 Rayleigh-Gans scattering.** Show that for backward scattering the interference factor (5.2.57) for a small sphere of radius  $a \ll \lambda$  and index of refraction  $n \approx 1$  is

$$|\mathcal{R}| \approx 1 - \frac{8\pi^2 a^2}{5\lambda^2}$$

(Hint: Divide the sphere into slices aligned perpendicular to the direction of incidence and emergence and first find the phase shift for such a thin disk.)



## ***Chapter 6***

### **AIRGLOWS, AURORAS, AND AERONOMY**

Aeronomy is a term introduced into the language by Sidney Chapman. Literally from the Greek it means the science of the air, but more precisely it is “the science of that part of the upper atmosphere where dissociation and ionization are important.” It may be used also in relation to the atmospheres of other planets. In 1954 the term was internationally adopted in this sense.

*Airglow* is the amorphous, optical radiation continuously emitted by a planetary atmosphere. It extends from the far ultraviolet into the near infrared, but the term excludes thermal emission in the long-wavelength infrared. We distinguish between airglow and aurora on the basis of the aurora’s geographic confinement to (magnetic) polar and sub-polar regions and its sporadic occurrence.

The Earth’s airglow arises mainly from discrete atomic and molecular transitions and thus has predominantly an emission-line and emission-band spectrum. An exception is a weak continuum in the green, probably due to *radiative association*,  $\text{NO} + \text{O} \rightarrow \text{NO}_2 + h\nu$ .

Historically airglow was discovered as being a localized component of the *light of the night sky*, which includes as well the diffuse galactic light due to the unresolved stars and the zodiacal light (sunlight scattered by interplanetary particles). Later, especially bright (by airglow standards) emissions were found in the twilight, arising from atmospheric regions illuminated directly by sunlight. In some cases airglow emissions can be observed from the ground in full daylight, but the instrumental techniques are difficult. In any case, to examine the airglows of the other planets, one observes from spacecraft flying

by or orbiting the planet, and scattered light from the lower atmosphere need not pose a problem.

Airglow arises from a multitude of sources; each spectral emission has to be examined individually to ascertain its origin. From the point of view of atmospheric physics and chemistry, it is useful to classify emissions into three categories: (a) those arising from direct scattering of sunlight, (b) emission associated with creation or destruction of the ionosphere, and (c) radiation resulting from the photochemistry of neutral constituents. Bear in mind that some radiations can be assigned to more than one category.

*Aurora* is also an optical emission from an upper atmosphere, but it is distinguished from airglow by its source of excitation, impact of electrons and ions precipitated from outside the atmosphere. Spectrally, part of component (b) of the day airglow, or *dayglow*, is nearly identical to a faint aurora; it is generated by *photoelectrons*, with energies up to tens of electron volts, produced in photoionization events. The source of auroral electrons and ions is a large subject in its own right, far beyond the scope of this book. However, their effects on atmospheres and their utility as diagnostics of atmospheric conditions and processes are included where appropriate.

## 6.1 Airglow Photometry

### 6.1.1 The Rayleigh: A Specialized Photometric Unit

Suppose that radiation crossing a surface, as illustrated in Fig. 6.1, has a *specific intensity* depending on the direction of  $I_v(\cos \theta, \phi)$  erg/cm<sup>2</sup> sec sr Hz. At a distance  $r$  from the origin, the energy crossing a unit area aligned normal to the beam and also passing through a unit area normal to the beam at the emitting surface (shown in the figure) is  $I_v d\omega$ , where  $d\omega = 1/r^2$  is the field of view of unit area at the receiver as seen from the origin. If the emitting surface is uniform in intensity, the observer at position  $\mathbf{r}$  with a field or view  $d\Omega$  will receive a total amount of energy across unit area of  $I_v d\omega r^2 d\Omega$ , since  $r^2 d\Omega$  is the perceived area of the emitting surface projected onto a plane normal to the line of sight. Thus the *specific surface brightness* as seen at distance  $r$  is the radiation crossing unit area per unit time from a cone of unit solid angle, which is simply  $I_v$ . Thus the surface brightness for an extended source is independent of the distance of the observer and is identical to the intensity emitted by the surface.

Suppose now that a plane-parallel atmosphere everywhere emits radiation at a rate independent of horizontal position but dependent on height  $z$ . The directional rate of emission is  $e_v(z|\mu, \phi)$  erg/cm<sup>3</sup> sec sr Hz, where  $\mu = \cos \theta$ . Each unit volume contributes to the total specific intensity emitted by the

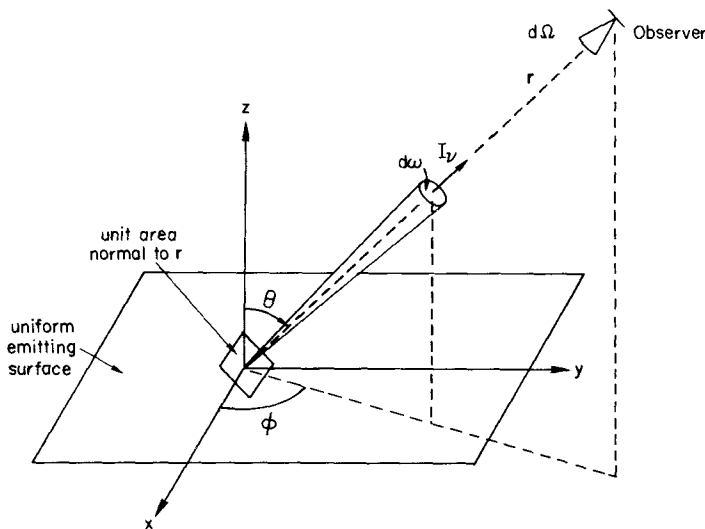


**Fig. 6.1** Specific surface brightness perceived by an observer at a distance  $r$  is equivalent to the specific intensity  $I_v$  and independent of  $r$ .

atmosphere and, if there is no loss due to absorption or scattering, the observer at  $\mathbf{r}$  will measure

$$I_v(\mu, \phi) = \int_0^\infty \varepsilon_v(z|\mu, \phi) \frac{dz}{\mu} \quad (6.1.1)$$

In airglow photometry one is usually concerned with the emission over a single spectral line or group of lines. Also, the energy emitted is usually of less intrinsic interest than the number of photons, which is a direct measure of the number of photochemical reactions occurring in the atmosphere. Thus the number of photons emitted in a given direction is

$$\mathcal{E}(\mu, \phi) = \int_0^\infty \mathcal{E}(z|\mu, \phi) \frac{dz}{\mu} \quad (6.1.2)$$

where

$$\mathcal{E}(z|\mu, \phi) = \int_{\text{line}} \frac{\varepsilon_v(z|\mu, \phi)}{h\nu} dv \quad \text{photon/cm}^3 \text{ sec sr} \quad (6.1.3)$$

The total rate of photon emission in all directions is then

$$E(z) = \int_0^{2\pi} \int_{-1}^1 \mathcal{E}(z|\mu', \phi') d\mu' d\phi' \quad \text{photon/cm}^3 \text{ sec} \quad (6.1.4)$$

For resonance scattering (see Section 6.2 and Problem 6.1), the emission rate  $\mathcal{E}$  may indeed have a directional dependence. But for chemical excitation the emission from unit volume is isotropic and  $E(z) = 4\pi\mathcal{E}(z|\mu, \phi)$ . Then we have for plane-parallel geometry

$$4\pi\mathcal{I}(\mu) = \frac{1}{\mu} \int_0^\infty E(z) dz \text{ photon/cm}^2 \text{ sec} \quad (6.1.5)$$

The *rayleigh* unit (R) is a measure of the *omnidirectional emission rate* in a column of unit cross section along the line of sight, with  $1 \text{ R} \equiv 10^6 \text{ photon/cm}^2 \text{ sec}$ . Thus if the frequency-integrated intensity  $\mathcal{I}(\mu)$  is expressed in units of megaphoton/cm<sup>2</sup> sec sr,  $4\pi\mathcal{I}(\mu)$  is in rayleighs.

Observations of airglow from spacecraft generally are made along a tangent to a spherical shell with radius  $r$  from the center of the planet. In that case the plane-parallel geometry is not valid and extracting the height distributions of emission is analogous to obtaining the electron densities  $N_e(r)$  from radio occultations (see Problem 5.7).

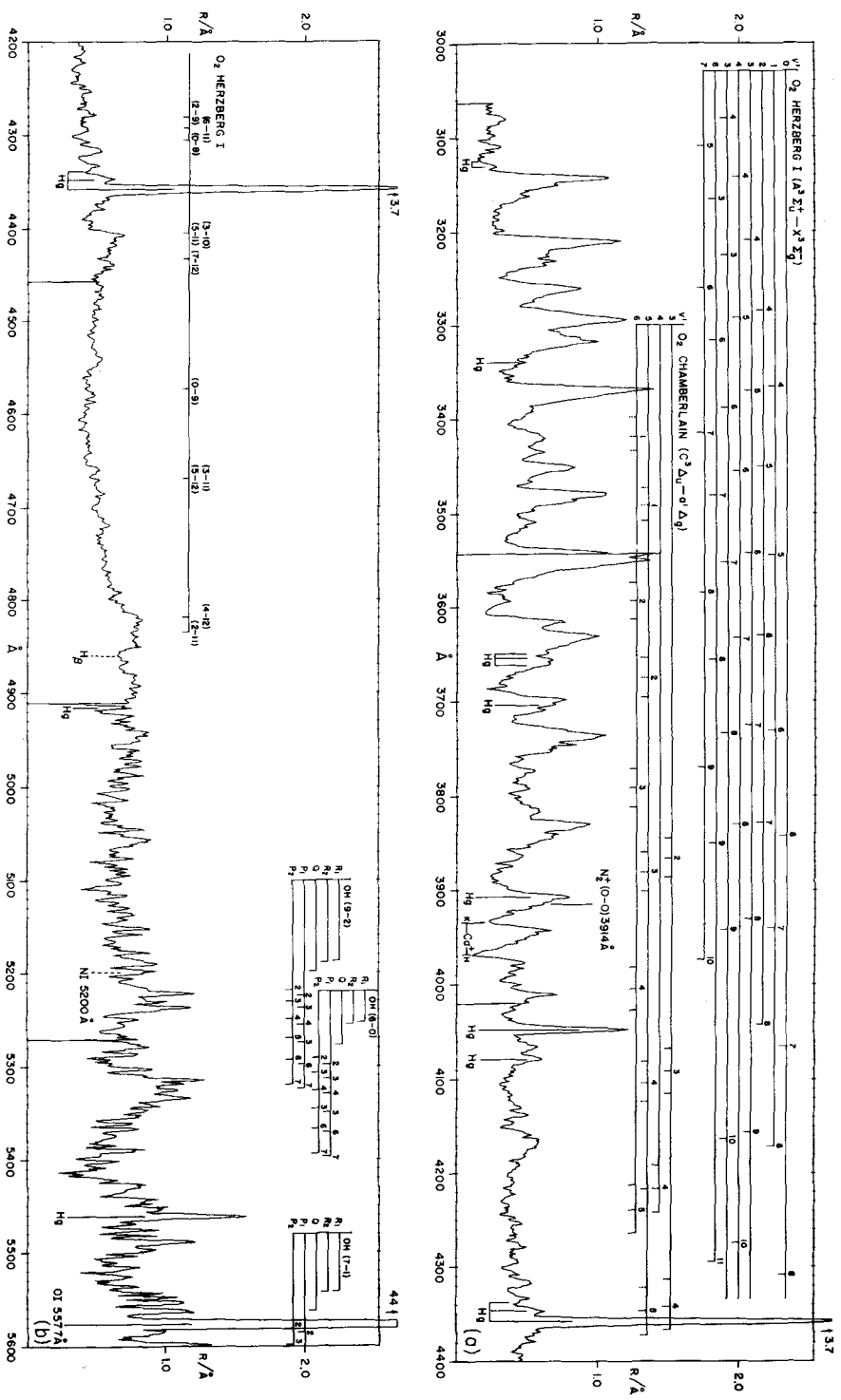
Most of the Earth's airglow emissions are confined to layers that have thicknesses of the order of a scale height, and except in the F regions, this scale factor is  $H \sim 10^6 \text{ cm}$ . Hence a total emission rate referred to the vertical of  $\mu 4\pi\mathcal{I}(\mu) = 1 \text{ R}$ , say, corresponds to 1 photon/cm<sup>3</sup> sec emitted from the layer.

### 6.1.2 Brightness and Composition of Night Airglow

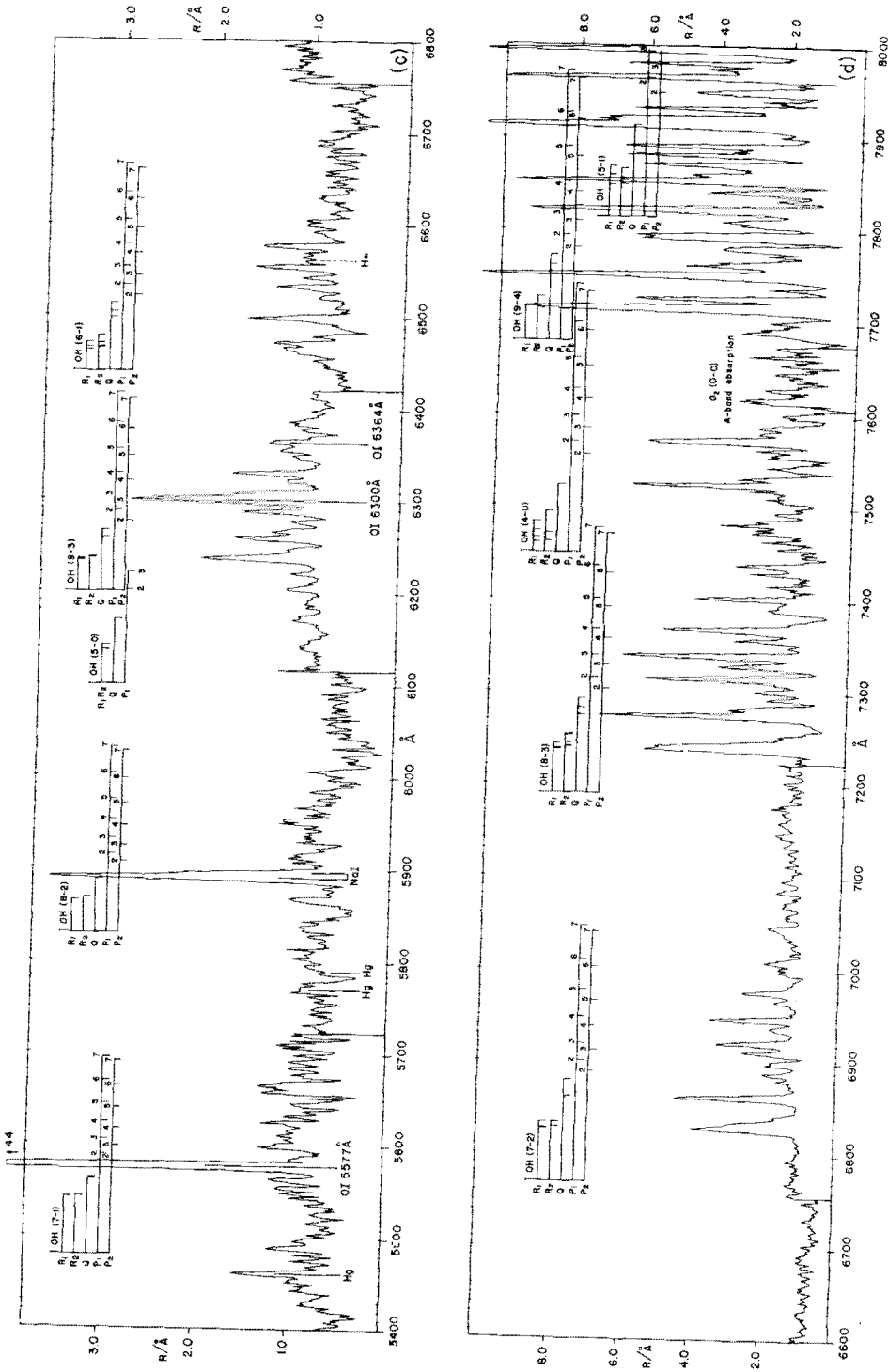
Figure 6.2 shows the spectrum of Earth's night airglow, which is dominated in the visible (Fig. 6.2c) by the green and red forbidden lines of neutral atomic oxygen [O I] and the yellow resonance doublet of Na I. (In discussions of spectra, square brackets indicate transitions forbidden by electric-dipole selection rules, rather than concentrations, and Roman numerals indicate the state of ionization: O I  $\equiv$  O; O II  $\equiv$  O<sup>+</sup>, etc.)

Figure 6.3 shows the energy-level diagram of the ground configuration of O I(2p<sup>4</sup>), along with lifetimes of the metastable levels and Einstein transition probabilities  $A$ . Much of the recombination and photochemical airglow arises from low-lying atomic and molecular levels because of the limited chemical energies available. These low levels are frequently metastable, with long lifetimes. Consequently, the altitude at which the emission occurs depends in part on whether collisional deactivation can occur within the radiative lifetime.

An exception to the above remarks is illustrated by the Na I resonance doublet, 5890–5896 Å, where the first excited electron level 3p(<sup>2</sup>P) lies 2.1 eV above ground, 3s(<sup>2</sup>S). A similar situation exists for the other alkali



**Fig. 6.2.** (a)—(f) Earth's airglow spectrum from about 3050 to 10,000 Å (0.3 to 1.0  $\mu\text{m}$ ). [After A. L. BROADFOOT and K. R. KENDALL, *J. Geophys. Res.* 73, 426-437 (1968).] (continues)



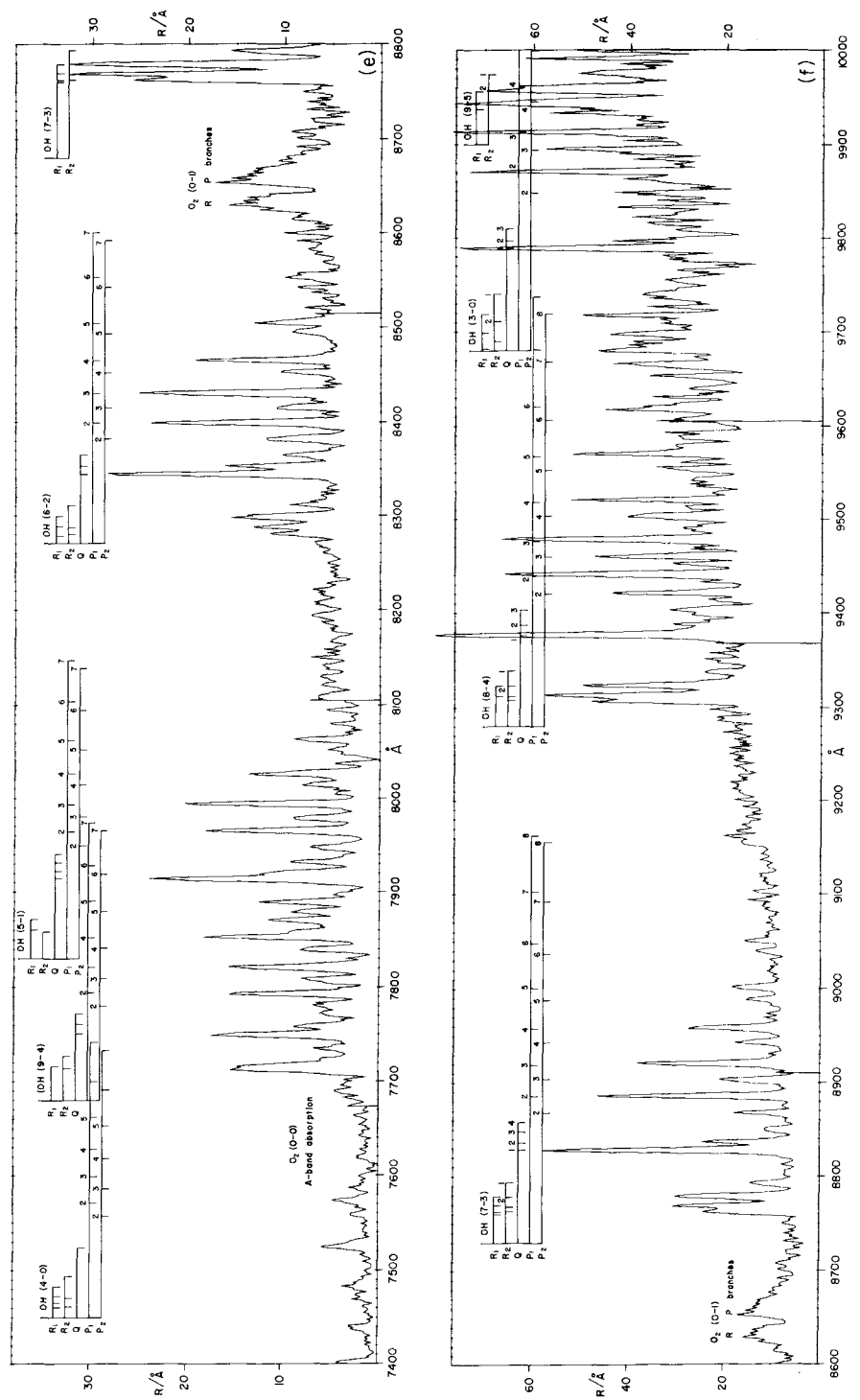
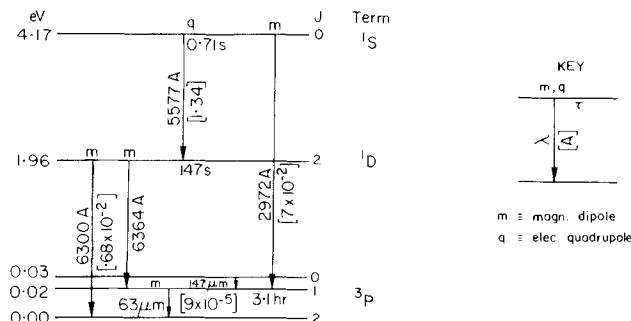


Fig. 6.2 (continued)

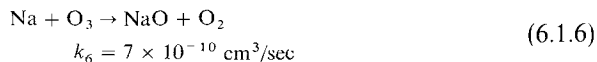
OI 2p<sup>4</sup>

**Fig. 6.3** Ground configuration, 1s<sup>2</sup>2s<sup>2</sup>2p<sup>4</sup>, of O I, showing term and level splitting. The diagram gives transition probabilities  $A$  (sec<sup>-1</sup>) for the forbidden transitions, the dominant multipole term ( $m$  or  $q$ ) in the transitions, the wavelengths, and mean lifetime  $\tau$  of the levels. The level splitting of the  $^3P$  term is exaggerated. The transition probability for  $^3P - ^1D$  is the total: the ratio for  $\lambda 6300/\lambda 6364$  is  $\frac{3}{1}$ . [Transition probabilities from R. H. GARSTANG: (1968), in "Planetary Nebulae," I.A.U. Symp. 34, 143; (1969), *Liege Colloq.*, p. 35; (1951), M.N.R.A.S. 111, 115.]

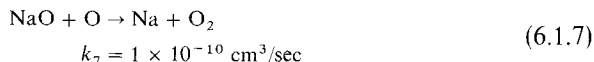
metals, such as Li I at 6708 Å, K I at 7699 Å, and Ca II at 3933–3968 Å, which appear in twilight.

The atomic lines in the green and red are all of the same order of brightness,  $10^2$  R, with Na having a strong seasonal variation and the red [O I] and Na lines having major twilight enhancements (for different reasons).

In twilight Na emits by resonance scattering and its abundance and height distribution can be ascertained. The maximum density of free Na is less than  $10^4$  cm<sup>-3</sup> at 90 km—a mixing ratio of one part in  $10^{10}$ . Its prominence in the night airglow is evidently due to a high reactivity with oxygen (or possibly hydrogen) compounds. Whether or not those reactions account for excitation of the D lines, the equilibrium abundance of Na is fixed mainly by



followed by



Consequently, the ratio of free sodium to sodium oxide is

$$\frac{[\text{Na}]}{[\text{NaO}]} = \frac{k_7[\text{O}]}{k_6[\text{O}_3]} \approx \frac{1}{7} \frac{[\text{O}]}{[\text{O}_3]} \quad (6.1.8)$$

For many years the green line of [OI] ( ${}^1\text{D}_2 - {}^1\text{S}_0$ ),  $\lambda 5577$ , originating from the 100-km region, was thought to be produced by the *Chapman mechanism*,



The actual excitation process, the *Barth mechanism*, is similar and also a direct result of oxygen association. The history of how the single-step Chapman mechanism was untangled from the two-step Barth mechanism makes a complicated but fascinating detective story. The Barth mechanism is



followed by



The major clue to the identification of the  $\text{O}_2^*$  state is the virtual absence ( $<5R$ ) of  $\lambda 5577$  in the Venus nightglow, even though the  $\text{A} {}^3\Sigma_u^+$  and  $\text{A}' {}^3\Delta_u$  molecular states, which are energetically capable of (6.1.9c), are abundant, as indicated by nightglow band systems. The state  $\text{O}_2^*$  is thus vibrationally excited  $c {}^1\Sigma_u^-$ , the upper state of the Herzberg II system (see Fig. 6.4). [The  $v = 0$  level of  $c {}^1\Sigma_u^-$  is populated on Venus but cannot transfer energy to  $\text{O}({}^1\text{S})$ .] It has also been established that  $\text{O}_2(a {}^1\Delta g)$ , which is likely to be plentiful in a region where (6.1.9b) is active, is an efficient deactivator of  $\text{O}({}^1\text{S})$ .

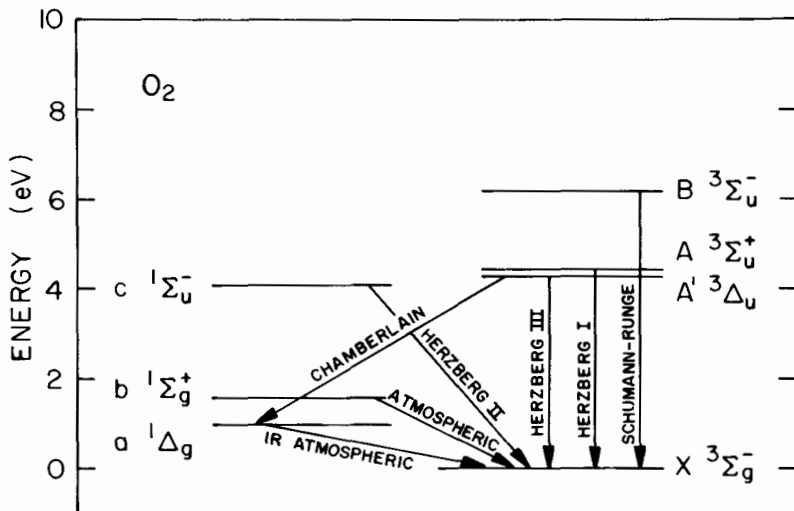


**Fig. 6.4** Energy-level diagram for  $\text{O}_2$  showing transitions important in airglow spectra. Compare Fig. 1.9. The energies for the electronic states are from K. P. HUBER and G. HERZBERG (1979), "Constants of Diatomic Molecules," Van Nostrand-Reinhold, New York.

Additional but weaker green-line emission arises as a result of ionospheric recombination, which also produces the major part of the nightglow [OI] red lines ( ${}^3P_{2,1} - {}^1D_2$ ),  $\lambda\lambda 6300-64$ , by



The product  ${}^1D$  has a yield of nearly unity and  ${}^1S$ , about 10 percent. The other main dissociative-recombination process in the F region produces [NI] ( ${}^4S_{3/2} - {}^2D_{5/2,3/2}$ ),  $\lambda 5200$ , by



This emission is barely detectable ( $\sim 1 R$ ) at night. The [OI] red lines have twilight enhancements due to the fast rate of F2 recombination after sunset (see Section 5.1.3), dissociation of  $O_2$  in the Schumann–Runge continuum,



and photoelectron impact. The latter may well precede morning twilight itself because photoelectrons in the southern hemisphere, say, can travel along magnetic-field lines and impact O atoms in the northern hemisphere at a point farther west and in total darkness, since the geomagnetic pole is displaced from the rotational pole.

Figure 6.2 also shows several of the weaker Meinel bands of hydroxyl (OH). These bands arise from vibrational transitions within the ground electronic state, and consequently their dipole moment is small but not zero. A harmonic oscillator has allowed transitions only for  $\Delta v = 1$  and the existence of sequences for  $\Delta v > 1$  is due to the anharmonicity of the OH potential well. For OH the strongest bands ( $\Delta v = 2$ ) appear in the  $\lambda = 1.5 \mu m$  region and have emission rates of the order of  $10^5 R$ , compared with  $10^1 - 10^2 R$  for the  $\Delta v = 6$  sequence.

The ground electronic state of OH is  ${}^2\Pi$ ; in addition to R and P branches, there is a Q branch in which the rotational lines are nearly superimposed and which appears as a strong spike at the band origin. In the open P branch, the spin doubling is shown for each rotational quantum number K as weak  $P_2$  and strong  $P_1$  lines, from the  ${}^2\Pi_{1/2}$  and  ${}^2\Pi_{3/2}$  levels, respectively.

The OH emission arises from the reaction



the H is recycled by



These reactions are part of the hydroxyl catalytic cycle for destruction of ozone (Section 3.2.2). The 3.34 eV available from (6.1.13) is adequate to excite

$v = 9$  but no higher levels and this is precisely what is observed. Photochemical theory and rocket observations agree in placing the emission layer around 90 km, but spectroscopic temperatures, while highly variable, are usually scattered around 250°K, which is warm for the emitting layer. The reason for this discrepancy is not clearly understood. Possibly the rotational distribution in the higher vibrational levels is not completely in thermal equilibrium with the surrounding gas; perhaps deactivation by O<sub>2</sub> is important at lower altitudes for certain vibrational levels, which then emit more strongly from higher, warmer regions. In any case a long series of spectrophotometric recordings near Moscow shows much less discrepancy with the kinetic temperature of the emitting environment, giving rotational temperatures between 200 and 225°K for a variety of bands.

The low electronic states of O<sub>2</sub> are shown in Fig. 6.4. The B  $^3\Sigma_u^-$  state dissociates into O( $^3P$ ) + O( $^1D$ ) from absorption in the Schumann-Runge continuum. All the other states illustrated dissociate in the weak Herzberg continuum and give two O( $^3P$ ) atoms. In the 100 km region where O<sub>2</sub> dissociation is important, the principal re-association mechanism is the three-body type,



where O<sub>2</sub>\* indicates a molecule in an excited state. Thus the newly formed molecule may be formed in any of the states A, A', a, b, or c, as well as the ground X  $^3\Sigma_g^-$  state.

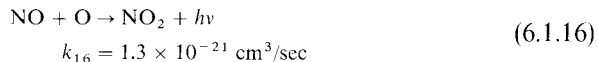
The O<sub>2</sub> Atmospheric ( $b\ ^1\Sigma_g^+ \rightarrow X\ ^3\Sigma_g^-$ ) and Infrared Atmospheric ( $a\ ^1\Delta_g \rightarrow X\ ^3\Sigma_g^-$ ) systems appear at the ground in the  $v' = 0 \rightarrow v'' = 1$  bands only. The 0-0 transitions are absorbed in the middle atmosphere. The total emission rate in the Atmospheric system is about 30 kR and in the IR Atmospheric, 75 kR. The relative intensities of the individual rotational lines are governed by the Boltzmann distribution of populations at the kinetic temperature of the emitting region.

The Herzberg I bands,  $A\ ^3\Sigma_u^+ \rightarrow X\ ^3\Sigma_g^-$ , violate the first-order dipole selection rule that  $\Sigma^+$  does not combine with  $\Sigma^-$ . The bands appear weakly in the 3100–4000 Å region and are somewhat stronger shortward of the ozone cutoff. Their total emission rate is of the order of 1 kR. All three of the above O<sub>2</sub> band systems observed in the terrestrial airglow give *rotational temperatures* of 200°K or under, consistent with their production in the 90–100 km region.

There are also two weak intercombination (singlet-to-triplet) O<sub>2</sub> systems in the ultraviolet. The Chamberlain  $A'\ ^3\Delta_u \rightarrow a\ ^1\Delta_g$  bands were first identified in airglow spectra and have a total emission rate of about 0.1 kR. The Herzberg II system,  $c\ ^1\Sigma_u^- \rightarrow X\ ^3\Sigma_g^-$ , first observed in absorption, was produced in the laboratory from oxygen association and identified in the Venus nightglow; it

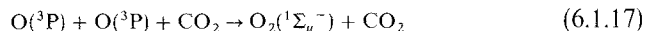
was finally identified in Earth's nightglow with the aid of computed synthetic spectra. Including the entire band systems, extending down to 2500 Å, the  $A \rightarrow X: A' \rightarrow a:c \rightarrow X$  emission ratios are 4:1:1, but in the observable region, 3100–4500 Å, they are 3:2:1.

The continuum radiation in the yellow-green region is probably due to radiative association,



which is also commonly seen in air afterglows in the laboratory.

**Venus Nightglow.** The Venera 9 and 10 spacecraft made observations from planetary orbit of a night airglow on Venus in the 3000–8000 Å region. The emission bands have been identified as the  $v' = 0$  progression of the Herzberg II ( $c\ ^1\Sigma_u^- \rightarrow X\ ^3\Sigma_g^-$ ) system of  $\text{O}_2$ . Laboratory afterglow studies demonstrate that this system is formed by reaction (6.1.15) where  $\text{CO}_2$  is the third body, namely,



Subsequently other bands were identified as the  $v' = 0$  progressions of the Chamberlain,  $A'\ ^3\Delta_u \rightarrow a\ ^1\Delta_g$ , and the Herzberg I,  $A\ ^3\Sigma_u^+ \rightarrow X\ ^3\Sigma_g^-$ ,  $\text{O}_2$  systems. Their intensities are quite different from those on Earth. Over the observed range the  $A \rightarrow X: A' \rightarrow a:c \rightarrow X$  emission rates in rayleighs are 140:200:2700. These relative populations, as well as the strong vibrational relaxation, are evidently due to deactivation by  $\text{CO}_2$ . The  $v = 0$  level of  $c\ ^1\Sigma_u^-$  cannot quite populate  $\text{O}(\ ^1\text{S})$  at the temperature (188°K) of Venus'  $\text{O}_2$  airglow level, and hence the green line is missing [see discussion around Eqs. (6.1.9)].

Pioneer Venus' orbiting spectrometer also detected the NO  $\gamma$  and  $\delta$  bands. Mapping these airglows on Venus gives some insight to the circulation in the upper atmosphere, since the local densities of O and N atoms on the night side are controlled by the rates of association and transport. Ground-based observations have disclosed the  $\text{O}_2$  Infrared Atmospheric ( $a \rightarrow X$ ) bands in the Venus nightglow and day airglow as well.

## 6.2 Resonant and Fluorescent Scattering of Sunlight

### 6.2.1 Photon Scattering Coefficient: The $g$ -Value.

Consider a three-level atom or molecule, as illustrated in Fig. 6.5. The ground state has two levels  $J_i$ , either of which can radiatively connect with the upper level  $J'$ . (The levels  $J_i$  may have further fine structure or hyperfine structure. Or they may, in the case of molecules, represent vibrational levels

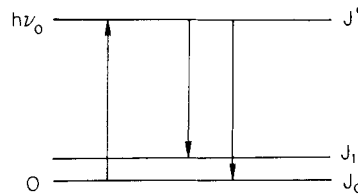


**Fig. 6.5** Simplified energy-level diagram with one level in the upper state and multiple levels in the ground state.

in the ground electronic states with each vibrational level being subdivided into rotational fine structure.)

The incident photon flux at energy  $h\nu_0$  from the sun is  $\pi\mathcal{F}_v(z) = \pi\mathcal{F}_v(\infty)\exp(-\tau_v/\mu_0)$ , where  $\pi\mathcal{F}_v(\infty)$  is the flux outside the atmosphere in units of photon/cm<sup>2</sup> sec Hz and the exponential  $\tau_v(z)/\mu_0$  is the *slant optical thickness* due to extinction (absorption plus scattering) of the flux in traversing the overhead atmosphere.<sup>1</sup> The photon intensity scattered by unit volume in a direction  $(\mu, \phi)$  at an angle  $\Theta$  to the solar direction  $(\mu_0, 0)$  in transition  $J' \rightarrow J_i$  is

$$\begin{aligned}\mathcal{E}(z|\mu, \phi) &= \frac{E(z)p(\Theta)}{4\pi} \\ &= N(z)\pi\mathcal{F}_v(z)\frac{\pi e^2}{mc} f(J_0 J') \tilde{\omega}(J' J_i) \frac{p(\Theta)}{4\pi} \text{ photon/cm}^3 \text{ sec sr}\end{aligned}\quad (6.2.1)$$

Here  $p(\Theta)$  is the phase function for single scattering;  $N(z)$  is the number density of scattering atoms or molecules;  $f$  is the oscillator strength or  $f$ -value, which is related to the transition probability by (1.6.5); and  $\tilde{\omega}$  is the albedo for single scattering, which is

$$\tilde{\omega}(J' J_i) = \frac{A(J' J_i)}{\sum_i \{A(J' J_i) + \eta(J' J_i)[M]\}} \quad (6.2.2)$$

where  $\eta$  is the rate coefficient for collisional deactivation. The phase angle  $\Theta$  is related to the incident and emergent polar angles,  $\cos^{-1}\mu_0$  and  $\cos^{-1}\mu$ , respectively, and their relative azimuth  $\phi$  by (4.1.35). Since  $\tilde{\omega}$  is carried explicitly in (6.2.1),  $p(\Theta)$  is normalized to unity [cf. Eq. (1.2.4)].

Scattering in the same transition  $J' \rightarrow J_0$  or frequency  $h\nu_0$  as the incident solar photon constitutes *resonance scattering*. When the downward transition follows a different route,  $J' \rightarrow J_1$ , it is called *fluorescent scattering*.

The height integration of (6.2.1) gives, for plane parallel geometry,

$$4\pi\mathcal{I}(\mu, \phi) = g\mathcal{N}_{eq}p(\Theta)/\mu \quad (6.2.3)$$

where

$$g(J' J_i) = \pi\mathcal{F}_v(\infty) \frac{\pi e^2}{mc} f(J_0 J') \frac{A(J' J_i)}{\sum_i A(J' J_i)} \text{ photon/sec molecule} \quad (6.2.4)$$

is the photon scattering in all directions per atom (or molecule) with no deactivation or extinction of incident flux and

$$\mathcal{N}_{\text{eq}} = \int_0^{\infty} \frac{N(z)e^{-\tau_{\nu}(z)/\mu_0} dz}{1 + [\mathbf{M}(z)] \sum_i \eta(J'J_i) / \sum_i A(J'J_i)} \quad (6.2.5)$$

is the *equivalent column-integrated density* of scattering molecules. The form (6.2.3) is convenient because  $g$ , the *photon scattering coefficient*, can be tabulated once and for all for any given transition (see Table 6.1).

When an atmosphere is viewed externally along a line of sight that is tangent to a spherical shell of radius  $r$ , the plane-parallel geometry is clearly inappropriate. In that case we can express the density integrated along a line of sight in terms of the local scale height  $H$  and the local density of scattering molecules  $N(r)$ . When both solar extinction and deactivation are negligible everywhere the factor  $\mathcal{N}_{\text{eq}}/\mu$  in (6.2.3) is replaced by the *tangentially integrated density*

$$\begin{aligned} \mathcal{N}_{\tan}(r) &\equiv \int_{-\infty}^{\infty} N(r') ds \\ &= \int_{-\pi/2}^{\pi/2} N(r)e^{-(r'-r)/H} r' \sec \beta d\beta \\ &= 2N(r)r e^{r'/H} K_1(r/H) \\ &\approx N(r)(2\pi r H)^{1/2}(1 + \frac{3}{8}H/r + \dots) \end{aligned} \quad (6.2.6)$$

where  $K_1$  is the modified Bessel function of the third kind. The integral is evaluated by writing  $r' = r \sec \beta$  and changing the independent variable to  $y \equiv \sec \beta$ . The leading term can be obtained most simply by expanding  $\sec \beta$ , but the correction term requires an asymptotic expansion of the exact solution for large arguments.

### 6.2.2 Anisotropy of Scattering, $p(\Theta)$

The anisotropy of scattering is directly related to the polarization of the scattered wave, just as Thomson scattering produces both polarization and anisotropy. In that case, if the electric vector is perpendicular to the plane of scattering, the scattered intensity is isotropic. But the scattered wave with  $\mathbf{E}$  in the plane of scattering has an intensity that varies as  $\cos^2 \Theta$ . Thus the total intensity is given by (5.2.55) (also, see Problem 5.9). The polarization produces the anisotropy and to know one is to know the other.

Thomson and Rayleigh scattering are classical effects. An electron is set in motion by the incident wave, and the direction of electron acceleration

TABLE 6.1 Photon Scattering Coefficients ( $g$ -values) at 1 AU from the Sun

| Atom or molecule                                  | Line or band  | $\lambda$ (Å) | $g$<br>(photon/sec-molecule) |
|---|---|---------------|------------------------------|
| [OI]  | $^3P_2 - ^1D_2$   | 6300          | $4.5 \times 10^{-10}$        |
| [OI]  | $^1D_2 - ^1S_0$   | 5577          | $1 \times 10^{-11}$          |
| [OI]  | $^3P_1 - ^1S_0$   | 2972          | $6 \times 10^{-13}$          |
| OI  | $2p^4 \ ^3P_{2,1,0} - 2p^3 3s \ ^3S_1^o$  | 1302–4–6      | $1 \times 10^{-4}$           |
| [NI]  | $^4S_{3/2} - ^2D_{3/2,5/2}^o$   | 5199          | $6 \times 10^{-11}$          |
| O <sub>2</sub> Atmospheric System                 | $b \ ^1\Sigma_g^+ \rightarrow X \ ^3\Sigma_g^-$<br>( $v' = 0 \rightarrow v'' = 1$ ) | 8645          | $5 \times 10^{-10}$          |
| O <sub>2</sub> Infrared Atmospheric               | $a \ ^1\Delta_g \rightarrow X \ ^3\Sigma_g^-$<br>( $v' = 0 \rightarrow v'' = 1$ )   | 15,803        | $1.2 \times 10^{-11}$        |
| Na I “D <sub>1</sub> + D <sub>2</sub> ”           | $^2S_{1/2} - ^2P_{1/2,3/2}^o$   | 5893          | 0.80                         |
| Ca II “K”   | $^2S_{1/2} - ^2P_{3/2}^o$   | 3933          | 0.3                          |
| Li I  | $^2S_{1/2} - ^2P_{1/2,3/2}^o$   | 6708          | 16                           |
| K I   | $^2S_{1/2} - ^2P_{1/2}^o$   | 7699          | 1.67                         |
| N <sub>2</sub> <sup>+</sup> First Negative System | $B \ ^2\Sigma_u^+ - X \ ^2\Sigma_g^+$<br>( $v' = 0 \rightarrow v'' = 0$ )           | 3914          | 0.05                         |
| H Lyman $\alpha$                                  | $1s \ ^2S - 2p \ ^2P^o$   | 1215          | $2.3 \times 10^{-3}$         |
| H Balmer $\alpha$                                 | $2s \ ^2S - 3p \ ^2P^o$   | 6563          | $2.6 \times 10^{-6}$         |
| He I  | $1s^2 \ ^1S_0 - 1s2p \ ^1P_1$   | 584           | $1.7 \times 10^{-5}$         |
| He I  | $2s \ ^3S_1 - 2p \ ^3P_{0,1,2}^o$   | 10,830        | 16.8                         |
| He II   | $1s \ ^2S - 2p \ ^2P^o$   | 304           | $1.1 \times 10^{-4}$         |

determines the allowed directions of emission of the scattered wave. Resonant (or fluorescent) scattering is a quantum effect: The electron is placed in a higher state, and then after a finite interval it cascades back to the lower state. If the molecule is in a magnetic field  $\mathbf{B}$ , the absorption places the molecule in a particular Zeeman state with a particular orientation of its angular momentum relative to the external field. If there are no collisions the molecule will re-emit from the same upper state. It can emit a  $\pi$  Zeeman component, which is polarized with the electric vector of the wave parallel to the magnetic field, or a  $\sigma$  component, which is polarized perpendicular to  $\mathbf{B}$ . If we observe along the field, for example, we can see only the  $\sigma$  component, and in general the intensity of a given Zeeman component depends on the geometry. Although it is not immediately obvious, it turns out that the total intensity of all Zeeman components in a specified direction also depends on the scattering angle.

With the polarization and consequent anisotropy dependent on the Zeeman effect (since a magnetic field provides a sense of direction in space), we might expect the polarization to disappear as  $\mathbf{B} \rightarrow 0$ . It does not, because the direction of radiation incidence still gives an orientation to the geometry.

The polarization without an external field is the same as if there were a weak field parallel to the incident electric vector.

To understand why this is so, we recall that the Zeeman states specify an orientation in space of the angular momentum of an atom relative to a given direction. If this direction is that of a field  $\mathbf{B}$ , the Larmor precession removes the energy degeneracy. But as long as an orientation is specified by an incident wave, we retain the formal distinctions of Zeeman states. The most obvious choice for orienting space might be to replace the field direction with the direction of propagation; but this arrangement gives the wrong answer, as we shall see.

Scattering that starts upward from level  $FM$  to level  $F'M'$  followed by cascading to the original level  $F'M' \rightarrow FM$  has coherence properties. This scattering contributes to the refractive index. Cascading to a different terminal state of the lower level,  $F'M' \rightarrow F''M''$ , is incoherent and has no effect on the refractive index. The average contribution to the refractive index per atom must be independent of the direction of the external magnetic field if it is weak, according to Heisenberg's *principle of spectroscopic stability*. However, applying a weak magnetic field parallel to the incident electric vector does not alter the plane of polarization, whereas a field in the direction of propagation makes  $\sigma$  components (circular polarization) responsible for the coherent scattering and the plane of polarization is rotated. Therefore, to treat polarization in the absence of a magnetic field, we assume a weak field parallel to the incident electric vector.

We now develop these concepts quantitatively for scattering through an angle  $\Theta$ . In Fig. 6.6 the  $xy$  plane is the plane of scattering; "perpendicular" and "parallel" subscripts on the incident specific flux  $\pi\mathcal{F}$ , and the scattered radiation rate  $\mathcal{E}$  will denote the direction of the electric vector relative to the scattering plane. For incident natural light,  $\mathcal{F}_\perp = \mathcal{F}_\parallel$ ; the incident flux is constant with frequency (white light). We assume that deactivating and depolarizing collisions are negligible.

The polarization and angular distribution of scattering depend critically on the level structure of the atom, including any hyperfine structure denoted by quantum number  $F$  due to nuclear spin  $I$ . The example of Na levels and the D lines is shown in Fig. 6.7. In addition, according to the discussion above, we assume there is an external magnetic field  $B_z$  that separates the Zeeman states  $M_F$ . Then the scattered emission rate per unit volume and solid angle polarized with  $\mathbf{E}$  along the  $z$  axis due to the incident flux component  $\pi\mathcal{F}_\perp$  is

$$\mathcal{E}_\perp = C\mathcal{F}_\perp \sum_{F'M'} (A_\pi^{F'M'})^2 \quad (6.2.7)$$

where  $C$  is a constant to be obtained presently and  $A_\pi^{F'M'}$  is total transition probability from state  $F'M'$  to all lower Zeeman states  $F''M''$  with emission

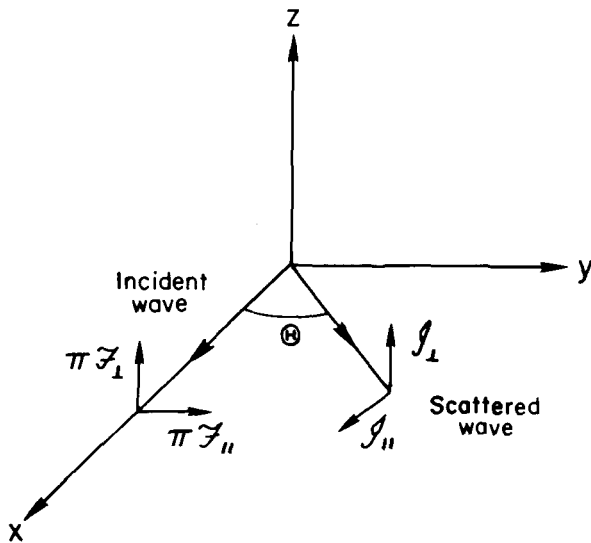


**Fig. 6.6** Geometry of scattering in the  $xy$  plane, with natural incident light divided into polarization components perpendicular and parallel to the plane of scattering.

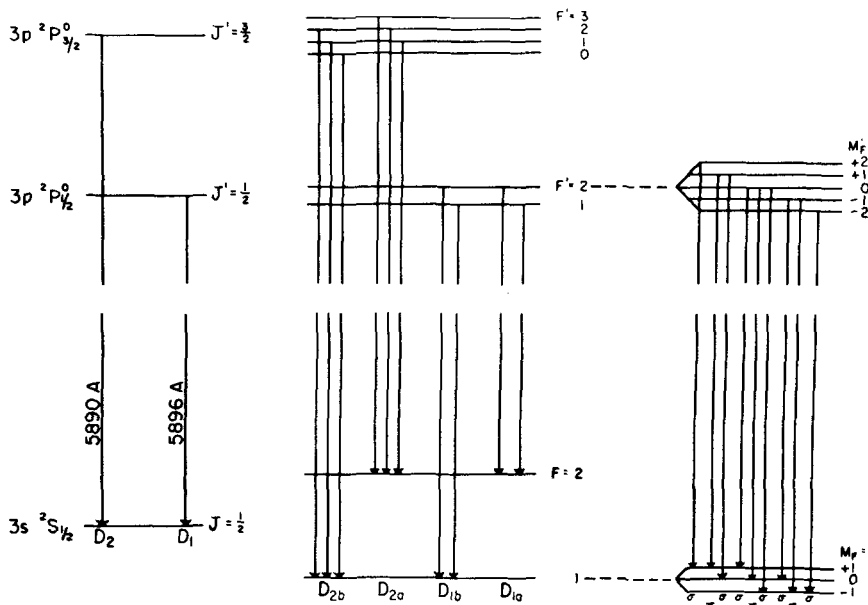


**Fig. 6.7** Energy-level diagram for the ground (3s) and first excited (3p) electron configurations of Na I. The hyperfine splitting (exaggerated in the figure) gives the hyperfine levels for a nuclear spin  $I = \frac{3}{2}$ . The right side shows the Zeeman states and the Zeeman line components, with their  $\pi$  or  $\sigma$  polarization character indicated. [After CHAMBERLAIN (1961).]

of a  $\pi$  Zeeman component ( $= \sum_{F''} \sum_{M''} A_\pi^{F'M'F''M''}$ ). Similarly, the emission rate polarized in the  $xy$  plane arising from scattering by  $\pi\mathcal{F}_\perp$  is

$$\mathcal{E}_{||} = C\mathcal{F}_\perp \sum_{F'M'} (\frac{1}{2}A_\pi^{F'M'} A_\sigma^{F'M'}) \quad (6.2.8)$$

where the  $\frac{1}{2}$  factor allows for the fact that perpendicular to the field  $\sigma$  components radiate with only one-half the efficiency of  $\pi$  components. (For example, the circularly polarized  $\sigma$  components are equivalent to two linearly polarized components aligned perpendicular to one another.) Equations (6.2.7–6.2.8) give the scattered intensity as being proportional to the absorption probability [which in turn is proportional to the emission probability for Zeeman components, whose statistical weights are unity; see (1.6.5)] times the re-emission probability.

To obtain the intensity scattered from  $\pi\mathcal{F}_{||}$  with an external magnetic field aligned along the  $z$  axis, we would proceed analogously, except that the absorption would be proportional to  $A_\sigma^{F'M'}/2$ . But as noted above, to treat the scattering of natural light in the limit of  $\mathbf{B} \rightarrow 0$ , we invoke a weak field  $B_y$  parallel to the electric vector. For the upward transitions, we again have to consider only  $\pi$  components. Thus to (6.2.7) and (6.2.8) we add

$$\mathcal{E}_\perp = C\mathcal{F}_{||} \sum_{F'M'} [A_\pi^{F'M'} (\frac{1}{2}A_\sigma^{F'M'})] \quad (6.2.9)$$

and

$$\mathcal{E}_{||} = C\mathcal{F}_{||} \sum_{F'M'} [A_\pi^{F'M'} (A_\pi^{F'M'} \cos^2 \Theta + \frac{1}{2}A_\sigma^{F'M'} \sin^2 \Theta)] \quad (6.2.10)$$

The total transition probability is

$$A = A_\pi^{F'M'} + A_\sigma^{F'M'} \quad (6.2.11)$$

which is independent of  $F'$  or  $M'$ . Summing over all  $2F' + 1$  Zeeman states in the upper level, we obtain

$$\sum_{M'} (A_\pi^{F'M'} + A_\sigma^{F'M'}) = (2F' + 1)A \quad (6.2.12)$$

and  $\tilde{\omega}(F') = 2F' + 1$  is the statistical weight of  $F'$ . For isotropic, unpolarized incident light, the scattered radiation is also unpolarized because of the spherical symmetry involved (i.e., spectroscopic stability obtains). If the scattered radiation is observed perpendicular to a weak magnetic field, the absence of polarization requires

$$\sum_{M'} A_\pi^{F'M'} = \frac{1}{2} \sum_{M'} A_\sigma^{F'M'} \quad (6.2.13)$$

We now define the auxiliary quantities

$$\alpha(F') = \sum_{M'} (A_{\pi}^{F'M'})^2 + \frac{2F' + 1}{3} A^2 \quad (6.2.14)$$

and

$$\beta(F') = \frac{3}{2} \sum_{M'} (A_{\pi}^{F'M'})^2 - \frac{2F' + 1}{6} A^2 \quad (6.2.15)$$

Then the intensities of scattered radiation components are

$$\mathcal{E}_{\perp} = \frac{C}{4} \sum_{F'} \{ [\alpha(F') + 2\beta(F')] \mathcal{F}_{\perp} + [\alpha(F') - 2\beta(F')] \mathcal{F}_{||} \} \quad (6.2.16)$$

and

$$\begin{aligned} \mathcal{E}_{||} &= \frac{C}{4} \sum_{F'} \{ [\alpha(F') - 2\beta(F')] \mathcal{F}_{\perp} \\ &\quad + [\alpha(F') - 2\beta(F') + 4\beta(F') \cos^2 \Theta] \mathcal{F}_{||} \} \end{aligned} \quad (6.2.17)$$

When the incident light is unpolarized, the polarization of radiation scattered at angle  $\Theta$  is

$$\mathcal{P}(\Theta) \equiv \frac{\mathcal{E}_{\perp} - \mathcal{E}_{||}}{\mathcal{E}_{\perp} + \mathcal{E}_{||}} = \frac{\sum_{F'} \beta(F') \sin^2 \Theta}{\sum_{F'} [\alpha(F') - \beta(F') \sin^2 \Theta]} \quad (6.2.18)$$

The total volume rate of emission in direction  $\Theta$  is

$$\mathcal{E}(\Theta) = \mathcal{E}_{\perp}(\Theta) + \mathcal{E}_{||}(\Theta) = \frac{C \mathcal{F}}{2} \sum_{F'} [\alpha(F') - \beta(F') \sin^2 \Theta] \quad (6.2.19)$$

where  $\mathcal{F}_{||} = \mathcal{F}_{\perp} = \frac{1}{2} \mathcal{F}$ , and the mean emission rate over a sphere is

$$\langle \mathcal{E} \rangle \equiv \frac{E(z)}{4\pi} = \frac{C \mathcal{F}}{2} \sum_{F'} [\alpha(F') - \frac{2}{3} \beta(F')] \quad (6.2.20)$$

With no collisions to deactivate or depolarize the emission (by collisionally altering the upper state  $F'$ ) and with  $f(JJ')$  related to  $A(J'J)$  by (1.6.5), a comparison of the total line ( $J' \rightarrow J$ ) emission given by (6.2.1) and (6.2.20) yields

$$C = \frac{9c^2 N(z)}{64\pi v^2 \tilde{\omega}(J) \sum_J A(J'J)} \quad (6.2.21)$$

where the total statistical weight of the lower level  $J$  is  $\tilde{\omega}(J) = (2J + 1)(2I + 1) = \sum_F (2F + 1)$ , and  $I$  is the nuclear spin.

The *anisotropy or scattering phase function* is then

$$p(\Theta) \equiv \frac{\mathcal{E}(\Theta)}{\langle \mathcal{E} \rangle} = \frac{\sum_{F'} [\alpha(F') - \beta(F') \sin^2 \Theta]}{\sum_{F'} [\alpha(F') - \frac{2}{3}\beta(F')]} \quad (6.2.22)$$

In the notation of Section 4.1.4, we may express  $p$  as

$$p(\cos \Theta) = a + b \cos^2 \Theta \quad (6.2.23)$$

Then defining

$$r = \sum_{F'} \beta(F') \Big/ \sum_{F'} \alpha(F') \quad (6.2.24)$$

we have coefficients

$$a = \frac{1 - r}{1 - \frac{2}{3}r}, \quad b = \frac{r}{1 - \frac{2}{3}r} \quad (6.2.25)$$

The relative intensities of all the Zeeman components in an unresolved multiplet must be known to compute  $\sum \alpha(F')$  and  $\sum \beta(F')$ . These intensities are most readily obtained in three steps. First, if there are two or more lines ( $J' \rightarrow J''$ ) in a multiplet ( $L' \rightarrow L''$ ), their relative intensities are given for  $LS$  coupling by well-known formulas found in texts on atomic spectra and involving the quantum numbers  $S', L'$ , and  $J'$ .

Then to find the relative intensities of hfs lines ( $F' \rightarrow F''$ ) within one line ( $J' \rightarrow J''$ ) when the nuclear spin  $I \neq 0$ , the same formulas apply with the quantum numbers  $S', L'$ , and  $J'$  replaced with  $I', J'$ , and  $F'$ , respectively. Some texts give convenient tables for quickly obtaining the relative intensities. An example is given in Problem 6.4.

Finally, the relative intensities of Zeeman components ( $M' \rightarrow M''$ ) in an hfs line ( $F' \rightarrow F''$ ) follow from the intensity sum rules, which state that the sum of all transitions starting (or stopping) on any Zeeman state is the same as the sum of all transitions starting (or stopping) on any other Zeeman state in the same hfs line. From these rules we obtain the following formulas: For a transition  $F' \rightarrow F'$  (i.e., for  $F'' = F'$ )

$$A_\pi^{F'M'F'M'} = aM'^2 \quad (6.2.26)$$

and

$$A_\sigma^{F'M'F'(M' \pm 1)} = \frac{1}{2}a(F' \pm M' + 1)(F' \mp M') \quad (6.2.27)$$

For a transition  $F' \rightarrow F' + 1$ ,

$$A_\pi^{F'M'(F'+1)M'} = b(F' + M' + 1)(F' - M' + 1) \quad (6.2.28)$$

and

$$A_\sigma^{F'M'(F'+1)(M' \pm 1)} = \frac{1}{2}b(F' \pm M' + 1)(F' \pm M' + 2) \quad (6.2.29)$$

For  $F' \rightarrow F' - 1$ ,

$$A_{\pi}^{F'M'(F'-1)M'} = c(F' + M')(F' - M') \quad (6.2.30)$$

and

$$A_{\sigma}^{F'M'(F'-1)(M' \pm 1)} = \frac{1}{2}c(F' - 1 \mp M')(F' \mp M') \quad (6.2.31)$$

Here  $a$ ,  $b$ , and  $c$  are constants that can be expressed in terms of  $A$  through (6.2.11) by summing the  $A_{\pi}$ 's and  $A_{\sigma}$ 's over all lower states  $F''M''$  and by considering the ratios of the strengths for the different hfs components  $F' \rightarrow F''$ .

### 6.3 Day Airglows of the Planets

Various reviews noted in the bibliography discuss the airglow emissions for the various planets. Our approach here will be to review airglow from the viewpoint of excitation mechanisms to see what the emissions can tell us about atmospheric structure and processes.

#### 6.3.1 Hydrogen and Helium

Lyman  $\alpha$  emission ( $1s^2S \leftarrow 2p^2P$ ) was first found in the Earth's night sky from a rocket flight and initially was thought to arise from H in the interplanetary medium. Subsequent analysis has made clear that the emission arises from resonant scattering by atmospheric H at very high altitudes. In the outer atmosphere H becomes the dominant constituent because of diffusive separation, and with the high temperature, low mass, and diminished gravity, the  $e$ -folding scale height  $kT/Mg$  reaches the order of the Earth's radius. The density distribution is then no longer given by simple consideration of hydrostatic equilibrium and the perfect-gas law (see Section 1.1) and we will develop the more complete theory in Chapter 7. For the moment we will suppose that theoretical models can be developed and compared with observations to obtain densities and temperatures.

When observed from outside the atmosphere, the resonant scattering gives the planet an extensive coronal glow. These *planetary coronas* have been observed on every planet from Mercury to Uranus and on Titan, and are confidently expected on Neptune. The Earth's corona has been mapped from the Moon. Other objects showing Lyman-alpha emission are Saturn's rings and a torus enveloping Titan's orbit. Hydrogen from interstellar space is also present throughout the solar system, although there is a cavity around the Sun because this hydrogen is ionized by ultraviolet and by charge exchange with the solar wind.

For accurate analysis of Ly  $\alpha$  it is necessary to allow for the anisotropy of the  $^2S_{1/2}-^2P_{3/2}$  fine-structure component ( $^2S_{1/2}-^2P_{1/2}$  emits isotropically). The H-term structure is the same as for Na (Fig. 6.7) except for the important difference that the nuclear spin is  $I = \frac{1}{2}$  and there is less hfs in the H spectrum. If the hfs were completely separated, the anisotropy of the  $^2P_{3/2}$  component would be given by (6.2.22), with

$$r \equiv \sum_{F'} \beta(F') / \sum_{F'} \alpha(F') = 0.203 \quad (6.3.1)$$

The isotropic  $^2P_{1/2}$  component contributes one-half times the mean intensity of the  $^2P_{3/2}$  component.

The actual situation is a little more complicated because  $^2P_{3/2}$  has a hyperfine splitting of  $\Delta v = 0.24 \times 10^8 \text{ sec}^{-1}$ , whereas the natural broadening is  $\Delta v = A/2\pi = 1 \times 10^8 \text{ sec}^{-1}$ . Thus the upper hyperfine levels are indistinct, being blurred together by the natural width. In this case the anisotropy and polarization are given by

$$r \equiv \sum_{F'} \beta(F') / \sum_{F'} \alpha(F') = 0.30 \quad (6.3.2)$$

The Ly  $\alpha$  emission at 1215 Å is by far the strongest H emission ( $\sim 8 \text{ kR}$  on the Earth's day side as seen by Apollo 16 on the moon) because it is a resonant transition and because Ly  $\alpha$  emission by the sun is strong. The solar Ly  $\beta$  (1s–3p) emission stimulates geocoronal scattering in Ly  $\beta$  at 1025 Å and Balmer  $\alpha$  fluorescence ( $2s \ ^2S \leftarrow 3p \ ^2P$ ) at 6563 Å. This latter emission can be detected from the ground but it is very weak, about 3 R at night.

On Mars the Mariners 6, 7, and 9 found comparable emission rates,  $\sim 5-6 \text{ kR}$ , whereas for Venus the bright dayside limb seen by Mariner 5 emitted about 40 kR. Some of these data are shown in Figs. 6.8 and 7.8; the latter also shows the interplanetary background, a little over 400 R. We will discuss the hydrogen planetary coronas of the terrestrial planets further in Section 7.3 after developing the theory for an outer atmosphere. The helium resonance lines 584 Å from He I and 304 Å from He II are present in the Earth's daytime spectrum, but they have not been studied intensively, as Ly  $\alpha$  has.

The Pioneer 10 spacecraft carried an ultraviolet photometer that measured 5.1 R of He I ( $1s^2 \ ^1S_0 - 1s2p \ ^1P_1$ ), 584 Å (as well as  $\sim 1 \text{ kR}$  Ly  $\alpha$ ) on Jupiter. With a model of the Jovian atmosphere, these measurements allow a determination of the  $[\text{He}]/[\text{H}_2]$  mixing ratio. The situation is a little confused because it is not clear whether the unexpected plasma temperature ( $\sim 10^{35} \text{ K}$ ) for the high Jovian ionosphere also implies high neutral temperatures (Section 5.3.3). With a low-temperature ( $\sim 150^\circ \text{K}$ ) model, the ratio is  $0 \lesssim [\text{He}]/[\text{H}_2] < 0.28$ , but high temperatures would allow more helium. The matter is of interest to theories for the origin and evolution of the solar system;

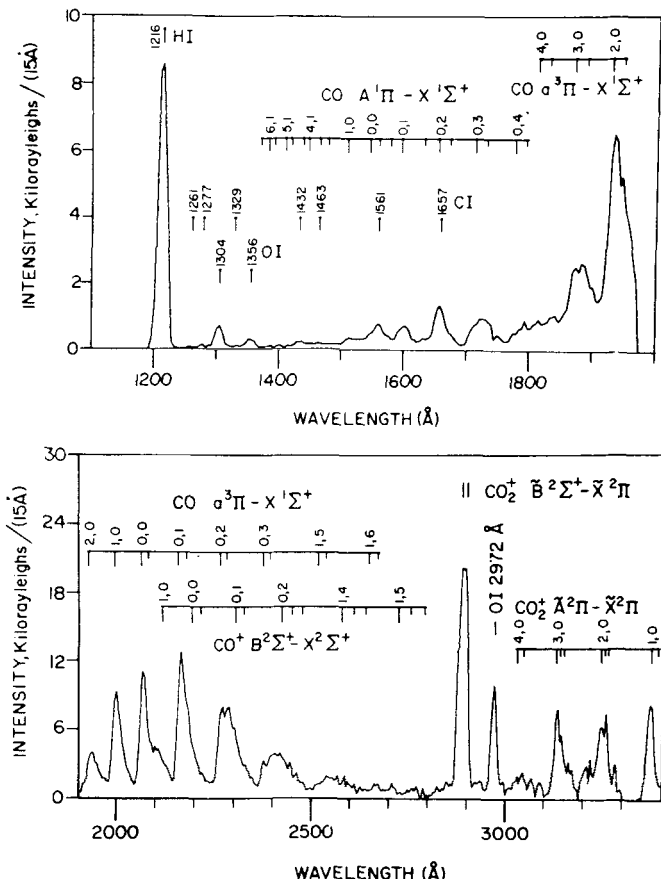


**Fig. 6.8** Ultraviolet airglow of Mars obtained from Mariner 9 orbiter. The spectral tracings are averages of 120 individual limb observations with a resolution of 15 Å. [After BARTH C.A.; STEWART, A. I.; HORD, C. W.; and LANE, A. L. (1972), *Icarus* **17**, 457.]

the He/H mixing ratio for the sun would give  $[\text{He}]/[\text{H}_2] \approx 0.14$ . Pioneer also detected emission from a torus associated with Io's orbit (see also Section 6.3.4), interpreted at the time as 300 R of Lyman alpha. However, the later Voyager spectra showed many other emission lines as well (Fig. 6.10). The Voyagers also found the disk and torus emissions to be much more intense, and it is surmised that the reason is a much higher solar activity than for the time of the Pioneer encounter. Re-interpretation of the Pioneer data for both torus and planet is discussed in Section 6.4.

On Venus the Mariner 10 measured He  $\lambda 584$  at about 600 R. A model analysis indicates an exospheric temperature of 375°K, and this determination does not suffer from the ambiguity of the Lyman alpha results (see

Section 7.3.3). Mariner 10 also found  $\lambda 584$  on the dayside of Mercury at about  $70\text{ R}$ , indicating a surface density of  $4500\text{ cm}^{-3}$  and a scale-height temperature of  $575^\circ\text{K}$ .

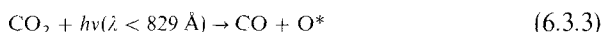
### 6.3.2 Atomic Oxygen

Another important emission is the resonance triplet of O I at  $1302\text{--}4\text{--}6\text{\AA}$  [ $2p^4\text{ }^3P_{2,1,0}\text{--}2p^3(^4S^0)3s\text{ }^3S_1^0$ ]. In the Earth's atmosphere the emission arises mainly from the  $190\text{ km}$  region and has an overhead emission rate of  $4\pi\mathcal{I} \sim 7.5\text{ kR}$ .

This  $\lambda 1304$  triplet, being excited at high altitudes by scattering of sunlight, offers the potential of obtaining the distribution of O in the high atmosphere, which itself is important to understanding atmospheric photochemistry and the ionosphere. In practice the analysis is complicated by an extraordinarily complex problem in radiative transfer. Absorption of sunlight from one of the lower levels in the  ${}^3P$  term can be followed by re-emission to another level. Hence the three lines are radiatively coupled. The fact that very little O is required for these resonance transitions to become optically thick means the interpretations require radiative-transfer analysis. Further, the emissions may be absorbed by such constituents as O<sub>2</sub> and CO<sub>2</sub> and produced by dissociative excitation of O<sub>2</sub> and impact of energetic photoelectrons.

Interpretations of the  $\lambda 1304$  emissions from Mars and Venus have generally been approached by comparing  $\lambda 1304$  with the  $1356\text{--}8\text{\AA}$  forbidden doublet of [OI] ( $2p^4\text{ }^3P_{2,1}\text{--}2p^3(^4S^0)3s\text{ }^5S_2^0$ ) observed simultaneously. The  ${}^5S$  and  ${}^3S$  terms are close together and  $\lambda 1356$  thus gives a means of roughly estimating the excitation due to photoelectron impact or *dissociative excitation* of CO<sub>2</sub> since  ${}^5S$  will not be excited by radiative absorption from the ground term. However, such use of the  $\lambda 1356$  line requires adequate spectral resolution, especially for Venus, because the  $\lambda 1353\text{--}1354$  region contains the 14-4 band of the CO fourth positive system. The unsuspected presence of this emission confused the interpretation of data from Venus for about a decade. Bands from the 14th vibrational level are anomalously strong because of an accidental overlap of the exciting transition with the strong, broad Lyman  $\alpha$  emission from the Sun. The intensity is proportional to the CO mixing ratio in the thermosphere, which, like that of O, is about an order of magnitude less on Mars than on Venus (see Sections 1.8.2 and 1.8.4).

Thus, on Mars the principal source is one depending on CO<sub>2</sub>, namely dissociative excitation:

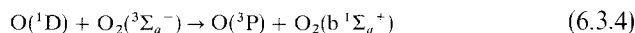


On Venus this source is dominated by electron impact on the more abundant O, and the greater abundance of CO makes the fluorescent band of this

molecule about twice as strong as the O line. On both planets the source of the allowed triplet, which is an order of magnitude fainter on Mars, is solar resonance scattering. A brightness factor of 4.5 comes from the different solar fluxes, and the remaining factor of 2 from the different O abundances.

### 6.3.3 Molecular Excitation

The principal molecular emissions in Earth's airglow arising from resonant/fluorescent scattering are the Atmospheric ( $b\ ^1\Sigma_g^+ \rightarrow X\ ^3\Sigma_g^-$ ) and IR Atmospheric ( $a\ ^1\Delta_g \rightarrow X\ ^3\Sigma_g^-$ ) systems of O<sub>2</sub>. Other mechanisms evidently contribute to these band systems, however. For example, O(<sup>1</sup>D) atoms, produced by Schumann–Runge dissociation of O<sub>2</sub>, may react by



which is a principal loss mechanism (along with collisional deactivation by N<sub>2</sub>) of O(<sup>1</sup>D) atoms.

The most important source of O<sub>2</sub>(<sup>1</sup>Δ<sub>g</sub>) molecules is photodissociation,



in the Hartley continuum,  $\lambda$ 2000–3100. Earth-based observations have disclosed this IR Atmospheric emission on Mars by detection of rotational lines in emission against the sunlit disk with very high spectral resolution. The O<sub>2</sub>(a <sup>1</sup>Δ<sub>g</sub>) molecules imply small amounts of ozone, about  $0.2 \times 10^{-4}$  atm-cm. Ultraviolet absorption measurements performed by Mariner 9 found ozone in amounts of  $50 \times 10^{-4}$  atm-cm over the winter polar caps, but could not detect amounts less than  $3 \times 10^{-4}$  atm-cm. The appearance of ozone at high winter latitudes implies that it favors dry conditions, and that water-related chemistry destroys it (see Section 6.4.1).

As mentioned in Section 6.1.2, the IR Atmospheric emission from Venus has also been measured from the Earth. About half of the dayside excitation is probably due to ozone photolysis, with the rest arising from the association of oxygen atoms from the thermosphere.

In the Earth's nitrogen–oxygen atmosphere, the chemistry of the 70–100 km region leads to the production of nitric oxide with concentrations of  $[NO] \sim 4 \times 10^7 \text{ cm}^{-3}$ , which appear in the ultraviolet  $\gamma$  bands ( $A\ ^2\Sigma^+ \rightarrow X\ ^2\Pi$ ) with emission rates of  $\sim 10^3$  R due to resonance scattering.

A day airglow of comparable emission rate arises from the Second Positive (C <sup>3</sup>Π<sub>u</sub> → B <sup>3</sup>Π<sub>g</sub>) system of N<sub>2</sub>. Although the bands are permitted, this excitation occurs from the ground state by photoelectron impact from the ground state X <sup>1</sup>Σ<sub>g</sub><sup>+</sup>, which requires a change of electron spin. Consequently, the Second Positive system is not subject to resonant scattering and is a

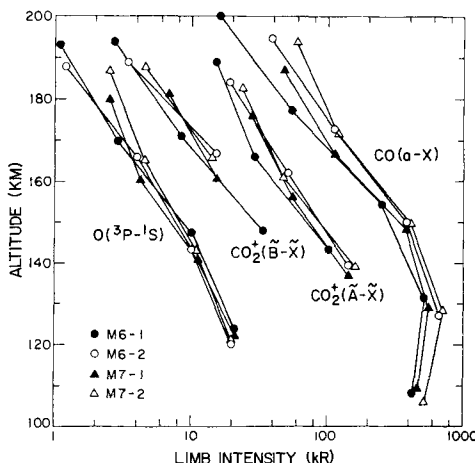


**Fig. 6.9** Height profiles of four airglow emissions on Mars. The data were obtained from four observation opportunities, as indicated: The first and second limb crossings for both the Mariner 6 and 7 fly-bys. [After STEWART (1972).]

good indication of excitation by photoelectron impact. Other band systems of  $\text{N}_2$  and  $\text{N}_2^+$  are present as well.

Similarly the Mariner spacecraft have observed intense airglows from CO, O, and  $\text{CO}_2^+$  on Mars. Figure 6.8 shows the spectra and Fig. 6.9 gives the limb (tangential) emission rates. The strongest of these airglow systems is the forbidden Cameron bands ( $a^3\Pi \rightarrow X^1\Sigma$ ) of CO, which have a maximum emission rate when seen tangentially of 600 KR. At  $\lambda 2972$  appears the forbidden “transauroral” line of O I; it is apparent from Fig. 6.3 that the “auroral” transition,  $\lambda 5577$ , must also be strong, but was out of range of the ultraviolet spectrometer. These emissions cannot be due to resonance scattering because the abundances are too small for the metastable states to become excited by absorption. Rather they arise from the direct action of sunlight on  $\text{CO}_2$ . There are three main possibilities: Dissociative excitation by photons,



or by fast photoelectrons,



and photoionization followed by dissociative recombination,



A physical discussion of these processes in terms of a model atmosphere can reproduce the scale height of the Cameron bands ( $19 \pm 4.5$  km) if the model has an exospheric temperature of  $315 \pm 75$ °K.

The Fourth Positive ( $A^1\Pi \rightarrow X^1\Sigma^+$ ) system of CO appears weakly in Fig. 6.8 and this permitted system, like the resonance line  $\lambda 1304$  of O I, is likely due to resonance scattering. There are also two band systems from  $CO_2^+$ : the Fox–Duffendack–Barker ( $\tilde{A}^2\Pi_u \rightarrow \tilde{X}^2\Pi_g$ ) and the “Doublet” ( $\tilde{B}^2\Sigma_u^+ \rightarrow \tilde{X}^2\Pi_g$ ) systems. These emissions may arise from resonance scattering or from photoionization-excitation,



The airglow radiation from the Martian upper atmosphere constitutes a major energy loss of the extreme ultraviolet sunlight that is deposited there.

Very similar phenomena are present in the Venus airglow, but there has been relatively little analysis because of the large body of direct data on the upper atmosphere from the Pioneer Venus orbiter.

On Jupiter and Saturn, and presumably also Uranus and Neptune, important  $H_2$  emissions in the Lyman ( $B^1\Sigma_u^+ - X^1\Sigma_g^+$ ) and Werner ( $C^1\Pi_u - X^1\Sigma_g^+$ ) bands are seen (“auroral  $H_2$  bands” in Fig. 6.12). They are excited by both resonance fluorescence and electron impact. The latter process operates primarily in the aurora, but as on the terrestrial planets photoelectrons give a dayglow component as well.

Titan’s sunlit disk has the spectrum shown in Fig. 6.10, which includes identifications for many of the emissions and a synthetic spectrum, computed for excitation by electron impact. Clearly, not all the intensity is explained, but the principal emitter is nitrogen, mostly in molecular form. This spectrum gave the first observational proof that  $N_2$  is the principal gas on Titan, followed quickly by the discovery from the IR and radio experiments that the molecular mass is close to 28 amu.

Jupiter, Saturn, and Titan all show two related anomalies: the intense UV emissions are several times brighter than can be accounted for by the energy in the incident solar UV, and these bright emissions are not seen on the dark side. Evidently some extra energy source is being triggered by the solar input; a speculative suggestion is that it might be related to electric fields of unknown origin. Such *electroglow* is even more prominent at Uranus.

### 6.3.4 Alkali Metals

The most extensively studied alkali metal is Na I, but twilight, and therefore presumably daytime, emissions are present also from Ca II, Li I, and K I. The seasonal and daily variations and the height distribution of [Na]

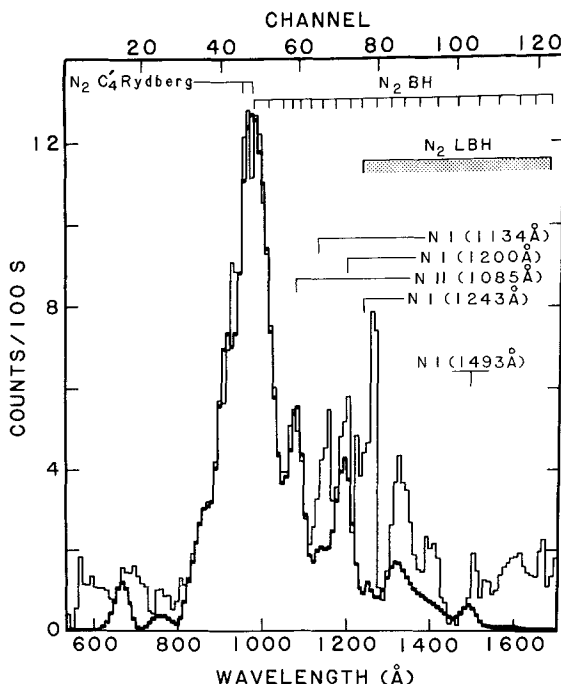


**Fig. 6.10** Ultraviolet spectrum of Titan's disk and a model fit involving the nitrogen lines and bands indicated. [After STROBEL and SHEMANSKY (1982).]

above the peak concentration around 90 km have not been well understood. There have been problems associated with the  $[Na^+]/[Na]$  ratio, the role of eddy diffusion, and the interaction between Na atoms and aerosols, all of which are suspected of being important as sources or sinks of free Na. With laser sounding techniques (*lidar*) the abundance of Na can be measured from the ground as a function of height. Observations of this nature promise to clarify the apparent peculiarities of Na distribution as well as the role of eddy transport near the mesopause.

Although not a conventional planetary airglow, the Na I emission from Io (Jupiter's inner Galilean satellite) is remarkably like airglow. The emission comes from an extensive cloud surrounding the satellite (see Fig. 6.11). The  $D_2$  and  $D_1$  emission rates are about 15 and 8 kR, respectively, and the excitation source seems to be resonance scattering of an optically thin, high-temperature cloud. High-dispersion spectra of the sodium near Io have consistently shown velocities of several kilometers per second, and 70 km/sec has been observed. Such velocities are far greater than any possible thermal speed, even at the  $1000^{\circ}\text{K}$  thought to apply to Io's exosphere. Collisional

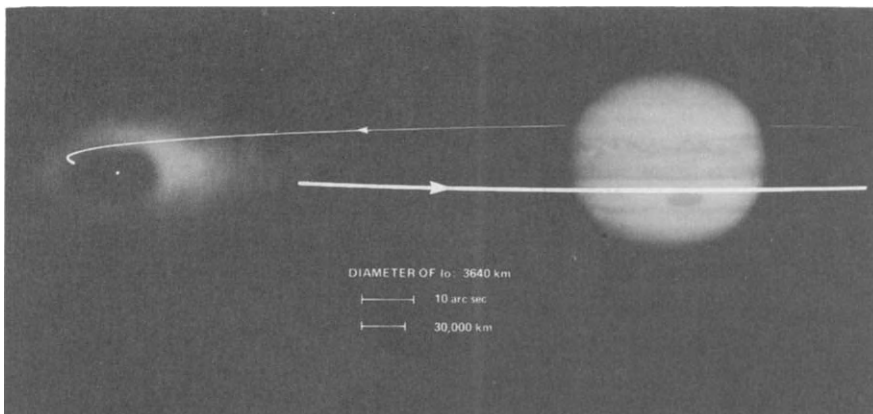


**Fig. 6.11** Image of Io's sodium cloud taken with the coude spectrograph at Table Mountain Observatory, California, on Feb. 19, 1977. The cloud was photographed in the  $D_1 + D_2$  emissions. The photograph of Jupiter and the white dot indicating the position of Io have been added for orientation purposes. The dark area within the sodium cloud is produced by an occulting disk used to exclude direct continuum light from Io. [After MATSON, D. L.; GOLDBERG, B. A.; JOHNSON, T. V.; and CARLSON, R. W. (1978). *Science*, **199**, 531.]

phenomena seem to be required to accelerate neutral atoms to such velocities; they are discussed in the next section.

### 6.3.5 Io's Plasma Torus

The Pioneer 10 ultraviolet photometer measured  $\sim 300$  R, attributed at the time to Lyman alpha radiation from a  $120^\circ$  segment of a torus in the orbit of Io. If the spectrum at that time was at all like that seen by the Voyagers, the broad passband of the Pioneer photometer would have included many of the lines seen in Fig. 6.12. These lines are excited by electron impact and are therefore in the category of aurora rather than airglow. Lines from the plasma torus were in fact discovered a few years before the Voyager encounters, and many of its properties had already been worked out. The most obvious effect on the sodium glow is to limit the lifetime of a sodium atom by ionizing it. This lifetime is about 24 hrs on the average, although it is considerably shorter in the region outside Io's orbit. It is likely that the ions of the plasma are also responsible for ejecting atoms of oxygen, sulfur, and sodium from Io in the first place.

Torus ions are trapped in Jupiter's magnetic field and therefore co-rotate with Jupiter at a speed of about 70 km/sec. Io's orbital speed is 17 km/sec, and the ions therefore overtake it at 55 km/sec, carrying a kinetic energy of 230 eV for oxygen and twice as much for sulfur. Their thermal energy in the rotating

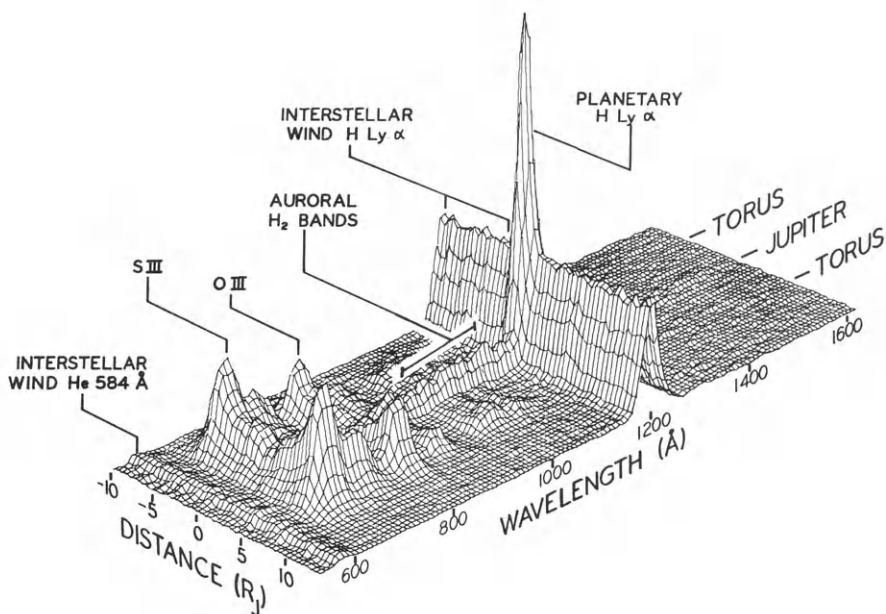


**Fig. 6.12** A panorama of ultraviolet spectra of the Jupiter system, viewed from a distance by Voyager 1. Light from Jupiter, the Io torus, and the interplanetary medium can all be seen. [After BROADFOOT *et al.* (1981).]

coordinate frame is typically 1–10 eV, and they are therefore confined rather closely to the centrifugal equator, the locus of those points on the magnetic-field lines farthest from Jupiter's axis of rotation. The electrons have about the same temperature as the ions and are responsible for ionizing the neutral atoms and exciting the observed ion emission lines. Freshly-created ions are moving with Io and therefore execute a cyclotron motion at 55 km/sec in addition to their co-rotation. This cyclotron motion is an important source of the energy that drives the whole system, although it may not be the only major source.

Io's upper atmosphere presumably is made up of atoms of O, S, and Na, with perhaps a considerable amount of SO<sub>2</sub> as well. Collisions of torus ions can eject them in the forward direction with velocities similar to the incident velocity, or sideways with considerably less. Atoms faster than 24 km/sec can leave the Jupiter system; the slower ones remain to contribute to the observed phenomena. Although these processes appear able to account for the supply of sodium atoms and torus ions, it is still necessary to explain in the first place the presence of sodium in the atmosphere. The relevant process is thought to be sputtering from the surface by heavy magnetospheric ions with energies in the hundreds of kiloelectron volts. The term *sputtering* refers to the multiple

collisions of atoms or molecules arising from the impact of a fast ion; there is a significant probability that one or more atoms will be ejected in the backward direction, with energies up to several electron volts. In the absence of an atmosphere, sputtered atoms could reach the torus region directly, but the required fluxes are more readily explained by the two-stage process, with the second stage involving much slower and more abundant ions.

## 6.4 Aeronomy of the Planets

The broad topic of aeronomy appears throughout this book. Chemical reactions are important at all levels—even in the Earth's troposphere where minor constituents and pollution products are concerned. The stratosphere was examined in some detail in Chapter 3 and aeronomic reactions involving ionospheres in Chapter 5. Here we look at aeronomy in the density regions of other planets that correspond roughly to the Earth's stratosphere.

### 6.4.1 Predominantly CO<sub>2</sub> Atmospheres

The problem of the low degree of dissociation of CO<sub>2</sub> on Mars and Venus has been noted earlier (Section 5.3.1) Basically it is that CO<sub>2</sub> dissociation produces O atoms that should associate to form O<sub>2</sub> by (5.3.9) faster than CO<sub>2</sub> by (5.3.8). Re-association of CO and O (or O<sub>2</sub>) requires catalytic processes involving odd hydrogen, as illustrated by Fig. 6.13. The odd H is

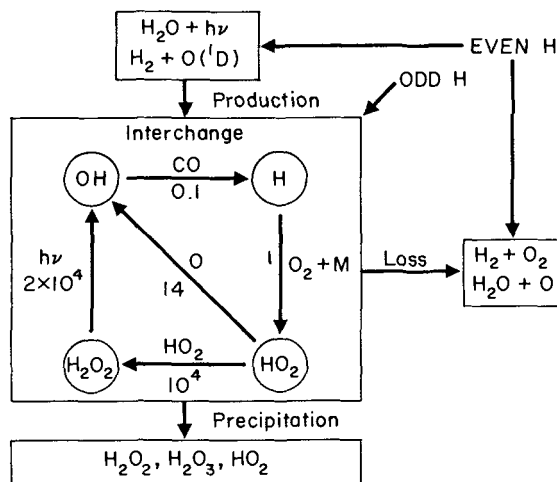
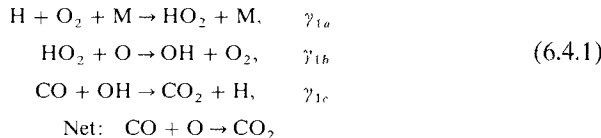


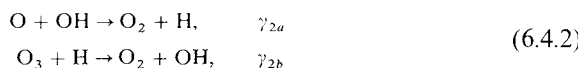
Fig. 6.13 Flow diagram for odd hydrogen near the surface of Mars. [After HUNTER (1979).]

produced by photolysis of  $\text{H}_2\text{O}$ , whose abundance can be much greater than in the Earth's middle atmosphere, and by reaction of  $\text{O}(\text{^1D})$  with  $\text{H}_2$ . Sinks of odd H are reaction of H with  $\text{HO}_2$ , shown at the right, and deposition on the surface, perhaps followed by further reactions to form superoxides in the soil. This cycle operates principally in the bottom 20–30 km of the atmosphere.

The inner cycle, involving H,  $\text{HO}_2$ , and OH, oxidizes a CO molecule and consumes an O atom; odd H and  $\text{O}_2$  act as catalysts:

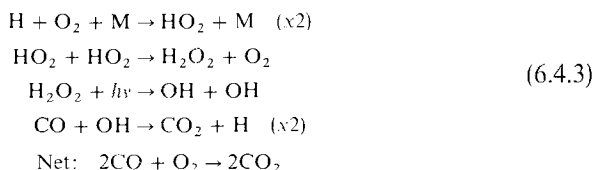


Molecular oxygen is produced, and odd O destroyed, by the reactions



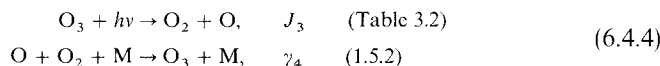
and the corresponding sink is photolysis of  $\text{O}_2$ , whose abundance is about 0.1 %. Additional O flows down from the thermosphere. The photolysis rate of  $\text{O}_2$  is fixed (at least over times of a few years), while the production rate varies as the square of the O density, since the OH in (6.4.2) depends on O. The O must be transported downward by eddy mixing. The scale height is very large; the density, therefore, varies as  $1/K$  (Fig. 2.7a), and the  $\text{O}_2$  production varies as  $1/K^2$ . The system balances with  $K \sim 10^8 \text{ cm}^2 \text{ sec}^{-1}$ , which is very large by comparison with the Earth's stratosphere. Perhaps this is because there is no true stratosphere on Mars: no temperature inversion to inhibit vertical motion. Nevertheless, the required value is uncomfortably large.

Carbon monoxide can be oxidized by  $\text{O}_2$  by way of the outer cycle in Fig. 6.13, and a smaller value of K might be acceptable. The sequence is



This mechanism, however, requires larger amounts of  $\text{HO}_x$  than does (6.4.1) and may have problems in that regard.

Ozone destruction on Mars is tied to the  $\text{HO}_x$  chemistry through (6.4.1) and through the dependence of  $[\text{O}_3]$  on [O] by the rapid sequence of



If  $\text{H}_2\text{O}_2$  can be neglected, the steady-state equations can easily be set up (Problem 6.10). The ratios of the three forms of odd H are

$$\frac{[\text{HO}_2]}{[\text{H}]} = \frac{\gamma_{1a}[\text{O}_2][\text{M}]}{\gamma_{1b}[\text{O}]} \quad (6.4.5)$$

$$\frac{[\text{OH}]}{[\text{H}]} = \frac{\gamma_{1a}[\text{O}_2][\text{M}] + \gamma_{2b}[\text{O}_3]}{\gamma_{1a}[\text{CO}] + \gamma_{2a}[\text{O}]} \quad (6.4.6)$$

These ratios are typically 16 and 0.073 at the surface, with the concentrations shown in Fig. 6.14. Similarly for odd O,

$$\frac{[\text{O}_3]}{[\text{O}]} = \frac{\gamma_4[\text{O}_2][\text{M}]}{J_3 + \gamma_{2b}[\text{H}]} \approx \frac{\gamma_4[\text{O}_2][\text{M}]}{J_3} \quad (6.4.7)$$

The production rate of odd O, mainly by  $\text{CO}_2$  photolysis, is represented by  $p(\text{O}) = 6 \times 10^5 \text{ cm}^{-3} \text{ sec}^{-1}$ ; if the smaller terms are dropped, the following equation implicitly gives the total amount of odd O produced:

$$\gamma_{1b}[\text{HO}_2][\text{O}] \left( 1 + \frac{\gamma_{2b}\gamma_4}{\gamma_{1a}J_3} [\text{O}] \right) \approx p(\text{O}) \quad (6.4.8)$$

This solution is illustrated in Fig. 6.14, along with the result for a “dry” atmosphere (one that contains no odd H but is constrained to have the observed amount of  $\text{O}_2$ ). The ozone abundance for the “wet” case is consistent with the observational upper limits for low latitudes, and the observed amounts around the winter pole are similar to the “dry” case.

As Fig. 6.13 indicates, the atmospheric sink of odd H is by the reaction of H and  $\text{HO}_2$ , which yields both  $\text{H}_2\text{O}$  and  $\text{H}_2$  in a poorly known ratio. The  $\text{H}_2$  is

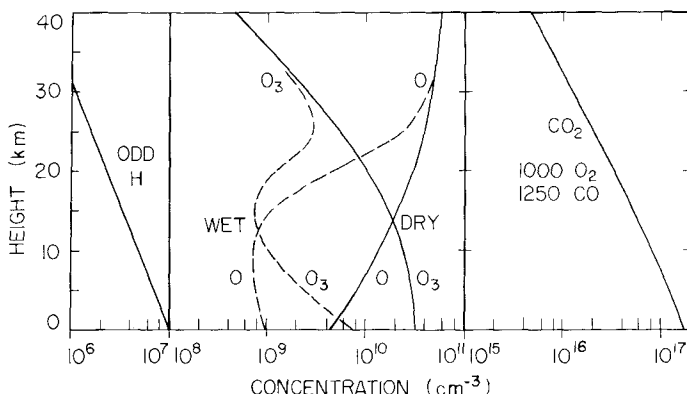


**Fig. 6.14** Densities of odd oxygen on Mars for models with no odd hydrogen (“dry”) and the amount shown on the left (“wet”). [After PARKINSON and HUNTER (1972).]

recycled by reaction with  $O(^1D)$ , which is produced in ozone photolysis. It also escapes from the atmosphere, partly in the form of H atoms. The predicted  $H_2$  mixing ratio is about 10 ppm, which is consistent with the observed amount of H in the corona. Thus the presence of  $O_3$  on Mars mainly over the winter polar cap (see Section 6.3.3) is likely due to the freezing out of  $H_2O_2$  and possibly  $HO_2$ , allowing  $O_3$  to form there. Frozen polyoxides ( $H_2O_3$ ,  $H_2O_4$ ) are probably formed from  $HO_2$ . In addition, the Viking landers have confirmed relatively high concentrations of metal oxides in the soil and these materials may exchange oxygen with the atmosphere, the soil liberating it mainly during warm periods of dust storms.

Although the dominant gas on Venus is also  $CO_2$ , the basic photochemistry is totally different from that of Mars. The  $O_2$  mixing ratio, already remarkably small on Mars, is far smaller on Venus, with an upper limit of  $3 \times 10^{-7}$  above the clouds. (The value below the clouds is not established, but may be considerably greater.) Carbon monoxide, at 45 ppm, is also much rarer, but not by nearly so large a factor. Although odd H may play a minor role in the oxidation of CO, the dominant catalysts are compounds of chlorine.

Another major feature of the Venus atmosphere is the cloud deck of concentrated  $H_2SO_4$ , extending from 50 to about 70 km. It is thought that the acid is thermally decomposed to  $SO_2$  in the deep, hot levels near the surface, and this gas must be re-oxidized to  $SO_3$ , even though free oxygen is

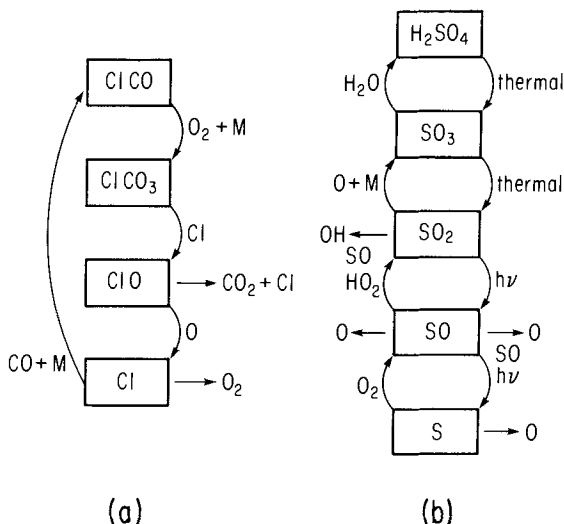


**Fig. 6.15** Simplified flow diagrams for (a) chlorine and (b) sulfur in the Venus middle atmosphere.

almost nonexistent. In fact, some free O atoms may be generated from  $\text{SO}_2$ . Only the general flavor of this complex system can be given here.

Flow diagrams for the chlorine and sulfur systems are given in Fig. 6.15. The chlorine cycle has the interesting and important property that it does not require any photons, except indirectly in the form of an input of atomic oxygen, primarily from the thermosphere. Thus, the net reaction  $\text{CO} + \text{O} \rightarrow \text{CO}_2$  runs as well on the night side as the day side, as required by Earth-based millimeter-wave data, which pertain to the upper mesosphere. The multiple sulfur cycles are powered by photons, with some contributions by thermal dissociation near the surface. Atomic oxygen is both produced and consumed; some of the atoms help to run the chlorine cycle, and others go into sulfuric acid. The small production of OH can help with the oxidation of CO. The eddy coefficient in the middle atmosphere can be treated as a free parameter, because there is almost no independent information. A value of  $10^5 \text{ cm}^2 \text{ sec}^{-1}$  from 70 to 95 km, increasing above and falling off below, gives the results shown in Fig. 6.16, which also includes the available observational constraints on  $\text{SO}_2$  and CO. The constraint of 1 ppm on  $\text{O}_2$  has since been pushed down another factor of three, and the new value does not appear to be met. However, the interpretation of an apparent spectroscopic upper limit is rather obscure for this scattering atmosphere, and a radiative-transfer analysis is needed to clarify it.

In the thermospheres of both Mars and Venus, the principal issue is the rate of vertical transport, whether expressed in terms of an eddy coefficient or

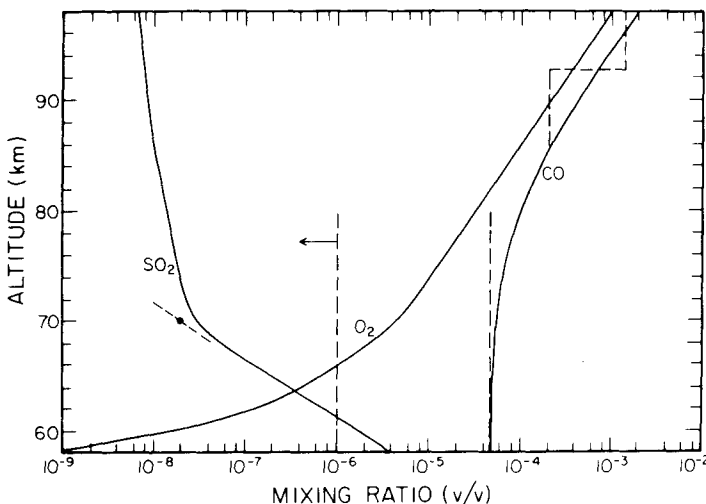


**Fig. 6.16** Computed densities of  $\text{SO}_2$ ,  $\text{O}_2$ , and CO above the Venus cloud tops, along with the observational constraints. [After YUNG and DEMORE (1982).]

a global circulation. These matters are discussed in Section 2.3.5; the chemistry of the middle atmosphere is important mainly in defining the densities and fluxes at the base of the thermosphere.

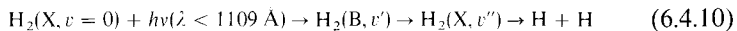
#### 6.4.2 Predominantly H<sub>2</sub> Atmospheres

Being farther removed from the sun, the major planets have much lower temperatures in their photochemically active middle atmospheres than does the Earth. This fact combined with the hydrogen dominated composition gives a photochemistry in which the main products are hydrocarbons—including some rather complex ones—and NH<sub>3</sub> (ammonia).

Atomic H is produced in the upper atmosphere by several processes, principally as follows: Photodissociation,



predissociation through absorption in the Lyman bands (B<sup>1</sup>Σ<sub>u</sub><sup>+</sup> ← X<sup>1</sup>Σ<sub>g</sub><sup>+</sup>),



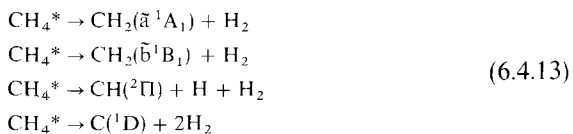
provided v'' > 14; predissociation through the Werner bands (C<sup>1</sup>Π<sub>u</sub> ← X<sup>1</sup>Σ<sub>g</sub><sup>+</sup>) for λ < 1009 Å; ionization of H<sub>2</sub> leading to



which breaks an H<sub>2</sub> bond; and ionization of He, which yields



The CH<sub>4</sub> (methane) molecule also undergoes predissociation. Absorption of Ly α leaves CH<sub>4</sub> in an excited state (CH<sub>4</sub><sup>\*</sup>) with internal energy exceeding the dissociation energy (4.5 eV). Then CH<sub>4</sub><sup>\*</sup> has a radiationless transition to the dissociation continuum of another state, such as



From these dissociation products, C<sub>2</sub>H<sub>6</sub> (ethane) is produced and then photodissociated into C<sub>2</sub>H<sub>4</sub> (ethylene), CH<sub>3</sub> (methyl radical), and CH<sub>2</sub>. Then C<sub>2</sub>H<sub>4</sub><sup>\*</sup> may predissociate into C<sub>2</sub>H<sub>2</sub> (acetylene). The principal reaction routes are shown in Fig. 6.17. The rate of photolysis of ethylene is considerably larger than that of the other two, so that this molecule is expected to be rare; in fact, it has not been observed on Jupiter and is scarce on Titan.

Although the detailed paths have not been traced, there is little doubt that heavier hydrocarbons are also produced. Because there is so much hydrogen,

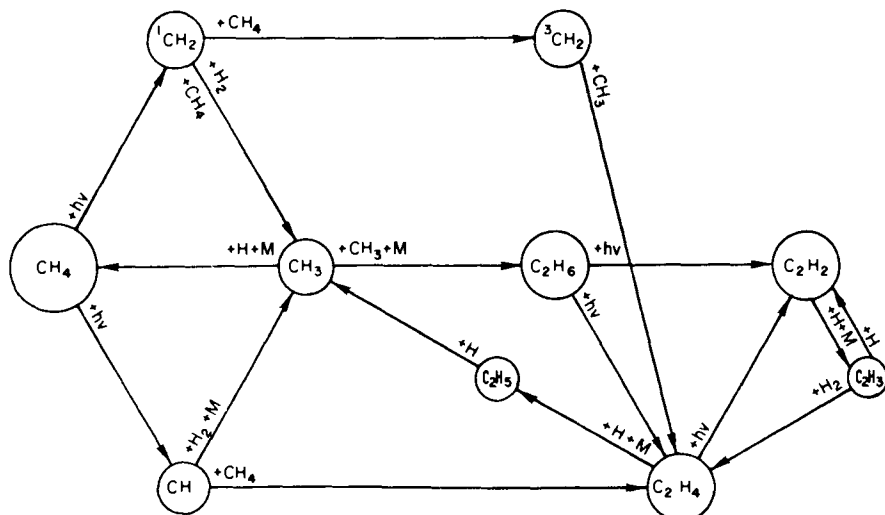


**Fig. 6.17** Principal reactions in the hydrocarbon photochemistry on Jupiter and other predominantly  $\text{H}_2$  atmospheres. The notation  ${}^1\text{CH}_2$  and  ${}^3\text{CH}_2$  refers to radicals produced in singlet and triplet states, respectively. [After STROBEL (1975).]

the yields are rather small. On Titan this inhibition is nearly absent, and the more complex molecules are abundant enough to have been detected (see the next section). Jupiter, Saturn, and Titan are all relatively dark in the ultraviolet, undoubtedly because of the presence of smog particles, often called *Danielson dust*. These particles are believed to have condensed from some of the heavier hydrocarbons. The major sink of all the more complex molecules is downward transport to regions of high temperature, where the thermodynamic equilibrium forms,  $\text{CH}_4$  and  $\text{NH}_3$ , are restored.

Photolysis of  $\text{NH}_3$  occurs primarily by



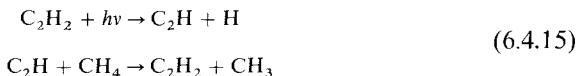
Other dissociation products are prevented by the screening of sunlight at  $\lambda < 1600 \text{ \AA}$  by the overhead  $\text{CH}_4$ .

At high pressures  $\text{NH}_2$  reacts with itself to form  $\text{N}_2\text{H}_4$  or with  $\text{H}$  to recycle  $\text{NH}_3$ . The  $\text{N}_2\text{H}_4$  may be converted into  $\text{N}_2$  and  $2\text{H}_2$  or it may, at low temperatures, contribute to the photochemical smog.

#### 6.4.3 Titan's Atmosphere

As summarized in Section 1.9.3, Titan has a fairly deep atmosphere of  $\text{N}_2$  with a few percent of methane, and a surface temperature of  $93^\circ\text{K}$ . In many ways, the methane photochemistry is like that of Jupiter, but more efficient in

the near absence of free hydrogen, which escapes rapidly. An important aspect of this higher efficiency is indirect photolysis of methane by processes of the form



Acetylene ( $\text{C}_2\text{H}_2$ ) acts as a catalyst, which is regenerated, but absorbs solar energy to much longer wavelengths than methane does; the available flux is an order of magnitude greater because the solar spectrum rises rapidly with wavelength. Polyacetylenes, though scarcer, absorb to still longer wavelengths with production of  $\text{C}_2\text{H}$ , as well as  $\text{C}_2$  which also attacks  $\text{CH}_4$ . Where hydrogen is abundant, (6.4.15) is replaced by a cycle that generates H atoms instead. As on Earth, nitrogen is almost but not quite inert; the principal source of dissociation is impact of charged particles, either cosmic rays at low altitudes or photoelectrons and magnetospheric electrons at high. Because of the low temperatures in the lower stratosphere (Fig. 1.31), most compounds condense and eventually fall to the surface, where they probably accumulate, rather than being recycled as on the Jovian planets. Methane must therefore be continuously replenished, presumably from the interior. The primary products are  $\text{H}_2$ , which escapes, and  $\text{C}_2\text{H}_6$ , which must therefore be the main constituent of the surface deposit: an *ethane ocean*. Such an ocean should also contain dissolved  $\text{N}_2$  and  $\text{CH}_4$ , with a total depth approaching a kilometer if the same processes as today have operated throughout most of geologic time. The corresponding fluxes, in  $\text{cm}^{-2} \text{ sec}^{-1}$  referred to the area of Titan's surface, are  $1.8 \times 10^{10}$  of  $\text{H}_2$ ,  $5.8 \times 10^9$  of  $\text{C}_2\text{H}_6$ , and, for replacement,  $1.5 \times 10^{10}$  of  $\text{CH}_4$ .

Very small amounts of CO and  $\text{CO}_2$  are observed. The only oxygen compound that could originate in the interior and reach the stratosphere is CO, which is somewhat unlikely on cosmochemical grounds. However,  $\text{H}_2\text{O}$  must be entering the atmosphere in the form of meteoroids, and is converted to CO with high efficiency.

Figure 6.18 is a flow chart for the chemistry that leads to the observed species (not all of which are shown). The initial part of the hydrocarbon chemistry is very similar to Fig. 6.17. The eddy coefficients required to match the model to the data are shown in Fig. 6.19. Production of smog particles has been modeled in some detail. The key radical is again  $\text{C}_2\text{H}$ , which reacts with acetylene and the polyacetylenes according to



A polyacetylene is a chain of carbon atoms with one hydrogen atom at each end, and condensation of the heavier ones is almost surely the principal source of the smog particles. The predicted rate of production is of the order

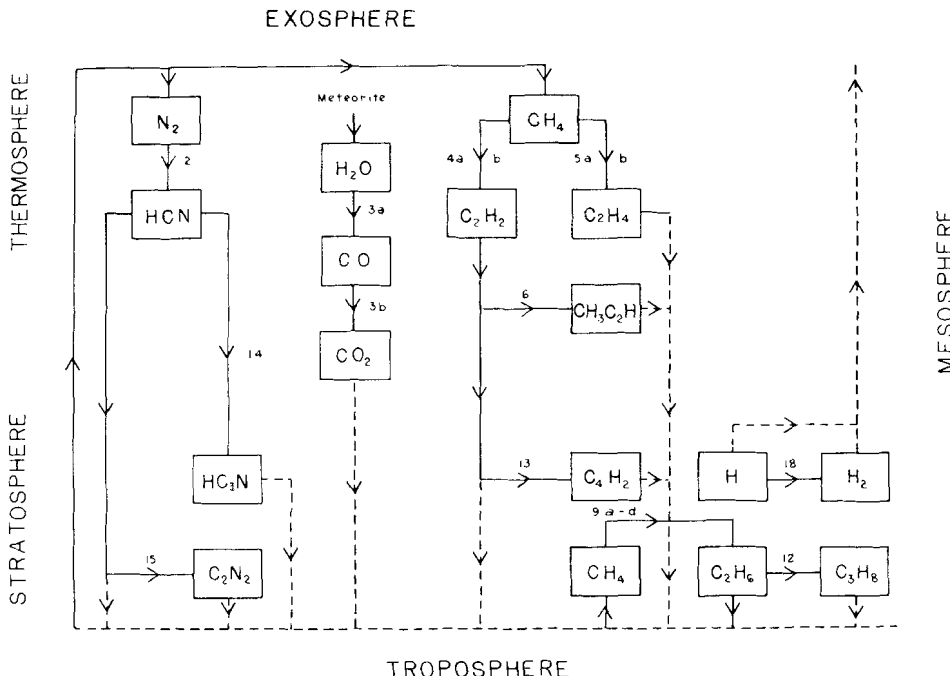


Fig. 6.18 Flow diagram for the aeronomy of Titan. [After YUNG *et al.* (1984).]

of  $10^8 \text{ cm}^{-2} \text{ sec}^{-1}$ , which may be a lower bound because only the first few polyacetylenes have been modelled. Analogous chemistry may be responsible for the production of soot in flames and, in interstellar clouds, of long carbon chains many of which are observed in the millimeter wavelength region. Polyacetylenes proper have no dipole moment and thus cannot be observed in this way; the relevant chemistry probably involves ions rather than photon-generated radicals.

Generation of smog particles on Jupiter and Saturn has not been modeled in detail; it is not clear whether the Titan chemistry or something rather different is active there.

#### 6.4.4 Galilean Satellites

As discussed in Section 1.9.4, Io has a tenuous atmosphere of  $\text{SO}_2$ , although the typical surface pressure is very uncertain and probably highly variable with latitude and solar zenith angle. Europa, Ganymede, and

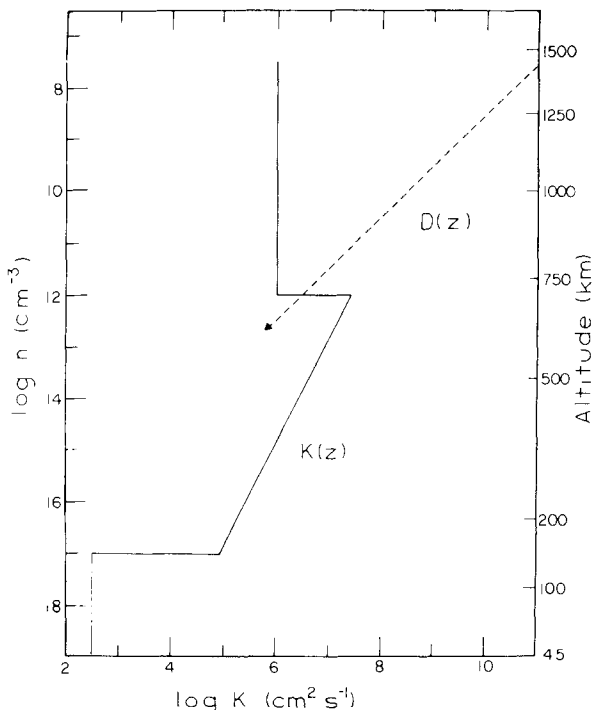


Fig. 6.19 The profile of eddy diffusion coefficient corresponding to Fig. 6.18. [After YUNG *et al.* (1984).]

Callisto are expected to have even more tenuous atmospheres of H<sub>2</sub>O. All four must have at least some O<sub>2</sub> of photochemical origin.

The aeronomy of sulfur and its oxides is fairly important on Earth and Venus; it is the whole story on Io. The principal reactions are illustrated in Fig. 6.20. Several rather arbitrary choices must be made before a model can be computed: the base pressure, the fluxes from the top of the atmosphere into the torus, and the fate of atoms and radicals hitting the surface. For the results shown in Fig. 6.21, escape fluxes were chosen at the large rates needed to populate the plasma torus. The surface provided SO<sub>2</sub> at the rate necessary to maintain the atmosphere, and S and O atoms striking the surface were absorbed. Another possible assumption is that the O atoms are converted to molecules and re-emitted; this case gives about 10% O<sub>2</sub> near the surface, and nearly pure O<sub>2</sub> on the night side.

The obvious diffusive separation in Fig. 6.21 leads to a problem in populating the torus with comparable amounts of O and S, since the O is considerably enriched at the higher levels. One possible resolution is that mutual drag forces are large enough to greatly reduce the diffusive separa-

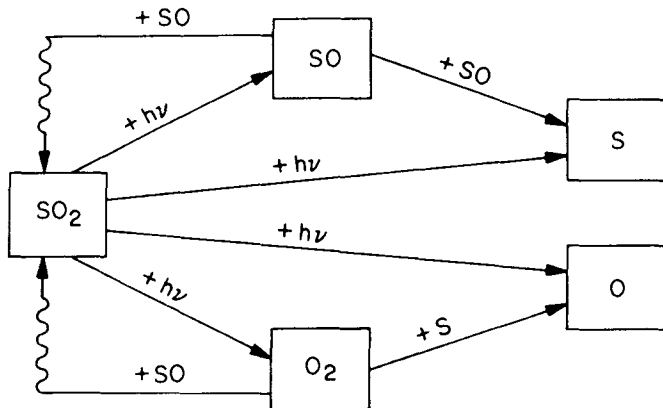


Fig. 6.20 Flow diagram for  $\text{SO}_2$  aeronomy on Io. [After KUMAR (1982).]

tion; such forces become appreciable when the gases are moving upward at speeds comparable to the sound speed, as they may be on Io (Section 7.3.6).

Satellites with exposed ice must have at least a small atmosphere of  $\text{H}_2\text{O}$ ; thermal evaporation may be supplemented by sputtering, especially on Europa which is subjected to a larger flux of ions than Ganymede or Callisto. Rapid escape of hydrogen must lead to a buildup of  $\text{O}_2$ , whose abundance rises until its escape comes into balance. Thermal escape is negligible for  $\text{O}$ ; the required energy is imparted by photodissociation of  $\text{O}_2$  by wavelengths

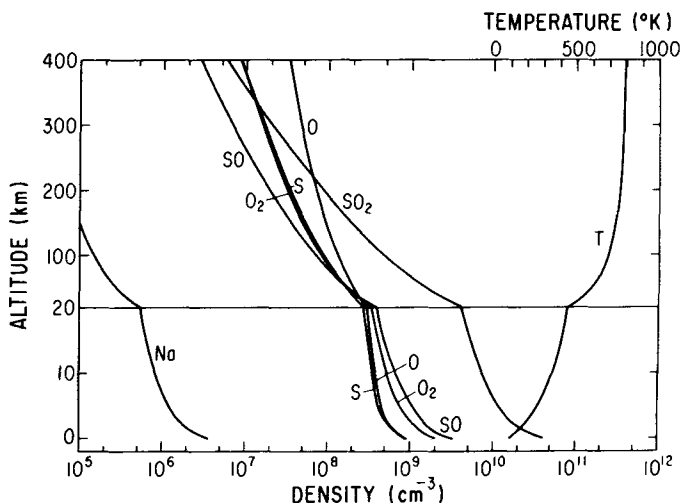


Fig. 6.21 Temperatures and densities for a possible Io atmosphere. The line at 20 km marks a change of the height scale. [After KUMAR (1985).]

well below threshold. There is thus a limit to the flux, obtained when the exobase has risen well above the surface; its global-mean value is  $4.2 \times 10^7$  atoms  $\text{cm}^{-2} \text{ sec}^{-1}$ . If the  $\text{H}_2\text{O}$  photolysis rate is less than this, the system can reach a steady state with a low surface pressure of  $\text{O}_2$ , up to a few times  $10^{-6} \mu\text{bar}$ . The corresponding  $\text{H}_2\text{O}$  pressure is around  $10^{-9} \mu\text{bar}$ . If it is a factor of 10 greater, oxygen is generated at a rate too large for the escape mechanism to handle; its partial pressure rises to around  $1 \mu\text{bar}$ , where it absorbs enough radiation to cut back the photolysis rate of  $\text{H}_2\text{O}$  and bring the system back into balance. For Ganymede, this situation is ruled out by the Voyager upper limit of  $10^{-5} \mu\text{bar}$ .

## BIBLIOGRAPHICAL NOTES

### Section 6.1 Airglow Photometry

There are observations on record as early as 1788 of nights with an unusually large sky brightness and an increase in brightness from the zenith to the horizon. That the light of the night sky has a terrestrial component—what is now termed *airglow*—was suspected by a number of astronomers around 1900 and was definitely established through careful photometry by

YNTEMA, L. (1909), On the brightness of the sky and total amount of starlight, *Publ. Astr. Groningen* No 22, 1–55.

The green line of [O I] had been found much earlier to be present, even when visible aurora was not, by

ÅNGSTRÖM, A. J. (1868), “Recherches sur le Spectre Solaire,” W. Schultz, Upsala, pp. 41–42, and others, but the fact that the green line is permanently present at night was established by

SLIPHER, V. M. (1919), On the general auroral illumination of the sky and the wavelength of the chief aurora line, *Astrophys. J.*, **49**, 266–275.

The principal early work was done by C. FABRY and J. DUFAY in France and the fourth Lord Rayleigh (R. J. STRUTT) in England. The first measurement of the absolute intensity of the night airglow was made by

RAYLEIGH, LORD (R. J. STRUTT) (1930), Absolute intensity of the aurora line in the night sky and the number of atomic transitions, *Proc. Roy. Soc. (London)* **A129**, 458–467.

Rayleigh's result for the zenith was  $4\pi\mathcal{I} = 1.81 \times 10^8$  quanta/ $\text{cm}^2 \text{ sec}$  or 181 rayleighs, not far from the value (250 R) usually adopted as the average today. Incidentally, it is Rayleigh's father, the third Lord Rayleigh (J. W. Strutt), who is remembered for the theory of molecular scattering, among other things.

One might question whether a specialized unit, generally unfamiliar to physicists and astronomers who do not work in the fields discussed here, was really necessary or even desirable. Before the rayleigh was introduced, there was widespread confusion in the airglow literature as to whether a measurement reported as “photon/ $\text{cm}^2 \text{ sec}$ ” referred to a vertical flux or a column emission rate; that is, there were uncertainties of a factor of two. To clarify matters, many writers started using the awkward unit, “photon/ $\text{cm}^2(\text{column})\text{sec}$ ” or “Megaphoton/ $\text{cm}^2(\text{column})\text{sec}$ ” for emission rates. This state of affairs led to the introduction of the rayleigh by

HUNTEM, D. M.; ROACH, F. E.; and CHAMBERLAIN, J. W. (1956), A photometric unit for the airglow and aurora, *J. Atm. Terr. Phys.* **8**, 345–346.

Shortly afterward, and largely due to the efforts of Roach, the unit was adopted by both the International Astronomical Union and the International Union of Geodesy and Geophysics.

An extensive review of terrestrial airglow, including references to the main historical works, is included in

CHAMBERLAIN, J. W. (1961), "Physics of the Aurora and Airglow," Academic Press, New York.

More recent reviews are

HUNTER, D. M. (1967), Spectroscopic studies of the twilight airglow, *Space Sci. Rev.* **6**, 493–573.

HUNTER, D. M. (1971), Airglow—Introduction and review, in "The Radiating Atmosphere," (B. M. McCormac, ed.), pp. 3–16, Springer-Verlag, New York.

The expanded sodium chemistry including NaOH and NaO<sub>2</sub> is discussed by

SWIDER, W. (1986), Sodium nightglow: Chemically independent of sodium content, *J. Geophys. Res.* **91**, 6742–6746.

The historical development of the theory of the airglow green line is recounted by

BATES, D. R. (1981), The green light of the night sky, *Planet. Space Sci.* **29**, 1061–1067.

The O<sub>2</sub>\* state that is the precursor to O(<sup>1</sup>D) in the Barth mechanism (6.1.9c) was identified, on the basis of the virtual absence of λ5577 in Venus' nightglow, as the c <sup>1</sup>Σ<sub>u</sub><sup>−</sup> state by

KRASNOPOLSKY, V. A. (1981), Excitation of oxygen emissions in the night airglow of the terrestrial planets, *Planet. Space Sci.* **29**, 925–929.

That the a <sup>1</sup>Δ<sub>g</sub> state is effective in deactivating O(<sup>1</sup>S) was established by

SLANGER, T. G. and BLACK, G. (1981), Quenching of O(<sup>1</sup>S) by O (a <sup>1</sup>Δ<sub>g</sub>), *Geophys. Res. Lett.* **8**, 535–538.

The problem of rotational temperatures of OH is discussed in

SUZUKI, K. and TOHMATSU, T. (1976), An interpretation of the rotational temperature of the airglow hydroxyl emissions, *Planet. Space Sci.* **24**, 665–671.

DICK, K. A. (1977), On the rotational temperature of airglow hydroxyl emissions, *Planet. Space Sci.* **25**, 595–596.

KRASSOVSKI, V. I.; POTAPOV, B. P.; SEMENOV, A. I.; SOBOLEV, V. G.; SHAGAEV, M. V.; and SHEFOV, N. N. (1977), On the equilibrium nature of the rotational temperature of hydroxyl airglow, *Planet. Space Sci.* **25**, 596–597.

The history of the identification of reaction (6.1.16) as the source of the airglow continuum is given in

CHAMBERLAIN, J. W. (1961), op. cit. pp. 543–545.

Satellite photometric observations of the emission and the rate coefficient of the reaction are discussed by

DONAHUE, T. M. (1974), An upper limit to the product of NO and O densities from 105 to 120 km, *J. Geophys. Res.* **79**, 4337–4339.

The A' <sup>3</sup>Δ<sub>u</sub> → a <sup>1</sup>Δ<sub>g</sub> bands were first identified as a new O<sub>2</sub> system on a long photographic exposure of the Earth's airglow spectrum by

CHAMBERLAIN, J. W. (1958), The blue airglow spectrum, *Astrophys. J.* **128**, 713–717.

The airglow spectra of Venus, obtained from Venera 9 and 10 by

KRASNOPOLSKY, V. A.; KRYSKO, A. A.; ROGASHEV, V. N.; and PARSHEV, V. A. (1976), Spectroscopy of the night-sky luminescence of Venus from the interplanetary spacecraft Venera 9 and Venera 10, *Cosmic Res.* **13**, 687–692,

showed the  $v' = 0$  progressions of three O<sub>2</sub> systems: The Herzberg II,  $c\ ^1\Sigma_u^- \rightarrow X\ ^3\Sigma_g^-$ , which was identified by

LAWRENCE, G. M.; BARTH, C. A.; and ARGABRIGHT, V. (1977), Excitation of the Venus night airglow, *Science* **195**, 573–574,

the Chamberlain,  $A'\ ^3\Delta_u \rightarrow a\ ^1\Delta_g$ , was identified by

SLANGER, T. G. and BLACK, G. (1978), The O<sub>2</sub>(C  $^3\Delta_u \rightarrow a\ ^1\Delta_g$ ) bands in the nightglow spectrum of Venus, *Geophys. Res. Lett.* **5**, 947–948,

and the Herzberg I,  $A\ ^3\Sigma_u^+ \rightarrow X\ ^3\Sigma_g^-$ , measured by

KRASNOPOLSKY, V. A. and TOMASHOVA, G. V. (1980), Variations in the nighttime emission of Venus, *Cosmic Res.* **18**, 556–562.

The identification of the Herzberg II system in Earth's nightglow is due to

SLANGER, T. G. and HUESTIS, D. L. (1981), O<sub>2</sub>(c  $^1\Sigma_u^- \rightarrow X\ ^3\Sigma_g^-$ ) emission in the terrestrial nightglow, *J. Geophys. Res.* **86**, 3551–3554.

The Pioneer Venus orbiter observed ultraviolet emissions, identified as the  $v' = 0$  progressions of the  $\gamma$  and  $\delta$  bands of NO by

FELDMAN, P. D.; MOOS, H. W.; CLARKE, J. T.; and LANE, A. L. (1979), Identification of the UV nightglow from Venus, *Nature* **279**, 221–222,

STEWART, A. I. and BARTH, C. A. (1979), Ultraviolet night airglow of Venus, *Science* **205**, 59–62.

The emission, which is produced by association of N and O in the 110 km region, has been photometrically mapped in the 0-1  $\delta$  band at 1980 Å to study the downward transport of atoms by

STEWART, A. I.; GERARD, J. -C.; RUSCH, D. W.; and BOUGHER, S. W. (1980), Morphology of the Venus ultraviolet night airglow, *J. Geophys. Res.* **85**, 7861–7870.

Emissions from the O<sub>2</sub> IR Atmospheric bands of Venus are reported by

CONNES, P.; NOXON, J. F.; TRAUB, W. A.; and CARLETON, N. P. (1979), O<sub>2</sub> ( $^1\Delta$ ) emission in the day and night airglow of Venus, *Astrophys. J. Lett.* **233**, 129–132.

### Section 6.2 Resonant and Fluorescent Scattering of Sunlight

The photon scattering coefficient, or  $g$ -value, is introduced in

CHAMBERLAIN, J. W. (1961), op. cit. Chapter 11, and a number of  $g$ -values are tabulated there (p. 425). Some additional and improved  $g$ -values are given by

HUNTEST, D. M. (1971), op. cit.

The tangentially integrated density (6.2.6) is due to

CHAPMAN, S. (1931), The absorption and dissociation or ionizing effect of monochromatic radiation in an atmosphere on a rotating Earth, *Proc. Phys. Soc.* **43**, 483–501.

The theory of resonance scattering was developed by HEISENBERG, WEISSKOPF, DIRAC, and BREIT. The discussion here follows

BREIT, G. (1933), Quantum theory of dispersion: Parts VI and VII, *Rev. Mod. Phys.* **5**, 91–140.

### Section 6.3 Day Airglow

Only the principal terrestrial emissions are discussed here. For additional information see reviews by

HUNTEST, D. M. (1971), op. cit.,

NOXON, J. F. (1968), Day airglow, *Space Sci. Rev.* **8**, 92–134,

LLEWELLYN, E. J. and EVANS, W. F. J. (1971), The dayglow, in "The Radiating Atmosphere," (B. M. McCormac, ed.), pp. 17–33, Springer-Verlag, New York,

RUNDLE, H. N. (1971), Dayglow and twilight excitation mechanisms for airglow, in "The Radiating Atmosphere," (B. M. McCormac, ed.), pp. 90–104, Springer-Verlag, New York.

BROADFOOT, A. L. (1971), Dayglow nitrogen band systems, in "The Radiating Atmosphere," (B. M. McCormac, ed.), pp. 34–44, Springer-Verlag, New York.

### Section 6.3.1 Hydrogen and Helium

Lyman  $\alpha$  was discovered in the night sky from a rocket flown in late 1955 by

BYRAM, E. T.; CHUBB, T. A.; FRIEDMAN, H.; and KUPPERIAN, J. (1957), Far ultraviolet radiation in the night sky, in "The Threshold of Space," (M. Zelikoff, ed.), pp. 203–210, Pergamon Press, London.

Observations of terrestrial Ly  $\alpha$  and Ly  $\beta$  from outside the atmosphere are reported in

CARRUTHERS, G. R.; PAGE, T.; and MEIER, R. R. (1976), Apollo 16 Lyman alpha imagery of the hydrogen geocorona, *J. Geophys. Res.* **81**, 1664–1672,

MEIER, R. R.; CARRUTHERS, G. R.; PAGE, T. L.; and LEVASSEUR-REGOURD, A.-C. (1977), Geocoronal Lyman  $\beta$  and Balmer  $\alpha$  emissions measured during the Apollo 16 mission, *J. Geophys. Res.* **82**, 737–739

The anisotropy and polarization of H scattering in Ly  $\alpha$  and other transitions is discussed by

BRANDT, J. C. and CHAMBERLAIN, J. W. (1959), Interplanetary gas. I. Hydrogen radiation in the night sky, *Astrophys. J.* **130**, 670–682.

AJELLO, J. M. and THOMAS G. E. (1985), Predicted interplanetary distribution of Lyman-alpha intensity and polarization, *Icarus* **61**, 163–170.

Observations of H resonance lines from Venus were made by

BARTH, C. A.; WALLACE, L.; and PEARCE, J. B. (1968), Mariner 5 measurements of Lyman alpha radiation near Venus, *J. Geophys. Res.* **73**, 2541–2545,

KURT, V. G.; ROMANOVA, H. H.; SMIRNOV, A. S.; BERTAUX, J. L.; and BLAMONT, J. (1976), Hydrogen observations at Lyman alpha of the upper atmosphere of Venus with Venera-9 and Venera-10, Paper presented at COSPAR meeting, Philadelphia, July 1976,

BROADFOOT, A. L. (1976), Ultraviolet spectrometry of the inner solar system from Mariner 10, *Rev. Geophys. Space Phys.* **14**, 625–627.

The latter paper also reviews the Mariner 10 measurements of He I on Venus and of H and He I on Mercury. Observations of H from Mariners 6, 7, and 9 at Mars are summarized in

BARTH, C. A.; STEWART, A. I.; HORD, C. W.; and LANE, A. L. (1972), Mariner 9 ultraviolet spectrometer experiment: Mars airglow spectroscopy and variations in Lyman alpha, *Icarus* **17**, 457–468.

The Lyman  $\alpha$  airglow on Jupiter may be interpreted to give the eddy diffusion coefficient for the upper atmosphere, since the H abundance there depends on the rate of downward transport to high-density regions where association of H<sub>2</sub> occurs. See

WALLACE, L. and HUNTER, D. M. (1973), The Lyman-alpha albedo of Jupiter, *Astrophys. J.* **182**, 1013–1031.

The ultraviolet spectrometers on board the Voyager spacecraft discovered a pronounced longitudinal asymmetry in the Lyman alpha brightness of Jupiter:

SANDEL, B. R.; BROADFOOT, A. L.; and STROBEL, D. F. (1980), Discovery of a longitudinal asymmetry in the H Lyman-alpha brightness of Jupiter, *Geophys. Res. Lett.* **7**, 5–8.

Different interpretations have been provided by

SHEMANSKY, D. E. (1984), An explanation for the H Ly-alpha longitudinal asymmetry in the equatorial spectrum of Jupiter, *J. Geophys. Res.* **90**, 2673–2694,

KILLEEN, R. M. and CHAMBERLAIN, J. W. (1984), The zonal distribution of hydrogen in the Jovian atmosphere, *Icarus* **60**, 640–653.

The observations of H and He resonance radiation from Jupiter and ultraviolet radiation from the torus associated with Io are described and analyzed by

- CARLSON, R. W. and JUDGE, D. L. (1974), Pioneer 10 ultraviolet photometer observations at Jupiter encounter, *J. Geophys. Res.*, **79**, 3623–3633,  
 CARLSON, R. W. and JUDGE, D. L. (1976), Pioneer 10 ultraviolet photometer observations of Jupiter: The helium to hydrogen ratio, in "Jupiter," (T. Gehrels, ed.), pp. 418–440, Univ. Arizona Press, Tucson,  
 CARLSON, R. W. and JUDGE, D. L. (1975), Pioneer 10 ultraviolet photometer observations of the Jovian hydrogen torus: The angular distribution, *Icarus* **24**, 395–399.

Voyager results for the Jupiter and Saturn systems are given in

- BROADFOOT, A. L.; BELTON, M. J. S.; TAKACS, P. Z.; SANDEL, B. R.; SHEMANSKY, D. E.; HOLBERG, J. B.; AJELLO, J. M.; ATREYA, S. K.; DONAHUE, T. M., MOOS, H. W., BERTAUX, J. L., BLAMONT, J. E., STROBEL, D. F.; MCCONNELL, J. C.; DALGARNO, A.; GOODY, R.; and MCELROY, M. B. (1979), Extreme ultraviolet observations from Voyager 1: Encounter with Jupiter, *Science* **204**, 979–982,  
 BROADFOOT, A. L.; SANDEL, B. R.; SHEMANSKY, D. E.; HOLBERG, J. B.; SMITH, G. R.; STROBEL, D. F.; MCCONNELL, J. C.; KUMAR, S.; HUNTER, D. M.; ATREYA, S. K.; DONAHUE, T. M.; MOOS, H. W.; BERTAUX, J. L.; BLAMONT, J. E.; POMPHREY, R. B.; and LINICK, S. (1981), Extreme ultraviolet results from Voyager 1 encounter with Saturn, *Science* **212**, 206–211.

### Section 6.3.2 Atomic Oxygen

The resonance lines of O I at 1304 Å were first detected in the terrestrial daytime airglow by

- CHUBB, T. A.; BYRAM, E. T.; FRIEDMAN, H.; and KUPPERIAN, J. E. (1958), The use of radiation absorption and luminescence in upper air density measurements, *Ann. Geophys.* **14**, 109–116.

The radiative transfer analysis of the terrestrial emission is due to

- STRICKLAND, D. J. and DONAHUE, T. M. (1970), Excitation and radiative transport of O I 1304 Å resonance radiation, I. The dayglow, *Planet. Space Sci.* **18**, 661–689,  
 CHAMBERLAIN, J. W. and WALLACE, L. (1974), Formation of coupled spectral lines in a planetary atmosphere, *Astrophys. J.* **190**, 487–495,  
 CHAMBERLAIN, J. W. and SMITH, G. R. (1975), Formation of coupled spectral lines in a planetary atmosphere: II Numerical evaluation of approximate solutions, *Astrophys. J.* **199**, 282–288,  
 STRICKLAND, D. J. and ANDERSON, D. E., JR. (1977), The O I 1304-Å nadir intensity/column production rate ratio and its application to airglow studies, *J. Geophys. Res.* **82**, 1013–1016.

Day airglow spectra of Mars obtained from Mariner 6, 7, and 9 are reviewed by

- BARTH, C. A. (1974), The atmosphere of Mars, *Ann. Rev. Earth Planet. Sci.* **2**, 333–368.

The analysis of Mariner Mars data on O I is given by

- THOMAS, G. E. (1971), Neutral composition of the upper atmosphere of Mars as determined from the Mariner uv spectrometer experiments, *J. Atmos. Sci.* **28**, 859–868,  
 STRICKLAND, D. J.; THOMAS, G. E.; and SPARKS, P. R. (1972), Mariner 6 and 7 ultraviolet experiment: Analysis of the O I 1304- and 1356-Å emissions, *J. Geophys. Res.* **77**, 4052–4068.

The O I emissions (along with Ly  $\alpha$ ) were observed on Venus with a rocket by

- MOOS, H. W. and ROTTMAN, G. J. (1971), O I and H I emissions from the upper atmosphere of Venus, *Astrophys. J. Lett.* **169**, L127–L130.

Mariner 5 and 10 Venus data are given by

- BARTH, C. A.; PEARCE, J. B.; KELLY, K. K.; WALLACE, L.; and FASTIE, W. G. (1967), Ultraviolet emission observed near Venus from Mariner V, *Science* **158**, 1675–1678,  
BROADFOOT, A. L.; KUMAR, S.; BELTON, M. J. S.; and McELROY, M. B. (1974), Ultraviolet observations of Venus from Mariner 10: Preliminary results, *Science* **183**, 1315–1318.

Analysis of Venus O I emission is due to

- STRICKLAND, D. J. (1973), The O I 1304- and 1356-Å emissions from the atmosphere of Venus, *J. Geophys. Res.* **78**, 2827–2836,  
ANDERSON, D. E., JR. (1975), The Mariner 5 ultraviolet photometer experiment: Analysis of Rayleigh-scattered and 1304-Å radiation from Venus, *J. Geophys. Res.* **80**, 3063–3067.

Explanation of the blend at  $\lambda$ 1356 on Venus is in

- DURRANCE, S. T. (1981), The carbon monoxide fourth positive bands in the Venus dayglow, *J. Geophys. Res.* **86**, 9115–9124.

### Section 6.3.3 Molecular Excitation

The Mariner observations are reviewed by

- BARTH, C. A. (1974), op. cit.

and have been analyzed by

- THOMAS, G. E. (1971), op. cit.,

- STEWART, A. I. (1972), Mariner 6 and 7 ultraviolet spectrometer experiment: Implications of  $\text{CO}_2^+$ , CO, and O airglow, *J. Geophys. Res.* **77**, 54–68.

Observations of O<sub>2</sub> Martian day airglow from Earth have been used to infer low levels of Martian O<sub>3</sub> by

- NOXON, J. F.; TRAUB, W. A.; CARLETON, N. P.; and CONNES, P. (1976), Detection of O<sub>2</sub> dayglow emission from Mars and the Martian ozone abundance, *Astrophys. J.* **207**, 1025–1035.

A comprehensive review of the O<sub>2</sub> emissions from Venus, Mars, and Earth and their excitation is given by

- KRASNOPOLSKY, V. A. (1983), Venus spectroscopy in the 3000–8000 Å region by Veneras 9 and 10, in "Venus" (D. M. Hunten, L. Colin, T. M. Donahue, and V. I. Moroz, eds.), pp. 459–483, Univ. Arizona Press, Tucson, Arizona.

Figures 6.10 and 6.11 are from

- BROADFOOT, A. L.; SANDEL, B. R.; SHEMANSKY, D. E.; McCONNELL, J. C.; SMITH, G. R.; HOLBERG, J. B.; ATREYA, S. K.; DONAHUE, T. M.; STROBEL, D. F.; and BERTAUX, J. L. (1981), Overview of the Voyager ultraviolet spectrometry results through Jupiter encounter, *J. Geophys. Res.* **86**, 8259–8284.

- STROBEL, D. F. and SHEMANSKY, D. E. (1982), EUV emission from Titan's upper atmosphere: Voyager 1 encounter, *J. Geophys. Res.* **87**, 1361–1368.

### Section 6.3.4 Alkali Metals

For Earth's airglow, see the reviews noted for Section 6.3, especially RUNDLE (1971). For a discussion of laser sounding of the free Na in the atmosphere see

- MEGIE, G. and BLAMONT, J. E. (1977), Laser sounding of atmospheric sodium: Interpretation in terms of global atmospheric parameters, *Planet. Space Sci.* **25**, 1093–1109.

A review of the emission features of Io with models that have been put forth to account for this unique phenomenon is given by

- BROWN, R. A. and YUNG, Y. L. (1976), Io, its atmosphere and optical emissions, in "Jupiter," (T. Gehrels, ed.), pp. 1102–1145, Univ. Arizona Press, Tucson.

### Section 6.3.5 Io's Plasma Torus

See the references to Section 1.9.4.

### Section 6.4 Aeronomy of the Planets

An excellent two-volume text on aeronomy, with emphasis on the terrestrial atmosphere, is

BANKS, P. M. and KOCKARTS, G. (1973), "Aeronomy," Academic Press, New York.

Aeronomy of  $\text{CO}_2$  atmospheres is reviewed by

KUMAR, S. (1975), The ionosphere and upper atmosphere of Venus, in "Atmospheres of the Earth and Planets." (B. M. McCormac, ed.), pp. 385-399, D. Reidel Publ. Co., Dordrecht, The Netherlands,

MCCONNELL, J. C. (1973), The atmosphere of Mars, in "Physics and Chemistry of Upper Atmospheres," (B. M. McCormac, ed.), pp. 309-334, D. Reidel Publ. Co., Dordrecht, The Netherlands,

HUNTER, D. M. (1974), Aeronomy of the lower atmosphere of Mars, *Rev. Geophys. Space Phys.* **12**, 529-535,

KONG, T. Y. and MCELROY, M. B. (1977a), Photochemistry of the Martian atmosphere, *Icarus* **32**, 168-189.

That  $\text{O}_2$  should be a principal constituent of the Mars upper atmosphere, regardless of the rarity of  $\text{O}_2$  in the lower atmosphere, was first advocated in

CHAMBERLAIN, J. W. (1962), Upper atmospheres of the planets, *Astrophys. J.* **136**, 582-293.

The model with a rapid downward flow of O is due to

MCELROY, M. B. and DONAHUE, T. M. (1972), Stability of the Martian atmosphere, *Science* **177**, 986-988.

Figure 6.13 is from

HUNTER, D. M. (1979), Possible oxidant sources in the atmosphere and surface of Mars, *J. Molec. Evolution* **14**, 71-78.

Figure 6.14 and the related discussion in the text are taken from

PARKINSON, T. D. and HUNTER, D. M. (1972), Spectroscopy and aeronomy of  $\text{O}_2$  on Mars, *J. Atmos. Sci.* **29**, 1380-1390.

which also contains the proposal for catalytic conversion of CO and  $\text{O}_2$  into  $\text{CO}_2$  by reaction (6.4.3).

Short-term fluctuations of Martian  $\text{O}_2$  due to interchange between oxidized solids and free  $\text{O}_2$  are discussed by

HUNTER, D. M. (1974), op. cit.,

and the oxidation of the surface is discussed in

HUGUENIN, R. L. (1974), The formation of goethite and hydrated clay minerals on Mars, *J. Geophys. Res.* 3895-3905.

The ozone distribution is analyzed by

KONG, T. Y. and MCELROY, M. B. (1977b), The global distribution of  $\text{O}_3$  on Mars, *Planet. Space Sci.* **25**, 839-857.

Alternate catalytic cycles that may be more appropriate for Venus are discussed in

PRINN, R. G. (1973), The upper atmosphere of Venus: A review, in "Physics and Chemistry of Upper Atmospheres," (B. M. McCormac, ed.), pp. 335-344, D. Reidel Publ. Co., Dordrecht, The Netherlands.

A thorough analysis of Venus' aeronomy is given by

- SZE, N. D. and McELROY, M. B. (1975), Some problems in Venus' aeronomy, *Planet. Space Sci.* **23**, 763–786,  
 LIU, S. C. and DONAHUE, T. M. (1975), The aeronomy of the upper atmosphere of Venus, *Icarus* **24**, 148–156.

More recent papers, which incorporate Pioneer Venus results, are

- KRASNOPOLSKY, V. A. and PARSHEV, V. A. (1983), Photochemistry of the Venus atmosphere, in "Venus" (D. M. Hunten, L. Colin, T. M. Donahue, and V. I. Moroz, eds.), pp. 431–458, Univ. Arizona Press, Tucson, Arizona,  
 YUNG, Y. L. and DEMORE, W. B. (1982), Photochemistry of the stratosphere of Venus: Implications for atmospheric evolution, *Icarus* **51**, 199–247.

Aeronomy of the Jovian atmosphere is treated in

- STROBEL, D. F. (1975), Aeronomy of the major planets: Photochemistry of ammonia and hydrocarbons, *Rev. Geophys. Space Phys.* **13**, 372–382.

The pioneering work on aeronomy of H<sub>2</sub> atmospheres was

- WILDT, R. (1937), Photochemistry of planetary atmospheres, *Astrophys. J.* **86**, 321–336.

Titan aeronomy is thoroughly discussed by

- YUNG, Y. L.; ALLEN, M.; and PINTO, J. P. (1984), Photochemistry of the atmosphere of Titan: Comparison between model and observations, *Astrophys. J. Suppl.* **55**, 465–506.

Aeronomy of the Galilean satellites is reviewed by

- KUMAR, S. and HUNTER, D. M. (1982), The atmospheres of Io and other satellites, in "Satellites of Jupiter" (D. Morrison, ed.), pp. 782–806, Univ. Arizona Press, Tucson, Arizona.

Figures 6.20 and 6.21 are from

- KUMAR, S. (1982), Photochemistry of SO<sub>2</sub> in the atmosphere of Io and implications on atmospheric escape, *J. Geophys. Res.* **87**, 1677–1684,

- KUMAR, S. (1985), The SO<sub>2</sub> atmosphere and ionosphere of Io: Ion chemistry, atmospheric escape, and models corresponding to the Pioneer 10 radio occultation measurements, *Icarus* **61**, 101–123.

## PROBLEMS

**6.1 Photometry for resonance scattering.** The phase function  $p(\cos \Theta)$  for resonance scattering is in general a linear combination of the isotropic and Rayleigh (4.3.2) phase functions. (a) Show that in the conservative case if

$$p(\cos \Theta) = a + b \cos^2 \Theta$$

then  $a = 1 - b/3$ , where  $p$  is normalized by (1.2.4). (b) Show that when scattering is not isotropic the relation (6.1.5) between the integrated intensity and total emission rate is replaced by

$$\mu 4\pi \mathcal{I}(\mu, \phi) = p(\cos \Theta) \int_0^\infty E(z) dz$$

(c) If sunlight is incident from a zenith angle of 60° and the observer is also at a zenith angle of 60°, what is the observer's azimuth from the sun if  $p(\cos \Theta) = 1$  when  $b = 0.3$ ?

**6.2 Polarization and anisotropy without hyperfine structure.** Neglect the hyperfine structure of the  $D$  lines of Na and assume that there is no external magnetic field (strong enough to separate the various Zeeman components). (a) Show that  $D_1$  is not polarized. (b) Find the polarization,  $\mathcal{P}(\Theta)$ , and anisotropy,  $\mathcal{E}(\Theta)/\langle \mathcal{E} \rangle$  for  $D_2$ . (Check: At  $\Theta = \pi/2$ ,  $\mathcal{P} = \frac{3}{7}$ .)

**6.3 Polarization and anisotropy with an external magnetic field.** Repeat Problem 6.2 with an external magnetic field perpendicular to the scattering plane.

**6.4 Polarization and anisotropy with hyperfine structure.** Repeat Problem 6.2 with the hfs shown in Fig. 6.7. Use the following tables for relative hfs intensities:

$$I = \frac{3}{2}$$

|      |     | $J = \frac{1}{2}$ |      |   |   | $J = \frac{1}{2}$ |     |
|------|-----|-------------------|------|---|---|-------------------|-----|
|      |     | 1                 | 2    |   |   | 1                 | 2   |
| $F'$ | $F$ | 0                 | 14.3 | — | — | 1                 | 20  |
| 0    | 1   | 35.7              | 7.1  | — | — | 100               | 100 |
| 1    | 2   | 35.7              | 35.7 | — | — | 100               | 100 |
| 2    | 3   | —                 | 100  | — | — | —                 | —   |
| 3    |     |                   |      |   |   |                   |     |

**6.5 Sum rules for Zeeman components.** For a transition  $F' \rightarrow F'$ , write the transition probabilities from (6.2.26) and (6.2.27) for all transitions starting on  $M' = F'$  and for all transitions starting on  $M' = F' - 1$  and show that the sum rule is obeyed.

**6.6 Magnetic dipole radiation.** The  $\lambda 6300-64$  lines of [OI] ( ${}^3P_{2,1}-{}^1D_2$ ) are forbidden by electric-dipole selection rules but permitted as magnetic-dipole transitions. To calculate their scattering replace the electric vector of the radiation field by the magnetic vector and proceed as usual. Obtain the intensity of Zeeman components with (6.2.26)–(6.2.31), where  $A_\pi$  and  $A_o$  are now partial transition probabilities for components polarized with the *magnetic* vector of the wave parallel and perpendicular, respectively, to the external magnetic field. Assume the incident fluxes at  $\lambda 6300$  and  $\lambda 6364$  are equal. The total transition probabilities are in the ratio  $A_{6300}/A_{6364} = 3$  and  ${}^{16}\text{O}$  has no nuclear spin. What is the degree of polarization of  $\lambda 6300$  when observed perpendicular to the direction of the sun in the absence of an external magnetic field? (Specify how you define polarization for this problem.)

**6.7 Green-line polarization.** Many years ago it was reported that the  $\lambda 5577$  line of [OI] ( ${}^1D_2-{}^1S_0$ ) is polarized in twilight. The conclusion drawn was that this polarization shows that the  $\lambda 5577$  twilight airglow has a component due to resonance scattering of sunlight. From general principles of the nature of polarization and atomic wave functions, state in one sentence why this conclusion was absurd. (Note:  $\lambda 5577$  arises from an electric quadrupole transition, and the dipole selection rules do not apply. However, the solution is *not* that  ${}^1S_0$  has a long lifetime and is subject to collisional depolarization.)

**6.8 Optical thickness of sodium on Io.** The  $D_2$  line ( $\lambda 5890$ ) of Na I has an oscillator strength  $f = 0.65$  and at the Earth its scattering coefficient is  $g = 0.6$  photon/sec molecule. When observed at maximum elongation from Jupiter, the Na cloud around Io has an apparent emission rate in  $D_2$  of 16 kR. What is the approximate minimum temperature of the cloud if it is excited by resonance scattering and its optical thickness at the center of  $D_2$  is small (i.e.,  $\tau \leq 1$ )? [Ignore the anisotropy of scattering for this purpose; the absorption cross section is related to  $f$  by (1.6.5).]

**6.9 Helium scattering.** The He I resonance line  $\lambda 584$  is observed at a zenith angle of  $60^\circ$  when the sun is in the local zenith. The total apparent emission rate is  $4\pi\mathcal{I}(\mu = \frac{1}{2}) = 100$  R. What is the true integrated emission rate for a vertical column of atmosphere? (The  ${}^4\text{He}$  nucleus has zero spin.)

**6.10 Mars odd hydrogen.** Complete the derivations of (6.4.7) and (6.4.8). Include estimates of the small terms omitted from (6.4.8). Verify the ground-level results in Fig. 6.14 for the given amounts of odd-H,  $\text{O}_2$ , and  $\text{CO}_2$ . [For rate coefficients, consult Chapter 3. The term  $p(\text{O})$  represents production of O atoms by  $\text{CO}_2$ , and is  $5 \times 10^5 \text{ cm}^{-3} \text{ sec}^{-1}$  between 10 and 25 km, rising smoothly to  $7.5 \times 10^5$  at the surface.]



## ***Chapter 7***

# **STABILITY OF PLANETARY ATMOSPHERES**

The stability of the Earth's atmosphere is a matter of urgent concern. We are aware of major climate changes in the past and (perhaps related in some cases) periods of selective faunal extinction. Human activities now have a major impact on the atmosphere and a potential to virtually ruin it. Hence, natural changes are not our principal concern, but an understanding of natural evolution should help our anticipation of alterations induced by society.

It may be quite fortuitous that planet Earth is habitable at all. Of the terrestrial planets, Mercury is too small and hot to hold much atmosphere. Venus, although receiving only twice the sunlight of Earth, evidently became unstable in the sense that the temperature rose until there was no surface water left (see Section 7.4.1). In spite of a low exospheric temperature on Mars, thermal escape is rapid, and a chemically induced loss of oxygen as well may have always kept a secondary atmosphere on Mars from developing fully (see Section 7.3.4).

Much of this chapter is concerned with exospheres and the escape of gases from the uppermost levels of an atmosphere. This is a subject that seemed fairly straightforward before space measurements were made of the exospheres of Earth and Venus. There were surprises in store that have considerably altered our understanding of atmospheric stability.

## 7.1 Quasi-Collisionless Exospheres

The uppermost fringes of a neutral planetary atmosphere constitute the *exosphere*; when the emphasis is on its scattered radiation (such as Lyman  $\alpha$  of H), an exosphere is frequently called a *planetary corona*. The base of an exosphere (the *critical level* or, according to most current usage, the *exobase*) is defined as the height where the overhead integrated density accounts for one mean free path  $l$  for a fast atom. Since an exosphere, to a first approximation, has a constant scale height  $H$ , the exobase is located at the radius  $r_c$  from the planetary center where

$$\int_{r_c}^{\infty} N(r)Q dr \approx QN(r_c)H = 1 \quad (7.1.1)$$

for local density  $N(r)$  and collision cross section  $Q$  ( $\approx 3 \times 10^{-15}$  cm $^2$ ). At constant density the mean free path is  $l = 1/NQ$ . Hence the exobase is at the height  $r_c$  where  $l(r_c) = H$ .

The classic exosphere is one that has a Maxwellian distribution of velocities at and below the exobase and no collisions whatever above that level. We will later modify the strict prohibition against collisions to account for a certain portion of the exospheric atoms called the *satellite population*.

### 7.1.1 Jeans Escape

Let the density of particles of mass  $M$  in six-dimensional phase space be  $f(\mathbf{r}, \mathbf{v})$ . If the velocity distribution function is Maxwellian,

$$f(\mathbf{r}, \mathbf{v}) = N(r) \frac{\exp(-Mv_r^2/2kT - Mv_\chi^2/2kT)}{(2\pi kT/M)^{3/2}} \quad (7.1.2)$$

where  $v_r$  is the radial velocity and  $v_\chi$  the transverse velocity. The escape flux at the exobase is, with the element of velocity space written in cylindrical coordinates,

$$\mathcal{F}(r_c) = \int_{v_r} \int_{v_\chi} \int_0^{2\pi} v_r f(r_c, \mathbf{v}) v_\chi d\phi dv_\chi dv_r \quad (7.1.3)$$

where  $\phi$  is the azimuthal angle for the transverse velocity component  $v_\chi$ . Some care is required in establishing the integration limits for  $v_r$  and  $v_\chi$ . If the radial velocity is below the escape velocity,

$$v_{\text{esc}} = \left( \frac{2GM}{r} \right)^{1/2} \quad (7.1.4)$$

(where  $G$  is the gravitational constant and  $\mathcal{M}$  is the mass of the planet), the atom can escape only if  $v_\chi^2 > v_{\text{esc}}^2 - v_r^2 \equiv v_2^2$ . Thus we have

$$\begin{aligned}\mathcal{F}_{\text{Jea}}(r_c) &= 2\pi \int_{v_r=0}^{v_{\text{esc}}} \int_{v_\chi=v_2}^{\infty} f(r_c, v) v_\chi v_r dv_\chi dv_r \\ &\quad + 2\pi \int_{v_r=v_{\text{esc}}}^{\infty} \int_{v_\chi=0}^{\infty} f(r_c, v) v_\chi v_r dv_\chi dv_r \\ &= \frac{N(r_c)U}{2\pi^{1/2}} e^{-v_{\text{esc}}^2/U^2} \left( \frac{v_{\text{esc}}^2}{U^2} + 1 \right) \\ &= \frac{N(r_c)U}{2\pi^{1/2}} e^{-\lambda} (\lambda + 1)\end{aligned}\quad (7.1.5)$$

where the *most probable velocity* of a Maxwellian distribution is

$$U = \left( \frac{2kT}{M} \right)^{1/2} \quad (7.1.6)$$

and  $\lambda$  is defined in (7.1.17).

Equation (7.1.5) is the *Jeans formula* for the rate of escape (atom/cm<sup>2</sup> sec) by *thermal evaporation* of a gas from a planetary atmosphere. The derivation is much simpler if (7.1.3) is written with the velocity space expressed in spherical coordinates (Problem 7.1), but in the following discussion we will occasionally find it convenient to use cylindrical velocity components.

### 7.1.2 Liouville's Equation and the Density in Phase Space

The theory throughout is developed for spherical symmetry. The atmospheric structure (density, composition, and temperature) is assumed uniform over the globe; there are no latitude or day-night effects, and the atmosphere does not rotate.

We assume initially a critical level or exobase above which collisions are negligible and below which collisions maintain a complete Maxwellian distribution of velocities. In the tenuous regions where atomic collisions are rare, the spatial and momentum distribution of particles is governed by Liouville's equation. It may be derived by analogy with the ordinary equation of continuity (2.1.1). A large group of particles distributed over spatial ( $q_i$ ) and momentum ( $p_i$ ) coordinates in six-dimensional phase space according to some function  $f(q_i, p_i)$  may then be said to have a "density" in phase space of  $f(q_i, p_i)$ . In (2.1.1) adapted to phase-space coordinates, the velocity component  $v_i$  is replaced by  $\dot{q}_i$  and  $\dot{p}_i$  and Liouville's equation is

$$\frac{\partial f}{\partial t} + \sum_{i=1}^3 \left( \frac{\partial}{\partial q_i} (f \dot{q}_i) + \frac{\partial}{\partial p_i} (f \dot{p}_i) \right) = 0 \quad (7.1.7)$$

The particles are subject to the equations of motion (in this case the particles are under the influence of gravitation). In Hamiltonian form, we have

$$\dot{q}_i = \frac{\partial \mathcal{H}}{\partial p_i}, \quad \dot{p}_i = -\frac{\partial \mathcal{H}}{\partial q_i} \quad (7.1.8)$$

where  $\mathcal{H} = \mathcal{H}(q_i, p_i)$  is the Hamiltonian function—the total energy expressed in terms of  $q_i$  and  $p_i$ . Expanding the derivatives in (7.1.7) and using (7.1.8) to eliminate  $\partial \dot{q}_i / \partial q_i = -\partial \dot{p}_i / \partial p_i$  gives

$$\frac{df}{dt} \equiv \frac{\partial f}{\partial t} + \sum_{i=1}^3 \left( \frac{\partial f}{\partial q_i} \dot{q}_i + \frac{\partial f}{\partial p_i} \dot{p}_i \right) = 0 \quad (7.1.9)$$

The term on the left side is the total derivative to be taken along the path (in phase space) followed by a closed element of “volume” as it “moves” according to the equations of motion. Liouville’s theorem thus states that the density in phase space remains constant along a dynamical trajectory.

Let us apply Liouville’s theorem to the density and velocity distribution in a corona. We shall assume an isotropic, Maxwellian distribution of velocities for temperature  $T_c$  just below the exobase, which is at radial distance  $r_c$  from the center of the planet, and a total density  $N(r_c) \equiv N_c$ . We shall then seek the distribution function at greater heights  $r$ . For spherical symmetry and a steady state ( $\partial f / \partial t = 0$ ), (7.1.9) is

$$\frac{\partial f}{\partial r} \frac{dr}{dt} = -\frac{\partial f}{\partial p_r} \frac{dp_r}{dt} \quad (7.1.10)$$

where  $p_r$  is the radial component of momentum.

One may readily show from the Lagrangian of a particle in a gravitational field that the second generalized momentum is  $P_\chi = Mr^2\dot{\chi}$ , where  $\dot{\chi}$  is the angular velocity. The Hamiltonian is thus written

$$\mathcal{H} = \frac{p_r^2}{2M} + \frac{P_\chi^2}{2Mr^2} - \frac{G\mathcal{M}M}{r} \quad (7.1.11)$$

where  $P_\chi$  is the angular momentum, a constant for an atom in free flight. That this is the correct form may be verified from equations (7.1.8), the first of which recovers the radial and angular velocities, whereas the second yields the equations of motion:

$$\frac{dp_r}{dt} = \frac{P_\chi^2}{Mr^3} - \frac{G\mathcal{M}M}{r^2} \quad (7.1.12)$$

and

$$\frac{dP_\chi}{dt} = 0 \quad (7.1.13)$$

At the exobase, the Maxwellian distribution,

$$f(r_c, p_r, P_\chi) = \frac{N_c e^{-p_r^2/2MkT_c} e^{-P_\chi^2/2MkT_c r_c^2}}{(2\pi M k T_c)^{3/2}} \quad (7.1.14)$$

gives

$$\frac{\partial f}{\partial p_r} = -\frac{p_r}{M k T_c} f \quad (7.1.15)$$

Substituting (7.1.12) and (7.1.15) into (7.1.10) yields

$$\frac{d(\ln f)}{dr} = -\left(\frac{G\mathcal{M}M}{k T_c r^2} - \frac{P_\chi^2}{M k T_c r^3}\right) \quad (7.1.16)$$

which is independent of  $p_r$  and can be integrated upwards from the exobase.

It is convenient to write the absolute value of the gravitational potential energy in units of  $k T_c$ :

$$\lambda(r) \equiv \frac{G\mathcal{M}M}{k T_c r} = \frac{v_{\text{esc}}^2}{U^2} \quad (7.1.17)$$

Then integrating (7.1.16) from  $r_c$  to  $r$  and using (7.1.14) for the boundary condition gives the distribution function at any height:

$$f(r, p_r, P_\chi) = \frac{N_c e^{-(\lambda_c - \lambda)} e^{-p_r^2/2MkT_c} e^{-P_\chi^2/2MkT_c r^2}}{(2\pi M k T_c)^{3/2}} \quad (7.1.18)$$

This equation is valid for all combinations of  $p_r$  and  $P_\chi$  allowed by the equations of motion.

If these momenta are independent and can take on all values ( $-\infty < p_r < \infty ; 0 < P_\chi < \infty$ ), as they do below the exobase, an integration over all momentum space gives a density we shall denote as  $N_b$ :

$$N_b(r) \equiv \int f(q_i, p_i) d^3 p_i = N_c e^{-(\lambda_c - \lambda)} \quad (7.1.19)$$

where  $d^3 p_i$  signifies that the integration is over all momentum coordinates. This is the generalized form (i.e., it allows for the variation with  $r$  of gravitational attraction) of the (isothermal) *barometric law* (1.1.4). The derivation in Section 1.1 used hydrostatic equilibrium and the perfect gas law, which are valid so long as the gas pressure is isotropic and the mean kinetic energy per atom is a constant times the temperature. The derivation of (7.1.19) from Liouville's equation is a direct consequence of the Maxwellian distribution holding even in the region free of collisions, provided the momenta do extend over all possible values. For then the mean energy per atom is unchanged and the barometric law naturally emerges.

All this depends, however, on having the entire range of molecular momenta allowed. At substantial distances above the exobase this is not the case and the barometric law breaks down. If strictly true (7.1.19) would predict a finite density and pressure is achieved as  $r \rightarrow \infty$  (and  $\lambda \rightarrow 0$ ), and to resolve this paradox it would be necessary to include the mass of the atmosphere within  $r$  in deriving a more accurate barometric equation.

In practice, the pressure at large distances is decidedly directional and the mean kinetic energy per atom decreases. Hence the barometric law must break down. Even with the macroscopic equations of hydrodynamics, the atmosphere is not strictly in hydrostatic equilibrium. It is expanding slightly—that is, some matter is being lost, which in the kinetic theory corresponds to evaporative loss. Thus the problem is one of hydrodynamics rather than hydrostatics. But to treat the density distribution accurately it is necessary to examine the individual Keplerian orbits of particles in the corona. This we shall do in the next section.

### 7.1.3 Distribution of Density with Height

The density  $N(r)$  is obtained by integrating (7.1.18) over the momentum space that is populated in accordance with the equations of motion (7.1.12–7.1.13). We shall write the density as a product of the barometric density of (7.1.19) and a *partition function*  $\zeta$ , which will describe how particles are partitioned in different classes of orbit. Thus we have

$$N(r) = N_b(r)\zeta(\lambda) = N_c e^{-(\lambda_c - \lambda)}\zeta(\lambda) \quad (7.1.20)$$

where

$$\zeta(\lambda) = \frac{2\pi}{r^2(2\pi M k T_c)^{3/2}} \iint e^{-p_r^2/2MkT_c - p_\chi^2/2MkT_c r^2} P_\chi dP_\chi dp_r \quad (7.1.21)$$

Introducing changes of variable to express the energies in units of  $kT_c$ , as with (7.1.17) for the potential, we let

$$v(r) = \frac{P_\chi^2}{2MkT_c r^2} = \frac{v_\chi^2}{U^2} \quad (7.1.22)$$

and

$$\xi(r) = \frac{p_r}{(2MkT_c)^{1/2}} = \frac{v_r}{U} \quad (7.1.23)$$

Alternatively, the total kinetic energy of a particle is

$$\psi(r) = \frac{Mv^2}{2kT_c} = \frac{v^2}{U^2} = \xi^2 + v \quad (7.1.24)$$

and the polar angle of the velocity vector is  $\theta = \cos^{-1} \mu$ , where

$$\mu = \frac{\xi}{(\xi^2 + v)^{1/2}} \quad (7.1.25)$$

The total energy, which is a constant for each particle, is from (7.1.11)

$$h = \mathcal{H}/kT_c = \xi^2 + v - \lambda = \psi - \lambda \quad (7.1.26)$$

With the substitution of (7.1.22–7.1.23), the partition function (7.1.21) becomes

$$\zeta(\lambda) = \frac{1}{\pi^{1/2}} \iint e^{-\xi^2 - v} dv d\xi \quad (7.1.27)$$

The particle orbits fall into three distinct categories with different integration limits. We shall consider each of these groups in turn. In general,  $\zeta$  may be regarded as the fraction of the isotropic, Maxwellian distribution that is actually present; for no dynamical restrictions on the orbits,  $\zeta = 1$ .

**Ballistic Orbits** The term *ballistic* will be used throughout to describe only those particles with negative energy ( $h < 0$ ) that rise from the critical level in elliptic orbits and eventually fall back. Clearly in this case there will be symmetry in positive and negative values of  $\xi$ .

The orbits are restricted, then, by the conditions that  $h < 0$  and that the orbits must intersect the exobase, designated by potential  $\lambda_c$ . From (7.1.22) and (7.1.26), remembering that  $P_\chi$  is constant, we express  $v$  as

$$v = h + \lambda - \xi^2 = \frac{\lambda^2}{\lambda_c^2} v_c = \frac{\lambda^2}{\lambda_c^2} (h + \lambda_c - \xi_c^2) \quad (7.1.28)$$

which yields

$$v = \frac{\lambda^2}{\lambda_c^2 - \lambda^2} (\lambda_c - \lambda - \xi_c^2 + \xi^2) \quad (7.1.29)$$

The condition that orbits intersect the exobase necessitates that  $\xi_c$  be real. Hence the conservation of  $P_\chi$  requires that

$$v \leq \frac{\lambda^2}{\lambda_c^2 - \lambda^2} (\lambda_c - \lambda + \xi^2) \equiv v_1(\xi) \quad (7.1.30)$$

The energy condition requires that

$$v < \lambda - \xi^2 \equiv v_2(\xi) \quad (7.1.31)$$

and for a given  $\xi$  the maximum  $v$  will be either  $v_1$  or  $v_2$ , whichever is smaller. The condition that  $v_1 < v_2$  imposes the requirement that

$$\xi^2 < \lambda(1 - \lambda/\lambda_c) \equiv \xi_1^2 \quad (7.1.32)$$

To review these conditions, we note that, with the energy limitation above (7.1.31) would be the only restriction between  $v$  and  $\xi$ . However, there exist *satellite* orbits, with  $v < v_2$ , which do not intersect the critical level; (7.1.30) and (7.1.32) exclude these orbits. We have, therefore, for ballistic orbits,

$$\begin{aligned}\zeta_{\text{bal}}(\lambda) &= \frac{2}{\pi^{1/2}} \int_{\xi=0}^{\xi_1} \int_{v=0}^{v_1(\xi)} e^{-\xi^2-v} dv d\xi \\ &+ \frac{2}{\pi^{1/2}} \int_{\xi=\xi_1}^{\lambda^{1/2}} \int_{v=0}^{v_2(\xi)} e^{-\xi^2-v} dv d\xi\end{aligned}\quad (7.1.33)$$

After some manipulation, including an integration by parts and a change of variable, this becomes (Problem 7.2)

$$\begin{aligned}\zeta_{\text{bal}}(\lambda) &= \frac{2}{\pi^{1/2}} \int_0^\lambda \psi^{1/2} e^{-\psi} [1 - \mu_0(\psi)] d\psi \\ &= \frac{2}{\pi^{1/2}} \left( \gamma\left(\frac{3}{2}, \lambda\right) - \frac{(\lambda_c^2 - \lambda^2)^{1/2}}{\lambda_c} e^{-\psi_1} \gamma\left(\frac{3}{2}, \lambda - \psi_1\right) \right)\end{aligned}\quad (7.1.34)$$

where we have used

$$\begin{aligned}\mu_0(\psi) &= \frac{(\lambda_c^2 - \lambda^2)^{1/2}}{\lambda_c} \left( 1 - \frac{\psi_1}{\psi} \right)^{1/2} \\ &= \left[ 1 - \frac{\lambda^2}{\lambda_c^2} \left( 1 + \frac{\lambda_c - \lambda}{\psi} \right) \right]^{1/2}, \quad \psi > \psi_1\end{aligned}\quad (7.1.35)$$

and

$$\mu_0(\psi) = 0, \quad \psi < \psi_1 \quad (7.1.36)$$

and where

$$\psi_1 = \frac{\lambda^2}{\lambda + \lambda_c} \quad (7.1.37)$$

In (7.1.34) the function  $\gamma$  is the *incomplete Γ function*,

$$\gamma(\alpha, x) \equiv \int_0^x y^{\alpha-1} e^{-y} dy \quad (7.1.38)$$

For a more direct derivation of (7.1.34), let  $\theta$  be the angle at which an orbit is inclined to the radius vector  $\mathbf{r}$  (Fig. 7.1). The maximum angle that a ballistic orbit may possess for a specific energy  $\psi$  and distance  $r$  will be denoted  $\theta_0(\psi)$ . Ballistic orbits will thus fill a cone of half width  $\theta_0$  centered on the radius vector; but outside this cone lie only satellite orbits, which do not touch the exobase. Within this cone there must be a uniform angular distribution, in accord with the orbits predicted from Liouville's equation, with particles moving in both directions along each orbit.

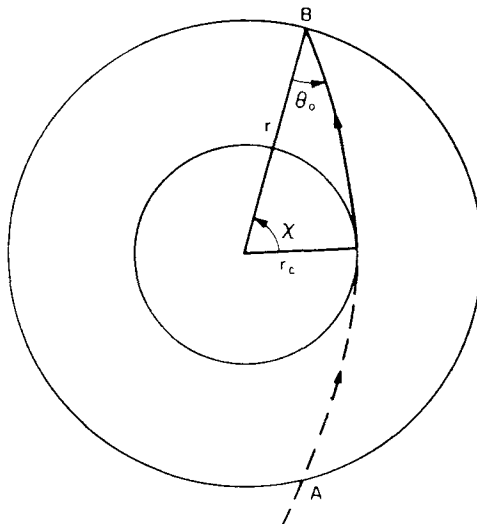


**Fig. 7.1** A hyperbolic orbit with velocity  $v(r) > v_{\text{esc}}(r)$  enters sphere  $r$  at  $A$  and exits at  $B$ . The orbit is tangent to the exobase at height  $r_c$  and crosses the sphere  $r$  at an angle  $\theta_0$ .

The partition function may be integrated directly with the distribution function  $f$  rewritten in polar velocity coordinates. We have

$$\zeta_{\text{bal}}(\lambda) = \frac{2}{\pi^{1/2}} \int_0^\lambda \int_{\theta=0}^{\theta_0(\psi)} \psi^{1/2} e^{-\psi} \sin \theta d\theta d\psi \quad (7.1.39)$$

Writing  $\mu_0(\psi) = \cos \theta_0(\psi)$ , this integral becomes equivalent to (7.1.34). It may be verified from the conservation of angular momentum that (7.1.35) is  $\cos \theta_0(\psi)$  (cf. Problem 7.3).

If the maximum angle  $\theta_0(\psi)$  is less than  $\pi/2$ , it designates an orbit that is tangent to the exobase (cf. Problem 7.3). A larger angle would correspond to a satellite orbit. When ballistic particles have  $\theta_0(\psi) = \pi/2$ , as they do for small energies  $\psi$ , the ballistic orbits for that and all smaller  $\psi$  are isotropic [cf. (7.1.36) and (7.1.37)].

There can be no satellite orbits with energies  $\psi < \psi_1$ . The satellite orbit with minimum energy  $\psi_1(\lambda)$  has an angle  $\theta = \pi/2$  at both  $r$  and  $r_c$ ; its apogee is at  $r$  and its perigee, on the opposite side of the planet, is at  $r_c$ .

**Satellite Orbits** These orbits, like ballistic ones, must have negative energies, but they do not intersect the critical level. While the full range of ballistic orbits is expected, the existence of satellite orbits depends on the balance of the rare collisions that do occur within the corona with the rare destructive processes, such as photoionization and the perturbation of orbits by radiation pressure.

The production and destruction of these particles in an atmosphere is discussed in Section 7.2.1; here we will suppose that there are no loss mechanisms other than by collisions. Then even exceedingly rare coronal collisions will eventually establish an isotropic distribution for all particles that are energetically allowed, according to Boltzmann's "H theorem."

Hence for all captive (ballistic plus satellite) orbits taken together, the integration limits to (7.1.27) are given by  $0 < v < \lambda - \xi^2$  and  $0 < \xi^2 < \lambda$ . These limits lead to a form analogous to (7.1.39),

$$\begin{aligned}\zeta_{\text{bal}}(\lambda) + \zeta_{\text{sat}}(\lambda) &= \frac{2}{\pi^{1/2}} \int_0^\lambda \psi^{1/2} e^{-\psi} d\psi \\ &= \frac{2}{\pi^{1/2}} \gamma\left(\frac{3}{2}, \lambda\right)\end{aligned}\quad (7.1.40)$$

This equation with (7.1.34) yields, for the maximum or full distribution of satellite orbits,

$$\begin{aligned}\zeta_{\text{sat}}(\lambda) &= \frac{2}{\pi^{1/2}} \int_{\psi=\psi_1}^\lambda \psi^{1/2} \mu_0(\psi) e^{-\psi} d\psi \\ &= \frac{2}{\pi^{1/2}} \frac{(\lambda_c^2 - \lambda^2)^{1/2}}{\lambda_c} e^{-\psi_1} \gamma\left(\frac{3}{2}, \lambda - \psi_1\right)\end{aligned}\quad (7.1.41)$$

where  $\psi_1$  is given by (7.1.37)

**Escaping Orbits** The selection of integration limits is here similar to the procedure for ballistic orbits. There are two conditions to be satisfied: the energy is positive ( $h \geq 0$ ) and the orbits must arise from the critical level. Note that for escaping orbits it is not sufficient to say that  $\xi_c$  must be real; it must now be positive, as particles falling to the planet from infinity must be excluded from the integration. The condition that the orbit intersects the critical level requires that  $v \leq v_1(\xi)$ , as with (7.1.30). The energy requirement gives  $v \geq v_2(\xi)$ , in analogy with (7.1.31). However,  $v_2$  may turn out to be negative and in that case we merely have  $v \geq 0$ . This latter limit on  $v$  is used, then, when  $\xi > +\lambda^{1/2}$  [cf. (7.1.31)].

A further caution to be observed is that we clearly cannot have  $v_2 \leq v \leq v_1$  unless  $v_2 \leq v_1$ . This condition necessitates, in analogy with (7.1.32), that  $\xi > \xi_1$ . Hence, we obtain

$$\begin{aligned}\zeta_{\text{esc}}(\lambda) &= \frac{1}{\pi^{1/2}} \int_{\xi=\xi_1}^{\lambda^{1/2}} \int_{v=v_2}^{v_1} e^{-\xi^2-v} dv d\xi \\ &\quad + \frac{1}{\pi^{1/2}} \int_{\xi=\lambda^{1/2}}^{\infty} \int_{v=0}^{v_1} e^{-\xi^2-v} dv d\xi\end{aligned}\quad (7.1.42)$$

This expression may be transformed to

$$\begin{aligned}\zeta_{\text{esc}}(\lambda) &= \frac{1}{\pi^{1/2}} \int_{\lambda}^{\infty} \psi^{1/2} e^{-\psi} [1 - \mu_0(\psi)] d\psi \\ &= \frac{1}{\pi^{1/2}} \left\{ \Gamma\left(\frac{3}{2}\right) - \gamma\left(\frac{3}{2}, \lambda\right) - \frac{(\lambda_c^2 - \lambda^2)^{1/2}}{\lambda_c} e^{-\psi} [\Gamma\left(\frac{3}{2}\right) - \lambda\left(\frac{3}{2}, \lambda - \psi_1\right)] \right\} \end{aligned}\quad (7.1.43)$$

where  $\mu_0(\psi)$  is given by (7.1.35) and  $\psi_1$  by (7.1.37); here  $\Gamma(\alpha) \equiv \gamma(\alpha, \infty)$  is the complete  $\Gamma$  function.

**Summary of Densities** The total partition function to be used in computing the density by (7.1.20) is

$$\zeta = \zeta_{\text{bal}} + \zeta_{\text{sat}} + \zeta_{\text{esc}} \quad (7.1.44)$$

as given by (7.1.34), (7.1.41), and (7.1.43). These components of  $\zeta$  are tabulated versus  $\lambda_c$  and  $\lambda$  in Appendix IX.

**Flux of Escaping Particles** At any height above the critical level the net number of particles moving outward across a square centimeter perpendicular to the radius vector may be expressed symbolically as

$$\mathcal{F}_{\text{esc}} = \int \frac{p_r}{M} f(q_i, p_i) d^3 p_i \quad (7.1.45)$$

where the integration is again over all allowed momentum coordinates. Writing  $f$  in terms of polar velocity coordinates in the manner of (7.1.39), we find

$$\mathcal{F}_{\text{esc}} = N_c e^{-(\lambda_c - \lambda)} \frac{U}{2\pi^{1/2}} \int_{\lambda}^{\infty} \psi e^{-\psi} [1 - \mu_0^2(\psi)] d\psi \quad (7.1.46)$$

where  $U = (2kT_c/M)^{1/2}$ .

With  $\mu_0(\psi)$  given by (7.1.35) the flux may be evaluated exactly and is

$$\mathcal{F}_{\text{esc}}(\lambda) = \frac{N_c e^{-\lambda_c} U}{2\pi^{1/2}} \frac{(\lambda_c + 1)\lambda^2}{\lambda_c^2} \quad (7.1.47)$$

This flux decreases as  $r^{-2}$ , as it must to satisfy continuity, and is the Jeans formula (7.1.5) at  $\lambda = \lambda_c$ .

#### 7.1.4 Integrated Densities

The *integrated density* is the total number of atoms per  $\text{cm}^2$  in a column of unit cross-sectional area above a specified height  $r_1$  and along a specified

direction  $\theta_1(r_1) = \cos^{-1} \mu_1(\lambda_1)$ . We designate it by

$$\begin{aligned}\mathcal{N}(\mu_1, \lambda_1) &\equiv \int_{r_1}^{\infty} N(r) \sec \theta(r, r_1) dr \\ &= N_c e^{-\lambda_c} \lambda_1 r_1 \int_0^{\lambda_1} \frac{e^{\lambda} \zeta(\lambda)}{\lambda^2 \mu(\lambda, \lambda_1)} d\lambda.\end{aligned}\quad (7.1.48)$$

where  $N(r)$  has been expressed by (7.1.20) and where  $\mu(\lambda, \lambda_1)$  is defined below by (7.1.49).

The importance of the integrated density is twofold. The probability of an atom escaping from the atmosphere is governed by the total number of atoms lying above it; hence the integrated density fixes the exobase. Moreover, optical observations of coronas may yield the integrated density directly. Integrated densities depend on the density of the observed species  $N_c$  and the temperature  $T_c$  at the exobase and on the contribution provided by satellite orbits. In order to extract this information from the observations, we must calculate the integrated densities for various conditions.

Rocket or satellite photometers might observe  $\mathcal{N}$  in any direction above the vehicle. But of special interest are observations made from outside the corona, where the line of sight passes through the corona along a chord that has its closest approach at  $r_1$ . This line of sight thus traverses an integrated density of  $2\mathcal{N}(\mu_1 = 0, \lambda_1)$ .

Except for the special case of radial integration,  $\theta$  is a function of both  $r_1$  and  $r$ . From the geometry of Fig. 7.2 and the law of sines, we have

$$\mu(\lambda, \lambda_1) = \left(1 - \frac{\lambda^2}{\lambda_1^2}(1 - \mu_1^2)\right)^{1/2}\quad (7.1.49)$$

We may then write (7.1.48) as

$$\begin{aligned}\mathcal{N}(\mu_1, \lambda_1) &= N_c e^{-(\lambda_c - \lambda_1)} \zeta(\lambda_1) \frac{r_1}{\lambda_1} K(\mu_1, \lambda_1) \\ &= N(r_1) H_1 K(\mu_1, \lambda_1)\end{aligned}\quad (7.1.50)$$

where

$$H_1 \equiv \frac{r_1}{\lambda_1} = \frac{k T_c r_1^2}{G M M} = \frac{k T_c}{M g(r_1)}\quad (7.1.51)$$

and

$$K(\mu_1, \lambda_1) = \int_0^{\lambda_1} \frac{\lambda_1^2 \zeta(\lambda) e^{-(\lambda_1 - \lambda)} d\lambda}{\lambda^2 \zeta(\lambda_1) [1 - (1 - \mu_1^2) \lambda^2 / \lambda_1^2]^{1/2}}\quad (7.1.52)$$

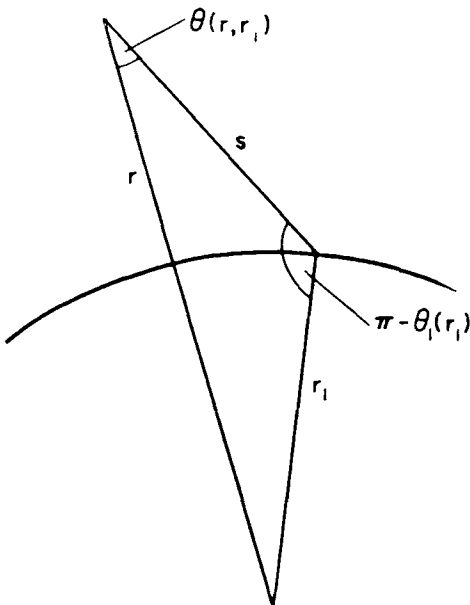


**Fig. 7.2** Geometry for integrated densities. The integration is along path  $s$ , extending from height  $r_1$  to infinity.

In (7.1.51) the acceleration of gravity at height  $r_1$  is  $g(r_1) = G\mathcal{M}/r_1^2$ , and  $H_1$  is the conventional *scale height* at temperature  $T_c$  used in plane-parallel models of atmospheric structure. When the variation of  $g(r)$  is neglected above  $r_1$ , as is frequently done in plane-parallel models, the integrated density is  $N(r_1)H_1\mu_1^{-1}$ . In practice, the error involved in taking  $g$  as a constant has a trivial effect on  $\mathcal{N}$  only if the distance over which  $g$  actually varies appreciably is very large compared with  $H_1$ —that is, if  $r_1 \gg H_1$  or, equivalently, if  $\lambda_1 \gg 1$ .

In coronal theory, where we necessarily abandon the approximation of constant gravity, it is necessary to examine the situation more thoroughly, since the generalized barometric formula (7.1.9) predicts  $N \rightarrow \text{const}$  as  $\lambda \rightarrow 0$  and therefore  $\mathcal{N} \rightarrow \infty$ . We may consider, then,  $\mu_1 K(\mu_1, \lambda_1)$  to be a correction factor for  $\mathcal{N}(\mu_1, \lambda_1)$  to the simple, plane-parallel approximation with constant gravity. In the general case, the integral (7.1.52) is so complicated that a reasonable simple analytic expression does not exist, although tables of numerical calculations for various  $\lambda_c$  and  $\lambda_1$  are given in Tables IX.3 and IX.4. For some purposes approximate expressions will suffice. First we evaluate  $K$  for  $\lambda_1 \gg 1$  and find to what extent  $\mathcal{N}$  may depart appreciably from the usual approximation. Then we shall consider the distant regions where  $\lambda_1 \gg 1$ , as observations of this region will be of particular use in disclosing the contribution from satellite orbits.

**Integrated Density for Large  $\lambda_1$**  When  $\lambda_1 \gg 1$  the integral (7.1.52) is conveniently evaluated in two parts: the contribution from large  $\lambda$  ( $\lambda_2 < \lambda < \lambda_1$ ), which we designate  $\Delta_1 K$ , and the part at small  $\lambda$  ( $0 < \lambda < \lambda_2$ ), called  $\Delta_2 K$ . Here  $\lambda_2$  is of order unity and designates the transition between large and small  $\lambda$ .

First consider the region of small  $\lambda$ . If there is a full population of particles in satellite orbits, the asymptotic density at small  $\lambda$  is given by (see Problem 7.4)

$$\zeta \approx \frac{4}{3\pi^{1/2}} \lambda^{3/2} \quad (7.1.53)$$

Letting  $\zeta(\lambda_1) = 1$ , we have

$$\begin{aligned} \Delta_2 K(\mu_1, \lambda_1) &\leq \frac{4}{3\pi^{1/2}} \int_0^{\lambda_2} \frac{\lambda_1^{-2}}{\lambda^{1/2}} e^{-(\lambda_1 - \lambda)} d\lambda \\ &= \frac{8}{3\pi^{1/2}} \lambda_1^{-2} \lambda_2^{1/2} e^{-\lambda_1} \end{aligned} \quad (7.1.54)$$

Since the approximate formula (7.1.53) actually overestimates  $\zeta(\lambda)$  around  $\lambda \approx 1$ , it is clear that (7.1.54) gives an upper limit and that  $\Delta_2 K \ll 1$ . When satellite orbits are depleted, the contribution to  $K$  is, of course, still smaller. This illustrates that, in contrast with the prediction of the barometric formula (7.1.19), the actual contribution to the integrated density at large distances is very small.

For the region  $\lambda_2 < \lambda < \lambda_1$ , we set  $\zeta(\lambda) = 1$ , corresponding to a full Maxwellian distribution. This is especially appropriate if the full component of satellite orbits is present and is likely to be a suitable approximation when  $\lambda_1 \gg 1$ , since most of the contribution to  $\Delta_1 K$  arises from large  $\lambda$ . We thus have

$$\begin{aligned} K(\mu_1, \lambda_1) \approx \Delta_1 K(\mu_1, \lambda_1) &\approx \int_{\lambda_2}^{\lambda_1} \frac{\lambda_1^{-2} e^{-(\lambda_1 - \lambda)} d\lambda}{\lambda^2 [1 - (1 - \mu_1^{-2})\lambda^2/\lambda_1^2]^{1/2}} \\ &= \int_0^{\lambda_1 - \lambda_2} \frac{e^{-x} dx}{(1 - x/\lambda_1)^2 [1 - (1 - \mu_1^{-2})(1 - x/\lambda_1)^2]^{1/2}} \end{aligned} \quad (7.1.55)$$

where  $x = \lambda_1 - \lambda$ .

We examine separately the two situations  $\mu_1 = 1$  and  $\mu_1 = 0$ . In the first case we have

$$K(\mu_1 = 1, \lambda_1) = \int_0^{\lambda_1 - \lambda_2} \frac{e^{-x} dx}{(1 - x/\lambda_1)^2} \quad (7.1.56)$$

The integrand on the right side is unity at  $x \equiv \lambda_1 - \lambda = 0$  (or  $\lambda = \lambda_1$ ) and decreases to a minimum at  $x = \lambda_1 - 2$  (or  $\lambda = 2$ ). At still larger  $x$  (or smaller

$\lambda$ ) the integrand increases and becomes infinite at  $x = \lambda_1$  (i.e.,  $\lambda = 0$ ). But the latter region is excluded by the integration limit and is included more appropriately in (7.1.54). Expanding  $(1 - x/\lambda_1)^{-2}$  by the binomial theorem, we may integrate term by term. These individual integrals may be expressed in closed form in terms of the *incomplete  $\Gamma$ -functions*, which can in turn be written in terms of the *truncated exponential series*. We find

$$K(\mu_1 = 1, \lambda_1) = \sum_{n=1}^{\infty} \frac{n!}{\lambda_1^{n-1}} [1 - e_{n-1}(\lambda_1 - \lambda_2) e^{-(\lambda_1 - \lambda_2)}] \quad (7.1.57)$$

where

$$e_n(\lambda_1 - \lambda_2) = 1 + (\lambda_1 - \lambda_2) + \frac{(\lambda_1 - \lambda_2)^2}{2!} + \cdots + \frac{(\lambda_1 - \lambda_2)^n}{n!} \quad (7.1.58)$$

When  $\lambda_1 \gg 1$  the first few terms in the series (7.1.57) will decrease rapidly because of the factor  $\lambda_1^{-(n-1)}$ . At higher members of the series,  $n!/\lambda_1^{n-1}$  will increase, but this occurs only after the exponential series  $e_{n-1}(\lambda_1 - \lambda_2)$  begins to converge. The  $n$ th term in (7.1.57) will then itself be a series whose leading term is

$$e^{-(\lambda_1 - \lambda_2)} \frac{(\lambda_1 - \lambda_2)^n}{\lambda_1^{n-1}} \quad (7.1.59)$$

which is small for  $\lambda_1 \gg 1$ . (If  $\lambda_2$  were allowed to be of order zero instead of unity, the convergence of the individual terms (7.1.59) as  $n \rightarrow$  large would be very gradual, in accord with the rapid increase of the integrand in (7.1.57) as  $x \rightarrow \lambda_1$ .)

Hence for  $\lambda_1 \gg 1$  and  $\lambda_2 \sim 1$  we find the integral (7.1.57) yields

$$K(\mu_1 = 1, \lambda_1) = 1 + \frac{2}{\lambda_1} + \cdots \quad (7.1.60)$$

as the correction factor imposed by the variation of gravity in a spherical atmosphere. For  $\lambda_1 = 10$ , the plane-parallel model is 20 percent in error; for still smaller  $\lambda_1$ , the discrepancy is worse.

When  $\mu_1 = 0$ , (7.1.55) yields

$$K(\mu_1 = 0, \lambda_1) \approx \frac{\lambda_1^{1/2}}{2^{1/2}} \int_0^{\lambda_1 - \lambda_2} \frac{e^{-x} dx}{x^{1/2}(1 - x/\lambda_1)^2(1 - x/2\lambda_1)^{1/2}} \quad (7.1.61)$$

Again expanding the denominator and integrating term by term, we have, to the same degree of approximation as (7.1.60) for  $\lambda_1 \gg 1$ ,

$$K(\mu_1 = 0, \lambda_1) \approx \left( \frac{\lambda_1 \pi}{2} \right)^{1/2} \left( 1 + \frac{9}{8\lambda_1} + \cdots \right) \quad (7.1.62)$$

From (7.1.50) the integrated density perpendicular to the radius vector is

$$\mathcal{N}(\mu_1 = 0, \lambda_1) \approx N(r_1) \left( \frac{\pi r_1 H_1}{2} \right)^{1/2} \left( 1 + \frac{9}{8\lambda_1} \right) \quad (7.1.63)$$

The leading term is half the density along a complete tangential traversal through the atmosphere given in the constant-gravity approximation by (6.2.6). The correction term  $9/8\lambda_1$ , is a rather crude approximation and should not be compared literally with the correction term  $3/8\lambda_1$ , in the constant-gravity expression (6.2.6).

**Integrated Density for Small  $\lambda_1$ .** When  $\lambda_1 \ll 1$  so that  $\zeta(\lambda)$  is represented adequately by asymptotic expansions in powers of  $\lambda$ , the exponential in (7.1.52) is of order unity. Let us now consider a single component (ballistic, satellite, or escaping particles) and suppose that the density of that component varies as some power of  $r$ ; that is,  $\zeta_{\text{com}}(\lambda) = \text{const } \lambda^{n+2}$ .

Equation (7.1.52) for a single component (or, more correctly, a single term in a power-law expansion of the density) is then

$$K_{\text{com}}(\mu_1, \lambda_1) = \lambda_1 \int_0^1 \frac{y^n dy}{[1 - (1 - \mu_1^2)y^2]^{1/2}} \quad (7.1.64)$$

Clearly we must have  $n > -1$  in this discussion or else the integrated density would be infinite, violating our basic assumption that the total gravitational mass of the atmosphere may be neglected.

For an arbitrary value of  $\mu_1$  the integral may be evaluated numerically, with the binomial expansion for the denominator. The convergence of terms in the integrated series is rather slow if  $\mu_1 \sim 0$ . However, the two special cases of most interest may be handled analytically. When  $\mu_1 = 1$  (7.1.64) becomes simply  $\lambda_1/(n+1)$ , and the integrated density of the component is, from (7.1.50)

$$\begin{aligned} \mathcal{N}_{\text{com}}(\mu_1 = 1, \lambda_1) &= N_c e^{-\lambda_c} \zeta_{\text{com}}(\lambda_1) \frac{r_1}{n+1} \\ &= N_{\text{com}}(r_1) \frac{r_1}{n+1} \end{aligned} \quad (7.1.65)$$

As  $\lambda_1 \rightarrow 0$ ,  $n = +\frac{1}{2}, -\frac{1}{2}$ , and 0 in the leading terms for ballistic, satellite, and escaping particles, respectively (see Problem 7.4). The integrated density in the radial direction at large distances  $r_1$  is thus computed with an effective scale height  $H_1 K(1, \lambda_1)$  the same order of magnitude as  $r_1$ .

For the transverse direction (7.1.64) gives

$$K_{\text{com}}(\mu_1 = 0, \lambda_1) = \frac{\lambda_1}{n+1} \frac{\Gamma[(n+3)/2]\Gamma(\frac{1}{2})}{\Gamma[(n+2)/2]} \quad (7.1.66)$$

where  $\Gamma$  is the *complete  $\Gamma$ -function*. The integrated density in the transverse direction is then

$$\mathcal{N}_{\text{com}}(\mu_1 = 0, \lambda_1) = N_{\text{com}}(r_1) \frac{r_1}{n+1} \frac{\Gamma[(n+3)/2]\Gamma(\frac{1}{2})}{\Gamma[(n+2)/2]} \quad (7.1.67)$$

The integrated density increases only moderately between the radial and transverse directions. The leading term in the ratio  $\mathcal{N}_{\text{com}}(\mu_1 = 0, \lambda_1)/\mathcal{N}_{\text{com}}(\mu_1 = 1, \lambda_1)$  is 1.79720 for ballistic orbits ( $n = \frac{1}{2}$ ); 1.57080 ( $=\pi/2$ ) for escaping orbits ( $n = 0$ ); and 1.31102 for satellite orbits ( $n = -\frac{1}{2}$ ).

### 7.1.5 Doppler Profiles of Spectral Lines

By the use of very sensitive detectors and high-resolution techniques, it is possible in principle to measure the line profile of radiation scattered by a planetary corona. With slightly less spectral resolution, one might measure the line width containing a specific fraction of the total intensity, that is, the integrated profile between two finite frequencies. Such measurements would be extremely useful for deriving the structure of the exosphere, especially if the intensities are measured in absolute units and at a variety of positions within the corona. In this section we derive expressions for those line profiles in terms of the basic parameters  $(\lambda_c, \lambda_{cs}, U, N_c)$  of the corona and the position and direction of observation.

The term *line profile* is used here in a rather special sense. Strictly speaking, we shall derive only the distribution of velocities in a specified direction in space, summing over all particles in the line of sight. This distribution is proportional to the spectral profile only when the corona is optically thin so that extinction and multiple scattering are negligible. Unfortunately, in practice these effects are likely to be troublesome. For example, outward observations from relatively near the planet might utilize the planet's shadow to obscure the atoms located below some height  $r_1$ . The setting or rising sun would then create an opportunity to collect data as a function of  $r_1$ . However, some of the incident sunlight passing through the corona is scattered before reaching the region to be observed ( $r > r_1$ ), producing a complex situation of radiation transfer.

Without these complications, it is merely necessary to multiply the particle densities in a velocity range  $dv_s$  by  $g/4\pi$ , where  $g$  is the total number of photons scattered per atom per second, to obtain the profile in absolute radiation units per unit velocity interval (photons/cm<sup>2</sup> sec sr cm sec<sup>-1</sup>). For the hydrogen geocorona,  $g \approx 2.3 \times 10^{-3}$  photons/sec. For very accurate measurements it would be necessary to correct this theoretical intensity by as much as 17 per cent for the anisotropy of resonance scattering in Ly  $\alpha$  (Section 6.3.1).

Consider a column of unit cross section extending above height  $r_1$  at an angle  $\theta_1(r_1)$  (see Fig. 7.2). This column contains an integrated density denoted in Eq (7.1.48) by  $\mathcal{N}(\mu_1, \lambda_1)$ . We shall let  $I(p_s, \lambda_1) dp_s$  be the optically thin intensity of photons scattered by atoms with a momentum component parallel to the column between  $p_s$  and  $p_s + dp_s$ , where  $\mathbf{s}$  specifies the direction along the column. Then the spectrum is

$$I(p_s, \lambda_1) = \frac{g}{4\pi} \int_{r_1}^{\infty} \int_{p_\beta} \int_{p_\alpha} \frac{f(p_s, p_\alpha, p_\beta) dp_\alpha dp_\beta dr}{\mu(\lambda, \lambda_1)} \quad (7.1.68)$$

and the integrated density, expressed in terms of the spectrum, is

$$\mathcal{N}(\mu_1, \lambda_1) = \frac{4\pi}{g} \int_{-\infty}^{\infty} I(p_s, \lambda_1) dp_s \quad (7.1.69)$$

Here  $p_\alpha$  and  $p_\beta$  are momentum components in the plane perpendicular to  $\mathbf{s}$ ,  $\mu$  specifies the direction of  $\mathbf{s}$  at any level and is given by (7.1.49), and the density in momentum phase space is a modified form of (7.1.18):

$$f(p_s, p_\alpha, p_\beta) = \frac{N_c e^{-(\lambda_c - \lambda)} e^{-(p_s^2 + p_\alpha^2 + p_\beta^2)/2MkT_c}}{(2\pi M k T_c)^{3/2}} \quad (7.1.70)$$

The integration limits in (7.1.68) are subject to the dynamical restrictions on coronal particles and are quite complicated in the completely general case.

The profile in the radial direction provides the simplicity of azimuthal symmetry and this special case is much less involved. Thus with  $r\lambda = r_1\lambda_1$  the radial profile is

$$I(p_r, \lambda_1) = \frac{g}{4\pi} \frac{N_c e^{-\lambda_c} r_1 \lambda_1 e^{-\xi^2}}{(2\pi M k T_c)^{1/2}} \mathcal{S}(\xi, \lambda_1) \quad (7.1.71)$$

where the *radial spectrum function* is

$$\mathcal{S}(\xi, \lambda_1) = \int_0^{z_1} \int_v \frac{e^\lambda e^{-v}}{\lambda^2} dv d\lambda \quad (7.1.72)$$

If  $\mathcal{S}$  were independent of  $\xi$ , then  $I(p_r, \lambda_1)$  would have the shape of  $\exp(-\xi^2)$ , as does the common Doppler profile for a Maxwellian distribution, where the absorption cross section per atom is, in frequency units,

$$\alpha_v = \frac{\pi e^2}{mc} f \frac{c}{v_0 U \pi^{1/2}} \exp \left[ -\frac{c^2}{U^2} \left( \frac{v - v_0}{v_0} \right)^2 \right] \quad (7.1.73)$$

for an oscillator strength  $f$ .

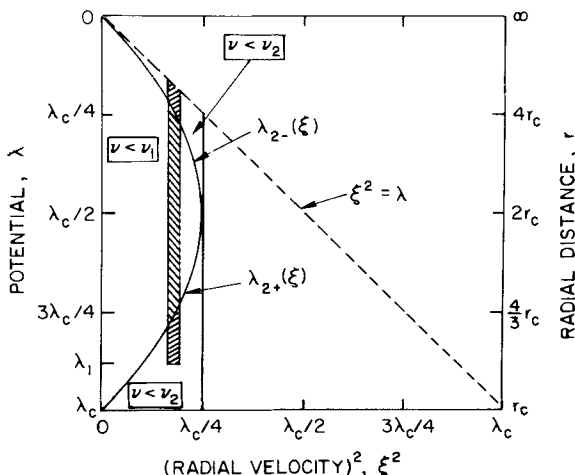


**Fig. 7.3** Integration limits in  $\lambda$ -space for a specified radial velocity  $\xi$  and a run of transverse energies  $v$ . The diagram relates the limits on  $\lambda$  to the corresponding limits on  $\xi$  when the  $v$  regime is specified. The shading shows an integration path in  $\lambda$  space for a ballistic orbit with  $\xi^2 < \lambda_c/4$ . The path covers three distinct regimes of  $v$ , such that  $\xi^2 < \lambda < \lambda_{2-}$  (for  $v < v_2$ );  $\lambda_{2-} < \lambda < \lambda_{2+}$  (for  $v < v_1$ ); and  $\lambda_{2+} < \lambda < \lambda_1$  (again for  $v < v_2$ ).

The evaluation of (7.1.72) still requires assignment of limits to  $v$  from the dynamical restrictions. The limits on  $v$  are derived in a similar manner to that used in Section 7.1.3; however, there the second integration was over  $\xi$  and here it is over  $\lambda$ . The relationship between the two sets of integration limits is illustrated in Fig. 7.3.

First consider ballistic orbits (with negative total energy). The limits on  $v$  are given by (7.1.30)–(7.1.31), defining  $v_1$  and  $v_2$ . We have  $0 < v < v_1$  if condition (7.1.32) is fulfilled. Expressed as a condition on  $\lambda$  instead of one on  $\xi$ , (7.1.32) becomes

$$\lambda \leq \lambda_{2\pm} = \frac{\lambda_c}{2} \left[ 1 \pm \left( 1 - \frac{4\xi^2}{\lambda_c} \right)^{1/2} \right] \quad (7.1.74)$$

We have to ascertain, however, which inequality is associated with the  $\pm$  signs of the radical. As shown in Fig. 7.3 the integration  $0 < v < v_1$  is valid when  $\lambda_{2-} < \lambda < \lambda_{2+}$ ; this interpretation of (7.1.74) may be checked analytically by (7.1.74) and (7.1.32) (see Problem 7.6). These are the ballistic orbits whose principal restriction is that they intersect  $r_c$ .

In a similar fashion we find  $0 < v < v_2$  when  $\lambda < \lambda_{2-}$  and when  $\lambda > \lambda_{2+}$ . These ballistic orbits are restricted only by the condition of negative energy; no satellite orbits are possible with these  $v, \lambda$  combinations because  $v < v_1$  (the intersection condition) is obeyed as well. It is interesting that one such

region for any particular  $\xi$ , lies at low altitudes ( $\lambda > \lambda_{2+}$ ) and the other at high ones ( $\lambda < \lambda_{2-}$ ). In intermediate heights and small values of  $\xi$ , satellite orbits are allowed [compare (7.1.77)].

For  $0 < \xi^2 < \lambda_c/4$  we have, therefore,

$$\begin{aligned}\mathcal{S}_{\text{bal}}(\xi, \lambda_1) = & \int_{\xi^2}^{\lambda_{2-}} \frac{e^\lambda}{\lambda^2} (1 - e^{-v_2}) d\lambda + \int_{\lambda_{2-}}^{\lambda_{2+}} \frac{e^\lambda}{\lambda^2} (1 - e^{-v_1}) d\lambda \\ & + \int_{\lambda_{2+}}^{\lambda_1} \frac{e^\lambda}{\lambda^2} (1 - e^{-v_2}) d\lambda\end{aligned}\quad (7.1.75)$$

When  $\xi^2 > \lambda_c/4$ , the limits  $\lambda_{2\pm}$  are imaginary and the three integrals in (7.1.75) coalesce into a single one. Hence for  $\lambda_c/4 \leq \xi^2 < \lambda_1$  the spectrum is obtained from

$$\mathcal{S}_{\text{bal}}(\xi, \lambda_1) = \int_{\xi^2}^{\lambda_1} \frac{e^\lambda}{\lambda^2} (1 - e^{-v_2}) d\lambda \quad (7.1.76)$$

For ballistic plus satellite orbits only the energy condition,  $0 < v < v_2$  prevails. Hence for all  $\xi^2 < \lambda_1$ , the spectrum function for all captive particles is given by (7.1.76). Thus we write

$$\mathcal{S}_{\text{bal+sat}}(\xi, \lambda_1) = \int_{\xi^2}^{\lambda_1} \frac{e^\lambda}{\lambda^2} (1 - e^{-v_2}) d\lambda \quad (7.1.77)$$

which may be evaluated with tabulated exponential integrals.

In practice, however, satellite orbits are never filled to capacity and one may estimate the actual contribution of ballistic plus satellite particles by the scheme used in Section 7.2.1. This involves defining the satellite critical level  $\lambda_{cs}$  and using (7.1.75) with  $\lambda_c$  everywhere replaced by  $\lambda_{cs}$  to describe all particles of negative energy. Escaping particles (see below) are still described with  $\lambda_c$ .

In Section 7.1.3 we established that escaping particles in the range  $v_2 < v < v_1$  are allowed when  $\xi$  is in the range  $[\lambda(1 - \lambda/\lambda_c)]^{1/2} < \xi < \lambda^{1/2}$ . This condition means for a fixed  $\xi$  that  $\lambda > \xi^2$  and that either  $\lambda > \lambda_{2+}$  or  $\lambda < \lambda_{2-}$ . The entire range  $0 < v < v_1$  is allowed for particles with  $\xi^2 > \lambda$ .

We therefore obtain the spectrum function for escaping particles ( $\xi > 0$ ) as

$$\begin{aligned}\mathcal{S}_{\text{esc}}(\xi, \lambda_1) = & \int_0^{\xi^2} \frac{e^\lambda}{\lambda^2} (1 - e^{-v_1}) d\lambda + \int_{\xi^2}^{\lambda_{2-}} \frac{e^\lambda}{\lambda^2} (e^{-v_2} - e^{-v_1}) d\lambda \\ & + \int_{\lambda_{2+}}^{\lambda_1} \frac{e^\lambda}{\lambda^2} (e^{-v_2} - e^{-v_1}) d\lambda\end{aligned}\quad (7.1.78)$$

Figure 7.4 shows some profiles for radially outward observations above various  $r_1$  with various assumed satellite critical levels (cf. Section 7.2.1).

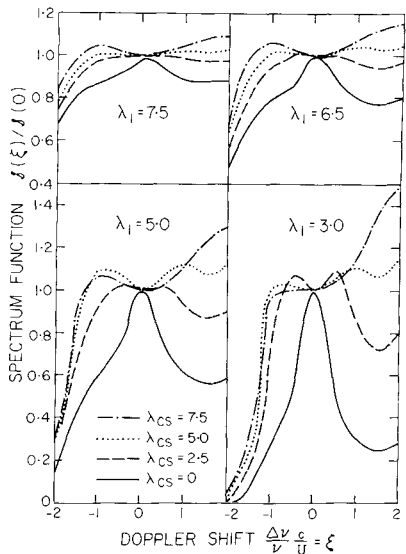


**Fig. 7.4** Spectrum functions for various shadow heights  $r_1$  and satellite critical level  $r_{cs}$  for zenith observations from below  $r_1$ . In all cases the base of the exosphere is specified by  $\lambda_c = 7.5$  (e.g., appropriate for 500 km altitude on Earth with H atoms at 940°K). For  $\lambda_{cs} = 7.5$  all satellite orbits are depleted; for  $\lambda_{cs} = 0$  all possible satellite orbits for negative total energy are filled, so that particles at any height are isotropic for all velocities less than  $\lambda^{1/2}$ . The curves, when multiplied by  $\exp(-\xi^2)$ , give the Doppler line profiles. [After CHAMBERLAIN (1976).]

### 7.1.6 Lateral Flow in Collisionless Atmospheres

The hydrogen and helium densities in the thermosphere and exosphere have a strong diurnal variation that arises from the diurnal temperature variation. Consequently, there is a lateral flow of matter that tends to smooth the densities. The flow rate is the order of  $10^{10}/\text{cm}^2 \text{ sec}$ . For helium the higher densities on the day side lead to a flow generally from day towards night. For hydrogen the simple density enhancement from diffusive separation is modified by the higher thermal escape from a region of higher temperature. Therefore, the net hydrogen flow tends to be from a nighttime bulge toward the day. Lateral transport has been treated both in terms of the upgoing and downcoming particles at the base of the exosphere and as hydrodynamic diffusion.

Interesting special cases arise for the Moon and Mercury, where the exospheric base is set by the solid planet, which produces peculiar problems. When particles strike the surface, a certain fraction will become adsorbed and not rebound (although they may liberate other particles). This fraction is the *accommodation coefficient*. If the particles are liberated from the surface according to a Maxwellian distribution, the atmosphere will be essentially barometric (at the temperature of the surface), as in a classical exosphere, but there seems to be no compelling reason to suppose that this distribution will be released. Furthermore, accommodation coefficients are temperature dependent and are generally quite low. The particle interaction energy of a

particle colliding with a surface is fixed mainly by its component of velocity normal to the local surface. The *energy accommodation* of particles to the solid surface is probably as low as 0.1 per collision. As a result the rate of thermal escape is drastically reduced from what would be expected for an atmosphere adjusted to the surface temperature.

## 7.2 Collisions in Exospheres

No exosphere is strictly collisionless, of course. Here we examine a variety of effects due to collisions and radiation pressure (i.e., photon-atom collisions).

### 7.2.1 Equilibrium of Satellite Particles

In order to estimate the population of satellite particles, we introduce the concept of *satellite critical level* at  $r_{cs}$ ; this level will assume a role for these particles analogous to that of the exobase  $r_c$  for ballistic and escaping particles. Specifically, we suppose that below  $r_{cs}$  there is, because of at least occasional collisions, a complete, isotropic distribution of the satellite particles that are energetically allowed ( $h < 0$ ). Above  $r_{cs}$  we suppose that the collisional creation of satellite orbits is negligible and that the only such orbits present are those that have perigees between  $r_c$  and  $r_{cs}$ .

With a sharply defined satellite critical level, we may compute the density with the complete distribution of allowable satellite orbits up to  $r_{cs}$ ; beyond, we may use the distribution for ballistic orbits alone as though these orbits arose from  $r_{cs}$  rather than  $r_c$ . Thus (7.1.40) is appropriate for  $\lambda > \lambda_{cs}$ , and for  $\lambda \leq \lambda_{cs}$  we may use (7.1.34) with  $\lambda_c$  replaced by  $\lambda_{cs}$ . The ballistic or escaping components are not actually affected by this modification. It is only that the ballistic formula and the numerical tables based on it may, with this approach, be used to describe satellite plus ballistic particles.

Similarly, the integrated densities may be obtained from  $K(\mu_1, \lambda_1)$  of (7.1.52) and published tables of that integral. Some caution is necessary if the point  $r_1$  is below  $r_{cs}$  (i.e., if  $\lambda_1 > \lambda_{cs}$ ). The total bound ( $h < 0$ ) population in the interval  $\lambda_1 > \lambda > \lambda_{cs}$  is evaluated with the entire permitted population ( $\zeta_{bal} + \zeta_{sat}$ ). For the interval  $\lambda_{cs} > \lambda > 0$ , the bound component is regarded as a ballistic component,  $K_{bal}(\mu_{cs}, \lambda_{cs})$ , where  $\mu_{cs}$  is related to  $\mu_1$ ,  $\lambda_1$ , and  $\lambda_{cs}$  in the manner of (7.1.49), and where  $\zeta_{bal}(\lambda)$  is found from (7.1.34) with  $\lambda_c$  replaced with  $\lambda_{cs}$ .

The location of  $\lambda_{cs}$  is specified by the condition that satellite particles are created, through collisions of ballistic particles with other particles, at the

same rate that they are destroyed, principally through particle collisions, radiation pressure, photoionization, and collisions with solar-wind ions.

Let  $f_{\text{sat}}(r, p)$  be the density in phase space of satellite particles with total momentum  $p$ , and let  $f_{\text{bal}}(r, p)$  be the density of particles whose orbits intersect the critical level  $r_c$ . For a given  $r$  and  $p$  (or  $\lambda$  and  $\psi$ ), satellite particles occupy a solid angle  $4\pi\mu_0$  and ballistic orbits fill the remaining portion of the sphere with solid angle  $4\pi(1 - \mu_0)$ , where  $\mu_0$  is given by (7.1.35) and (7.1.36).

The rate of change of the population of satellite particles, with changes in total particle momentum ignored, is (for isotropic scattering)

$$4\pi\mu_0 \frac{d}{dt} f_{\text{sat}}(r, p) = N'Qv[4\pi(1 - \mu_0)f_{\text{bal}}(r, p)]\mu_0 - N'Qv[4\pi\mu_0 f_{\text{sat}}(r, p)](1 - \mu_0) - \frac{4\pi\mu_0}{\tau_{\text{loss}}} f_{\text{sat}}(r, p) \quad (7.2.1)$$

Here  $N'$  is the total number density of particles available for collisions,  $Q$  the cross section for a collision, and  $\tau_{\text{loss}}$  the lifetime for a  $1/e$  probability of loss of an exospheric atom in the absence of neutral collisions. The first term on the right side is the rate of collisional injection of ballistic atoms (which fill a fraction  $1 - \mu_0$  of a sphere) into a fraction  $\mu_0$  of a sphere—that is, it represents the rate of creation of satellite orbits. Similarly, the second term is the rate of loss of satellite orbits by collisions that change satellite orbits into ballistic ones. The last term is the destruction rate of satellite particles through external forces.

The equilibrium ratio of densities in phase space is then

$$\frac{f_{\text{bal}}(r, p)}{f_{\text{sat}}(r, p)} = 1 + \frac{\tau_{\text{coll}}}{\tau_{\text{loss}}(1 - \mu_0)} \quad (7.2.2)$$

where  $\tau_{\text{coll}} = (N'Qv)^{-1}$  is the lifetime for a  $1/e$  probability of a particle having a collision. The ratio depends on  $p$  as well as  $r$ . But we may obtain an upper limit to  $\lambda_{cs}$ , the potential at which satellite orbits effectively cease to be created, by evaluating (7.2.2) for the maximum kinetic energy,  $\psi = \lambda$ , that captive particles may possess. Particles with lower kinetic energy may enter satellite orbits at still smaller values of  $\lambda$ , so this procedure will yield the lowest height at which a significant number of bound orbits are absent.

Satellite orbits with  $\psi = \lambda_{cs}$  are filled to one-half capacity when  $f_{\text{sat}}/f_{\text{bal}} = \frac{1}{2}$ , which yields from (7.2.2)

$$N(\lambda_{cs})\lambda_{cs}^{1/2}[1 - \mu_0(\lambda_{cs})]QU\tau_{\text{loss}} = 1 \quad (7.2.3)$$

The most effective type of collision in a hydrogen corona is likely to involve charge transfer between H and H<sup>+</sup>, since at low velocities the cross section

may be quite large. Coulomb collisions continually work toward an isotropic distribution of proton velocities so that the distribution of proton density may approximate the barometric formula (7.1.19) (for a mean molecular weight of one-half that of hydrogen), remaining nearly constant at great distances, with the ionized gas confined by a planetary magnetic field.

For such charge-transfer collisions (7.2.1) must be replaced by an expression in which the total momentum of the neutral and ion are, in effect, interchanged. Writing  $f'(r, p)$  for the density in phase space of the ions and  $N$  for the total density of neutrals, we have

$$4\pi\mu_0 \frac{d}{dt} f_{\text{sat}}(r, p) = [4\pi\mu_0 f'(r, p)] QvN - N' Qv [4\pi\mu_0 f_{\text{sat}}(r, p)] - \frac{4\pi\mu_0}{\tau_{\text{loss}}} f_{\text{sat}}(r, p) \quad (7.2.4)$$

So long as few of the neutral particles are escaping and the satellite orbits are filled almost to capacity ( $f_{\text{sat}} \approx f_{\text{bal}}$ ) and so long as the ions and neutrals follow the same Maxwellian distribution for temperature  $T_c$ , we may write

$$\frac{f'}{(1 - \mu_0)f_{\text{bal}} + \mu_0 f_{\text{sat}}} \approx \frac{N'}{N} \quad (7.2.5)$$

which states that the relative abundance of ions and neutrals is approximately independent of momentum. In this case (7.2.4) reduces to (7.2.1).

In practice it is difficult to evaluate (7.2.3) accurately because  $N'$  and  $\tau_{\text{loss}}$  vary with time and position and because  $\lambda_{\text{cs}}$  varies inversely as their squares. The destruction of satellite particles occurs by photoionization with  $\tau \sim 2.2 \times 10^6$  sec (= 25 days). However, charge exchange with fast solar-wind protons may be more efficient, especially at large distances where screening of the exosphere by the geomagnetic field is unimportant. Radiation pressure destroys satellite orbits efficiently, as we shall now show.

## 7.2.2 Radiation Pressure from Solar Lyman-Alpha

Radiation pressure from the scattering of solar Lyman  $\alpha$  distorts the orbits in a way that usually lowers their perigees. The theory of orbital perturbations of elliptical orbits is rather complicated. There are two general methods for treating the problem. In dynamical astronomy it is common to work with the six orbital elements that completely specify a Keplerian orbit.

These elements are the semi-major axis  $a$  and eccentricity  $e$ , which together specify the ellipse;  $a$  also gives the period through Kepler's third law,  $P = 2\pi a^{3/2}/(GM)^{1/2}$ . The longitude of the ascending node  $\Omega$  measured from the vernal equinox is the point where the body crosses the plane of the

ecliptic from south to north. The inclination  $i$  to the plane of the ecliptic fixes with  $\Omega$  the position of the orbital plane. The orientation of the ellipse in its plane is defined by  $\omega$ , the longitude of the perihelion point measured from the node. Finally, the time of perihelion passage  $t_0$  fixes the body in its orbit. Having the perturbed elements as a function of time, one may compute altered positions and velocities if desired. Alternatively, one can consider the variations of the satellite coordinates directly.

The first approach, analysis of the changes in the orbital elements, is the more useful one when there is a steady perturbation acting over a long time. It is also mathematically elegant. One can relate four of the elements,  $a$ ,  $e$ ,  $i$ , and  $\Omega$ , to the total energy (per unit mass),

$$E = -\frac{GM}{2a} \quad (7.2.6)$$

and the three components of the angular momentum (per unit mass),

$$\mathbf{H} = \mathbf{r} \times \frac{d\mathbf{r}}{dt} \quad (7.2.7)$$

where  $M$  is the mass of the planet. If we forget about the particle passing through the Earth's shadow, the sun's radiation pressure does not vary significantly over the orbit and the particle does not change its total energy or, by (7.2.6), the length of its semi-major axis. If the orbit is not circular its angular momentum does change. Imagine an elliptic orbit in a plane containing the Earth and the sun. The Earth is at the origin, perigee is on the  $x$  axis, which is normal to the Earth-sun line, and the  $y$  axis points away from the sun. Because the particle spends more time in the apogee half-plane than near perigee, there is a net torque on the particle about the Earth. There are two effects. The magnitude of the angular momentum ( $r^2 d\theta/dt$ ) is increased or decreased, depending on the direction of the particle motion in the orbit, and the position of perigee slips or *precesses*. The change in angular momentum  $H$  causes a change in the eccentricity  $e$ ; the precession of perigee means that a torque that increases  $e$  will eventually reverse and become a torque that decreases  $e$ .

With the geometry specified above, the vector equation of motion is

$$\frac{d^2\mathbf{r}}{dt^2} = -\frac{GM\mathbf{r}}{r^3} + \mathbf{f}_y \quad (7.2.8)$$

where  $\mathbf{f}_y$  is the acceleration due to radiation pressure,

$$f_y = hvg/M_H c \quad (7.2.9)$$

and  $g$  is the mean number of Ly  $\alpha$  photons scattered per second by an atom. With  $g = 2.3 \times 10^{-3}$  photon/sec (Table 6.1), the acceleration is  $f_y = 0.75$

cm/sec<sup>2</sup>. (We neglect, for this illustration, the screening of sunlight by the Earth on the nightside and the anisotropy of Ly  $\alpha$  scattering; cf. Section 6.3.1.) Equation (7.2.8) is equivalent to the two scalar equations

$$\begin{aligned} \frac{d}{dt}(r^2\dot{\theta}) &= f_y r \cos \theta \\ \frac{d^2r}{dt^2} - r\dot{\theta}^2 &= -\frac{G\mathcal{M}}{r^2} + f_y \sin \theta \end{aligned} \quad (7.2.10)$$

where superdots denote time derivatives. We will be concerned here with only the first or angular-momentum equation. Without the perturbing influence of radiation, the right side of that equation would be zero and the angular momentum a constant  $H$ , which is a statement of Kepler's law of areas. Taking that constancy as a first-order solution to (7.2.10), we obtain the integral over one revolution,

$$\begin{aligned} r^2\dot{\theta} &= H + \int_0^{2\pi} \frac{f_y r \cos \theta d\theta}{d\theta/dt} \\ &= H + \frac{f_y a^3 (1 - e^2)^3}{H} \int_0^{2\pi} \frac{\cos \theta d\theta}{(1 + e \cos \theta)^3} \\ &= H - \frac{3\pi e f_y a^3 (1 - e^2)^{1/2}}{H} \end{aligned} \quad (7.2.11)$$

where we use the equation for a Keplerian ellipse,

$$r = \frac{a(1 - e^2)}{1 + e \cos \theta} \quad (7.2.12)$$

and regard the particle as moving directly ( $\dot{\theta} > 0$ ).

The Newtonian solution to the two-body gravitational problem gives an angular momentum (the law of areas) of

$$H = [G\mathcal{M}a(1 - e_0^2)]^{1/2} \quad (7.2.13)$$

for an unperturbed eccentricity  $e_0$ , and the harmonic law, relating period  $P$  to semi-major axis  $a$ ,

$$P = \frac{2\pi}{\omega_0} = \frac{2\pi a^{3/2}}{(G\mathcal{M})^{1/2}} \quad (7.2.14)$$

where  $\omega_0 = \langle \dot{\theta} \rangle$ . The perigee distance is  $r_p = a(1 - e)$  and the area of an ellipse is  $\pi a^2(1 - e^2)^{1/2}$ . Thus the difference in areas swept out by the radius vector in one revolution, with the perturbation and without it, can be

written in terms of the change in  $e$ , which in turn gives the change in  $r_p$ . Averaged over a period (7.2.11) shows that the perigee drops at the rate

$$\left\langle \frac{dr_p}{dt} \right\rangle = -\frac{3}{2} \frac{f_y}{\omega_0} (1 - e^2)^{1/2} \quad (7.2.15)$$

This result can be readily generalized to the case where perigee is at an angle  $\theta_0$  to the  $x$  axis by replacing  $f_y$  with  $f_y \cos \theta_0$ . Although this equation can give us a sense of the radiation-pressure perturbation, the orbits have to be integrated directly from (7.2.10) for actual situations. One such study indicates that H atoms with perigees at  $2R_E$  will decay within times  $\tau_{\text{rad}} \sim 5 \times 10^5$  sec, more or less independent of the apogee height. This lifetime is the same order as the orbital period for particles with apogees at  $15R_E$  (Problem 7.5).

With this  $\tau_{\text{rad}} = \tau_{\text{loss}}$  and ion densities of  $N' \sim 3 \times 10^3 \text{ cm}^{-3}$ , and with  $T_c = 10^{3.0} \text{ K}$ ,  $U = 4 \times 10^5 \text{ cm/sec}$ ,  $\lambda_c = 7.04$ , and  $Q = 5 \times 10^{-15} \text{ cm}^2$ , (7.2.3) yields  $\lambda_{cs} = 2.1$  or  $r_{cs}/r_c \approx 3.35$ . At this height  $\mu_0$  (for  $\psi = \lambda_{cs}$ ) = 0.84. This example is little more than illustrative, however. Observations indicate a strong day-night difference with satellites much more depleted at several  $R_E$  on the day side. Also the assumption above that the ion and neutral temperatures are equal is not correct, and their difference probably has profound effects on the exospheric structure (Section 7.2.4).

### 7.2.3 Departures from a Maxwellian Distribution near the Exobase

The collisionless theory invokes the Maxwellian velocity distribution at the exobase, except for particles moving downward with velocities exceeding the escape velocity  $v_{\text{esc}}$ . This assumption is equivalent to postulating partition functions (7.1.21) of

$$\zeta(\lambda_c) = \begin{cases} 1, & \psi < \lambda, \quad -1 < \mu < 1 \\ 1, & \psi > \lambda, \quad 0 < \mu < 1 \\ 0, & \psi > \lambda, \quad -1 < \mu < 0 \end{cases} \quad (7.2.16)$$

With the occurrence of collisions, such sharp demarcations are clearly unrealistic. At energies  $\psi \sim \lambda$ , the sudden truncation in  $\psi$  for  $\mu < 0$  must be smoothed, and at  $\mu \sim 0$ , deflecting collisions will smooth the angular distribution for  $\psi > \lambda$ . The question is, how much will such smoothing decrease the Jeans escape flux?

A particle with  $\psi > \lambda$  that is moving upward has a finite chance of having a collision in the exosphere that changes its direction or energy, or both, in

ways that prevent its escape. In a complete Maxwellian distribution, these collisions that alter the momentum coordinates from state  $p_j$ , say, to state  $p_i$  are exactly balanced by inverse collisions that alter momentum  $p_i$  into  $p_j$ . This *detailed balancing* occurs because the Maxwellian distribution is a description of matter in thermodynamic equilibrium, wherein all processes are balanced. In the planetary geometry, compensating collisions do not generally occur, and we have to ascertain what is the equilibrium situation.

The analytic approach to this problem is through the *Boltzmann equation*, the extension of Liouville's equation (7.1.9) to include effects of collisions. With the equation of motion (7.1.12) for a particle in a gravitational field, the steady-state extension of (7.1.10) is

$$\begin{aligned} v_r \frac{\partial f(r, p_i)}{\partial r} + \left( \frac{P_\chi^2}{Mr^3} - \frac{G\mathcal{M}M}{r^2} \right) \frac{\partial f(r, p_i)}{\partial p_r} \\ = \int [f^*(r, p_k)f(r, p_j) - f^*(r, p_k)f(r, p_i)]Qg d^3p_k \quad (7.2.17) \end{aligned}$$

Here  $Q$  is the collisional cross section,  $g$  is the relative scalar velocity of collision (which has the same magnitude before and after collision). We suppose that the escaping substance, with phase-space density  $f$ , is a minor constituent having most of its collisions with the major constituent of density  $f^*$ . The first term in the integral represents collisions that produce a particle with momentum  $p_i$ . For a given final momentum  $p_i$  and initial momentum  $p_k$ , the conservation of energy and momentum fix the other initial momentum  $p_j$  and the relative velocity  $g$ . The final term gives the loss rate of particles with momentum  $p_i$ .

It is possible to obtain a first-order solution to  $f(r, p_i)$  when the departures from a Maxwellian are not great, and we shall deal with a related problem in the next section. The only way in which an accurate solution has been obtained for the flux at the exobase is by the *Monte Carlo* computing technique. Monte Carlo is a kind of numerical experiment involving a large number of test particles whose paths are followed through the background gas (say, H atoms in a gas of O atoms) by the computer. At every collision a number of parameters—those describing the collision itself and the distance to the next collision—are specified by random numbers.

The “particles” may be initially released several mean free paths below the exobase to assure a reasonably complete Maxwellian, and followed until they either escape or return to the level of initial release. An alternative and more efficient method involves the consideration that, above the atmosphere,  $\zeta = 0$  for  $\psi \gtrsim \lambda_c$  and  $-1 < \mu < 0$ . Thus one can release these “virtual” or absent particles with a Maxwellian density  $f(\psi > \lambda_c, \mu < 0)$ , and see how they migrate through the gas and eventually escape. Since the real population

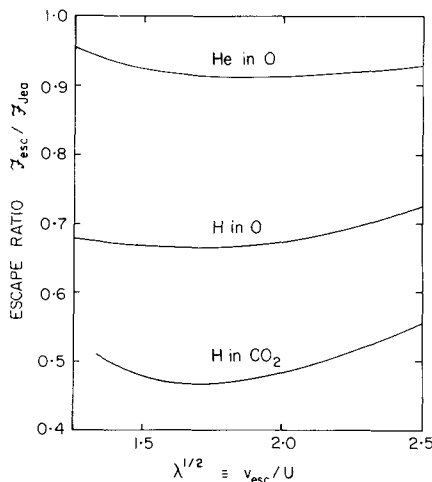


Fig. 7.5 Ratio of actual escape flux, obtained from Monte-Carlo analysis, to the flux computed from the Jeans formula (7.1.5). The correction factor is close to unity when the escaping gas has a mass close to that of the background gas and decreases to about 0.5 for a ratio of 1/44 (H in  $\text{CO}_2$ ). For H in the Earth's atmosphere ( $T_c \approx 10^3$  K),  $\lambda_c^{1/2} \approx 2.6$ ; for H in Mars' atmosphere ( $T_c \approx 350$  K),  $\lambda_c^{1/2} \approx 2.0$ . [Based on data of CHAMBERLAIN and SMITH (1971).]

is a Maxwellian less the virtual particles caused by the absent component from outer space, the number of virtual particles that escape gives the depletion of the real escape flux from the Jeans formula.

The loss of light particles from the top of an atmosphere also has an effect on the density distribution below the exobase. Instead of being in strict hydrostatic equilibrium, the upward flowing gas is in hydrodynamic diffusive equilibrium, and the density gradient is distorted from the barometric distribution accordingly.

Figure 7.5 shows the correction factor of  $F_{\text{esc}}/F_{\text{Jea}}$  for a variety of temperatures for H and He in a background atmosphere of O. If the background gas is  $\text{CO}_2$ , the departures from the Jeans fluxes are slightly greater, with  $F_{\text{esc}}/F_{\text{Jea}} \sim 0.5$ .

#### 7.2.4 Charge-Exchange Collisions in a Hot Plasmasphere

On a planet with a magnetic field such as Earth the direct escape of  $\text{H}^+$  is prevented, except possibly near the magnetic poles where field lines tend to be open. However, if the ions have a temperature  $T^* > T_c$ , then charge-exchange collisions provide a source of fast H atoms. In the collision, the electron moves from a slow H atom to the fast ion forming a fast H atom.

It appears that such a mechanism can account for a discrepancy between the upward flux of total H in all chemical forms in the mesosphere and the Jeans flux of H inferred from exospheric observations of  $T_c$  and the H concentration.

The basic Boltzmann equation is (7.2.17), where  $f^*$  is the ion density and  $f$  is the neutral density. To solve this equation we adopt a perturbation technique. Let

$$f(r, p_j) = f_0(r, p_j) + \Phi(r, p_j)f_0(r, p_j) \quad (7.2.18)$$

where  $f_0$  is the known solution to Liouville's equation. The Liouville equation says simply that the density in phase space  $f_0$  is constant along a dynamical trajectory. Hence, when the collision term is added, we integrate along a collisionless dynamical trajectory to find the gain and loss of density  $\Phi f_0$ .

For resonant charge exchange we can introduce a greatly simplifying approximation. The collision has a relatively large cross section at low velocities, which means that the collision normally occurs at large internuclear distances with little momentum transfer. Thus in (7.2.17) the only collision that produces an H atom with momentum  $p_i$  is one that involves an incident  $H^+$  with  $p_k = p_i$ . Similarly, the incident H atom can then take on any momentum, and we replace  $p_j$  with  $p_k$ .

The cross section is only mildly velocity dependent. Theoretical cross sections have been confirmed by experiments down to thermal energies ( $\sim 0.1$  eV). Within the thermal regime  $Q$  varies as  $g^{-0.2}$  and may be regarded as being effectively constant at  $Q_0 = 5 \times 10^{-15} \text{ cm}^2$ .

A final simplification to (7.2.17) is that the velocities of collision, insofar as escape is concerned, are mainly ones close to the local escape velocity  $v_{\text{esc}} = (2GM/r)^{1/2}$ . Little error should result from adopting  $g = v_{\text{esc}}$ .

With these approximations the Boltzmann equation appropriate to H—H<sup>+</sup> charge-transfer collisions is

$$\begin{aligned} & \frac{p_r}{M} \frac{\partial f(r, p_i)}{\partial r} + \left( \frac{P_\chi^2}{Mr^3} - \frac{GMM}{r^2} \right) \frac{\partial f(r, p_i)}{\partial p_r} \\ &= Q_0 v_{\text{esc}}(r) \int [f^*(r, p_i)f(r, p_k) - f^*(r, p_k)f(r, p_i)] d^3 p_k \end{aligned} \quad (7.2.19)$$

To evaluate the collision term, we assume that the H population entering a collision is given by the Liouville equation (or Boltzmann equation without collisions). Then on the right side,  $f(r, p_k)$  becomes

$$f_0(r, p_r, P_\chi) = \frac{N e^{-(\lambda_c - \lambda)} \exp(-p_r^2/2MkT_c) \exp(-P_\chi^2/2MkT_c r^2)}{(2\pi M k T_c)^{3/2}} \quad (7.2.20)$$

for all combinations of  $p_r$  and  $P_\chi$  allowed by the equations of motion.

We transform to the dimensionless notation of Section 7.1. For ions the temperature will be  $T^* = \alpha T_c$ . Since the electric attraction caused by the

tendency for ions and electrons to separate gravitationally reduces the net downward force by a factor of 2 [for a single-component plasma, see (5.1.25)] the potential for  $H^+$  is

$$\lambda^* = \frac{G\mathcal{M}M}{2\alpha k T_c r} = \frac{\lambda}{2\alpha} \quad (7.2.21)$$

With the ions following a Maxwellian distribution (out to some cut-off distance) the Boltzmann equation becomes

$$\begin{aligned} -\xi \frac{\partial f(\lambda, \xi, v)}{\partial \lambda} + \left( \frac{v}{\lambda} - \frac{1}{2} \right) \frac{\partial f(\lambda, \xi, v)}{\partial \xi} \\ = r_c \lambda_c Q_0 \lambda^{-3/2} N_c N_c^* \exp[-(\lambda_c - \lambda)(1 + 1/2\alpha)] (2\pi M k T_c)^{-3/2} \\ \times \left[ \frac{\zeta(\lambda)}{\alpha^{3/2}} \exp\left(-\frac{\xi^2 + v}{\alpha}\right) - \exp[-(\xi^2 + v)] \right] \end{aligned} \quad (7.2.22)$$

With (7.2.18) substituted on the left side, we have

$$-\xi \frac{\partial \Phi}{\partial \lambda} + \left( \frac{v}{\lambda} - \frac{1}{2} \right) \frac{\partial \Phi}{\partial \xi} = \frac{K e^{\lambda/2\alpha}}{\lambda^{3/2}} \left\{ \frac{\zeta(\lambda)}{\alpha^{3/2}} \exp\left[(\xi^2 + v)\left(\frac{\alpha - 1}{\alpha}\right)\right] - 1 \right\} \quad (7.2.23)$$

where the *collision coefficient* is

$$K = r_c \lambda_c Q_0 N_c^* e^{-\lambda_c/2\alpha} \quad (7.2.24)$$

In writing (7.2.23) we have used the fact that the coefficient of a term in  $\Phi$  on the left side vanishes identically through the Liouville equation, which governs  $f_0$ .

Equation (7.2.23) is to be integrated along dynamical trajectories for free ballistic flight. Along such a path,  $\Phi$  then represents (in units of  $f_0$ ) the accumulation (or loss) of particles due to collisions. The integration path is fixed by conservation of energy and angular momentum, or

$$\xi^2(\lambda) = (\xi_c^2 + v_c - \lambda_c) + \lambda - v \quad (7.2.25)$$

$$v/\lambda^2 = v_c/\lambda_c^2 \quad (7.2.26)$$

Thus (7.2.23) may be written as

$$\frac{d\Phi}{ds} = \frac{K e^{\lambda/2\alpha}}{\lambda^{3/2}} \left\{ \frac{\zeta(\lambda)}{\alpha^{3/2}} \exp\left[(\xi^2 + v)\left(\frac{\alpha - 1}{\alpha}\right)\right] - 1 \right\} \quad (7.2.27)$$

where the element of trajectory is

$$ds = -d\lambda/\xi \quad (7.2.28)$$

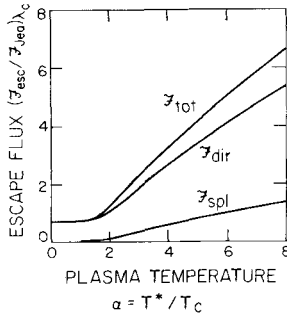


Fig. 7.6 Escape fluxes relative to Jeans escape, for H-H<sup>+</sup> charge exchange in Earth's atmosphere as a function of the plasma temperature. Curves are computed for  $\lambda_c = 7.5$  ( $T_c = 940^\circ\text{K}$ ), a plasmapause at  $\lambda = 5.0$ , and  $K = 0.175 \exp(-\lambda_c/2\alpha)$ . The curve for  $\mathcal{F}_{\text{dir}}$  is the enhancement of the direct, upward moving flux while  $\mathcal{F}_{\text{spl}}$  is the splash component, which has no Jeans analogue. [After CHAMBERLAIN (1977).]

and

$$d\xi/d\lambda = (1 - 2v_c\lambda/\lambda_c^2)/2\xi \quad (7.2.29)$$

Integrating (7.2.27) along such a trajectory in  $\lambda, \xi$  phase space for a specified  $v_c = \text{const}$  yields a contribution to the density and flux at any height. Trajectories corresponding to positive energy terminate at  $\lambda = 0$ ; those for negative energy turn over at  $\xi = 0$  and return to the exobase.

An interesting particle-reflection or “splash” phenomenon arises when fast neutral H atoms are produced within the exosphere. We noted in Section 7.2.2 that one technique for treating the departures from a Maxwellian is to examine “virtual” incoming particles from space. Roughly 30 percent of such entrants are reflected back out according to the Monte Carlo calculations. Hence if we here follow trajectories from  $\lambda = 0$  to the exobase for particles that exceed  $v_{\text{esc}}$  (i.e.,  $\psi > \lambda$ ), we obtain a “splash” component of escape, which arises from collisions that produce particles initially with a downward velocity.

Some sample results of calculations of this sort are shown in Fig. 7.6.

### 7.2.5 Lateral Flow

A typical value of the Earth's exospheric temperature for moderate solar activity is  $900^\circ\text{K}$ , with a diurnal variation of about  $300^\circ\text{K}$  peak-to-peak. According to (7.1.5), the thermal escape flux of H therefore varies by an order of magnitude, and one might expect the number density to vary inversely. Considerable study was therefore applied to the process of lateral flow in the exosphere, which can greatly reduce the magnitude of the effect. Inclusion of other escape processes, such as the charge exchange discussed above, greatly reduces the day-night asymmetry of the total flux; however, the lateral flow itself is still of interest, partly because it generates a significant asymmetry of

its own. This asymmetry, like thermal escape, depends on temperature differences and is particularly pronounced on Mercury, whose helium atmosphere can be considered as a thin exosphere in contact with the surface (cf. Section 7.1.6).

Thermospheric winds cause a related effect. Such winds blow toward the winter pole on Earth and from day to night on Venus. In the presence of diffusive separation, the height-integrated flux of each gas is proportional to its scale height. Thus, the light gases can be enriched downstream by an order of magnitude (44 for H in CO<sub>2</sub>); but this factor depends on the strength of the return flows, which may be at lower or higher altitudes. The mechanism has been called the *Johnson pump* or *wind-induced diffusion*. Its effects are observed on Earth as a winter helium bulge and on Venus as a nightside hydrogen and helium bulge; no other planet has been observed in enough detail to define such a phenomenon. A complete treatment should simultaneously include both modes of lateral flow, all the escape processes, and the upward flow from the lower atmosphere.

Exospheric flow due to a density gradient can be visualized as a kind of diffusion, or random walk, of particles in ballistic orbits between different spots on the exobase. The corresponding mean free path is the mean length of such a hop. For a parabolic orbit, it is well known that the range for a particle launched at a zenith angle  $\chi$  and speed  $U$  is

$$L = (U^2/g) \sin 2\chi = 2H \sin 2\chi \quad (7.2.30)$$

where  $U$  has been set equal to the most probable thermal speed (7.1.6) and  $H$  is the scale height. If all values of  $\chi$  are equally probable, the mean range is  $4H/\pi$ , or approximately  $H$ . The quantity of interest is the height-integrated flux, which is proportional to the integrated density  $NH$ , to the speed  $U$ , and to the range, where  $N$  is the exobase density of the light atom in question. Collecting all the factors of  $T$ , we obtain

$$\text{height-integrated flux} \propto NT^{5/2} \quad (7.2.31)$$

A correction to the integrated density (of ballistic particles only) can be made; it is somewhat smaller than the value for all particles given in (7.1.60), but cancels out of (7.2.31) unless there is a very large range of temperatures. Thus, if the diurnal variation of a light element is dominated by ballistic lateral flow, the number density tends to vary as  $T^{-5/2}$ .

A detailed study requires formulation of several integrals, which can be solved numerically or by asymptotic expansions. In Fig. 7.7, the point under consideration has colatitude  $\theta$  and longitude  $\phi$ ; a typical source point is given primed variables. The azimuth of a particle trajectory is  $\psi$  and, as above, its zenith angle at the exobase is  $\chi$ . The Earth rotates with angular velocity  $\Omega$ . The net flux at the point is given by the two Maxwell distributions  $f_u(v)$  and

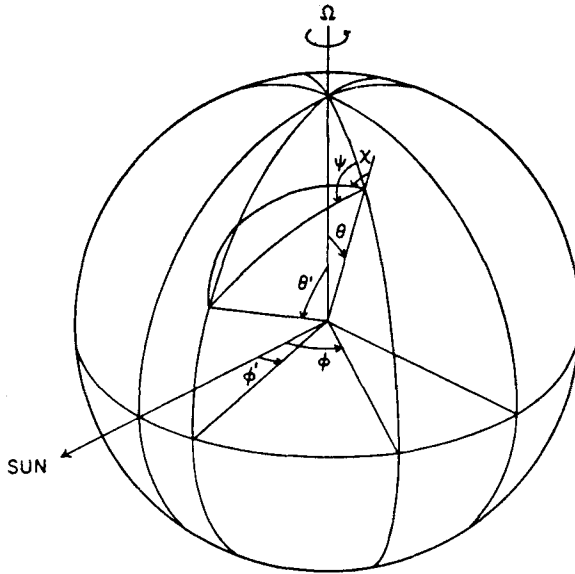


**Fig. 7.7** Coordinates for computation of lateral flow. [After PATTERTON (1970).]

$f_d(v)$  (upward and downward); the downward part is a function of the primed variables

$$\Phi(\theta, \phi) = \int_0^{2\pi} d\psi \int_0^{V_{esc}} v^3 dv \int_0^{\pi/2} \sin \chi \cos \chi [f_u(v) - f_d(v)] d\chi \quad (7.2.32)$$

$$f_u(v) = N(\theta, \phi) \left( \frac{m}{2\pi k T} \right)^{3/2} \times \exp \left\{ -\frac{m}{2kT} [v^2 + 2\Omega r v \sin \chi \sin \psi \sin \theta + \Omega^2 r^2 \sin^2 \theta] \right\} \quad (7.2.33)$$

and

$$f_d(v) = N(\theta', \phi') \left( \frac{m}{2\pi k T'} \right)^{3/2} \times \exp \left\{ -\frac{m}{2kT'} [v^2 - 2\Omega r v \sin \chi \sin \psi \sin \theta + \Omega^2 r^2 \sin^2 \theta'] \right\} \quad (7.2.34)$$

Solution of these equations requires some specified distribution of temperature and hydrogen density over the exobase, or instead of the latter the assumption of zero net ballistic flux, ZNBF. Numerical integrations for ZNBF of  $H$  on the Earth have been carried out by several authors, and the

ratio of maximum to minimum density has been found to be between 1.5 and 2.5, consistent with (7.2.31) but often formulated as linear with the ratio (temperature difference)/(mean temperature)<sup>2</sup>. The observed distribution is similar, implying that the asymmetries in the escape processes are fairly small, at least in comparison with the magnitude of the ballistic flux.

Another approach is to obtain a power series expansion, which can include the effects of a horizontal velocity field (planetary rotation and thermospheric winds) as well as the ballistic flux. Once this is done, the escape fluxes and the input from below can be added to obtain a fairly comprehensive solution.

Global winds are believed to be responsible for the terrestrial winter helium bulge and the light-element nightside bulge on Venus. Escape is probably negligible, and there is little or no smoothing by planetary rotation. The bulges mark the convergent point of the wind system, and the size and magnitude depend on the strength of any return flows, which include ballistic lateral flow and subsidence along with the heavier gases. The relative importance of these two paths is uncertain, but it is instructive to compare the ballistic flow with the incoming flux due to the winds. Ballistic flow can be thought of as diffusion, and the diffusion coefficient as the product of the thermal velocity  $U$  with the mean free path  $H$ . The height-integrated diffusion coefficient is therefore  $D \sim UH^2$ . If the radius and peak density of the bulge are  $L$  and  $N$ , the density gradient is  $-N/L$  and the diffusive flux is  $F_D \sim UH^2N/L$ . Like any diffusive process, this one is less effective for greater distances. The horizontal convective flux at velocity  $u$ , again height-integrated, is  $NHu$ . Equating these two expressions gives an estimate of the scale:

$$L \sim HU/u \quad (7.2.35)$$

The speed of the Venus wind is thought to approach the speed of sound, which is not much different from  $U$ ; thus, the diameter of the bulge could be as little as 2 hydrogen scale heights, only a few hundred kilometers. The observed size (Fig. 1.17) is perhaps 6000 km and must, therefore, be controlled by additional effects. One possibility is simply that the convergent point of the thermospheric flow wanders around by this much.

The tenuous helium atmosphere of Mercury was detected by Mariner 10 through resonance scattering of its 584 Å line. The surface density is much less than that of an exobase; the only significant collisions are with the surface, whose temperature varies between about 600 and 100°K. The ZNBF condition would therefore call for a density variation of  $6^{5/2}$ , or 88. Detailed models give an even larger ratio, about 200, much greater than is observed. The explanation is incomplete accommodation: an atom striking the surface does not fully equilibrate before leaving. A fast atom retains a fraction of its original velocity, and a slow one remains slower than an atom at the local surface temperature. The ultraviolet data are fitted with an accommodation

coefficient (ratio of energy lost or gained in a collision to incident energy) of less than 10%, which is consistent with the limited laboratory data available. These results are obtained by Monte-Carlo methods rather than analytic modeling.

## 7.3 Atmospheric Escape

### 7.3.1 Escape Mechanisms and the Limiting Flux

The loss of H and He from a planet may occur by several means. The Jeans “thermal evaporation” (as slightly modified in Section 7.2.2) gives a lower limit to the escape flux, but other processes may work as well. The importance of the other mechanisms—and how they might vary over geologic periods—has not been appreciated until recent years. Consequently, much of the earlier (and some of the current) literature on atmospheric evolution should be read with caution.

A summary of the known nonthermal mechanisms is given in Table 7.1. With the exception of 3(b), photodissociation, they all involve ions or electrons. Generally speaking, charged particles have difficulty escaping because they are trapped in magnetic fields; even a body that has no internal field is generally enveloped in fields of external origin. However, ions can sometimes escape directly, an option indicated as process 7. A charge exchange, process 1, can get rid of the charge while any excess kinetic energy is largely retained, as discussed in the previous section. In processes 2 and 4, chemical energy is converted into kinetic energy of the atoms as a molecule flies apart; process 3 is somewhat similar, but the energy comes from the incident electron or photon. Process 5 involves collisions with an incident fast particle, which can in principle be either an ion or a neutral atom. In practice, it is nearly always an ion, which is much easier to accelerate; such an acceleration is indicated as process 8. In a single collision, the accelerated atom tends to have a large forward component of velocity because of conservation of momentum; there is no well-established term for this process, but a frequently-used one is “knock-on.” “Sputtering” refers to a process that depends on multiple collisions, originally near the surface of a solid, in which a few particles of relatively low energy are ejected in the backward direction. The term arose in vacuum practice, where redistribution of atoms takes place in a glow discharge; the process is useful for the production of some types of thin films. It can be highly relevant in a planetary exosphere as well as the surface. Process 6 indicates the fate of an ion that is produced far enough from a planet to be in the solar wind, in which magnetic fields are sweeping by at hundreds of kilometers per second. The ion sees a motional electric field that

TABLE 7.1 *Nonthermal Processes Leading to Escape<sup>a</sup>*

| Process                       | Examples   | Product | Remarks   |
|-------------------------------|--|---------|---|
| 1. Charge exchange            | (a) $H + H^{+*} \rightarrow H^+ + H^*$<br>(b) $O + H^{+*} \rightarrow O^+ + H^*$ | N       |   |
| 2. Dissociative recombination | (a) $O_2^+ + e \rightarrow O^* + O^*$<br>(b) $OH^+ + c \rightarrow O + H^*$      | N       | Energy divided equally<br>H takes nearly all the energy               |
| 3. Impact dissociation        | (a) $N_2 + e^* \rightarrow N^* + N^*$  | N       | $e^*$ may be a photoelectron or an accelerated one                    |
| Photodissociation             | (b) $O_2 + h\nu \rightarrow O^* + O^*$   | N       |   |
| 4. Ion-Neutral reaction       | $O^+ + H_2 \rightarrow OH^+ + H^*$   | N       | Sputtering requires kilovolt or greater energies                      |
| 5. Sputtering or knock-on     | $Na + S^{+*} \rightarrow Na^* + S^{+*}$<br>$O^* + H \rightarrow O^* + H^*$       | N       | Knock-on requires much less   |
| 6. Solar-wind pickup          | $\{O + h\nu \rightarrow O^+ + e\}$<br>$\{O^+ \text{ picked up}$                  | I       | Also electron impact<br>Also magnetospheric wind for satellites       |
| 7. Ion escape                 | $H^{+*} \text{ escapes}$   | I       | Requires open magnetic-field lines                                    |
| 8. Electric fields            | $X^+ + eV \rightarrow X^{+*}$  | I       | Generates fast ions and electrons that participate in other processes |

<sup>a</sup> An asterisk represents excess kinetic energy. In the third column, N means neutral and I means ion.

quickly accelerates it to wind speed. Exactly analogous effects occur in a co-rotating magnetosphere and are very prominent in the inner Jovian system.

The fate of a fast particle depends on the conditions of its production. If it is aimed downward, it will probably be stopped in the atmosphere, or it may be reflected as mentioned at the end of the previous section, probably with reduced energy. If it is produced below the exobase, it will probably be stopped. If it does not have escape energy it will contribute to a nonthermal corona; such coronal particles may make several passes, losing energy each time they are reflected from the top of the atmosphere. Formation of a corona is favored for a massive planet such as Earth or Venus; escape is the more probable for Mars and the satellites of the outer solar system. Coronas are strongly favored for Jovian planets.

As a prelude to the following sections, Table 7.2 summarizes the significant processes thought to be operating on terrestrial bodies: the four inner planets

**TABLE 7.2** *Summary of Escape Mechanisms for the Terrestrial Bodies; Corona-Forming Processes (C) Are Also Shown*

| Planet               | Gas                                    | Mechanisms <sup>a</sup> |
|----------------------|--|-------------------------|
| Earth                | H                                      | 1, CE; J; 7, IE         |
|                      | D                                      | same                    |
|                      | He                                     | 7, IE                   |
|                      | O (C)                                  | 2a, DR                  |
| Venus                | H                                      | 2b, DR or 5b, KO        |
|                      | H (C)                                  | 1, CE; 4, I-N           |
|                      | O (C)                                  | 2a, DR                  |
| Mars                 | H                                      | J                       |
|                      | H <sub>2</sub>                         | J                       |
|                      | N                                      | 3a, ID; 2, DR           |
|                      | O                                      | 2a, DR                  |
| Moon                 | H                                      | J; 6, SWP               |
| Mercury              | He, Ar,---                             | 6, SWP                  |
| Io                   | H, C, N,---                            | J?                      |
|                      | SO <sub>2</sub> , S, O, O <sub>2</sub> | ?                       |
|                      | Na, K                                  | 5, Sp                   |
| E, G, C <sup>b</sup> | H, H <sub>2</sub>                      | J                       |
|                      | O                                      | 2a, DR                  |
|                      |  |                         |
| Titan                | H                                      | J                       |
|                      | H <sub>2</sub>                         | J; 2, DR                |
|                      | N                                      | 3a, ID                  |
| Pluto                | CH <sub>4</sub>                        | J                       |

<sup>a</sup> See Table 7.1. J stands for Jeans or thermal escape.

<sup>b</sup> E, G, C are the Galilean satellites Europa, Ganymede, and Callisto.

and the Moon, the Galilean satellites of Jupiter, Titan, and Pluto. Corona-forming processes are indicated by (C), and the mechanisms in the third column are keyed to Table 7.1.

All escape processes are at least somewhat mass dependent, with lighter atoms escaping more readily than heavier ones. The magnitude of the effect can be very large if say, helium, is being compared with xenon. Here, however, we shall focus on differential isotopic effects within the same element. In thermal escape, the exponential term involving  $\lambda$  in (7.1.5) is strongly mass dependent, especially if  $\lambda$  is large. However, a large  $\lambda$  means a small flux and a small ability to affect the composition of the remaining atmosphere. If fluxes are large they may become diffusion limited, as discussed below; there is still fractionation, but only by virtue of the mass dependence of the diffusion coefficient. The nonthermal processes tend to be mass independent, except for one important thing: they operate at high altitudes where the atmosphere is diffusively separated and therefore enriched in lighter masses. In most actual cases it is this diffusive separation that is mainly responsible for fractionation.

Whatever the cause, the fractionation can be represented by a *fractionation factor*  $1 + y$  as follows:

$$\begin{aligned} dN_1/dt &= -(1 + y)AN_1 \\ dN_2/dt &= -AN_2 \end{aligned} \quad (7.3.1a)$$

where  $N_1$  and  $N_2$  are the *inventories* of the two isotopes in question (*not* the local densities!) and  $A$  is a constant which will shortly cancel out. If isotope 1 is lighter than isotope 2, then  $y$  will be positive, but usually only by a few hundredths. These two equations can be combined into

$$\begin{aligned} dN_1/dN_2 &= (1 + y)N_1/N_2 \\ d \ln N_1 &= (1 + y) d \ln N_2 \end{aligned} \quad (7.3.1b)$$

The isotopic ratio  $R$  is defined as  $N_1/N_2$ ; thus

$$\begin{aligned} d \ln R &= d \ln N_1 - d \ln N_2 \\ &= y d \ln N_2 \\ &= [y/(1 + y)] d \ln N_1 \end{aligned} \quad (7.3.1c)$$

In integral form, with initial values  $R^0$ ,  $N_1^0$ , and  $N_2^0$ , these relations are

$$R/R^0 = (N_2/N_2^0)^y = (N_1/N_1^0)^{y/(1+y)} \quad (7.3.1d)$$

This class of process is often called *Rayleigh fractionation*. The implications are best seen through a numerical example, which is in the proper range for nitrogen on Mars (Section 7.3.4):  $y = 0.2$ ,  $R/R^0 = \frac{1}{2}$ ,  $N_2/N_2^0$  and  $N_1/N_1^0$

must be  $2^{-5}$  and  $2^{-6}$  respectively, or 0.031 and 0.016. Significant isotopic fractionation occurs only if a very small part of the original material is left. Much smaller values of  $y$  are common: 0.02 gives exponents of 50 and 51; and  $y = 0.0043$  for separation of the 235 and 238 isotopes of uranium as  $\text{UF}_6$ .

Care is needed in defining the inventories  $N_1$  and  $N_2$ . The situation is straightforward if all the gas is present in the atmosphere from the beginning. It is, however, easy to think of situations in which (7.3.1a) is not valid or must be qualified. A major part of the inventory may be in the crust but able to exchange with the atmosphere, or may be degassed episodically or continuously over the entire planetary history. In the limit of continuous degassing of a large reservoir, a steady state is set up with  $R = R^0/(1 + y)$ ; this case is approximated by the helium isotopes on the Earth.

There are several links in a full description of escape. For hydrogen, some volatile compound must be in the atmosphere; it must be converted to  $\text{H}_2$  or  $\text{H}$  at some level; they must be transported to the exobase; and finally they must escape. The escape flux may be controlled by any one, or more than one, of these steps. The first is necessarily involved; on Earth the major compounds are  $\text{H}_2\text{O}$  and  $\text{CH}_4$ , and the condensation processes that control the  $\text{H}_2\text{O}$  abundance in the stratosphere are very important. The other controlling process turns out to be the upward transport, as discussed next.

Regardless of the manner of escape from the high atmosphere, the rate of escape is likely to be fixed in the lower portions of the atmosphere. So long as some mechanism is at work to remove atoms from the top of the atmosphere, their rate of removal in a steady state must be equivalent to the rate of supply from below. There is a common misconception that, if the exospheric temperature were to increase, the Jeans escape flux would increase dramatically because of its exponential dependence on temperature. For this to occur the atmosphere would have to be nearly in hydrostatic, diffusive equilibrium capable of quickly replenishing lost atoms. In fact, the hydrogen flux is transported mainly by mixing in the *homosphere*—that portion of the atmosphere that is strongly mixed by vertical motions (frequently but not necessarily turbulent)—and mainly by molecular diffusion at higher levels. As this concept is important to atmospheric escape, we will develop it in detail.

The vertical flux from molecular diffusion and eddy diffusion (see Section 2.3) of a minor, light-weight constituent of density  $N_1$  is

$$\Phi_1 = -DN_1 \left( \frac{1}{N_1} \frac{\partial N_1}{\partial z} + \frac{M_1 g}{kT} + \frac{\alpha_T + 1}{T} \frac{\partial T}{\partial z} \right) - KN \frac{\partial(N_1/N)}{\partial z} \quad (7.3.2)$$

where  $N$  is the “background” density of the atmosphere. At low densities only the molecular or  $D$ -term is important; at high densities  $D$  is small

and the eddy-diffusion or  $K$ -term dominates. The height where  $D = K$  may be defined as the *homopause*.

We define the fractional abundance  $f_1 = N_1/N$  and the actual density scale height  $H^*$  by

$$\frac{1}{H^*} = -\frac{1}{N} \frac{\partial N}{\partial z} \quad (7.3.3a)$$

Then the reciprocal density scale height in equilibrium is (cf. Section 1.1, with the thermal-diffusion term incorporated)

$$\frac{1}{H_E^*} = \frac{Mg}{kT} + \frac{\alpha_T + 1}{T} \frac{\partial T}{\partial z} \quad (7.3.3b)$$

Thus we have

$$\Phi_1 = -b_1 f_1 \left( \frac{1}{H_{1E}^*} - \frac{1}{H_1^*} \right) - KN \frac{\partial f_1}{\partial z} \quad (7.3.4)$$

where we have extracted the density dependence of the diffusion coefficient by  $D = b_1/N$ . Here  $b_1$  is the *binary collision parameter*, which must be measured for each pair of colliding substances; for  $\text{H}_2$  in air,  $b_1 \sim 1.4 \times 10^{19} \text{ cm}^{-1} \text{ sec}^{-1}$  (Appendix VII).

The maximum rate of diffusion occurs for complete mixing,  $\partial f_1 / \partial z = 0$ , since  $\partial f_1 / \partial z$  cannot be negative when  $M_1 < M$ . When a light-weight constituent of mass  $M_1$  is completely mixed, then  $H_1^* = H^* \equiv H_E^*$ , and the diffusion is said to have its *limiting flow rate* of

$$\begin{aligned} \Phi_l &= b_1 f_1 \left( \frac{1}{H_E^*} - \frac{1}{H_{1E}^*} \right) \\ &\approx \frac{b_1 f_1}{H} \left( 1 - \frac{M_1}{M} \right) \approx \frac{b_1 f_1}{H} \end{aligned} \quad (7.3.5)$$

Then in general the flux from molecular and eddy diffusion combined is

$$\begin{aligned} \Phi_1 &= \Phi_l + b_1 f_1 \left( \frac{1}{H_1^*} - \frac{1}{H^*} \right) - KN \frac{\partial f_1}{\partial z} \\ &= \Phi_l - (D + K)N \frac{\partial f_1}{\partial z} \end{aligned} \quad (7.3.6)$$

When the minor constituent (say, H) occurs in many forms ( $\text{H}_2\text{O}, \text{CH}_4, \text{H}_2$ ), it is merely necessary to add the several equations of the form (7.3.5) or (7.3.6), weighted by the number of H atoms in a molecule to obtain the total H flux. Thus if  $N_1, f_1, H_1$ , and  $\Phi_1$  pertain to H atoms in all forms and

$N_a$  is the total density, the equations here are still valid, although  $D$  and  $b_1$  have to be regarded as weighted mean values for the various constituents.

To summarize, the maximum vertical transport occurs when a region is well mixed ( $\partial f_1 / \partial z = 0$ ) and conversely a well-mixed region fixes the limit on the rate of upward flow and hence the escape flux. In this case, no matter how hot the exosphere, the loss rate cannot be increased. The density  $N_1$  has its steepest possible gradient and cannot be buoyed upward any faster.

At the other extreme, when the loss at the exobase is small, that region effectively controls the loss. In the mixing region ( $K > D$ ), hydrogen may then not be well mixed because molecular diffusion will increase its scale height giving  $H_1^* > H^*$ . In the limit of no escape, there is a balance between mixing ( $H_1^* = H^*$ ) and hydrostatic, diffusive equilibrium ( $H_1^* = H_{1E}^*$ ). At the homopause this balancing yields  $H_1^* = 2H^*$  (Problem 7.7).

The developments above are restricted to a minor constituent but can readily be extended to a major one, as long as the background gas is stationary. The expression for the limiting flux (7.3.5) is valid if  $f_1$  is replaced by the mole fraction  $X_1 = N_1/(N_1 + N_2) = f_1/(1 + f_1)$ , but the other expressions retain a somewhat more complicated form.

With mechanisms at work in addition to Jeans escape, one cannot be certain the escape rate is known. If the escape rate at the top of the atmosphere (or in the case of helium the production rate in the lower atmosphere) is not known it is necessary to examine the upward flow by ascertaining mixing ratios at more than one height.

### 7.3.2 Earth's Loss of H and He

As an example, the Earth's atmosphere is well mixed to about 100 km. The mixing ratio of  $H_2$  at 100 km is about  $f_1 = 9 \times 10^{-6}$ , not greatly different from the mixing ratio for H in all forms (mainly  $H_2O$ ,  $CH_4$ , and  $H_2$ ) in the stratosphere. Then (7.3.5) gives the limiting flux for H atoms in all forms as about  $2 \times 10^8 \text{ cm}^2/\text{sec}$ .

Direct measurements of the exospheric temperature by satellite drag and the hydrogen abundance from the Lyman  $\alpha$  emission allow the Jeans escape to be computed. Not only is the Jeans escape too low by a factor of 3 to 5, but its variations with exospheric temperature  $T_c$  and density  $N_c(H)$  do not give the constant flux expected. Jeans escape has an exponential relationship with  $T_c$ , and hence an increase in  $T_c$  should be accompanied by a drastic drop in  $N_c(H)$ . The actual decrease in  $N_c(H)$  is not enough to compensate for the temperature excursion. However, charge-exchange loss varies as the integrated overhead density,  $\mathcal{N}_c(H) \approx N_c(H)H_c$ , and  $N_c$  requires much less adjustment to keep the loss rate constant.

Helium loss is limited by the loss mechanism at the top of the atmosphere. For the case of  ${}^4\text{He}$  produced by  $\alpha$ -particle decay of radioactive elements, the crust exhales  $2 \times 10^6 \text{ atom/cm}^2 \text{ sec}$ . But (7.3.5) predicts a flux of  $\Phi_l = 10^8 \text{ cm}^{-2} \text{ sec}^{-1}$  for a mixing ratio  $f = 5.24 \times 10^{-6}$ . Moreover, He approximates the scale height of the atmosphere over most of the homosphere, although it does increase slightly at higher altitudes. However, it is estimated that at the exobase  $N_c({}^4\text{He}) \approx 3 \times 10^6 \text{ cm}^{-3}$ , and at  $T_c = 10^3 \text{ }^\circ\text{K}$ ,  $\mathcal{F}_{\text{Jea}} \approx 2.4 \text{ atom/cm}^2 \text{ sec}$ . The discrepancy in fluxes is thus a factor of  $10^6$ .

In addition,  ${}^3\text{He}$ , thought to be produced by cosmic-ray bombardment in the atmosphere, also escapes too slowly by Jeans evaporation. If the temperature of the exobase were higher, a fit could be obtained for either  ${}^3\text{He}$  or  ${}^4\text{He}$ . For many years a satisfactory simultaneous solution to both isotopes was pursued as a means of ascertaining  $T_c$ . The problem is that no single  $T_c$  will fit the data, and therefore the accuracy of the  ${}^3\text{He}$  data was often challenged.

The problem will not go away and it is unsolved. It appears now that He escape, like the loss of H, must occur through some process other than Jeans thermal evaporation, although much of the He loss may occur in the form of  $\text{He}^+$  out the open magnetic field lines over the poles. Another possibility that holds promise is charge exchange between He or H and hot  $\text{He}^+$  in the plasmasphere to produce energetic He atoms (Section 7.2.3).

### 7.3.3 Venus' Dual Exosphere and Escape

Mariner 5 presented an anomalous situation for Venus. The preliminary analysis of the observations indicated that a single exospheric temperature could not explain the data but that two components with scale heights in the ratio 2:1 or 3:1 could mimic the observations. One possibility seemed to be a large deuterium abundance on Venus, which, though present, is not large enough.

Later analysis (Fig. 7.8) supports a two-temperature interpretation. If the low-temperature ( $T_c \approx 275 \text{ }^\circ\text{K}$ ) component represents the thermal corona, the hotter one ( $T_c \approx 1020 \text{ }^\circ\text{K}$ ) may arise from a different mechanism. In such a dual exosphere, the thermal escape from the cooler component is trivial in magnitude. On the other hand, spectroscopic evidence for  $\text{H}_2\text{O}$  and  $\text{HCl}$  near the cloud tops and photochemical theory for hydrogen compounds together indicate from (7.3.5) an escape flux about the same as for Earth,  $\mathcal{F}_{\text{esc}} \approx \Phi_l \gtrsim 10^8 \text{ cm}^{-2} \text{ sec}^{-1}$ .

Several of the escape mechanisms (cf. Table 7.1) could also account for the hot component. Dissociative recombination of molecular ions containing H atoms ( $\text{OH}^+$ ,  $\text{CO}_2\text{H}^+$ ) would produce high-velocity atoms. To provide the

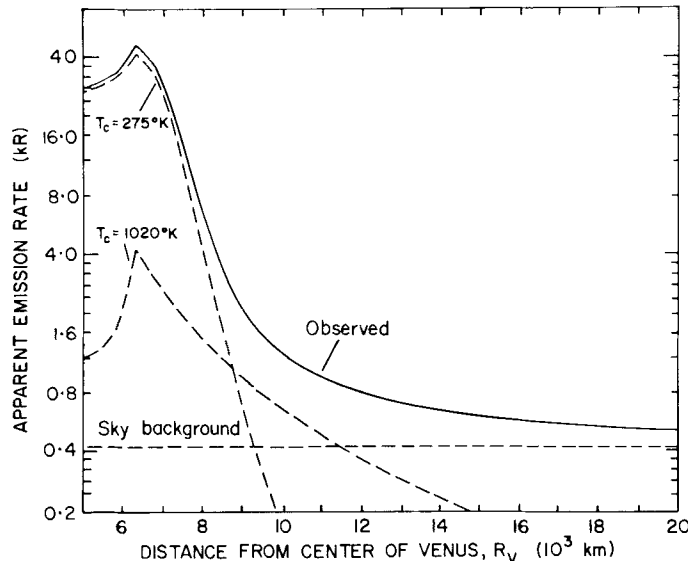


**Fig. 7.8** Dual exosphere of Venus. The Ly  $\alpha$  observations of the bright limb by Mariner 5 can be reproduced by a model that includes (in addition to the sky background) two exosphere components with  $T_c = 275^\circ\text{K}$ ,  $N_c = 2 \times 10^5 \text{ cm}^{-3}$  and  $T_c = 1020^\circ\text{K}$ ,  $N_c = 1.3 \times 10^3 \text{ cm}^{-3}$ . [After ANDERSON (1976).]

ions, these reactions require a larger H<sub>2</sub> abundance in the upper ionosphere than likely exists.

Charge exchange with hot protons, or oxygen (Section 7.2.4),



may be especially important at night, when the density of H in the lower exosphere is 100 times larger than on the day side; H is favored over D.

Finally, momentum transfer from fast O atoms to thermal H atoms, propelling the latter to escape speeds, may be important. The source of hot O atoms is dissociative recombination of O<sub>2</sub><sup>+</sup>, and although the resultant O atoms are not moving fast enough to escape (as they are on Mars—see below), H (but not D) atoms that ricochet off them can escape. The escape of O atoms is confined to those ionized by photon and electron collisions and subsequently swept away by the solar wind.

#### 7.3.4 Mars' Hydrogen and Oxygen Escape

As with so many other aeronomic matters involving the two CO<sub>2</sub> atmospheres, the exosphere of Mars seemed (before the Viking landers) much

easier to comprehend than did its counterpart on Venus. According to Mariner data the exobase has  $T_c \approx 350^\circ\text{K}$  and there is no complication of a second exosphere. Quite possibly the bottleneck for H (and  $\text{H}_2$ ) escape is the exobase itself. There we find  $\lambda_c \approx 4.2$ , and such a small value indicates rapid thermal evaporation. With  $N_c(\text{H}) = 3 \times 10^4 \text{ atom/cm}^3$ , we have  $\mathcal{F}_{\text{Jea}}(\text{H}) \approx 1.5 \times 10^8 \text{ atom/cm}^2 \text{ sec}$ , comparable to Earth's loss rate. Nevertheless, if the limiting diffusive flow is estimated with (7.3.5), we obtain a similar value (as we would expect for a diffusion bottleneck), so it is really not clear where the limitation occurs.

In any case, if one supposes that escape varies as the density of hydrogen at the exobase, an amusing hypothesis can be developed, namely, that the thermal evaporation of hydrogen is twice the nonthermal loss of oxygen:

$$\mathcal{F}_{\text{Jea}}(\text{H}) + 2\mathcal{F}_{\text{Jea}}(\text{H}_2) = 2\mathcal{F}(\text{O}) \quad (7.3.8)$$

The nonthermal loss of O is presumed to occur by



with the O atoms having escape velocities. If the reaction rate of (7.3.9) were to change, the total abundance of  $\text{O}_2$  would, after a time to achieve equilibrium, change in the opposite sense by about the same factor since the source of  $\text{O}_2$  should remain constant. This source is



and it remains constant if  $\text{H}_2\text{O}$  (the source of OH) and  $\text{CO}_2$  (the main source of O) remain constant.

Suppose the rate of (7.3.9) increases. The decreased  $\text{O}_2$  in the lower atmosphere is accompanied by an  $\text{O}_3$  decrease, thence an  $\text{O}({}^1\text{D})$  decrease and an increase in the lifetime of  $\text{H}_2$  against destruction by  $\text{O}({}^1\text{D})$ . Other reactions increase H, effectively taking it out of storage in  $\text{HO}_2$  and OH. The overall effect is to increase the free H and  $\text{H}_2$  throughout the atmosphere leading to an increase in escape flux of  $\text{H} + \text{H}_2$  and Eq. (7.3.8).

The hypothesis is especially fascinating because it implies that the nonthermal escape of O controls the escape of H. The result is that  $\text{H}_2\text{O}$  escapes from Mars!

The nonthermal escape of O would have a selective effect in escaping  $^{16}\text{O}$  compared with  $^{18}\text{O}$  (as would, of course, thermal evaporation). In view of the likelihood that large amounts of O have escaped over geologic periods, interesting questions arise regarding isotopic compositions of oxygen-containing materials on Mars, since the isotopic ratio would be related to their period of formation.

Both Viking landers obtained density distributions during descent that imply a completely unexpected temperature structure in the thermosphere.

The profiles oscillate as much as 40°K over vertical distances of the order of 20 km, perhaps indicating a wave motion originating in the lower atmosphere. The average temperature between 120 and 200 km is under 200°K (compare Fig. 1.22).

### 7.3.5 Escape from Titan and Io

The major processes operating on these two satellites could hardly be more different: escape of H from Titan is almost purely thermal, while on Io the major processes seem to involve bombardment by ions from the magnetosphere and torus.

As discussed in Section 6.4.3, photochemistry on Titan converts methane to ethane, acetylene, heavier hydrocarbons, and free hydrogen. Destruction of two methane molecules releases one hydrogen molecule if ethane is the product; production of acetylene and further evolution into heavier molecules releases somewhat more hydrogen. The production rate of  $\text{H}_2$ ,  $7.2 \times 10^9 \text{ cm}^{-2} \text{ sec}^{-1}$ , is thus about half the destruction rate of  $\text{CH}_4$ ,  $1.5 \times 10^{10} \text{ cm}^{-2} \text{ sec}^{-1}$ . (These values are global averages, referred to the area of Titan's surface.) There is an additional production and escape of  $5.5 \times 10^9 \text{ H atoms cm}^{-2} \text{ sec}^{-1}$ , mostly well above the homopause where there is no influence on the flux of  $\text{H}_2$ .

The exobase height and temperature are well established by the Voyager ultraviolet stellar occultation as 1600 km and 186°K (Section 1.9.3). At this height the gravitational acceleration is  $51 \text{ cm sec}^{-2}$  and the escape parameter  $\lambda$  for  $\text{H}_2$  is 2.75. With such a small value there can be no doubt that the escape rate is diffusion limited, no matter what the mix of atoms and molecules; in turn, the mixing ratio of hydrogen should be controlled by the balance of production and escape. If the homopause is at 740 km as indicated by Fig. 6.19, the  $\text{H}_2$  flux referred to that level is  $4 \times 10^9 \text{ cm}^{-2} \text{ sec}^{-1}$ . Substitution into (7.3.5), the limiting-flux relation, predicts an  $\text{H}_2$  mixing ratio of 0.2%, just the value observed by Voyager. The indirect photolysis of methane illustrated in (6.4.15) must be included to obtain these numbers, which would be considerably smaller in its absence.

The escaped H and  $\text{H}_2$  go into the Titan torus; the H flux quoted above is of the right order to account for the observed density. The lifetimes of both H and  $\text{H}_2$  are probably determined by electron impact and should be similar; in the absence of other sources, the torus should therefore contain comparable amounts of each. Dissociation of  $\text{H}_2$  however may be an additional source of atoms, and Saturn itself is another possible source. In both cases the velocity distributions are likely to be quite different from that exhibited by the thermal Titan source. Ionic recombination in Titan's ionosphere is expected to be

another source of fast H atoms. There are several unresolved questions here, and further experimental input is unlikely for a long time because detection of the small quantities of H<sub>2</sub> is not currently possible.

As indicated in Table 7.2, impact dissociation of N<sub>2</sub> produces a significant flux of fast N atoms, estimated as  $3.6 \times 10^8 \text{ cm}^{-2} \text{ sec}^{-2}$  in global mean. The fast electrons are assumed to be of magnetospheric origin, and their flux is estimated from the intensity of the ultraviolet airglow. Many of the N atoms are fast enough (8 or more km/sec) to escape the Saturn system, but some will join the torus if their direction is favorable or if they are slowed down in leaving the atmosphere. If the estimated loss rate from Titan is correct and representative of past times, about 10% of the atmosphere could have been lost. Even though the loss is undoubtedly somewhat isotopically selective, the fraction of the total gas lost is too small to have any significant effect on the isotopic composition of the remaining gas (Section 7.3.1).

A possible atmospheric structure for Io is shown in Fig. 6.21; it is intended to represent conditions on the day side, but far from the subsolar point. This model postulates the large escape fluxes believed necessary to populate the plasma torus. The mechanism or mechanisms at work must satisfy the following requirements:

1. At least part, perhaps all, of the escaping gas is neutral, not ionized.
2. Fluxes of O and S must be approximately in a 2:1 ratio.
3. These fluxes must supply at least  $10^{28}$  atoms/sec to the torus, or  $4 \times 10^{10} \text{ atoms cm}^{-2} \text{ sec}^{-1}$  in global mean.
4. Several percent of the flux must be sodium, and at least some of the sodium must have velocities of several kilometers per second, ranging up to tens of kilometers per second.

In all probability, some of the oxygen and sulfur atoms are fast also, but there is no evidence either way.

At the high exospheric temperature, approaching 1000°K, thermal escape of O could be important, but it cannot apply to S or SO<sub>2</sub> and cannot supply fast atoms. The best candidate seems to be one or both of the processes stemming from ion bombardment; sputtering or knock-on (Table 7.1, process 5). Fast magnetospheric ions should be able to penetrate a thin atmosphere and sputter sodium atoms and SO<sub>2</sub> molecules from the surface; SO<sub>2</sub> should also be raised by sublimation, especially on the day side. The actual ejection from Io's gravity field is probably due to torus ions, which are incident at a relative velocity of 55 km/sec. The energies are 280 and 560 eV for oxygen and sulfur, and the total flux is about  $7 \times 10^9 \text{ cm}^{-2} \text{ sec}^{-1}$ . Sputtering yields (atoms ejected per incident ion) are 20, 10, and 2.5, respectively, for ejection of S, O, and SO<sub>2</sub>. Multiplication by  $1.3 \times 10^{17} \text{ cm}^2$ , the projected area of a hemisphere at the exobase, gives an escape rate of

$1.6 \times 10^{28}$  atoms/sec, in the range of the values required to populate the torus.

A remaining problem is the composition of the ejected gas. In Fig. 6.21, the exobase is close to 200 km, and the approximate composition (in terms of column abundance) is 20% SO<sub>2</sub>, 56% O, 13% S, and 11% O<sub>2</sub>. If the gases are swept away in these proportions, the ratio of S to O is 0.28; if only the atoms contribute, it is 0.23. Taking account of the difference in sputtering yields reduces the latter number to 0.12. Analyses of the torus require 0.5 or even larger (point 2 above). Although the discrepancy may be within the combined uncertainties, it is disturbing. A possible resolution, discussed in the next section, is that the upward fluxes in the atmosphere are so large as to generate significant drag forces between the various components and greatly reduce the degree of diffusive separation.

Atoms ejected by sputtering tend to have energies of a few electron volts or less. Individual collisions can occur in the exosphere in a ring normal to the impact direction and can give velocities up to, or even exceeding, the incident velocity. The height of this ring is of the order of an O scale height, 360 km, and its inner diameter is that of the exobase, for an area of  $4.6 \times 10^{16} \text{ cm}^2$ . A rough but simple approximation is that each ion traversing this ring ejects one atom; the total rate is thus  $3 \times 10^{26} \text{ sec}^{-1}$ , much smaller than the sputtering rate but potentially an important source of faster atoms.

### 7.3.6 Atmospheric Blowoff

An atmosphere is said to be in the blowoff state when an escaping light gas is able to carry heavier constituents along with it, even though such gases could not escape according to the Jeans formula. Although the concept seems intuitively reasonable, a quantitative expression has proved somewhat elusive. For the case of a single gas, the analogy of the solar wind is helpful. If the inner part of the flow is isothermal, the flow goes through a critical point at  $\lambda = 2$  where the Mach number is unity: the flow velocity is equal to the sound speed. At greater distances the flow becomes moderately supersonic. However, the flux is easily evaluated at the  $\lambda = 2$  point, which we shall call the sonic point to avoid confusion with the older name (critical level) of the exobase. For a number density  $N_s$  and a sound speed  $C_s$ , the flux is  $N_s C_s$ . If the sonic level is coincident with the exobase, the Jeans equation (7.1.5) with  $\lambda = 2$  gives a flux  $(3N_s U / 2\sqrt{\pi})e^{-2}$ . Since  $U$  and  $C_s$  are almost the same, these two fluxes differ only slightly by the factor  $e^{-2}$ . It is reasonable to define this situation as the borderline between kinetic-theory thermal escape (sonic level above the exobase) and hydrodynamic blowoff (sonic level below the exobase).

If a light gas is moving at speeds approaching sonic, large drag forces arise with any other gases. The form of the diffusion equation discussed in Sections 2.3.1 and 7.3.1 assumes that all gases are at rest or moving very slowly compared with molecular (or sound) speeds. However, if two gases have vertical fluxes  $F_1, F_2$ , their diffusion equations are

$$\begin{aligned}\frac{dN_1}{dz} &= -\frac{M_1 g}{kT} N_1 + \frac{1}{b}(N_1 F_2 - N_2 F_1) \\ \frac{dN_2}{dz} &= -\frac{M_2 g}{kT} N_2 + \frac{1}{b}(N_2 F_1 - N_1 F_2)\end{aligned}\quad (7.3.11)$$

where we have omitted the terms in  $dT/dz$  and  $K$ . Setting  $F_2$  to zero and ignoring the  $F_1$  term in the second equation recovers the cases previously discussed. If the two equations (7.3.11) are added, the result is the hydrostatic equation. The definition of mole fraction,  $X_2 = N_2/(N_1 + N_2) = N_2/N$ , can be logarithmically differentiated and the terms in  $dN_2/dz, dN/dz$  eliminated. A little algebra gives an expression for the flux of the heavier gas:

$$F_2 = \frac{X_2}{X_1} F_1 \left[ 1 - \frac{bgX_1}{kTF_1} (M_2 - M_1) \right] = \frac{X_2}{X_1} F_1 \left( \frac{M_c - M_1}{M_c - M_2} \right) \quad (7.3.12)$$

where the *crossover mass*  $M_c$  is

$$M_c = M_1 + \frac{kTF_1}{bgX_1} \quad (7.3.13)$$

Equation (7.3.12) is valid only if it gives a positive result, or equivalently, for  $M_2 < M_c$ . For greater masses the flux is zero, although the scale height is increased over the diffusive-equilibrium value. Comparison with (7.3.5) shows that  $M_c = 2M_1$  when  $F_1$  is equal to the limiting flux; much larger values are necessary if  $M_c$  is to be in the tens or hundreds of a.m.u. Up to this mass, the flux has a strong mass dependence, and large elemental and isotopic fractionations can be imagined.

Maintenance of a blowoff state requires a sufficient energy input to the proper parts of the atmosphere. Exospheres are usually taken as isothermal because the long mean free path implies rapid heat transfer. However, rapid escape carries away heat so fast that this assumption is no longer valid; the heat balance must be solved along with the transport equations, and the temperature profile found as part of the solution. Solar energy inputs in the contemporary solar system are not large enough to maintain any atmosphere in a blowoff state, but the primitive atmosphere of Venus, and perhaps that of the Earth, may have experienced blowoff. Another possible energy source is the heat of accretion, during perhaps the first  $10^8$  years of a planet's existence. There is a suspicion that Io's atmosphere is being blown off or, more

properly, stripped off at rates similar to those characteristic of blowoff by impact of torus ions. Some of these examples are now discussed.

The great enhancement of deuterium on Venus encourages the idea that an original endowment roughly equivalent to an Earth ocean may have been lost, and the latter parts of this process, when most of the isotopic fractionation would have taken place, are described in Section 7.3.3. The likely cause of a still earlier blowoff situation would be an atmosphere very rich in water vapor, leading to an upper atmosphere rich in hydrogen, both molecular and atomic. It appears that such an atmosphere could undergo hydrodynamic escape even with current solar fluxes. Computations of this complex coupled system have not yet found the expected supersonic flow far from the planet, probably because of numerical difficulties. However, the subsonic solutions that have been obtained (Fig. 7.9) should give nearly as great a flux; the peak velocity, reached at about 50,000 km altitude, is not far below the sound speed. The great extent of the atmosphere is noteworthy; the density profile (Fig. 7.10) approaches inverse-square behavior, illustrating that gravity has essentially lost control of the outer atmosphere. Temperatures, shown in Fig. 7.11, tend to peak in the 2000–3000 km range; the presence of the peak indicates that this is where most of the heat is being deposited, at a density of  $10^{-16}$  g/cm<sup>3</sup> or  $10^8$  atoms/cm<sup>3</sup>. The heat source is, therefore, ionizing radiation. The energy limitation in this kind of blowoff is determined by this tiny, but strongly absorbed, fraction of the solar flux. The case of a molten planet, which has not been studied in as much detail, is totally different.

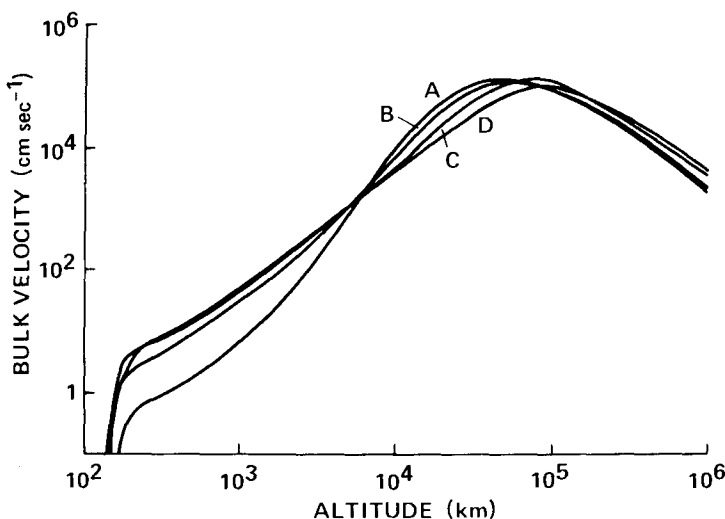


**Fig. 7.9** Velocity profiles of atmospheric blowoff in a model of primitive Venus. [After KASTING and POLLACK (1983).]

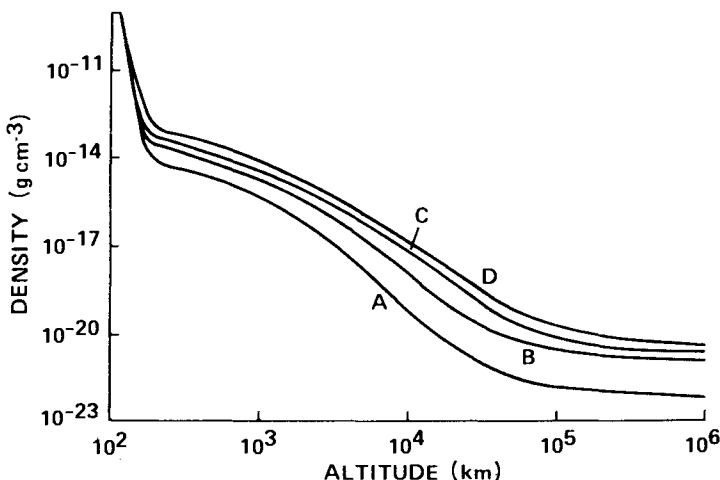


**Fig. 7.10** Density profiles corresponding to Fig. 7.9; the huge extent of the atmosphere is noteworthy. [After KASTING and POLLACK (1983).]

Loss of hydrogen from a primitive Earth by heating of the upper atmosphere is also possible; it depends mainly on the behavior of the cold trap near the tropopause. If the primitive atmosphere lacked a trap as efficient as we have today, much larger fluxes could have existed. Since we do not fully understand this aspect of the present atmosphere, extrapolation to the past is not justified.

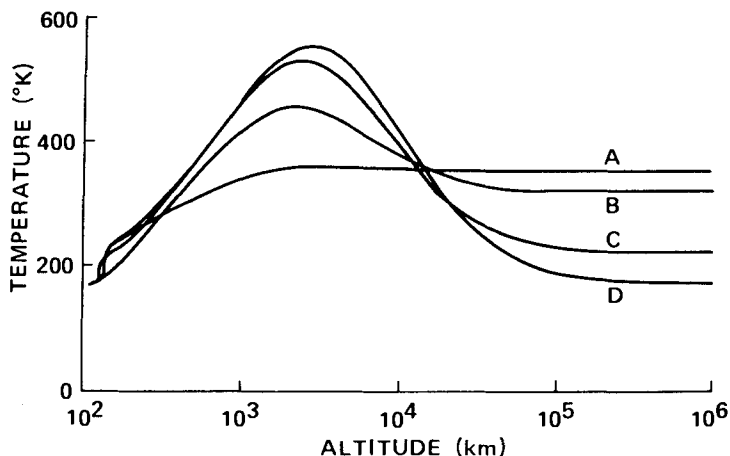


**Fig. 7.11** Temperature profiles corresponding to Fig. 7.9, illustrating the strong cooling at high altitudes that limits the flux. [After KASTING and POLLACK (1983).]

Pluto has a methane atmosphere that would blow off if it had an isothermal exosphere at the Gold-Humphreys skin temperature  $T_0$  [Fig. 1.4 and Eq. (1.2.30)]. The limited ionospheric heating rate again comes to the rescue; the loss rate that it could sustain limits the escape to a tolerable value of  $4 \times 10^{10} \text{ cm}^{-2} \text{ sec}^{-1}$  (referred to the surface). As seems to be typical, the atmosphere is highly extended with the heating level at a radial distance of 3.5 Pluto radii. If it is assumed that 20 times more energy is deposited by some kind of charged particles, the flux is six times greater, and the heating level drops to 2 Pluto radii.

Escape rates from Io are uncertain, but the available numbers indicate that the limiting fluxes may be approached or exceeded. Io's atmosphere has four main components (Fig. 6.21), while (7.3.5) and (7.3.6) are appropriate for two. However, it should still be true that the mutual drag effects are important in tending to equalize the scale heights of the various gases. Escape due to ion bombardment should be effective over the area ( $2.1 \times 10^{17} \text{ cm}^2$ ) of the trailing hemisphere, on which the co-rotating plasma impinges. If an appropriate mole fraction  $X$  for O is 0.15, the limiting flux (7.3.5) is  $8 \times 10^{10} \text{ cm}^{-2} \text{ sec}^{-1}$ , and the escape rate for a hemisphere is  $1.7 \times 10^{28} \text{ sec}^{-1}$ . Supply rates to the torus are estimated in several ways, which give values in the range  $(0.5\text{--}4) \times 10^{28} \text{ sec}^{-1}$ . None of these values includes the faster atoms that quickly leave the torus region. It thus appears probable that blowoff effects are significant to Io's atmospheric structure, but more detailed studies are needed for a firmer conclusion.

## 7.4 Atmospheric Evolution and Climate

### 7.4.1 Development of Atmospheres of the Terrestrial Planets

The principal feature of the atmospheres of the terrestrial planets Venus, Earth, and Mars is that they are composed mainly of elements in the *oxygen group*—the second row of the periodic table of the elements—which account for only about 0.1 percent of the atoms of the sun or the universe. Jupiter and the other major planets, on the other hand, are mainly composed of H and He, with traces of C, N, and O that show up spectroscopically as CH<sub>4</sub> (methane), NH<sub>3</sub> (ammonia), and H<sub>2</sub>O. Whether the H/He ratio coincides with the solar abundance is still uncertain (see Section 6.3.1), but the evidence does not rule out that possibility.

The Earth has retained water in its atmosphere because it has retained its oceans. Were the oceans to evaporate, H<sub>2</sub>O would become the most abundant constituent (about 300 times the present atmosphere), resembling the situation that may one day have existed on Venus (see below).

The atmospheres of the terrestrial planets must be secondary atmospheres. The primary atmospheres that may have existed after the time of planetary formation have long since disappeared; the present abundance ratios are very different from those of the sun. The composition of the crust-ocean-atmosphere system can be accounted for only by incorporating into the system the steady volcanic flow of volatiles (H, C, N, O, S, Cl) upward from the mantle. Except for the volatiles, the erosion of elements in crustal rocks (Si, Al, Fe, Ca) leads to a reasonably accurate composition of the oceans, sedimentary rocks, and the atmosphere.

The abundance of O<sub>2</sub> in the Earth's atmosphere is particularly remarkable, since the crust is suboxidized—quite the opposite of Mars. Photosynthesis of green plants is probably responsible in part for today's high abundance, but past photodissociation of H<sub>2</sub>O with subsequent escape of the H may also have been a factor.

The atmosphere of Saturn's major satellite Titan holds special interest since Titan is comparable to the Earth's moon in size and mass, but it was likely formed earlier from the same region of the protosun that formed the major planets. The major gases to be accounted for are CH<sub>4</sub> and N<sub>2</sub>, since all the other observed compounds can be derived from them aeronomically. Both have high enough condensation temperatures to exist as gases in the present atmosphere; if similar temperatures were present in the nebula from which Titan condensed, their incorporation in their present form is unlikely. Methane readily enters into clathrates (cage compounds) with H<sub>2</sub>O ice with a low enough vapor pressure to make this a reasonable vehicle for accretion. Subsequent slow degassing could explain the continuous supply needed to maintain the atmospheric abundance. Nitrogen also forms a clathrate, but tends to be displaced by methane. A more attractive source is NH<sub>3</sub>, which is readily photolyzed with production of N<sub>2</sub> and escape of H<sub>2</sub>. This process could not occur at present; any ammonia vapor is trapped near the surface by the low temperature, and little or no solar ultraviolet penetrates that deep. More probably the photolysis occurred early in Titan's history when the atmospheric conditions could have been sufficiently different. A model of these processes has yielded enough nitrogen to supply the present atmosphere, as well as the amount thought to be dissolved in the ethane ocean.

Also, Mercury has an anomalous atmosphere that may indicate the rate of exhalation of elements from its crust and capture from the solar wind. Escape from Mercury should be rather rapid because of the small surface gravity and high temperatures on the sunlit side. However, there are difficulties in estimating the distribution of velocities of atoms that are thermally ejected from Mercury's surface.

The low abundance of water on Mars is unknown, although probably low; it resides in the crust and polar caps in the forms of ice and water of

hydration. While O may also be escaping by the nonthermal mechanism (7.3.9), isotope analyses by Viking on Mars indicate, as do Venus CO<sub>2</sub> spectra, that the <sup>18</sup>O/<sup>16</sup>O ratio is close to that on Earth. This ratio may place important constraints on the evolutionary history of Martian oxygen and other volatiles. The lack of enrichment of <sup>18</sup>O may imply, for example, interchange of atmospheric and subsurface oxygen on a time scale of 10<sup>9</sup> years. Geochemical analyses of measurements of isotopic ratios (<sup>40</sup>Ar/<sup>36</sup>Ar) and abundances of heavy gases indicate that Mars has not outgassed as completely as Earth. In addition, it seems that Mars, like the moon, may have had a small initial endowment of volatile elements, but just why is not clear.

Although liquid water cannot exist for long on Mars' surface today, the altitude slope of branched channels indicates that ancient water flowed from a set of tributaries toward a main trunk (as distinct from volcanic flow from a main stem downward and outward into a family of branches). The early atmosphere must have been much more massive than the remnant left today. In the past Mars' atmosphere probably had a surface pressure of the order of 1 atm of CO<sub>2</sub>, and a greenhouse including H<sub>2</sub>O that would have produced a global mean surface temperature around 295°K.

Venus is currently poor in H<sub>2</sub>O, but its D/H ratio of 1.6 × 10<sup>-2</sup>, an enhancement of 100 times over the Earth's value, means that Venus has outgassed (and subsequently lost through escape) a large amount of H<sub>2</sub>O—perhaps as much as the Earth outgassed.

Compared with the massive atmosphere of Venus, that of Earth seems anomalously thin and poor in CO<sub>2</sub>. The resolution of this dilemma probably lies in the large amounts of liquid water on Earth, through which CO<sub>2</sub> has formed carbonates and thence sedimentary rocks. But why Venus should have lost so much water (compared with Earth) in its early stages is an interesting problem that has led to the concept of a *runaway greenhouse effect*, a positive feedback between increasing temperature and increasing opacity.

It is apparent that, so long as there is water on the surface, the upper part of a convecting atmosphere must be saturated. Convection acting alone would tend to supersaturate the entire troposphere. The only process that prevents the atmosphere from being saturated at all heights is the descent of relatively dry air. At the tropopause, where the temperature becomes essentially constant or reverses, there is negligible descent of air from above and the air arriving there from below will be saturated.

The crucial feature of the runaway greenhouse is that, above a certain threshold of solar flux (when the infrared-active substance is condensable), an atmosphere cannot exist in radiative equilibrium. The energy discrepancy is in the sense that more solar energy is absorbed than emitted, and hence the condensed vapor (i.e., the oceans) will evaporate. The atmosphere will then

heat up until the vapor is no longer condensable and the atmosphere achieves radiative equilibrium. With the water totally mixed in the atmosphere, it is photodissociated and the H can flow upward and escape.

We will examine the basic feature of this scenario—namely, the departure from radiative equilibrium—with the gray-atmosphere two-stream approximation of Section 1.2.3. From (1.2.43) we have

$$B(\tau) = B(0)(1 + \frac{3}{2}\tau) = \frac{\sigma}{\pi} T^4(\tau) \quad (7.4.1)$$

where  $B(0)$  is the Planckian radiation characteristic of the skin temperature  $T_0 \equiv T(\tau = 0)$  (cf. Fig. 1.4). In radiative equilibrium the atmosphere radiates the absorbed solar flux, which is

$$B(\tau = \frac{2}{3}) = 2B(0) \quad (7.4.2)$$

For a mass absorption coefficient  $\kappa$  (independent of frequency in the gray approximation), the optical thickness is

$$\tau(z) = \int_z^\infty \kappa_1 \rho_1 dz = \frac{M_1 \kappa_1}{Mg} p_1(z) \quad (7.4.3)$$

where subscripts 1 refer to the absorbing-radiating substance and where we have used hydrostatic equilibrium (1.1.1).

If liquid exists in large quantities on the surface, then the partial pressure of the vapor at the top of the convective zone  $z_c$  will be approximately the saturation vapor pressure, or  $p_1(z_c) \approx p_s(T_c)$ . Thus the condition imposed by saturation is

$$p_s(T_c) = \frac{Mg}{M_1 \kappa_1} \tau_c \equiv p_0 \tau_c \quad (7.4.4)$$

which defines  $p_0$ . For the Earth we may take  $\kappa_1 = 0.1 \text{ cm}^2/\text{gm}$  (appropriate for the 8–20  $\mu\text{m}$  window),  $M_1 = 18$ ,  $M = 29$ ,  $g = 980 \text{ cm/sec}^2$ , obtaining  $p_0 \approx 1.5 \times 10^{-2} \text{ atm}$ . Figure 7.12 shows from (7.4.1)  $T(\tau)$  for radiative equilibrium for two values of  $T_0$  and from (7.4.4) the  $T_c(\tau_c)$  imposed by the saturation condition. We see that if  $T_0$  were to exceed about 250°K, a gray atmosphere in radiative equilibrium could not be saturated. Alternatively, if the vapor in the upper troposphere were saturated, the atmosphere could not be in radiative equilibrium, because it would be too cool to re-radiate all the energy absorbed.

There is some ambiguity in this analysis in principle, but it is not serious in practice. One does not know in advance either the  $T_c$  or  $\tau_c$  of the top of the convective region; in practice we can require without serious error that the  $T(\tau)$  curves defined by (7.4.1) and (7.4.4) merely intersect somewhere.

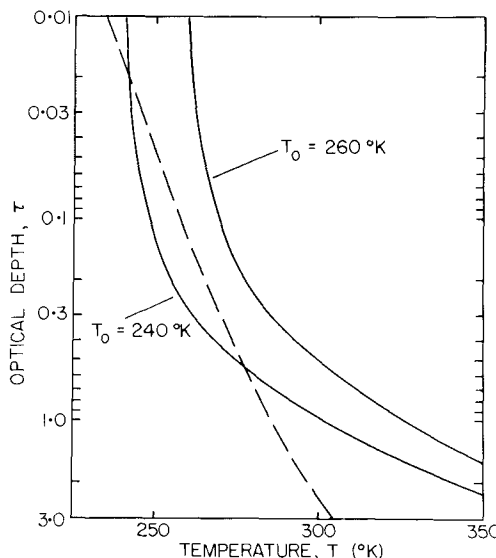


**Fig. 7.12** Model atmospheres in radiative equilibrium at two skin temperatures,  $T_0$  (solid lines), and the saturation condition (7.4.4). The higher temperature model cannot exist in an equilibrium situation where there is liquid water on the surface, since there is no way for the atmosphere to convert vapor back to liquid.

#### 7.4.2 Climate Variations

Changes in climate may arise from (a) alterations in the solar radiation output, or its spectral distribution, or changes in solar or terrestrial magnetism that affect the incident charged-particle flux; (b) orbital changes of the planet that alter the incident solar flux or its distribution over the planet; (c) redistribution of energy among a planet's internal storage modes, which can in turn be triggered by external or evolutionary factors or simply arise from oscillations within the internal energy system; or (d) modifications to the planet's opacity or albedo, which can arise from a host of sources.

**Solar Radiation and Solar System Magnetism** The very young sun,  $t < 10^7$  yr, was probably a T-Tauri star, possessing X-ray and ultraviolet emission enormously greater than today's sun. Also, the stellar wind and surface flaring must have been extremely strong and possibly erratic. To what extent the atmospheres of the protoplanets were formed at this stage, and therefore influenced by the activity of the sun, is uncertain. As the early sun evolved along the main sequence ( $t > 10^7$  yr), the solar luminosity was 20–30% lower than now. A lowering of temperature would expand the current polar ice caps, according to straightforward energy-balance modeling, and the resultant increase in planetary albedo would expand the ice caps

still further. Consequently, the reduced solar luminosity with ice-albedo feedback leads to a primitive ice-covered Earth, whereas the entire geologic record indicates substantial liquid water was present. To escape the dilemma, one must invoke large compositional differences (e.g., a large CO<sub>2</sub> enhancement to elevate the greenhouse effect) or invent cloud feedbacks that modify both the greenhouse heating and planetary albedo. Increases in the solar flux may have occurred at other periods when the solar system passed through clouds of Galactic dust.

Over a time scale of days, the sun is an erratic variable star, with fluctuations no more than a few tenths of one percent overall but possibly greater in the ultraviolet. Indeed, the obscuration of the areas covered by sunspots can reduce the solar flux by 0.1%. In the far ultraviolet, solar emission lines originating from the chromosphere or lower corona have strong variations with solar activity and the sunspot cycle, but these emissions, while important to the ionosphere, have no known direct connection with tropospheric energy balance. In the near ultraviolet differential fluctuations in the solar spectrum will produce changes in the ozone abundance. Conversely, an upper limit on the global 11-yr variation of ozone sets a rather restrictive limit on the solar ultraviolet variability, and the combined energy of the solar wind, cosmic rays, and extreme ultraviolet radiation is only one-millionth of the energy in the visual radiation. Furthermore, most of this energy is absorbed at very high altitudes, and thus directly affects only a tiny fraction of the mass of the atmosphere. Significant effects on tropospheric weather are therefore inherently improbable, and it is necessary to lay a strong burden of proof on any claimed correlations or suggested mechanisms. Such mechanisms must involve a great deal of amplification, which in the extreme could be analogous to the trigger of a gun. The next few paragraphs discuss some of the more plausible suggestions.

An indirect connection between solar activity and climatic change may occur through magnetic and particle interactions. The magnetic field lines that emanate from the sun and extend toward the Earth, embedded in the solar wind, are predominantly of one sign in any one large spatial sector. When the boundaries between two such sectors sweep past the Earth, a change in magnetic polarity of this interplanetary/solar field occurs, and, to some investigators, has seemed to be associated with a supposed "measure of storminess" called the *vorticity area index*; but the statistics are weak, and a causal link between solar activity and weather continues to be more hoped for than real.

The most likely indirect or "trigger" mechanism for relating *climate* to solar magnetic and particle activity is through a modification of the opacity of the middle atmosphere. The sequence might progress from decreased magnetic shielding to increased particle bombardment to formation of NO<sub>x</sub>.

to destruction of  $O_3$ . An  $O_3$  loss admits more ultraviolet, but more importantly it lets more infrared escape to space, thus cooling the surface. The Little Ice Age, a period of generally depressed temperatures in northern Europe in the seventeenth century, occurred during a long period of low sunspot activity (*the Maunder minimum*) and may have arisen from increased particle bombardment (primarily Galactic cosmic rays) into the stratosphere/mesosphere at high latitudes.

The stratospheric ozone contributes directly to the tropospheric greenhouse effect by absorption in the  $9.6\ \mu m$  band. There could, however, be even more important interactions. Reduced ozone will lower the stratospheric heating, leading to increased condensation of stratospheric water vapor (which is close to the saturation pressure at the tropical tropopause; see Section 1.5.3). This ice could increase the Earth's albedo or it could simply reduce the  $H_2O$  vapor content of the stratosphere and thereby reduce the greenhouse heating of the troposphere. Either way, the direction is the same: any reduction of ozone promises to lower the mean temperature at the ground.

**Milankovitch Theory of Orbital Variations** Three variable elements of the Earth's orbit influence the total solar radiation received and its geographical distribution. They are the eccentricity ( $e$ ), the obliquity of the ecliptic ( $\varepsilon$ ), and the longitude of perihelion ( $\omega$ ) measured from the vernal equinox (which itself is in motion).

Integrated over the Earth and over a year, the total energy influx (*insolation*) depends only on  $e$ . The present value of  $e$  is 0.017 and its range over the past million years is 0.001–0.054. The total insolation varies by less than 0.1%, and a major problem has been to show that this small triggering perturbation could lead to ice ages. The dominant term in the series expansion for  $e$  has a period of 413,000 yr. Eight of the next 12 terms range from 95,000 to 136,000 yr, and at low resolution they appear as a single broad peak around 100,000 yr.

The geographic and seasonal distribution of irradiation depends on  $\varepsilon$  and on  $e \sin \omega$ . The spectrum of obliquity  $\varepsilon$  is dominated by components with periods near 41,000 yr. Over the past million years,  $\varepsilon$  has varied from  $22.0^\circ$  to  $24.5^\circ$ ; currently  $\varepsilon = 23.4^\circ$ . The vernal equinox precesses as the pole moves over the sky with a 26,000 yr period due to lunar perturbations. The variation of  $e \sin \omega$  has a spectral doublet at 23,000 and 19,000 yr, which appears as a single broad peak around 22,000 yr. The *precession index*,  $\Delta(e \sin \omega)$ , defined as the departure from the current value of  $e \sin \omega$ , has ranged from  $-0.069a$  to  $+0.037a$ , where  $a$  is Earth's (invariant) semimajor axis.

The largest and most abrupt changes in climate are the ice ages. It has been established for some time that for the past 730,000 years, the climate system is driven in some way by insolation changes at the frequencies of variation in

obliquity and precession (1 cycle per 41,000 yr and 1/22,000 yr, respectively). There has been considerable doubt in the past, however, that the pronounced 100,000-yr recurrence cycle of ice ages shown in the geologic record could arise from the 100,000-yr orbital cycle of changing eccentricity. The change in insolation seemed too small for a cause-effect relationship.

However, some of the orbital cycles have now been used to sharpen up the geologic record. That is, the known orbital variations were used to fine tune the dating of oxygen isotope ratios (which specify the amount of glacial ice present). The amplitude of each of the main eccentricity cycles of the past 800,000 yr was thus found to be proportional to the amplitude of the corresponding 100,000-yr glacial cycle.

The question remains as to how the climate effects of the eccentricity cycle are magnified. Most likely the climatic feedback mechanism involves the temperature-sensitive rate at which the abundant microscopic life near the ocean's surface takes up dissolved carbonate. Such a mechanism of removing large amounts of CO<sub>2</sub> from the atmosphere would account for long-period CO<sub>2</sub> variations found in polar ice cores and inferred from <sup>18</sup>O/<sup>16</sup>O ratios in deep-sea sediment cores. Glacial ice sheets evolve asymmetrically, waxing more rapidly than they decay; once an ice sheet is formed, insolation cycles favor its growth. Ice-albedo feedback constitutes an important coupling between glacial and climate models, but it is not clear that this class of feedback alone is sufficient to produce ice ages. What seems to be needed in addition is a decrease in atmospheric CO<sub>2</sub> or H<sub>2</sub>O as the planet cools; this (or a similar change in the Earth's radiation balance) would further amplify the temperature response to insolation changes.

**Redistribution of Internal Energy** Not all climatic variations are driven by changes in the external energy available to the system. For example, a large reservoir of energy is in the oceans. The upper layer of 50–100 m is thoroughly mixed and interacts with air. The deep layers turn over with characteristic periods of 10<sup>3</sup> yr. Given a suitable driving function, the temperature of the mixed layer at a given latitude might oscillate over long periods. Random fluctuations in climate can be studied by analogy with Brownian motion. Short-term weather fluctuations are the high-frequency random events; the oceans are analogous to the slowly responding large particles.

A breakdown in the normal coupling of sea and air in the equatorial Pacific is El Niño, which often brings disastrous consequences. The typical El Niño, which occurs every 3–10 yrs, begins with the appearance of warm water off the South American coast around Christmas (which is how the event gets its name). Southern hemisphere trade winds, blowing stronger than normal, pile up water in the western Pacific near Indonesia. Normally the air rises in the Indonesian low-pressure area and its water rains out. During El

Niño, the Indonesian low weakens, the trade winds abate, and the sea warms all along the equatorial Pacific. The anomalously warm coastal waters and equatorial ocean off Ecuador and Peru are greatly diminished in nutrients, plankton, fish, and seabirds.

In 1982–1983 El Niño was an extreme event. It did not follow the usual time schedule (the warming began in May, not December) and it first appeared in the central Pacific and spread eastward. (In 1940–41 El Niño was similarly strong and atypical.) The 1982–1983 event was the strongest warming of the twentieth century. It was associated with (and probably caused) a major Australian drought, an abnormally wet Indian monsoon season, and heavy rains along the South American coast. In June 1983 the rainfall at Quito, Ecuador was 58 cm—this during the “dry season,” with normal precipitation of 1.3 cm/month. At its peak the tongue of unseasonably warm water stretched 13,000 km across the Pacific. The maximum warming was 5°C in the central ocean and an amazing 7°C near the South American coast.

Certain agricultural regions of the Earth, such as the western plains of North America and the Sahel of northern Africa, are subject to severe drought from time to time. Much effort has been made to associate these periods with the sunspot cycle—with only limited success. The 1975–1976 drought in southern England, which was characterized as “unprecedented since 1698,” was to be expected statistically once in 200 years. The persistent high-pressure areas normally accompanying droughts are frequently related to anomalous sea-surface temperatures. In addition, an established drought condition tends to be self-perpetuating: the lack of local moisture and sources of latent heat inhibits the development of local convective storms. Sometimes, as with the Sahel in 1973 and the U.S. Great Plains during the “dust bowl years” of the mid-1930s, a climatic fluctuation is aggravated by unwise exploitation of the land (too much grazing or tilling) and produces a catastrophe.

**Variations in Albedo and Opacity** We have already noted some changes in insolation that result from albedo feedbacks (the polar ice caps) and opacity (ozone destruction by particle bombardment). In virtually any kind of climatic change the question arises as to what will be the change (and feedback) of cloudiness, not only to the overall global energy balance but to latitudinal redistributions of energy as well.

(a) *The Role of Clouds.* As the global surface temperature responds to a specified change in the energy budget (for example, from a change in the CO<sub>2</sub> atmospheric content or a long-term change in solar flux), the amount of cloud cover varies. The cloud latitudinal distributions and cloud-top heights also vary. There are difficulties in taking into account all these factors in climate modeling. Formerly the prevailing view was that an increase in the

amount of global cloud cover would lead to global surface cooling. Further studies throw doubt on this commonly accepted conclusion. In fact, it now seems that the cloud amount may not even be a significant feedback mechanism, since the albedo change in the solar portion of the spectrum and the greenhouse change in the infrared largely compensate one another when the change in outgoing longwave flux is properly averaged.

(b) *Catastrophic Impacts.* Climatic changes due to modified atmospheric opacity may be conveniently divided into two broad categories: catastrophic and evolutionary. The prototype of catastrophic climate events is the impact of an asteroid or comet with the Earth 65 million years ago, at the end of the Cretaceous and beginning of the Tertiary Period. The projectile was some 10 km in diameter and probably struck with a speed of at least 25 km/sec, and much more if it was a comet in a retrograde orbit. The associated kinetic energy would exceed  $4 \times 10^{30}$  erg or the equivalent of  $10^8$  megatons of TNT explosive. Asteroids of this size are rare, but one would be expected to strike the Earth about once every 40 million years or so. More recent but controversial evidence has suggested a 26 Myr periodicity to impact extinctions, which suggests in turn that comet showers regularly bombard the inner solar system. It has been hypothesized that the comets are triggered loose from their normal habitat in the *Oort cloud*, thousands of astronomical units from the Sun by a small, dark companion star of the Sun. However, we must reiterate that the impact periodicity is itself in serious doubt.

The initial evidence for an asteroid (or comet) impact took the form of a large iridium enhancement in a thin layer in marine sedimentary rocks laid down at precisely the time of the Cretaceous-Tertiary extinctions. Iridium is rare in the Earth's crust but comparatively rich in meteors and presumably comets.

The extinction itself is the most recent of five major extinctions since the beginning of the Cambrian Period (i.e., during the time span of easily observed fossils) 570 million years ago. Marine reptiles, the flying reptiles, and all species of dinosaurs were suddenly wiped out, as were microscopic floating animals and plants and most species of plankton, which in turn led to a dramatic loss of sea life. Groups that were less affected included a variety of land plants, crocodiles, snakes, mammals, and many kinds of invertebrates. This extinction was not the biggest of all time; that honor belongs to the one occurring at the Permian-Triassic boundary, 225 million years ago. This extinction has generally been attributed to coalescence of the world's continents into the supercontinent, Pangea, with enormous sea-level and geographic changes. Over 96 percent of living species were destroyed. (Alas, today we mourn the passenger pigeon and fret over the California condor.) However, the Permian extinction does fit the supposed 26 Myr periodicity and was also associated with an iridium layer.

It has been established that the iridium dust settled worldwide. Circulation in the stratosphere between hemispheres takes more than a year, whereas the comet dust (diluted by 20 to 100 times with terrestrial matter), responsible for obscuring the sun, would have settled out in only 3–6 months. However, the explosive impact of a comet would generate a fireball with convective winds strong enough to propel the dust into ballistic orbits and populate the entire world.

A strong candidate for the major kill mechanism is the cessation of photosynthesis for the several months of darkness. Most of the plankton in the surface levels of the sea would have died and disrupted the food chain for the larger animals. A similar situation would have occurred on land when most of the plants died. Other possible kill mechanisms are (a) excessive greenhouse heating from water vapor sent into the atmosphere by an asteroid or comet impact in the ocean; (b) an extended period of severe cold, caused by the obscuration of the sun; and (c) acid rain created by the enormous amounts of nitrogen oxides that are produced in the rising fireball, just as in a nuclear explosion (see Section 3.2.4).

(c) *Nuclear Winter*. A similar but scaled down scenario might develop in the event of a major exchange of nuclear weapons. It has been estimated that the two major nuclear powers possess 50,000 weapons. If they all went off, the energy released would be  $10^4$  MT ( $1\text{ MT} = 4.2 \times 10^{22}\text{ erg}$ ), or some  $10^{-4}$  the energy of the Cretaceous asteroid or comet. Attacks on urban-industrial areas would generate large amounts of smoke from fire storms; attacks on an underground nuclear-missile silo would normally involve high-yield ground bursts that produce fine dust. Additional smoke would come from air bursts that ignite forest fires.

Climatic models of nuclear exchanges, with a variety of military scenarios, have suggested that the destruction would far exceed that commonly expected from blast, fire, and radiation. The dust and smoke generated would encircle the Earth within two weeks, reducing visual light levels to a few percent of ambient and dropping land temperatures to  $-20^\circ\text{C}$ , for a major weapons exchange. The obscuring particles would be transported into the stratosphere and across the equator by large thermal gradients that would arise from sunlight absorption by smoke and dust clouds. Nitrogen oxides generated by the fireballs would largely deplete stratospheric ozone. At first, plant growth would be stunted by the diminished photosynthesis and later further damaged by exposure to ultraviolet light (which disrupts the DNA molecule). Survivors of the initial nuclear exchange would face a postwar environment characterized by long-term nuclear radiation, below freezing temperatures, a vanishing food supply, disease and pestilence, and, as the smoke and dust eventually cleared, harsh ultraviolet radiation transmitted by a wounded ozone layer.

One should be cautious about giving too much credence to the nuclear-winter predictions. It is a young study, and many assumptions have been built into the calculations without adequate understanding:

(1) The strong horizontal gradients of temperature and the resultant winds that will develop over fairly short distances near the edges of the soot-laden zone are not handled at all well by the models but are likely to be exceedingly important.

(2) The amount of soot remaining in the atmosphere after it becomes widely dispersed over the temperate zone and its altitude distribution are poorly known at best.

(3) The interaction between soot and water has not been studied. For example, how much soot is scavenged by the rains that can be expected to accompany fire storms (as they did at Hamburg, Dresden, Hiroshima, and Nagasaki, the most intensely bombed cities of World War II)? Will fog and water-coated soot form and provide infrared blanketing, which would keep ground temperatures warm beneath the blanket?

(4) There will be literally hundreds of compounds liberated into the atmosphere by the ignition of a city or forest; what will be the infrared blanketing (i. e., greenhouse) properties of these gases?

On a greatly reduced scale, volcanic eruptions that deposit dust and gas in the stratosphere, where they may live for months or years, are suspected of climatic influence.

(d) *Changes in Chemical Composition.* Evolutionary changes in the Earth's opacity have undoubtedly occurred. We have already mentioned the likelihood that the  $\text{CO}_2$  abundance was very much greater  $4.5 \times 10^9$  yr ago, and the added greenhouse effect offset the reduced (75% of present) solar constant, allowing liquid water to flow on the surface. About  $2.5 \times 10^9$  yr ago the transition to an oxidizing atmosphere, induced by green-plant photosynthesis, brought a major increase in  $\text{O}_2$  and the virtual disappearance of  $\text{CO}_2$ .

Model calculations show that ozone grew to a level to provide an effective biological screen (about 0.2 atm-cm) when the total  $\text{O}_2$  content reached one-tenth of the present level. Although the calculations are rather imprecise, there is a possibility that this level was reached after the Cambrian Period (i.e., later than 500 Myr ago) and that the screening was a causative factor in the emergence of land life during the Silurian (350–390 Myr ago).

In modern times the chemical composition of the atmosphere can be changed by man's industrial activities in ways that impact the climate. Most important is the growth of atmospheric  $\text{CO}_2$  due primarily to the burning of fossil fuels (see Fig. 7.13). This increase is occurring at the alarming rate of 3.8%/decade, and this rate may itself be increasing. Nevertheless the  $\text{CO}_2$  released into the atmosphere since the beginning of the industrial revolution

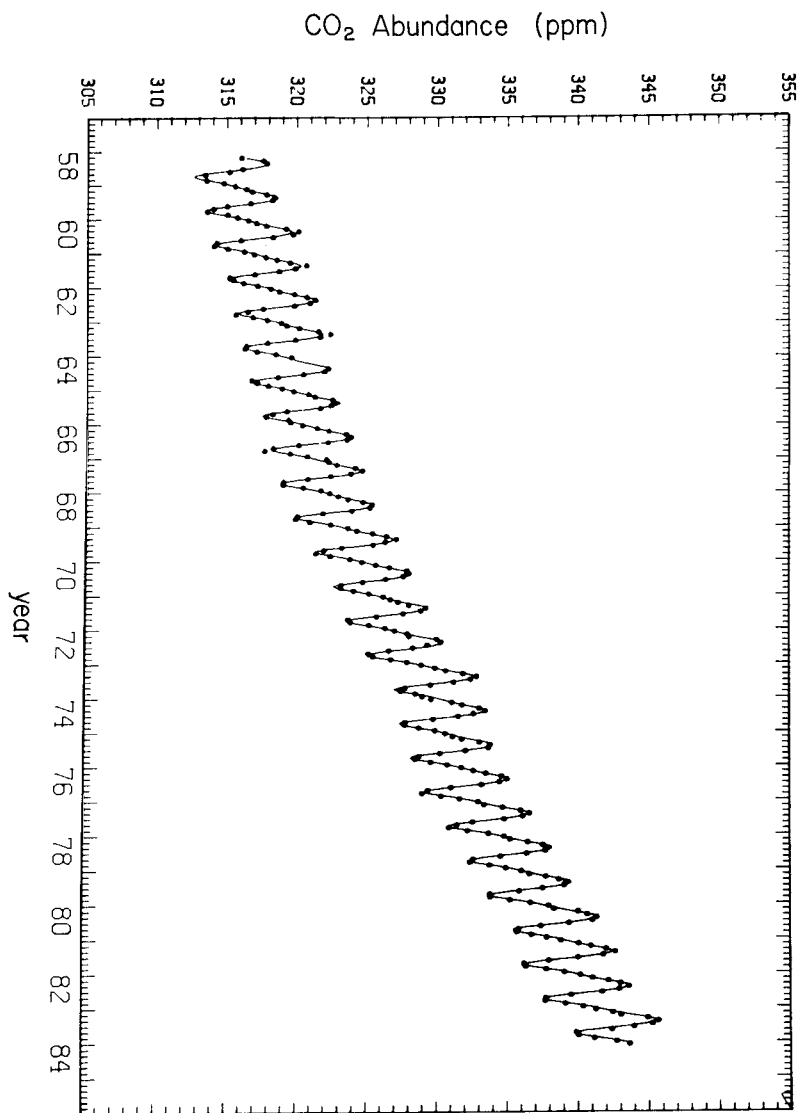


**Fig. 7.13** The growth of the CO<sub>2</sub> mixing ratio (in parts per million) over Mauna Loa, Hawaii, since 1958. The dots represent monthly averages of a continuous record obtained with a nondispersive infrared analyzer. The smooth curve was obtained as a spline fit of the seasonally adjusted concentration plus a four-harmonic representation of the annual cycle, assumed to increase linearly with time. (Courtesy of Charles D. Keeling and Scripps Institution of Oceanography.)

by the burning of fossil fuels is not all accounted for. Less than half of it is in the atmosphere. The excess CO<sub>2</sub> is not in the upper layers of the oceans, and their deep circulation is commonly thought to be much too slow to provide the missing sink. Also, this excess CO<sub>2</sub> does not seem to be locked in the world's trees. Indeed, the harvesting of tropical forests and clearing of land for agricultural use may have led to a net transfer of CO<sub>2</sub> from the biota to the atmosphere, perhaps accounting in recent years for about 50% of the annual increase.

Several types of models (global radiative balance, zonal radiative-convective heat balance, general circulation) treated with various levels of sophistication (i. e., complexity) agree in predicting that a doubling of CO<sub>2</sub> will lead to an increase in global mean temperature of 2–3°C. The increase is enhanced at high latitudes, in part because of ice-albedo feedback—the shrinking of the polar snow and ice caps lowers the peripheral albedo, which further raises the polar temperature. In addition, sea ice reduces the heat exchange between the air and underlying seawater. However, partially offsetting these effects is the water vapor feedback: an increase in temperature increases the absolute humidity, which further increases the greenhouse opacity; this effect tends to amplify the heating in the tropics.

Constituents other than CO<sub>2</sub> may influence climate. Minor constituents that absorb in the 9–14 μm transparency window of the atmosphere (see Fig. 1.11) are especially effective in enhancing the greenhouse effect. Such molecules include N<sub>2</sub>O, CH<sub>4</sub>, O<sub>3</sub>, and the halomethanes, CCl<sub>4</sub>, CF<sub>2</sub>Cl<sub>2</sub>, and CFCl<sub>3</sub>. In addition, the naturally occurring background haze in the atmosphere has a climatic effect—it lowers the mean temperature by 2–3°C. Hence, variations in the aerosol burden or its composition and size distribution can induce changes in climate.

An increase in the mean temperature of the Earth would have profound economic and sociological impacts. The optimum agricultural belts for various crops would move toward higher latitudes. On the whole, arid regions would likely expand, but fuel consumption for heating would diminish. The partial melting of polar ice could raise the sea level. The detachment or melting of the West Antarctic ice sheet, which extends into the ocean south of South America but is resting on the continental shelf, would raise the global sea level by 5–6 m and flood many coastal cities. (In Washington, D.C., the White House and the Capitol would be dry, but Pennsylvania Avenue connecting the two would be flooded by the Potomac estuary.)

There is some indication that the global sea level has already risen since 1940, although satellite observations have not yet established a definite decrease in polar ice. The discharge of ice into the sea and its subsequent

melting extracts atmospheric heat that would otherwise appear as an increase in the global mean temperature.

Finally, some secular changes in temperature are occurring in and near urban-industrial centers. Photochemical smog (see Section 7.4.4) and aerosols, due to automotive and industrial burning, create localized greenhouse warmings. In some instances the effects can be found over large regions near cities, primarily leeward of the sources. In the 1960s when passenger transport by jet aircraft came into wide use, many urban airports moved from locations near the central cities to outlying areas and took the official thermometers along. For this reason one must be careful in drawing conclusions about changes in mean temperatures if such weather stations were involved.

### 7.4.3 Climatic Conditions Hospitable to Emerging Intelligence

In speculative discussions on the existence of intelligent life elsewhere in the Galaxy, it is generally assumed that, given a stellar planetary system, suitable conditions for life forms to develop and evolve into an intelligent, communicative civilization would likely be found one time in a hundred or better. That is, the probability for the eventual emergence of very intelligent life is of the order of 1% per planetary system. This number seems excessive in view of our present knowledge of the precariousness of intelligent life in the solar system.

A slightly higher solar flux than the Earth now has would lead to a runaway greenhouse in the planet's early atmosphere. A slightly lower flux for a sustained period would allow the ice caps to spread to lower latitudes. The additional ice cover would (other things remaining unchanged) significantly increase the Earth's albedo, causing a further spread of ice, and so forth: a runaway polar ice cap! An ice-covered Earth would be difficult to reverse; simply reversing the solar flux with time is not enough because the ice albedo requires a higher flux to thaw. This hysteresis effect would likely make permanent any ice cover, once it was established.

The development of intelligent life requires that the planet's evolution successfully navigate through a sea of catastrophes, and there is no charting or evaluating these events. Our first response to the theory of the Cretaceous asteroid might be concern over when the next event will occur. However, had the Age of Reptiles not been brought to a halt, civilized life might never have developed or, if it had, we might have hatched from eggs and had scaly features.

Much is made these days of a search for extraterrestrial intelligence (SETI). The subject has, as a spinoff, the further stimulation of interest in planetary

sciences among an educated public that is properly fascinated by the accomplishments of space exploration. This situation is a little like astrology stimulating college students to study astronomy. The desire to find extraterrestrial intelligence is blind to the combined facts that it must be exceedingly rare and that, even where it exists, it would be undetectable by presently known techniques.

It can scarcely be doubted that intelligence is much more rare than the conventional probabilities presume. Factors generally omitted from the calculation are: (a) the precarious situation of a terrestrial type planet lying in a narrow band between a runaway greenhouse or global ice cover; (b) the restrictions on surface gravity and escape mechanisms, which allow retention of a planet's water but development of an oxidizing atmosphere; (c) the probability of well-behaved orbital parameters, such that excursions in planetary temperatures over geologic eras are not too wild; (d) the existence of a sufficiently long time interval between natural disasters, such that intelligent life has time to evolve; and (e) the lifetime of a civilization learning to communicate electromagnetically and to self-destruct with nuclear energy almost simultaneously.

Given an intelligent civilization with the capacity to beam coded messages Earthward, there is little likelihood that its scientists and engineers will do so. The project of sending and then waiting for a reply would take so long ( $10^4$  yr, with the most optimistic assumptions), that no government would likely fund the enterprise.

#### 7.4.4 Pollution

Ankara, Athens, Mexico City, Santiago, São Paulo, Seoul, Taipei—none of these cities is in a highly developed industrialized country. Yet they rank among the most polluted cities in the world. Widespread coal burning and dirty automotive burning of gasoline are aggravated by local topography to build up high levels of pollutants.

In addition to  $\text{CO}_2$  a number of wastes are injected into the atmosphere through the burning of hydrocarbons. Most of the physical-chemical research on tropospheric pollutants has so far concentrated on identifying and measuring the secondary products and the complex photochemistry that is responsible for creating them from the primary automobile exhausts and power-plant discharges. Much additional work has been directed toward their toxicity on humans and their impact on ecosystems. It is too early to predict what will be the effects on climate, if any, of both the gases and aerosols, but there are indications of changes occurring in the average weather conditions many kilometers downwind from major urban centers.

The principal primary pollutants in urban areas are the hydrocarbons, the aldehydes (e.g., formaldehyde,  $\text{CH}_2\text{O}$ ), nitrogen oxides, and carbon monoxide. The major oxidant in smog is ozone, and the question is, How is ozone formed? The central reactions start with  $\text{NO}_2$ , which can be dissociated by sunlight reaching the ground. Thus we have



followed by



The ozone is then destroyed by

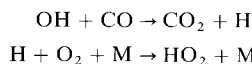


completing the catalytic cycle. This sequence goes rapidly once O is formed and gives an equilibrium  $\text{O}_3$  abundance of

$$[\text{O}_3] = J_5[\text{NO}_2]/k_7[\text{NO}] \quad (7.4.8)$$

where  $J$  is a dissociation rate ( $\text{sec}^{-1}$ ) and  $k$  is a rate coefficient ( $\text{cm}^3 \text{ sec}^{-1}$ ). However, (7.4.5)–(7.4.7) do not account for the observed diurnal variations of ozone and  $\text{NO}_2$ . There are other problems: reactive hydrocarbons are oxidized faster than they should be if the O and  $\text{O}_3$  concentrations were those due only to the ozone cycle.

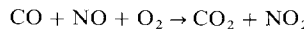
The resolution of both dilemmas appears to lie in the effect of  $\text{HO}_x$  chemistry on the system by the cycle



and



giving a net



Thus ozone follows the cycle of (7.4.5)–(7.4.7), but NO is converted to  $\text{NO}_2$  by (7.4.9), in addition to (7.4.7).

Regarding pollution of the troposphere by industrial by-products, OH plays a kind of scavenger role whose cleansing effects may soon become overworked. The main OH reactions are

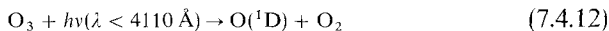


and



which are the principal sinks for  $\text{CH}_4$  and CO, although oxidation of  $\text{CH}_3$  provides the main natural source of CO. Probably OH also controls the concentrations of  $\text{H}_2\text{S}$ ,  $\text{SO}_2$ ,  $\text{CH}_3\text{Cl}$ , and other less soluble trace gases.

A major decrease in OH in the troposphere may have repercussions that are only beginning to become apparent. It can not only affect the natural disposal of technological products in the air, but also impact on the stratospheric chemistry. One danger is the fact that a major portion of the CO produced is technological and increasing. Another is that the stratosphere and troposphere may couple in both directions; a man-induced change in stratospheric  $\text{O}_3$  could affect tropospheric OH (and hence  $\text{CH}_4$ ), just as  $\text{CH}_4$  produced in the troposphere eventually enters the stratosphere chemistry. The main source of tropospheric OH is photodissociation of tropospheric ozone,



followed by



The possibilities for feedbacks of all this tropospheric chemistry on the thermal balance of the atmosphere are numerous and complex. What is certain is that the time constants are the order of decades, and pollution problems that were local a few years ago are rapidly becoming global.

In industrial North America and Europe acid rain has attracted growing concern. The ecological effects are far reaching, with acidic levels reaching 4 and below on the logarithmic pH scale (neutral is 7.0) in some lakes. Outdoor statuary, such as that on the Athenian Acropolis, shows erosion effects. Although attention has been focused mainly on precipitation containing sulfuric and nitric acids ( $\text{H}_2\text{SO}_4$  and  $\text{HNO}_3$ ), dry deposition of sulfate may be equally important.

International problems arise in attempts to place blame, and hence responsibility, for a clean up. Are Scandinavia's acidic lakes poisoned from the industrial English Midlands or from the German Ruhr Valley? The smokestack industry in the Ohio River Valley is polluting eastern Canada as well as northeastern U.S.; some retaliation is provided by the huge smelters in southern Ontario that send fumes across the longest "friendly frontier" in the world, into New England.

There are distinct differences in the geography of the fallout of  $\text{SO}_2$  and  $\text{NO}_x$ . The latter is largely an automobile pollutant and appears in the U.S. relatively stronger in the west—as in Lake Tahoe, a volcanic lake in the Sierra Nevada.

Interest in sulfur compounds in the atmosphere centers on hydrogen sulfide ( $\text{H}_2\text{S}$ ) and sulfur dioxide ( $\text{SO}_2$ ) chemistry. Natural sources provide the

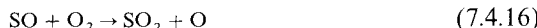
bulk of  $\text{H}_2\text{S}$ , while  $\text{SO}_2$  is mainly man-made. Their chemistry is the same after  $\text{H}_2\text{S}$  is oxidized to  $\text{SO}_2$ ; again,  $\text{OH}$  is the key player:



followed by removal of HS (thiyl radical) by  $\text{O}_2$ , which regenerates the odd hydrogen,



Finally,  $\text{SO}$  (sulfur monoxide) is oxidized by



Again,  $\text{HO}_x$  is called into play to transform  $\text{SO}_2$  into acid. Thus



with  $\text{SO}_3$  (sulfate) transformed into sulfuric acid by



The lifetime for conversion of  $\text{H}_2\text{S}$  to  $\text{SO}_2$  is set by reaction (7.4.14) and is under a day. The lifetime for  $\text{SO}_2$  conversion to acid is of the order of 10 days, as set by the conversion to  $\text{SO}_3$ ; the final step, (7.4.18), proceeds in microseconds for normal concentrations of  $\text{H}_2\text{O}$ .

Complications that arise in acid-rain chemistry are several;

(1) The reactions do not have to proceed in the gas phase or via "homogeneous chemistry." In heterogeneous chemistry a gas molecule attaches to a solid or liquid aerosol, and rates may be quite different.

(2) If the conversion chemistry proceeds in an urban environment, hydrocarbons become important. For example, the peroxy radical  $\text{CH}_3\text{O}_2$  may play the role of  $\text{HO}_2$  in (7.4.17).

(3) There can be interactions between  $\text{NO}_x$  and  $\text{HO}_x$  that affect the relative production of  $\text{HNO}_3$  and  $\text{H}_2\text{SO}_4$ . Since  $\text{NO}_x$  is a frequent precursor to the formation of the strong oxidants  $\text{O}_3$ ,  $\text{H}_2\text{O}_2$ , and  $\text{HO}_x$ , the obvious implication is that a high  $\text{NO}_x$  concentration may enhance the oxidation of  $\text{SO}_2$  into  $\text{SO}_4^{2-}$ , the ion of sulfuric acid. Schematically the route is



The situation is clouded, however, because (a)  $\text{HO}_x$  can be formed without assistance from  $\text{NO}_x$  and (b)  $\text{HO}_x$  can be destroyed by  $\text{NO}_x$ . The abundances of all these minor constituents vary widely and are never known with much certainty.

(4) It is unclear whether the final conversion to acid before deposition is really necessary for most ecological damage to occur.

## BIBLIOGRAPHICAL NOTES

**Section 7.1 Quasi-Collisionless Exospheres**

The escape of light gases from the planets, the moon, and the sun was first discussed in a paper read to the Royal Society in 1846 by J. J. WATERSTON. The paper was mainly concerned with matters of kinetic theory and first advanced the principle that the mean kinetic energy of each molecular species is proportional to the temperature. Thus the subject matter of this chapter is as old as the kinetic theory of gases, and older than Maxwell's law of the distribution of velocities. Waterston's manuscript was rejected, however, and was published eventually only because Lord Rayleigh, then secretary of the Royal Society, later found the manuscript in the Society's archives and recognized its historical importance. The original paper appears as

WATERSTON, J. J. (1892), On the physics of media that are composed of free and perfectly elastic molecules in a state of motion, *Phil. Trans. Roy. Soc. (London)* **A183**, 1-80.

The Jeans formula for escape by a Maxwellian velocity distribution over the upward hemisphere was developed in

JEANS, J. H. (1916), "The Dynamical Theory of Gases," Chapter 15, Cambridge University Press (4th ed., 1925).

Although out of date in some respects, a classic review of the escape problem is contained in

SPITZER, L., JR. (1949), The terrestrial atmosphere above 300 km, in "The Atmospheres of the Earth and Planets," (G. P. Kuiper, ed.), Univ. Chicago Press, Chicago, (2nd ed., 1952).

Hydrogen exospheres, their escape, and their observation (optically and otherwise) are treated in

TINSLEY, B. A. (1974), Hydrogen in the upper atmosphere, *Fundam. Cosmic Phys.* **1**, 201-300.

Currently the definitive review, with some 370 references, is

FAHR, H. J. and SHIZGAL, B. (1983), Modern exospheric theories and their observational relevance, *Rev. Geophys. Space Phys.* **21**, 75-124.

The mathematical analysis of the collisionless exosphere follows

CHAMBERLAIN, J. W. (1963), Planetary coronae and atmospheric evaporation, *Planet. Space Sci.* **11**, 901-960.

Line profiles due to Doppler broadening by the non-Maxwellian velocity distributions of an exosphere have been computed by

CHAMBERLAIN, J. W. (1976), Spectral line profiles for a planetary corona, *J. Geophys. Res.* **81**, 1774-1776,

PRISCO, R. A. and CHAMBERLAIN, J. W. (1978), Spectral line profiles in a planetary corona: A collisional model, *J. Geophys. Res.* **83**, 2157-2161,

PRISCO, R. A. and CHAMBERLAIN, J. W. (1979), Doppler line profiles in a planetary corona: An extended approach, *J. Geophys. Res.* **84**, 4363-4370.

Observations have been obtained of Lyman-alpha line shapes from OGO by

BERTAUX, J. L. (1978), Interpretation of OGO-5 line shape measurements of Lyman-alpha emissions from terrestrial exospheric hydrogen, *Planet. Space Sci.* **26**, 431-447,

and of Balmer-alpha from the ground with Fabry-Perot interferometers by

MERIWETHER, J. W., Jr.; ATREYA, S. K.; DONAHUE, T. M.; and BURNSIDE, R. G. (1980), Measurements of the spectral line profile of Balmer alpha emissions from the hydrogen geocorona, *Geophys. Res. Lett.* **7**, 967-970,

KERR, R. B.; ATREYA, S. K.; MERIWETHER, J. W., Jr.; TEPLEY, C. A.; and BURNSIDE, R. G. (1986), Simultaneous H alpha line profile and radar measurements at Arecibo, *J. Geophys. Res.* **91**, 4491–4512,

SHIH, P.; ROESLER, F. L.; and SCHERB, F. (1985), Intensity variations of geocoronal Balmer alpha emission. I. Observational results, *J. Geophys. Res.* **90**, 477–490,

YELLE, R. V. and ROESLER, F. L. (1985), Geocoronal Balmer alpha line profiles and implications for the exosphere, *J. Geophys. Res.* **90**, 7568–7580.

Computer models of exospheres have made it possible to remove the restrictions imposed at the beginning of Section 7.1.2 in order to have an analytically simple problem. See, for example,

HARTLE, R. E. and MAYR, H. (1976), Wind-enhanced escape with application to terrestrial helium, *J. Geophys. Res.* **81**, 1207–1212,

HARTLE, R. E. (1973), Density and temperature distributions in nonuniform rotating planetary exospheres with applications to Earth, *Planet. Space Sci.* **21**, 2123–2138.

VIDAL-MADJAR, A.; CAZES, S.; and EMERICH, C. (1974), Influence of Earth's rotation and of possible perturbations on the exobase and exospheric hydrogen densities, *Planet. Space Sci.* **22**, 1375–1402.

Lateral flow in the exosphere has been discussed for the Earth by a number of authors including

MCAFEE, J. R. (1967), Lateral flow in the exosphere, *Planet. Space Sci.* **15**, 599–609,

HODGES, R. R., Jr. (1973), Differential equation of exospheric lateral transport and its application to terrestrial hydrogen, *J. Geophys. Res.* **78**, 7340–7346.

The exospheres of Mercury and the Moon, which offer special problems because of interaction of the atmosphere with the surface, have been examined by

SHEMANSKY, D. E. and BROADFOOT, A. L. (1977), Interaction of the surfaces of the Moon and Mercury with their exospheric atmospheres, *Rev. Geophys. Space Phys.* **15**, 491–500.

Also see references for Section 7.2.5.

## Section 7.2 Collisions in Exospheres

The concept of a satellite critical level was introduced in

CHAMBERLAIN, J. W. (1963), op. cit.

Perturbation theory of Keplerian orbits subjected to a small second force (such as radiation pressure) is developed in textbooks on dynamical astronomy and in

SHAPIRO, I. I. (1962), The prediction of satellite orbits, in "Dynamics of Satellites," (M. Roy, ed.), pp. 257–312. Academic Press, New York.

A clear and simple presentation of the perturbations on the orbital elements by an external force is given in

BURNS, J. A. (1976), Elementary derivation of the perturbation equations of celestial mechanics, *Amer. J. Phys.* **44**, 944–949.

The importance of radiation pressure in removing H atoms in satellite orbits was demonstrated by

BERTAUX, J. L. and BLAMONT, J. E. (1973), Interpretation of Ogo 5 Lyman alpha measurements in the upper geocorona, *J. Geophys. Res.* **78**, 80–91.

Orbital perturbations by radiation pressure and the gradual decay of H atoms into the atmosphere have been examined in

CHAMBERLAIN, J. W. (1979), Depletion of satellite atoms in a collisionless exosphere by radiation pressure, *Icarus* **39**, 286–294.

CHAMBERLAIN, J. W. (1980), Exospheric perturbation by radiation pressure. II. Solution for orbits in the ecliptic plane, *Icarus* **44**, 651–656.

The asymmetric shape of the geocorona under the influence of solar radiation pressure and charge-exchange collisions with the plasmasphere has been treated by

BISHOP, J. (1985), Geocoronal structure: The effects of solar radiation pressure and the plasmasphere interaction, *J. Geophys. Res.* **90**, 5235–5245.

The standard work on elastic-collision effects in neutral gases is

CHAPMAN, S. and COWLING, T. G. (1970), "The Mathematical Theory of Non-Uniform Gases," 3rd ed., Cambridge University Press, Cambridge.

Results of Monte Carlo calculations of the departures of thermal escape fluxes from the Jeans rate are given by

BRINKMANN, R. T. (1971), More comments on the validity of Jeans' escape rate, *Planet. Space Sci.* **19**, 791–794,

CHAMBERLAIN, J. W. and SMITH, G. R. (1971), Comments on the rate of evaporation of a non-Maxwellian atmosphere, *Planet. Space Sci.* **19**, 675–684.

The application of the Boltzmann equation to escape by charge-exchange collisions follows the treatment in

CHAMBERLAIN, J. W. (1977), Charge exchange in a planetary corona: Its effect on the distribution and escape of hydrogen, *J. Geophys. Res.* **82**, 1–9.

Further calculations on the effects of charge exchange are given in

MAHER, L. J. and TINSLEY, B. A. (1977), Atomic hydrogen escape rate due to charge exchange with hot plasmaspheric ions, *J. Geophys. Res.* **82**, 689–695,

TINSLEY, B. A. (1981), Neutral atom precipitation—a review, *J. Atmos. Terr. Phys.* **43**, 617–632,

HODGES, R. R., Jr.; ROHRBAUGH, R. P.; and TINSLEY, B. A. (1981), The effect of the charge exchange source on the velocity and 'temperature' distributions and their anisotropies in the Earth's exosphere, *J. Geophys. Res.* **86**, 6917–6925,

SHIZGAL, B. and LINDENFELD, M. J. (1982), A simple kinetic theory calculation of terrestrial atomic hydrogen escape fluxes induced by charge exchange collisions, *J. Geophys. Res.* **87**, 853–858.

Ballistic lateral flow was first discussed by

HANSON, W. B. and PATTERSON, T. N. L. (1963), Diurnal variation of the hydrogen concentration in the exosphere, *Planet. Space Sci.* **11**, 1035–1052.

The definitive formulation (in the approximation of a discrete exobase) and an approximate numerical solution were given by

MCAFEE, J. R. (1967), Lateral flow in the exosphere, *Planet. Space Sci.* **15**, 599–609.

A convenient review of the first decade, and some improved numerical results, are in

PATTERSON, T. N. L. (1970), Diurnal variations in thermospheric hydrogen, *Rev. Geophys. Space Phys.* **8**, 461–467.

The differential equation based on a series expansion of the McAfee integrals is derived and applied in

HODGES, R. R. and JOHNSON, F. S. (1968), Lateral transport in planetary atmospheres, *J. Geophys. Res.* **73**, 7307–7317,

HODGES, R. R. (1973), Differential equation of exospheric lateral flow and its application to terrestrial hydrogen, *J. Geophys. Res.* **78**, 7340–7346,

TINSLEY, B. A.; HODGES, R. R.; and STROBEL, D. F. (1975), Diurnal variations of atomic hydrogen: Observations and calculations, *J. Geophys. Res.* **80**, 626–634.

The Venus light-element bulge is discussed by

MAYR, H. G.; HARRIS, I.; NIEMANN, H. B.; BRINTON, H. C.; SPENCER, N. W.; TAYLOR, H. A.; HARTLE, R. E.; HOEGY, W. R.; and HUNTER, D. M. (1980), Dynamic properties of the thermosphere inferred from Pioneer Venus mass spectrometer measurements, *J. Geophys. Res.* **85**, 7841–7847.

A discussion of the Mercury problem is given by

SMITH, G. R.; SHEMANSKY, D. E.; BROADFOOT, A. L.; and WALLACE, L. (1978), Monte carlo modeling of exospheric bodies: Mercury, *J. Geophys. Res.* **83**, 3783–3790.

Opinions still differ in this area; see

HODGES, R. R. (1980), Methods for monte carlo simulation of the exospheres of the Moon and Mercury, *J. Geophys. Res.* **85**, 164–170,

SHEMANSKY, D. E. (1980), Comment on ‘Methods of Monte Carlo simulation of the exospheres of the Moon and Mercury’ by R. R. Hodges, Jr., *J. Geophys. Res.* **85**, 221–222.

### Section 7.3.1 Escape Mechanisms and the Limiting Flux

The suggestion that charge exchange with a hot plasma could be important to escape is due to

COLE, K. D. (1966), Theory of some quiet magnetospheric phenomena related to the geomagnetic tail, *Nature* **211**, 1385–1387.

The direct escape of ions from high geomagnetic latitudes was proposed by

NICOLET, M. (1961), Helium, an important constituent in the lower exosphere, *J. Geophys. Res.* **66**, 2263–2264.

This mechanism is the ion analog of Jeans escape, made possible by the down-wind opening of geomagnetic field lines. An additional mechanism, the *polar wind*, involves the existence of two or more positive ions and a resulting electrostatic acceleration, to supersonic speeds at high altitudes, once escape begins. See

BANKS, P. M. and KOCKARTS, G. (1973), “Aeronomy” Part B, Academic Press, New York, pp. 206–235,

for a summary of the physics and references to the original literature.

Solar wind sweeping of newly created charges from the upper region of an unmagnetized planet is treated by

MICHEL, F. C. (1971), Solar-wind induced mass loss from magnetic field-free planets, *Planet. Space Sci.* **19**, 1580–1583.

The upward splash of O atoms from the atmosphere as a result of O<sup>+</sup> auroral-type bombardment is a suggestion of

TORR, M. R.; WALKER, J. C. G.; and TORR, D. G. (1974), Escape of fast oxygen from the atmosphere during geomagnetic storms, *J. Geophys. Res.* **79**, 5267–5271.

Chemical reactions that lead to energetic atoms that may escape are listed by

SZE, N. D. and McELROY, M. B. (1975), Some problems in Venus’ aeronomy, *Planet. Space Sci.* **23**, 763–786.

The concept of a limiting flow for H in the thermosphere was implicit in the work on atmospheric diffusion being pursued actively around 1960; see

MANGE, P. (1961), Diffusion in the thermosphere, *Ann. Géophys.* **17**, 63–77 (reprinted as “Symposium d’Aéronomie,” Intern. Assoc. Geomagn. Aeron. Symposium No. 1).

The concept, however, was clearly formulated and applied to a number of escape problems in

HUNTEST, D. M. (1973), The escape of light gases from planetary atmospheres, *J. Atmos. Sci.* **30**, 1481–1494.

The discussion of nonthermal escape mechanisms is based on

HUNTEST, D. M. (1982), Thermal and nonthermal escape mechanisms for terrestrial bodies, *Planet. Space Sci.* **30**, 773–783.

“Rayleigh diffusion” was first treated by

RAYLEIGH, Lord (1895), Theoretical considerations respecting the separation of gasses by diffusion and similar processes, *Phil. Mag.* **42**, 493–498.

Application to Mars is discussed by

MCELROY, M. B. and YUNG, Y. L. (1976), Oxygen isotopes in the Martian atmosphere: implications for the evolution of volatiles, *Planet. Space Sci.* **24**, 1107–1113.

MCELROY, M. B.; KONG, T. Y; and YUNG, Y. L. (1977), Photochemistry and evolution of Mars’ atmosphere: A Viking perspective, *J. Geophys. Res.* **82**, 4379–4388.

The parameter  $R$  used in these papers is equivalent to  $1/(1+y)$ .

### Section 7.3.2 Earth’s Loss of H and He

Direct determinations of Jeans escape of H from satellite data and the implied loss from other mechanisms are discussed by

BERTAUX, J. L. (1976), Observations of hydrogen in the upper atmosphere, *J. Atmos. Terr. Phys.* **38**, 821–827,

HUNTEST, D. M. and DONAHUE, T. M. (1976), Hydrogen loss from the terrestrial planets, *Ann. Rev. Earth Planet Sci.* **4**, 265–292.

BREIG, E. L.; HANSON, W. B.; HOFFMAN, J. H., and KAYSER, D. C. (1976). In situ measurements of hydrogen concentration and flux between 160 and 300 km in the thermosphere, *J. Geophys. Res.* **81**, 2677–2686.

The difficulties of accounting for He escape by the Jeans formula are treated in

MACDONALD, G. J. F. (1963), The escape of helium from the Earth’s atmosphere, *Rev. Geophys.* **1**, 305–349,

and an update is contained in

HUNTEST, D. M. (1973), op. cit.

### Section 7.3.3 Venus’ Dual Exosphere and Escape

Analysis of the Mariner 5 data in terms of one mass (H) and two temperatures (as well as one temperature and two masses, D or H<sub>2</sub>) is due to

WALLACE, L. (1969), Analysis of the Lyman-Alpha observations of Venus made from Mariner 5, *J. Geophys. Res.* **74**, 115–131.

Of the two-mass solutions, deuterium was subsequently eliminated by a rocket-borne spectrometer flown by Wallace and his associates. And H<sub>2</sub> photodissociation (producing H with the H<sub>2</sub> scale height) is eliminated on grounds of continuity: The production rate of H would have to grossly exceed the rate at which it will diffuse to lower regions of the atmosphere and reassociate. The two-temperature model has been reanalyzed by

ANDERSON, D. E., JR. (1976), The Mariner 5 ultraviolet photometer experiment: Analysis of hydrogen Lyman alpha data, *J. Geophys. Res.* **81**, 1213–1216.

The analysis of Mariner 10 data is given in

TAKACS, P. Z.; BROADFOOT, A. L.; SMITH, G. R.; and KUMAR, S. (1980), Mariner 10 observations of hydrogen Lyman alpha emission from the Venus exosphere: Evidence of complex structure, *Planet. Space Sci.* **28**, 687–701.

Analyses of Soviet Venera 9–12 observations are given by

- BERTAUX, J. L.; BLAMONT, J. E.; MARCELIN, M.; KURT, V. G.; ROMANOVA, N. N.; and SMIRNOV, A. S. (1978), Lyman alpha observations of Venera 9 and 10. I. The nonthermal hydrogen population in the exosphere of Venus, *Planet. Space Sci.* **26**, 817–831,  
 BERTAUX, J. L.; BLAMONT, J. E.; LEPINE, V. M.; KURT, V. G.; ROMANOVA, N. N.; and SMIRNOV, A. S. (1981), Venera 11 and Venera 12 observations of E. U. V. emissions from the upper atmosphere of Venus, *Planet. Space Sci.* **29**, 149–166,  
 BERTAUX, J. L.; LEPINE, V. M.; KURT, V. G.; and SMIRNOV, A. S. (1982), Altitude profile of H in the atmosphere of Venus from Lyman  $\alpha$  observations of Venera 11 and Venera 12 and origin of the hot exospheric component, *Icarus* **52**, 221–244.

As a source for the hot exospheric component, mechanism A (dissociative recombination) has been advocated by

- KUMAR, S. and HUNTER, D. M. (1974), Venus: An ionospheric model with an exospheric temperature of 350°K, *J. Geophys. Res.* **79**, 2529–2532,  
 SZE, N. D. and MCELROY, M. B. (1975) op. cit.

The H<sub>2</sub> abundance in the thermosphere is treated in

- KUMAR, S.; HUNTER, D. M.; and TAYLOR, H. A., Jr. (1981), H<sub>2</sub> abundance in the atmosphere of Venus, *Geophys. Res. Letts.* **8**, 237–240,  
 HARTLE, R. E. and TAYLOR, H. A., Jr. (1983), Identification of deuterium ions in the ionosphere of Venus, *Geophys. Res. Letts.* **10**, 965–968.

Mechanism B (charge exchange with a hot plasmasphere) was proposed with a tentative model exosphere in

- CHAMBERLAIN, J. W. (1977), Charge exchange in a planetary corona: Its effect on the distribution and escape of hydrogen, *J. Geophys. Res.* **82**, 1–9,

and developed more thoroughly by

- HODGES, R. R., Jr., and TINSLEY, B. A. (1981), Charge exchange in the Venus ionosphere as the source of the hot exospheric hydrogen, *J. Geophys. Res.* **86**, 7649–7656,  
 HODGES, R. R., Jr., and TINSLEY, B. A. (1982), The influence of thermospheric winds on exospheric hydrogen on Venus, *Icarus* **51**, 440–447.

Mechanism C (momentum transfer) was proposed by

- MCELROY, M. B.; PRATHER, M. J.; and RODRIGUEZ, J. M. (1982), Escape of hydrogen from Venus, *Science* **215**, 1614–1615.

The most thorough treatment of exospheric hydrogen on Venus is

- RODRIGUEZ, J. M.; PRATHER, M. J.; and MCELROY, M. B. (1984), Hydrogen on Venus: Exospheric distribution and escape, *Planet. Space Sci.* **32**, 1235–1255.

The day- and night-side concentrations of H were derived by

- BRINTON, H. C.; TAYLOR, H. A., Jr.,; NIEMANN, H. B.; MAYR, H. G.; NAGY, A. F.; CRAVENS, T. E.; and STROBEL, D. F. (1980), Venus nighttime hydrogen bulge, *Geophys. Res. Lett.* **7**, 865–868,

from *in-situ* measurements of [H<sup>+</sup>], [O<sup>+</sup>], [O], and [CO<sub>2</sub>]. The analysis uses a slight refinement of the charge-exchange equilibrium

$$[H] \approx (8/9) [O] [H^+]/[O^+]$$

used extensively in studies of ionization in gaseous nebulae and thermospheres:

- CHAMBERLAIN, J. W. (1957), Excitation in nebulae: Charge transfer and the Cassiopeia radio source, *Astroph. J.* **123**, 390–398.

The production of hot O atoms and their escape are treated by

- NAGY, A. F.; CRAVENS, T. E.; YEE, J.-H.; and STEWART, A. I. F. (1981), Hot oxygen atoms in the upper atmosphere of Venus, *Geophys. Res. Lett.* **8**, 629–632,  
 McELROY, M. B.; PRATHER, M. J.; and RODRIGUEZ, J. M. (1982), Loss of oxygen from Venus, *Geophys. Res. Lett.* **9**, 649–651.

#### Section 7.3.4 Mars' Hydrogen and Oxygen Escape

A detailed analysis of data from three Mariners is given by

- ANDERSON, D. E., JR. (1974), Mariner 6, 7, and 9 ultraviolet spectrometer experiment: Analysis of hydrogen Lyman alpha data, *J. Geophys. Res.* **79**, 1513–1518.

The Viking composition measurements are given by

- NIER, A. O. and McELROY, M. B. (1977), Composition and structure of Mars' upper atmosphere: Results from the neutral mass spectrometers on Viking 1 and 2, *J. Geophys. Res.* **82**, 4341–4349.

The near equivalence of the escape losses of O and H<sub>2</sub> was first noted by

- McELROY, M. B. (1972), Mars: An evolving atmosphere, *Science* **175**, 443–445.

Further investigation by

- LIU, S. C. and DONAHUE, T. M. (1976), The regulation of hydrogen and oxygen escape from Mars, *Icarus* **28**, 231–246,

demonstrated that the HO<sub>x</sub> photochemistry of the lower atmosphere keeps the relative abundances in the correct ratio for the oxygen and hydrogen escape to remain matched. The <sup>18</sup>O/<sup>16</sup>O abundance ratio and its increase with time for nonthermal escape has been discussed by

- McELROY, M. B. and YUNG, Y. L. (1976), Oxygen isotopes in the Martian atmosphere: Implications for the evolution of volatiles, *Planet. Space Sci.* **24**, 1107–1113.

#### Section 7.3.5 Escape from Titan and Io

Non-thermal escape of H and N from Titan has been evaluated by

- STROBEL, D. F. (1982), Chemistry and evolution of Titan's atmosphere, *Planet. Space Sci.* **30**, 839–848.

Comprehensive papers on the aeronomy of Titan, and on Titan as a whole, are

- YUNG, Y. L.; ALLEN, M.; and PINTO, J. P. (1984), Photochemistry of the atmosphere of Titan: comparison between theory and observations, *Astrophys. J. Suppl.* **55**, 465–506,  
 HUNTER, D. M.; TOMASKO, M. G.; FLASAR, F. M.; SAMUELSON, R. E.; STROBEL, D. F.; and STEVENSON, D. J. (1984), Titan, in "Saturn" (T. Gehrels and M. S. Matthews, eds.), pp. 671–759. Univ. Arizona Press, Tucson, Arizona.

Escape mechanisms of Io are treated in

- KUMAR, S. (1982), Photochemistry of SO<sub>2</sub> in the atmosphere of Io and implications on atmospheric escape, *Planet. Space Sci.* **30**, 773–783,  
 SMYTH, W. H. and SHEMANSKY, D. E. (1983), Escape and ionization of atomic oxygen from Io *Astrophys. J.* **271**, 865–875.

Loss by sputtering and elastic collisions in Io's exosphere is treated and advocated in

- SUMMERS, M. E.; YUNG, Y. L.; and HAFF, P. K. (1983), A two-stage mechanism for escape of Na and K from Io, *Nature* **304**, 710–712,  
 CHENG, A. F. (1984), Escape of sulfur and oxygen from Io, *J. Geophys. Res.* **89**, 3939–3944,  
 KUMAR, S. (1984), Sulfur and oxygen escape from Io and a lower limit to atmospheric SO<sub>2</sub> at Voyager 1 encounter, *J. Geophys. Res.* **89**, 7399–7406.  
 SIEVEKA, E. M. and JOHNSON, R. E. (1984), Ejection of atoms and molecules from Io by plasma-ion impact, *Astrophys. J.* **287**, 418–426.

The mutual drag forces were introduced by

- HUNTER, D. M. (1985), Blowoff of an atmosphere and possible application to Io, *Geophys. Res. Lett.* **12**, 271-273.

Reviews are also cited in Sections 1.9.3 and 1.9.4. See also

- HUNTER, D. M.; PEPIN, P. O.; and WALKER, J. C. G. (1986), Mass fractionation in hydrodynamic escape, *Icarus* (submitted).

#### Section 7.3.6 Atmospheric Blowoff.

The idea of blowoff was discussed by

- SHKLOVSKII, I. S. (1951), On the possibility of explaining the difference in chemical composition of the Earth and Sun by thermal dissipation of light gases (in Russian), *Astron. Zh.* **28**, 234-243,

- OPIK, E. J. (1963), Selective escape of gases, *Geophys. J. Roy. Astron. Soc.* **7**, 490-509.

The treatment in the text is based on

- HUNTER, D. M. et al. (1986), *op. cit.*

Blowoff driven by accretional heat is discussed by

- WALKER, J. C. G. (1982), The earliest atmosphere of the Earth, *Precamb. Res.* **17**, 141-171.

An idealized model for the rapid escape of a hydrogen thermosphere has been developed by

- WATSON, A. J.; DONAHUE, T. M.; and WALKER, J. C. G. (1981), The dynamics of a rapidly escaping atmosphere, *Icarus* **48**, 150-166,

based on the equations of continuity, motion, and heat conduction as introduced for the solar wind by

- CHAMBERLAIN, J. W. (1961), Interplanetary gas. III. A hydrodynamic model of the corona, *Astrophys. J.* **133**, 675-687.

The implications of hydrodynamic escape for the loss of water from Venus are discussed by

- KASTING, J. F. and POLLACK, J. B. (1983), Loss of water from Venus. I. Hydrodynamic escape of hydrogen, *Icarus* **53**, 479-508,

- KUMAR, S.; HUNTER, D. M.; and POLLACK, J. B. (1983), Nonthermal escape of hydrogen and deuterium from Venus and implications for loss of water, *Icarus* **55**, 369-389.

Also, see Section 7.4.1.

A substantial CH<sub>4</sub> atmosphere on Pluto appears at first sight to be unstable against blowoff, but the difficulty disappears when the thermospheric temperature is treated realistically:

- HUNTER, D. M. and WATSON, A. J. (1982), Stability of Pluto's atmosphere, *Icarus* **51**, 665-667.

#### Section 7.4.1 Development of Atmospheres of the Terrestrial Planets

The origin and early chemical evolution of the atmospheres of the Earth and other terrestrial planets have been reviewed by

- WALKER, J. C. G. (1977), "Evolution of the Atmosphere," MacMillan, New York,  
POLLACK, J. B. and YUNG, Y. L. (1980), Origin and evolution of planetary atmospheres, *Ann. Rev. Earth Planet. Sci.* **8**, 425-487,

- POLLACK, J. B. and BLACK, D. C. (1982), Noble gases in planetary atmospheres: Implications for the origin and evolution of atmospheres, *Icarus* **51**, 169-198,

- WALKER, J. C. G. (1982), The earliest atmosphere of the Earth, *Precambrian Res.* **17**, 147-171,

- PRINN, R. G. (1982), Origin and evolution of planetary atmospheres: An introduction to the problem, *Planet. Space Sci.* **30**, 741-753.

LEWIS, J. S. and PRINN, R. G. (1984), "Planets and Their Atmospheres: Origin and Evolution," Academic Press, New York.

Computer simulations of the development of the Earth's atmospheric composition, albedo, greenhouse effect, and surface temperature have been made by

HART, M. H. (1978), The evolution of the atmosphere of the Earth, *Icarus* **33**, 23–39.

An analysis of the atmosphere of Saturn's massive satellite Titan is given in

HUNTER, D. M. (1977), Titan's atmosphere and surface, in "Planetary Satellites," (J. A. Burns, ed.), pp. 420–437. University of Arizona Press, Tucson.

High resolution measurements of the H<sub>2</sub> absorption by Titan, with references to the earlier observations, are reported by

MUNCH, G.; TRAUGER, J. T.; and ROESLER, F. L. (1977), A search for the H<sub>2</sub> (3, 0) S1 line in the spectrum of Titan, *Astrophys. J.* **216**, 963–966.

The problems associated with estimating the escape flux from the surface of Mercury or the moon are summarized in

SHEMANSKY, D. E. and BROADFOOT, A. L. (1977), Interaction of the surfaces of the moon and Mercury with their exospheric atmospheres, *Rev. Geophys. Space Phys.* **15**, 491–500.

The various factors contributing to the low abundance of atmospheric gases on Mars are reviewed and weighed in importance in

ANDERS, E. and OWEN, T. (1977), Mars and Earth: Origin and abundance of volatiles, *Science* **198**, 453–465.

A Martian atmosphere composed primarily of CO<sub>2</sub> and capable of supporting liquid water on the surface has been treated by

POLLACK, J. B. (1979), Climatic change on the terrestrial planets, *Icarus* **37**, 479–553,  
CESS, R. D.; RAMANATHAN, V.; and OWEN, T. (1980), The Martian paleoclimate and enhanced atmospheric carbon dioxide, *Icarus* **41**, 159–165,

HOFFERT, M. I.; CALLEGARI, A. J.; HSIEH, C. T.; and ZIEGLER, W. (1981), Liquid water on Mars: An energy balance climate model for CO<sub>2</sub>/H<sub>2</sub>O atmospheres, *Icarus* **47**, 112–129.

The D/H ratio on Venus has been measured and its implications discussed by

DONAHUE, T. M.; HOFFMAN, J. H.; HODGES, R. R., Jr.; and WATSON, A. J. (1982), Venus was wet: A measurement of the ratio of deuterium to hydrogen, *Science* **216**, 630–633,

HARTLE, R. E., and TAYLOR, H. A., Jr. (1983), Identification of deuterium ions in the ionosphere of Venus, *Geophys. Res. Lett.* **10**, 965–968.

The concept of the runaway greenhouse for Venus is due to

INGERSOLL, A. P. (1969), The runaway greenhouse: A history of water on Venus, *J. Atmos. Sci.* **26**, 1191–1198.

Additional discussion is given in

RASOOL, S. I. and DE BERGH, C. (1970), The runaway greenhouse and the accumulation of CO<sub>2</sub> in the Venus atmosphere, *Nature* **226**, 1037–1039.

POLLACK, J. B. (1971), A nongray calculation of the runaway greenhouse: Implications for Venus' past and present, *Icarus* **14**, 295–306.

LINDZEN, R. S.; HOU, A. Y.; and FARRELL, B. F. (1982), the role of convective model choice in calculating the climate impact of doubling CO<sub>2</sub>, *J. Atmos. Sci.* **39**, 1189–1205,

KASTING, J. F.; POLLACK, J. B.; and ACKERMAN, T. P. (1984), Response of Earth's atmosphere to increases in solar flux and implications for loss of water from Venus, *Icarus* **57**, 335–355.

The basic idea behind the runaway greenhouse—namely, the radiative-equilibrium temperature near the top of the Earth's troposphere cannot be so high that water vapor is unsaturated—was anticipated in the classic work of

SIMPSON, G. C. (1928), Further studies in terrestrial radiation, *Mem. Roy. Meteorol. Soc.* **3**, No. 21, 1–26.

#### Section 7.4.2 Climate Variations

The problem with the early sun being poor in luminosity and Earth's temperature being compensated by an enhanced greenhouse is treated by

ZAHNLE, K. J. and WALKER, J. C. G. (1982), The evolution of solar ultraviolet luminosity, *Rev. Geophys. Space Phys.* **20**, 280–292,

EDDY, J. A.; GILLILAND, R. L.; and HOYT, D. V. (1982), Changes in the solar constant and climatic effects, *Nature* **300**, 689–693,

OWEN, T.; CESS, R. D.; and RAMANATHAN, V. (1979), Enhanced CO<sub>2</sub> greenhouse to compensate for reduced solar luminosity on early Earth, *Nature* **277**, 640–642,

VISCONTI, G. (1982), Radiative-photochemical models of the primitive terrestrial atmosphere, *Planet. Space Sci.* **30**, 785–793,

ROSSOW, W. B.; HENDERSON-SELLERS, A.; and WEINREICH, S. K. (1982), Cloud feedback: A stabilizing effect for the early Earth, *Science* **217**, 1245–1247.

A survey of the effects resulting from the passage of the solar system through an interstellar cloud of gas and "dust" is given by

TALBOT, R. J., Jr. and NEWMAN, M. J. (1977), Encounters between stars and dense interstellar clouds, *Astrophys. J. Suppl.* **34**, 295–308.

The relation between solar ultraviolet emission and stratospheric ozone is treated in

CHAMBERLAIN, J. W. (1982), The influence of solar ultraviolet variability on climate, *Planet. Space Sci.* **30**, 147–150.

The possible relationship of sunspot activity with climate is developed from historical records by

EDDY, J. A. (1976), The Maunder minimum, *Science* **192**, 1189–1202,

and is developed from correlations of <sup>14</sup>C production with solar magnetic activity on the one hand and with climate on the other by

SUESS, H. E. (1968), Climate changes, solar activity, and the cosmic-ray production rate of natural radiocarbon, *Meteor. Monog.* **8**, 146–150.

Geomagnetic correlations with climate to 1.2 million years have been reported by

WOLLIN, G.; ERICSON, D. B.; and RYAN, W. B. F. (1971), Variations in magnetic intensity and climatic changes, *Nature* **232**, 549–551.

A speculative mechanism relating long-term magnetic activity to climate, through effects of cosmic rays on the stratosphere, was proposed by

CHAMBERLAIN, J. W. (1977), A mechanism for inducing climatic variations through the stratosphere: Screening of cosmic rays by solar and terrestrial magnetic fields, *J. Atmos. Sci.* **34**, 737–743.

The depletion of mesospheric ozone during a solar proton event has been studied by

THOMAS, R. J. et al. (1983), Mesospheric ozone depletion during the solar proton event of July 13, 1982. Part I. Measurement, *Geophys. Res. Lett.* **10**, 253–255,

SOLomon, S.; REID, G. C.; RUSCH, D. W.; and THOMAS R. J. (1983), Mesospheric ozone depletion during the solar proton event of July 13, 1982. Part II. Comparison between theory and measurements, *Geophys. Res. Lett.* **10**, 257–260.

The astronomical theory of ice ages was first suggested in

CROLL, J. (1864), On the physical cause of the change of climate during geological epochs, *Philos. Mag.* **28**, 121–137;

the earliest thorough exposition of the theory is

MILANKOVITCH, M. (1930), Mathematische Klimalehre und astronomische Theorie der Klimaschwankungen, *Handbuch der Klimatologie*, I. Teil A, W. Koeppen and R. Geiger, eds., Gebrueder Borntraeger Berlin.

Interest in the theory was revived by

HAYS, J. D.; IMBRIE, J.; and SHACKLETON, N. J. (1976), Variations in the Earth's orbit: Pacemaker of the ice ages, *Science* **94**, 1121–1132.

Further evidence for these climate cycles is summarized in

CESS, R. D. and WRONKA, J. C. (1979), Ice ages and the Milankovitch theory: A study of interactive climate feedback mechanisms, *Tellus* **31**, 185–192,

IMBRIE, J. and IMBRIE, J. Z. (1980), Modeling the climatic response to orbital variations, *Science* **207**, 943–953,

HELD, I. M. (1982), Climate models and the astronomical theory of the ice ages, *Icarus* **50**, 449–461,

KERR, R. A. (1983), Precisely measuring the past million years, *Science* **221**, 1041,

BERGER, A.; IMBRIE, J.; HAYS, J.; KUKLA, G.; and SALTZMAN, B., eds. (1984), "Milankovitch and Climate: Understanding the Response to Astronomical Forcing," NATO Advanced Science Institute Series, Ser. C, Vol. 126, Pts. 1 and 2, D. Reidel Publ., Dordrecht.

Application of the Milankovitch theory to Mars has been made by

TOON, O. B.; POLLACK, J. B.; WARD, W.; BURNS, J.; and BILSKI, K. (1980), The astronomical theory of climate change on Mars, *Icarus* **44**, 552–607,

CHRISTIE-BLICK, N. (1982), Pre-pleistocene glaciation on Earth: Implications for climatic history of Mars, *Icarus* **50**, 423–443,

POLLACK, J. B. and TOON, O. B. (1982), Quasi-periodic climate changes on Mars: A review, *Icarus* **50**, 259–287.

The analogy of climate fluctuations with Brownian motion is due to

HASSELMANN, K. (1976), Stochastic climate models, Part 1. Theory, *Tellus* **28**, 473–485.

El Niño, with emphasis on the great 1982–1983 event, is reviewed in a series of three papers:

CANE, M. A. (1983), Oceanographic events during El Niño, *Science* **222**, 1189–1195,

RASMUSSEN, E. M. and WALLACE, J. M. (1983), Meteorological aspects of the El Niño/Southern Oscillation, *Science* **222**, 1195–1202,

BARBER, R. T., and CHAVEZ, F. P. (1983), Biological consequences of El Niño, *Science* **222**, 1203–1210.

The energy budget of the Earth and climatological effects of a change in it are discussed by

BUDYKO, M. I. (1969), The effect of solar radiation variations on the climate of the Earth, *Tellus* **21**, 611–619,

SELLERS, W. D. (1969), A global climate model based on the energy balance of the Earth-Atmosphere system, *J. Appl. Meteorol.* **8**, 392–400,

NORTH, G. (1975), Analytical solution to a simple climate model with diffuse heat transport, *J. Atmos. Sci.* **32**, 1301–1307,

LINDZEN, R. S., and FARRELL, B. (1977), Some realistic modifications of simple climate models, *J. Atmos. Sci.* **34**, 1487–1501,

CESS, R. D. (1976), Climate change: An appraisal of atmospheric feedback mechanisms employing zonal climatology, *J. Atmos. Sci.* **33**, 1831–1843,

- LIAN, M. S., and CESS, R. D. (1977), Energy balance climate models: A reappraisal of ice-albedo feedback, *J. Atmos. Sci.* **34**, 1058–1062,
- CESS, R. D., and RAMANATHAN, V. (1978), Averaging of infrared cloud opacities for climate modeling, *J. Atmos. Sci.* **35**, 919–922,
- SCHNEIDER, S. H.; WASHINGTON, W. M.; and CHERVIN, R. M. (1978), Cloudiness as a climatic feedback mechanism: Effects on cloud amounts of prescribed global and regional surface temperature changes in the NCAR GCM, *J. Atmos. Sci.* **35**, 2207–2221,
- WETHERALD, R. T. and MANABE, S. (1980), Cloud cover and climate sensitivity, *J. Atmos. Sci.* **37**, 1485–1510,
- NORTH, G. R.; CAHALAN, R. F.; and COAKLEY, J. A., Jr. (1981), Energy balance climate models, *Rev. Geophys. Space Phys.* **19**, 91–121,
- STEPHENS, G. L. and WEBSTER, P. J. (1981), Clouds and climate: Sensitivity of simple systems, *J. Atmos. Sci.* **38**, 235–247,
- POTTER, G. L. et al. (1981), Climate change and cloud feedback: The possible radiative effects of latitudinal redistribution, *J. Atmos. Sci.* **38**, 489–493,
- HANSEN, J. et al. (1983), Efficient three dimensional global models for climate studies: Models I and II, *Mon. Weather Rev.* **111**, 609–662,
- ROBOCK, A. (1983), Ice and snow feedbacks and the latitudinal and seasonal distribution of climate sensitivity, *J. Atmos. Sci.* **40**, 986–997.

A book that contains a number of pertinent articles is

- HANSEN, J. E. and TAKAHASHI, T., eds. (1984), "Climate Processes and Climate Sensitivity," American Geophysical Union, Washington, D. C.

The asteroid impact theory of extinctions is developed in

- ALVAREZ, L. W.; ALVAREZ, W.; ASARO, F.; and MICHEL, H. V. (1980), Extraterrestrial cause for the Cretaceous-Tertiary extinction, *Science* **208**, 1095–1108,
- ALVAREZ, L. W. (1983), Experimental evidence that an asteroid impact led to the extinction of many species 65 million years ago, *Proc. Natl. Acad. Sci.* **80**, 627–642.

The 26-Myr periodicity in the fossil record of extinctions was proposed by

- RAUP, D. M. and SEPkoski, J. J. (1984), Periodicity of extinctions in the geologic past, *Proc. Natl. Sci.* **81**, 801–805.

This study led to the hypothesis of an unseen solar companion, travelling in a moderately eccentric orbit that brings it into the Oort cloud of comets were it perturbs the cometary orbits, being advocated by

- DAVIS, M.; HUT, P.; and MULLER, R. A. (1984), Extinction of species by periodic comet showers, *Nature* **308**, 715–717,

and independently and simultaneously, by

- WHITMIRE, D. P. and JACKSON, A. A. (1984), Are periodic mass extinctions driven by a distant solar companion? *Nature* **308**, 713–715.

Nevertheless, serious challenges have been leveled at both the reality of a periodicity in the extinctions and the capability of a companion "Star X" to produce the required perturbations on the comet orbits. See the news item by

- KERR, R. A. (1985) Periodic extinctions and impacts challenged, *Science* **227**, 1451–1453.

Climate changes accompanying a major nuclear war are treated in

- PETERSON, J., ed., (1983), "The Aftermath: The Human and Ecological Consequences of Nuclear War," Pantheon (reprinted from *Ambio*, **2**, Nos. 2–3, 1982).

TURCO, P.; TOON, O. B.; ACKERMAN, T. P.; POLLACK, J. B.; and SAGAN, C. (1983), Nuclear winter: Global consequences of multiple nuclear explosions, *Science* **222**, 1283-1292, EHRLICH, P. R. et al. (1983), Long-term biological consequences of nuclear war, *Science* **222**, 1293-1300.

The principal source of data for nuclear explosions is

GLASSTONE, S. and DOLAN, P. J., eds., (1977), "The Effects of Nuclear Weapons," U. S. Government Printing Office, Washington, D. C.

The possible role of volcanic clouds in affecting climate through changes in albedo, opacity, or both are discussed in a series of papers introduced by

POLLACK, J. B. et al. (1983), The El Chichon volcanic cloud: An introduction, *Geophys Res. Lett.* **10**, 989-992.

Also see

KRUEGER, A. J. (1983), Sighting of El Chichon sulfur dioxide clouds with the Nimbus 7 total ozone mapping spectrometer, *Science* **220**, 1377-1379.

The development of Earth's oxygen and ozone is treated in

KASTING, J. F.; LIU, S. C.; and DONAHUE, T. M. (1979), Oxygen levels in the prebiological atmosphere, *J. Geophys. Res.* **84**, 3097-3107,

KASTING, J. F. and DONAHUE, T. M. (1980), The evolution of atmospheric ozone, *J. Geophys. Res.* **85**, 3255-3263.

Models of carbon dioxide increases have been reported in

CLARK, W. C., ed., (1982), "Carbon Dioxide Review: 1982," Oxford Univ. Press, London.

HAMEED, S.; CESS, R. D.; and HOGAN, J. S. (1980), Response of the global climate to changes in atmospheric chemical composition due to fossil fuel burning, *J. Geophys. Res.* **85**, 7537-7545,

HANSEN, J. et al. (1981), Climate impact of increasing atmospheric carbon dioxide, *Science* **213**, 957-966,

MANABE, S. (1983), Carbon dioxide and climatic change, *Adv. Geophys.* **25**, 39-82, E. P. A. (1983), "Can We Delay a Greenhouse Warming?" U. S. Environmental Protection Agency, Washington, D. C.,

NATIONAL RESEARCH COUNCIL (1983), "Changing Climate," National Academy Press, Washington, D. C.,

Analyses of the exchange of CO<sub>2</sub> between the atmosphere, oceans, and biomass are given in

WOODWELL, G. M.; WHITTAKER, R. H.; REINERS, W. A.; LIKENS, G. E.; DELWICHE, C. C.; and BOTKIN, D. B. (1978), The biota and the world carbon budget, *Science* **199**, 141-146, STUIVER, M. (1978), Atmospheric carbon dioxide and carbon reservoir changes, *Science* **199**, 253-258,

MCELROY, M. B. (1983), Marine biology: Controls on atmospheric CO<sub>2</sub> and the climate, *Nature* **302**, 328-329,

WOODWELL, G. M. et al. (1983), Global deforestation: Contribution to atmospheric carbon dioxide, *Science* **222**, 1081-1086.

The CO<sub>2</sub> increases have been studied at the South Pole and at Mauna Loa; the results from the latter site are given in

KEELING, C. D. et al. (1976), Atmospheric carbon dioxide variations at Mauna Loa Observatory, Hawaii, *Tellus* **28**, 538-551.

The greenhouse effect of minor constituents has been treated in

YANG, W. C.; YUNG, Y. L.; LACIS, A. A.; MO, T.; and HANSEN, J. E. (1976). Greenhouse effects due to man-made perturbations of trace gases, *Science* **194**, 685-690,

LACIS, A.; HANSEN, J.; LEE, P.; MITCHELL, T.; and LEBEDEFF, S. (1981), Greenhouse effect of trace gases, 1970-1980. *Geophys. Res. Letts.* **8**, 1035-1038.

Recent changes in sea level are reviewed by

GORNITZ, V.; LEBEDEFF, S.; and HANSEN, J. (1982), Global sea level trend in the past century, *Science* **215**, 1611-1614,

ETKINS, R. and EPSTEIN, E. S. (1982), The rise of global mean sea level as an indication of climate change, *Science* **215**, 287-289,

ZWALLY, H. J.; PARKINSON, C. L.; and COMISO, J. C. (1983), Variability of Antarctic sea ice and changes in carbon dioxide, *Science* **220**, 1005-1012.

The U. S. Department of Energy has published (1985) four so-called "State-of-the-Art" volumes on different aspects of the carbon dioxide problem. They are:

"Detecting the Climatic Effects of Increasing Carbon Dioxide" (DOE/ER-0235),

"Projecting the Climatic Effects of Increasing Carbon Dioxide" (DOE/ER-0237),

"Atmospheric Carbon Dioxide and the Global Carbon Cycle" (DOE/ER-0238), and

"Direct Effects of Increasing Carbon Dioxide on Vegetation" (DOE/ER-0239).

These reports are available in many libraries or can be obtained from the National Technical Information Service, U. S. Department of Commerce, Springfield, VA 22161. Two companion reports are also being published (1986):

"Characterization of Information Requirements for Studies of CO<sub>2</sub> Effects: Water Resources, Agriculture, Fisheries, Forests, and Human Health," and

"Glaciers, Ice Sheets, and Sea Level: Effects of a CO<sub>2</sub>-Induced Climatic Change."

#### Section 7.4.3 Climatic Conditions Hospitable to Emerging Intelligence

A paper that cautions against too much exuberance over the prospects of finding extraterrestrial life is

TIPLER, F. J. (1981), Extraterrestrial beings do not exist, *Phys. Today*, April, p. 9,

and it is followed by a vigorous debate in the March 1982 issue of *Physics Today*. Additional arguments questioning the universal development or survivability of life are given by

ORNSTEIN, L. (1982), A biologist looks at the numbers, *Phys. Today*, March, p. 27.

CHAMBERLAIN, J. W. (1978), The geophysical importance of searching for intelligent life in the Galaxy, *EOS*, December, p. 900.

The argument that a government would not likely fund a SETI project that required 10,000 yr for a response is developed by

BATES, D. R. (1978), On making radio contact with extraterrestrial civilizations, *Astroph. Space Sci.* **55**, 7-13.

#### Section 7.4.4 Pollution

Tropospheric pollution by automobile exhaust and industrial sources, its photochemistry and toxicity, and the associated ecological problems are thoroughly surveyed in

National Academy of Sciences (1977), "Ozone and other photochemical oxidants," N. A. S., Washington, D. C. 20418.

National Academy of Sciences (1977), "Nitrogen Oxides," N. A. S., Washington D. C. 20418.

The wide-range importance of OH as a cleansing agent was noted by

LEVY, H. (1972), Photochemistry of the lower troposphere, *Planet. Space Sci.* **20**, 919-935, and future implications have been examined in a preliminary way by

CHAMEIDES, W. L.; LIU, S. C.; and CICERONE, R. J. (1977), Possible variations in atmospheric methane, *J. Geophys. Res.* **82**, 1795-1798,

SZE, N. D. (1977), Anthropogenic CO emissions: Implications for the atmospheric CO - OH-CH<sub>4</sub> cycle, *Science* **195**, 673-675,

- LOGAN, J. A.; PRATHER, M. J.; WOFSY, S. C.; and McELROY, M. B. (1981), Tropospheric chemistry: A global perspective, *J. Geophys. Res.* **86**, 7210–7254,  
 KHALIL, M. A. K. and RASMUSSEN, R. A. (1984), Carbon monoxide in the Earth's atmosphere: Increasing trend, *Science* **224**, 54–56.

A vast measurement program of trace gases and aerosols was called Project Gametag. A dozen papers on the project are introduced by

- DAVIS, D. D. (1980), Project Gametag: An overview, *J. Geophys. Res.* **85**, 7285–7292.

The definitive compendium of atmospheric pollutants is

- GRAEDEL, T. E. (1978), "Chemical Compounds in the Atmosphere," Academic Press, New York.

An excellent, thorough review of halogens is

- CICERONE, R. J. (1981), Halogens in the atmosphere, *Rev. Geophys. Space Phys.* **19**, 123–139.

Acid rain is the subject of an NAS/NRC report,

- NATIONAL RESEARCH COUNCIL (1983), "Acid Deposition: Atmospheric Processes in Eastern North America," National Academy of Sciences, Washington, D.C.

An independent report is

- CHAMBERLAIN, J.; FOLEY, H.; HAMMER, D.; MACDONALD, G.; ROTHAUS, O.; and RUDERMAN, M. (1985), "Acid Deposition," The MITRE Corporation, McLean, VA 22102, 450 pp + Appendices and References.

A report from the National Academy of Sciences' Board on Atmospheric Sciences and Climate is

- NATIONAL RESEARCH COUNCIL (1984), "Global Tropospheric Chemistry: A Plan for Action," National Academy of Sciences, Washington, D.C.

## PROBLEMS

**7.1 Jeans escape flux.** Write (7.1.3) with the velocity components expressed in spherical coordinates and derive (7.1.5).

**7.2 Ballistic partition function.** Starting with (7.1.33), change the velocity components to  $\mu$  and  $\psi$  and derive (7.1.34).

**7.3 Cone of acceptance for ballistic orbits.** From the conservation of angular momentum and energy, show that the maximum angle  $\theta_0(\psi)$  in the integral (7.1.39) is given by (7.1.35), where  $\mu_0 = \cos \theta_0$ .

**7.4 Asymptotic expansions of partition functions.** (a) From the exact integrals (7.1.34), (7.1.41), and (7.1.43), show that as  $\lambda \rightarrow 0$ ,

$$\zeta_{\text{bal}} \rightarrow \frac{2}{\pi^{1/2}} \frac{\lambda^{5/2}}{\lambda_c}, \quad \zeta_{\text{sat}} \rightarrow \frac{4}{3\pi^{1/2}} \lambda^{3/2} \quad \text{and} \quad \zeta_{\text{esc}} \rightarrow \frac{\lambda^2}{4\lambda_c^2} (1 + 2\lambda_c)$$

(b) Show that the integrated column density above  $r_1$ , when  $\lambda_1 \ll 1$  and in the absence of satellite particles, is

$$\mathcal{N}(\mu_1 = 1, \lambda_1) = N_c e^{-\lambda_c r_c} \left( \frac{(1 + 2\lambda_c)\lambda_1}{4\lambda_c} + \frac{2\lambda_1^{3/2}}{3\pi^{1/2}} \right)$$

**7.5 Orbital period.** (a) Show that the time spent by a ballistic particle in free flight above the exosphere is

$$\tau = \frac{2r_c\lambda_c}{U} \int_{\lambda_a}^{\lambda_c} \frac{d\lambda}{\lambda^2(h + \lambda - v_c\lambda^2/\lambda_c^2)^{1/2}}$$

where  $\lambda_a$  is the potential at the particle's apogee. (b) Evaluate the integral for an elliptical orbit when  $\lambda_c$  is at the perigee. Then show that for the special case of a circular orbit at  $r_c$  the orbital period is

$$\frac{2\pi r_c}{(GM/r_c)^{1/2}}$$

which is Kepler's harmonic law. (c) Compare the circular orbital period at  $1.05 R_E$  with the period of an orbit having an apogee at  $15 R_E$  and perigee at  $2 R_E$ .

**7.6 Integration limits for spectrum function.** Verify that if  $v_1 < v_2$  so that  $0 < v < v_1$ , the  $\lambda$  limits corresponding to (7.1.32) for ballistic particles are  $\lambda_{2-} < \lambda < \lambda_{2+}$ , where  $\lambda_{2\pm}$  are given by (7.1.74).

**7.7 Limiting flow.** Consider a planet with the radius and surface gravity of Earth. The major constituent is  $\text{CO}_2$  with trace amounts of hydrogen compounds that are completely dissociated near and above the homopause. The binary collision parameter is  $b_1 = 2 \times 10^{19} \text{ cm}^{-1} \text{ sec}^{-1}$ . Just below the homopause the eddy diffusion coefficient is  $K = 5 \times 10^7 \text{ cm}^2/\text{sec}$ ,  $D = K$ , and the mixing ratio is  $f_1(\text{H}) = 10^{-4}$ . Above the homopause  $K = 0$ . The temperature is everywhere constant at  $400^\circ$ . The gas-kinetic cross section is  $Q = 3 \times 10^{-15} \text{ cm}^2$  and the only loss mechanism is Jeans escape.

- (a) What is the H density at the exobase and what is the Jeans escape flux?
- (b) What is the ratio of the actual H scale height to the hydrostatic, diffusive-equilibrium scale height for H above the homopause?
- (c) Immediately below the homopause, what is the ratio of the actual H scale height to that of  $\text{CO}_2$ ?
- (d) Compute the limiting flow from (7.3.5),  $\Phi_l \approx b_1 f_1 / H$ , below the homopause and explain why it differs from  $\mathcal{F}_c$  found in part (a).

# *Appendix I*

## A TABLE OF PHYSICAL CONSTANTS

### Fundamental Constants

|   |  |
|---|--|
| Velocity of light   | $c = 2.998 \times 10^{10}$ cm/sec  |
| Gravitational constant  | $G = 6.670 \times 10^{-8}$ dyne cm <sup>2</sup> /gm <sup>2</sup>         |
| Planck's constant   | $h = 6.624 \times 10^{-27}$ erg sec                                      |
| Mass of unit atomic weight  | $M_0 = 1.66053 \times 10^{-24}$ gm                                       |
| Mass of hydrogen atom   | $M_H = 1.673 \times 10^{-24}$ gm   |
| Mass of electron  | $m = 9.1096 \times 10^{-28}$ gm  |
| Electronic charge   | $e = 4.8025 \times 10^{-10}$ esu<br>$= 1.602 \times 10^{-20}$ emu        |
| Avogadro's number   | $1/M_0 = 6.0222 \times 10^{23}$ molecule/mole                            |
| Loschmidt's number (gas density<br>at 273°K and 1 atmosphere<br>pressure) | $N_0 = 2.687 \times 10^{19}$ molecule/cm <sup>3</sup>                    |
| Density of air at STP   | $\rho_0 = 1.293 \times 10^{-3}$ gm/cm <sup>3</sup>                       |
| Standard atmosphere   | $p_0 = 1.013250 \times 10^6$ dyne/cm <sup>2</sup>                        |
| Boltzmann constant (gas constant<br>per atom)                             | $k = R_0 M_0 = 1.380 \times 10^{-16}$ erg/deg                            |
| Gas constant per mole   | $R_0 = k/M_0 = 1.987$ cal/deg mole<br>$= 8.314 \times 10^7$ erg/deg mole |
| Gas constant for mass $M$<br>(molecular wt. $\mu = M/M_0$ )               | $R = k/M = R_0/\mu$<br>$= 8.314 \times 10^7/\mu$ erg/deg gm              |

### Atomic and Radiation Constants

|                               |   |
|-------------------------------|---|
| Radius of first Bohr orbit    | $a_0 = 0.529 \times 10^{-8}$ cm                     |
| Area of first Bohr orbit      | $\pi a_0^2 = 0.880 \times 10^{-16}$ cm <sup>2</sup> |
| Rydberg constant for hydrogen | $R_H = 109,677.58$ cm <sup>-1</sup>                 |

|   |  |
|---|--|
| Rydberg constant for infinite mass                                | $R_\infty = 2\pi^2 me^4/ch^3 = 109,737.31 \text{ cm}^{-1}$   |
| Energy per unit wave number                                       | $hc = 1.986 \times 10^{-16} \text{ erg cm}$  |
| Integrated absorption coefficient<br>per atom for unit $f$ -value | $\pi e^2/mc = 2.647 \times 10^{-2} \text{ cm}^2/\text{sec}$<br>$\alpha = 2\pi e^2/hc = 7.297 \times 10^{-3}$ |
| Fine structure constant   |  |
| First radiation constant<br>(specific intensity, $\lambda$ units) | $c_1 = 2hc^2 = 1.191 \times 10^{-5} \text{ erg cm}^2/\text{sec sr}$  |
| Second radiation constant   | $c_2 = hc/k = 1.439 \text{ cm deg}$  |
| Wien displacement-law constant                                    | $\lambda_{\max} T = 0.2898 \text{ cm deg}$   |
| Stefan-Boltzmann constant   | $\sigma = 5.67 \times 10^{-5} \text{ erg/cm}^2 \text{ deg}^4 \text{ sec}$                                    |

## The Earth

|  |  |
|--|--|
| Radius (mean)                            | $R_E = 6.37 \times 10^8 \text{ cm}$              |
| Surface area                             | $4\pi R_E^2 = 5.10 \times 10^{18} \text{ cm}^2$  |
| Mass                                     | $\mathcal{M} = 5.98 \times 10^{27} \text{ gm}$   |
| Acceleration of gravity (at the surface) | $g = 9.807 \times 10^2 \text{ cm/sec}^2$         |
| Magnetic moment of the dipole            | $M = 8.1 \times 10^{25} \text{ G cm}^3$          |
| Velocity (mean) about the sun            | $= 3.0 \times 10^6 \text{ cm/sec}$               |
| Distance (mean) from sun                 | $1 \text{ AU} = 1.496 \times 10^{13} \text{ cm}$ |

## The Sun

|  |   |
|--|---|
| Radius (mean)  | $= 6.96 \times 10^{10} \text{ cm}$  |
| Surface area   | $= 6.09 \times 10^{22} \text{ cm}^2$  |
| Mass   | $= 1.99 \times 10^{33} \text{ gm}$  |
| Acceleration of gravity (at the surface)   | $= 2.740 \times 10^4 \text{ cm/sec}^2$  |
| Acceleration of gravity (at 1 AU from the sun)   | $= 0.593 \text{ cm/sec}^2$  |
| Magnitude, absolute photovisual  | $= +4.84$   |
| Magnitude, apparent photovisual  | $= -26.73$  |
| Effective temperature (total energy radiated is equivalent to a black body with $T = T_{\text{eff}}$ ) |   |
| Flux at sun's surface  | $T_{\text{eff}} = 5710^\circ\text{K}$<br>$= 6.25 \times 10^{10} \text{ erg/cm}^2 \text{ sec}$ |

## Conversion Factors

|                             |  |
|-----------------------------|--|
| 1 day                       | $= 8.64 \times 10^4 \text{ sec}$   |
| 1 year                      | $= 3.1557 \times 10^7 \text{ sec}$   |
| 1 electron volt             | $\varepsilon_0 = 1.602 \times 10^{-12} \text{ erg}$  |
|                             | $\varepsilon_0/hc = 8.067 \times 10^3 \text{ cm}^{-1}$   |
| 1 erg                       | $1/hc = 5.035 \times 10^{15} \text{ cm}^{-1}$  |
| 1 $\text{cm}^{-1}$ (kayser) | $1/\varepsilon_0 = 6.242 \times 10^{11} \text{ eV}$<br>$hc = 1.986 \times 10^{-16} \text{ erg}$<br>$hc/\varepsilon_0 = 1.2397 \times 10^{-4} \text{ eV}$ |

|                                       |  |
|---------------------------------------|--|
| 1 eV/molecule                         | = 23.053 kcal/mole   |
| Speed of 1 eV electron                | $(2\varepsilon_0/m)^{1/2} = 5.93 \times 10^7 \text{ cm/sec}$   |
| Speed of 1 eV proton                  | $(2\varepsilon_0/M_H)^{1/2} = 1.38 \times 10^6 \text{ cm/sec}$ |
| Wavelength equivalent of 1 eV         | $hc/\varepsilon_0 = 12,397 \times 10^{-8} \text{ cm}$          |
| Temperature associated with 1 eV      | $\varepsilon_0/k = 11,605^\circ\text{K}$                       |
| Thickness of dry atmosphere           | $\mathcal{N} = 2.15 \times 10^{25} \text{ molecule/cm}^2$      |
| 1 gm/cm <sup>2</sup> H <sub>2</sub> O | $\xi = 8.0 \times 10^5 \text{ atm-cm}$                         |
| 1 kiloton of TNT                      | $= 1245 \text{ atm-cm}$<br>$= 4.18 \times 10^{19} \text{ erg}$ |

## ***Appendix II***

### **PLANETARY CHARACTERISTICS**

| Planet  | Mean Solar Distance (AU)<br>(1 AU = $1.496 \times 10^{13}$ cm) | Period of Solar Revolution | Rotational Period<br>(Sidereal, Eastward, Equatorial) | Orbital Eccentricity        | Equatorial Inclination to Orbital Plane |
|---------|--|----------------------------|---|-----------------------------|---|
| Mercury | 0.387  | 88.0 day                   | 59 day  | 0.206                       | <28°                                    |
| Venus   | 0.723  | 224.7 day                  | —243 day  | 0.007                       | 3°                                      |
| Earth   | 1.000  | 365.26 day                 | 23 <sup>h</sup> 56 <sup>m</sup> 4 <sup>s</sup>        | 0.017                       | 23°27'                                  |
| Mars    | 1.524  | 687 day                    | 24 <sup>h</sup> 37 <sup>m</sup> 23 <sup>s</sup>       | 0.093                       | 23°59'                                  |
| Jupiter | 5.203  | 11.86 yr                   | 9 <sup>h</sup> 50 <sup>m</sup> 30 <sup>s</sup>        | 0.048                       | 3°05'                                   |
| Saturn  | 9.539  | 29.46 yr                   | 10 <sup>h</sup> 14 <sup>m</sup>                       | 0.056                       | 26°44'                                  |
| Uranus  | 19.18  | 84.01 yr                   | —17 <sup>h</sup> 17 <sup>m</sup>                      | 0.047                       | 82°05'                                  |
| Neptune | 30.06  | 164.8 yr                   | 18.2 <sup>h</sup>                                     | 0.009                       | 28°48'                                  |
| Pluto   | 39.44  | 247.7 yr                   | 6 <sup>d</sup> 9 <sup>h</sup>                         | 0.25                        | —                                       |
| Planet  | Mass<br>(Earth = 1)  | Equatorial radius<br>(km)  | Surface gravity<br>(Earth = 1)                        | Escape velocity<br>(km/sec) | Bond albedo                             |
| Mercury | 0.0554   | 2425                       | 0.37  | 4.2                         | 0.056                                   |
| Venus   | 0.815  | 6070                       | 0.88  | 10.3                        | 0.72                                    |
| Earth   | 1.000  | 6378                       | 1.00  | 11.2                        | 0.29                                    |
| Mars    | 0.1075   | 3395                       | 0.38  | 5.0                         | 0.16                                    |
| Jupiter | 317.8  | 71,300                     | 2.64  | 61                          | 0.343                                   |
| Saturn  | 95.15  | 60,100                     | 1.15  | 37                          | 0.342                                   |
| Uranus  | 14.54  | 24,500                     | 1.17  | 22                          | 0.34                                    |
| Neptune | 17.2   | 25,100                     | 1.18  | 25                          | 0.29                                    |
| Pluto   | 0.0026   | 1500                       | 0.046   | 1.17                        | 0.4                                     |

## Selected Satellites

| System  | Satellite | Mean<br>Distance<br>from<br>Planet<br>( $10^6$ km) | Period  | Radius<br>(km) | Mass<br>( $10^{24}$ gm) | Gravity<br>( $\text{cm sec}^{-2}$ ) | Escape<br>Velocity<br>(km/sec) |
|---------|-----------|--|---|----------------|-------------------------|-------------------------------------|--------------------------------|
| Jupiter | Io        | 422  | 1 <sup>d</sup> 18 <sup>h</sup> 29 <sup>m</sup>  | 1815           | 89.2                    | 181                                 | 2.56                           |
|         | Europa    | 671  | 3 <sup>d</sup> 13 <sup>h</sup> 18 <sup>m</sup>  | 1569           | 49.7                    | 135                                 | 2.06                           |
|         | Ganymede  | 1070   | 4 <sup>d</sup> 04 <sup>h</sup> 00 <sup>m</sup>  | 2631           | 149                     | 144                                 | 2.75                           |
|         | Callisto  | 1883   | 16 <sup>d</sup> 18 <sup>h</sup> 05 <sup>m</sup> | 2400           | 108                     | 125                                 | 2.45                           |
| Saturn  | Titan     | 1222   | 15 <sup>d</sup> 23 <sup>h</sup> 15 <sup>m</sup> | 2575           | 134.6                   | 135                                 | 2.64                           |
| Neptune | Triton    | 355 <sup>a</sup>                                   | 5 <sup>d</sup> 21 <sup>h</sup> 03 <sup>m</sup>  | ~ 1600         | ~ 340                   |                                     |                                |

<sup>a</sup>Eccentricity 0.75

## *Appendix III*

### A MODEL OF EARTH'S ATMOSPHERE

The tables given in this appendix are adapted from

"U.S. STANDARD ATMOSPHERE, 1976," (1976), National Oceanic and Atmospheric Administration, National Aeronautics and Space Administration, U.S. Air Force, NOAA-S/T 76-1562, Supt. Documents, U.S. Gov. Printing Office, Washington, D.C. 20402.

"SATELLITE ENVIRONMENT HANDBOOK," (1961), (F. S. Johnson, ed.), Stanford University Press, Stanford, California.

In the tables the notation  $a(b)$  stands for  $a \times 10^b$ .

TABLE III.1 *Model Atmosphere*

| Height<br>$z$ (km) | Geopotential<br>height<br>$\Phi/g_0$ (km) | Temperature<br>$T$ (°K) | Pressure<br>$p$ (mb) | Number<br>density<br>$N$ ( $\text{cm}^{-3}$ ) | Mean<br>molecular<br>weight<br>$\langle \mu \rangle$ (gm/mole) | Pressure<br>scale<br>height<br>$H$ (km) | Acceleration<br>of<br>gravity<br>$g$ ( $\text{cm/sec}^2$ ) |
|--------------------|---|-------------------------|----------------------|---|--|---|--|
| 0                  | 0   | 28.8                    | 1.013(3)             | 2.547(19)                                     | 28.96  | 8.434                                   | 980.7  |
| 5                  | 4.996                                     | 25.6                    | 5.405(2)             | 1.531(19)                                     | 28.96  | 7.496                                   | 979.1  |
| 10                 | 9.98                                      | 22.3                    | 2.650(2)             | 8.598(18)                                     | 28.96  | 6.555                                   | 977.6  |
| 15                 | 14.97                                     | 21.7                    | 1.211(2)             | 4.049(18)                                     | 28.96  | 6.372                                   | 976.1  |
| 20                 | 19.94                                     | 21.7                    | 5.529(1)             | 1.849(18)                                     | 28.96  | 6.382                                   | 974.5  |
| 25                 | 24.90                                     | 22.2                    | 2.549(1)             | 8.334(17)                                     | 28.96  | 6.536                                   | 973.0  |
| 30                 | 29.86                                     | 22.7                    | 1.197(1)             | 3.828(17)                                     | 28.96  | 6.693                                   | 971.5  |
| 35                 | 34.81                                     | 23.7                    | 5.746(0)             | 1.760(17)                                     | 28.96  | 7.000                                   | 970.0  |
| 40                 | 39.75                                     | 25.0                    | 2.871(0)             | 8.308(16)                                     | 28.96  | 7.421                                   | 968.4  |
| 45                 | 44.68                                     | 26.4                    | 1.491(0)             | 4.038(16)                                     | 28.96  | 7.842                                   | 966.9  |
| 50                 | 49.61                                     | 27.1                    | 7.978(-1)            | 2.135(16)                                     | 28.96  | 8.047                                   | 965.4  |
| 55                 | 54.53                                     | 26.1                    | 4.253(-1)            | 1.181(16)                                     | 28.96  | 7.766                                   | 963.9  |
| 60                 | 59.44                                     | 24.7                    | 2.196(-1)            | 6.439(15)                                     | 28.96  | 7.368                                   | 962.4  |
| 65                 | 64.34                                     | 23.3                    | 1.093(-1)            | 3.393(15)                                     | 28.96  | 6.969                                   | 960.9  |
| 70                 | 69.24                                     | 22.0                    | 5.221(-2)            | 1.722(15)                                     | 28.96  | 6.570                                   | 959.4  |
| 75                 | 74.13                                     | 20.8                    | 2.388(-2)            | 8.300(14)                                     | 28.96  | 6.245                                   | 957.9  |
| 80                 | 79.00                                     | 19.8                    | 1.052(-2)            | 3.838(14)                                     | 28.96  | 5.962                                   | 956.4  |

|      |        |      |            |           |       |       |
|------|--------|------|------------|-----------|-------|-------|
| 85   | 83.89  | 189  | 4.457(-3)  | 1.709(14) | 28.96 | 5.678 |
| 86   | 84.85  | 187  | 3.734(-3)  | 1.447(14) | 28.95 | 5.621 |
| 90   | 88.74  | 187  | 1.836(-3)  | 7.121(3)  | 28.91 | 5.64  |
| 95   | 93.60  | 189  | 7.597(-4)  | 2.921(3)  | 28.73 | 5.73  |
| 100  | 98.45  | 195  | 3.201(-4)  | 1.191(3)  | 28.40 | 6.01  |
| 110  | 108.13 | 240  | 7.104(-5)  | 2.141(2)  | 27.27 | 7.72  |
| 120  | 117.78 | 360  | 2.538(-5)  | 5.11(11)  | 26.20 | 12.09 |
| 130  | 127.40 | 469  | 1.250(-5)  | 1.93(11)  | 25.44 | 16.29 |
| 140  | 136.98 | 560  | 5.403(-6)  | 9.32(10)  | 24.75 | 20.03 |
| 150  | 146.54 | 634  | 4.542(-6)  | 5.19(10)  | 24.10 | 23.38 |
| 160  | 156.07 | 696  | 3.040(-6)  | 3.16(10)  | 23.49 | 26.41 |
| 180  | 175.04 | 790  | 1.527(-6)  | 1.40(10)  | 22.34 | 31.70 |
| 200  | 193.90 | 855  | 8.474(-7)  | 7.189(9)  | 21.30 | 36.18 |
| 220  | 212.64 | 899  | 5.015(-7)  | 4.049(9)  | 20.37 | 40.04 |
| 240  | 231.27 | 930  | 3.106(-7)  | 2.429(9)  | 19.56 | 43.41 |
| 260  | 249.78 | 951  | 1.989(-7)  | 1.529(9)  | 18.85 | 46.35 |
| 280  | 268.19 | 966  | 1.308(-7)  | 9.818(8)  | 18.24 | 48.93 |
| 300  | 286.48 | 976  | 8.770(-8)  | 6.518(8)  | 17.73 | 51.19 |
| 350  | 331.74 | 990  | 3.450(-8)  | 2.528(8)  | 16.64 | 55.83 |
| 400  | 376.32 | 996  | 1.452(-8)  | 1.068(8)  | 15.98 | 59.68 |
| 450  | 420.25 | 998  | 6.248(-9)  | 4.687(7)  | 15.25 | 63.64 |
| 500  | 463.54 | 999  | 3.024(-9)  | 2.197(7)  | 14.33 | 68.79 |
| 750  | 670.85 | 1000 | 2.260(-10) | 1.646(6)  | 6.58  | 161.1 |
| 1000 | 864.07 | 1000 | 7.514(-11) | 5.445(5)  | 3.94  | 785   |
|      |        |      |            |           | 288.2 | 732   |

**TABLE III.2** *Composition of Dry Atmosphere<sup>a</sup> (by Volume)*

| Species                         | Fractional volume | Molecular weight |
|---------------------------------|-------------------|------------------|
| N <sub>2</sub>                  | 0.780840          | 28               |
| O <sub>2</sub>                  | 0.209476          | 32               |
| Ar                              | 9.34(-3)          | 40               |
| CO <sub>2</sub>                 | 3.33(-4)          | 44               |
| Ne                              | 1.818(-5)         | 20.2             |
| He                              | 5.24(-6)          | 4                |
| CH <sub>4</sub>                 | 2(-6)             | 16               |
| Kr                              | 1.14(-6)          | 83.8             |
| H <sub>2</sub>                  | 5(-7)             | 2                |
| O <sub>3</sub>                  | 4(-7)             | 48               |
| N <sub>2</sub> O                | 2.7(-7)           | 44               |
| CO                              | 2(-7)             | 28               |
| Xe                              | 8.7(-8)           | 131.3            |
| H <sub>2</sub> CO               | 1(-8)             | 30               |
| NH <sub>3</sub>                 | 4(-9)             | 17               |
| H <sub>2</sub> O <sub>2</sub>   | 1(-9)             | 34               |
| SO <sub>2</sub>                 | 1(-9)             | 64               |
| NO <sub>2</sub>                 | 1(-9)             | 46               |
| NO                              | 5(-10)            | 30               |
| CF <sub>2</sub> Cl <sub>2</sub> | 2(-10)            | 121              |
| CFCl <sub>3</sub>               | 1(-10)            | 137.5            |
| CCl <sub>4</sub>                | 1(-10)            | 154              |
| H <sub>2</sub> S                | 5(-11)            | 34               |
| HO <sub>2</sub>                 | 3(-11)            | 33               |
| HBr, BrO                        | ~1(-11)           | 81, 96           |
| OH                              | ~2(-13)           | 17               |

<sup>a</sup> Total thickness of the dry atmosphere is  $\xi = 8.0 \times 10^5$  atm-cm or  $\mathcal{N} = 2.15 \times 10^{25}$  molecule/cm<sup>2</sup>.

**TABLE III.3** *Mid-Latitude Ozone Model*

| Height<br><i>z</i> (km) | Number<br>density<br>[O <sub>3</sub> ] (cm <sup>-3</sup> ) | Local<br>thickness<br>$\Delta\xi = 10^5 [\text{O}_3]/N_0$<br>atm-cm/km | Volume<br>mixing ratio<br>[O <sub>3</sub> ]/ <i>N</i> |
|-------------------------|--|--|---|
| 2                       | 6.8(11)  | 2.5(-3)  | 3.2(-8)   |
| 6                       | 5.7(11)  | 2.1(-3)  | 4.2(-8)   |
| 10                      | 1.13(12)   | 4.2(-3)  | 1.3(-7)   |
| 15                      | 2.65(12)   | 9.9(-3)  | 6.5(-7)   |
| 20                      | 4.77(12)   | 1.77(-2)   | 2.6(-6)   |
| 25                      | 4.28(12)   | 1.59(-2)   | 5.1(-6)   |
| 30                      | 2.52(12)   | 9.38(-3)   | 6.5(-6)   |
| 35                      | 1.40(12)   | 5.21(-3)   | 7.9(-6)   |
| 40                      | 6.07(11)   | 2.26(-3)   | 7.3(-6)   |
| 45                      | 2.22(11)   | 8.26(-4)   | 5.4(-6)   |
| 50                      | 6.64(10)   | 2.47(-4)   | 3.1(-6)   |
| 60                      | 7.33(9)  | 2.73(-5)   | 1.1(-6)   |
| 70                      | 5.4(8)   | 2.0(-6)  | 3.1(-7)   |

**TABLE III.4** *Thermospheric Composition*

| Height<br><i>z</i> (km) | Concentrations (cm <sup>-3</sup> ) |         |                   |         |        |        |
|-------------------------|------------------------------------|---------|-------------------|---------|--------|--------|
|                         | [N <sub>2</sub> ]                  | [O]     | [O <sub>2</sub> ] | [Ar]    | [He]   | [H]    |
| 86                      | 1.13(14)                           | 8.6(10) | 3.0(13)           | 1.4(12) | 7.6(8) | ---    |
| 90                      | 5.5(13)                            | 2.4(11) | 1.5(13)           | 6.5(11) | 4.0(8) | ---    |
| 100                     | 9.2(12)                            | 4.3(11) | 2.2(12)           | 9.5(10) | 1.1(8) | ---    |
| 150                     | 3.1(10)                            | 1.8(10) | 2.8(9)            | 5.0(7)  | 2.1(7) | 3.7(5) |
| 200                     | 2.9(9)                             | 4.1(9)  | 1.9(8)            | 1.9(6)  | 1.3(7) | 1.6(5) |
| 250                     | 4.8(8)                             | 1.4(9)  | 2.5(7)            | 1.5(5)  | 9.7(6) | 1.2(5) |
| 300                     | 9.6(7)                             | 5.4(8)  | 3.9(6)            | 1.6(4)  | 7.6(6) | 1.0(5) |
| 400                     | 4.7(6)                             | 9.6(7)  | 1.3(5)            | 2.1(2)  | 4.9(6) | 9.0(4) |
| 500                     | 2.6(5)                             | 1.8(7)  | 4.6(3)            | 3.4(0)  | 3.2(6) | 8.0(4) |
| 750                     | 2.7(2)                             | 3.7(5)  | 1.8(0)            | 2.0(-4) | 1.2(6) | 6.2(4) |
| 1000                    | 4.6(-1)                            | 9.6(3)  | 1.3(-3)           | 2.2(-8) | 4.9(5) | 5.0(4) |

**TABLE III.5** *Solar Fluxes at Earth Orbit and Absorption Cross Sections*

| Wavelength<br>(Å) | Flux <sup>a</sup> | Cross sections <sup>b</sup> ( $10^{-20}$ cm $^2$ ) |                 |                  |                |
|-------------------|-------------------|--|-----------------|------------------|----------------|
|                   |                   | O <sub>2</sub>                                     | CO <sub>2</sub> | H <sub>2</sub> O | O <sub>3</sub> |
| 1000              | 0.091             |  |                 |                  |                |
| 1050              | 0.053             | 1–100  |                 |                  |                |
| 1100              | 0.033             | 1–100  |                 |                  |                |
| 1150              | 0.046             | 1–1000   |                 |                  |                |
| 1200              | 3.44              | 1.05   | 3.7             | 1440             |                |
| 1250              | 0.094             | 5.0  | 27              | 588              |                |
| 1300              | 0.118             | 36   | 59              | 660              |                |
| 1350              | 0.177             | 600  | 82              | 340              |                |
| 1400              | 0.183             | 1380   | 61              | 82               |                |
| 1450              | 0.365             | 1430   | 59              | 51               |                |
| 1500              | 0.72              | 1130   | 48              | 108              |                |
| 1550              | 1.33              | 780  | 32              | 216              |                |
| 1600              | 2.58              | 480  | 18              | 354              |                |
| 1650              | 4.15              | 156  | 6.6             | 460              |                |
| 1700              | 7.02              | 86   | 2.3             | 413              |                |
| 1750              | 10.6              | 26   | 0.60            | 260              |                |
| 1800              | 17.2              | 0.5–10   | 0.14            | 78               |                |
| 1850              | 26.1              | 0.1–5  | 0.029           | 5.6              |                |
| 1900              | 39.2              | 0.02–0.5   | 0.006           | 0.4              |                |
| 1950              | 54.0              | 0.01–0.2   | 0.0018          | 0.005            |                |
| 2000              | 70.5              | 0.00128  | 0.00025         |                  | 32             |
| 2050              | 93                | 0.00115  |                 |                  | 34             |
| 2100              | 153               | 0.00099  |                 |                  | 54             |
| 2150              | 260               | 0.00082  |                 |                  | 99             |
| 2200              | 343               | 0.00062  |                 |                  | 180            |
| 2250              | 397               | 0.00040  |                 |                  | 290            |
| 2300              | 417               | 0.00025  |                 |                  | 450            |
| 2350              | 379               | 0.00015  |                 |                  | 620            |
| 2400              | 411               | 0.00009  |                 |                  | 800            |
| 2450              | 481               | 0.00004  |                 |                  | 986            |
| 2500              | 478               |  |                 |                  | 1110           |
| 2550              | 719               |  |                 |                  | 1160           |
| 2600              | 916               |  |                 |                  | 1090           |
| 2650              | 1330              |  |                 |                  | 960            |
| 2700              | 1700              |  |                 |                  | 774            |
| 2750              | 1520              |  |                 |                  | 577            |
| 2800              | 1690              |  |                 |                  | 380            |
| 2850              | 2440              |  |                 |                  | 240            |
| 2900              | 3800              |  |                 |                  | 134            |
| 2950              | 4680              |  |                 |                  | 73             |
| 3000              | 4610              |  |                 |                  | 43             |
| 3050              | 5140              |  |                 |                  | 22             |
| 3100              | 5930              |  |                 |                  | 11             |
| 3150              | 6500              |  |                 |                  | 6              |
| 3200              | 6850              |  |                 |                  | 3              |

<sup>a</sup> In units of  $10^{11}$  photons cm $^{-2}$  sec $^{-1}$  per 50 Å band.<sup>b</sup> Somewhat smoothed.

**TABLE III.6** *Other Tables in Text*

| Table | Topic  | Page |
|-------|--|------|
| 1.1   | Deposition of solar flux                               | 12   |
| 1.2   | Constants for thermal conductivity                     | 35   |
| 1.3   | Characteristics of the Jovian planets                  | 52   |
| 3.1   | Dissociation energies of neutral molecules             | 120  |
| 3.2   | Daily mean photolysis rates                            | 121  |
| 4.1   | Composition of atmospheres                             | 189  |
| 4.2   | Selected molecular bands                               | 194  |
| 5.1   | The ionosphere   | 228  |
| 5.2   | Designations of radio bands                            | 229  |
| 5.3   | Microwave bands  | 229  |
| 6.1   | Photon scattering coefficients<br>at 1 AU from the Sun | 293  |
| 7.1   | Nonthermal escape processes                            | 366  |
| 7.2   | Escape mechanisms by planet                            | 367  |

## ***Appendix IV***

### **PLANETARY SPACECRAFT MISSIONS**

| Planet        | Spacecraft | Launch      | Mission summary  | Notes |
|---------------|------------|-------------|--|-------|
| Venus         | Mariner 2  | 27 Aug. 62  | Fly-by 14 Dec. 62  |       |
| Venus         | Venera 3   | 16 Nov. 65  | Venus impact 1 Mar. 66   |       |
| Venus         | Venera 4   | 12 June 67  | Soft atmospheric entry 18 Oct. 67  | 1, 2  |
| Venus         | Mariner 5  | 14 June 67  | Fly-by 19 Oct. 67  | 1     |
| Venus         | Venera 5   | 5 Jan. 69   | Soft atmospheric entry 16 May 69   | 2     |
| Venus         | Venera 6   | 10 Jan. 69  | Soft atmospheric entry 17 May 69   | 2     |
| Venus         | Venera 7   | 17 Aug. 70  | Soft surface landing 15 Dec. 70  | 2     |
| Venus         | Venera 8   | 27 Mar. 72  | Soft surface landing 22 July 72  | 2     |
| Venus/Mercury | Mariner 10 | 3 Nov. 73   | In solar orbit: Venus fly-by, 5 Feb. 74;<br>Mercury fly-by, 29 Mar. 74;<br>additional Mercury encounters in<br>Sept. 74 and in Mar. 75 | 3     |
| Venus         | Venera 9   | 8 June 75   | Orbiter and surface lander 22 Oct. 75  | 4     |
| Venus         | Venera 10  | 14 June 75  | Orbiter and surface lander 25 Oct. 75  | 4     |
| Venus         | Pioneer    | 20 May 78   | Orbiter: 4 Dec 78  | 5     |
|               | Venus 1    |             |  |       |
| Venus         | Pioneer    | 8 Aug. 78   | Multiprobes; enter atmosphere 9 Dec. 78  | 5     |
|               | Venus 2    |             | week after arrival of Orbiter  |       |
| Venus         | Venera 11  | 9 Sept. 78  | Fly-by; soft lander,<br>day side; 25 Dec. 78   |       |
| Venus         | Venera 12  | 14 Sept. 78 | Fly-by; soft lander,<br>day side; 21 Dec. 78   |       |
| Venus         | Venera 13  | 30 Oct. 81  | Soft lander; 1 Mar. 82   |       |
| Venus         | Venera 14  | 4 Nov. 81   | Soft lander; 5 Mar. 82   |       |
| Venus         | Venera 15  | 2 June 83   | Radar mapper; 10 Oct. 83   |       |
| Venus         | Venera 16  | 7 June 83   | Radar mapper; 14 Oct. 83   |       |

| Planet                               | Spacecraft                      | Launch     | Mission summary   | Notes |
|--------------------------------------|---------------------------------|------------|---|-------|
| Venus                                | Venera-<br>Halley 1<br>(VEGA 1) | 15 Dec. 84 | Balloon; 11 June 85<br>Halley's Comet, 6 Mar. 86  | 5     |
| Venus                                | Venera-<br>Halley 2<br>(VEGA 2) | 21 Dec. 84 | Balloon; 14 June 85<br>Halley's Comet, 9 Mar. 86  | 5     |
| Mars                                 | Mariner 4                       | 28 Nov. 64 | Fly-by 14 July 65   |       |
| Mars                                 | Mariner 6                       | 25 Feb. 69 | Fly-by 31 July 69   |       |
| Mars                                 | Mariner 7                       | 27 Mar. 69 | Fly-by 5 Aug. 69  |       |
| Mars                                 | Mars 2                          | 19 May 71  | Orbiter; hard landing probe 27 Nov. 71  |       |
| Mars                                 | Mars 3                          | 28 May 71  | Orbiter; soft landing probe 2 Dec. 71   | 6     |
| Mars                                 | Mariner 9                       | 30 May 71  | Entered Mars orbit 13 Nov. 71   | 6     |
| Mars                                 | Viking 1                        | 20 Aug. 75 | Orbiter; soft landing probe 20 July 76  | 7     |
| Mars                                 | Viking 2                        | 9 Sept. 75 | Orbiter; soft landing probe 3 Sept. 76  | 7     |
| Jupiter                              | Pioneer 10                      | 3 Mar. 72  | Fly-by 4 Dec. 73  | 8     |
| Jupiter/Saturn                       | Pioneer 11                      | 6 Apr. 73  | Fly-by Jupiter 5 Dec. 74; fly-by Saturn<br>1 Sept. 79   | 8     |
| Jupiter/Saturn                       | Voyager 1                       | 5 Sept. 77 | Jupiter fly-by 5 Mar. 79; Saturn fly-by<br>12 Nov. 80   | 9     |
| Jupiter/Saturn/<br>Uranus<br>Neptune | Voyager 2                       | 20 Aug. 77 | Jupiter fly-by 9 July 79; Saturn fly-by<br>25 Aug. 81; Uranus 24 Jan. 86,<br>Neptune 24 Aug. 89 | 9     |
| Jupiter                              | Galileo                         | 89-91      | Orbiter and atmospheric entry probe;<br>expected arrival 95-97                                  | 10    |

*Notes on publication of scientific results*

1. Preliminary results of the American Mariner 5 fly-by of Venus are given in several brief articles by the participating investigators in

*Science* **158**, No. 3809, 29 Dec. (1967), pp. 1665-1688.

In March 1968, Soviet and American investigators met in Tucson, Arizona to discuss results of the Venera 4 and Mariner 5. The collected papers of this "Second Arizona Conference on Planetary Atmospheres" are published in

*J. Atmos. Sci.* **25**, No. 4, July (1968), pp. 533-671.

2. Summary articles on the Soviet series of Venus entry probes, Venera 4-8, are

VAKHNIN, V. M. (1968), A review of the Venera 4 flight and its scientific program, *J. Atmos. Sci.* **25**, pp. 533-534;

AVDUEVSKY, V. S.; MAROV, M. Ya.; and ROZHDESTVENSKY, M. K. (1970), A tentative model of the Venus atmosphere based on the measurements of Veneras 5 and 6, *J. Atmos. Sci.* **27**, pp. 561-579;

AVDUEVSKY, V. S.; MAROV, M. Ya.; ROZHDESTVENSKY, M. K.; BORODIN, N. F.; and KERZHANOVICH, V. V. (1971), Soft landing of Venera 7 on the Venus surface and preliminary results of the investigations of the Venus atmosphere, *J. Atmos. Sci.* **28**, pp. 263-264;

- MAROV, M. YA. *et. al.* (1973a), Preliminary results on the Venus atmosphere from the Venera 8 descent module, *Icarus* **20**, 407–421;
- MAROV, M. YA. (1973b), Venera 8: Measurements of temperature, pressure, and wind velocity on the illuminated side of Venus, *J. Atmos. Sci.* **30**, pp. 1210–1214;
- AVDUEVSKY, V. S.; MAROV, M. YA.; MOSHKIN, B. E.; and EKONOMOV, A. P. (1973), Venera 8: Measurements of solar illumination through the atmosphere of Venus, *J. Atmos. Sci.* **30**, 1215–1218.
3. Preliminary analyses of the U.S. Mariner 10 Venus fly-by are given in *Science* **183**, No. 413; 29 Mar. (1974), pp. 1289–1321.
- Preliminary reports of the first Mercury encounter of M 10 were published in *Science* **185**, No. 4146, 12 July (1974), pp. 141–180.
4. Results of the Venera 9 and 10 orbiter/lander missions are reported in a series of papers, available in English translation from the Russian (*Kosmicheskie Issledovaniya*) in *Cosmic Res.* **14**, No. 5, Sep.–Oct. (1976), pp. 573–701.
- A summary article is
- KELDYSH, M. V. (1977), Venus exploration with the Venera 9 and 10 spacecraft, *Icarus* **30**, 605–625.
5. The exploration of Venus, with particular emphasis on the Pioneer Venus program, is reviewed in
- Science* **203**, No. 4382, 23 Feb. (1979), pp. 743–808, *Ibid.*, **205**, No. 4401, 6 July (1979), pp. 41–121,
- J. Geophys. Res.* **85**, No. A13, 30 Dec. (1980), pp. 7573–8337 [Pioneer Venus Special Issue], “Pioneer Venus” (1983) (R. O. Fimmel *et al.*, eds.), NASA SP-461, U.S. Govt. Printing Office, 253pp [contains a Pioneer Venus bibliography].
- An international conference on “The Venus Environment” was held at Palo Alto, California in November 1981. The results of that conference are published in two issues of *Icarus* and a book:
- Icarus* **51**, No. 2, Aug. (1982), pp. 167–459, *Icarus* **52**, No. 2. Nov. (1982). pp. 209–372, “Venus” (1983) (D. M. Hunten, L. Colin, T. M. Donahue, and V. I. Moroz, eds.), Univ. Arizona Press, Tucson, Arizona 1143pp.
- The two VEGA spacecraft were launched as a joint Soviet-French-American mission, carried balloons to Venus and then continued on to Comet Halley. The tracking of the balloons from a network of observation stations on Earth, the meteorologic data obtained, and the implications of the data for defining the atmospheric dynamics of Venus are treated in a special issue of *Science* **231**, No. 4744, 21 March 1986, pp. 1349, 1369, 1407–1425.
6. Preliminary results from the Mariner 9 orbiter of Mars are given in *Science* **175**, No. 4019, 21 Jan. (1972), pp. 293–323.
- A number of papers on results of Mariner 9 and the Soviet Mars 3 are collected in *Icarus* **17**, No. 2, Oct. (1972), pp. 289–327.
7. A series of three issues of *Science* were largely devoted to preliminary reports on Viking 1 and 2. They are
- Science* **193**, No. 4255, 27 Aug. (1976), pp. 759–815.
- Ibid.* **194**, No. 4260, 1 Oct. (1976), pp. 57–109.
- Ibid.* **194**, No. 4271, 17 Dec (1976), pp. 1274–1353.

Later discussion of the results by the experimenters appears in three special issues:

*J. Geophys. Res.* **82**, No. 28, 30 Sept. (1977), pp. 3959-4681, "Scientific Results of the Viking Project"

*Ibid.* **84**, No. B6, 10 June (1979), pp. 2793-3007,

*Ibid.* **84**, No. B14, 30 Dec. (1979), pp. 7909-8519,

A special issue of *Icarus* is largely devoted to "Dust on Mars":

*Icarus* **66**, No. 1, April (1986), pp. 1-142.

8. The Pioneer 10 and 11 preliminary reports appear, respectively, in

*Science* **183**, No. 4122, 25 Jan. (1974), pp. 301-324.

*Ibid.* **188**, No. 4187, 2 May. (1975), pp. 445-477.

The preliminary report of the Pioneer 11 encounter with Saturn appears in

*Science* **207**, No. 4429, 25 Jan. (1980), pp. 400-453,

and detailed papers are in a special issue of

*J. Geophys. Res.* **85**, No. A11, Nov. (1980), pp. 5651-6082.

Detailed analyses have been collected, following a conference on the Pioneer results, in

"Jupiter" (1976) (T. Gehrels, ed.), Univ. Arizona, Tucson, 1254 pp.

9. Twelve papers on various aspects of the Voyager missions are published together in

*Space Sci. Rev.* **21**, Nos. 2-3 (1977), pp. 75-376.

The preliminary reports for the encounters with Jupiter by Voyager 1 and Voyager 2, respectively, are in

*Science* **204**, No. 4396, 1 June (1979), pp. 945-1008,

*Science* **206**, No. 4421, 23 Nov. (1979), pp. 925-996.

Nature also issued a special supplement devoted to preliminary papers on the Voyager 1 encounter with Jupiter and Io:

*Nature* **280**, No. 5725, 30 Aug. (1979), pp. 725-806.

Voyager 1 and 2 observations on the atmosphere and magnetosphere of Jupiter are treated in a special issue of

*Geophys. Res. Letts.* **7**, No. 1, Jan. (1980), pp. 1-68,

The principal papers on the Jupiter observations are in

*J. Geophys. Res.* **86**, No. A10, Sept. (1981), pp. 8123-8841.

For the Saturn encounters, the preliminary reports appear in

*Science* **212**, No. 4491, 10 Apr. (1981), pp. 159-243,

*Science* **215**, No. 4532, 29 Jan. (1982), pp. 499-594.

*Nature* **292**, No. 5825, 20 Aug. (1981), pp. 675-755.

The Voyager observations at Saturn are treated in depth in a special issue of

*J. Geophys. Res.* **88**, No. A11, 1 Nov. (1983), pp. 8625-9018.

Saturn is the subject of another post-Voyager collection of papers, including three on Titan:

"Saturn" (1984) (T. Gehrels and M. Matthews, eds.), Univ. Arizona, Tucson, 980 pp.

A preliminary report on this conference, with papers on Saturn, its rings, and satellites is

*Icarus* **53**, No. 2, Feb. (1983), pp. 163-387.

"The Jovian Atmospheres" was the subject of a highly successful conference held at NASA's Goddard Institute for Space Studies in New York during May 1985. Many of the review, as well as contributed, papers are published in a special issue of *Icarus*:

*Icarus* **65**, Nos. 2/3, Feb./Mar. (1986), pp. 159–466.

The Voyager spacecraft yielded especially valuable observations of the planetary satellites. Papers presented at conferences on the satellites have been published in

*Icarus* **44**, No. 2, Nov. (1980), pp. 225–547,

"Satellites of Jupiter" (1982) (D. Morrison, ed.), Univ. Arizona Press, Tucson, Arizona, 974 pp,

*Icarus* **58**, No. 2, May (1984), pp. 135–329,

"Satellites of the Solar System" (1985) (J. A. Burns and M. S. Matthews, eds.), Univ. Arizona Press, Tucson, Arizona, 1026 pp.

Preliminary accounts of the Voyager 2 encounter with the Uranian system are published in *Science* **233**, No. 4759, 4 July (1986), pp. 39–109.

**10.** The launch of Galileo by the Space Shuttle was postponed after the Challenger explosion on 28 January 1986.

## ***Appendix V***

### **SUPPLEMENTARY READING**

In order to develop the physics and chemistry of planetary atmospheres in some mathematical detail qualitative descriptions of atmospheric phenomena have been kept at a minimum. Several excellent sources of such material are available, and some students may wish to use one or more of them in conjunction with this book. Two texts that are mainly oriented toward physical and dynamical meteorology are

- WALLACE, J. M. and HOBBS, P. V. (1977), "Atmospheric Science: An Introductory Survey," Academic Press, New York, 467 pp.  
HOUGHTON, J. T. (1977), "The Physics of Atmospheres," Cambridge Univ. Press, Cambridge, 203 pp.

A number of undergraduate astronomy texts contain overviews of the planetary system. Particularly useful for supplementary reading are

- ABELL, G. O. (1982), "Exploration of the Universe," 4th ed., Saunders, Philadelphia, Pennsylvania, 721 pp.  
JASTROW, R. and THOMPSON, M. H. (1984), "Astronomy, Fundamental and Frontiers," 4th ed., John Wiley & Sons, New York, 564 pp.  
PASACHOFF, J. M. (1984), "Contemporary Astronomy," 3rd ed., Saunders, Philadelphia, Pennsylvania, 490 pp.

A text that deals exclusively with the solar system is

- HARTMANN, W. K. (1983), "Moons and Planets," 2nd ed., Wadsworth, Belmont, California, 509 pp.

There are several important texts dealing with atmospheric radiation:

- GOODY, R. M. (1964), "Atmospheric Radiation," Oxford Univ. Press, London and New York, 436 pp.  
KONDRATYEV, K. YA. (1969), "Radiation in the Atmosphere," Academic Press, New York, 912 pp,

- KONDRATYEV, K. YA. and MOSKALENKO, N. I. (1977), "Teplovoye Izlucheniye Planet" ["Thermal Radiation of the Planets"], Gidrometeoizdat, Leningrad, 263 pp.  
 LIOU, K. N. (1980), "An Introduction to Atmospheric Radiation," Academic Press, New York, 392 pp.  
 MCCARTNEY, E. J. (1983), "Absorption and Emission by Atmospheric Gases: The Physical Processes," John Wiley & Sons, New York, 320 pp.

The U.S.S.R. State Committee for Science and Technology has published a very useful monograph as Volume 19 in its Series on Space Research:

- KONDRATYEV, K. YA. and MOSKALENKO, N. I. (1983), "Kluchevie Problemi Issledovaniia Planet Solnechnoi Sisteme: Parnikovii Effekt Atmosfer Planet" ["Key Problems in Research on the Planets of the Solar System: The Greenhouse Effect in Planetary Atmospheres"], Academy of Sciences, Moscow, 155 pp.

The comparative meteorology of Earth, Venus, Mars, and Jupiter is the emphasis in

- KONDRATYEV, K. YA. and HUNT, G. E. (1982), "Weather and Climate on Planets," Pergamon Press, Oxford, 755 pp.

This book is an excellent compendium on the properties of planetary atmospheres and surfaces, and contains nearly 1400 references.

Another scholarly work with an emphasis on chemistry and atmospheric evolution (and valuable as well for its more than 2000 references) is

- LEWIS, J. S. and PRINN, R. G. (1984), "Planets and Their Atmospheres: Origin and Evolution," Academic Press, New York, 470 pp.

Additional recent books are

- BRASSEUR, G. and SOLOMON, S. (1984), "Aeronomy of the Middle Atmosphere," D. Reidel, Dordrecht, 441 pp.  
 KRASNOPOLSKY, V. A. (1986), "Photochemistry of the Atmospheres of Mars and Venus," Springer-Verlag, Berlin, 329 pp.

From time to time the U.S. National Research Council (NRC) issues reports on some aspect of atmospheric physics and chemistry. The NRC is the operational arm of the National Academy of Sciences and National Academy of Engineering and as such undertakes these studies at the request of government agencies. Among the advantages of these reports are that they are written by committees of (unpaid) experts and are very authoritative and timely when issued; they are published rapidly and inexpensively, once completed and reviewed internally; they are addressed to nonspecialists and hence generally develop the current state of knowledge in a field before assessing the particular problem area that may have inspired the report; and they contain excellent bibliographies. Among the disadvantages are that they are not widely advertised; not widely available in libraries; and usually do not contain subject indices. To obtain a current list of titles one may write

National Academy Press  
 2101 Constitution Avenue, N.W.  
 Washington, D.C. 20418

In recent years several reports have dealt with environmental factors that might deplete ozone in the stratosphere:

- "Environmental Impact of Stratospheric Flight" (1975), Climatic Impact Committee, 348 pp,  
 "Halocarbons: Environmental Effect of Chlorofluoromethane Release" (1976), Committee on Impacts of Stratospheric Change, 126 pp,

"Causes and Effects of Changes in Stratospheric Ozone: Update 1983" (1984), Environmental Studies Board, 254 pp.

Several other reports have addressed the problems of atmospheric and water pollution, including

"Ozone and Other Photochemical Oxidants" (1977), Committee on Medical and Biologic Effects of Environmental Pollutants, 719 pp,

"Nitrogen Oxides" (1977), Committee on Medical and Biologic Effects of Environmental Pollutants, 333 pp,

"Acid Deposition: Atmospheric Processes in Eastern North America" (1983), Environmental Studies Board, 375 pp.

In recent years the Academy has become increasingly concerned with the future direction of climate change and man's impact upon it:

"Solar Variability, Weather, and Climate" (1982), Geophysics Research Board, 106 pp,

"Carbon Dioxide and Climate: A Second Assessment" (1982), Climate Board, 72 pp,

"Changing Climate" (1983), Carbon Dioxide Assessment Committee, Board on Atmospheric Sciences and Climate, 496 pp.

## **Appendix VI**

### **THE PLANCK FUNCTION**

The intensity per unit frequency or wavelength of black-body radiation is defined as the Planck function (Fig. VI.1)

$$B_v(T) = \frac{2hv^3}{c^2(e^x - 1)} \quad (\text{VI.1})$$

$$B_\lambda(T) = \frac{v^2}{c^2} B_v(T) = \frac{c_1 \lambda^{-5}}{e^x - 1} \quad (\text{VI.2})$$

where

$$x = \frac{hv}{kT} = \frac{hc}{\lambda kT} = \frac{c_2}{\lambda T} \quad (\text{VI.3})$$

and  $c_1 = 2hc^2$  and  $c_2 = hc/k$ ;  $h$  and  $k$  are Planck's and Boltzmann's constants, respectively,  $c$  is the speed of light, and  $T$  the temperature. Other definitions of  $c_1$  are commonly used, giving either flux or energy density of radiation; the one used here gives intensity.

The dashed curve in Fig. VI.1 shows  $\lambda B_\lambda$ , which has the useful property of giving ordinates proportional to energies. Study of the wavelength scales for 250 and 6000°K reveals that there is essentially no overlap of Planck functions at these two temperatures: the 6000°K curve has only 0.4% of its energy above 5 μm, and the 250°K curve has the same fraction below 5 μm. This is the basis of the common procedure of regarding solar and planetary radiation fields as distinct.

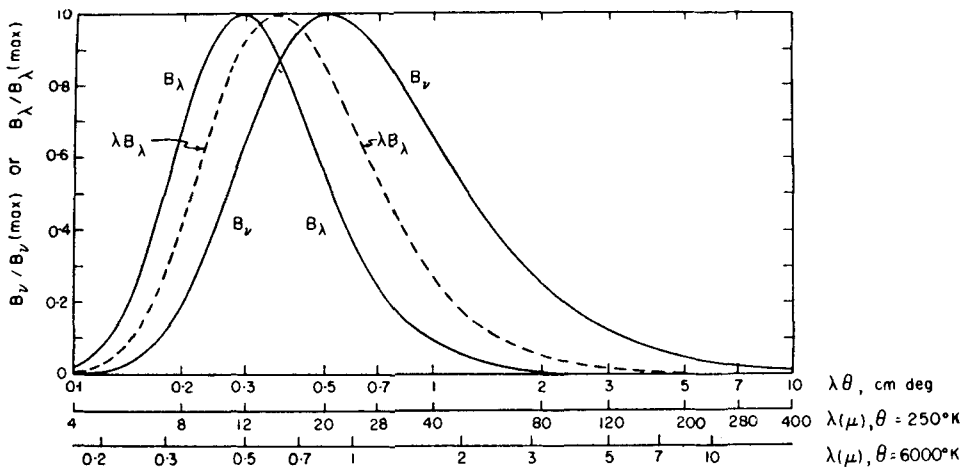


**Fig. VI.1** Normalized Planck functions plotted against the logarithm of the wavelength for two different temperatures and against the product of wavelength and temperature  $\theta$ . [After Goody (1964).]

The asymptotic forms of (VI.1) and (VI.2) are known as the Rayleigh-Jeans approximation for low frequencies, and the Wien approximation for high frequencies:

$$B_\nu(\text{RJ}) = 2kT\nu^2/c^2, \quad B_\lambda(\text{RJ}) = 2kTc/\lambda^4 \quad (\text{VI.4})$$

$$B_\nu(\text{W}) = \frac{2hv^3}{c^2} e^{-x}, \quad B_\lambda(\text{W}) = c_1 \lambda^{-5} e^{-x} \quad (\text{VI.5})$$

Wien's Law gives the wave number or wavelength of peak intensity

$$cT/v_{\max} = 0.510 \text{ cm deg}, \quad T\lambda_{\max} = 0.290 \text{ cm deg} \quad (\text{VI.6})$$

This summary of the Planck function follows Section 2.2.1 of GOODY, R. M. (1964), "Atmospheric Radiation," Oxford Univ. Press (Clarendon), London and New York. There are misprints in Goody's Eqs. (2.33) and (2.35).

## *Appendix VII*

### DIFFUSION COEFFICIENTS

Diffusion and thermal conduction in gases are related phenomena, and both can be represented over a reasonable temperature range by equations of the same form

$$DN = b = AT^s \quad (\text{VII.1})$$

(cf. 1.7.21). The binary parameter  $b$  is the product of the diffusion coefficient  $D$  and the total number density  $N$ . In terms of pressure instead of  $N$ , the exponent appears as  $s + 1$ . The quantities  $A$  and  $s$  can be found for many gas pairs in the article by Mason and Marrero (1970); a few are given here in Table VII.1.

If data are lacking, one can use the hard-sphere approximation

$$b = \frac{3}{64Q} \left[ \frac{2\pi kT(m_1 + m_2)}{m_1 m_2} \right]^{1/2} \quad (\text{VII.2})$$

The collision cross section is

$$Q = (\pi/16)(\sigma_1 + \sigma_2)^2 \quad (\text{VII.3})$$

where  $\sigma_1$  and  $\sigma_2$  are the collision diameters of the two atoms or molecules, which have masses  $m_1$  and  $m_2$ . The value of  $s$  in the hard-sphere formula is 0.5, rather than the more typical value of 0.7–0.8; a more realistic soft sphere could be regarded as having a cross section that decreases at higher collision velocities.

**TABLE VII.1** Parameters for use in Eq. (VII.1).  
Neon is included because it should be an analog  
for atomic oxygen.

| Gas 1            | Gas 2                  | $10^{-16} \text{ A}$ | $s$   |
|------------------|------------------------|----------------------|-------|
| H                | H <sub>2</sub>         | 145                  | 1.61  |
|                  | Air                    | 65                   | 1.7   |
|                  | CO <sub>2</sub>        | 84                   | 1.597 |
| H <sub>2</sub>   | Air                    | 26.7                 | 0.750 |
|                  | CO <sub>2</sub>        | 22.3                 | 0.750 |
|                  | N <sub>2</sub> (100°K) | 18.8                 | 0.82  |
| H <sub>2</sub> O | Air                    | 1.37                 | 1.072 |
| CH <sub>4</sub>  | N <sub>2</sub>         | 7.34                 | 0.749 |
| Ne               | N <sub>2</sub>         | 11.7                 | 0.743 |
| Ar               | Air                    | 6.73                 | 0.749 |

Thermal diffusion is sensitive to the force law in a collision, and there is no simple recipe. In practice, the thermal diffusion factor is taken as  $-0.25$  for hydrogen and helium, and zero for other gases.

The diffusion coefficient can be written in terms of the mean thermal speed  $\bar{c}$  and mean free path  $L$  as

$$D = (3\pi/16\sqrt{2})\bar{c}L = 0.42\bar{c}L \quad (\text{VII.4})$$

The *mixing-length approximation* for eddy diffusion is based on this expression, which is the product of a characteristic velocity and a characteristic distance. For example, in free thermal convection, the speed can be taken as that of the convecting elements, and the mixing length as the scale height.

## REFERENCES

- MASON, E. A. and MARRERO, T. R. (1970), The diffusion of atoms and molecules, in "Advances in Atomic and Molecular Physics" (D. R. Bates and I. Estermann, eds.), pp. 155-232, Academic Press, New York.  
 CHAPMAN, S. and COWLING, T. G. (1961), "The Mathematical Theory of Non-Uniform Gases." Cambridge Univ. Press, London and New York.

## **Appendix VIII**

### **ORTHO AND PARA HYDROGEN**

The lowest rotational energy levels of  $\text{H}_2$  are illustrated in Fig. VIII.1. The energies are shown beside each level, calculated from  $BJ(J + 1) + DJ^2(J + 1)^2$ , where  $B = 59.322 \text{ cm}^{-1}$ ,  $D = 0.0471 \text{ cm}^{-1}$ , and  $J$  is the rotational quantum number. Quantum mechanics requires that the total wave function be antisymmetric with respect to interchange of the nuclei, which have spin  $\frac{1}{2}$ , and that transitions with  $\Delta J = \pm 1$  be highly forbidden. The paired arrows in Fig. VIII.1 show the behavior of the proton spins; the symmetry of the electronic part of the wave function is  $s$  and  $a$  for para and ortho levels, respectively. The nuclear part of the statistical weight alternates between 1 and 3; the rotational part is  $2J + 1$ .

The even states (spins antiparallel) are called *para* and the odd states (spin parallel) *ortho*. Transitions between the two sets are nearly impossible and are caused only by some suitable external perturbation, most commonly by collision with an atom or molecule having a large magnetic moment (a paramagnetic catalyst). Another possibility is reaction with a free H atom, forming a temporary  $\text{H}_3$  molecule that can break up again, forming  $\text{H}_2$  in either set of states. This process occurs once in a million collisions at room temperature, because of its activation energy, and much more slowly at temperatures found in the atmospheres of the Jovian planets. At and above room temperature, several levels of each species are significantly populated, and the ortho–para ratio is that of the nuclear statistical weights, or 3. This mixture is called *normal*. If normal  $\text{H}_2$  is cooled to a much lower temperature, only the two lowest levels are populated, and they retain the 3:1 ratio for times of weeks to years, with the conversion rate determined mainly by the presence of paramagnetic catalysts. Once the conversion is complete, the gas

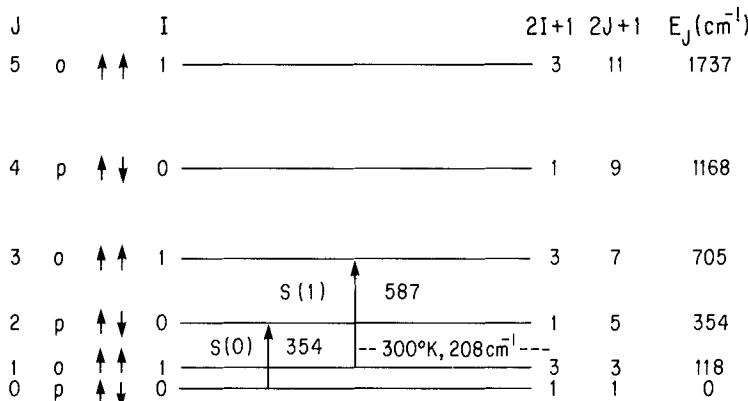


**Fig. VIII.1** The six lowest rotational levels of  $\text{H}_2$ , showing the rotational quantum number  $J$ , the para-ortho alternation, the spin state of the protons with the quantum number  $I$ , the spin and rotational degeneracies, and the excitation energies in  $\text{cm}^{-1}$ . Arrows indicate the two lowest transitions, and the dashed line shows the energy ( $kT$ ) corresponding to  $T = 300^\circ\text{K}$ .

is called *equilibrium hydrogen*. Normal hydrogen would be expected on the Jovian planets because vertical mixing should be much faster than any of the conversion processes.

Figure VIII.1 shows the two transitions  $S(0)$  and  $S(1)$  that can be observed in the far infrared at  $354$  and  $587 \text{ cm}^{-1}$  (Fig. 4.22). Since  $\text{H}_2$  has no dipole moment, the transitions are normally forbidden, but the required moment can be induced during a collision; the lines are very broad because the collision is very brief. Transitions can also occur, through the quadrupole moment, to vibrational levels higher than the zeroth one shown in Fig. VIII.1. The  $3-0$  lines can be observed in the  $8000 \text{ \AA}$  region, and a few  $4-0$  lines in the visible. In every case, the ortho-para ratio is less than 3, with values near those expected for the local atmospheric temperature. These results seem to require either a more rapid conversion process or slower vertical mixing in the atmosphere.

If conversion is rapid, a large peak in the specific heat appears between  $50$  and  $120^\circ\text{K}$ , with corresponding effects on the lapse rate. If the conversion is confined to a layer, the effect can resemble that of latent heat, with possible large effects on the buoyancy of an atmospheric parcel. Current practice is to ignore the heat of conversion and use a specific heat that is the weighted mean of the ortho and para values, evaluated at the local temperature. Gas that behaves this way is called *intermediate hydrogen*.

Recent papers on ortho and para hydrogen are

MASIE, S. T. and HUNTER, D. M. (1982), Conversion of para and ortho hydrogen in the Jovian planets, *Icarus* **49**, 213–226.

CONRATH, B. J. and GIERASCH, P. J. (1984), Global variation of the para hydrogen fraction in Jupiter's atmosphere and implications for dynamics on the outer planets, *Icarus* **57**, 184–204.

## **Appendix IX**

### **PARTITION FUNCTIONS FOR A SPHERICAL EXOSPHERE**

In Sections 7.1.3 and 7.1.4, integrals are given for the calculation of particle densities and integrated densities along a specified line of sight for a spherically symmetric planetary corona. Even though such an ideal geometry is not likely to be approximated in the solar system, this first-order model is useful in reducing data that can be expressed in terms of small departures from the spherically symmetric case. Tables in this appendix will be helpful in this regard.

Table IX.1 gives the total partition function  $\zeta(\lambda)$  for all bound orbits, as obtained from (7.1.40). The total density of bound (i.e., ballistic plus satellite) particles is then given by (7.1.20), provided that all allowed particles are present. Note that  $\zeta_{\text{bal}} + \zeta_{\text{sat}}$  is independent of the location of the exobase  $\lambda_c$ .

Table IX.2 gives the partition functions  $\zeta_{\text{bal}}(\lambda)$  and  $\zeta_{\text{esc}}(\lambda)$  for finding the ballistic and escaping particle components.

Table IX.3 contains straightforward integrations of equation (7.1.52) for computing the integrated densities from (7.1.50) for  $\mu_1 = 1$  and 0. In using these tables to compute the integrated density, it is necessary to compute  $\mathcal{N}(\mu_1, \lambda)$  separately for each component (ballistic and escape) from Eq. (7.1.50) with  $\zeta(\lambda)$  for that component obtained from Table IX.2 and then to add the component  $\mathcal{N}$ 's.

Table IX.4 gives the integral (7.1.52), as obtained from the  $\zeta$ 's of Table IX.1 and evaluated between limits  $\lambda_{\text{cs}} < \lambda < \lambda_1$ , for an overhead integration (i.e.,  $\mu_1 = 1$ ). Thus if one desires the total integrated density above height  $r_1$ , the

**TABLE IX.1** Partition Function for Bound Orbit

| $\lambda$ | $\zeta_{\text{bal}} + \zeta_{\text{sat}}$ | $\lambda$ | $\zeta_{\text{bal}} + \zeta_{\text{sat}}$ |
|-----------|---|-----------|---|
| 0.1       | 0.0224107                                 | 2.6       | 0.8422755                                 |
| 0.2       | 0.0597575                                 | 2.7       | 0.8552564                                 |
| 0.3       | 0.1035676                                 | 2.8       | 0.8672216                                 |
| 0.4       | 0.1505329                                 | 2.9       | 0.8782433                                 |
| 0.5       | 0.1987480                                 | 3.0       | 0.8883897                                 |
| 0.6       | 0.2469956                                 | 3.5       | 0.9281022                                 |
| 0.7       | 0.2944652                                 | 4.0       | 0.9539883                                 |
| 0.8       | 0.3406101                                 | 4.5       | 0.9707090                                 |
| 0.9       | 0.3850650                                 | 5.0       | 0.9814339                                 |
| 1.0       | 0.4275932                                 | 5.5       | 0.9882745                                 |
| 1.1       | 0.4680516                                 | 6.0       | 0.9926172                                 |
| 1.2       | 0.5063653                                 | 6.5       | 0.9953637                                 |
| 1.3       | 0.5425104                                 | 7.0       | 0.9970952                                 |
| 1.4       | 0.5765000                                 | 7.5       | 0.9981837                                 |
| 1.5       | 0.6083748                                 | 8.0       | 0.9988663                                 |
| 1.6       | 0.6381949                                 | 8.5       | 0.9992936                                 |
| 1.7       | 0.6660347                                 | 9.0       | 0.9995605                                 |
| 1.8       | 0.6919778                                 | 9.5       | 0.9997269                                 |
| 1.9       | 0.7161138                                 | 10.0      | 0.9998306                                 |
| 2.0       | 0.7385358                                 | 11.0      | 0.9999351                                 |
| 2.1       | 0.7593381                                 | 12.0      | 0.9999754                                 |
| 2.2       | 0.7786146                                 | 13.0      | 0.9999908                                 |
| 2.3       | 0.7964579                                 | 14.0      | 0.9999967                                 |
| 2.4       | 0.8129582                                 | 15.0      | 0.9999990                                 |
| 2.5       | 0.8282028                                 |           |   |

procedure depends on the relative values of  $\lambda_1$  and  $\lambda_{\text{cs}}$ . Case (a), if  $\lambda_1 < \lambda_{\text{cs}}$ : The escaping component of  $\mathcal{N}$  is computed from equation (7.1.50) with  $\zeta_{\text{esc}}$  and  $K_{\text{esc}}$  obtained from Tables IX.2 and IX.3, respectively, and evaluated with the  $\lambda_c$  appropriate to the exobase. The ballistic plus satellite component is similarly computed but with  $\zeta_{\text{bal}}$  and  $K_{\text{bal}}$  evaluated with  $\lambda_c$  replaced by  $\lambda_{\text{cs}}$ . Case (b), if  $\lambda_1 > \lambda_{\text{cs}}$ : The escaping component is evaluated exactly as before. The ballistic plus satellite component is computed in two intervals. The integrated density in the first interval,  $\lambda_1 > \lambda > \lambda_{\text{cs}}$ , is evaluated with  $\zeta$  and  $\Delta K$  obtained from Tables IX.1 and IX.4. For the second interval,  $\lambda_{\text{cs}} > \lambda > 0$ , we take  $\zeta(\lambda_{\text{cs}})$  and  $K(1, \lambda_{\text{cs}})$  from the ballistic columns of Tables IX.2 and IX.3,

(Text continues on p. 455)

**TABLE IX.2** Partition Functions for Ballistic and Escaping Orbits

| $\lambda_c = 1.0$ |                      |                      | $\lambda_c = 2.0$    |                      |
|-------------------|----------------------|----------------------|----------------------|----------------------|
| $\lambda$         | $\zeta_{\text{bal}}$ | $\zeta_{\text{esc}}$ | $\zeta_{\text{bal}}$ | $\zeta_{\text{esc}}$ |
| 0.1               | 0.0031541            | 0.0054313            | 0.0016478            | 0.0021737            |
| 0.2               | 0.0158253            | 0.0182501            | 0.0086060            | 0.0071668            |
| 0.3               | 0.0388161            | 0.0355262            | 0.0218891            | 0.0136826            |
| 0.4               | 0.0711837            | 0.0556409            | 0.0414704            | 0.0209618            |
| 0.5               | 0.1115230            | 0.0777011            | 0.0668653            | 0.0285147            |
| 0.6               | 0.1584466            | 0.1013701            | 0.0973691            | 0.0360195            |
| 0.7               | 0.2108664            | 0.1269113            | 0.1321862            | 0.0432664            |
| 0.8               | 0.2683348            | 0.1555973            | 0.1705066            | 0.0501251            |
| 0.9               | 0.3321255            | 0.1916387            | 0.2115528            | 0.0565225            |
| 1.0               | 0.4275932            | 0.2862033            | 0.2546090            | 0.0624283            |
| 1.1               |                      |                      | 0.2990377            | 0.0678453            |
| 1.2               |                      |                      | 0.3442906            | 0.0728034            |
| 1.3               |                      |                      | 0.3899154            | 0.0773571            |
| 1.4               |                      |                      | 0.4355640            | 0.0815874            |
| 1.5               |                      |                      | 0.4810061            | 0.0856088            |
| 1.6               |                      |                      | 0.5261605            | 0.0895902            |
| 1.7               |                      |                      | 0.5711717            | 0.0938043            |
| 1.8               |                      |                      | 0.6166366            | 0.0987735            |
| 1.9               |                      |                      | 0.6645299            | 0.1058662            |
| 2.0               |                      |                      | 0.7385358            | 0.1307320            |
| $\lambda_c = 3.0$ |                      |                      | $\lambda_c = 4.0$    |                      |
| $\lambda$         | $\zeta_{\text{bal}}$ | $\zeta_{\text{esc}}$ | $\zeta_{\text{bal}}$ | $\zeta_{\text{esc}}$ |
| 0.1               | 0.0011154            | 0.0013295            | 0.0008430            | 0.0009523            |
| 0.2               | 0.0059134            | 0.0043529            | 0.0045046            | 0.0031064            |
| 0.3               | 0.0152638            | 0.0082590            | 0.0117200            | 0.0058754            |
| 0.4               | 0.0293366            | 0.0125751            | 0.0227057            | 0.0089191            |
| 0.5               | 0.0479653            | 0.0169971            | 0.0374208            | 0.0120195            |
| 0.6               | 0.0707944            | 0.0213247            | 0.0556711            | 0.0150339            |
| 0.7               | 0.0973625            | 0.0254273            | 0.0771688            | 0.0178698            |
| 0.8               | 0.1271557            | 0.0292223            | 0.1015702            | 0.0204692            |
| 0.9               | 0.1596422            | 0.0326615            | 0.1285021            | 0.0227990            |
| 1.0               | 0.1942969            | 0.0357213            | 0.1575804            | 0.0248434            |
| 1.1               | 0.2306169            | 0.0383953            | 0.1884238            | 0.0265991            |
| 1.2               | 0.2681325            | 0.0406901            | 0.2206628            | 0.0280718            |
| 1.3               | 0.3064139            | 0.0426207            | 0.2539470            | 0.0292729            |
| 1.4               | 0.3450743            | 0.0442084            | 0.2879492            | 0.0302181            |
| 1.5               | 0.3837724            | 0.0454782            | 0.3223688            | 0.0309256            |

TABLE IX.2 (continued)

| $\lambda_c = 3.0$ |                      |                      | $\lambda_c = 4.0$    |                      |
|-------------------|----------------------|----------------------|----------------------|----------------------|
| $\lambda$         | $\zeta_{\text{bal}}$ | $\zeta_{\text{esc}}$ | $\zeta_{\text{bal}}$ | $\zeta_{\text{esc}}$ |
| 1.6               | 0.4222115            | 0.0464580            | 0.3569330            | 0.0314152            |
| 1.7               | 0.4601389            | 0.0471770            | 0.3913976            | 0.0317071            |
| 1.8               | 0.4973445            | 0.0476651            | 0.4255469            | 0.0318214            |
| 1.9               | 0.5336582            | 0.0479527            | 0.4591931            | 0.0317782            |
| 2.0               | 0.5689490            | 0.0480704            | 0.4921747            | 0.0315964            |
| 2.1               | 0.6031222            | 0.0480491            | 0.5243559            | 0.0312943            |
| 2.2               | 0.6361199            | 0.0479206            | 0.5556242            | 0.0308891            |
| 2.3               | 0.6679210            | 0.0477188            | 0.5858892            | 0.0303966            |
| 2.4               | 0.6985453            | 0.0474811            | 0.6150808            | 0.0298317            |
| 2.5               | 0.7280631            | 0.0472530            | 0.6431474            | 0.0292081            |
| 2.6               | 0.7566176            | 0.0470948            | 0.6700545            | 0.0285385            |
| 2.7               | 0.7844794            | 0.0470996            | 0.6957824            | 0.0278346            |
| 2.8               | 0.8122052            | 0.0474424            | 0.7203260            | 0.0271070            |
| 2.9               | 0.8412825            | 0.0485820            | 0.7436928            | 0.0263659            |
| 3.0               | 0.8883897            | 0.0558051            | 0.7659024            | 0.0256205            |
| 3.5               |                      |                      | 0.8611442            | 0.0221587            |
| 4.0               |                      |                      | 0.9539883            | 0.0230058            |
| $\lambda_c = 5.0$ |                      |                      | $\lambda_c = 7.5$    |                      |
| $\lambda$         | $\zeta_{\text{bal}}$ | $\zeta_{\text{sec}}$ | $\zeta_{\text{bal}}$ | $\zeta_{\text{sec}}$ |
| 0.1               | 0.0006775            | 0.0007404            | 0.0004545            | 0.0004745            |
| 0.2               | 0.0036380            | 0.0024094            | 0.0024567            | 0.0015391            |
| 0.3               | 0.0095123            | 0.0045483            | 0.0064675            | 0.0028978            |
| 0.4               | 0.0185221            | 0.0068921            | 0.0126828            | 0.0043806            |
| 0.5               | 0.0306831            | 0.0092718            | 0.0211637            | 0.0058796            |
| 0.6               | 0.0458852            | 0.0115769            | 0.0318873            | 0.0073248            |
| 0.7               | 0.0639381            | 0.0137363            | 0.0447743            | 0.0086716            |
| 0.8               | 0.0845997            | 0.0157060            | 0.0597070            | 0.0098926            |
| 0.9               | 0.1075971            | 0.0174609            | 0.0765414            | 0.0109728            |
| 1.0               | 0.1326409            | 0.0189898            | 0.0951166            | 0.0119056            |
| 1.1               | 0.1594359            | 0.0202909            | 0.1152607            | 0.0126909            |
| 1.2               | 0.1876891            | 0.0213694            | 0.1367970            | 0.0133327            |
| 1.3               | 0.2171163            | 0.0222348            | 0.1595472            | 0.0138376            |
| 1.4               | 0.2474455            | 0.0228999            | 0.1833347            | 0.0142145            |
| 1.5               | 0.2784207            | 0.0233795            | 0.2079873            | 0.0144733            |
| 1.6               | 0.3098037            | 0.0236892            | 0.2333387            | 0.0146245            |
| 1.7               | 0.3413754            | 0.0238452            | 0.2592300            | 0.0146786            |
| 1.8               | 0.3729367            | 0.0238633            | 0.2855109            | 0.0146463            |

(continues)

TABLE IX.2 (continued)

| $\lambda$          | $\lambda_c = 5.0$    |                      | $\lambda_c = 7.5$    |                      |
|--------------------|----------------------|----------------------|----------------------|----------------------|
|                    | $\zeta_{\text{bal}}$ | $\zeta_{\text{esc}}$ | $\zeta_{\text{bal}}$ | $\zeta_{\text{esc}}$ |
| 1.9                | 0.4043083            | 0.0237593            | 0.3120403            | 0.0145377            |
| 2.0                | 0.4353311            | 0.0235480            | 0.3386868            | 0.0143625            |
| 2.1                | 0.4658647            | 0.0232437            | 0.3653290            | 0.0141298            |
| 2.2                | 0.4957879            | 0.0228594            | 0.3918555            | 0.0138484            |
| 2.3                | 0.5249966            | 0.0224075            | 0.4181652            | 0.0135259            |
| 2.4                | 0.5534036            | 0.0218992            | 0.4441668            | 0.0131696            |
| 2.5                | 0.5809370            | 0.0213449            | 0.4697785            | 0.0127860            |
| 2.6                | 0.6075394            | 0.0207537            | 0.4949283            | 0.0123810            |
| 2.7                | 0.6331664            | 0.0201343            | 0.5195526            | 0.0119600            |
| 2.8                | 0.6577855            | 0.0194940            | 0.5435969            | 0.0115276            |
| 2.9                | 0.6813752            | 0.0188396            | 0.5670143            | 0.0110881            |
| 3.0                | 0.7039237            | 0.0181771            | 0.5897658            | 0.0106449            |
| 3.5                | 0.8011886            | 0.0149050            | 0.6926384            | 0.0084732            |
| 4.0                | 0.8746162            | 0.0119878            | 0.7765107            | 0.0065348            |
| 4.5                | 0.9289265            | 0.0096776            | 0.8421618            | 0.0049265            |
| 5.0                | 0.9814339            | 0.0092830            | 0.8918194            | 0.0036538            |
| 5.5                |                      |                      | 0.9282875            | 0.0026801            |
| 6.0                |                      |                      | 0.9544006            | 0.0019546            |
| 6.5                |                      |                      | 0.9727474            | 0.0014270            |
| 7.0                |                      |                      | 0.9856534            | 0.0010573            |
| 7.5                |                      |                      | 0.9981837            | 0.0009081            |
| $\lambda_c = 10.0$ |                      | $\lambda_c = 15.0$   |                      |                      |
| $\lambda$          | $\zeta_{\text{bal}}$ | $\zeta_{\text{esc}}$ | $\zeta_{\text{bal}}$ | $\zeta_{\text{esc}}$ |
| 0.1                | 0.0003420            | 0.0003487            | 0.0002287            | 0.0002277            |
| 0.2                | 0.0018545            | 0.0011292            | 0.0012444            | 0.0007361            |
| 0.3                | 0.0048995            | 0.0021232            | 0.0032996            | 0.0013821            |
| 0.4                | 0.0096434            | 0.0032057            | 0.0065191            | 0.0020842            |
| 0.5                | 0.0161540            | 0.0042978            | 0.0109642            | 0.0027911            |
| 0.6                | 0.0244367            | 0.0053483            | 0.0166556            | 0.0034695            |
| 0.7                | 0.0344551            | 0.0063248            | 0.0235868            | 0.0040986            |
| 0.8                | 0.0461430            | 0.0072076            | 0.0317320            | 0.0046658            |
| 0.9                | 0.0594135            | 0.0079859            | 0.0410510            | 0.0051642            |
| 1.0                | 0.0741651            | 0.0086555            | 0.0514939            | 0.0055914            |
| 1.1                | 0.0902866            | 0.0092163            | 0.0630029            | 0.0059475            |
| 1.2                | 0.1076602            | 0.0096716            | 0.0755155            | 0.0062348            |

TABLE IX.2 (continued)

| $\lambda$ | $\lambda_c = 10.0$   |                      | $\lambda_c = 15.0$   |                      |
|-----------|----------------------|----------------------|----------------------|----------------------|
|           | $\zeta_{\text{bal}}$ | $\zeta_{\text{esc}}$ | $\zeta_{\text{bal}}$ | $\zeta_{\text{esc}}$ |
| 1.3       | 0.1261649            | 0.0100266            | 0.0889653            | 0.0064569            |
| 1.4       | 0.1456785            | 0.0102880            | 0.1032836            | 0.0066182            |
| 1.5       | 0.1660789            | 0.0104631            | 0.1184008            | 0.0067237            |
| 1.6       | 0.1872463            | 0.0105599            | 0.1342465            | 0.0067785            |
| 1.7       | 0.2090636            | 0.0105862            | 0.1507507            | 0.0067880            |
| 1.8       | 0.2314178            | 0.0105498            | 0.1678442            | 0.0067573            |
| 1.9       | 0.2542002            | 0.0104584            | 0.1854591            | 0.0066912            |
| 2.0       | 0.2773072            | 0.0103191            | 0.2035290            | 0.0065946            |
| 2.1       | 0.3006408            | 0.0101386            | 0.2219893            | 0.0064718            |
| 2.2       | 0.3241087            | 0.0099233            | 0.2407776            | 0.0063270            |
| 2.3       | 0.3476242            | 0.0096789            | 0.2598337            | 0.0061639            |
| 2.4       | 0.3711069            | 0.0094107            | 0.2791000            | 0.0059859            |
| 2.5       | 0.3944822            | 0.0091234            | 0.2985212            | 0.0057961            |
| 2.6       | 0.4176819            | 0.0088214            | 0.3180449            | 0.0055973            |
| 2.7       | 0.4406431            | 0.0085085            | 0.3376212            | 0.0053920            |
| 2.8       | 0.4633092            | 0.0081881            | 0.3572031            | 0.0051823            |
| 2.9       | 0.4856288            | 0.0078633            | 0.3767460            | 0.0049703            |
| 3.0       | 0.5075563            | 0.0075367            | 0.3962084            | 0.0047576            |
| 3.5       | 0.6100652            | 0.0059457            | 0.4910461            | 0.0037273            |
| 4.0       | 0.6986411            | 0.0045380            | 0.5791505            | 0.0028233            |
| 4.5       | 0.7722627            | 0.0033792            | 0.6581367            | 0.0020849            |
| 5.0       | 0.8314909            | 0.0024689            | 0.7268622            | 0.0015092            |
| 5.5       | 0.8778145            | 0.0017773            | 0.7851346            | 0.0010751            |
| 6.0       | 0.9131511            | 0.0012647            | 0.8334304            | 0.0007561            |
| 6.5       | 0.9395052            | 0.0008918            | 0.8726492            | 0.0005260            |
| 7.0       | 0.9587566            | 0.0006246            | 0.9039130            | 0.0003627            |
| 7.5       | 0.9725498            | 0.0004354            | 0.9284158            | 0.0002482            |
| 8.0       | 0.9822550            | 0.0003028            | 0.9473205            | 0.0001687            |
| 8.5       | 0.9889730            | 0.0002106            | 0.9616937            | 0.0001140            |
| 9.0       | 0.9935690            | 0.0001472            | 0.9724720            | 0.0000767            |
| 9.5       | 0.9967392            | 0.0001046            | 0.9804492            | 0.0000513            |
| 10.0      | 0.9998306            | 0.0000846            | 0.9862797            | 0.0000342            |
| 11.0      |                      |                      | 0.9934941            | 0.0000150            |
| 12.0      |                      |                      | 0.9970901            | 0.0000065            |
| 13.0      |                      |                      | 0.9988011            | 0.0000027            |
| 14.0      |                      |                      | 0.9995809            | 0.0000011            |
| 15.0      |                      |                      | 0.9999990            | 0.0000005            |

**TABLE IX.3** Integrated-Density Functions for Ballistic and Escaping Particles

| $\lambda_c$ | $\lambda_1$ | $K_{\text{bal}}(1, \lambda_1)$ | $K_{\text{esc}}(1, \lambda_1)$ | $K_{\text{bal}}(0, \lambda_1)$ | $K_{\text{esc}}(0, \lambda_1)$ |
|-------------|-------------|--------------------------------|--------------------------------|--------------------------------|--------------------------------|
| 1           | 0.3         | 0.2043                         | 0.3313                         | 0.3646                         | 0.5055                         |
|             | 0.4         | 0.2732                         | 0.4415                         | 0.4870                         | 0.6733                         |
|             | 0.5         | 0.3417                         | 0.5475                         | 0.6089                         | 0.8360                         |
|             | 0.6         | 0.4093                         | 0.6466                         | 0.7295                         | 0.9905                         |
|             | 0.7         | 0.4751                         | 0.7351                         | 0.8476                         | 1.1322                         |
|             | 0.8         | 0.5376                         | 0.8066                         | 0.9615                         | 1.2531                         |
| 2           | 0.9         | 0.5935                         | 0.8460                         | 1.0664                         | 1.3335                         |
|             | 1.0         | 0.6064                         | 0.7142                         | 1.1038                         | 1.1708                         |
|             | 0.3         | 0.1953                         | 0.3419                         | 0.3537                         | 0.5175                         |
|             | 0.4         | 0.2583                         | 0.4614                         | 0.4691                         | 0.6958                         |
|             | 0.5         | 0.3204                         | 0.5814                         | 0.5834                         | 0.8747                         |
|             | 0.6         | 0.3815                         | 0.7012                         | 0.6963                         | 1.0531                         |
| 3           | 0.7         | 0.4415                         | 0.8202                         | 0.8079                         | 1.2305                         |
|             | 0.8         | 0.5003                         | 0.9376                         | 0.9181                         | 1.4060                         |
|             | 0.9         | 0.5579                         | 1.0530                         | 1.0268                         | 1.5790                         |
|             | 1.0         | 0.6142                         | 1.1655                         | 1.1338                         | 1.7486                         |
|             | 1.1         | 0.6692                         | 1.2745                         | 1.2391                         | 1.9140                         |
|             | 1.2         | 0.7227                         | 1.3791                         | 1.3425                         | 2.0742                         |
| 4           | 1.3         | 0.7745                         | 1.4782                         | 1.4437                         | 2.2279                         |
|             | 1.4         | 0.8245                         | 1.5705                         | 1.5427                         | 2.3733                         |
|             | 1.5         | 0.8725                         | 1.6541                         | 1.6390                         | 2.5083                         |
|             | 1.6         | 0.9182                         | 1.7263                         | 1.7322                         | 2.6294                         |
|             | 1.7         | 0.9610                         | 1.7829                         | 1.8215                         | 2.7310                         |
|             | 1.8         | 0.9999                         | 1.8156                         | 1.9053                         | 2.8025                         |
| 5           | 1.9         | 1.0321                         | 1.8045                         | 1.9793                         | 2.8167                         |
|             | 2.0         | 1.0251                         | 1.5515                         | 1.9868                         | 2.4826                         |
|             | 0.3         | 0.1919                         | 0.3458                         | 0.3495                         | 0.5217                         |
|             | 0.4         | 0.2525                         | 0.4680                         | 0.4620                         | 0.7032                         |
|             | 0.5         | 0.3116                         | 0.5917                         | 0.5726                         | 0.8862                         |
|             | 0.6         | 0.3692                         | 0.7164                         | 0.6814                         | 1.0701                         |
| 6           | 0.7         | 0.4254                         | 0.8415                         | 0.7884                         | 1.2545                         |
|             | 0.8         | 0.4802                         | 0.9667                         | 0.8936                         | 1.4388                         |
|             | 0.9         | 0.5336                         | 1.0917                         | 0.9972                         | 1.6228                         |
|             | 1.0         | 0.5857                         | 1.2161                         | 1.0990                         | 1.8060                         |
|             | 1.1         | 0.6363                         | 1.3396                         | 1.1991                         | 1.9881                         |
|             | 1.2         | 0.6856                         | 1.4620                         | 1.2975                         | 2.1688                         |
| 7           | 1.3         | 0.7336                         | 1.5828                         | 1.3941                         | 2.3478                         |
|             | 1.4         | 0.7801                         | 1.7019                         | 1.4890                         | 2.5246                         |
|             | 1.5         | 0.8253                         | 1.8189                         | 1.5821                         | 2.6989                         |

**TABLE IX.3** (*continued*)

| $\lambda_c$ | $\lambda_1$ | $K_{\text{bal}}(1, \lambda_1)$ | $K_{\text{esc}}(1, \lambda_1)$ | $K_{\text{bal}}(0, \lambda_1)$ | $K_{\text{esc}}(0, \lambda_1)$ |
|-------------|-------------|--------------------------------|--------------------------------|--------------------------------|--------------------------------|
| 3           | 1.6         | 0.8691                         | 1.9334                         | 1.6734                         | 2.8703                         |
|             | 1.7         | 0.9114                         | 2.0451                         | 1.7628                         | 3.0384                         |
|             | 1.8         | 0.9523                         | 2.1535                         | 1.8504                         | 3.2026                         |
|             | 1.9         | 0.9917                         | 2.2582                         | 1.9360                         | 3.3623                         |
|             | 2.0         | 1.0296                         | 2.3584                         | 2.0196                         | 3.5168                         |
|             | 2.1         | 1.0659                         | 2.4536                         | 2.1012                         | 3.6653                         |
|             | 2.2         | 1.1007                         | 2.5429                         | 2.1806                         | 3.8066                         |
|             | 2.3         | 1.1338                         | 2.6251                         | 2.2578                         | 3.9394                         |
|             | 2.4         | 1.1651                         | 2.6987                         | 2.3326                         | 4.0617                         |
|             | 2.5         | 1.1946                         | 2.7617                         | 2.4048                         | 4.1710                         |
| 4           | 2.6         | 1.2221                         | 2.8109                         | 2.4742                         | 4.2631                         |
|             | 2.7         | 1.2471                         | 2.8412                         | 2.5402                         | 4.3313                         |
|             | 2.8         | 1.2691                         | 2.8430                         | 2.6015                         | 4.3627                         |
|             | 2.9         | 1.2860                         | 2.7919                         | 2.6549                         | 4.3239                         |
|             | 3.0         | 1.2744                         | 2.4423                         | 2.6560                         | 3.8533                         |
|             | 0.3         | 0.1901                         | 0.3478                         | 0.3474                         | 0.5240                         |
|             | 0.4         | 0.2494                         | 0.4714                         | 0.4582                         | 0.7070                         |
|             | 0.5         | 0.3068                         | 0.5969                         | 0.5668                         | 0.8920                         |
|             | 0.6         | 0.3625                         | 0.7238                         | 0.6731                         | 1.0784                         |
|             | 0.7         | 0.4165                         | 0.8517                         | 0.7774                         | 1.2659                         |
| 5           | 0.8         | 0.4689                         | 0.9803                         | 0.8796                         | 1.4540                         |
|             | 0.9         | 0.5196                         | 1.1093                         | 0.9799                         | 1.6425                         |
|             | 1.0         | 0.5689                         | 1.2384                         | 1.0783                         | 1.8310                         |
|             | 1.1         | 0.6166                         | 1.3675                         | 1.1747                         | 2.0194                         |
|             | 1.2         | 0.6630                         | 1.4963                         | 1.2694                         | 2.2074                         |
|             | 1.3         | 0.7079                         | 1.6246                         | 1.3622                         | 2.3949                         |
|             | 1.4         | 0.7514                         | 1.7523                         | 1.4533                         | 2.5815                         |
|             | 1.5         | 0.7935                         | 1.8792                         | 1.5426                         | 2.7672                         |
|             | 1.6         | 0.8342                         | 2.0052                         | 1.6302                         | 2.9517                         |
|             | 1.7         | 0.8737                         | 2.1300                         | 1.7160                         | 3.1348                         |
| 6           | 1.8         | 0.9118                         | 2.2534                         | 1.8001                         | 3.3164                         |
|             | 1.9         | 0.9486                         | 2.3754                         | 1.8824                         | 3.4961                         |
|             | 2.0         | 0.9840                         | 2.4956                         | 1.9631                         | 3.6739                         |
|             | 2.1         | 1.0182                         | 2.6139                         | 2.0420                         | 3.8494                         |
|             | 2.2         | 1.0511                         | 2.7301                         | 2.1191                         | 4.0224                         |
|             | 2.3         | 1.0826                         | 2.8440                         | 2.1945                         | 4.1926                         |
|             | 2.4         | 1.1129                         | 2.9552                         | 2.2682                         | 4.3597                         |
|             | 2.5         | 1.1419                         | 3.0635                         | 2.3401                         | 4.5233                         |
|             | 2.6         | 1.1696                         | 3.1685                         | 2.4103                         | 4.6832                         |
|             | 2.7         | 1.1960                         | 3.2699                         | 2.4787                         | 4.8387                         |

*(continues)*

**TABLE IX.3** (*continued*)

| $\lambda_e$ | $\lambda_1$ | $K_{\text{bal}}(1, \lambda_1)$ | $K_{\text{esc}}(1, \lambda_1)$ | $K_{\text{bal}}(0, \lambda_1)$ | $K_{\text{esc}}(0, \lambda_1)$ |
|-------------|-------------|--------------------------------|--------------------------------|--------------------------------|--------------------------------|
| 4           | 2.8         | 1.2212                         | 3.3673                         | 2.5454                         | 4.9894                         |
|             | 2.9         | 1.2450                         | 3.4601                         | 2.6102                         | 5.1347                         |
|             | 3.0         | 1.2676                         | 3.5478                         | 2.6733                         | 5.2737                         |
|             | 3.5         | 1.3608                         | 3.8725                         | 2.9602                         | 5.8303                         |
|             | 4.0         | 1.3943                         | 3.3654                         | 3.1473                         | 5.2590                         |
|             | 0.3         | 0.1890                         | 0.3491                         | 0.3460                         | 0.5254                         |
|             | 0.4         | 0.2475                         | 0.4735                         | 0.4558                         | 0.7093                         |
|             | 0.5         | 0.3039                         | 0.6001                         | 0.5631                         | 0.8955                         |
|             | 0.6         | 0.3583                         | 0.7283                         | 0.6679                         | 1.0834                         |
|             | 0.7         | 0.4109                         | 0.8578                         | 0.7704                         | 1.2726                         |
| 5           | 0.8         | 0.4616                         | 0.9883                         | 0.8706                         | 1.4629                         |
|             | 0.9         | 0.5106                         | 1.1195                         | 0.9687                         | 1.6538                         |
|             | 1.0         | 0.5580                         | 1.2512                         | 1.0647                         | 1.8453                         |
|             | 1.1         | 0.6038                         | 1.3832                         | 1.1587                         | 2.0370                         |
|             | 1.2         | 0.6480                         | 1.5154                         | 1.2507                         | 2.2289                         |
|             | 1.3         | 0.6907                         | 1.6476                         | 1.3408                         | 2.4206                         |
|             | 1.4         | 0.7320                         | 1.7797                         | 1.4291                         | 2.6122                         |
|             | 1.5         | 0.7719                         | 1.9115                         | 1.5155                         | 2.8034                         |
|             | 1.6         | 0.8104                         | 2.0429                         | 1.6002                         | 2.9942                         |
|             | 1.7         | 0.8475                         | 2.1739                         | 1.6831                         | 3.1843                         |
| 6           | 1.8         | 0.8834                         | 2.3042                         | 1.7643                         | 3.3736                         |
|             | 1.9         | 0.9180                         | 2.4338                         | 1.8438                         | 3.5620                         |
|             | 2.0         | 0.9513                         | 2.5625                         | 1.9217                         | 3.7495                         |
|             | 2.1         | 0.9834                         | 2.6903                         | 1.9979                         | 3.9358                         |
|             | 2.2         | 1.0142                         | 2.8170                         | 2.0725                         | 4.1208                         |
|             | 2.3         | 1.0439                         | 2.9425                         | 2.1454                         | 4.3044                         |
|             | 2.4         | 1.0724                         | 3.0667                         | 2.2168                         | 4.4865                         |
|             | 2.5         | 1.0997                         | 3.1895                         | 2.2866                         | 4.6669                         |
|             | 2.6         | 1.1259                         | 3.3106                         | 2.3548                         | 4.8454                         |
|             | 2.7         | 1.1509                         | 3.4301                         | 2.4214                         | 5.0219                         |
| 7           | 2.8         | 1.1749                         | 3.5477                         | 2.4865                         | 5.1962                         |
|             | 2.9         | 1.1977                         | 3.6632                         | 2.5500                         | 5.3682                         |
|             | 3.0         | 1.2194                         | 3.7766                         | 2.6120                         | 5.5375                         |
|             | 3.5         | 1.3123                         | 4.303                          | 2.8992                         | 6.336                          |
|             | 4.0         | 1.3800                         | 4.733                          | 3.1496                         | 7.021                          |
|             | 4.5         | 1.4241                         | 4.986                          | 3.3637                         | 7.488                          |
|             | 5.0         | 1.4301                         | 4.310                          | 3.5087                         | 6.688                          |
|             | 7.5         | 0.3                            | 0.1875                         | 0.351                          | 0.527                          |
|             | 0.4         | 0.2448                         | 0.476                          | 0.4526                         | 0.712                          |
|             | 0.5         | 0.2998                         | 0.604                          | 0.5580                         | 0.900                          |

TABLE IX.3 (continued)

| $\lambda_c$ | $\lambda_1$ | $K_{\text{bal}}(1, \lambda_1)$ | $K_{\text{esc}}(1, \lambda_1)$ | $K_{\text{bal}}(0, \lambda_1)$ | $K_{\text{esc}}(0, \lambda_1)$ |
|-------------|-------------|--------------------------------|--------------------------------|--------------------------------|--------------------------------|
| 7.5         | 0.6         | 0.3525                         | 0.734                          | 0.6606                         | 1.090                          |
|             | 0.7         | 0.4029                         | 0.865                          | 0.7605                         | 1.281                          |
|             | 0.8         | 0.4514                         | 0.998                          | 0.8579                         | 1.474                          |
|             | 0.9         | 0.4978                         | 1.132                          | 0.9527                         | 1.668                          |
|             | 1.0         | 0.5424                         | 1.267                          | 1.0452                         | 1.863                          |
|             | 1.1         | 0.5852                         | 1.403                          | 1.1353                         | 2.059                          |
|             | 1.2         | 0.6263                         | 1.539                          | 1.2233                         | 2.255                          |
|             | 1.3         | 0.6657                         | 1.676                          | 1.3092                         | 2.452                          |
|             | 1.4         | 0.7036                         | 1.813                          | 1.3931                         | 2.650                          |
|             | 1.5         | 0.7399                         | 1.951                          | 1.4750                         | 2.847                          |
| 1.6         | 0.7748      | 2.088                          | 1.5550                         | 3.045                          |                                |
|             | 0.8084      | 2.226                          | 1.6331                         | 3.243                          |                                |
|             | 0.8405      | 2.364                          | 1.7096                         | 3.441                          |                                |
|             | 0.8714      | 2.502                          | 1.7843                         | 3.639                          |                                |
|             | 0.9011      | 2.640                          | 1.8573                         | 3.836                          |                                |
|             | 0.9296      | 2.778                          | 1.9287                         | 4.034                          |                                |
|             | 0.9569      | 2.915                          | 1.9986                         | 4.231                          |                                |
|             | 0.9831      | 3.052                          | 2.0669                         | 4.428                          |                                |
|             | 1.0082      | 3.189                          | 2.1338                         | 4.624                          |                                |
|             | 1.0323      | 3.325                          | 2.1992                         | 4.820                          |                                |
| 2.1         | 1.0553      | 3.461                          | 2.2632                         | 5.015                          |                                |
|             | 1.0774      | 3.597                          | 2.3258                         | 5.210                          |                                |
|             | 1.0985      | 3.732                          | 2.3870                         | 5.404                          |                                |
|             | 1.1187      | 3.866                          | 2.4469                         | 5.598                          |                                |
|             | 1.1380      | 4.000                          | 2.5055                         | 5.790                          |                                |
|             | 3.5         | 1.2216                         | 4.657                          | 2.7798                         | 6.740                          |
|             | 4.0         | 1.2857                         | 5.290                          | 3.0248                         | 7.661                          |
|             | 4.5         | 1.3328                         | 5.891                          | 3.2428                         | 8.545                          |
|             | 5.0         | 1.3649                         | 6.449                          | 3.4361                         | 9.380                          |
|             | 5.5         | 1.3842                         | 6.952                          | 3.6073                         | 10.149                         |
| 6.0         | 1.3927      | 7.38                           | 3.7588                         | 10.83                          |                                |
|             | 6.5         | 1.3926                         | 7.68                           | 3.8931                         | 11.4                           |
|             | 7.0         | 1.3854                         | 7.78                           | 4.0125                         | 11.6                           |
|             | 7.5         | 1.3688                         | 6.74                           | 4.1087                         | 10.3                           |
|             | 0.3         | 0.1868                         | 0.352                          | 0.3433                         | 0.528                          |
|             | 0.4         | 0.2435                         | 0.478                          | 0.4509                         | 0.714                          |
|             | 0.5         | 0.2977                         | 0.607                          | 0.5554                         | 0.902                          |
|             | 0.6         | 0.3494                         | 0.737                          | 0.6569                         | 1.093                          |
|             | 0.7         | 0.3988                         | 0.870                          | 0.7554                         | 1.286                          |
|             | 0.8         | 0.4460                         | 1.004                          | 0.8512                         | 1.480                          |

(continues) 451

TABLE IX.3 (continued)

| $\lambda_c$ | $\lambda_1$ | $K_{\text{bar}}(1, \lambda_1)$ | $K_{\text{esc}}(1, \lambda_1)$ | $K_{\text{bar}}(0, \lambda_1)$ | $K_{\text{esc}}(0, \lambda_1)$ |
|-------------|-------------|--------------------------------|--------------------------------|--------------------------------|--------------------------------|
| 10          | 0.9         | 0.4911                         | 1.139                          | 0.9442                         | 1.675                          |
|             | 1.0         | 0.5342                         | 1.275                          | 1.0348                         | 1.872                          |
| 1.1         | 1.1         | 0.5753                         | 1.413                          | 1.1228                         | 2.070                          |
|             | 1.2         | 0.6147                         | 1.551                          | 1.2086                         | 2.268                          |
|             | 1.3         | 0.6522                         | 1.690                          | 1.2920                         | 2.468                          |
|             | 1.4         | 0.6882                         | 1.829                          | 1.3734                         | 2.668                          |
|             | 1.5         | 0.7225                         | 1.969                          | 1.4526                         | 2.868                          |
|             | 1.6         | 0.7553                         | 2.110                          | 1.5299                         | 3.069                          |
|             | 1.7         | 0.7867                         | 2.251                          | 1.6053                         | 3.270                          |
|             | 1.8         | 0.8168                         | 2.392                          | 1.6788                         | 3.472                          |
|             | 1.9         | 0.8455                         | 2.534                          | 1.7506                         | 3.673                          |
|             | 2.0         | 0.8729                         | 2.675                          | 1.8207                         | 3.875                          |
| 2.1         | 2.1         | 0.8992                         | 2.817                          | 1.8891                         | 4.077                          |
|             | 2.2         | 0.9243                         | 2.959                          | 1.9560                         | 4.280                          |
|             | 2.3         | 0.9483                         | 3.101                          | 2.0214                         | 4.482                          |
|             | 2.4         | 0.9713                         | 3.243                          | 2.0853                         | 4.684                          |
|             | 2.5         | 0.9933                         | 3.384                          | 2.1478                         | 4.886                          |
| 2.6         | 2.6         | 1.0143                         | 3.526                          | 2.2089                         | 5.088                          |
|             | 2.7         | 1.0343                         | 3.668                          | 2.2687                         | 5.289                          |
|             | 2.8         | 1.0535                         | 3.809                          | 2.3272                         | 5.491                          |
|             | 2.9         | 1.0718                         | 3.951                          | 2.3845                         | 5.692                          |
|             | 3.0         | 1.0893                         | 4.092                          | 2.4405                         | 5.893                          |
| 3.5         | 3.5         | 1.1653                         | 4.793                          | 2.7037                         | 6.892                          |
|             | 4.0         | 1.2245                         | 5.484                          | 2.9410                         | 7.879                          |
|             | 4.5         | 1.2694                         | 6.160                          | 3.1552                         | 8.849                          |
|             | 5.0         | 1.3021                         | 6.82                           | 3.3485                         | 9.80                           |
|             | 5.5         | 1.3243                         | 7.45                           | 3.5229                         | 10.72                          |
| 6.0         | 6.0         | 1.3377                         | 8.06                           | 3.6805                         | 11.61                          |
|             | 6.5         | 1.3436                         | 8.64                           | 3.8230                         | 12.47                          |
|             | 7.0         | 1.3435                         | 9.18                           | 3.9524                         | 13.28                          |
|             | 7.5         | 1.3387                         | 9.67                           | 4.0705                         | 14.0                           |
|             | 8.0         | 1.3303                         | 10.1                           | 4.1790                         | 14.7                           |
| 8.5         | 8.5         | 1.3194                         | 10.4                           | 4.2795                         | 15.3                           |
|             | 9.0         | 1.3068                         | 10.6                           | 4.3736                         | 15.7                           |
|             | 9.5         | 1.2932                         | 10.6                           | 4.4622                         | 16                             |
|             | 10.0        | 1.2781                         | 9.2                            | 4.5436                         | 14                             |
| 15          | 0.3         | 0.1860                         | 0.353                          | 0.3423                         | 0.529                          |
|             | 0.4         | 0.2421                         | 0.480                          | 0.4492                         | 0.715                          |
|             | 0.5         | 0.2955                         | 0.609                          | 0.5527                         | 0.905                          |
|             | 0.6         | 0.3463                         | 0.740                          | 0.6530                         | 1.096                          |
|             | 0.7         | 0.3946                         | 0.874                          | 0.7501                         | 1.290                          |

**TABLE IX.3** (*continued*)

| $\lambda_c$ | $\lambda_1$ | $K_{\text{bal}}(1, \lambda_1)$ | $K_{\text{esc}}(1, \lambda_1)$ | $K_{\text{bal}}(0, \lambda_1)$ | $K_{\text{esc}}(0, \lambda_1)$ |
|-------------|-------------|--------------------------------|--------------------------------|--------------------------------|--------------------------------|
| 15          | 0.8         | 0.4405                         | 1.009                          | 0.8442                         | 1.486                          |
|             | 0.9         | 0.4841                         | 1.146                          | 0.9354                         | 1.683                          |
|             | 1.0         | 0.5256                         | 1.283                          | 1.0239                         | 1.881                          |
|             | 1.1         | 0.5650                         | 1.423                          | 1.1097                         | 2.081                          |
|             | 1.2         | 0.6025                         | 1.563                          | 1.1930                         | 2.281                          |
|             | 1.3         | 0.6381                         | 1.703                          | 1.2739                         | 2.483                          |
|             | 1.4         | 0.6719                         | 1.845                          | 1.3524                         | 2.685                          |
|             | 1.5         | 0.7040                         | 1.988                          | 1.4288                         | 2.888                          |
|             | 1.6         | 0.7346                         | 2.131                          | 1.5030                         | 3.092                          |
|             | 1.7         | 0.7636                         | 2.275                          | 1.5752                         | 3.296                          |
|             | 1.8         | 0.7913                         | 2.419                          | 1.6455                         | 3.501                          |
|             | 1.9         | 0.8175                         | 2.563                          | 1.7139                         | 3.707                          |
|             | 2.0         | 0.8425                         | 2.709                          | 1.7806                         | 3.912                          |
|             | 2.1         | 0.8662                         | 2.854                          | 1.8456                         | 4.119                          |
|             | 2.2         | 0.8888                         | 3.000                          | 1.9090                         | 4.325                          |
|             | 2.3         | 0.9103                         | 3.146                          | 1.9709                         | 4.532                          |
|             | 2.4         | 0.9308                         | 3.292                          | 2.0313                         | 4.739                          |
|             | 2.5         | 0.9502                         | 3.439                          | 2.0902                         | 4.946                          |
|             | 2.6         | 0.9687                         | 3.586                          | 2.1478                         | 5.154                          |
|             | 2.7         | 0.9864                         | 3.733                          | 2.2042                         | 5.361                          |
|             | 2.8         | 1.0032                         | 3.880                          | 2.2592                         | 5.569                          |
|             | 2.9         | 1.0191                         | 4.027                          | 2.3131                         | 5.777                          |
|             | 3.0         | 1.0344                         | 4.175                          | 2.3659                         | 5.985                          |
|             | 3.5         | 1.1002                         | 4.912                          | 2.6139                         | 7.024                          |
|             | 4.0         | 1.1517                         | 5.648                          | 2.8391                         | 8.062                          |
|             | 4.5         | 1.1917                         | 6.380                          | 3.0448                         | 9.095                          |
|             | 5.0         | 1.2224                         | 7.11                           | 3.2336                         | 10.12                          |
|             | 5.5         | 1.2453                         | 7.83                           | 3.4075                         | 11.14                          |
|             | 6.0         | 1.2616                         | 8.54                           | 3.5681                         | 12.15                          |
|             | 6.5         | 1.2725                         | 9.24                           | 3.7166                         | 13.14                          |
|             | 7.0         | 1.2787                         | 9.93                           | 3.8543                         | 14.13                          |
|             | 7.5         | 1.2810                         | 10.61                          | 3.9822                         | 15.10                          |
|             | 8.0         | 1.2801                         | 11.27                          | 4.1014                         | 16.05                          |
|             | 8.5         | 1.2766                         | 11.92                          | 4.2127                         | 16.99                          |
|             | 9.0         | 1.2710                         | 12.55                          | 4.3173                         | 17.90                          |
|             | 9.5         | 1.2639                         | 13.17                          | 4.4159                         | 18.81                          |
|             | 10.0        | 1.2557                         | 13.77                          | 4.5095                         | 19.69                          |
|             | 11.0        | 1.2375                         | 14.9                           | 4.6845                         | 21.3                           |
|             | 12.0        | 1.2187                         | 16.0                           | 4.8473                         | 23.2                           |
|             | 13.0        | 1.2007                         | 17.3                           | 5.0016                         | 25.0                           |
|             | 14.0        | 1.1842                         | 18                             | 5.1498                         | 27                             |
|             | 15.0        | 1.1694                         | 20                             | 5.2933                         | 30                             |

**TABLE IX.4** Integrated-Density Functions for Ballistic plus Satellite Particles

| $\lambda_{\text{cs}}$ | $\lambda_1$ | $\Delta K_{\text{bal+sat}}(1, \lambda_1; \lambda_{\text{cs}})$ | $\lambda_{\text{cs}}$ | $\lambda_1$ | $\Delta K_{\text{bal+sat}}(1, \lambda_1; \lambda_{\text{cs}})$ |
|-----------------------|-------------|--|-----------------------|-------------|--|
| 1                     | 1.1         | 0.09997  | 2                     | 6.0         | 1.50335  |
|                       | 1.2         | 0.19923  |                       | 6.5         | 1.49009  |
|                       | 1.3         | 0.29700  |                       | 7.0         | 1.46717  |
|                       | 1.4         | 0.39264  |                       | 7.5         | 1.43939  |
|                       | 1.5         | 0.48566  |                       | 8.0         | 1.40997  |
|                       | 1.6         | 0.57567  |                       | 8.5         | 1.38089  |
|                       | 1.7         | 0.66237  |                       | 9.0         | 1.35332  |
|                       | 1.8         | 0.74552  |                       | 9.5         | 1.32784  |
|                       | 1.9         | 0.82497  |                       | 10.0        | 1.30468  |
|                       | 2.0         | 0.90058  |                       | 10.5        | 1.28383  |
|                       | 2.1         | 0.97228  |                       | 11.0        | 1.26518  |
|                       | 2.2         | 1.04003  |                       | 11.5        | 1.24852  |
|                       | 2.3         | 1.10383  |                       | 12.0        | 1.23365  |
|                       | 2.4         | 1.16369  |                       | 12.5        | 1.22035  |
|                       | 2.5         | 1.21965  |                       | 13.0        | 1.20844  |
|                       | 2.6         | 1.27179  |                       |             |  |
|                       | 2.7         | 1.32017  | 3                     | 3.5         | 0.44449  |
|                       | 2.8         | 1.36490  |                       | 4.0         | 0.78192  |
|                       | 2.9         | 1.40607  |                       | 4.5         | 1.02489  |
|                       | 3.0         | 1.44380  |                       | 5.0         | 1.19035  |
|                       | 3.5         | 1.58543  |                       | 5.5         | 1.29565  |
|                       | 4.0         | 1.66124  |                       | 6.0         | 1.35646  |
|                       | 4.5         | 1.68827  |                       | 6.5         | 1.38583  |
|                       | 5.0         | 1.68166  |                       | 7.0         | 1.39395  |
|                       | 5.5         | 1.65372  |                       | 7.5         | 1.38847  |
|                       | 6.0         | 1.61380  |                       | 8.0         | 1.37485  |
|                       | 6.5         | 1.56850  |                       | 8.5         | 1.35685  |
|                       | 7.0         | 1.52222  |                       | 9.0         | 1.33698  |
|                       | 7.5         | 1.47769  |                       | 9.5         | 1.31680  |
|                       | 8.0         | 1.43637  |                       | 10.0        | 1.29726  |
|                       |             |  |                       | 10.5        | 1.27887  |
| 2                     | 2.1         | 0.09848  | 4                     | 11.0        | 1.26187  |
|                       | 2.2         | 0.19378  |                       | 11.5        | 1.24633  |
|                       | 2.3         | 0.28567  |                       | 12.0        | 1.23220  |
|                       | 2.4         | 0.37397  |                       | 12.5        | 1.21940  |
|                       | 2.5         | 0.45857  |                       | 13.0        | 1.20782  |
|                       | 2.6         | 0.53939  |                       | 13.5        | 1.19732  |
|                       | 2.7         | 0.61636  |                       | 14.0        | 1.18780  |
|                       | 2.8         | 0.68946  |                       | 14.5        | 1.17914  |
|                       | 2.9         | 0.75871  |                       | 15.0        | 1.17124  |
|                       | 3.0         | 0.82411  |                       |             |  |
|                       | 3.5         | 1.09573  |                       | 4.5         | 0.43500  |
|                       | 4.0         | 1.28383  |                       | 5.0         | 0.75347  |
|                       | 4.5         | 1.40355  |                       | 5.5         | 0.97724  |
|                       | 5.0         | 1.47079  |                       | 6.0         | 1.12764  |
|                       | 5.5         | 1.50004  |                       | 6.5         | 1.22339  |

TABLE IX.4 (continued)

| $\lambda_{\text{es}}$ | $\lambda_1$ | $\Delta K_{\text{bal+sat}}(1, \lambda_1; \lambda_{\text{es}})$ | $\lambda_{\text{es}}$ | $\lambda_1$ | $\Delta K_{\text{bal+sat}}(1, \lambda_1; \lambda_{\text{es}})$ |
|-----------------------|-------------|--|-----------------------|-------------|--|
| 4                     | 7.0         | 1.27989  | 5                     | 10.0        | 1.26577  |
|                       | 7.5         | 1.30914  |                       | 10.5        | 1.25782  |
|                       | 8.0         | 1.32014  |                       | 11.0        | 1.24786  |
|                       | 8.5         | 1.31941  |                       | 11.5        | 1.23704  |
|                       | 9.0         | 1.31152  |                       | 12.0        | 1.22607  |
|                       | 9.5         | 1.29960  |                       | 12.5        | 1.21536  |
|                       | 10.0        | 1.28579  |                       | 13.0        | 1.20517  |
|                       | 10.5        | 1.27115  |                       | 13.5        | 1.19559  |
|                       | 11.0        | 1.25673  |                       | 14.0        | 1.18667  |
|                       | 11.5        | 1.24292  |                       | 14.5        | 1.17841  |
|                       | 12.0        | 1.22995  |                       | 15.0        | 1.17076  |
|                       | 12.5        | 1.21792  |                       |             |  |
|                       | 13.0        | 1.20685  | 7.5                   | 8.0         | 0.41733  |
|                       | 13.5        | 1.19669  |                       | 8.5         | 0.70151  |
|                       | 14.0        | 1.18739  |                       | 9.0         | 0.89148  |
|                       | 14.5        | 1.17887  |                       | 9.5         | 1.01579  |
|                       | 15.0        | 1.17106  |                       | 10.0        | 1.09498  |
|                       |             |  |                       | 10.5        | 1.14362  |
| 5                     | 5.5         | 0.42810  |                       | 11.0        | 1.17184  |
|                       | 6.0         | 0.73299  |                       | 11.5        | 1.18665  |
|                       | 6.5         | 0.94325  |                       | 12.0        | 1.19279  |
|                       | 7.0         | 1.08317  |                       | 12.5        | 1.19346  |
|                       | 7.5         | 1.17232  |                       | 13.0        | 1.19080  |
|                       | 8.0         | 1.22579  |                       | 13.5        | 1.18619  |
|                       | 8.5         | 1.25483  |                       | 14.0        | 1.18054  |
|                       | 9.0         | 1.26762  |                       | 14.5        | 1.17442  |
|                       | 9.5         | 1.26994  |                       | 15.0        | 1.16817  |

wherein the parameter  $\lambda_c$  is replaced with  $\lambda_{\text{es}}$ . Of course, whenever  $\lambda_{\text{es}}$  is used in evaluating  $\zeta$  and  $K$  in order to account for satellite particles,  $N_c \exp(-\lambda_c)$  in (7.1.50) is unchanged and is still computed for the original exobase  $\lambda_c$ . These tables are from J. W. CHAMBERLAIN (1963), *Planet. Space Sci.* **11**, 901–960, except that Table IX.4 has been recomputed. For values of  $\mu_1 \neq 1$ , the second integration interval is not stated correctly on p. 929 of this paper, because  $\mu_1 = \cos \theta_1$  is not constant along the integration path.

## AUTHOR INDEX

### A

Abell, G. O., 433  
Ackerman, T. P., 408, 412  
Adams, W. S., 219  
Ajello, J. M., 323, 324  
Allen, C. W., 24, 95, 97, 272  
Allen, M., 112, 113, 157, 327, 406  
Allison, M., 66, 115  
Alvarez, L. W., 411  
Alvarez, W., 411  
Anders, E., 408  
Anderson, D. E., Jr., 324, 325, 373, 404,  
    406  
Anderson, J. D., 67  
Anderson, L. G., 153  
Andrew, B. H., 115  
Angstrom, A. J., 320  
Anicich, V. G., 154  
Appleby, J. F., 57, 67  
Appleton, E. V., 271, 274  
Argabright, V., 322  
Atreya, S. K., 267, 276, 324, 325, 400, 401  
Avduevsky, V. S., 64, 429, 430

### B

Bailey, A. D., 273  
Baluteau, J. P., 66, 220

Banks, P. M., 326, 403  
Barber, R. T., 410  
Barcilon, A., 114  
Barfield, R. H., 271  
Barker, E. S., 65  
Barnett, M. A. F., 271  
Barrett, A. H., 64  
Barrett, J. W., 157  
Barron, D. W., 272  
Barshay, S. S., 112  
Barth, C. A., 65, 275, 301, 322, 323, 324,  
    325  
Bates, D. R., 22, 63, 69, 154, 271, 272, 321,  
    413, 439  
Bauer, E., 156  
Bauer, S. J., 273  
Baurer, T., 273  
Beebe, R. F., 115  
Bellman, R. E., 217  
Belton, M. J. S., 66, 191, 192, 218, 219,  
    220, 221, 324, 325  
Benedict, W. S., 221  
Berger, A., 410  
Bergstrahl, J. T. 67, 116  
Bertaux, J. L., 323, 324, 325, 400, 401,  
    404, 405

- Bevilacqua, R. M., 223  
 Bezard, B., 220  
 Biemann, K., 220  
 Biller, J. E., 220  
 Bilski, K., 410  
 Binder, A. B., 196  
 Birnbaum, A., 220  
 Bishop, J., 402  
 Bjerknes, J., 111  
 Black, D. C., 407  
 Black, G., 321, 322  
 Blamont, J. E., 323, 324, 325, 401, 405  
 Bologna, J. M., 223  
 Booker, H. G., 274  
 Borodin, N. F., 64, 429  
 Bortner, M. H., 273  
 Botkin, D. B., 412  
 Bouger, S. W., 322  
 Bowles, K. L., 275  
 Boyer, C., 113  
 Brace, L. H., 275  
 Bradbury, N. E., 271  
 Brandt, J. C., 217, 323  
 Branscomb, L. M. 273  
 Brasseur, G., 134, 434  
 Breig, E. L., 404  
 Breit, G., 271, 322  
 Brenkle, J., 65  
 Brewer, A. W., 63  
 Briggs, F. H., 115  
 Briggs, G. A., 114  
 Brinkmann, R. T., 402  
 Brinton, H. C., 40, 64, 275, 403, 405  
 Broadfoot, A. L., 65, 66, 67, 113, 219, 283,  
     308, 323, 324, 325, 401, 403, 404, 408  
 Brown, R. A., 325  
 Budyko, M. I., 410  
 Burch, D. E., 221  
 Burns, J. A., 67, 401, 408, 410, 432  
 Burnside, R. G., 400, 401  
 Busse, F. H., 114  
 Butler, D. M., 276  
 Byram, E. T., 323, 324
- C**
- Cahalan, R. F., 411  
 Caldwell, J. J., 220  
 Calfee, R. F., 221  
 Callegari, A. J., 408  
 Calvert, J. G., 153  
 Camichel, H., 113  
 Cane, M. A., 410
- Carleton, N. P., 322, 325  
 Carlson, R. W., 307, 323  
 Carruthers, G. R., 323  
 Cazes, S., 400  
 Cess, R. D., 408, 409, 410, 411, 412  
 Chahine, M., 223  
 Chamberlain, J. W., 63, 156, 180, 181, 183,  
     186, 218, 219, 238, 272, 276, 295,  
     320, 321, 322, 323, 324, 326, 350,  
     358, 361, 400, 401, 402, 405, 407,  
     409, 413, 414  
 Chameides, W. L., 155, 413  
 Chandrasekhar, S., 61, 114, 167, 217, 222  
 Chapman, C. R., 114  
 Chapman, S., 62, 63, 112, 114, 154, 208,  
     271, 322, 402, 439  
 Charney, J. G., 111, 115  
 Chase, S. C., 65  
 Chavez, F. P., 410  
 Chedin, A., 66, 220  
 Cheng, A. F., 406  
 Chervin, R. M., 411  
 Christensen, E., 65  
 Christie-Blick, N., 410  
 Chubb, T. A., 323, 324  
 Cicerone, R. J., 155, 156, 157, 413, 414  
 Clark, J. T., 322  
 Clark, W. C., 412  
 Clough, S. A., 221  
 Cloutier, P. A., 326  
 Coakley, J. A., Jr., 62, 411  
 Cochran, W. D., 218  
 Cole, K. D., 403  
 Colegrove, F. D., 112  
 Colin, L., 65, 113, 220, 275, 325, 327, 430  
 Comiso, J. C., 413  
 Connes, J., 188, 219  
 Connes, P., 188, 219, 322, 325  
 Conrath, B. J., 66, 114, 115, 220, 222, 441  
 Cowling, T. G., 112, 402, 439  
 Cravens, T. E., 64, 275, 276, 405, 406  
 Crawford, S. L., 276  
 Croll, J., 410  
 Cruikshank, D. P., 66, 67, 196  
 Crutzen, P. J., 154, 155, 156  
 Cuong, P. G., 115  
 Curtis, A. R., 63, 218
- D**
- Dalgarno, A., 324  
 Daniell, R. E., Jr., 326  
 Danielson, R. E., 218

- Davis, D. D., 414  
Davis, M., 411  
de Bergh, C., 408  
Deepak, A., 223  
Deirmendjian, D., 221  
Delwiche, C. C., 412  
Deming, L. S., 62, 154  
DeMore, W. B., 112, 153, 313, 327  
Denison, J. S., 272  
dePater, 213, 221, 223  
deZafra, R., 157  
Dessler, A. J., 64, 67, 326  
Dick, K. A., 321  
Dicke, R. H., 220  
Dickinson, R. E., 64  
Dirac, P. A. M., 322  
Dolan, P. J., 412  
Donahue, T. M., 65, 113, 155, 220, 267,  
    275, 276, 321, 324, 325, 326, 327, 400,  
    404, 406, 407, 408, 412, 430  
Dufay, J., 320  
Dungey, J. W., 272  
Dunham, T., Jr., 187, 219  
Durrance, S. T., 325
- E**
- Eccles, W. H., 273  
Eddington, A. S., 272  
Eddy, J. A., 409  
Ehhalt, D. H., 155  
Ehrlich, P. R., 412  
Ekonomov, A. P., 430  
Elkins, J. W., 155  
Elliot, J., 223, 276  
Emden, R., 62  
Emerich, C., 401  
Epstein, E. S., 413  
Ericson, D. B., 409  
Eshleman, V. R., 64, 66, 67, 274, 275  
Estermann, I., 439  
Etkins, R., 413  
Evans, F. J., 322  
Evenson, K. M., 154
- F**
- Fabry, C., 320  
Fahr, H. J., 400  
Farless, D., 65  
Farrell, B., 408, 410
- Fastie, W. G., 325  
Fehsenfeld, F. C., 272  
Feldman, P. D., 322  
Ferguson, E. E., 243, 244, 272, 273, 276  
Fimmel, R. O., 430  
Fink, U., 219, 220  
Fjeldbo, G., 48, 64, 65, 274, 276  
Flasar, F. M., 66, 67, 220, 222, 406  
Foley, H. M., 155, 414  
Fox, K., 221  
French, R. G., 223, 276  
Fricke, K. H., 112  
Friedman, H., 323, 324
- G**
- Garing, J. S., 221  
Garneau, G. W., 115  
Garriott, O. K., 273, 274  
Garstang, R. H., 286  
Garvin, D., 153  
Gauss, C. F., 271  
Gautier, D., 66, 220, 222, 223  
Gehrels, T., 66, 67, 115, 219, 220, 221,  
    223, 276, 324, 431  
Geiger, R., 410  
Gerard, J. C., 322  
Gibbons, C. J., 223  
Giersch, P. J., 43, 65, 67, 114, 115, 222,  
    223, 276, 441  
Gille, J. C., 221  
Gilliland, R. L., 409  
Gilmore, F. R., 156  
Glasstone, S., 412  
Godson, W. L., 218  
Gold, E., 63  
Goldberg, B. A., 307  
Golden, D. M., 153  
Goldstein, S., 274  
Golitsyn, G. S., 111  
Gombosi, T. I., 275, 276  
Goody, R. M., 43, 61, 62, 63, 65, 218, 220  
    324, 433, 437  
Gordon, W. E., 275  
Gornitz, V., 413  
Graedel, T. E., 414  
Greenstein, J. L., 217  
Greiman, P. W., 113  
Gross, S. H., 64  
Grossi, M., 65  
Grossman, K., 217

**H**

- Hadley, G., 110  
 Haff, P. K., 406  
 Hambridge, G., 79  
 Hameed, S., 412  
 Hampson, R. F., 153  
 Hamilton, K., 114  
 Hammer, D., 414  
 Hanel, R. A., 54, 66, 210, 211, 220, 222  
 Hansen, J. E., 198, 200, 205, 217, 222,  
     411, 412, 413  
 Hanson, W. B., 46, 65, 112, 262, 276,  
     402, 404  
 Hapke, B., 222  
 Harries, J. E., 158  
 Harris, D. L., 221  
 Harris, I., 403  
 Hart, M. H., 408  
 Hartle, R. E., 401, 403, 405, 408  
 Hartmann, W. K., 433  
 Hartree, D. R., 274  
 Hasselmann, K., 410  
 Hays, J. D., 410  
 Heath, D. F., 156  
 Heaviside, O., 271  
 Hedin, A. E., 64  
 Heisenberg, W., 322  
 Held, I. M., 410  
 Henderson-Sellers, A., 409  
 Henry, R. M., 65  
 Henyey, L. G., 217  
 Herath, L., 66  
 Herlofson, N., 275  
 Herschel, Sir John, 271  
 Herzberg, G., 220, 287  
 Herzberg, L., 19  
 Hess, S. L., 45, 65, 104, 113, 114  
 Hidalgo, H., 155  
 Hill, T. W., 326  
 Hines, C. O., 19  
 Hobbs, P. V., 433  
 Hodges, R. R., Jr., 401, 402, 403, 405, 408  
 Hoegy, W. R., 403  
 Hoffert, M. I., 408  
 Hoffman, J. H., 404, 408  
 Hogan, J. S., 412  
 Holberg, J. B., 66, 67, 113, 324, 325  
 Holton, J. R., 77, 78, 80, 87, 111, 157  
 Holmes, J. C., 232  
 Hord, C. W., 301, 323  
 Horn, L. 67  
 Hou, A. Y., 408

- Houghton, J. T., 111, 433  
 Hovenier, J. W., 205, 222  
 Howard, C. J., 153, 154  
 Howard, H. T., 64  
 Howarth, D. W., 220  
 Howell, H. B., 217  
 Hoyt, D. V. 409  
 Hsieh, C. T., 408  
 Hubbard, W. B., 66, 275  
 Huber, K. P., 287  
 Hudson, R. D., 153  
 Huestis, D. L., 322  
 Huguenin, R. L., 326  
 Hunt, G. E., 434  
 Hunten, D. M., 37, 38, 58, 64, 65, 66, 67,  
     92, 112, 157, 218, 219, 220, 221, 223,  
     275, 276, 309, 311, 320, 321, 322, 323,  
     324, 325, 326, 327, 403, 404, 405, 406,  
     407, 408, 430  
 Huntress, W. T., Jr., 154  
 Husson, N., 66, 220  
 Hut, P., 411

**I**

- Imbrie, J., 410  
 Imbrie, J. C., 410  
 Ingersoll, A. P., 114, 115, 116, 221, 408  
 Inn, E. C. Y., 18  
 Irvine, W. M., 217  
 Isaken, I. S. A., 156

**J**

- Jackson, A. A., 411  
 Jacobowitz, M., 217  
 Jakowsky, B. M., 65  
 Jastrow, R., 433  
 Jeans, J. H., 400  
 Johnson, C. Y., 232  
 Johnson, F. S., 112, 402, 421  
 Johnson, R. E., 406  
 Johnson, T. V., 307  
 Johnston, H. S., 121, 143, 154, 155  
 Judge, D. L., 324

**K**

- Kalaba R., 217  
 Kalnay de Rivas, 99  
 Kaplan, L. D., 223  
 Kasprzak, W. T., 64  
 Kasting, J. F., 379, 380, 407, 408, 412

- Kattawar, G. W., 218  
Kawabata, K., 217  
Keeling, C. D., 286, 295, 393, 412  
Keldysh, W. V., 430  
Kelly, K. K., 325  
Kendall, K. R., 283  
Kennelly, A. E., 271  
Kerr, R. A., 410, 411  
Kerr, R. B., 401  
Kerzhanovich, V. V., 64, 429  
Khalil, M. A. K., 414  
Kieffer, H. H., 43, 65  
Killen, R. M., 323  
King-Hele, D. G., 232  
Kirk, D. B., 44, 65  
Kliore, A., 64, 66, 275, 276  
Knudsen, W. C., 275  
Kockarts, G., 31, 64, 326, 403  
Koeppen, A. W., 410  
Kondratyev, K. Ya., 61, 218, 433, 434  
Kong, T. Y., 219, 326, 404  
Koppany, R., 67  
Krankowsky, D., 112  
Krasnopolksky, V. A., 221, 321, 322, 325,  
    327, 434  
Krassovski, V. I., 321  
Krauss, R. J., 115  
Krueger, A. J., 156, 412  
Krysko, A. A., 321  
Kuiper, G. P., 22, 63, 111, 112, 219, 220,  
    221, 222  
Kukla, G., 410  
Kumar, S., 65, 220, 222, 276, 319, 324,  
    325, 326, 327, 404, 405, 406, 407  
Kunde, V., 50, 66, 220, 222  
Kupperian, J. E., 323, 324  
Kurt, V. G., 323, 405  
Kurylo, M. J., 153
- L**
- Lacis, A. A., 217, 412, 413  
Ladenberg, R., 218  
Lafleur, A. L., 220  
Landau, L. D., 110  
Lane, A. L., 301, 322, 323  
Larmor, J., 273  
Larson, H. P., 219, 220  
Lassen, H., 274  
Lawrence, G. M., 322  
Lebedeff, S., 413  
Lee, T. H., 221
- LeLevier, R. E., 273  
Lenard, P., 62  
Leovy, C. B., 63, 65, 103, 113  
Lepine, V. M., 405  
Levasseur-Regourd, A. C., 323  
Levine, J. S., 153  
Levy, G. S., 67  
Levy, H., 413  
Lewis, J. S., 408, 434  
Lian, M. S., 411  
Lifshitz, E. M., 110  
Light, E. S., 218  
Likens, G. E., 412  
Limaye, S. S., 110, 115  
Lindal, G. F., 67  
Lindenfeld, M. J., 402  
Lindzen, R. S., 114, 408, 410  
Linick, S., 324  
Liou, K. N., 218, 434  
Liu, S. C., 155, 321, 406, 412  
Llewellyn, E. J., 322  
Logan, J. A., 414  
London, J., 16  
Lorentz, H. A., 273  
Lorenz, E. N., 111  
Louis, J. F., 149, 150, 151, 152  
Lowman, P., 222  
Lyot, B., 204, 222
- M**
- McAfee, J. R., 401  
MacDonald, G.J.F., 404, 414  
McCartney, E. J., 221, 434  
McClatchey, R. A., 221  
McConnell, J. C., 51, 66, 67, 112, 113, 154,  
    155, 269, 324, 325, 326  
McCord, T. B., 219  
McCormac, B. M., 63, 112, 273, 321, 322,  
    326, 327  
McElroy, M. B., 112, 121, 127, 130, 142,  
    154, 155, 156, 157, 217, 219, 324, 325,  
    326, 327, 403, 404, 405, 406, 412, 414  
McEwan, M. J., 309  
Maguire, W., 66, 222  
Maher, L. J., 402  
Maillard, J. P., 219  
Manabe, S., 16, 62, 411, 412  
Mange, P., 111, 272, 403  
Marcelin, M., 405  
Marov, M. Ya., 64, 429, 430  
Marrero, T. R., 439

**M**

- Marten, A., 66, 220  
 Mason, E. A., 439  
 Massey, H. S. W., 271, 272  
 Massie, S. T., 41, 65, 112, 212, 213, 221,  
     223, 441  
 Matson, D. L., 307  
 Matthews, M. S., 66, 67, 220, 431, 432  
 Mauersberger, K., 112  
 Maxwell, J. C., 400  
 Maxworthy, T., 115  
 Mayr, H. G., 64, 111, 401, 403, 405  
 Megie, G., 325  
 Mehta, J., 65  
 Meier, R. R., 323  
 Menzel, D. H., 221  
 Meriwether, J. W. Jr., 400, 401  
 Michael, W., Jr., 65  
 Michel, F. C., 403  
 Middlehurst, B. M., 221  
 Milankovitch, M., 410  
 Miner, E., 65  
 Mintz, Y., 103, 113  
 Mitchell, J. L., 115  
 Mitchell, T., 413  
 Mitra, S. K., 274  
 Mo, T., 412  
 Molina, M. J., 153, 157  
 Moos, H. W., 322, 324  
 Morgan, T., 66  
 Moroz, V. I., 65, 113, 220, 275, 325,  
     327, 430  
 Morrison, D., 67  
 Moshkin, B. E., 64, 430  
 Moskalenko, N. I., 434  
 Mukherjee, N. R., 157  
 Muller, J. P., 115  
 Muller, R. A., 411  
 Munch, G., 65, 221, 408

**N**

- Nagy, A. F., 64, 261, 275, 276, 405, 406  
 Namias, J., 111  
 Narcisi, R. S., 273  
 Nath, N., 115  
 Nawrocki, P. J., 19  
 Neher, H. V., 134  
 Neugebauer, G., 65, 221  
 Newman, M. J., 409  
 Newton, C. W., 111

Nichols, H. W., 274

- Nicolet, M., 63, 111, 112, 134, 153, 154,  
     155, 156, 158, 403  
 Niemann, H. B., 39, 41, 64, 220, 403, 405  
 Nier, A. O., 112, 406  
 North, G., 410, 411  
 Norton, R. B., 272  
 Noxon, J. F., 154, 322, 325

**O**

- Olivero, J. J., 223  
 Opik, E. J., 222, 407  
 Orstein, L., 413  
 Orton, G. S., 57, 67, 214, 221, 223  
 Owen, T., 220, 408, 409

**P**

- Page, T. L., 323  
 Palmén, E., 111  
 Pannekoek, A., 272  
 Panofsky, H. A., 114  
 Parkinson, C. L., 413  
 Parkinson, T. D., 311, 326  
 Parrish, A., 157  
 Parshev, V. A., 321, 327  
 Pasachoff, J. M., 433  
 Patterson, T. N. L., 363, 402  
 Pearce, J. B., 323, 325  
 Pearl, J., 66, 222  
 Pederson, P. O., 62  
 Penner, J. E., 154  
 Peterson, J., 411  
 Phillips, L. F., 309  
 Pilcher, C. B., 196, 219  
 Pinto, J. P., 113, 327, 406  
 Pirraglia, J. A., 66, 115, 222  
 Pitts, J. N., Jr., 153  
 Plass, G. N., 218  
 Poll, J. D., 220  
 Pollack, J. B., 64, 113, 379, 380, 407,  
     408, 410, 412  
 Pollard, D., 115  
 Pomphrey, R. B., 324  
 Ponnampерuma, C., 67, 222  
 Potapov, B. P., 321  
 Potter, A., 66  
 Potter, G. L., 411  
 Prather, M., 66, 405, 406, 414  
 Prinn, R. G., 112, 219, 220, 327,  
     407, 408, 434  
 Prisco, R. A., 400

**R**

- Ramanathan, V., 62, 408, 409, 411  
Rasool, S. I., 408  
Rasmussen, E. M., 410  
Rasmusson, R. A., 414  
Ratcliffe, J. A., 63, 274  
Raup, D. M., 411  
Ravishankara, A. R., 153  
Rawer, K., 274  
Rayleigh, Lord [Strutt, J. W.], 320, 400,  
    404  
Rayleigh, Lord [Strutt, R. J.], 320  
Redekopp, L. G., 115  
Reiche, F., 218  
Reid, G. C., 156, 273, 276, 321, 409  
Reiners, W. A., 412  
Reiter, E. R., 149, 150, 151, 152, 157  
Revercomb, H. E., 115  
Ridgeway, S. T., 219  
Rishbeth, H., 227, 272, 273  
Roach, F. E., 320  
Robbins, D. E., 157  
Robinson, J. B., 108, 114  
Robock, A., 411  
Rodriguez, J. M., 405, 406  
Roesler, F. L., 401, 408  
Rogashev, V. N., 321  
Rohrbaugh, R. P., 402  
Romanova, H. H., 323, 405  
Ronomov, A. E., 64  
Rossby, C.-G., 79, 111  
Rosseland, S., 272  
Rossow, W. B., 409  
Rothaus, O., 414  
Rothman, L. S., 221  
Rottman, G. J., 324  
Rowland, F. S., 157  
Roy, M., 401  
Rozhdestvensky, M. K., 64, 429  
Ruderman, M. A., 155, 156, 414  
Rundle, H. N., 323  
Rusch, D. W., 322, 409  
Rushneck, D. R., 220  
Ryabov, O., 64  
Ryan, J. A., 65, 157  
Ryan, W. B. F., 409

**S**

- Sagan, C., 276, 412  
Salby, M. L., 111  
Saltzman, B., 111, 410
- Samuelson, E. E., 220  
Samuelson, R., 66, 67, 222, 406  
Sanatani, S., 65, 276  
Sandel, B. R., 66, 67, 113, 323, 324, 325  
Santek, D. A., 115  
Sato, M., 217  
Schelleng, J. C., 274  
Schneider, S. H., 411  
Schubert, G., 113  
Schunk, R. W., 275  
Schuster, A., 271  
Schwartz, P. R., 223  
Scott, N., 66, 220  
Seidel, B., 65, 276  
Seiff, A., 37, 44, 65, 113  
Sellers, W. D., 410  
Selwyn, G. S., 121, 155  
Semenov, A. I., 321  
Sepkoski, J. J., 411  
Shackleton, N. J., 410  
Shagaev, M. V., 321  
Shapiro, I. I., 401  
Shefov, N. N., 321  
Shemansky, D. E., 65, 66, 67, 113, 306,  
    323, 324, 325, 401, 403, 406, 408  
Shih, P., 401  
Shizgal, B., 400, 402  
Shklovskii, I. S., 407  
Sieveka, E. M., 406  
Sill, G. T., 222  
Silverstein, S. D., 62  
Simpson, G. C., 409  
Slanger, T. G., 321, 322  
Slipher, V. M., 320  
Smirnov, A. S., 323, 405  
Smith, F. L., III, 274  
Smith, G. R., 55, 59, 66, 67, 113, 324,  
    325, 358, 402, 403, 404  
Smith, L. G., 19  
Smith-Rose, R. L., 271  
Smith, S. G., 275  
Smyth, W. H., 406  
Sobolev, V. G., 321  
Solomon, P. M., 157  
Solomon, S., 409, 434  
Sowell, D. R., 65, 112  
Sparks, P. R., 324  
Spencer, J. E., 157  
Spencer, N. W., 64, 403  
Spitzer, L., Jr., 63, 400

Sromovsky, L. A., 115  
 Staelin, D. H., 64  
 Stephens, G. L., 411  
 Stevenson, D. J., 67, 220, 406  
 Stewart, A. I., 301, 304, 322, 323, 325, 406  
 Stewart, B., 270, 271  
 Stokes, G. G., 217, 222  
 Stolarski, R. S., 156, 157  
 Stone, P. H., 105, 113, 114, 115, 116  
 Strickland, D. J., 324, 325  
 Strickler, R. F., 16, 62  
 Strobel, D. F., 64, 66, 67, 113, 220, 306  
     315, 323, 324, 325, 327, 403, 405, 406  
 Strong, J., 218  
 Strutt, J. W., 320, 400, 404  
 Strutt, R. J., 320  
 Stuiver, M., 412  
 Suchy, K., 274  
 Suess, H. E., 409  
 Summers, M. E., 406  
 Suomi, V. E., 100, 115  
 Suzuki, K., 321  
 Sweetnam, D., 65, 276  
 Sze, N. D., 327, 403, 413

**T**

Takacs, P. Z., 324, 404  
 Takahashi, T., 411  
 Talbot, R. J., Jr., 409  
 Tanaka, Y., 18  
 Taylor, H. A., Jr., 64, 275, 403, 405, 408  
 Taylor, R., 271  
 Teifel, V. G., 220  
 Tepley, C. A., 401  
 Telegadas, K., 144, 145, 146, 147  
 Thacker, D. J., 223  
 Thomas, G. E., 323, 324, 325  
 Thomas, R. J., 409  
 Thompson, M. H., 433  
 Tinsley, B. A., 400, 402, 403, 405  
 Tipler, F. J., 413  
 Tohmatsu, T., 321  
 Tomashova, G. V., 322  
 Tomasko, M. G., 67, 218, 220, 406  
 Toon, O. B., 410, 412  
 Torr, D. G., 403  
 Torr, M. R., 403  
 Trafton, L. M., 66  
 Traub, W. A., 322, 325  
 Trauger, J. T., 408  
 Travis, L. D., 198, 200, 217, 222

Tull, R. G., 190  
 Turcor, P., 412  
 Tuve, M. A., 271  
 Twomey, S., 217, 223  
 Tyler, G. L., 54, 67

**U**

Ueno, S., 217

**V**

Vakhnin, V. M., 429  
 van de Hulst, H. C., 217, 219, 275  
 vanZandt, T. E., 272  
 Vergison, E., 155  
 Neverka, J., 66, 223, 276  
 Vidal-Madjar, A., 401  
 Visconti, G., 409  
 Volland, H., 111  
 VonZahn, U., 112, 220

**W**

Walker, J.C.G., 403, 407, 409  
 Wallace, J. M., 158, 410, 433  
 Wallace, L., 66, 112, 116, 218, 220, 221,  
     323, 324, 325, 403, 404  
 Wallio, A., 65  
 Wang, W. C., 412  
 Wannier, P. G., 218  
 Ward, W., 410  
 Warneck, P., 156  
 Washington, W. M., 411  
 Wasserman, L., 276  
 Watanabe, K., 19  
 Waters, J. W., 112, 157  
 Waterston, J. J., 400  
 Watson, A. J., 407, 408  
 Watson, R. T., 153, 154  
 Wattson, R. B., 64  
 Webster, P. J., 411  
 Weidman, P. D., 115  
 Weinreich, S. K., 409  
 Weisskopf, V., 322  
 Westman, H. P., 229  
 Wetherald, R. T., 411  
 Whitehead, J., 113  
 Whitmire, D. P., 411  
 Whittaker, R. H., 412  
 Wickramasinghe, N. C., 221  
 Wildt, R., 327

- Williams, G. P., 108, 114, 115  
Wofsy, S. C., 142, 154, 155, 156, 157, 414  
Woiceshyn, P., 276  
Wollin, G., 409  
Wood, A. T., Jr., 64  
Wood, G. E., 67  
Wook, R. W., 62  
Woodwell, G. M., 412  
Wronka, J. C., 410  
Wulf, O. R., 62, 154
- Y**
- Yagi, G. M., 115  
Yee, J. H., 406  
Yntema, L., 320
- Young, A. T., 222  
Young, J. M., 232  
Young, R. E., 113  
Yung, Y. L., 112, 113, 154, 157, 313, 317,  
    318, 325, 327, 404, 406, 407, 412
- Z**
- Zahnle, K. J., 409  
Zelikoff, M., 323  
Ziegler, W., 408  
Zuccaro, D. R., 65, 276  
Zuev, V. E., 61  
Zurek, R. W., 114  
Zwally, H. J., 413

## SUBJECT INDEX

Boldface page numbers give the location of definitions of terms or defining equations. Atoms and molecules are listed under their chemical formulae; thus methane appears under CH<sub>4</sub>. Band systems and continua are listed under the molecule.

### A

- A (argon)
  - Earth, 189
  - Mars, 189
- Absorption coefficient, 5, 24, 26, 161, 177
  - Chandrasekhar mean, 11
  - in ionosphere, 247
  - for photoionization, 229
  - Roseland mean, 11
- Absorption cross section, 118, 177, 229
- Absorption-ratio parameter, 178
- Accidental resonance, see H-0 charge exchange equilibrium
- Accommodation coefficient, 350
- Activation energy, 119
- Adiabatic gradient, *see* Temperature lapse rate
- Adiabatic law
  - differential, 14, 83
  - integral, 72, 84
- Advection, 75
  - of temperature, 85
- of vorticity, 85-87
- Airglow continuum, 279, 290, 321
- Airglow spectra, *see also* specific molecule
  - as data on chemical composition
- Earth, day, 299-309, 320-325
- Earth, night, 282-290, 320-322
- Jupiter, day, 299-309, 323
- Mars, day, 299-309, 324-325
- Venus, day, 299-309, 324-325
- Venus, night, 290, 322
- Air-mass factor
  - scattering atmosphere, weak lines, 181, 182, 225
  - transparent atmosphere, strong lines, 175
  - transparent atmosphere, weak lines, 174
- Albedo, Bond, 12, 201, 225
  - Earth, 12
  - effect of a change in, on climate, 389
  - feedback of change in ice or clouds on greenhouse effect, 386
- Jupiter, 105
  - table of, 419
- Albedo, geometric, 201, 225

- Albedo, ground, **165**  
   equivalent value for semi-infinite atmosphere, **168**, 224–225
- Albedo, planetary omnidirectional, *see* Albedo, Bond
- Albedo, single scattering, **5**, **28**, **161**, 177, **191**
- Apollo 16, 300, 323
- Appleton dispersion formula, 258, 274
- Astronomical theory of climate, *see* Milankovitch theory
- Asymmetry factor, *see* Phase function
- Atmo-centimeter, **3**
- Atom-atom interchange, **30**
- Atom-ion interchange, **33**, **233**
- Attachment, *see* Electron attachment
- Aurora, 279–280  
   on Uranus, **56**
- B**
- Banded structure, Jupiter, 104–110
- Band strength, **27**
- Baroclinic atmosphere, **81**, 106
- Baroclinic disturbance, **87**  
   instability, 106, 109
- Barometric law, **3**, **68**, 218  
   generalized **334**
- Barometric pressure (high-low) regions, development of, **87**  
   from gradient wind, **78**
- Barotropic atmosphere, **81**  
   Jupiter, **106**
- Barth, mechanism, OI airglow excitation, **287**
- Bénard problem, **107**, **114**, **117**
- Bergen school, modern meteorology, **111**
- Bessel functions, **175**, **257**, **292**
- Beta-plane approximation, **88**
- Beta recombination, *see* Bradbury recombination
- Binary collision parameter, **89**, **370**, 483–439
- Biota, storage of CO<sub>2</sub> in, **394**
- Black-body radiation, *see* Planck function
- Blowoff, theory of, **377**–**381**  
   velocity, density, temperature profiles  
   for primitive Venus, **379**–**380**
- Boltzmann continuity equation (in six dimensional space), **357**
- Boltzmann excitation equation, **27**–**29**, **34**, **176**
- Born approximation, **254**
- Boundary layer, **75**
- Boussinesq approximation, **72**, **107**
- Br (bromine)  
   in stratosphere, **140**, **157**  
   tropospheric sources of, **140**, **157**
- Bradbury recombination, **234**–**235**
- Broadening, line, *see* Collisional damping, Doppler broadening, Natural broadening
- C**
- <sup>14</sup>C (carbon isotope 14)  
   climate, correlation with, **409**  
   solar activity, correlation with, **409**  
   stratospheric mixing, as tracer for, **144**–**147**
- Ca (calcium) airglow **286**, **293**
- Catalytic chemistry of ozone, **122**–**140**  
   coupling of cycles of, **138**
- Catastrophic climate events  
   Cretaceous-Tertiary boundary, **390**  
   energy released in asteroid impact, **390**  
   faunal extinctions, **390**–**391**  
   iridium enhancement, **390**  
   kill mechanisms, **391**  
   Permian-Triassic boundary, **390**
- CCl<sub>4</sub> (carbon tetrachloride)
- Centimeter-amagat, *see* Atmo-centimeter
- Centimeter-atmosphere, *see* Atmo-centimeter
- Centrifugal force, **73**–**74**
- CFC<sub>13</sub> (trichlorofluoromethane, *F-11*), **138**–**139**
- CF<sub>2</sub>Cl<sub>2</sub> (dichlorofluoromethane, *F-12*), **138**–**139**
- CH<sub>3</sub> (methyl)  
   on Jupiter, **268**, **314**  
   in OH formation, **124**
- CH<sub>4</sub> (methane)  
   destruction of OH, **139**–**140**  
   dissociation energy, **120**
- Earth, **189**
- Jupiter, abundances on, **189**  
   atmospheric cooling, **52**  
   photochemistry of, **268**–**270**, **314**  
   spectrum of, **188**–**196**
- Mars, **189**
- $\nu_3$  fundamental ( $3.3 \mu$ ), **52**  
 $\nu_4$  fundamental ( $7.7 \mu$ ), **52**  
   in OH formation, **124**
- Pluto, **49**
- Titan, **59**, **316**
- Triton, **49**

- C<sub>2</sub>H in Titan photochemistry, 316  
 C<sub>2</sub>H<sub>2</sub> (acetylene)  
   on Jupiter, 56, 193, 212, 314  
   on Titan, 316  
 C<sub>2</sub>H<sub>4</sub> (ethylene) on Jupiter, 314  
 C<sub>2</sub>H<sub>5</sub> ion on Jupiter, 268  
 C<sub>2</sub>H<sub>6</sub> (ethane)  
   on Jupiter, 212, 314  
   on Titan, 316  
 CH<sub>2</sub>O (formaldehyde), 397  
 CH<sub>3</sub>O<sub>2</sub> (peroxy radical) in urban photochemistry, 399  
 Chahine algorithm, 214  
 Chapman layer, *see also* O<sub>3</sub> (Earth's stratosphere), Ionosphere  
   for F2 diffusion, 239  
   for dissociation, 23  
   history and references, 63  
   for ionization, 229–234  
   on Mars, 260–264  
   peak, 20, 68  
   on Venus, 260–264  
 Chapman mechanism for airglow OI excitation, 287  
 Chapman production function  
   in dimensionless units, 208  
   ionosphere formation, 230  
   stratosphere formation, 23, 63  
   as weighting function of radiative transfer source function, 207  
 Chapman reactions (of oxygen allotropes), 17–21, 62–63, 68, 122, 154  
 Characteristic equation (in radiative transfer theory), 164  
 Charge exchange, 232  
   atmospheric escape induced by, 358–361, 402  
 CH<sub>3</sub>Cl (chloromethane or methyl chloride), 138–139, 398  
 CHFCl<sub>2</sub> (*F*-21), 139  
 CHF<sub>2</sub>Cl (*F*-22), 139  
 Chlorofluoromethanes, *see* Halomethanes  
 Circulation, *see* Wind systems  
 Cl (chlorine)  
   in ClO<sub>x</sub> cycle, 136–138  
   isotopic splitting of HCl in Venus spectra, 189  
   production from halomethanes, 138–139  
 Clathrate, 382  
 Climatic variations, 62  
   cloudiness as source of, 389–390  
   physical causes of, 385–395  
   stratosphere as source of, 136  
 ClNO<sub>3</sub> (chlorine nitrate)  
   dissociation energy, 120  
   interaction between NOx and ClO cycle, 138, 157  
 ClO (chlorine monoxide)  
   in ClO<sub>x</sub> cycle, 136–138  
   dissociation energy, 120  
 ClO<sub>x</sub> (odd chlorine), 123  
   catalytic cycle, 136–138, 157–158  
   interaction with HOx cycle, 137  
   interaction with NOx cycle, 138, 158  
   natural stratospheric sources, 138, 157  
   production from halomethanes, 138–139, 157  
 Clouds on Jupiter, 205; *see also* Banded structure  
 Clouds on Neptune, 56  
 Clouds on Uranus, absence of, 56  
 Clouds on Venus, 97–102, 204–205, 222  
 CO (carbon monoxide)  
   airglow, Mars, 263, 304  
   Cameron (forbidden) band system, on Mars, 304  
   destruction by OH, 139–140  
   dissociation energy, 120  
   Earth, abundance on, 189  
   fourth positive band system, on Mars, 305  
   Jupiter, abundance on, 189  
   Mars, abundance on, 189  
   role in cooling thermosphere, 33  
   in Titan chemistry, 316  
   Venus, abundance on, 189  
 CO<sub>2</sub> (carbon dioxide)  
   absence of  $\mu_1$  mode, 25  
   angular momentum of vibration, 26  
   deactivation coefficient, 29, 35  
   dissociation energy, 120  
   Earth, annual variation, 394  
   Earth, climatic effect, 389–395  
   Earth, cooling to space, 1, 22, 25–29, 68  
   Earth, increase with time from burning of fossil fuels, 394  
   Earth, inventory (atmosphere, oceans, biota) [does not account for CO<sub>2</sub> production from fossil fuel since start of industrial revolution], 394  
   Earth, mixing ratio, 189  
   Earth, present rate of increase in abundance, 394

- Earth, temperature increase due to doubling abundance, 394
- Earth, transport of radiation, 25, 28, 68
- Earth, variation over lifetime of solar system, 392
- fundamental vibrational modes, 26
- hot bands, 22
- isotopic bands, 22
- linear structure, 25
- Mars, 43, 103, 176, 189, 218
- Mars, aeronomy on, 309–313
- Mars, airglow on, 304–305
- Mars, condensation on ice cap, 104
- Mars, dissociation, 309
- $\nu_2$  fundamental ( $15\mu$ ), 25, 29
- in Titan chemistry, 316
- Venus, 97, 186–189
- Venus, aeronomy of, 309–313
- Venus, carbonates, 383
- Venus, dissociation, 309
- vibrational quantum numbers, 26
- vibrational relaxation, 25–29
- vibration-rotation bands, 187
- $\text{CO}_2^+$  (carbon dioxide ion)
- Doublet bands, Mars
  - Fox-Duffendack-Barker bands, Mars
- $\text{CO}_3^-$  (carbonate) negative ion, *D* region, 243
- $\text{CO}_4^-$ , negative ion, *D* region, 243
- Collisional broadening, *see* Collisional damping
- Collisional cross section, 20, 118, *see also* Rate coefficient
- Collisional damping, 174, 195  
of  $\text{CO}_2$  on Mars, 175–176
- Collisional detachment, 241
- Collisional narrowing, 195
- Collision frequency, 245
- Composition of atmospheres of planets, *see also* specific planetary regions and specific molecules
- Earth, 189, 381
  - Io, 308
  - Jupiter, 189
  - Mars, 103, 189
  - Mercury, 48
  - Neptune, 189
  - Saturn, 189
  - Titan, 189
  - trace gases, 189, 424
  - Uranus, 189
  - Venus, 189
- Conduction, thermal in Earth's ionosphere, 5, 34–36
- Continuity, equation of, 71, 145  
for incompressible fluid, 71  
in isobaric coordinates, 83, 106  
with source, sink terms, 140, 236
- Convection
- in Earth's troposphere, 13–15, 84–87
  - on Jupiter, 104–109
  - on Venus, 99–101
- Coriolis force, 73–79
- component of vorticity, 85
  - on Jupiter, 106
  - on Mars, 103
  - parameter, 76, 85
  - on Venus, 98
- Coupled catalytic chemistry, 138
- Critical frequency, 226, 247–248
- Critical level, *see* Exobase, Satellite critical level
- Critical reflection, 245, 247
- absorption associated with, 277
  - extraordinary wave, 260
  - ordinary wave, 259
- Cross section, *see* Absorption cross section, Collisional cross section
- Cryosphere
- origin of terminology, 113
  - on Venus, 39, 40–42
- Curtis-Godson approximation, *see* Strong-Plass formula
- Curve of growth, 174, 182, 219
- linear regime, 174, 179, 185–186
  - square-root regime, 174, 181, 182, 185, 219
- Cyclonic disturbances
- origin in baroclinic instabilities, 106, 111
  - relation to moving fronts, 109
- Cyclostrophic wind, 78

**D**

- Damping constant, 174
- effective value, inhomogeneous atmosphere, 225
  - pressure dependence, 174
- Danielson dust, 315
- Deactivation coefficient, 28
- relation to excitation coefficient, 28
- Debye screen length, 255–256
- Degeneracy, *see* Statistical weight
- Delta function, 161

- Denitrification, 132  
branching ratio, 132
- Detailed balancing, 241, 277, 357
- Differentiation of vector in rotating frame, 73
- Diffraction by drops, 198
- Diffusion, molecular, 4, 32, 89, 111, 370; *see also*, Eddy diffusion  
ambipolar, 231, 235–240, 272  
coefficient of, 89, 371, 438–439  
equilibrium, 32, 67, 69, 89, 234  
in Mars' ionosphere, 264  
thermal diffusion factor, 89, 369  
time characteristic, 32, 89
- Diffusive equilibrium, 89–94  
electrostatic equilibrium, 236
- Dissociation energy, 30, 120
- Dissociative excitation, 302
- Dissociative photoionization, 268
- Dissociative recombination, 30, 232, 263, 265
- Disturbances, propagation on planetary scale, 83–89  
“Do-nothing” catalytic cycle, 128
- Doppler broadening, 347
- Doppler profiles of exospheric scattering, 346–351, 400, 415
- Doppler shift  
Fraunhofer lines in planetary spectra, double tilt of, 190  
of Jupiter spectral lines, 190  
between spacecraft-Earth in radio occultation experiments, 252
- Doppler width, 176
- Doubling method (in radiative transfer), 170–172, 217
- D* region of Earth's ionosphere  
characteristics, summary of, 228  
effective ionization rate in, 242  
ion species in, 242–244, 273  
recombination processes in, 240–244, 277
- Dust on Mars, 42–45, 65, 205
- E**
- Earth, atmospheric characteristics, *see* specific atom and molecule, specific characteristic (e.g., Composition, Density, Pressure, Temperature), specific ionospheric region (*D*, *E*, *F1*, *F2*), and specific atmospheric region, (e.g., Troposphere)
- Eddy diffusion, 75, 90, 112, 141, 158, 159, 370  
coefficient of, 97  
in Mars' upper atmosphere, 310  
mixing time, 141  
in stratosphere, 141, 157  
in tropospheric convection, 140  
in Venus' upper atmosphere, 310
- Eddy viscosity, 75, 106–107  
coefficient, 75  
mixing length, 75
- Einstein radiation coefficients, 27
- Electric-dipole transition, 18
- Electron affinity, 241
- Electron attachment, 30  
radiative, 240  
three-body, 240
- Electroglow, 305
- Electrostatic equilibrium, *see* Diffusive equilibrium
- El Niño, 388–389  
climate changes, association with short-term, 388–389  
periodicity, 389  
southeast Asian drought, 389  
water temperature changes across Pacific, 389
- Emission coefficient for thermal radiation, 5–6, 26
- Energy accommodation, 351
- Energy-exchange collisions, 30
- Energy conservation, equation of, 73, *see also* Thermodynamics, first law
- Enforced dipole transition (pressure-induced absorption), 195
- Equilibrium temperature, *see* Temperature, mean planetary emission
- Equivalent width, 174, 218
- E* region of Earth's ionosphere  
Chapman layer, 232  
characteristics, summary of, 228  
ion composition, 232  
metallic ions, 232  
recombination in, 232  
sporadic E, 233, 252, 255, 265
- E* region of Mars, 261–264
- Escape flux, 340  
Earth, H and He, 371–372  
Io, Na, *et al.*, 376  
Mars, H and O, 373–375

- Mercury, 382  
 Titan, H, H<sub>2</sub>, 375  
 Venus, H, 372–373  
 Escape mechanisms, 366–367  
 Escape velocity, 331  
     in dimensionless units, 334  
     table of, 419  
 Euler's equation, 72  
     isobaric coordinates, approximate 83, 116  
     for rotating planet, approximate, 76  
 Excitation coefficient, 29  
     relation to deactivation coefficient, 29  
 Exobase, 331  
 Exosphere  
     collisions in, 351–353, 358–361  
     integrated density, 340–346  
     lateral flow, 350, 361  
     radial distribution of density, 330–340  
     radiation pressure of solar Ly-alpha, 353–356  
     spectral line profiles, 346–349  
 Exospheric temperature  
     Earth, 31, 371–372  
     Jupiter, 51–53  
     Mars, 45–47, 373–375  
     Mercury, 302, 323  
     Saturn, 55  
     Uranus, 56  
     Venus, 37–38, 372–373  
 External climate modulations, 385–388  
 Extinction coefficient, 5
- F**
- Faunal extinctions, 330  
 Fermi resonance, 187  
 Ferrel cell, 80, 148  
 Fertilizer as source of N<sub>2</sub>O, 132, 155  
 Fixation of N<sub>2</sub>, 132  
 Fluorcarbons, see Halomethanes, Halocarbons  
 Flux, 7  
     divergence, 8  
 FO<sub>x</sub> (odd fluorine)  
     catalytic cycle, 139  
     stratospheric sink, 140  
 Forbidden transitions, 33, 68,  
     *see also* Magnetic dipole radiation,  
     Quadrupole (electric) transition  
 CO, 304  
 H<sub>2</sub>, 188  
 O, 282, 286, 328
- Four-day rotation, Venus  
 Fourier spectroscopy, 188  
 Fraunhofer spectrum, 190  
 Fractionation factor, 368  
 F1 region of Earth's ionosphere  
     Chapman layer, 232  
     characteristics, summary of, 228  
     ion composition, 232  
     recombination in, 233  
 F2 region of Earth's ionosphere  
     characteristics, summary of, 228  
     ion composition, 232  
     recombination process in, 234–240, 277  
 Freon, *see* Halomethanes, specific molecule  
 Fresnel formulae, 198, 252, 275  
 Fundamental transitions between lowest  
     molecular vibrational levels, 194  
 f-value, *see* Oscillator strength
- G**
- Galactic cosmic rays  
     eleven-year cycle, 133  
     relation to ozone 11-yr cycle, 133–135  
 Galilean satellites, 60–61, 317–320,  
     *see also* Io  
     surface characteristics, Europa,  
         Ganymede, Callisto, 60–61  
     surface pressures of Europa, Ganymede,  
         Callisto, upper limits to, 60–61  
 Galileo spacecraft (Jupiter), 429  
 Gamma function, 175  
     incomplete, 337  
 Gas constant, R, 3  
 Gas-kinetic collision, 121  
 Gaussian quadrature, 162–163, 223  
 Generalized momentum, 333  
 Geometric albedo, *see* Albedo, geometric  
 Geopotential, 81, 84  
     height, 69, 422–423  
     tendency 86  
 Geostrophic wind, 75–77, 80, 84–86  
 Glory, 199  
 Golitsyn number, 98  
 Gradient wind, 78, 116  
 Gravitational contraction, *see* Helmholtz  
     contraction  
 Gravity wave, 87, 158  
     on Jupiter, 276  
 Gray atmosphere, *see* Local thermodynamic  
     equilibrium

Greenhouse effect, 13, 43, 61, *see also CO<sub>2</sub>*, Sea level change  
on Mars, 43  
minor constituents, role of, 394  
runaway, 383–384, 386  
Green's function, 254  
*g*-values, 293, 322  
table of, 293  
Gyrofrequency, 258

## H

**H** (atomic hydrogen), *also see Escape flux*  
anisotropy of scattering, 300, 323  
height distribution in stratosphere, 129  
in HO<sub>x</sub> cycle, 123–129  
hyperfine splitting, 300  
Jupiter, 97, 267–270, 314–315  
Lyman-alpha airglow, 97, 293,  
299–301, 323  
Lyman continuum, solar, 233  
H<sub>2</sub> (molecular hydrogen)  
dissociation energy, 120  
Earth, 189  
photochemistry in predominantly H<sub>2</sub>  
atmospheres, 314–315  
Jupiter, 189, 268, 314–315  
Lyman bands, 305  
Mars, 189  
ortho, para, 211, 440–441  
Titan, 316, 382  
Werner auroral bands, 305  
Hadley circulation, 79–80, 148  
on Venus, 101  
Halocarbons, 139  
Halomethanes, 138–139, 156, *see also*  
specific molecule  
partially halogenated  
methanes, 139  
Hamiltonian, particle in gravitational  
field, 333  
HCl (hydrogen chloride)  
dissociation energy, 120  
interaction with ClO<sub>x</sub> cycle, 136–138  
Venus' abundance, 189  
in Venus' spectrum, 188  
He (helium)  
Earth, 189, 372  
Earth's stratosphere, 63  
<sup>3</sup>He/<sup>4</sup>He escape flux discrepancy, 372,  
404  
Jupiter, 189, 190, 268, 300, 323  
Mercury, 301, 323

resonance scattering by, 190, 293,  
299–302, 329  
solar emission lines, 233  
Heating efficiency, 31, 33  
Helmholtz (gravitational) contraction  
of Jovian planets, 50, 53, 56, 201  
Henyey–Greenstein phase function, *see*  
Phase function  
HF (hydrogen fluoride)  
dissociation energy, 120  
sink for FO<sub>x</sub> cycle, 139  
Venus' abundance, 189  
*H*-functions, Chandrasekhar's 166,  
169, 217  
physical meaning of, 224  
HNO<sub>3</sub> (nitric acid)  
in acid rain, 399  
dissociation energy, 120  
diurnal variation, 159  
height distribution in stratosphere, 129  
interaction with HO<sub>x</sub> and NO<sub>x</sub> cycles, 128  
photolysis rate, 120  
H–O charge exchange equilibrium,  
239–240, 405  
HO (hydroxyl), *see OH*  
HO<sub>2</sub> (hydroperoxyl)  
dissociation energy, 189  
height distribution in stratosphere, 127  
in HO<sub>x</sub> cycle, 123–127  
HO<sub>x</sub> (odd hydrogen), 123  
acid rain, photochemistry in formation of,  
399  
aeronomy on Mars, Venus, 309–314  
catalytic cycles, 123–127, 154  
interaction with ClO<sub>x</sub> cycle, 136  
interaction with itself, 125  
interaction with NO<sub>x</sub> cycle, 128, 154  
in pollution chemistry, 397  
H<sub>2</sub>O (water), dissociation energy, 120  
H<sub>2</sub>O in Earth's stratosphere  
cold trap, 25, 63  
in formation of OH, 124  
impact on climatic variations, 136  
mixing ratio, 25, 148, 158  
transport of radiation, 22  
H<sub>2</sub>O, Earth's troposphere  
abundance, 189  
transport of radiation, 15, 24–25  
tropopause height, effect on, 16  
H<sub>2</sub>O, Jupiter, 109, 114, 189  
H<sub>2</sub>O, Mars, 189  
spectrum, 191

- $\text{H}_2\text{O}$ , Venus, 189  
 $\text{H}_2\text{O}_2$  (hydrogen peroxide)  
dissociation energy, 120  
height distribution, stratosphere, 127  
interaction with  $\text{HO}_x$  cycle, 125  
on Mars, 310–311
- $\text{H}_2\text{O}_3$ ,  $\text{H}_2\text{O}_4$  (polyoxides), on Mars, 312
- Homonuclear molecule  
dipole moment, absence of, 25, 30  
forbidden transitions, 195, 212, 289, 303
- Homopause, 370
- Homosphere, 369
- Horizontal circulation, 75–79, 110–111  
*see also* Meridional circulation, Wind systems  
Earth's stratosphere, 142–153, 157, 158  
Earth's troposphere, 75–89  
Jupiter, 104–109, 114–115  
Mars, 42, 103–104, 113–114  
Venus clouds, 100–102  
Venus troposphere, 97–102, 113
- $\text{H}_2\text{S}$  (hydrogen sulfide), photochemistry in formation of acid rain, 399
- $\text{H}_2\text{SO}_4$  (sulfuric acid)  
in acid rain, 399  
in clouds of Venus, 205  
refractive index, 205
- Humidity, see  $\text{H}_2\text{O}$
- Hydration  
*D* region, 242–244  
Venus aerosols, 204–205
- Hydrocarbon chemistry, Jupiter, 314–315, 327
- Hydrodynamic equations, *see also* specific equations, Time scales  
in inertial frame, 71–73  
in isobaric coordinates, 83–89, 116  
in rotating atmosphere, 73–89
- Hydrostatic approximation, 76, 80, 83
- Hydrostatic equilibrium, 1, 2–4, 89  
departure from, 335
- Hyperfine structure, 295–299, 328
- I**
- Ice covered Earth, 386
- Inclination, geometric, 236
- Incoherent scattering, 255–258, 275
- Incompressible fluid, 71
- Inertial oscillation, 116
- Infrared radiometer experiment, 43, 65
- Inhomogeneous atmosphere, 218
- Insolation, 387
- Integrated density, 3  
atmo-centimeter unit, 3  
for Earth, vertical, 174, 424 (footnote)  
exospheric, radial, 340–346  
tangential, 292, 322
- Intelligence, extraterrestrial, 395–396
- Internal energy redistribution, as source of climate variations, 388–389
- Inversion of thermal emissions, 213–215
- Io  
composition of upper atmosphere, 307  
escape flux, 376  
ionosphere, 306  
Na torus around Jupiter, 61, 307  
source of Jupiter plasma torus, 307–308  
surface pressure, 60–61  
surface, characteristics of, 60–61
- Ionization energy, 30
- Ion-molecule association, 243
- Ionosphere, *see also* specific characteristics (e.g., recombination coefficient)  
specific planet, specific ionospheric region for Earth (e.g., *D*, *E*, *F1*, *F2*)  
Chapman layer, 229  
characteristics for Earth, summary of, 228  
discovery and history, 270–275
- Ions, *see* Metallic ions, Negative ions, Positive ions, specific ionosphere region, specific recombination process
- Isentropic flow, 72
- Isobaric coordinates, 80, 81, 83, 116
- Isotope comparisons, Mars vs. Earth  
 $^{40}\text{A}/^{36}\text{A}$ , 383  
 $^{18}\text{O}/^{16}\text{O}$ , 383
- J**
- Jeans escape, 331–332, 400, 414  
correction for collisional model, 356–358, 403
- Jet stream, 80–82, 116
- Johnson pump mechanism, *see* Wind-induced diffusion
- Jupiter, *see also* specific characteristic, molecule, spacecraft  
circulation, 104–109, 114–115  
clouds, 205  
composition, 189  
internal heating, 105–108, 152, 160

- Jupiter (*cont.*)  
 ionosphere, 276  
 Lyman-alpha, 97  
 mesosphere temperature, 56  
 rotation, 104  
 temperatures, 201, 276  
 vertical structure, 49–53  
 Jupiter Orbiter/Probe, *see* Galileo,
- K**
- K (potassium) airglow, 286, 293  
 on Mercury, 48  
 Kelvin resonance mode, 104  
 Keplerian ellipse, 355  
 Keplerian orbits  
   elements of, 353  
   in exosphere, 335  
   perturbation by radiation pressure, 353  
 Kepler's harmonic law, 355, 415  
 Kepler's law of areas, 355  
 Kirchhoff's law, 4, 5, 26–29
- L**
- Ladenberg-Reiche formula, 174  
 Lagrangian, particle in gravitational field, 333  
 Lambert's law of exponential extinction, 5, 24 (footnote)  
 Lambert's reflection law, 165  
 Laguerre polynomial, 237  
 Legendre polynomial, 168  
 Li (lithium) airglow, 286, 293  
 Limiting flow, 370–371, 375, 403–404, 415  
 Line absorption parameter, 178  
 Linear law of cooling, 24  
 Line strength, 174  
 Little ice age, 387  
 Liouville equation, 332–335  
 Local thermodynamical equilibrium, 5  
   departures from, 28–29  
   gray atmosphere, 10–13  
 Lorentz force, 239, 258  
 Lorentz line profile, 174, 218  
 Lorentz width, 174, 193  
   collisional damping constant, relation to, 174  
 Lyman-alpha radiation, *see* H
- M**
- Magnetic birefringence, 259, 274  
 Magnetic dipole radiation, 286, 328

- Magneto-ionic theory, 258–260, 274  
 Mariner 2, 428  
 Mariner 4, 65, 429  
 Mariner 5, 36, 64, 248, 300, 323, 325, 372, 428  
 Mariner 6, 44, 65, 300, 304, 323–325, 406, 429  
 Mariner 7, 44, 65, 300, 304, 323–325, 406, 429  
 Mariner 9, 43, 65, 300–301, 323–324, 406, 429  
 Mariner 10, 64, 65, 100, 222, 301, 323–325, 404, 428  
 Mars, *see also* specific characteristic, molecule, spacecraft  
   circulation, 42–45, 103–104, 113–114  
   composition, 42, 103, 189, 218  
   dust, 65, 205  
   ionosphere, 47, 260–264, 275  
   mesopause height, 47  
   rotation, 103  
   surface pressure, 65, 103, 176, 218  
   temperatures, 65  
   vertical structure, 42–48  
 Mars 2, 65  
 Mars 3, 65, 429  
 Maxwellian velocity distribution, 6, 331, 333  
 Maxwell's equations, 244–245  
 Mean free path  
   for particle collisions, 331  
   for photons in a scattering atmosphere, 185  
 Mean intensity, 6, 8  
 Mean mass, 3–4  
 Mercury,  
   escape flux, 382  
   exosphere, 48, 66, 302, 323  
 Meridional circulation, 17, 22, *see also*  
   Horizontal circulation, Wind systems  
   in stratosphere, from  $^{14}\text{C}$  measurements, 144–147  
   in stratosphere, from  $\text{O}_3$  measurements, 143  
   in stratosphere, from temperature measurements, 144–153  
 Mesopause condition, 35, 63, 68  
 Mesopause on Earth, 2, 25–29, 34–36, 63  
 Mesopause on Mars, 47  
 Mesosphere, Earth, 2, 25–29, 422–423  
 Mesosphere of Jupiter, 47, 50, 56, 66  
 Mesospheres of Jovian planets,

- temperatures of, 56
- Mesosphere of Venus, 37, 64
- Metallic ions, 232  
in *E* region, 232  
Venus' ionosphere, 264–267, 276
- Methanes, halogenated, see Halomethanes
- Mg (magnesium) ions, Venus' ionosphere
- Michelson interferometer, 188
- Microwave band of frequencies, 229
- Microwave emission by Venus, 13, 64
- Mie scattering, *see* Scattering
- Milankovitch (astronomical) theory of climate, 387
- Mixing, 4, 90, 140  
stratosphere-troposphere interchange, 142–153
- Mixing length, 75  
stratosphere, 140  
troposphere, 75
- Mixing-length approximation, 438–439
- Mixing time, 89  
diffusion, 89  
eddy diffusion, 140
- Model atmosphere, 1
- Molecular energy levels, 194  
normal modes of vibration, polyatomic molecules, 194
- Monochromatic radiative equilibrium, 7–9  
temperature discontinuity, 9
- Monte carlo numerical experiment, 357–358, 402
- Motion, hydrodynamic equations of, *see* Euler's equation, Hydrodynamic equations, Navier-Stokes equation
- Moving flame mechanism, 102, 113
- Mutual neutralization 30, 241  
on Venus, 266
- N**
- N (atomic nitrogen) airglow production in thermosphere
- N<sub>2</sub> (molecular nitrogen)  
airglow, 304  
dissociation continuum, absence of, 32  
dissociation energy, 120  
second positive auroral bands, 302
- Na (sodium)  
day, twilight airglow, 286, 293, 305–306  
energy diagram, 295
- Io emission, 307
- Io optical thickness, 329
- ions on Venus' nightside, 265
- lidar measurements of, 306
- night airglow, 286, 321
- nuclear spin, 295
- NaO (sodium oxide), 286
- Natural broadening, 300
- Natural coordinates (meteorology), 76–77
- Navier-Stokes equation, 72–75
- Negative ions  
*D* region, 242–243  
Venus' ionosphere, 266–267
- Neptune  
mesosphere temperature, 56  
Voyager 2 encounter, 429
- Newtonian cooling, *see* Linear law of cooling
- NH<sub>2</sub>, 315
- NH<sub>3</sub> (ammonia)  
Earth, 189  
Jupiter, abundance, 189  
Jupiter, aeronomy, 314, 315  
Jupiter, solid crystal clouds on, 105  
Jupiter, spectrum, 195–196  
Mars, 189
- NH<sub>4</sub> (ammonium), 132
- N<sub>2</sub>H<sub>4</sub> (hydrazine), 315
- Nitrification, 132
- NO (nitric oxide)  
airglow bands, 303  
airglow continuum, 279  
artificial sources, 131–133  
dissociation energy, 120  
Earth abundance, 189  
formation in thermosphere, 32  
height distribution in stratosphere, 129  
ionization by solar Ly-alpha, 30  
Mars abundance, 189  
in NO<sub>x</sub> cycle, 127–130  
positive ion in Earth's ionosphere, 232, 272
- production from N<sub>2</sub>O, 131  
role in cooling thermosphere, 33
- NO<sub>2</sub> (nitrogen dioxide)  
airglow continuum, 279  
dissociation energy, 120  
in NO<sub>x</sub> cycle, 127–130  
photolysis rate, 121  
terminal negative ion, *D* region, 242–243
- NO<sub>3</sub> (nitrate)  
dissociation energy, 120  
height distribution in stratosphere, 129  
in NO<sub>x</sub> cycle, 128  
product of nitrification, 132  
terminal negative ion, *D* region, 243–244

- NO<sub>x</sub> (odd nitrogen) 123**  
     in acid rain chemistry, 399  
     in aircraft exhaust, 131, 155  
     catalytic cycle, 127–130, 154, 158  
     interaction with ClO<sub>x</sub> cycle, 138, 158  
     interaction with HO<sub>x</sub> cycle, 128, 154  
     production by cosmic rays, 133–135, 156  
     production from N<sub>2</sub>O, 131–132, 155  
     production by nuclear explosions, 132, 155–156
- N<sub>2</sub>O (nitrous oxide)**  
     biological production, 131–132  
     dissociation energy, 120  
     NO formation from, 131  
     photolysis rate, 121
- N<sub>2</sub>O<sub>5</sub> (nitrous oxide)**  
     height distribution in stratosphere, 129  
     interaction with NO<sub>x</sub> cycle, 128
- Nuclear explosions**  
     NO production by, 132–133  
     radio blackout from gamma rays, 242, 273
- Nuclear winter**  
     inadequacies of current oversimplified scenarios, 392  
     nuclear energy available (worst case), 391  
     ozone depleted in stratosphere for high-altitude fireball, 391  
     sunlight obscured by smoke from nuclear firestorm, 391
- Numerical methods in radiative transfer, 170–173, 217**  
     inhomogeneous atmospheres, 218
- O**
- O (atomic oxygen)**  
     airglow, Earth, 279–280, 282–290, 302  
     airglow, Mars and Venus, 290, 301–303  
     association in the thermosphere, 31–32  
     forbidden doublet, 1356-Å airglow, 302  
     forbidden airglow green and red lines, 286  
     height distribution in stratosphere, 22  
     photochemical equilibrium, 122  
     resonance triplet, 1302-Å airglow, 302  
     term structure, ground configuration, 286
- O(<sup>1</sup>D) (first metastable term)**  
     deactivation of, 303  
     dissociation product, formation as a, 20, 23, 123, 288  
     height distribution in stratosphere, 127
- NO formation, 131**  
     OH formation, 124  
     upper term of red airglow, 286
- O(<sup>3</sup>P) (ground term)**  
     dissociation product, formation as a, 17, 20  
     fine-structure transitions, 33–34, 68  
     role in cooling thermosphere, 33–34
- O(<sup>1</sup>S) (second metastable term)**  
     Barth excitation mechanism, 287  
     Chapman excitation mechanism, 287  
     deactivation of, 287, 321  
     dissociation product, formation as a, 20  
     upper term of green airglow, 286
- O<sub>2</sub> (molecular oxygen)**  
     airglow, 33  
     dissociation energy, 120  
     Earth abundance, 189  
     ionization, 2  
     Mars abundance, 189  
     negative ion, D region, 240–241, 273  
     photolysis, 2, 17, 121  
     positive ion, Mars, Venus, 263  
     potential-energy diagram, 20, 287  
     stratospheric chemistry, 17–21, 122
- O<sub>2</sub> Atmospheric bands, 288–290, 303**
- O<sub>2</sub> Chamberlain bands, 287, 289–290, 321**
- O<sub>2</sub> Herzberg bands**  
     airglow excitation of, 187–189  
     system I, 287–290  
     system II, 287–290  
     system III, 287
- O<sub>2</sub> Herzberg continuum, 17, 19, 20, 23, 68, 289**  
     photoysis rate, 121
- O<sub>2</sub> Infrared Atmospheric bands, 287, 289, 303**
- O<sub>2</sub> Schumann–Runge continuum, 18, 20, 29, 31, 35, 277**
- O<sub>3</sub> (ozone) in Earth's ionosphere, 242–243**
- O<sub>3</sub> (ozone) in Earth's stratosphere**  
     abundance, 18, 23, 424  
     biological screen, allowing development of land life, 392
- Chapman layer, 23**
- dissociation energy, 120**
- heating, 1, 22–24, 68**
- height distribution, 22, 143**
- latitudinal variation, 15–17, 143**
- photochemical-equilibrium lifetime, 122–123**
- photochemical-production lifetime, 143**

- photodissociation, 17  
 photolysis rate, 121  
 $O_3$  (ozone) in Earth's troposphere, 189  
 397, 424  
 $O_3$  Hartley bands and continuum, 18,  
 23, 68  
 $O_3$  on Mars, 189, 310  
 $O_4$  negative ion,  $D$  region, 243  
 Oceans, storage of  $CO_2$  in, 394  
 Odd oxygen ( $O, O_3$ ), 17, 122–123  
     height distribution of production and loss  
     rates in the stratosphere, 130  
 OH (hydroxyl)  
     airglow temperatures, 289, 321  
      $CH_4$  destruction, 142, 397  
     dissociation energy, 120  
     height distribution in stratosphere, 127  
     in  $HO_x$  cycle, 123–127, 288  
     interaction with  $ClO_x$  cycle, 137  
     interaction with  $NO_x$  cycle, 128, 137  
     tropospheric scavenger, 139–140, 397  
     vibration-rotation (Meinel) bands in  
         airglow, 283–285, 288–289  
 Ohm's law, 245–246  
 Oort comet cloud, 390  
 Optical thickness,  
     in ionosphere, 230  
     slant, 7  
     in stratosphere, 119  
     vertical, 7, 119  
 Orbital characteristics, 419–420  
 Oscillator strength, 27, 291
- P**
- Partial reflection, 252–255, 277  
 Partition function, 335–336, 414  
     ballistic orbits, 336–337  
     captive orbits, 339  
     escaping orbits, 339–340  
     satellite orbits, 338–339  
     tables of, 442–455  
 Perfect gas law, 2, 72, 83  
 Phase angle, *see also* Phase function,  
     planetary, 182  
     scattering, 197  
 Phase function, 5, 161; *see also* Albedo  
     for single scattering, Scattering  
     asymmetry factor, 169  
     Henyey-Greenstein, 169, 217  
     normalization of, 5, 199, 291  
     phase matrix, 204
- polarization, relation to, 197, 292–299  
 resonance scattering, 298, 327–328  
 similarity relations for, 170, 197, 217  
 spectrum variation with planetary phase,  
     effect on, 197  
 Phase integral, 201, 225  
 Phase space, 332  
 Phase variation,  
     of absorption bands, 173–183, 219  
     of polarization of Venus, 200, 218–219  
 Photochemical equilibrium, 20–21, 122  
     lifetime to achieve, 122  
 Photochemical reactions, 118–121, *see also*  
     specific atom and molecule  
     dissociation energy, 120  
     photolysis rate, 119, 121  
 Photochemistry, principles of, 118–121  
 Photodetachment, 240  
 Photodissociation, 17–24, 30–32, 120,  
     *see also* Photolysis rate  
 Photoionization, 29, 230, 232, 261, 268  
     with excitation, 304–305  
 Photolysis rate, 119, 121  
     effect of atmospheric scattering on, 121  
     (footnote), 153  
 Photon scattering coefficient, *see*  $g$ -values  
 Pioneer 10, 52, 60–61, 105, 190, 201, 221,  
 267, 300, 307, 429  
 Pioneer 11, 52, 201, 221, 276, 429  
 Pioneer Venus 1 and 2 (orbiter and atmos-  
     pheric probes), 37, 39, 64–65, 307, 428  
 Planck function, 6, 436–437  
 Plane of scattering, 295  
 Planetary corona, 331  
 Planetary spacecraft, 428–432, *see also*  
     specific mission  
 Planetary wave, *see also* Gravity wave,  
     Rossby wave  
     in stratospheric mixing, 140, 158  
     thermospheric propagation, 111  
 Plasma frequency, 246  
 Plasmasphere, 358  
 Pluto,  $CH_4$ , 49  
 Polar cap absorption events  
      $D$  region, effect on, 242, 273  
     relation to solar protons, 135  
     stratospheric ozone, effect on, 135, 156  
 Polar convection cell, 79, 148  
 Polarization, theory of  
     general scattering, 202–205, 222  
     Mie scattering, 199–205

- Polarization, theory of (*cont.*)  
 Rayleigh scattering, 204  
 resonance scattering, 292–299, 327–328  
 scattering matrix, 204  
 Stokes parameters in, 202–204, 222
- Polarization, radio waves in ionosphere, 260
- Polarization, Venus, 200, 202–205, 222
- Polar wind, 403
- Pollution  
 acid rain, 397–398  
 hydrocarbons, burning of, 396  
 OH, role of scavenger  
 ozone, other oxidants, importance in urban environment, 397–398  
 statuary, erosion of, 397–398  
 sulfates, dry deposition on plants, 397–398  
 urban, 396–399, 413–414
- Positive-ion composition, Earth's ionosphere, 232, 244
- Potential temperature, 84
- Precession index, 387
- Pressure broadening, *see* Collisional damping
- Pressure profile, *see also* Surface pressure  
 Earth, 422–423  
 Jupiter, 50  
 Mars, 45
- Principle of invariance, 166
- Principle of reciprocity, 166
- Profile of absorption line, 173–182
- Q**
- Quadrupole (electric) transition, 195  
 286, 328
- Quantum yield, 118
- Quasi-biennial oscillation, 133
- R**
- Radiation pressure, 353  
 perturbation of exosphere particles, 353–356, 401–402
- Radiative association, 32, 279
- Radiative-convective equilibrium, 13–14  
 Mars, 42  
 modeling techniques, 62
- Radiative cooling  
 CO rotational spectrum, upper atmospheres Mars and Venus emitting, 33
- Radiative equilibrium, 4–13, 62, 68
- Radiative recombination, 233  
 on Venus, 266
- Radiative transfer, equation of, 4, 6, 19, 28, 160–173  
 for anisotropic scattering (first order), 168–169
- Feautrier method, 171–173  
 formal solution of, 7, 14, 166  
 historical references, 61–62  
 for isotropic scattering, 163–168  
 numerical methods, 170–173, 217  
 thermal radiation, 206–208  
 two-stream approximation, 7, 163–168
- Radio-aurora, 252
- Radio-band frequencies, 229
- Radio occultation experiments, 66, 248–252, 274–277, 282
- Rainbow, 199
- Random-walk theory, 182–185
- Rate coefficient, 20  
 gas-kinetic, 120  
 sources of, 153, 273  
 three-body, 120  
 two-body, 119
- Rayleigh fractionation, 368
- Rayleigh-Gans approximation, 257, 275
- Rayleigh number, 107
- Rayleigh photometric unit, 280–282  
 history of, 320
- Rayleigh scattering, *see* Scattering
- Recombination coefficient of ionosphere, alpha, 231  
 beta (Bradbury), 234–242  
 effective, 227–228, 242
- Refractive index  
 plasma, for radio wave in, 244–245, 249–252  
 Venus aerosols, 205
- Resonance scattering  
 in airglow, 286  
 anisotropy of, 292–299, 327–328  
 g-values for, 293  
 polarization of, 292–299, 327
- Rossby wave, 87, 111  
 on Mars, 264
- Rotational temperature, 176, 289–290, 321
- Runaway greenhouse, 383–384, 386, 395, 408–409
- Runaway ice cap, 385–386, 395

**S**

- Saha ionization equation, 240, 277  
 Satellite critical level, 351  
 Saturn,  
   mesosphere, 54–56  
   temperature, 54–56  
 Scale height (e-folding height in pressure),  
   3  
   density scale height, 3, 370  
   in exosphere, 341  
   for ion-electron gas, 235, 276  
   linear variation, 68  
   pressure, 3, 22  
 Scattering, *see also* Albedo for single scattering, Phase function, Resonance scattering  
   anisotropic (first order), 168–170, 199, 224  
   coherent, 160  
   isotropic, 6, 163–168, 199  
   Mie, 160, 169, 197–199  
   plane of, 295  
   polarization by, 202–205, 292–299  
   Rayleigh, 160, 199  
   Rayleigh phase matrix, 204  
   Rayleigh with polarization, 199  
 Scattering angle, 197–198  
 Scattering atmosphere, 177–183  
 Scattering coefficient, 5, 161  
 Sea breeze, 116  
 Sea level change  
   polar ice, partial melting of, 394  
 Sidereal period, 264  
 Similarity relations, 170, 197, 217  
 Sink function, 185–186, *see also* Source function  
 Size parameter of scattering drops, 198  
 Skin temperature, Gold–Humphreys, *see*  
   Temperature, skin  
 SO<sub>2</sub> (sulfur dioxide), 398–399  
 SO<sub>3</sub> (sulfate), 399  
 Solar constant, 12  
 Solar heating, *see also* Dust on Mars  
   deposition of, 12  
   stratosphere, 22–25, 68  
   thermosphere, 29–36  
 Solar flux spectrum at Earth, 426  
 Solar wind  
   effect on cosmic rays, 133  
 Source function, 6, 19, 165, 185,  
   *see also* Radiative transfer  
 Specific abundance, 178  
 Specific heat, 13, 23  
 Specific volume, 13  
 Spectra of planets, 219  
   Jupiter, 188–189, 196  
   Mars, 190  
   variation across the disk, 173–182, 162  
   variation with phase, 173–186  
   Venus, 187–188  
 Spectroscopic stability, 294, 296  
 Spectroscopy, theoretical  
   absorption lines, formation of, 160, 173–182  
   temperature response, 176, 219, 289  
 Spontaneous emission, 27–28  
 Sputtering (loss mechanism on Io), 60–61, 308–309, 377  
 State, equation of, *see* Perfect gas law  
 Static stability parameter, 85, 116  
   Jupiter, 107  
 Statistical weight, 27  
 Stellar occultations, 215–216  
 Stimulated emission, 27–28  
 Stirling's formula, 184  
 Stochastic theory, *see* Random walk theory  
 Stokes parameters, 202, 222, 225  
 Stratosphere, Earth, 2  
   absorption of solar radiation, 17–30  
   Chapman chemistry, 17–21, 62, 68  
   composition, 424  
   discovery, 62  
   heating and cooling, 22–24, 468  
   H<sub>2</sub>O mixing ratio, 25, 148, 158  
   mass exchange with troposphere, 142–152  
   meridional circulation, 17, 22, 63,  
     142–152, 157  
   O<sub>3</sub> production region, 143  
   O<sub>3</sub> residence region, 143  
   planetary-scale waves in, 140, 158  
   temperature, 422  
 Stratosphere on Jupiter, *see* Mesosphere on Jupiter  
 Stratosphere on Venus, *see* Mesosphere on Venus  
 Stratopause on Earth, 2  
   latitudinal isotherms  
 Strength (line or band), *see* Oscillator strength, Transition probability  
 Strong–Plass formula, 175, 218  
   Curtis–Godson approximation, 175, 218  
 Substantial derivative, 71

- Surface brightness, 280–281  
 Surface pressure  
   Earth, 422–423  
   Mars, 43, 65  
   Venus, 64, 97
- T**
- Taylor number, 107  
 Taylor–Proudman theorem, 106  
 Temperature lapse rate  
   dry adiabatic, 14  
   radiative equilibrium, 12  
   saturation (wet) adiabatic, 14  
 Temperature, mean planetary emission  
   or equilibrium, 12  
   Earth, 12  
   Jupiter, 13, 105, 201, 222  
   Venus, 13, 98  
 Temperature, measures of  
   brightness (radiometric), 13, 201, 222  
   bolometric, 13  
   kinetic, 6  
   Planckian, 6, 13, 27  
   satellite drag, 371  
   scale height, 302, 375  
   spectroscopic, 176, 219  
 Temperature profile  
   Earth, 1–2, 35, 422–423  
   Jupiter, 49–50, 66  
   Mars, 42–44, 65  
   Venus, 37, 41, 64, 97  
 Temperature, skin, 9, 10, 13, 15, 384  
 Temperature, surface  
   discontinuity, 9  
   Earth, 12, 16  
   Mars, 43, 65  
   Venus, 13, 64  
 Thermal capacity, 98  
 Thermal conductivity, 34, 73, 112  
   for Earth's thermosphere, 35  
 Thermal diffusion, 90  
 Thermal diffusivity, 75, 107  
 Thermal emission  
   Earth, 210–211  
   Jupiter, 210–211  
   Mars, 210  
   Saturn, 210  
   Titan, 210–211  
 Thermal excitation, 5  
 Thermal opacities, with pressure induced  
   absorption, 206–212
- Thermal radiation, 6–13  
 Thermal tides on Mars, 89, 103, 114  
 Thermal wind, 80–82  
 Thermodynamic equilibrium, 6, 277;  
   *see also* Local thermodynamic  
   equilibrium  
 Thermodynamics, first law, 13, 73, 83, 146  
 Thermosphere  
   Bates' analytical model, 69  
   on Earth, 2, 29–36, 63, 69, 422–423, 425  
   on Jupiter, 52–53  
   on Mars, 45–48  
   on Saturn, 52  
   on Uranus, 52  
   on Venus, 40–42  
 Thomson scattering cross section, 256  
   278  
 Three-body association, 33  
 Three-body collision, 120  
 Tides, atmospheric, 114  
   Earth's ionosphere, 89, 111  
   Earth's troposphere, 89  
   Mars, 89, 103, 114  
 Time scales, hydrodynamic and radiative  
   Earth's troposphere, 76  
   Jupiter, 104–105  
   Mars' troposphere, 103  
   Venus' troposphere, 98  
 Titan  
   absorbers, principal, 193  
   atmosphere, principal constituents, 382  
   density profile, 59  
   escape flux, 376  
   H<sub>2</sub> mixing ratio, 375  
   ionosphere, 59, 270, 375  
   photochemistry, 59, 315–317  
   spectra, 210  
   temperature profile, 58–59  
   torus (around Saturn), 375  
 Topography of Mars  
   effects on surface winds, 104  
   spectroscopic determination of, 218  
 Tornado pressure, 116  
 Trade winds, 79, 110  
 Transition probability, 27, *see also* Einstein  
   radiation coefficients  
   for Zeeman components, 298–299  
 Transparent approximation, 24  
 Transparent atmosphere, 173–177  
 Triton, CH<sub>4</sub>, 49, 60

- Tropopause on Earth, 1–2  
 cold-trap analogy, 25, 62–63  
 discontinuity (“gap”) in, 82  
 latitudinal variation, 15–17, 62  
 mean temperature, 12  
 pollution, 396–399
- Troposphere on Earth  
 composition, 189, 424  
 density, 422  
 horizontal circulation, 75–89  
 latitudinal isotherms, 15  
 mass exchange with stratosphere, 143–153  
 pressure (table), 422  
 temperature profile, 2 (diagram), 422 (table)
- Turbulence, 75, 90
- Two-stream approximation, *see* Radiative transfer, equation of
- U**
- Uranus  
 aurora, 56  
 seasons, 110  
 temperature, mesosphere, 56
- V**
- Venera 3, 428  
 Venera 4, 189, 428  
 Venera 5, 64, 189, 428  
 Venera 6, 64, 189, 428  
 Venera 7, 189, 428  
 Venera 8, 37, 64, 189, 428  
 Venera 9, 98, 290, 323, 428  
 Venera 10, 98, 290, 323, 428  
 Venus, *see also* specific characteristic, molecule, spacecraft  
 circulation, 97–102, 113–114  
 clouds, 100–102, 204–205, 222  
 composition, 189  
 deuterium/hydrogen ratio, 383  
 ionosphere, 260–267, 275–276  
 rotation, 97–102, 265  
 surface pressure, 64, 97  
 temperatures, 13, 64–65, 97–102  
 vertical structure, 36–42
- Vertical motion (convection), 13–15  
 in isobaric coordinates, 84–87
- Vertical structure, atmospheric, 1  
 Earth, 1–36, 422–423, 425  
 Io, 60
- Jupiter, 49–53  
 Mars, 42–47  
 Neptune, 56  
 Pluto, 56  
 Saturn, 53–55  
 Titan, 58–59  
 Triton, 60  
 Uranus, 56  
 Venus, 36–42
- Vertical transport, 89–97, *see also* Convection, Diffusion, Eddy diffusion
- Vibrational relaxation, 25–29, 33, 35, 63, 68
- Viking 1, 44–47, 65, 103, 104, 189, 312, 374, 406, 429  
 Viking 2, 44–47, 65, 104, 189, 312, 374, 406, 429
- Virtual height, 226–227, 271
- Viscosity, 112, *see also* Eddy viscosity  
 coefficient, dynamic viscosity, 72, 75  
 coefficient, kinematic viscosity, 72, 75  
 stress tensor, 72
- Volatiles, evolution from crust, 382, 408
- Vorticity  
 absolute, 85  
 geostrophic, 86  
 horizontal advection of, 85–87, 116  
 on Jupiter, 104–106  
 planetary, 85–86  
 quasi-geostrophic, 86  
 relative, 85
- Vorticity area index, 386
- Voyager, 66, 97, 115, 212, 375  
 Voyager 1, 52, 60–61, 211, 307–308, 311, 429  
 Voyager 2, 52, 429
- W**
- Water, *see* H<sub>2</sub>O
- Wave equation, 245, 277
- Wind-induced diffusion, 42, 362
- Wind systems, *see also* Horizontal circulation, Meridional circulation  
 Jupiter, 104–109, 114–115  
 Mars, 104–106, 113–114  
 stratosphere, 17, 22, 142–153  
 thermosphere, 31  
 Venus, 97–102, 113
- Z**
- Zeeman splitting, 295, 298–299, 328